ГЕОГРАФИЧЕСКИЙ ФАКУЛЬТЕТ
МГУ имени М.В. Ломоносова

НИИЯФ
МГУ

Воздушные и водные потоки поллютантов в Российской Арктике

2024

ГЕОГРАФИЧЕСКИЙ ФАКУЛЬТЕТ
МГУ имени М.В. Ломоносова

НИИЯФ
МГУ

Atmospheric and riverine pollutants in Russian Arctic

2024

ВОЗДУШНЫЕ И ВОДНЫЕ ПОТОКИ ПОЛЛЮТАНТОВ В РОССИЙСКОЙ АРКТИКЕ

Под редакцией

академика Н.С. Касимова, проф. С. Р. Чалова, внс. О.Б Поповичевой

В сборнике представлены статьи, опубликованные коллективом авторов в ведущих российских и зарубежных высокорейтинговых журналах: Nature Geoscience, Environmental Research Letters, Arctic and Antarctic Research, Atmospheric Chemistry and Physics, Science of the Total Environment, Land Degradation and Development, Water Resources Research, Catena, Арктика: экология и экономика, Оптика Атмосферы и Океана и др. Статьи подготовлены в ходе крупнейших международных и российских проектов Российского фонда научный исследований (РФФИ), Российского научного фонда (РНФ), Русского географического общества (РГО) и Министерства науки и высшего образования РФ. Разработаны технологии современного комплексного подхода проведения измерений и высококачественного анализа состояния окружающей среды Арктики.

ATMOSPHERIC AND RIVERINE POLLUTANTS IN RUSSIAN ARCTIC

Editors

academician N.S. Kasimov, professor S.R. Chalov, leading scientist O.B. Popovicheva

The collection presents articles published by a team of authors in leading Russian and foreign high-ranking journals: Nature Geoscience, Environmental Research Letters, Arctic and Antarctic Research, Atmospheric Chemistry and Physics, Science of the Total Environment, Land Degradation and Development, Water Resources Research, Catena, Arctic: ecology and economics, Optics of the Atmosphere and Ocean, etc., carried out during the largest international and Russian projects of the Russian Foundation for Scientific Research (RFBR), Russian Science Foundation (RSF), Russian Geographical Society (RGO) and the Ministry of Science and Higher Education education of the Russian Federation. Technologies for a modern integrated approach to measurements and high-quality analysis of the state of the Arctic environment have been developed.

Фото на обложке с сайта
Climate & Clean Air Coalition
https://www.ccacoalition.org/short-lived-climate-pollutants/black-carbon

СОДЕРЖАНИЕ

1. Потоки микрочастиц в атмосфере Российской Арктики, по данным исследований на российских полярных станциях

2. Климатический трассер – черный углерод

3. Высокоширотные источники пылевых и органических аэрозолей

4. Водные потоки в речных бассейнах

5. Водные потоки в арктических дельтах

ВВЕДЕНИЕ

Исследования экологического состояния окружающей среды Арктики и климатических изменений связаны с необходимостью решения фундаментальных научных задач анализа составляющих загрязненной атмосферы, снежного покрова, речных вод и актуальностью проведения оценок степени опасности антропогенного воздействия климатически – активных и токсичных компонентов на экосистему и климат Арктики. В настоящем издании приводятся результаты экологических междисциплинарных исследований коллектива сотрудников географического факультета (кафедры геохимии ландшафтов и географии почв, гидрологии суши, лаборатории эрозии почв и русловых процессов), НИИ ядерной физики и факультета почвоведения МГУ совместно с нашими партнерами из различных организаций. Мы предлагаем читателю электронный дайджест, состоящий из 18 статей, опубликованных в ведущих зарубежных и российских журналах.

В четвертом и пятом разделах приводятся результаты исследований полевых кампаний на опорных створах гидролого-геохимического мониторинга на р. Обь, Енисей, Лена и Колыма, выполненные в 2019-2022 годах, на основе которых охарактеризованы химический сток взвешенных и растворенных веществ крупнейших сибирских рек в арктические моря. Впервые разработаны и реализованы технологии определения потоков наносов крупных рек, основанные на комбинированном использовании доплеровских измерителей ADCP и авторских методов пробоотбора, на алгоритме оценки расхода взвешенных наносов по связи мутности воды, методике недеструктивного определения трансформации состава поглощенного комплекса речных наносов и алгоритме расчета вклада русловых деформаций в сток наносов. Выявлены характерные особенности механического и химического состава взвешенных наносов замыкающих створов сибирских рек. Исследована широтная зональность параметров эрозии, рассмотрен тренд по увеличению интенсивности эрозии с севера на юг. Бассейны Оби, Енисея, Лены и Колымы в современных гидроклиматических условиях представляют собой области аккумуляции, темпы которой значительно превышают объемы выноса за пределы речного бассейна. На примере крупнейшего внутриматерикового обнажения мерзлых пород – Дуванного яра р. Колымы, показана ведущая роль подобных локальных участков размыва берегов в формировании стока наносов и органического вещества крупных рек. Выполнена комплексные гидролого-геохимические исследования потоков в дельте р. Лены, существенно подверженной климатически обусловленным изменениям мерзлотных процессов. Получены новые данные о сезонном и многолетнем режиме баланса взвешенных наносов дельт рек Лена и Колыма на основе методики дешифрирования концентраций взвешенных наносов по данным дистанционного зондирования Landsat 5, Landsat 7, Landsat 8. Впервые системно доказан эрозионный режим транспорта взвешенных наносов в этих дельтах, возрастание мутности в рукавах дельты, обусловленное совокупностью метеорологических и местных факторов. В дельтах наблюдается климатически обусловленное убыстрение разрушения берегов: в условиях роста температур воздуха за период с 2000 по 2021 гг. по сравнению с 1964 по 2000 гг. средняя скорость горизонтальных деформаций в дельте увеличилась.

Первые разделы посвящены разработанным уникальным современным методам анализа физико-химических свойств аэрозолей, созданию инструментальной базы портативных приборов для проведения непрерывных экспедиционных измерений в удаленных районах Арктики. Впервые с высоким временным разрешением выполнены измерения уровня аэрозольного загрязнения атмосферы Белого и Карского моря, архипелага Северная Земля, побережья моря Лаптева. На российских полярных станциях ГМО Тикси и Ледовая база «Мыс Баранова» установлены специализированные системы непрерывного отбора проб аэрозолей арктической атмосферы, выполнены измерения сезонной изменчивости климатического трассера – черного углерода и экологически-опасных компонентов в химическом составе аэрозолей. Изучена варьируемость и источники повышенных концентраций во время Сибирских лесных пожаров. Проводится анализ данных по составу, сезонности и региональному происхождению арктических аэрозолей, полученных на российских станциях, в сравнении с международными полярными станциями. С целью улучшения сети наблюдений в Российской Арктике с августа 2019 года на острове Белый (Карское море) функцианирует Аэрозольный комплекс МГУ. Уникальность его месторасположения на пути выноса крупномасштабных эмиссий из газонефтедобывающих регионов в Арктику позволяет получать данные о сезонной динамике и годовых трендах аэрозольного загрязнения атмосферы западносибирского сектора Арктики. Исследования беспрецедентного по масштабам дымового загрязнения Севера Западной Сибири в августе 2021 года выполнены в рамках междисциплинарного исследования влияния дымов лесных пожаров на окружающую среду и здоровье людей. Представлена научная основа проведения оценок содержания и состава полиароматических углеводородов (ПАУ) в твердой фракции снежного покрова, приведены результаты двухлетних исследований в районах ЯНАО. По профильному распределению ПАУ выделен состав снеговых осадков зоны эмиссий факельного сжигания газоконденсата на объектах ТЭК и территорий с низким уровнем техногенной нагрузки удаленных арктических районов.

В дайджесте приводятся только тексты статей, без списков литературы и приложений, которые можно найти по ссылке на оригинальную публикацию каждой статьи.

1. ПОТОКИ МИКРОЧАСТИЦ В АТМОСФЕРЕ РОССИЙСКОЙ АРКТИКИ, ПО ДАННЫМ ИССЛЕДОВАНИЙ НА РОССИЙСКИХ ПОЛЯРНЫХ СТАНЦИЯХ

Региональные источники загрязнения атмосферы Арктики черным углеродом по данным измерений на острове Белый*

1. ВВЕДЕНИЕ

Климатические изменения, вызванные аэрозольным загрязнением атмосферы, являются серьезной проблемой во всем мире. Вследствие индустриализации и роста численности населения увеличиваются выброс в атмосферу аэрозольных веществ и частота крупномасштабных лесных пожаров. Арктический регион особенно подвержен эмиссиям источников сжигания природных топлив и биомасс. В зимне весенний период из за комбинации интенсивного дальнего переноса антропогенных эмиссий с низких широт и температурной инверсии наблюдается Арктическая дымка [1]. С увеличением солнечной активности весной устойчивость атмосферы уменьшается, концентрация аэрозолей падает, влияние локальных источников прибрежных районов Арктики становится более значительными по сравнению с зимой.

Черный углерод (BC, black carbon) в составе продуктов сжигания хорошо поглощает солнечное излучение, является короткоживущей климатически значимой составляющей, оказывает значительное воздействие на климат Арктики [2]. Совместное влияние BC и охлаждающих атмосферу сульфатов вызывает увеличение температуры поверхности Арктики на +0,29 К и составляет ~ 20% от всех факторов потепления в Арктике с начала 1980-х гг. [3]. Накопление BC в нижней тропосфере усиливает энергетический обмен между облаками и снежным покровом [4]. Осаждение BC на снег приводит к уменьшению альбедо подстилающей поверхности и ускорению таяния снега и льда [5].

Высокомолекулярный органический углерод, называемый коричневым углеродом (BrC), поглощает солнечное излучение в ультрафиолетовом диапазоне, демонстрируя существенные различия между дымами при сжигании древесины и эмиссиями транспорта [6, 7]. BrC, накапливающийся в арктических аэрозолях в результате переноса дымовых эмиссий пожаров, вносит значительный вклад в нагрев атмосферы региона с радиационным форсингом ~ 30% по отношению к BC [8].

До 62% BC в атмосферу высокоширотной Арктики (севернее 66° с.ш.) поступает с российских территорий [9]. Данные самолетных измерений подтверждают, что тропосферный BC над побережьем российских арктических морей сильно изменчив в пространстве и времени и среди его источников преобладают антропогенные [10]. Несмотря на сокращение антропогенных выбросов за последние десятилетия [11] наблюдения сезонных циклов BC на 10 полярных обсерваториях, включая ГМО Тикси (побережье моря Лаптевых, восточно сибирский сектор Арктики), продемонстрировали ежегодно повторяющееся зимой явление – Арктическую дымку. В весенне летние сезоны в прибрежных лесных районах Арктики регистрируются шлейфы природных пожаров [12]. Перенос BC шлейфами пожаров летом был зарегистрирован в измерениях физико химических характеристик атмосферных аэрозолей на полярной станции «Ледовая база “Мыс Баранова”» (арх. Северная Земля, восточно сибирский сек тор Арктики) [13, 14]. Сельскохозяйственные пожары в европейской части РФ и на юге Сибири – значимый источник эмиссий и загрязнений Арктики [15].

Из за больших объемов выбросов и близости к исследуемому региону факельное сжигание газа на нефтегазовых промыслах [16] обусловливает до 42% среднегодовых концентраций BC в Арктике [17]. Крупнейшие нефтегазодобывающие регионы Западной Сибири и северо востока европейской части России, расположенные на пути переноса воз душных масс в Арктику, вносят непропорционально большой вклад в загрязнение арктической тропосферы[18, 19]. Вынос шлейфов загрязнений из этих районов в моря Северного Ледовитого океана приводит к возрастанию концентраций BC до 400 нг/м^3 в сравнении с уровнем в несколько нг/м^3 при об ратном направлении ветра [20]. Однако достоверность оценок вклада эмиссий факельного сжигания газа на действующих в настоящее время в Европейском и Канадском секторах Арктики полярных станциях низка из за их значительной удаленности от индустриальных источников [17], а существующие модели воспроизводят концентрации BC в Арктическом регионе с большой неопределенностью [21].

Высокие концентрации BC, определенные на ГМО Тикси, обусловлены эмиссиями жилого сектора и дальним переносом из индустриальных районов преимущественно в зимне весенний период, более низкие концентрации летом – результат го рения биомасс во время природных пожаров [22]. Данные радиоуглеродного анализа на ст. ГМО Тикси продемонстрировали преобладающее влияние сжигания

---

* О.Б. Поповичева. М.А. Чичаева, В.О. Кобелев, Н.С. Касимов, //Оптика атмосферы и океана. 2022;35:1-7
DOI: 10.15372/ AOO20221212

природных топлив по сравнению со сжиганием биомасс – на 32± 16% [23]. Ранее было показано [24], что транспортная дисперсионная модель частиц с базой данных антропогенных эмиссий и эмиссий сжигания биомассы хорошо определяет вклад источников ВС в Европейском секторе Арктики. Однако для ГМО Тикси с помощью этой модели был получен непредсказуемо малый вклад ~ 6% эмиссий факельного сжигания газа, что объясняется значительной неопределенностью в данных о пространственном распределении источников ВС по территории Сибири, отсутствием инвентаризации выбросов и большой удаленностью станции от нефтегазодобывающих регионов.

Для оценки климатических последствий эмиссий углеродосодержащих аэрозолей необходимы комплексные измерения свойств арктических аэрозолей, включающих поглощающую способность в широком спектре солнечного излучения. С целью проведения длительных комплексных наблюдений за составом арктической атмосферы и для оценки влияния эмиссий нефтегазового сектора в 2019 г. на о-ве Белый, расположенном в Карском море (ЯНАО, западно сибирский сектор Арктики), была установлена новая исследовательская полярная аэрозольная станция МГУ «Остров Белый» (https:// peexhq.home.blog/2019/12/ll/new research aerosol stations in the russian arctic). Предварительно были проведены трехмесячные непрерывные измерения массовых концентраций ВС на аэрозольном комплексе вблизи г. Салехарда [25]. Месторасположение станции на севере ЯНАО на пути выноса крупномасштабных эмиссий из индустриальных регионов Западной Сибири, густонаселенных и промышленных районов Евразии в Арктику предоставляет уникальную возможность для изучения аэрозольного загрязнения атмосферы западно сибирского сектора Арктики [26].

Цель данной работы – анализ результатов измерений концентрации ВС, выполненных на инструментальном комплексе ст. «Остров Белый», и исследование распределения источников загрязнений арктических аэрозолей на о-ве Белый в холодное и теплое время года.

ИЗМЕРЕНИЯ И ОБРАБОТКА ДАННЫХ

Остров Белый находится в Карском море, отделен проливом Малыгина от п-ва Ямал. Среднегодовая температура составляет –10,6°С. Зимы продолжительные и холодные: в феврале средняя температура –24,2°С (может достигать –59°С), летом характерны туманы, средняя температура воздуха +5,3 °С. Месячное количество осадков – более 20 мм.

Анализируются данные наблюдений с августа по декабрь 2019 г. и с января по ноябрь 2020 г. Период с 1 ноября 2019 г. по 1 апреля 2020 г., а также ноябрь 2020 г., когда температура опускалась ниже –10°С, обозначим как «холодный», остальное время – как «теплый». В холодный период доминировал континентальный ветер (Ю–ЮВ). С июня по сентябрь средняя температура держалась выше 0°С, доминировали С–СВ ветра, что определило преобладание океанических воздушных масс, приходящих в акватории Северного Ледовитого океана. В октябре с уменьшением инсоляции температура воздуха снизилась и держалась ниже 0 °С. Средняя скорость ветра за весь период наблюдений составила 5–10 м, с.

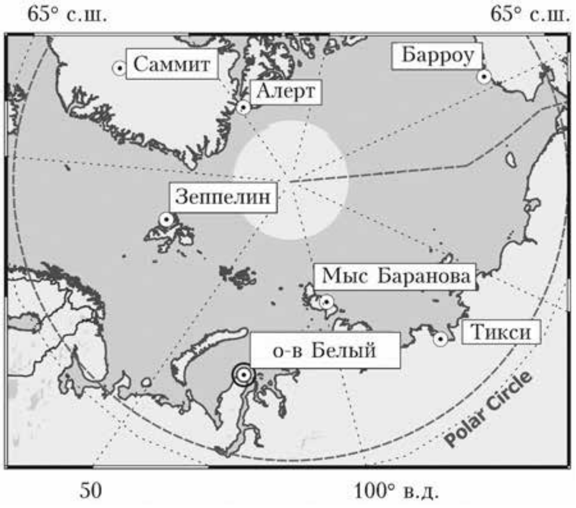

Рис. 1. Карта полярных аэрозольных станций

Исследовательская станция МГУ «Остров Белый» работает непрерывно с августа 2019 г. Не положение на севере Западной Сибири (73°20’7,57» с.ш., 70°4’49,05” в.д.) относительно арктических ст. Зеппелин, Алерт, Барроу, Саммит, Тикси и «Ледовая база “Мыс Баранова»» показано на рис. 1. Павильон аэрозольного комплекса находится в полу километре к юго-востоку оист гидрометеорологической станции, где работает дизельный генератор – единственный на острове локальный источник загрязнения. Измерения, проведенные при направлении ветра со станции, исключались из массива данных. Изоляция ст. «Остров Белый» от антропогенных источников является основным преимуществом месторасположения инструментального аэрозольного комплекса, в отличие от ГМО Тикси, находящейся под значительным воздействием эмиссий близлежащего пос. Тикси [22].

В павильоне станции установлена система непрерывного отбора проб, разработанная для суровых арктических условий. Аэталометр AE33 (Magee Scientific, Aerosol d.o.o.) используется для определения поглощательной способности частиц, осаждающихся на фильтре при прокачке воздуха с разными скоростями потока, которые дают коэффициент коррекции на поглощение внутри фильтра [27]. Измерения проводятся на семи длинах волн в диапазоне от ультрафиолетового (370 нм) до инфракрасного (950 нм) с разрешением 1 мин. Эффективность поглощения на длине волны 880 нм пересчитывается в эквивалентную концентрацию черного углерода eBC (880) с массовым коэффициентом 7,7 м^2/г. Спектральная зависимость поглощения позволяет учесть увеличенное поглощение высокомолекулярного органического углерода в ультрафиолетовом диапазоне излучения по сравнению с инфракрасным [28]. Разница между eBC(370) п eBC(880), называемая параметром Delta C, оказывается значительной в эмиссиях сжигания биомасс [29, 30]. В данной работе параметр Delta-C используется в качестве индикатора влияние сжигания древесины в жилом секторе и лесных пожаров.

Определение фоновых аэрозольных концентраций в Арктическом регионе проводится при отсутствии влияния локального и регионального загрязнений [22, 31]. В данной работе за фоновую концентрацию принимается уровень 10 нг/м^3, равный 20 перцентилям выборки за весь период измерений. Длительные события, в течение которых концентрации eBC превышали пороговое значение 90 нг/м^3, равное 80 перцентилям выборки, идентифицируют эпизоды загрязнения.

С целью определения зоны влияния возможных удаленных источников эмиссий BC на уровень загрязнений на о-ве Белый с помощью модели HYSPLIT лаборатории Air Resources Laboratory [32] был рассчитан массив (кратных траекторий переноса воздушных масс за все время наблюдений со временным интервалом 1 ч и 240 ч назад на высотах 100 и 500 м над уровнем земли (AGL) с пространственным разрешением 1° широты и 1° долготы. На его основе выполнен кластерный анализ сходных по происхождению и близости траекторий, в котором критерием разделения на кластеры служат угловые расстояния [33]. Траектория, вычисленная путем усреднения угловых расстояний между всеми траекториями, представляет данный кластер.

Метод отнесения траекторий переноса воздушных масс к концентрации загрязнений в момент их прихода в точку наблюдений (Concentration Weight Trajectories, CWT) является эффективным инструментом для анализа переноса загрязняющих атмосферу веществ и выявления их возможных источников [34]. При определении пространственных источников рассчитываются концентрации загрязнений *Cjj* для каждой ячейки сетки (i, j):

$$\ln(\bar{C}_{ij}) = \frac{1}{\sum_{k=1}^{N}\tau_{ijk}} \sum_{k=1}^{N} \ln(Ck)\tau_{ijk}, \qquad (1)$$

где i и j – широта и долгота ячейки; k – индекс траектории; N – общее число рассчитанных траекторий; C^* – концентрация, измеренная в момент при хода k-ik траектории в место измерений; τ_{ijk} – время пребывания k и траектории в ячейке (i, j).

Получаемые по результатам длительных наблюдений поля концентраций С,у позволяют установить связь между высокой С* и траекториями движения воздушных масс, т.е. показывают области пространства с повышенной интенсивностью эмиссии и вероятное расположение источника. В данной работе региональное распределение источников BC определялось путем отнесения траекторий, рассчитываемых за весь период наблюдений, к концентрации в момент их прихода на станцию «Остров Белый». Метод основан на совместном анализе траекторий переноса воздушных масс и результатов аэталометрических измерений концентраций eBC.

Расположение газовых факелов определялось по спутниковым данным MODIS и VIIRS о свечении объектов с температурой выше 1200 °С, соответствующей факельному сжиганию газа (https:// viirs. skytmth.org/apps heatmap/). Данные о пожарной активности получены из системы Resource Mana gement System (FIRMS), созданной NASA/ GSFC Earth Science Data Information System (https: - ‘/firms. modaps.eosdis.nasa.gov/ map), спутникового зондирования термоактивных точек на поверхности Земли.

РЕЗУЛЬТАТЫ И ОБСУЖДЕНИЯ

Результаты многолетних исследований изменений аэрозольных компонентов на полярных станциях указывают на характерные для Арктики сезонные тренды [35]. Временной ряд среднемесячных значений eBC на ст. «Остров Белый» представлен на рис. 2. Самые высокие концентрации наблюдались с ноября по апрель (до 160 нг/м^3), а самые низкие – с июня по август (около 20 нг/м^3). Арктическая дымка регистрировалась с ноября 2019 г. по март 2020 г. Максимальная медианная концентрация составила 127 нг/м^3 идекабре 2019 г. В сред нем летом концентрации были в 10 раз ниже, чем зимой, при минимальном значении 30 нг/м^3 в июле 2020 г. В течение второго года наблюдений низкий уровень концентраций летом и высокий зимой повторился. В сентябре 2020 г. eBC достигала аномально высокого значения 72 нг/м^3, превысив в два раза значения в сентябре 2019 г.

Похожая варьируемость ежемесячной eBC наблюдалась в 2015–2016 гг. на ГМО Тикси и характеризовалась высокими значениями (~ 130 – 230 нг/м^3) в зимне весенний период и низкими (~ 20 нг/м^3) с мая по октябрь [22]. Наст. «Ледовая база “Мыс Баранова”» в этот же период зимой были зарегистрированы концентрации 1.42 ± 120 нг/м^3 с максимумом 350 нг/м^3 13 января 2016 г. и 67 ± ± 43 нг/м^3 летом [13].

Таким образом, во время Арктической дымки значения eBC на трех российских станциях «Остров Белый», ГМО Тикси и «Ледовая база “Мыс Баранова”» оказались выше уровня, измеренного в этот период на канадской ст. Алерт (100 ± ± 65 нг/м^3), который, в свою очередь, был самым высоким среди значений, зарегистрированных всеми другими станциями в Арктике [36]. Такой результат подтверждает выводы [37] и [23] о том, что сибирская Арктика является наиболее загрязненной крупномасштабными эмиссиями евразийского континента среди других областей Арктики.

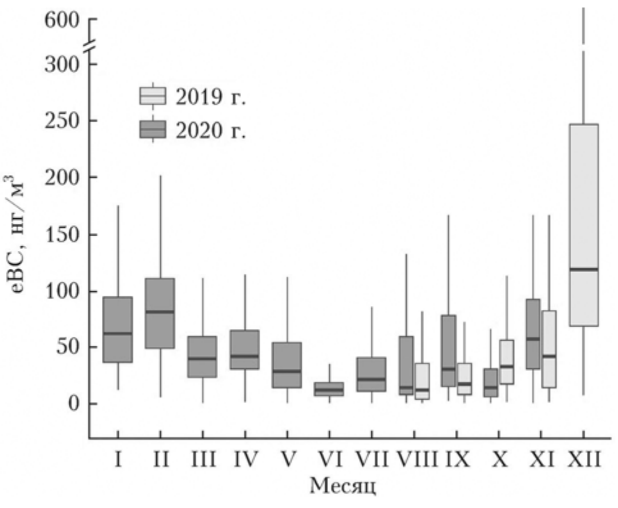

Рис. 2. Ежемесячная динамика медианных концентраций eBC в 2019 и 2020 гг. Высота прямоугольников показывает значения между первым и третьим квартилями, вертикальные линии — максимальное и минимальное значения, а горизонтальные – медианы

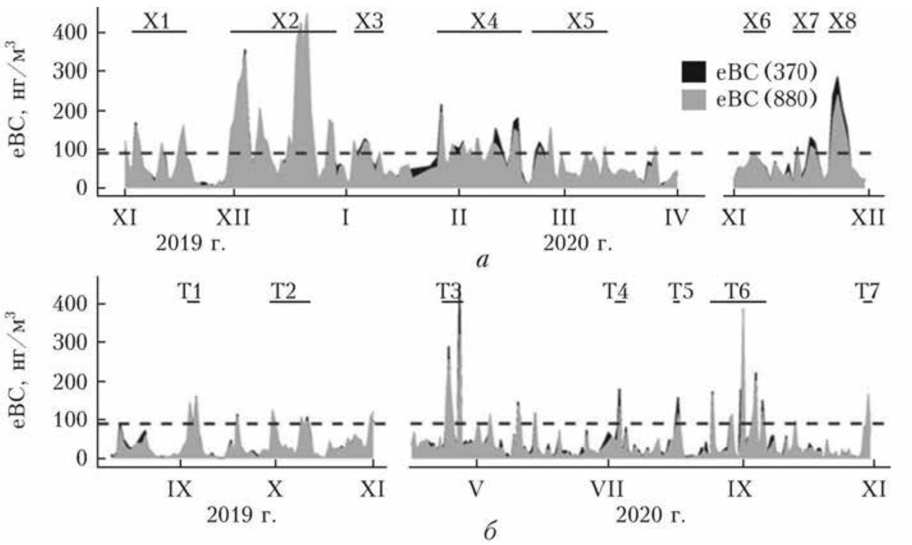

Рис. 3. Суточные медианные значения eBC (880) и eBC (370) в холодный (а) и теплый (б) периоды года; X1–X8, T1–T7 – эпизоды загрязнений; пунктирная линия указывает пороговое значение загрязнения атмосферы 90 нг/м^3

Анализ суточных данных, полученных в холодный и теплый периоды года, показал высокую варьируемость eBC на фоне сезонного хода (рис. 3).

Выделяются эпизоды загрязнений, во время которых eBC превышает пороговое значение 90 нг/м^3. В холодный период наблюдалось восемь эпизодов загрязнений (рис. 3, б). Во время первого эпизода XI высокие концентрации eBC случались трижды. Декабрь 2019 г. (X2) характеризовался максимальными суточными значениями eBC за все время наблюдений – 350 и 420 нг/м^3 4 и 19 декабря. Второй по интенсивности эпизод загрязнения случился 24, 25 ноября 2020 г. ~ 300 нг/м^3.

Кластерный анализ обратных траекторий в холодный период выявил, что зона влияния возможных источников BC располагается в основном на континентальной части Евразии и имеет характерные размеры в несколько тысяч километров (рис. 4, цв. вкладка). Доминирует кластер C1 траекторий, проходящих через север Скандинавии (рис. 4, а), включающий 46% всех траекторий за данный период. Кластеры C2 и C3 охватывают обширные территории Восточной Европы, европейской части РФ, Урала и Западной Сибири, частично Казахстана (24 и 16%). В меньшем объеме воздушные потоки приходят из приполярных областей Северного Ледовитого океана. Перенос воздушных масс из Восточной Сибири и с акватории Северного Ледовитого океана (кластер C4) оказался наименее значительным (13%).

В теплый период циркуляция воздушных масс существенно меняется. Воздушные потоки сильно смещаются к побережью Северного Ледовитого океана и охватывают его акваторию, а также полярные области северных провинций Канады, Аляски и районы Чукотского моря и Берингова пролива (рис. 4, б). В кластере C1 перенос происходил в основном из акватории океана с запада, в C2 и C3 – с северных территорий РФ (26 и 23%). В меньшей степени зона влияния располагается над континентальной частью Евразийского региона и островными арх. Северная Земля, Шпицберген, Новая Земля, Земля Франца Иосифа и о в Гренландия; 10% траекторий кластера C4 приходили с востока через обширный регион Северного Ледовитого океана.

В холодный период eBC (370) был выше, чем eBC (880) во время эпизодов загрязнения X4, 5, 7 и 8 (рис. 5, а, цв. вкладка). Они характеризуются значениями Delta C от 20 (19 ноября 2020 г.) до 56 нг/м^3 (24 ноября 2020 г.), определяемыми преобладанием в это время эмиссий сжигания древесины в целях отопления жилого сектора. Отметим, что согласно базе данных российских эмиссий сжигание древесины составляет ~61% от общего объема выбросов в жилом секторе, особенно в районах ограниченного снабжения газом [38]. В теплый период наблюдались низкие значения eBC, которые редко превышали пороговое значение эпизодов загрязнения (рис. 5б).

Расчеты полей концентраций BC по формуле (1) на основе результатов наблюдений на ст. «Остров Белый» дали возможность оценить пространственное распределение основных источников эмиссий сжигания природных топлив и биомасс на материковой части евроазиатского континента в зависимости от сезона. В холодное время года воздушные массы приходили на о в Белый с территории густо населенных и индустриальных районов Восточной Европы, европейской части РФ и Кольского п-ва. Распределение источников eBC в декабре 2019 г., в период, когда были зарегистрированы самые высокие загрязнения, показано на рис. 5, а. Самые высокие эмиссии BC обнаружены в Западно Сибирском и Волго Уральском нефтегазоносных бассейнах, в регионах – лидерах по добыче нефти и газа: Ханты Мансийском и Ямало-Ненецком АО. Спутниковые данные о расположении газовых факелов крупнейших месторождений указывают на факельное сжигание газа как основной источник эмиссий BC в этих регионах (рис. 5, а). Региональное распределение источников BC, идентифицированных в июле, значительно отличается от декабрьского локализацией преимущественно на побережье Северного Ледовитого океана (рис. 5, б). В работе [39] было показано, что специфические условия циркуляции в атмосфере, сопутствующие лесным сибирским пожарам, могут способствовать снижению в это время эффективности переноса атмосферных примесей в арктические районы.

Особое влияние на загрязнение Арктики в теплый период года оказывает сжигание биомасс. Во

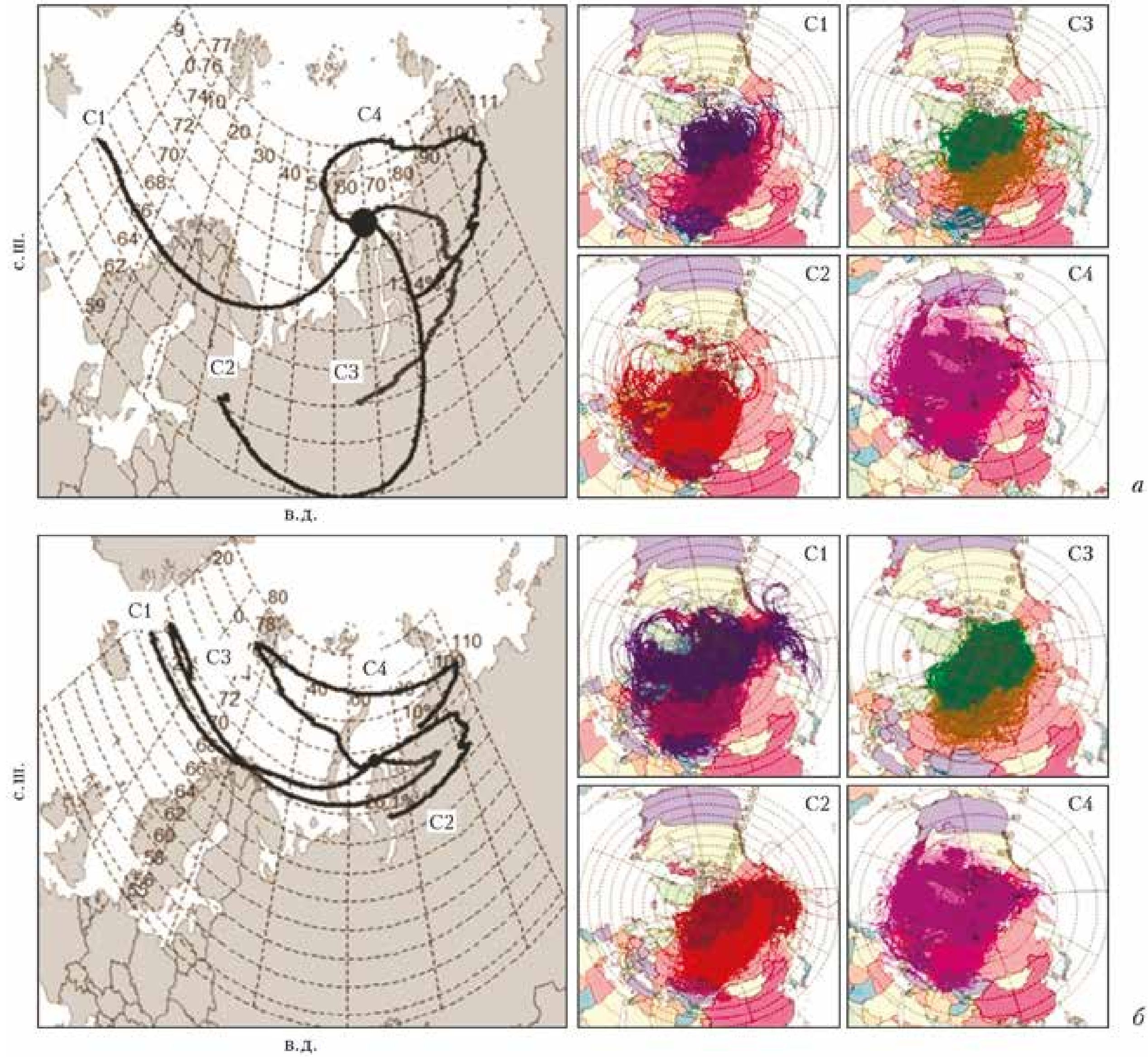

Рис. 4. Результаты расчета усредненных траекторий кластеров С1–С4 (слева) и обратных траекторий воздушных масс (справа) в холодный (а) и теплый (б) периоды года; черная точка – о-в Белый

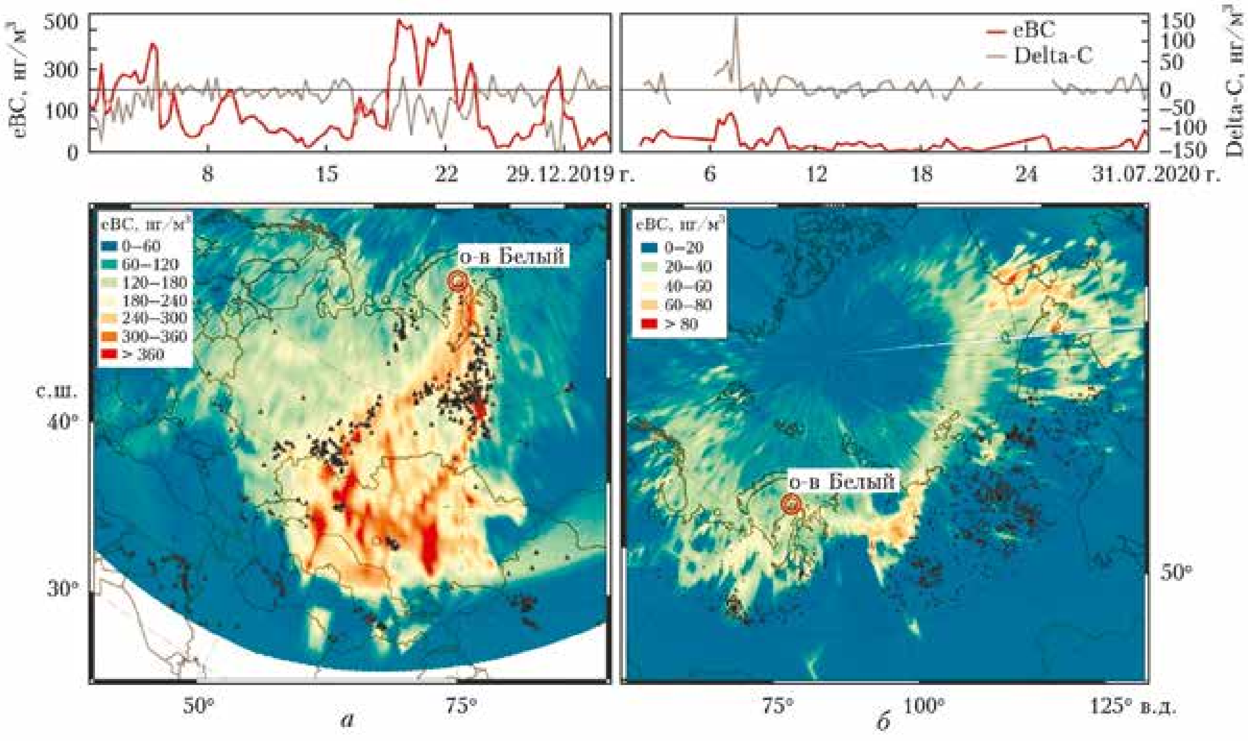

Рис. 5. Концентрация eBC и Delta-C на о-ве Белый (вверху) и пространственное распределение источников BC в декабре 2019 г. (а) и июле 2020 г. (б); треугольники и точки — факельные установки нефтегазовых месторождений и очаги пожаров севернее 60°с.ш. соответственно

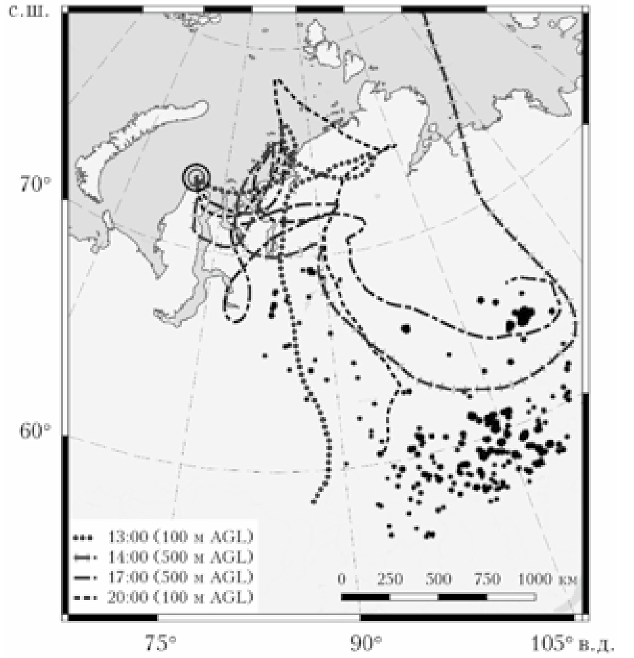

Рис. 6. Обратные траектории воздушных масс 1 сентября 2020 г. на высотах 100 и 500 м AGL в период эпизода загрязнения Т6; пожары в Красноярском крае в районе прохождения траекторий

время наших измерений интенсивные лесные пожары были зарегистрированы на севере Красноярского края, в Республике Саха, Центральной и Южной Сибири; с апреля по ноябрь 2020 г. выгорело около 7 000 000 га леса (https://aviales.ru/popup.aspx? news-6286). Обширные сельскохозяйственные пожары на юге Сибири стали причиной сильного весенне го загрязнения Т3 (18 и 23 апреля 2020 г.), когда Delta_C достигла 214 нг/м^3 (рис. 5, б), указывая на значительный вклад сжигания биомасс. Воздействие лесных пожаров отмечается в Т4 (7 июля 2020 г.) при Delta_C – 100 нг/м^3 (рис. 5, б).

Самые высокие значения eBC наблюдались в сентябре 2020 г. во время эпизода Т6 (см. рис. 3, б). Максимум eBC(880) – 534 нг/м^3 (1 сентября 2020 г.) превысил пороговое значение в 5 раз, а арктический фоновый уровень – в 20 раз. Высокие значения Delta_C – 209 нг/м^3 указывают на преимущественное загрязнение дымовыми эмиссия ми пожаров. Траекторный анализ, проведенный на высотах 100 и 500 м AGL 1 сентября 2020 г., указывает на Красноярский край как регион источников многочисленных пожаров (рис. 6).

Таким образом, вынос дымовых шлейфов из регионов Сибири, а именно из Красноярского края и Якутии, где выгорело около миллиона гектаров леса, повлекло беспрецедентное загрязнение атмосферы Арктики в сентябре 2020 г. эмиссиями горения лесных биомасс.

ЗАКЛЮЧЕНИЕ

Непрерывные измерения поглощающей способности аэрозолей в широком диапазоне спектра солнечного излучения, выполненные на полярной ст. «Остров Белый», позволили впервые определить уровень аэрозольного загрязнения в западно-сибирском секторе Российской Арктики по концентрации черного углерода. Полученный годовой ход eBC характеризуется высокими значениями зимой во время арктической дымки и низкими — летом. В течение 16 мес наблюдений на ст. «Остров Белый» зарегистрировано 15 эпизодов загрязнений с концентрациями, достигавшими 420 нг/м^3 зимой и 534 нг/м^3 летом. Эпизоды в холодный период оказались более длительными, частыми и с большей интенсивностью, чем в теплый.

Основной причиной загрязнения Арктики в зимне-весенний период явился дальний перенос воздушных масс из низких широт. Благодаря уникальному месторасположению аэрозольного комплекса на пути выноса крупномасштабных эмиссий из индустриально развитых регионов определено пространственное распределение эмиссий факельного сжигания газа как основного источника черного углерода на территориях газовых и нефтяных месторождении Западной Сибири и Волго-Уральской нефтегазоносной провинции, подтверждаемое спутниковыми данными о расположении газовых факелов в этих регионах. Индикатор влияния сжигания биомасс указал на преобладающее влияние сжигания древесины в жилом секторе густонаселенных районов Восточной Европы и европейской части РФ в холодный период, сельскохозяйственных и лесных пожаров на территории Красноярского края, Республики Саха, Центральной и Южной Сибири в теплое время года.

Полученные данные по поглощающей способности BC в широком спектре солнечного излучения используются для оценки влияния источников сжигания природных топлив и биомасс.

Финансирование. Исследования проведены при финансовой поддержке РНФ (проект № 22 17 00 102) и по Программе развития Междисциплинарной научно-образовательной школы Московского государственного университета им. М.В. Ломоносова «Будущее планеты и глобальные изменения окружающей среды». Методология развития инфраструктуры аэрозольного комплекса внедрена, при финансовой поддержке Министерства науки и высшего образования РФ (проект № 075-15-2021-938).

East Siberian Arctic background and black carbon polluted aerosols at HMO Tiksi*

1. INTRODUCTION

Arctic atmospheric data are critical to evaluate trends and global impacts of climate-active species (Breider et al., 2017). Currently, risks and uncertainties regarding climate change have become the focus of intense research efforts. Warming in the Arctic has been accompanied by ice loss, reduction of the surface albedo, changes in the hydrological balance and positive feedbacks leading to further warming (Quinn et al., 2000). Carbonaceous aerosols have contributed 1.09 ± 0.81 °C to the observed Arctic temperature increase of 1.48 ± 0.28 °C from 1976 to 2007 (Shindell and Faluvegi, 2009). In winter-spring, the combination of intense isentropic transport from mid-latitudes to the Arctic and strong surface-based temperature inversions results in a large increase of tropospheric aerosol concentration known as Arctic Haze (Quinn et al., 2007). The springtime, when the sunlight returns, is the most critical time for aerosol induced Arctic warming. In contrast to the Arctic Haze period, pollutant concentrations during summer are much lower due to their limited long-range transport into the Arctic from lower latitudes, as the polar front retreats to the high arctic (Stone et al., 2014). However, the influence of potential local sources may then become relatively stronger.

Black carbon (BC) is the climate-active fraction of aerosols absorbing sunlight. Originating from local and regional combustion sources, together with organic carbon (OC), BC exerts a warming effect that contrasts the cooling effect of scattering sulfates. BC residing in the lowest atmospheric layer impacts aerosol-cloud interactions (Yun et al., 2013) and produces the Arctic warming because of cloud and sea-ice feedback (Flanner, 2013). BC decreases the snow albedo when precipitating out of the atmosphere, absorbing sunlight on the surface and accelerating snowmelt (Quinn et al., 2008). OC could result in either positive or negative feedbacks to global warming (Tomasi et al., 2007), making the understanding of the role of organics in the Arctic atmosphere crucial for quantifying the direct and indirect aerosol effects (Fu et al., 2009). Organic functional group composition provides important insight on the sources and composition of springtime Arctic haze and the substantial organic matter contributions into season-dependent mass concentrations (Shaw et al., 2010).

Studies of aerosol composition have significantly expanded the knowledge about BC and OC pollution in the Arctic (Chang et al., 2011; Nguyen et al., 2013; Stohl et al., 2007). Source apportionment has relied on a combination of elemental carbon (EC) and OC tracers (Barrett et al., 2015; Chang et al., 2011; von Schneidemesser et al., 2009). Transport, industry, gas flaring, and residential emissions are assumed to be responsible for anthropogenic BC and OC in the Arctic (Stohl et al., 2013; Wang et al., 2011). The isotope-constrained source apportionment pinpointed that biomass burning was dominant during low BC concentration periods in summer whereas fossil sources impacted mostly during the Arctic haze seasons (Winiger et al., 2017). However, the sources and chemical composition of arctic aerosols are still poorly represented in models. Even the most recent emission inventory has an estimated range of total BC emissions that spans one order of magnitude (Huang et al., 2015).

High levels of the Arctic pollution due to BC transport from Eurasian Russia have been recorded at several Arctic stations, including Barrow (Alaska), Alert (Canada), Summit (Greenland), and Zeppelin, Ny-Ålesund (Svalbard) (Sharma et al., 2013; Sharma et al., 2004; Treffeisen et al., 2007). BC monthly climatology has been compared, documenting the marked maxima in winter and minima in summer and early autumn (Stone et al., 2014); nevertheless, Siberian arctic atmospheric aerosol data are still very limited. Currently, a few BC measurements are available in East Siberian Arctic, mostly from campaigns that measured BC in the Arctic sea (Popovicheva et al., 2017a; Sakerin et al., 2015; Stohl et al., 2013), and from remote sensing measurements of aerosol optical depth on the drifting station "North Pole" (Stock et al., 2012).

The Hydrometeorological Observatory (HMO) Tiksi (71.36N; 128.53E), located on the coast of Laptev sea in Northern Siberia, is closer to the BC source regions of high-latitude Eurasia than other arctic stations. It has been previously a site for short-term BC and aerosol composition (elements, ions, OC, EC) measurements (Golobokova et al., 2013; Makarov et al., 2007; Rahn et al., 1997; Sakerin et al., 2012). Continuous observations of equivalent black carbon (EBC) with an aethalometer started at the HMO Tiksi in 2009 (Eckhardt et al., 2015), followed by aerosol number density and size distribution measurements (Asmi et al., 2016). In 2009–2010, the annual mean EBC concentration was found 2.5 times higher than for other arctic stations due to the possible influence of regional and local sources. However, ongoing Arctic aerosol studies consider mostly the average levels, while episodes of high BC concentrations are scarcely discussed. Analysis of BC data along with aerosol composition data is expected to increase our ability to identify the BC episodes that are related with potential pollution sources in the Arctic atmosphere.

In this framework, the present work is focused on EBC observations, coupled with comprehensive aerosol characterization performed at the HMO Tiksi during seven sampling periods of a two-year study, namely in September 2014, 2015 and 2016, November 2014, March 2015, May–June 2015, and June 2016. Analysis of wind and EBC pollution roses combined with long-range transport analysis assist in identifying the sources of the observed pollution episodes, demonstrating impacts either from

---

* O. Popovicheva, E. Diapouli, A. Makshtas, N. Shonija, M. Manousakas, D. Saraga, T. Uttal, K. Eleftheriadis // Science of the Total Environment.2019; 655:924-938
DOI: 10.1016/j.scitotenv.2018.11.165

lower latitudes or/and local emissions from the adjacent urban Tiksi area. EBC levels are assessed together with aerosol composition, such as carbon fractions (OC, EC), inorganic and organic functionalities of chemical compounds, ionic and elemental components, providing insight into the source-influenced and season-dependent composition of East Siberian Arctic aerosols.

2. EXPERIMENTAL

2.1. Sampling

The International HMO Tiksi was established through a cooperation during the 2007 International Polar Year (Uttal et al., 2013) which included the construction of the weather station, Clean Air Facility (CAF) for aerosol and gas sampling, and meteorological flux tower. The aerosol measurements described here were taken at the CAF that is located approximately 1 km north from the weather station Polyrka, 500 m from the Laptev sea coast, and 5 km from the Tiksi settlement, from which it is separated by a hill (Fig. 1). The 20 meter Tiksi meteorological flux tower is located around 300 m from the CAF; multiple levels are instrumented for the measurement of air temperature, relative humidity, and wind speeds allowing calculations of profiles in the near surface boundary layer. The basic meteorological parameters, such as wind speed, wind direction, temperature, relative humidity, and pressure were obtained every 3 h at the weather station Polyrka. All local values were converted to UTC time.

The area of the Tiksi settlement is separated in two parts which are located in the direction north and north-

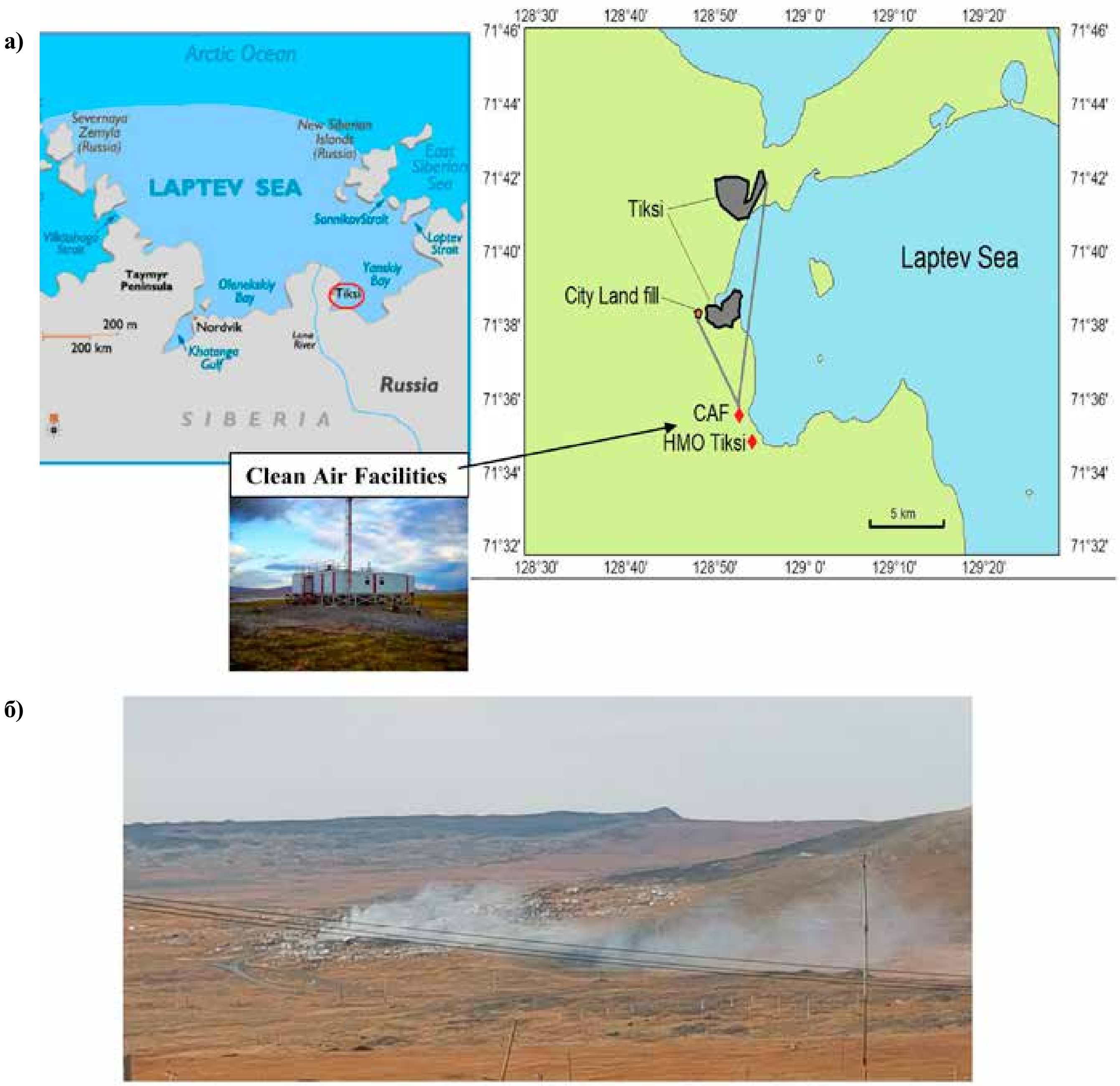

Fig. 1. a) Tiksi settlement in Northern Siberia; the area near Tiksi, the aerosol measurement site Clean Air Facility (CAF) and HMO Tiksi (71.36N; 128.53E) are indicated. "Local Pollution Influence (LPI) sector", the sector of wind directions for which local pollution affects the CAF, is also shown.
b) Landfill burning plume at 15.09.2016; the photo was taken on the way from CAF to Tiksi.

east from the CAF (Fig. 1). Aeroport Tiksi is situated in the northern part of a city. There are a few urban emission sources in the Tiksi settlement, such as a power plan using crude oil, central residential heating stations, and transport. Tiksi settlement is located on the Arctic Ocean coast of the remote Far East and serves as one of the biggest ports for accessing the Laptev Sea, therefore shipping emission in warm season can be another important source of BC. These local pollution emission sources may disturb the background aerosol and gaseous measurements at the CAF. Data collected during periods with wind directions at 300–360 and 0–50° are flagged accordingly. Therefore, the sector of the north-west – north – north-east wind is marked as "Local Pollution Influenced (LPI)" on Fig. 1. In Asmi et al. (2016) the wind direction was used to define a marine sector from the 45–150°, and a continental sector from the 150–315°, flagging out the remaining sector as polluted and indicating the three types of air mass direction.

A seven wavelength aethalometer (AE-31, Magee Scientific) is operated at the CAF, measuring aerosol optical properties by detecting the attenuation of light transmitted through particles that are accumulated on a quartz fiber filter tape with a time resolution of 5-min. Data obtained during the period September 2014–September 2016 were analyzed. Equivalent black carbon (EBC) was calculated at 880 nm using the instrument specific mass absorption coefficient (16.6 m2 g^{-1}). During a very clean period (May–June 2015), the EBC data obtained at 660 nm was used because at 880 nm the absorption was recorded at the noise level. Three short duration extreme EBC values appeared on 24.09, 30.09, and 24.11 of 2014 and were removed from the database, since they appeared to be the result of an instrument malfunction.

Table 1. Sampling periods at the CAF of HMO Tiksi; temperature T, pressure p, and EBC averaged over each sampling period and from the analysis of collected samples.

Sampling dates	Sampling, h period	T, °C	p, mbar	EBC, ng/m^3	OC/EC
Autumn 2014					
21.09–24.09	69	4	997	14	78.0
24.09–27.09	68.5	−0.6	1002	5	LOD
27.09–30.09a	69	−1.9	1004	18	–
30.09b	1.2	0.2	1011	97	–
30.09–01.10a	46	0.4	1013	125	–
Winter 2014					
20.11–22.11	48.6	−28	1001	141	10.9
22.11–24.11	44.3	−27	1019	179	9.0
24.11–26.11	45.9	−31	1008	237	2.8
26.11–27.11	20.3	−30	1013	146	6.1
Spring 2015					
19.03–20.03	22.5	−12,6	1000	150	18.4
20.03–21.03	22.5	−18	1000	220	15.2
21.03–22.03	23	−20	1009	158	22.4
Early summer 2015					
30.05–31.05	22.3	−1	1015	1.9	LOD
31.05–02.06	40.8	−0.4	1012	15.3	71.4
02.06–03.06	26.8	−1	1013	73.4	10.8
Autumn 2015					
06.09–08.09	47.3	11.2	1002	~	80.8
08.09–10.09	43	8.5	1011	40	42.2
Early summer 2016					
04.06–05.06	23.1	1.6	1012	50	86.5
05.06–07.06	45	4.1	1021	70	29.5
07.06–08.06	27.7	7.8	1018	100	50.8
Autumn 2016					
11.09–13.09	49.1	10.2	1026	61	80.9
13.09–15.09	43.2	7.7	1024	94	44.5

LOD - the EC concentration was below the limit of detection.
a Teflon filter.
b Ti foil.

An aerosol sampling system was installed at the CAF in September of 2014 to provide aerosol samples complementary to the real-time BC monitoring. A total suspended particle (TSP) inlet was installed approximately 1.5 m above the CAF roof and 5 m above the ground. The TSP inlet is equipped with an electric heating wire to prevent rimming and ice blocking the system. Aerosols were sampled at an air flow of ~45 l/min and collected into a temperature controlled room. The flow rate is regulated by a valve and measurement of the pressure drop and reported in standard conditions, using the in situ meteorological data presented in Table 1.

TSP was collected on 47 mm quartz fiber (Pallflex) and teflon (Zefluor) filters for subsequent analyses in the laboratory. The low concentrations of ambient aerosols necessitated sampling times ranging from one day in November up to three days in September, to allow the loading to exceed the detection limit for relevant aerosol chemistry analyses. In addition, a custom-made two-stage cascade impactor, with aerodynamic cut-offs at 5.5 and 0.33 μm for the first and second stage, respectively, was utilized to collect particles on metal substrate (Ti foil) installed on the second stage. The collection duration (typically 30–50 min) was adjusted to avoid overloading.

Due to harsh winter conditions and the remoteness of the CAF site, sampling was possible during only a limited number of periods. Sampling was performed in September and November of 2014, in March, May–June, and September 2015, and in June and September 2016. The sampling dates, periods, and average ambient conditions are presented in Table 1. Stability of the atmospheric surface layer during the sampling periods was estimated by the stratification parameter Z/L at the altitude Z = 10 m where L is the Monin-Obukhov's length in the semi-empirical theory of the turbulent atmosphere (Makshtas et al., 2012). For estimations of the stratification parameter, hourly averaged profile data were taken from the meteorological flux tower.

Air mass backward trajectories were generated to portray the atmospheric transport and evaluate the general flow patterns of air masses during sampling days. NOAA HYbrid Single-Particle Lagrangian Integrated Trajectory (HYSPLIT) model of the Air Resources Laboratory (ARL) (Stein et al., 2015) was used. The potential source areas were investigated using 7-day back trajectories for air masses arriving each 6 h to the HMO Tiksi at 250, 500 and 1000 m heights above sea level (A.S.L.). Forward trajectories from Kamchatka were generated in order to assess the possible plume transportation from volcano eruptions. Fire maps covering the studied period were obtained from the Fire Information for Resource Management System (FIRMS), operated by the NASA/GSFC

Earth Science Data Information System (ESDIS). Daily maps were related to the computed trajectories, providing a clear picture of the geographical location of fires.

2.2. Analytical methods

Table 2 presents the techniques used for the aerosol sample analysis. Organic (OC) and elemental carbon (EC) were measured by thermo-optical transmittance (TOT) analysis (Lab OC-EC Aerosol Analyzer, Sunset Laboratory, Inc.). Quartz filter samples were heated first up to 650 °C in He and then up to 850 °C in an mixture of 2% O_2 in He, using the controlled heating ramps of the EUSAAR_2 thermal protocol (Cavalli et al., 2010). This protocol has been initially developed for regional background sites. OC evolved in the inert atmosphere, while EC was oxidized in the He-O_2 atmosphere. Charring correction was applied by monitoring the sample transmittance throughout the heating process. The limit of detection (LOD) for the TOT analysis is 0.2 μg C cm^{-2}. Before sampling, the quartz fiber filters were pre-treated at 500 °C for 6 h to remove possible OC contaminations. Lab and field blanks were prepared and run following the same procedures as adopted for the samples. The QA/QC procedures described in EN 16909:2017 were followed during TOT analysis.

Water soluble ion components were measured by capillary electrophoresis using the Capel 103 system (Lumex) with the UF detection, as described elsewhere (Popovicheva et al., 2017c). One quarter of the sample was extracted in 5 ml of distilled water by ultrasonic agitation for 45 min and then the extract was filtered. Inorganic anions and cations (Table 2) were measured in aqueous extracts with a relative standard deviation of 10%. A mixture of benzimidazole, tartaric acid, and 18 crown 6 ether was used as an electrolyte in cation measurements. Anions were analyzed in the chromate buffer prepared from chromium oxide (VI), diethanolamine, and cetyl trimethyl ammonium hydroxide solution. The LOD for ion concentrations was in the range of 0.1–0.5 mg/l depending on the ion type. A few extracts were analyzed by both capillary electrophoresis and ion chromatography as described in Mass concentrations of non-sea salt (nss) SO_4^{2-} and (nss) K^+ ions were derived by subtracting the sea salt contribution estimated from Na^+ mass concentration and sea water weight ratio for sulfates and potassium, taken as $SO_4^{2-}/Na^+ = 0.252$ and $K^+/Na^+ = 0.0353$, respectively.

The functionalities of various inorganic and organic compounds in the entire aerosol composition were analyzed by Fourier Transform Infrared (FTIR) spectroscopy, as described elsewhere (Popovicheva et al., 2015a). Shimadzu IRPrestige-21 spectrometer was used in the diffuse reflectance mode. Spectra were measured at 4 cm^{-1} resolutions for a wavenumber range from 4000 to 500 cm^{-1}. In the case of samples collected on quartz filters, spectral bands with wave numbers in the range below to 1400 cm^{-1} were not considered because of the strong absorption of filter material in this range. The spectra were obtained from five different spots to address the possible inhomogeneity of the sample loading. If four from five spectra demonstrated the same absorption features, we considered these bands as the representative spectrum for the entire sample. IR Solution software was applied to subtract the FTIR spectrum of blank substrates, to correct the baseline absorbance as well as to perform the Kubelka-Munk (K-M) conversion into a quasi-quantitative spectrum which correlates with the sample concentration. Because of the possible overlapping of vibration bands the functionality identification was accomplished through the use of the Shimadzu FTIR database and a set of authentic chemical standards measured in the same FTIR setup, in agreement with the approach followed in previous studies (Coury and Dillner, 2009; Maria et al., 2002).

Teflon filter samples were analyzed by an ED-XRF system (E5 Panalytical). The instrument is calibrated for aerosol filters by means of Micro Matter thin standards (evaporated on Mylar 6.3 μm film), as well as NIST CRMs 2584 and 2583 dust deposited on PTFE filters for 35 elements Analytical uncertainty ranges from 0.3 to 10% and detection limit from 1 to 30 ng/cm^2 depending on the element analyzed.

Table 2. Description of techniques used for aerosol sample analysis.

Technique	Instrument	Type of substrates	Variables
Optical attenuation	Magee Scientific Aethalometer	Quartz	EBC
Thermo-optical transmittance	Lab OC-EC Aerosol Analyzer	Quartz	OC, EC
Capillary electrophoresis	Capel 103 System (Lumex)	Quartz	Water soluble inorganic anions (SO_4^{2-}, NO_3^-, Cl^-, F^-, PO_4^{3-}), cations (Na^+, NH_4^+, K^+, Mg^{2+}, Ca^{2+}), organic ions ($HCOO^-$, CH_3COO^-, $(COO^-)_2$)
Fourier Transform Infrared Spectroscopy (FTIR)	Shimadzu IR Prestige-21 Spectrometer	Quartz Ti foil	Organic and inorganic functionalities
X-Ray Florescence (XRF)	ED-XRF system	Teflon	Elements Z = 11–38 plus Ag, Cd, Sn, Sb, Cs, Ba, Ce, Pt, Au, Hg
Scanning Electron Microscopy, Energy Dispersive X-ray Spectroscopy (SEM/EDX)	LEO 1430-vp Zeiss system	Ti foil	Individual particles morphology and composition

3. RESULTS AND DISCUSSION

3.1. Seasonal variability of the arctic aerosol

Meteorological variables (i.e., temperature, pressure, solar radiation, wind speed and direction, and air mass origin) in the Tiksi region have a strong seasonal cycle (Asmi et al., 2016). Median temperatures stay above 0 °C for four months each year, between June and September. This period is characterized by the highest-frequency occurrence of marine air masses and the most stable wind speeds with median values ranging from 3 to 5 m/s. In October, solar insolation is decreased, resulting in a temperature shift to below 0 °C until January–February, after which the increasing solar radiation results in an increasing temperature. The cold month winds are primarily continental. Specifically, for the study period, very high wind speeds were recorded during October through December, with half hour averages up to 20 m/s, indicating stormy weather conditions. January through March was the calmest period of the year, with median wind speeds between 1 and 3 m/s. A shift in weather conditions occurred in April–May with increasing temperatures and stronger winds and the onset of more frequent marine air flow.

3.1.1. EBC climatology

As shown by studies at various Arctic locations, such as Ny-Alesund, Alert, and Barrow, the Arctic aerosols display peak concentrations during winter and spring months, due to the well-known Arctic Haze, an Arctic pollution phenomenon (Stone et al., 2014). The climatology of atmospheric transport from surrounding regions has shown that all these stations are highly sensitive to emissions from high-latitude Eurasia (Eleftheriadis et al., 2009; Sharma et al., 2004). The EBC monthly climatology in Tiksi during the period of our study shows a very similar trend (Fig. 2) The highest concentrations were observed from December to March (130–230 ng/m^3) and the lowest from June to August (about 20 ng/m^3), in agreement with the typical seasonal trend of the arctic aerosol concentrations (Stone et al., 2014). On average, concentrations in summer were about 10 times lower than those in winter. Very similar monthly trends were also recorded in 2009–2010 at Tiksi, with maximum concentrations reaching above 100 ng/m^3 during winter-spring and lowest concentrations of about 20 ng/m^3 observed during summer and early autumn (Eckhardt et al., 2015). (Sharma et al., 2004) also reported low EBC concentrations (~8 ng/m^3) during June–September at the Alert station (82° 30′ 30.4308″ N, 62° 24′ 37.8936″ W), well in the range of the arctic background. During winter months, the mean EBC concentration was found equal to 187 ± 38 and 127 ± 28 ng/m^3 in 2014–2015 and 2015–2016, respectively; these concentrations levels are high in comparison to the levels observed at the Alert station (100 ± 65 ng/m^3). We note that observations at the Alert station display the maximum concentrations among all other Arctic stations. This finding confirms the conclusion of Eckhardt et al. (2015) and Winiger et al. (2017) that the HMO Tiksi is the station mostly influenced by emissions from high-latitude Siberia.

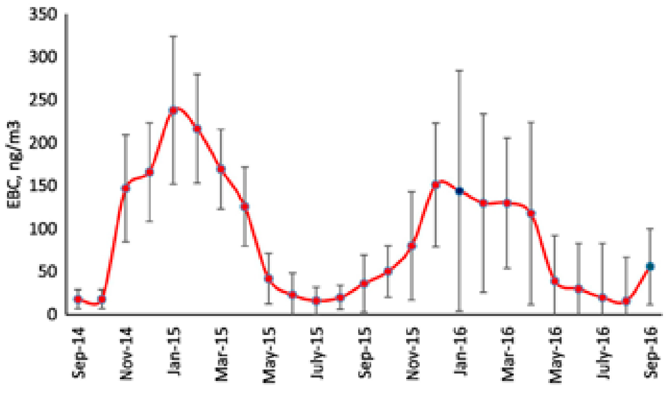

Fig. 2. EBC monthly climatology from September 2014 to September 2016 at HMO Tiksi. Monthly means are presented by points with ±1σ indicated by bars. Large σ value for January and September of 2016 (marked by blue) is decreased 3 times on the plot. (For interpretation of the references to color in this figure legend, the reader is referred to the web version of this article.)

3.1.2. Aerosol chemistry

Long-term surface measurements indicate that arctic aerosols consist mainly of sulfates and to a lesser extent of organics, ammonium, nitrates, and BC (Quinn et al., 2007). The biological activity of the ocean and Arctic pack ice are resulting in a significant production of dimethyl sulfide CH_3SCH_3 which oxidizes and forms various sulfur-containing products such as sulfuric acid H_2SO_4 and methyl sulfonic acid CH_3SO_3H (Yin et al., 1990), recently found to be associated with the growing nuclei aerosol mode. High sulfate concentration may relate to regional sources of secondary sulfate during periods of air mass transportation from continental areas (Eckhardt et al., 2015). A strong correlation between BC and sulfate concentrations (Hirdman et al., 2010) indicates that they both have anthropogenic sources and are mainly transported to high-latitude Arctic through similar pathways (Eleftheriadis et al., 2009; Sharma et al., 2013). Na^+, Cl^-, K^+, and Mg^{2+} are the major ions in the sea-salt aerosols which are ubiquitous in the marine boundary layer and significantly impact the particle concentrations in coastal regions (Li and Winchester, 1989). Ammonium is mainly produced by soil and emission from biota and the ocean; it is commonly found in the form of $(NH_4)_2SO_4$ and NH_4Cl. Similar to sulfates, ammonium is influenced by regional sources of secondary aerosol formation and transport.

Fig. 3 shows the mass concentrations of elemental (EC) and organic carbon (OC) and inorganic ions (SO_4^{2-}, Na^+, Cl^-, NH_4^+, K^+, Mg^{2+}, NO_3^-, PO_4^{3-}, and F^-) in the water-soluble fraction of aerosols, during the sampling periods at the HMO Tiksi. EBC averaged over the time of the corresponding sample collection is shown in Table 1; the averaged EBC/EC ratio was found equal to 1.33. The EBC/EC ratio found in our study is well within the expected difference for the two methods measuring EBC and EC, respectively (Baumgardner et al., 2012). In addition, EC concentrations correlated well with the corresponding average EBC concentrations (correlation coefficient R2 = 0.78; Fig. S1). As expected, similarly to EBC, EC maximum concentrations were observed during the cold period. Winiger et al. (2017) also reported a strong seasonality of EC concentrations (ranging from 8 to 302 ng/m^3 from July to February as measured by radiocarbon and stable carbon isotope analysis) during a two-year sampling campaign at the RAS Polar Geocosmophysical (PGC) Observatory, which is located at

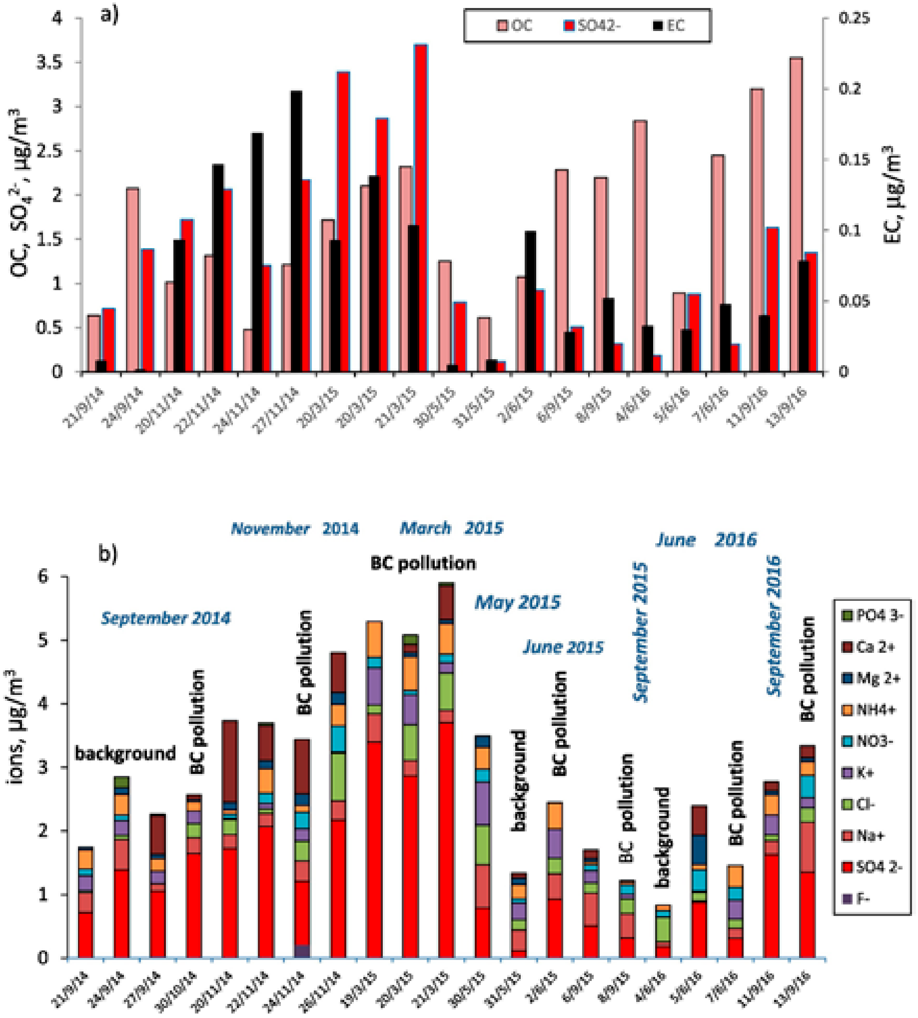

Fig. 3. a) EC, OC, and $SO4^{2-}$, and b) ion concentrations in sampling periods from September 2014 to September 2016.

10 km south from HMO Tiksi. In (Barrett et al., 2015), six week-long winter samples collected at the Barrow station (71°17′26″N, 156°47′19″W) showed the EC concentration (measured by using the NIOSH 5040 method) ranging from 40 to 100 ng/m^3, from December to February, respectively. Higher concentrations were recorded at HMO Tiksi during the cold period (93 to 199 ng/m^3, Fig. 3).

Organic carbon (OC) composes a significant fraction of the aerosol mass in the Arctic (Chang et al., 2011). OC tends to be elevated due to biogenic emissions and secondary aerosol formation from biogenic volatile organic compounds, wind-induced bubbles bursting from the sea surface (Frossard et al., 2014), fossil fuel combustion (Barrett et al., 2015) as well as biomass burning (agricultural and wildfires) (Stohl et al., 2007; Warneke et al., 2010). At the HMO Tiksi, OC concentrations in winter-spring sampling periods were found in the range 0.6 µg/m^3 in May to 2.3 µg/m^3 in November (Fig. 3a), followed by a decreasing trend in summer-autumn, in agreement with the typical seasonal trend of arctic aerosols. However, OC concentrations were found to be fairly high in September during all years (concentrations up to 3.6 µg/m^3), while some high OC values were also recorded during June 2016. These peak OC concentrations during periods that arctic aerosol levels are expected to be low, may be indicators of local OC pollution in early autumn and in summer (for the year 2016).

The high OC/EC ratio observed (Table 1) is typical for sites characterized as natural background, and results from relatively high OC concentrations (due to biogenic emissions and secondary organic aerosol formation) coupled with negligible EC concentrations (due to minimum anthropogenic activities, and specifically combustion sources). By contrast, in the urban environment which is dominated by traffic and in general fossil fuel combustion, OC is comparable to EC (Samara et al., 2014). High OC/EC ratios (40–80) were observed in September, while the lowest values for this ratio corresponded to November and March. A similar trend was observed at the PGC Observatory, with highest ratios in summer and autumn (reaching up to 30), and lowest in winter and spring (going down to 5 (Winiger et al., 2017)).

Total ion mass concentration demonstrates the typical seasonal variation of Arctic aerosol. On the other hand, the seasonal cycle of sulfates shows a clear maximum during the Arctic Haze and a minimum in summer/early autumn but also displays fairly high values in September, similar to OC. Our data show a weak correlation between EC and sulfates (R2 = 0.3); this result suggests that sulfate is not always related with high-temperature combustion (where EC emissions are also expected to be high). Low-temperature combustion such as biomass and waste burning can contribute to EC and sulfates (Kalogridis et al., 2018; Wiedinmyer et al., 2014) at different extent. It should be noted that during the winter-time high-concentration period, OC levels are always significantly lower than the respective SO_4^{2-} levels. In contrast, during the peak OC events in autumn and summer, the sulfate to OC ratio is different. These results suggest that the local pollution source observed mainly in early autumn is related to biomass or waste burning.

3.2. Pollution episodes due to long range transport and local sources

Pollution episodes recorded at the HMO Tiksi are separated from the background (clean) conditions based on the long-term EBC time series. Background air conditions are generally defined as a state without any detectable influence of local or regional pollution (Eleftheriadis et al., 2004; Mikhailov et al., 2017). In this study we relate the arctic background to the lowest 20th percentile of EBC data. Local meteorology and air mass back trajectory analysis have been combined, in order to understand the characteristics and origin of the different pollution events and assess their seasonal trends. Focus was given to the episodes observed during the aerosol filter sampling periods, for which chemical composition data are also available.

3.2.1. Autumn episodes

EBC climatology during August to September of 2014, 2015 and 2016 is presented in Fig. 4a. Background conditions were characterized by low EBC concentrations while a number of episodes with elevated EBC are clearly visible, lasting typically 1–3 days.

September 2014 was characterized by EBC background concentrations around 7 ng/m^3. During this period, the wind was blowing from south-west, while the tundra was snow-free. Back-trajectory analysis revealed two distinct origins of air masses: the central Siberian Plateau (until 26.09) and the Arctic Ocean (after 26.09), with the air masses passing from coastal areas before arriving to the Tiksi region (Fig. 5a). A background OC concentration of 0.6 µg/m^3 was observed, originating from biogenic and marine activity. The organic functional group composition provided an important insight on the sources and composition. Analyses of absorption bands showed aliphatic C C H (2931–2855 cm^{-1}), carbonyl C O (1731 cm^{-1}), amino N H (3247 cm^{-1}), and hydroxyl C OH (3547 cm^{-1}) groups in alkanes, esters/lactones, amino-compounds and alcohols/phenols, respectively (Fig. S2). Carbonyl and amino functionalities are particularly relevant to biogenic aerosols, being characteristic of primary and secondary organic aerosol formed by oxidation of biogenic volatile organic compounds (BVOC) (Hawkins and Russell, 2010). Impact of BVOC emissions from Siberian boreal regions on the aerosol number size distribution at the HMO Tiksi was shown in Asmi et al. (2016). Russell et al. (2010) suggested that hydroxyl functional groups with a broad absorbance between 3200 and 3500 cm^{-1} of carbohydrate-like compounds, including saccharides, are associated with ocean-derived particles emitted by bubble bursting during wave breaking. Bands of CO_3^{2-} (at 871 cm^{-1}) and ammonium $NH4^+$ (3247 cm^{-1}) indicate the absorption of inorganic natural aerosol. During this background conditions period, the concentration of Na^+ and Cl^- was found ~300 and 30 ng/m^3, respectively. It should be noted that the Na^+/Cl^- ratio was 16 times higher than in natural sea-salt aerosols (SSA), indicating a strong Cl depletion; this phenomenon is general-

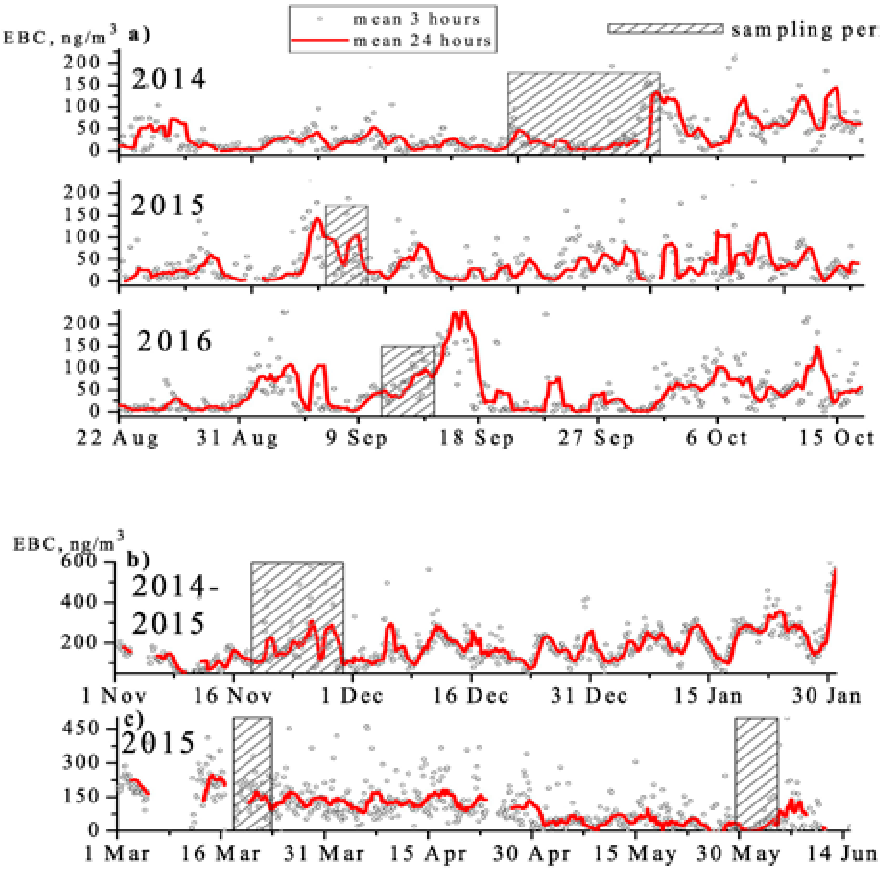

Fig. 4. Time series of EBC concentrations from a) August to October of 2014, 2015, and 2016 year, b) November of 2014 to January 2015, and c) March to June 2015. 3 h means (points) and 24 h running means (curve). Periods of sampling are marketed.

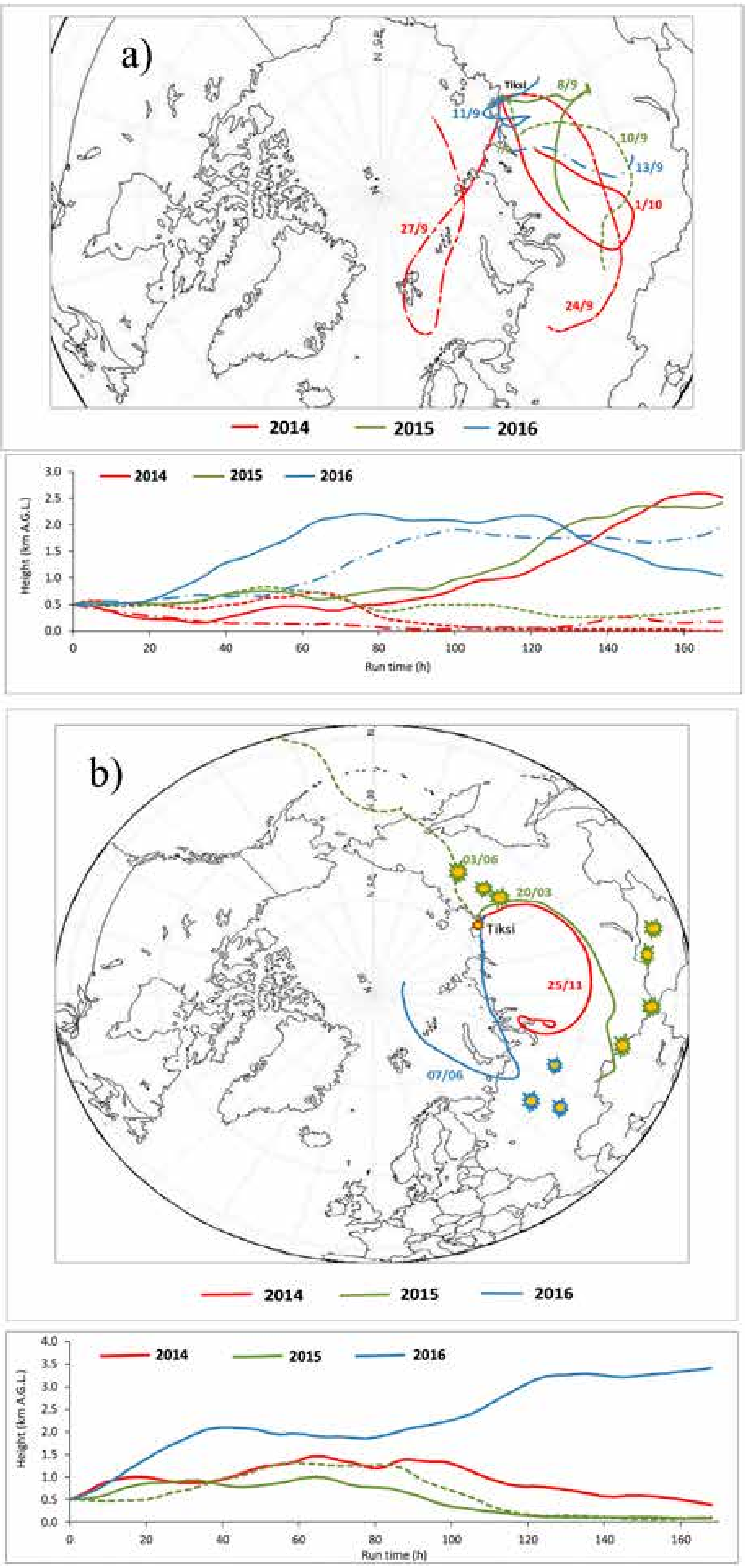

Fig. 5. 7-day back trajectories of the air masses arriving to HMO Tiksi a) during days with background conditions (dashed lines) and EBC pollution episodes (solid lines), in September 2014, 2015 and 2016, and b) during EBC pollution episodes in November 2014, March 2015, May–June 2015, and June 2016. Trajectories generated for date indicated in 2014, 2015, and 2016 are marked in red, green, and blue color, respectively. Height A.G.L. of arrival is shown. (For interpretation of the references to color in this figure legend, the reader is referred to the web version of this article.)

ly observed in the arctic atmosphere, due to interaction of SSA with reactive gaseous species, mainly with NOx (or HNO_3) (Gard et al., 1998; Geng et al., 2010). This is further confirmed by the relatively high concentration of nitrates NO_3^- (~80 ng/m^3). Additionally, S, Fe, Na, Al, Si, Ca, Cl, K, Ti, Mn, Co, Cu, Zn, Ga, Sr, Ba, Hg, and Pb were detected above the LOD in the background aerosol, with sulfur displaying the highest concentration, followed by Fe, Na, and Al (Fig. S3).

An episode of high OC concentrations was observed on 24.09 when a change in the wind direction brought pollution plumes from the Tiksi urban area to the measurement site, resulting in an increase of the OC concentration (up to 2.1 μg/m^3). During this OC pollution episode, C C H (3041 cm^{-1}), NO_2 (1507 cm^{-1}), and C O (1052 cm^{-1}) groups were added to the organic spectral features (Fig. S2), indicating polyaromatics, nitro- and oxygenated compounds (alcohols/esters). Since at that time EC concentrations were below LOD, while EBC was found at background levels, this pollution episode seems to be related to low-temperature pyrolysis (smoldering) aerosols dominated by organic compounds (Popovicheva et al., 2015b) and high OC/EC ratio. These findings exclude high-temperature traffic-related combustion (Samara et al., 2014) and engine exhaust or biomass burning smoke (residential, agriculture and forest fires) in the flaming phase. This observation led to identification of combustion sources related to high OC emissions in the Tiksi area, namely, open air waste burning occurs at the landfill site, situated to the west of the Tiksi urban area (see map in Fig. 1). In addition, an increase in sulfate concentration (up to 1.4 μg/m^3) was observed, which is composed of 90% non-sea-salt sulfates (nss-SO_4^{2-}) and also showed a twofold increase of SO_4^{2-} absorption at 3232, 1144, 620 and 573 cm^{-1} (Fig. S1), in sulfuric acid and salts such as $(NH_4)_2SO_4$, CaSO4, Na_2SO_4, and K_2SO_4, produced by heterogeneous reactions and secondary formation. Moreover, vibrations at 1144 cm^{-1} observed in the FTIR spectrum of particles can be associated to organic sulfates such as RSO_2O^- in sulfonate salts, and R S(O)2 R in sulfones. The wide nitrate band at 831 cm^{-1} indicates possible Cl depletion, with SSA acting as a sink for nitric acid and nitrogen oxides species (Graedel and Keene, 1995). Furthermore, almost the entire mass of K^+ (near 200 ng/m^3) was composed of nss-K^+, pointing towards waste burning, which produces K^+ at concentrations similar to biomass burning (Christian et al., 2010). PO_4^{3-} concentration was also found elevated (160 ng/m^3), in comparison to the background aerosol and has been proposed as a specific tracer for plastics burning (Simoneit et al., 2005). Thus, it may be concluded that local waste burning may lead to local pollution episodes as observed in September 2014.

This full characterization of local aerosol pollution observed at the CAF during this period provides further evidence in order to screen measurements when the wind blows from the LPI sector especially during the warm period of the year. It appears that water soluble ions provide adequate evidence to evaluate an LPI event and continuous monitoring would benefit from an EMEP/EANET operation at the Tiksi site.

Following the OC pollution episode, a significant EBC episode was observed on 30.09–01.10 with EBC concentrations increasing up 160 ng/m^3 (Fig. 6). Analyses of the wind direction (Fig. S4) showed that the southwest winds were the most frequent during that period, while, the neutral stratification of the atmospheric boundary layer was indicated by a Z/L near zero (Fig. S5). Thus, we can hardly assume the impact of local sources from the Tiksi direction on increased EBC level. Back-trajectory analysis indicated that the air masses reaching the HMO Tiksi on 01.10 originated from northern Siberia (Yamal-Nenetz) and central Siberia (Khanty-Mansisky) regions (around 300 km from Tiksi), where the most significant gas flaring, industrial and residential emission sources in Siberia are located, as evaluated by Huang et al. (2015) and Winiger et al. (2017). It is interesting to note that during this episode, the transported air masses descended from high altitudes, around 4 km A.S.L. (Fig. 5), where vertical EBC profiles have been shown to display the highest concentrations (Brock et al., 2011; Eckhardt et al., 2015). These results highlight the impact of the different atmospheric layers mixing processes.

The newly reconstructed inventory of Huang et al. (2015) indicates significant emissions from a large residential and industrial region near Norilsk in Krasnoyarsk Krai, as well as distributed transport emissions, including intense shipping, in Lena river delta. High-latitude Eurasia has been shown to be the dominant BC and sulfates source region for other arctic stations such as Ny-Ålesund, Alert and Barrow, due to its metal smelting complexes (Hirdman et al., 2010). Since the days of EBC pollution were characterized by wind speeds around 5 m/s followed by stagnant weather, we associate this episode with long-range transport (LRT) of polluted masses (Fig. 6) which resulted in the accumulation of pollution in the HMO Tiksi area, due to stagnant conditions although it is difficult to exclude the local pollution accumulation as well.

Regarding the detailed chemical composition during the September 2014 BC pollution episode, aerosols are characterized by elevated concentrations of aliphatic C C H, carboxylic acid C O (1706 cm^{-1}), aldehydes C O (1657 cm^{-1}), C O (1074–1021 cm^{-1}), and NH_4^+, CO_3^{2-}, and SO_4^{2-} functional groups (Fig. S2). N-alkanes serve as a good indicator of BC urban and diesel emissions (Coury and Dillner, 2009; Popovicheva et al., 2017b). During long-term transportation anthropogenic and biomass burning emission becomes more oxygenated due to secondary organic aerosol formation (Popovicheva et al., 2014). Ammonium nitrates and sulfates are known anthropogenic secondary species well correlating with oxygenated secondary species (Coury and Dillner, 2009). Thus, the change of aerosol composition observed is well identified by a pattern of functional markers which can be reasonably related to long range transport (LRT) from industrial and urban emission sources. A significant increase of SO_4^{2-} concentration is also observed (up to 1.6 μg/m^3), and it is in agreement with the recorded 3 times higher sulfur concentration during this episode in comparison to the background conditions (Fig. S3). The increase of the relative contribution of SO_4^{2-} to total PM mass from 50 to 70% indicates the strong impact of LRT from gas flaring, industrial and residential emission sources in Western Siberia, Krasnoyarsk Krai and Lena river delta (Fig. 5a), where sulfur-containing oil and diesel fuel are used (Klonecki et al., 2003). It is worth noting that a layer of alkanes, organic-rich and scattering aerosols, unambiguously attributed to anthropogenic emissions, was observed at 4–6 km altitude (Warneke et al., 2010), which coincides with the high traveling height of the air masses reaching the HMO Tiksi during

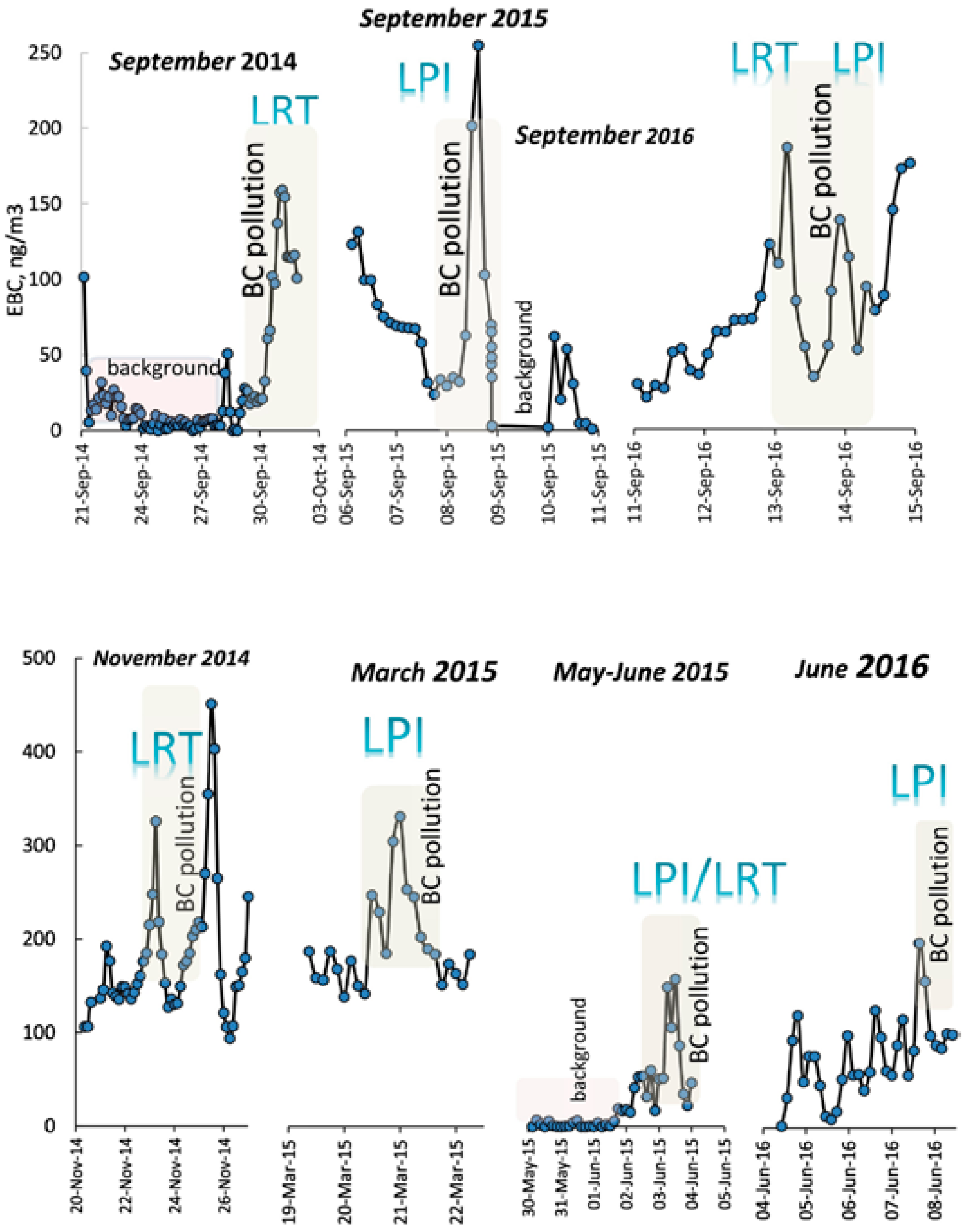

Fig. 6. 3 h mean EBC concentrations during the filter sampling periods. Background is identified by lowest absorption. The episodes of the highest EBC pollution are indicated as impacted by long-range air masses transportation (LRT) or local pollution influenced (LPI).

the BC pollution episode. Additionally, we should note that volcano eruptions may impact the sulfate loading at the regional level. Intensive eruptions of the volcano in Kamchatka were observed at the beginning of September 2014 (http://argumenti.ru/society/2014/09/363718). Forward trajectory at 30.09 to the Tiksi region clearly indicated the arrival of air masses from the Zhupanovskyi volcano, at an altitude of 4 km.

During the September 2015 sampling campaign, a period of high EBC concentrations was captured in its declining phase, followed by a second episode, with EBC levels reaching up to 250 ng/m^3 (Fig. 6). Back-trajectory analysis for 04–08.09 revealed that the air masses arriving to Tiksi region originated from central Yakutia (Fig. 5a) where transport and industrial emissions are quite abundant (Huang et al., 2015). At the end of the sampling period, on 10.09, EBC was lower but above the background, and the origin of back trajectories changed to the north-western region of Krasnoyarsk Krai, where there are low urban and industrial BC emissions.

Unlike the EBC episode of September 2014, during September 2015, calm winds (~1 m/s) from the North dominated (Fig. S4). During the observed EBC pollution episode, north-east winds with speed ~5 m/s were followed by calm conditions and northern wind directions (coinciding with the LPI sector), while a significant increase of the stratification parameter Z/L was observed (reaching values up to 8) (Fig. S5). Such combination of meteorological characteristics indicates favorable conditions for accumulation of pollutants in the atmosphere, due to strong stratification of the boundary layer (stagnant weather conditions). Therefore, a maximum of the EBC concentration observed during that period (Fig. 6) may be the result of high impact from the local urban emissions rather than long-range transport of pollution, coupled with stagnant weather conditions that inhibit the dispersion of pollution, OC/EC ratios in this period is indicted in Table 2 The aerosol composition was dominated by aliphatic, oxygenated compounds and ammonium (Fig. S1). The high concentration of OC, above 2 μg/m^3, recorded during this month (Fig. 3a), points towards impact from the landfill continuously burning in the Tiksi area. A decreased Na^+/Cl^- ratio was also observed (on average around 1.6), still indicating a Cl depletion phenomenon, but not so prominent in comparison with the background period. The higher abundance of Cl^- further supports the local origin of this episode (landfill emissions), since Cl^- is considered a marker for waste burning. Concentrations of SO_4^{2-} and NH_4^+ (~500 and 40 ng/m^3, respectively) were significantly lower than in 2014, again pointing towards a decreased impact from long-range transport of secondary aerosol from continental regional sources. Sea-salts production from the ocean was indicated by hydroxyls at 3560 cm^{-1} (Fig. S1).

The sampling campaign in September 2016 coincided with the beginning of a high EBC period (Fig. 6). Concentrations rose from a background level of around 20 ng/m^3 on 11.09, when air masses originated from the ocean (Fig. 5a), to three maxima of 172, 130, and 160 ng/m^3 (Fig. 6). Back-trajectory analysis during whole period indicated air mass transport from central Yakutia (Fig. 5a). Low winds from the North dominated (with a frequency of about 13%; Fig. S4); however this sampling period was characterized by a high variability of the wind directions, including western and north-eastern winds. The first and third maxima of EBC were observed when the wind was blowing from the West, while a north-east wind brought the second EBC maximum, which seems to be related to local urban emissions from the LPI sector (Fig. 6). It should be also noted that when EBC approached the second maximum the wind decreased significantly to calm conditions, leading to an increase of the stratification parameter Z/L, up to 12, indicating stable atmospheric conditions (Fig. S5) and accumulation of pollution. Thus, we assign these episodes of BC pollution to complex LRT and local source impacts.

The aerosol composition during that period also reflects the combined impact of LRT and LPI. Higher OC concentrations (above 3.0 μg/m^3 and reaching up to 3.5 μg/m^3) in comparison to the previous September sampling periods were recorded, indicating a strong impact from a prominent organic emission source. Since such OC pollution appears to be reproducible in the month of September, visual inspection of the area around the HMO was again performed and revealed again smoke plumes spreading from the Tiksi landfill site. A photograph taken on 15.09 (Fig. 1) clearly shows the white smoke emitted from the site, demonstrating that the smoldering combustion phase was dominant. This OC pollution was related to aliphatic, ester/lactones (1740 cm^{-1}), and acids/ketones (1710 cm^{-1}), as well as aromatic compounds, observed during the whole sampling period of September 2016 by the specific spectral absorption C C H and C C bands at 3064 and 1617 cm^{-1}, respectively (Fig. S2). The north-east winds dominating during days of high EBC concentrations also point towards harbour emissions (from ship traffic and the surrounding ocean) (Xie et al., 2007). Alkanes, esters, and polyaromatic compounds, which are well recognized as functional markers of on-road and off-road diesel emission (Popovicheva et al., 2015a) were found in ship exhaust residuals (Popovicheva et al., 2012). Measurements at the Barrow station during autumn months showed averaged organic matter (OM) concentrations below 500 ng/m^3, related to alkane and hydroxyl functional groups, equally contributing to the functional group composition (Shaw et al., 2010).

The total concentration of water-soluble ions approached 3.5 μg/m^3 in that period, again demonstrating higher levels in comparison to the previous September periods. Ion concentration was dominated by secondary sulfate, pointing towards impact from LRT from central Yakutia, as well as from Tiksi urban area, where the local power plant, heating stations, and diesel and marine transport use crude oil and sulfur-containing fuel. The Na^+/Cl^- ratio was calculated at 3.1 ± 0.8 on average, indicating Cl depletion, consistently found in the Tiksi BC polluted atmosphere. Overall, the OC and BC pollution episodes observed during September 2016 display features of waste burning and fossil fuel combustion from both local and regional sources, pointing towards the mixed impact of LRT from central Yakutia and LPI. The latter in such cases averts clear characterization of LRT events at the Tiksi station.

3.2.2. Winter episodes

November and March are winter months on the Laptev sea coast, with continental winds prevailing (>50% of the time), opening the gates for low altitude transport of Eurasian pollution into the Arctic (Asmi et al., 2016). During these months, the ocean was frozen and deep snow cover was observed near the HMO Tiksi. Low wind speeds and cold temperatures led to shallow boundary layers, which favor the accumulation of pollution.

The winter-time EBC climatology was assessed for the period November 2014 to January 2015 (Fig. 4). Polar night in the Tiksi region lasts from 19 November to 24 January; therefore, winter sampling took place in the absence of sunlight, with temperatures dropping down to a minimum of −31 °C (Table 1). Similar to the warm months described above, the cold months also displayed periods of low EBC interrupted by episodes of increased EBC; nevertheless the lowest levels of aerosol light absorption, corresponding to background reached up to EBC concentration levels close to 100 ng/m^3, and EBC maximum concentrations around 300 ng/m^3. During the sampling campaign of November 2014, the south-west wind direction was dominant, with wind speeds higher than 1 m/s. Calm conditions (wind speeds <1 m/s) occurred at a frequency around 36% (Fig. S4). The stagnant weather conditions, further documented by a Z/L ~12 (Fig. S5), which indicates stable stratified atmosphere, coincided with high EBC concentrations due to the accumulation of pollution, characteristic of high atmospheric stability in the Arctic during winter, also reported elsewhere (Quinn et al., 2008). During the whole sampling period air masses arrived to the HMO Tiksi from the center of the Siberian Plateau (Fig. 5b). The highest EBC concentration (up to 450 ng/m^3) was observed on 23.11 and 25.11 when the wind blew from south-west and air masses arrived from Yakutia (Fig. 6). During this month, OC was on average 0.97 ± 0.33 μg/m^3, significantly lower than the levels measured during the warm period. For comparison, the OC concentrations during winter at the Barrow station were equal to 0.33 ± 0.07 ng/m^3 (Barrett et al., 2015). Organic functional groups analysis showed similar aerosol composition during the entire sampling period. Winter-time aerosol was characterized by the strong carbonyl (1702 cm^{-1}) but low aliphatic (2856 cm^{-1}) and aromatic (3063 cm^{-1}) bands for all sampling days, including the period of highest EBC concentrations (Fig. S2). In comparison to the aerosol collected in September, winter-time (November) aerosols displayed much higher (68 times) abundance of oxygenated compounds with respect to alkanes, as determined by the ratio C O/C C H of bands peak areas. All sampling days were under strong influence of consistent LRT from central Yakutia; therefore a substantial portion of dicarboxylic acids/ketones was likely derived from atmospheric oxidation of aerosol during long range transport also observed in aerosol traveling from Siberia to Pacific Ocean (Agarwal et al., 2010). It clearly demonstrates the processes of chemical transformation during the aging of gaseous and aerosol emissions in the atmosphere. Prominent absorption of ammonium (3247 cm^{-1}) and sulfates (704 cm^{-1}) demonstrates the high impact of secondary inorganic aerosol formation and transportation to Laptev sea region, mixed with silicate ions SiO_4^{4-} (978 cm^{-1}) in various aluminosilicates and carbonates (874, 1428 cm^{-1}) in dust (Fig. S2).

Regarding the ionic composition, the winter-time aerosols were characterized by increased sum of common ions and sulfate concentrations in comparison to the warm period (September), in agreement with the general trend of increase in aerosol concentrations in the Arctic during winter. On average, SO_4^{2-} was 1.79 ± 0.43 μg/m^3, higher than OC, as is typically observed during Arctic Haze events where secondary SO_4^{2-} formation and aging is shaped by several processes like heterogeneous oxidation of SO_2, coagulation and cloud processing (Yun et al., 2013). Ammonium as well as sulfates relate to secondary inorganic aerosol formation, this is why the high NH_4^+ concentrations (on average 0.22 ± 0.16 μg/m^3) may support the pronounced secondary inorganic aerosol formation during this period. We note that the average NH_4^+ is 0.26 ± 0.17 μg/m^3 over whole sampling period. The averaged Na^+/Cl^- ratio was calculated ~0.74, indicating fresh SSA; the latter is more probable since NO_3^- concentration was high (up to 410 ng/m^3 on 26.11).

3.2.3. Spring-summer episodes

As sunlight returns to the Arctic in spring, the atmospheric stability is reduced. Air mass transport from lower latitudes is less frequent during that period compared to winter (Stohl, 2006). Fig. 4 shows the EBC climatology from March to June 2015. The sampling period of March 2015 is characterized by even higher level of the lowest BC values, around 120 ng/m^3, than in winter (Fig. 4). Analysis of both the wind (Fig. S4) and EBC pollution roses (Fig. 7) showed that low wind speed (<2 m/s) north winds occurred with the highest frequency (28%). High EBC levels (>180 ng/m^3), observed almost during the whole sampling period, were related mostly to these north winds (with a frequency of around 30%) and also to north-east winds, i.e. from the LPI sector. The stable stratification of the atmosphere was also quite prominent (Fig. S5). During the highest EBC concentrations (reaching >300 ng/m^3), on 20–21.03, the wind was blowing from the LPI sector. Air mass transport from lower latitudes (central Yakutia) was also observed at that time (Fig. 5b).

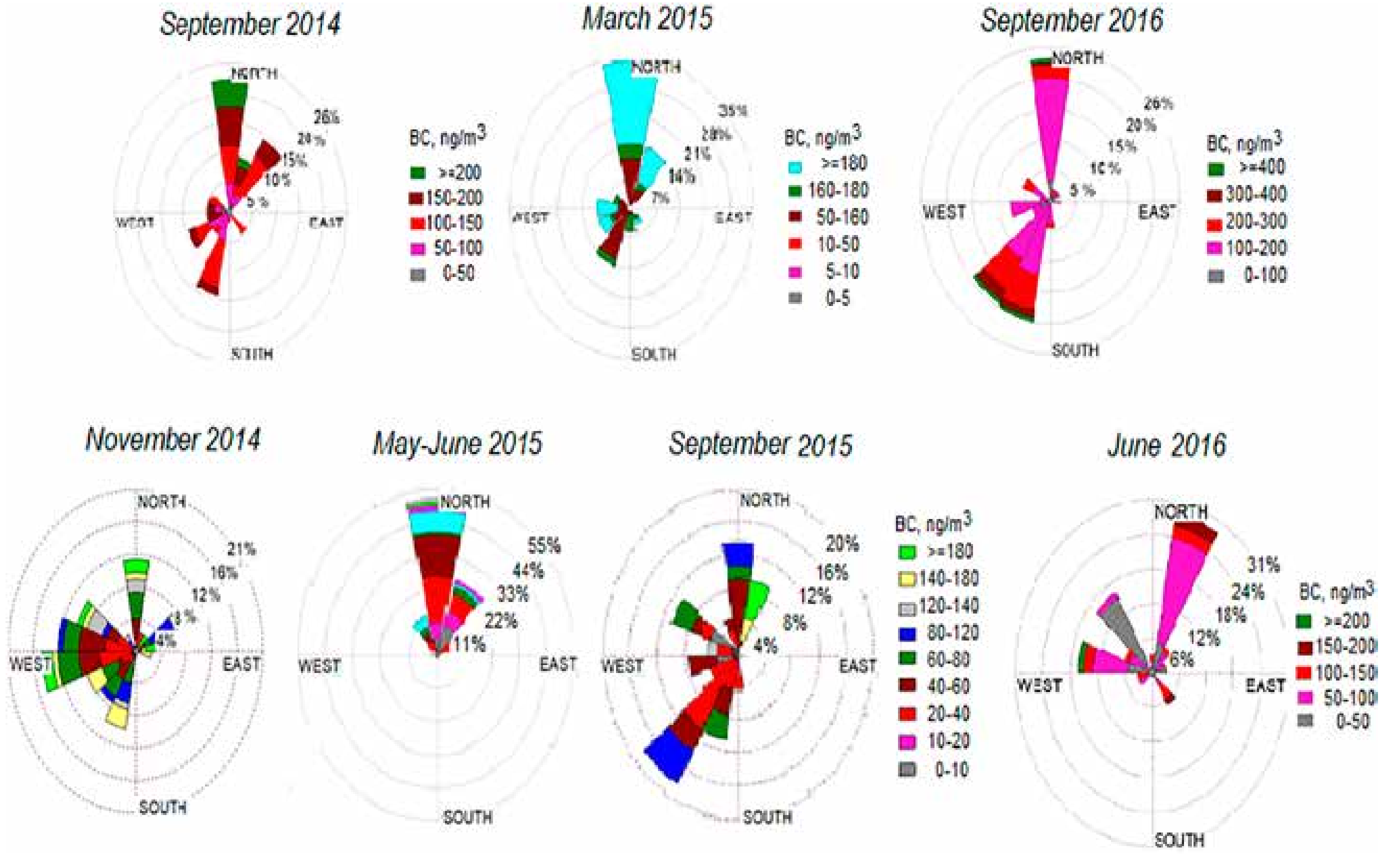

Fig. 7. Pollution roses of hourly averaged EBC concentrations during the sampling periods of 2014, 2015 and 2016.

Ion concentrations were the highest during this period, with sulfates and total ions up to 3.7 and 6 μg/m^3, respectively. OC also displayed higher levels in comparison to November (on average 2.1 ± 0.3 μg/m^3). Nevertheless, the organic composition was similar to the winter period, characterized by high contribution from carbonyl groups and low contribution from aliphatic functional groups (Fig. S2). This finding supports the impact of long range transport from lower latitudes during both November and March. 24 h average organic matter concentrations higher than 1 μg/m^3 have been recorded at the Barrow station during spring months. Organic matter consisted of approximately half alkane groups with the other half split between carboxylic acid and hydroxyl groups (Shaw et al., 2010). Abundance of carbohydrate-like hydroxyls was associated to organic-salt coatings raised during sea ice formation. However, hydroxyls were not observed in the composition of the spring-time aerosol at HMO Tiksi, probably due to the low impact of ocean-derived sources; the dominant wind at that time was from west and north, while back trajectory analysis showed air mass transport consistently from the continent. The increased concentrations of nss-K^+ ions (with the highest value reaching up to 580 ng/m^3), along with the rather high OC levels, point towards biomass burning and may be related to residential emissions.

As sunlight returns in spring, the solar radiation provides favorable conditions for the enhancement of the reaction of NOx (or HNO_3) and SSA. (Gard et al., 1998) observed that such active heterogeneous chemical reactions primarily occurred during the daytime and they completely converted SSA, mostly into $NaNO_3$ particles. At Ny-Ålesund, the all-day-long daytime during the spring period enhanced photochemical activity, consequently resulting in the production of nitric acid that readily reacted with sea-salt particles (Geng et al., 2010). However, during the sampling days of March 2015, the average Na^+/Cl^- ratio was 0.7, near the fresh SSA composition, as in November. Furthermore, it is suggested by Fenger et al. (2013) be originated from frost flowers torn at high wind speeds. Thus, both frost flowers and the marine snow pack near HMO Tiksi can be sources of sea salt.

In the transition period of late spring–early summer, the Arctic front retreats furthest north and the lower Arctic atmosphere is nearly closed off from continental influence (Sharma et al., 2004). This phenomenon is associated with a general trend of EBC concentration decrease from March to June (Fig. 4) and more frequent transport of air masses from the Arctic and Pacific Ocean. In the beginning of the sampling period in May–June 2015 the EBC background was near the detection limit showing extremely clean atmosphere (Fig. 6); at that time air masses arrived from Bereng sea along the coast of East Siberian sea. A BC pollution episode observed on 03.06 may be related to air masses transported from Eastern Siberia, which was covered by numerous fires at that time (Fig. 5b). Fires in Russia typically occur during the springtime snowmelt and may more than double the already high Arctic atmospheric background observed during this season, impacting climate-relevant species, including black carbon and organic aerosols (Warneke et al., 2010). Analysis of the EBC pollution rose indicated that the whole range of EBC concentrations during this sampling period related to the wind direction of the LPI sector, with a frequency of 55% (Fig. 7), including the EBC pollution episode of 130 ng/m^3, which occurred in almost neutral atmosphere (Fig. S5).

During the background conditions period, OC, originating from biogenic and marine activity, was low (~800 ng/m^3). The background aerosol was characterized by a similar pattern of functionalities as observed in September: hydroxyl C OH (3470 cm−1), amino N H/ammonium NH_4^+ (3218 cm^{-1}), carbonyl C O (1710 cm^{-1}), NO_2 (1539 cm^{-1}), NO_3^- (815 $^{cm-1}$), and SO_4^{2-} (681, 588 cm^{-1}) groups with negligible aliphatic compounds (Fig. S2). The EBC pollution episode observed on 03.06 was related with significant increase of aliphatic C C H (2908–2841 cm^{-1}) and SO_4^{2-} (704 cm^{-1}). The aerosol chemical composition during this period suggests impact from the both LPI sector (adjacent Tiksi urban area) and LRT, since alkanes are associated with dominant functionalities of diesel emissions (Popovicheva et al., 2017b).

The EBC variability during June 2016 showed frequently repeated episodes of increased concentrations (Fig. 4). The wind direction during the sampling period varied between west and north-east, with the LPI sector displaying the highest frequency (around 30%; Fig. S4). The variability of EBC concentrations was quite well related to the atmosphere stratification (Fig. S5). Air masses arrived from the arctic region on days of increased EBC; on 07.06, when the highest EBC concentration was recorded, air masses were transported through the Eurasian coast from western Siberia and Yamal peninsula, where numerous fires were observed (Fig. 5b). A descent of air masses from 3.5 km altitude was observed. It is worth noting that chemical compounds released by large fires may be injected into the atmosphere up to altitudes of several kilometers (Trentmann et al., 2006). The significant impact from biomass burning during this period is further supported by high OC concentrations (2.83 and 2.44 μg/m^3 on 04–05.06 and 07–8.06, respectively). The photochemical aging processes during long-range transport of fire plumes, such as condensation of semi-volatile organic compounds, tend to further increase OC concentrations in the plumes (Konovalov et al., 2015). The OC polluted aerosol displayed much higher abundance of acid and non-acid (1719 cm^{-1}) functional groups in carboxylic acids and ketones, respectively (by 4 times with respect to alkanes) (Fig. S2). In addition to carboxylic acid groups, non-acidic carbonyls (functional marker of forest fire emissions) were found and were assigned to aldehyde/ketone, ester/lactone, and acid anhydride groups (Hawkins and Russell, 2010). During the period of OC and EBC pollution, a prominent aromatic C C band at 1594 cm^{-1} was also observed, which may be related to local emission sources (diesel transport emissions and shipping). The BC pollution episode of the highest EBC, up to 170 ng/m^3, happened when north-east wind (50–100°) was blowing from the Tiksi area and the harbour location (Fig. 1); therefore we should also emphasize the potential impact from shipping emissions.

At the Ny-Alesund station, the spring-to-summer switch was confirmed by the reduction of the seasonal average of the nss-SO_2^{4-} concentrations by 91% (Bazzano et al., 2015). A similar trend is observed during our summer sampling periods. Sulfate concentrations averaged over the whole sampling periods of May–June 2015 and June 2016 were decreased by 82 and 87% in comparison with the maximum concentrations observed in March 2015. SO_4^{2-} no longer dominated the ion composition; sea salts, potassium, nitrates, ammonium, and calcium made up most of the aerosol inorganic mass in early summer. During the days of June 2016 with high OC levels, K^+ concentrations were also found elevated, confirming the strong influence of wildfires on the local aerosol burden.

Sampling period of June 2016 was different from 2015 by a rapid change of aerosol chemistry related to strong EBC variations almost each day. OC was found as high as of semi-volatile organic compounds tend to increase OC in particulate matter (Konovalov et al., 2015). Much higher abundance of acid and non-acid (1719 cm^{-1}) functional groups in carboxylic acids and ketones, respectively, is distinguished by 4 times with respect to alkanes in OC polluted aerosols (Fig. S2). Non-acidic carbonyls in addition to carboxylic acid groups were found as the functional marker of forest fire emissions and were assigned to aldehyde/ketone, ester/lactone, and acid anhydride groups (Hawkins and Russell, 2010). Specific spectral absorption observed during those days when OC pollution correlates with highly increased EBC is prominent aromatic C C bands at 1594 cm^{-1}, respectively, which is related to diesel transport emission as well as shipping in local sources.

At Ny-Alesund station the presence of spring-to-summer switch was confirmed by the reduction of the seasonal average of the nss-SO_2^{4-} daily concentrations by 91% (Bazzano et al., 2015). The similar trend is observed during our yearly summer sampling periods. In May–June 2015 and June 2016 mass concentrations of sulfates averaged over the sampling period were decreased by 82 and 87% in comparison with maximum observed in March 2015. SO_4^{2-} ions no more dominate the ion composition, sea salts, potassium, nitrates, ammonium, and calcium make up the aerosol inorganic mass in early summer. In days of high OC K^+ ions approached 302 ng/m^3, confirming the strong influence of wildfires on the local aerosol burden.

4. CONCLUSIONS

The long-time gap in aerosol observations in the Siberian Arctic strongly limited the estimations of rapid climate forcing. This work provides the opportunity in quantification of East Siberian Arctic background and black carbon polluted aerosols, the source and season impacts on their concentrations and composition done by comprehensive characterization of aerosol optical and physico-chemical properties. It is shown that the Hydrometeorological Observatory (HMO) Tiksi surrounded by the Arctic Ocean from one side and by the continent from other side, is affected by both marine, biogenic and anthropogenic sources from lower latitudes as well as influenced by local emissions. EBC time series analysis during two years of observations indicates that EBC concentrations undergo the frequent variations imposed upon the seasonal trends. Aerosol sampling of one-three days better resolves the irregular episodes of increased EBC which bring the extensive amount of pollutants to arctic aerosols. Chemical characterization of aerosols performed at HMO Tiksi is highly valuable for evaluation of episodes of increased EBC as the events of anthropogeneous pollution due to long-range air mass transport from lower latitudes in Siberia and emissions from adjacent urban area. Focus on source-dependent aerosol characteristics during EBC pollution episodes combined with the analyses of wind direction and air mass transportation allows the quantification of the pollution with respect to background. Since the times for sampling campaigns were arbitrary we can put the observations of the background and BC pollution episodes in the context of the long-term BC variability and conclude that two year EBC monitoring at the HMO Tiksi in September shows quite well repeatability with respect to relatively frequent pollution events, thus giving us the opportunity to analyze both the background arctic aerosols and polluted ones from the point of view of the increased BC concentration.

In September, the major components of background aerosols are characterized by low EBC, alkanes, carboxylic acids/ketones, aminocompounds, and saccharides, as well as organic and inorganic sulfates, sea salts, and windblown dust. The reason for a lack of Cl^- is the chemical transformation of sea-salt in the atmosphere polluted by nitrogen oxides. High sulfate concentrations in September originate from biological activity near the coast of Laptev sea and secondary sulfate formation. Increased mass concentrations of EBC and SO_4^{2-} indicate the combustion emission, in accordance with the abundance of aliphatic and carbonyls as functional markers of urban and industrial sources identified by the long-range air masses transport from gas flaring, industrial, and residential regions in Western Siberia, Krasnoyarsk Krai, and Central Yakutia. Ionic markers for waste burning PO43−, K^+, and Cl^- support the identification of the Tiksi city landfill plumes carrying the hazardous compounds. Reproduction of high OC concentrations in September of both 2014, 2015, and 2016 years demonstrates that municipal waste burning could be an intensive local source of atmospheric pollution at the HMO Tiksi.

Elevated EBC, sulfates, and OC during the winter and spring are a result of the intensification of meridional transport from the midlatitudes to the Arctic as well as of high stability of the atmospheric surface layer leading to the increase of both the background and pollution level. Organic aerosols of the Arctic Haze are composed almost from carboxylic acid and alkanes indicating that not only mass concentrations are enhanced within the Arctic troposphere but also aerosol chemistry is changing under long-range air mass transportation from low latitudes. In early summer, less pollutant transport into the Arctic decrease the mass concentrations of EBC and sulfates almost to the level of early autumn. However, wildfire events in Siberia impact to increased OC dominated by highly-oxidized acid compounds. BC pollution episodes are connected with local emissions originating in industrial, traffic, and harbour activities indicated by markers of diesel transport and shipping emissions.

This study firstly quantifies the BC-polluted aerosols during sampling periods at the HMO Tiksi by comprehensive analyses of atmospheric particle chemistry combined with meteorological parameter, stratification of the boundary layer and air mass transportation. It is supported by the identification of source-specific chemical, functional and ionic markers and increases the state of scientific understanding for aerosol/climate interactions and dangerous impacts on climate. Therefore, further strategy for understanding, documenting, and identifying the local and regional origin of Arctic air pollution episodes in the vastly understudied Siberian Arctic should be developed. Although at present there are few high Arctic sources of BC, emissions are expected to grow due to increased human activity in the Arctic, therefore demanding special attention to the local sources of pollution.

Aerosol carbonaceous, elemental and ionic composition variability and origin at the Siberian High Arctic, Cape Baranova*

1. INTRODUCTION

The Arctic is the most sensitive region in the world with respect to temperature increases and the climatic effects of air pollution (Shindell and Faluvegi, Citation2009). Ice melting is accelerated when carbonaceous particles are deposited on snow and ice surfaces, reducing surface albedo, and leading to a temperature-albedo feedback that amplifies Arctic warming (Dou et al., Citation2012; Jacobi et al., Citation2019; Stone et al., Citation2014). Aerosol particles are major climate forcers in the Arctic, as they scatter and absorb incoming solar radiation, modify clouds properties and affect surface albedo (Shindell and Faluvegi, Citation2009). The chemical composition of aerosols is an important parameter that defines their impact on climate, as various chemical components have different global warming potential (Breider et al., Citation2017). Most of the absorption of radiation by accumulation-mode aerosol is due to black carbon (BC), which also influences cloud radiative properties (Yun et al., Citation2013).

BC is a very important contributor to global warming, having a contribution equal to about two thirds of that from carbon dioxide (Bond et al., Citation2004; Khan et al., Citation2012). Originating from local and regional fossil fuel and biofuel combustion sources, in addition to natural and anthropogenic biomass burning, it is emitted and transported together with organic carbon (OC) (Stohl et al., Citation2013; Wang et al., Citation2011) and exerts a warming effect that contrasts the cooling effect of sulfates through scattering and induced cloud formation.

Arctic Haze is a phenomenon that was first reported in 1950s but it took almost 20 years for scientists to realize that the haze was pollution transported to the Arctic region from middle latitudes (Barrie, Citation1986). The Arctic Haze is a mixture of sulfate and particulate organic matter and to a lesser extent ammonium, nitrate, BC, trace metal and dust aerosols (Law and Stohl, Citation2007) and has an important impact on optical properties (Zanatta et al., Citation2018). The Arctic Haze has a seasonal cycle (Eleftheriadis et al., Citation2009) with a maximum in late winter and early spring. This is due to more frequent poleward atmospheric transport of pollution from the mid-latitudes to the Arctic in winter and spring, on one hand, and to the expansion of the polar vortex southwards, on the other (Klonecki, Citation2003; Sharma et al., Citation2013, Stone et al., Citation2014). Furthermore, the boundary layer is shallower in winter, enhancing BC concentrations at low altitudes, which may then be mixed to the surface (Sharma et al., Citation2013).

The AMAP (Arctic Monitoring Assesement Programme) assessment includes observation results from six Arctic stations, including Alert (82.45°N, 62.52°W), Barrow (71.32°N, 156.6°W), Summit (72.60°N, 38.42°W), Zeppelin (78.91°N, 11.88°E), Pallas (67.97°N, 24.12°E) and Station Nord (81°36’N,16°39’W) (AMAP, Citation2015). These Arctic stations record aerosol optical properties and provide concentrations of aerosol components (Schmeisser et al., Citation2018; Uttal et al., 2016). Such studies have significantly expanded our knowledge about BC and OC pollution into the Arctic (Chang et al., Citation2011; Nguyen et al., Citation2013; Stohl et al., Citation2007).

Long-range pollution transport to the Arctic is known to carry aerosol compounds that can be used as tracers of anthropogenic activities and wildfires, and help to identify the regions of pollutant origin (Frossard et al., Citation2014; Koch et al., 2009; Warneke et al., Citation2010). According to results from previous studies in the region (Tiksi station, Russian high Arctic), the isotope-constrained source apportionment pinpoint that biomass burning sources dominate during low BC concentration periods in summer, whereas fossil sources sources mostly prevail during the Arctic Haze season (Winiger et al., Citation2017). In many studies, statistical trajectory methods such as potential source contribution function (PSCF) (Chang et al., Citation2011; Polissar et al., Citation1998) and concentration weight trajectories (CWT) (Hsu et al., Citation2003) have been used in combination with aerosol data to identify potential source areas. Transport, industry, gas flaring, and residential emissions have been found to be responsible for anthropogenic BC and OC in the Arctic (Popovicheva et al., Citation2017a; Stohl et al., Citation2013; Wang et al., Citation2011). The source-related chemical composition of Arctic aerosols are still poorly represented in models having for a long time struggled to capture the distribution of aerosol characteristics. This is due to difficulties in simulating aerosol removal processes, missing emission sources or incorrect spatiotemporal distribution of emissions in the inventories (Huang et al., Citation2015; Schacht et al., Citation2019).

In the Siberian high Arctic, the knowledge of the aerosol chemical composition has poor spatiotemporal coverage, due to the small number of monitoring sites and logistical difficulties associated with these sites. Recently, a few BC measurements were performed in the Siberian Arctic, mostly from field campaigns over the Arctic (Popovicheva et al., Citation2017a; Sakerin et al., Citation2015; Stohl et al., Citation2013), and from the drifting station “North Pole” (Stock et al., Citation2012). Model validation has been benefited from observations performed in the proximity of the major industrial sources (Popovicheva et al., Citation2017a). The only station reporting results for long-term BC (Eckhardt et al., 2015), aerosol number density and size distribution (Asmi et al., Citation2016), and aerosol composition (ions, OC, EC) measurements (Popovicheva et al., Citation2019) is the Hydrometeorological Observatory (HMO) Tiksi (71.36 N; 128.53E) station, located in the East Northern Siberia on the coast of the Laptev Sea. The extensive knowledge about aerosol chemical components in the Siberian high Arctic provides valuable information about the seasonal variability, trends, and sources that affect air quality in this part of the Arctic region.

The research station “Ice Base Cape Baranova” is newly developed at the cape Baranova, Bolshevik Is-

---

* M. Manousakas , O. Popovicheva , N. Evangeliou , E. Diapouli , N. Sitnikov , N. Shonija & K. Eleftheriadis // TELLUS SERIES B-CHEMICAL AND PHYSICAL METEOROLOGY.2020;72 1-14 DOI: 10.1080/16000889.2020.1803708

land, at the Severnaya Zemlya archipelago (79.16 N; 101.45E). It is located at the same latitude as Ny-Ålesund station of Spitsbergen archipelago, but is closer to the BC source regions of Eurasia. In this work, results from a comprehensive characterization of aerosol composition and the geographical origin of PM sources are reported for this station. Carbonaceous, elemental, and ionic composition, were determined during 2015–2016. Statistical Trajectory Methods (STMs) were used to identify the main transport pathways of aerosols providing a better understanding of the origin of aerosol pollution in the Siberian High Arctic.

2. SAMPLING AND ANALYSIS

2.1. Sampling site

The research station "Ice Base Cape Baranova" is located on the coast (at sea level) of the Shokal Strait, which divides Bolshevik and Oktiabrskay Revolution islands of the Severnya Zemlya Archipelago (Fig. 1). The area adjacent to the station is characterized by a wide range of natural sea ice (drifting and soldering), lake and river origin, powerful (up to 800 m) dome-shaped glaciers and numerous icebergs. This area has a pronounced landscape of polar desert. The polar night and day last from October 22 to February 22 and from April 22 to August 22, respectively. The air temperature in summer (June-August) is from 0 to 4°C. In winter (October–April) temperatures range from −25° to − 45°C. The area is characterized by stable winds mainly from the southern direction with an average speed of 10–15 m/s, which during the transition periods of the year can reach 50 m/s. The prevailing wind is southwest.

For atmospheric composition observations and sampling, the aerosol pavilion was purposely built approximately 1 km southeastst from the main station (Fig. 1). The basic meteorological parameters, such as wind speed, wind direction, temperature, relative humidity, and pressure were obtained every 1 hour by the station weather service. Also, the major advantage of this station is its location far from any local anthropogenic sources. For instance, previous research has shown significant impact of local sources on measurements performed on the HMO Tiksi station (Popovicheva et al., Citation2019).

2.2. Aerosol light absorbing carbon measurements

Highly time resolved measurements of the aerosol absorption coeffient were obtained from 18/10/15 to 5/4/16 by operating a portable aethalometer. It was purposely designed by the Moscow State University (MSU)/Central Aerological Observatory (CAO) and was used in a number of previous campaigns (Popovicheva et al., Citation2017a, Citation2017b). In this instrument, light attenuation caused by the particles depositing on a quartz fiber filter is measured at three wavelengths (450, 550, and 650 nm). In previous studies eBC concentrations were determined by converting the time-resolved light attenuation to eBC mass using the 650 nm channel and characterized by a specific mean mass attenuation coefficient as described elsewhere (Popovicheva et al., Citation2017a). Calibration of eBC was performed during parallel long-term measurements against an AE33 aethalometer (Magee Scientific) that operates at seven wavelengths, three of them identical with the MSU unit. As the principle of operation for the two instruments is the same, with the exception of the improved compensation regarding the loading effect offered by the AE33 (Drinovec et al., Citation2015), data analysis from this AE33 calibration experiment can be also adjusted to provide the scheme of calculation for the absorption coefficient (σ0). In any case the loading effect can be disregarded for the longest wavelength output reported here and the low arctic BC loadings. The multiple scattering factor Cref is a parameter required for data processing and conversion to absorption coefficents. It has been determined for the arctic aerosol close to 3.5 in a previous study and can be adjusted to 2.5 given the already incorporated factor in the AE33 (Backman et al., Citation2017). The attenuation coefficient batn is defined as:

$$b_{atn} = A\,(m^2)\cdot\delta ATN/V\,(m^3) \qquad (1)$$

where A is the filter exposed area, V is the volume of air sampled, and δATN is the light attenuation defined as follows:

$$\delta ATN=\ln(Io/I) \qquad (2)$$

where Io and I is the light intensity transmitted through unexposed and exposed parts of the filter, respectively.

Fig. 1. Geographical location of «Ice Base Cape Baranova station» on the Bolshevik Island (http://globalcryospherewatch.org) (left panel), and aerosol pavilion (right panel).

A good linear correlation between the attenuation coefficient batn and A σ0 calculated by the AE33 aethalometer (at 660 nm) was achieved (R2 = 0.92). This allowed estimating the absorption coefficientas follows:

$$\sigma_0(Mm^{-1})=1.32 \times 10^3 \cdot A\ (m^2).\delta ATN/V\ (m^3) \qquad (3)$$

where 1.32 × 10^3 is the correction factor that includes the appropriate Cref factor for arctic aerosol.

The data retrieved from the aethalometer were post-processed in order to remove outlier values. A value is considered as an outlier if it exceeds its previous value in the time-series by more than 3 times the standard deviation of the last 10 values. If this criterion was met, then the value was removed from the dataset. With this approach, extremely high concentrations that do not follow the general trend and can be attributed to local contamination (e.g., from diesel generators operating at the station) were removed. The outliers were less than 5% of the total number of values for every season. Data screening/cleaning is a standard procedure in Arctic stations. For example, monitoring data from Barrow and Alert are routinely cleaned, while Zeppelin measurements are generally not strongly influenced by local emission sources (AMAP, Citation2015; Eckhardt et al., Citation2013).

2.3. Aerosol sample collection

An 18-month campaign was conducted from April 2015 to December 2016. Particles of mean aerodynamic diameter less than 10 µm (PM_{10}) were collected using the Comde Derenda sampling system with 2.3 m^3 per hour pumped airflow. The sampling time was 48-72 hours per sample depending on the season, atmospheric particulate loading, and weather conditions. Sampling volume was corrected to standard atmosphere conditions (0 °C, 1 atm). Teflon and quartz filters, heated prior to their use at 500 °C for 6 h, were used for elemental and ionic/carbon analyses. In total, 120 samples were collected and analyzed.

To determine whether samples had been affected by local emissions from the station diesel generator, polar plots and wind roses were also analyzed. In general, EC is expected to have the highest local influence, due to the use of diesel generators operating in the nearby monitoring station settlement, as it has been previously seen (Popovicheva et al., Citation2019). Fig. 2 shows the CPF (Conditional Probability Function) for EC. Even though winds from the NW sector (location of the station settlement) are not infrequent, no significantly high EC concentrations were observed from that location.

2.4. Off-line aerosol chemical characterization

Bulk composition of collected samples were analyzed with a number of analytical tools. For the elemental analysis of PM_{10} samples, the high energy, polarization geometry energy dispersive XRF spectrometer Epsilon 5 by PANalytical was used. Epsilon 5 is constructed with optimized Cartesian-triaxial geometry composing of several secondary targets for attaining lower spectral background and with extended K line excitation provided by the capability to operate the X-ray tube at the maximum high voltage of 100 kV. The secondary target-XRF spectrometer includes a side-window low power X-ray tube with a W/Sc anode (spot size 1.8–2.1 cm, 100 kV max voltage, 6 mA current, 600 W maximum power consumption). The characteristic X-rays emitted from the sample are detected by a Ge X-ray detector with 140 eV FWHM at MnKα, 30 mm^2 and 5 mm thick Ge crystal with 8 µm Be window. The used spectrometer is equipped with eight secondary targets (Al, CaF_2, Fe, Ge, Zr, Mo, Al_2O_3, KBr and LaB_6) that can polarize the X-ray tube generated incident radiation through the Barkla scattering. The methodology that was used for the elemental composition analysis is described in detail elsewhere (Manousakas

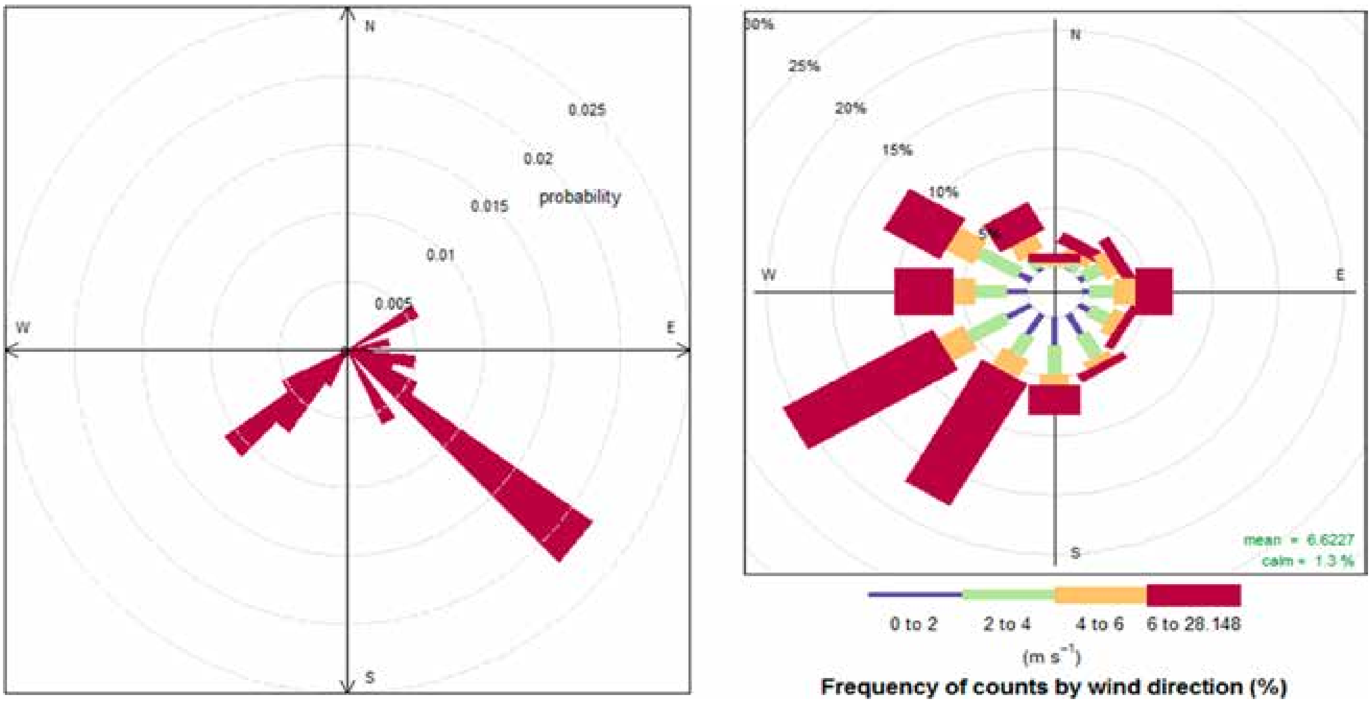

Fig. 2. Left: CPF for the 95th percentile for EC. Right: Wind rose for the study period.

et al., Citation2018). The 20 elements determined by the ED-XRF method were Na, Mg, Al, Si, S, Cl, K, Ca, Ti, V, Cr, Mn, Fe, Co, Ni, Cu, Zn, Br, Sr, and Pb, but only 5 of them were found in a concentration higher than the detection limit (Na, S, Cl, Ca, Fe).

Carbon fractions were measured by thermo-optical transmittance (TOT) analysis (Lab OC-EC Aerosol Analyzer, Sunsett Laboratory, Inc.) (Diapouli et al., Citation2017). Quartz filter samples were heated up to 650 °C in He, at first, and then up to 850 °C in a mixture of 2% O_2 in He, using the controlled heating ramps of the EUSAAR_2 thermal protocol (Cavalli et al., Citation2010). This protocol has been initially developed for regional background sites. Organic carbon (OC) evolved in the inert atmosphere, while elemental carbon (EC) was oxidized in the He-O_2 atmosphere. Charring correction was applied by monitoring the sample transmittance throughout the heating process. The limit of detection (LOD) for the TOT analysis is 0.2 μg C cm^{-2}. Before sampling, the quartz fiber filters were pre-treated at 500 °C for 6 h to re- move possible OC contaminations. Lab and field blanks were prepared and run following the same procedures as adopted for the samples. The QA/QC procedures described in EN 16909:2017 were followed during TOT analysis.

Water-soluble ion components were measured by capillary electrophoresis using the Capel 103 system (Lumex) with the UF detection, as described elsewhere (Popovicheva et al., Citation2017b). One quarter of the sample was extracted in 5 ml of distilled water by ultrasonic agitation for 45 min, and then the extract was filtered. Inorganic anions and cations were measured in aqueous extracts with a relative standard deviation of 10%.

2.5. Atmospheric transport modelling

To accurately investigate the possible origin of the observed particles, the Lagrangian particle dispersion model FLEXPART (FLEXible PARTicle dispersion model) version 10.4 was used (Pisso et al., Citation2019). The model was driven with 3-hourly operational meteorological analyses from the European Centre for Medium-Range Weather Forecasts (ECMWF) with 137 vertical layers and a horizontal resolution of 1°×1°. Computational particles were released from Ice Cape Baranova station and were tracked 30 days back in time in FLEXPART's so-called "retroplume" mode, which is a sufficient time to include most aerosol emissions arriving at the station, given a typical aerosol lifetime (~1 week).

The tracking includes gravitational settling characteristics for spherical particles of the size observed. FLEXPART differs from trajectory models due to its ability to simulate dry and wet deposition of gases or aerosols (Grythe et al., Citation2017), turbulence (Cassiani et al., Citation2015), unresolved mesoscale motions (Stohl et al., Citation2005) and includes a deep convection scheme (Forster et al., Citation2007). The model output consists of an emission sensitivity, which is a quantitative measure for the particle mass concentration at the sampling location that would result from a unit emission flux at the Earth's surface. The emission sensitivity can also be interpreted as a probability distribution field of the particle's origin. We used it here to identify possible source regions of particles, as described in the previous section.

2.6. Potential source contribution function analysis

To identify the spatial origin of the aerosol components, the Potential Source Contributions Function (PSCF) was used in combination with FLEXPART emission sensitivities. PSCF calculates the probability of a source region to be located at a certain latitude and longitude. The basis of PSCF is that if a source is located at (i,j), an air parcel passing through that location indicates that material from the source can be collected and transported along the trajectory to the receptor site. PSCF is given by the following the equation:

$$PSCF=m_{ij}n_{ij} \qquad (4)$$

where n_{ij} is the number of times that the trajectories passed through the cell (i,j) and m_{ij} is the number of times that a source concentration was high when the trajectories passed through the cell (i,j). The criterion for determining mij is controlled by percentiles. In the present study, the 70th percentile was used for PSCF calculation.

3. RESULTS AND DISCUSSION

3.1. Absorption coefficients and black carbon

The 3-hourly Absorption coefficients during the period of our study ranged from 0.01 to 3.05 Mm^{-1} (Fig. 3). The highest monthly averaged Absorption coefficients were observed in January (1.01 ± 0.70 Mm^{-1}) and the lowest ones in April and October (0.39 ± 0.36 Mm^{-1}). Absorption coefficient measurements were used together with the EC data to estimate the MAC for this Arctic site. MAC was calculated at 650 nm wavelengtgh equal to 4.12 m^2/g. This rather low values are in line with the expected range of values for bare BC particles as we are

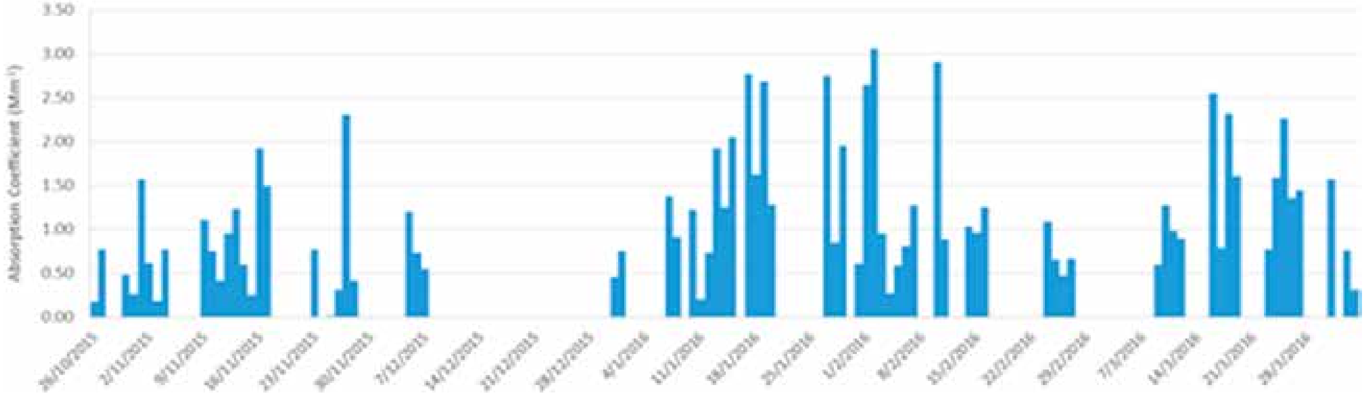

Fig. 3. Time series of 3 h average aerosol Absorption coefficient (Mm^{-1}) at the wavelength of 650 nm.

using the EC concentration for the calculation, as described in Zanatta et al., (2018).

Using the calculated MAC value with the Absorption coefficients, eBC was estimated to compare the data with the available information of BC concentrations in the Arctic. In general, Arctic BC shows peak concentrations during winter and early spring months, due to the Arctic Haze phenomenon (Stone et al., Citation2014). The average 3-hourly eBC concentrations during the period of our study was 139 ± 120 ng/m^3. Similarly to Absorption coefficients, eBC variation shows that the highest monthly averaged concentrations were observed in January (245 ± 169 ng/m^3) and the lowest ones in April and October (94.6 ± 87.4 ng/m^3). The climatology of atmospheric transport from surrounding regions has shown that Arctic stations are highly sensitive to high-latitude emissions from Eurasia (Eleftheriadis et al., Citation2009; Popovicheva et al., Citation2019; Sharma et al., Citation2004). This is in good agreement with the winter seasonal trend of Arctic aerosol concentrations reported by Eleftheriadis et al. (Citation2009), who measured an average annual concentration of 39 ng/m^3, and an average wintertime concentration of 300 ng/m^3 in Ny-Ålesund. Furthermore, the mean eBC concentration at HMO Tiksi during winter was found equal to 187 ± 38 and 127 ± 28 ng/m^3 in 2014–2015 and 2015–2016, respectively (Popovicheva et al., Citation2019). eBC concentrations during winter at Ice Base Cape Baranova and HMO Tiksi stations are high compared with respective levels observed at Alert (100 ± 65 ng/m^3) (Sharma et al., Citation2004) or any other of the Arctic stations. For instance, eBC concentrations at Alert, Barrow, Zeppelin and Summit show monthly median concentrations of 20–80 ng/m^3 in late winter/early spring and <10 ng/m^3 in summer/early autumn (AMAP, Citation2015). Seasonal variation of eBC concentrations was weaker at the southernmost Pallas station, where summer concentrations were double reflecting a decrease in the seasonal minimum with latitude. This finding leads to the conclusion that the Ice Base Cape Baranova station is significantly influenced by emissions from high-latitude sources of Siberia.

To capture the origin of the air masses ariving at this station and, in turn, the potential sources, PSCF analysis for eBC was performed (Fig. 4). PSCF probability is enhanced over the gas flaring regions (shown as red dots in Fig. 4) of (Khanty-Mansiysk Okrug, Nenets-Komi, and Yamal- Nenetzk Okrug Peninsula) and Kazakhstan, where BC emissions are high. Gas flaring is reported to be the major source of BC in Siberian Arctic having a contribution of 36.2%, followed by residential emissions, transportation, industry, and power plants, that contribute 25.0%, 20.3%, 13.1%, and 5.4%, respectively (Huang et al., Citation2015). Based on an estimate of the BC emission from flaring, up to 12% of the total BC emissions from the Arctic Council nations in 2000, primarily originates from northern part of Siberia (AMAP,

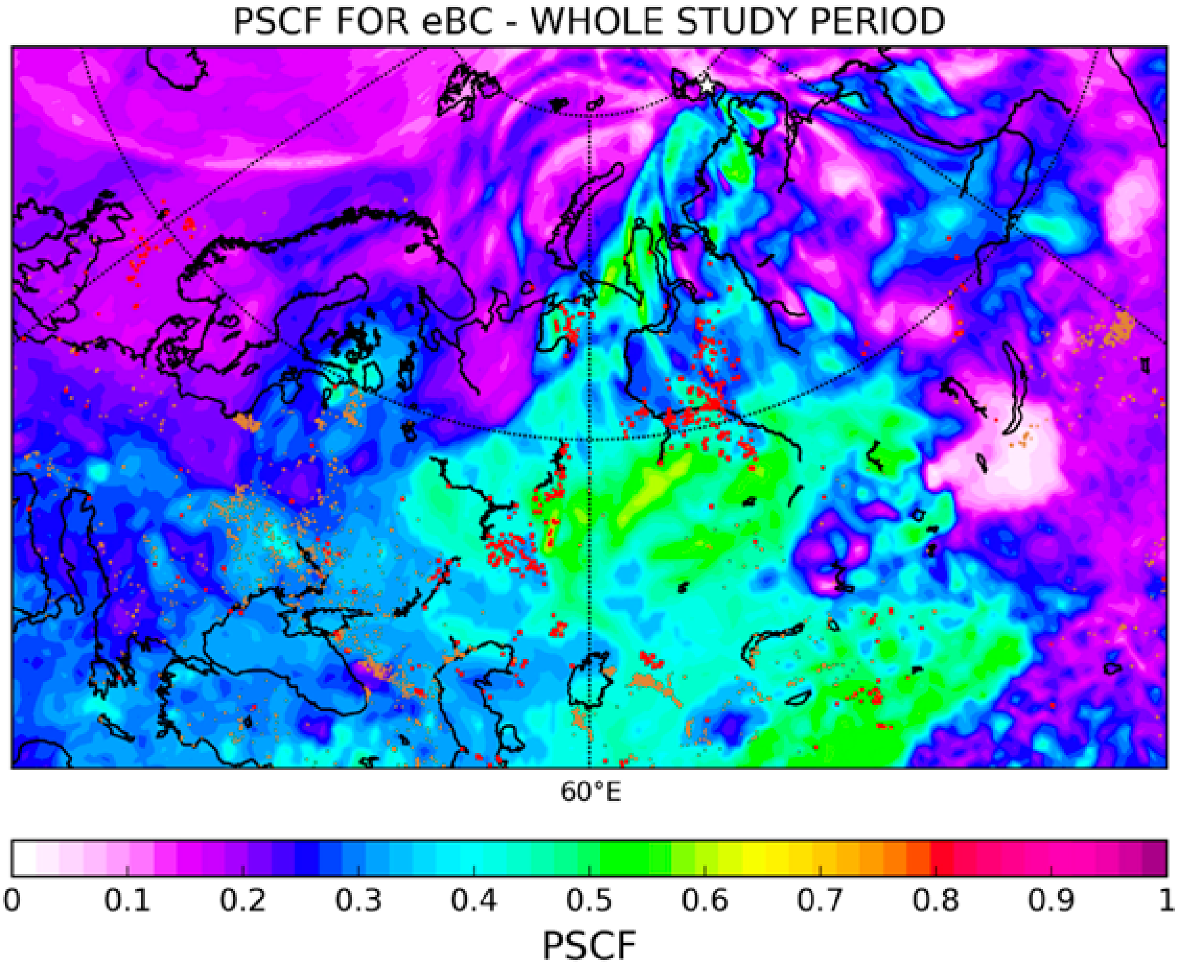

Fig. 4. PSCF analysis for eBC. The red dots in the map represent the gas flaring regions from the Global Gas Flaring Reduction Partnership (GGFR), http://www.worldbank.org/en/programs/gasflaringreduction) while the brown dots represent active fires from MODIS (Giglio et al., Citation2003).

Citation2015). It is noteworthy that biomass burning emissions are not expected to have large contribution on eBC concentrations in Ice Cape Baranova, because eBC measurements took place from November to April only, when forest fire activity in boreal regions is limited. This is also proved by MODIS active fires (brown dots), which were plotted in Fig. 4 for the measurement period, and are shown to be limited in mid-latitudes. Other potential sources that may contribute to eBC concentrations in this high Arctic station are inhabited and industrial regions of Siberia, as well as north China and Kazakhstan. One of the possible transport patterns of aerosols to the Arctic from lower latitudes is a 10–15 day low level transport of already cold air masses into the polar dome, which is associated with further diabatic cooling (Stohl, Citation2006). The transport patterns intensify the climatic risk of BC with respect to its ability to act as light absorbing impurity when deposited on snow and ice surfaces (Shindell and Faluvegi, Citation2009).

3.2. Organic carbon and elemental carbon

Organic carbon (OC) accounts for a significant fraction of the Arctic aerosol masses (Chang et al., Citation2011). OC tends to be elevated, due to biogenic emissions and secondary aerosol formation from biogenic volatile organic compounds, wind-induced bubbles bursting from the sea surface (Frossard et al., Citation2014), fossil fuel combustion (Barrett et al., Citation2015) as well as biomass burning (agricultural and wildfires) (Stohl et al., Citation2007; Warneke et al., Citation2010). The descriptive statistics of PM10 size mode EC/OC measured in Ice Base Cape Baranova station are presented in Table 1 for the whole study period and per season. The average concentration of OC for the sampling period was estimated as 677 ± 322 ng/m^3 and is dominant over other aerosol compounds, with a maximum in winter (760 ± 398 ng/ m^3).

Fig. 5. shows time-serie concentrations of OC, with maxima of up to 1400 ng/m3 in January. For comparison, OC concentrations at the HMO Tiksi have been found as high as 2300 ng/m^3 in winter-spring followed by a decreasing trend in summer-autumn, which is in agreement with typical seasonal trends of Arctic aerosols (Popovicheva et al., Citation2019). However, OC concentrations were found to be higher in September (up to 3600 ng/ m3), while some high OC values were also recorded during June 2016. These peak concentrations of OC were observed during periods when Arctic aerosol levels are expected to be low and are likely attributed to local OC pollution.

The average concentration of EC was estimated to be 82.0 ± 70.0 ng/m^3 in winter (maximum: 142 ± 120 ng/m^3) (Table 1). EC concentrations were higher than those from other Arctic stations (AMAP, Citation2015) and comparable with those reported by Popovicheva et al., Citation2017a. Popovicheva et al. (Citation2017a) measured

Table 1. Descriptive statistics (average, stdev, min, max) for EC and OC in ng/m^3 per season (Winter: Dec-Feb, Spring: Mar-May, Summer: Jun-Aug, Autumn: Sep-Nov).

	Winter (DJF)		Spring (MAM)		Summer (JJA)		Autumn (SON)	
	OC	EC	OC	EC	OC	EC	OC	EC
Aver	760	142	702	60.6	688	67.6	637	80.1
STDEV	398	112	177	50.4	251	71.9	375	61.1
MIN	322	10.4	397	0.70	381	1.30	187	0.0
MAX	1520	357	1040	186	1230	249	1390	172

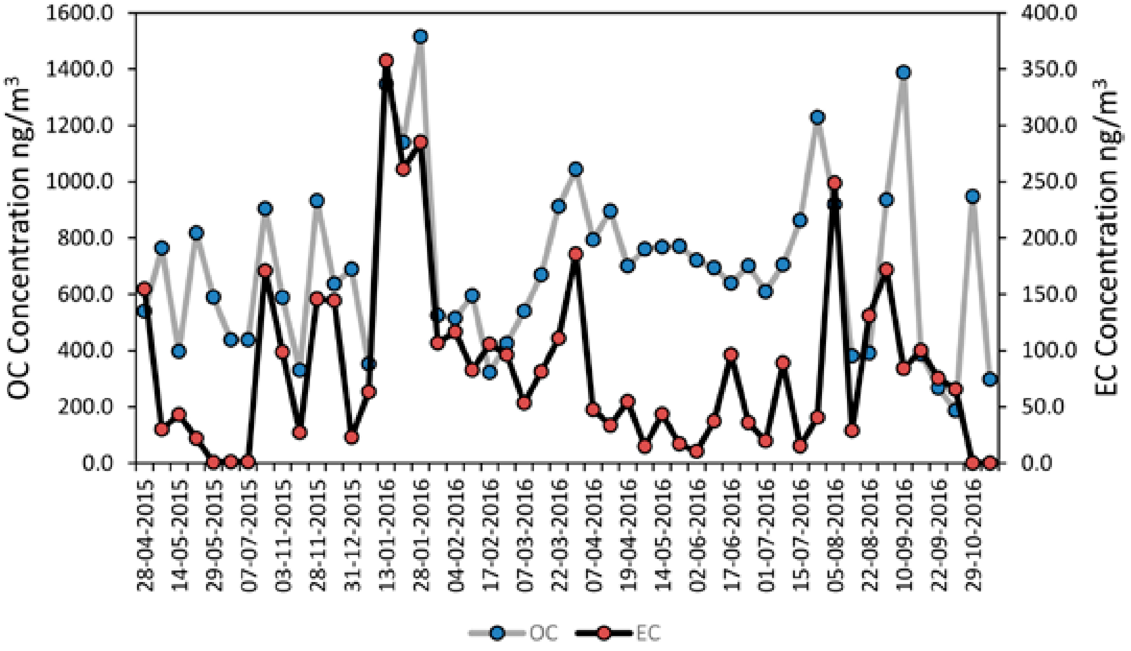

Fig. 5. Time series of EC and OC in ng/m^3 (EC correspond to secondary axis).

eBC concentrations of the order of 200–400 ng/m^3 during a research ship cruise in the White, Barents and Kara seas, north of the region characterized by high flaring emissions. The seasonal variation of EC concentrations is more pronounced than for OC showing large peaks attributed to haze events in January followed by significantly lower concentrations in the next month (Fig. 5), although sporadic maxima were present. The average OC/EC ratio was found equal to 12. High OC/EC ratios are typical for natural background sites; they result from high OC concentrations (due to biogenic emissions and secondary organic aerosol formation) coupled with negligible EC concentrations (due to minimum anthropogenic activities, and specifically combustion sources) (Popovicheva et al., Citation2019).

The PSCF analysis for EC and OC is presented in Fig. 6. High PSCFs of continental origin were observed for EC and OC (Fig. 6). As shown in previous studies (Fu et al., Citation2009, Citation2013), primary organic aerosols from biogenic emissions, due to long-range transport, sea-to-air emission of marine organics, and photooxidation of biogenic VOCs, are important factors controlling the organic chemical composition of marine aerosols in the Arctic. This shows that while EC is transported to Arctic regions, OC might be formed as secondary product when solar activity is higher.

The characteristic contribution from the industrial and gas-flaring sources (red dots) of Northern Siberia (Nenets-Komi, Yamal-Nenetz Okrug, peninsula and Khanty-Mansiysk Okrug) is also shown for all seasons both for EC and OC. As mentioned in the previous section for eBC, gas-flaring is of major importance in the Arctic region (Eckhardt et al., 2015; Stohl et al., Citation2013). Even though EC is higher during winter, it is not negligible during spring as well. This might be due to biomass burning emissions (brown dots), as these emissions has been found to contribute 36% to total BC with the highest peaks occurring in late spring and summer months (Hyvärinen et al., Citation2011). EC concentrations in Ice Cape Baranova are mainly affected by nearby industrial sources in winter and from forest fires and other European and Asian sources during the other seasons, as maximum observed PSCF regions have shifted further south (Fig. 6). OC shows similar maxima as for EC indicating large impact from the Northern Siberian flaring regions throughout the whole year, as these sources are more or less constant (Klimont et al., Citation2017).

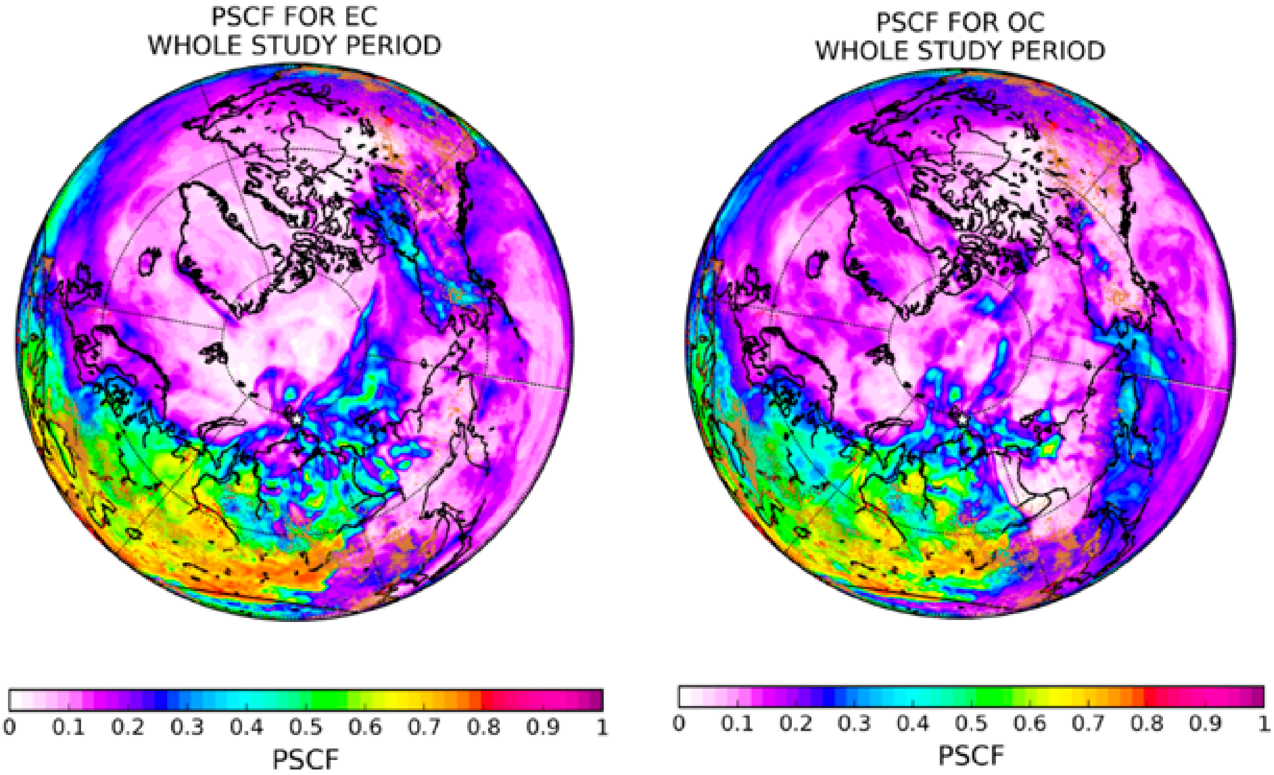

Fig. 6. PSCF analysis for EC and OC. The red dots in the map represent the gas flaring regions from (Global Gas Flaring Reduction Partnership (GGFR), http://www.worldbank.org/en/programs/gasflaringreduction) while the brown dots represent active forest fires from MODIS (Giglio et al., Citation2003).

3.3. Ionic and elemental composition

Long-term surface measurements indicate that aerosols in the North American, Norwegian, Finnish and Russian Arctic mainly consist of sulfates and to a lesser extent of organics, ammonium, nitrates, and BC during the spring months (March and April) (Quinn et al., Citation2007). Sulfates may originate from biological activity, such as oxidation of dimethyl sulfide. High sulfate concentrations are related to transport from regional sources and secondary sulfates from continental regions (Eckhardt et al., 2015). Sulfates designate the distinct temporal pattern of the Arctic Haze defining whether or not the observed concentration in the sampling site have been affected by long-range transport.

Table 2 presents the ionic and elemental composition of aerosols observed in the Ice Base Cape Baranova station from April 2015 to December 2016. The av-

Table 2. Average concentrations ± standard deviation of measured PM components (ions and elements) in ng/m^3 from April 2015 to December 2016 (Warm: summer, Cold: winter, spring).

Specie	Total	Warm	Cold	Specie	Total	Warm	Cold
K^+	170 ± 155	192 ± 159	146 ± 97	$SO_4{}^{2-}$	390 ± 370	184 ± 170	603 ± 462
Na^+	270 ± 255	257 ± 189	291 ± 232	$NO_3{}^-$	62.7 ± 25	0	62.7 ± 36.3
$NH4^+$	160 ± 150	99.0 ± 90.0	252 ± 240	Na	90.7 ± 56.0	130 ± 76.8	69.2 ± 17.1
Mg^{2+}	65.0 ± 33.0	62.0 ± 280	68.0 ± 33.0	S	151 ± 124	133 ± 120	172 ± 138
Ca^{2+}	300 ± 268	333 ± 271	251 ± 217	Cl	113 ± 58.0	58.6 ± 51.1	135 ± 130
Cl^-	230 ± 220	173 ± 91	322 ± 286	Ca	93.5 ± 71.1	151.7 ± 71.1	10 ± 6.70
				Fe	11.2 ± 4.50	16.8 ± 6.4	6.7 ± 2.14

erage concentration of sulfates was 390 ± 290 ng/m^3 for the whole study period. Sulfates were also observed to present high seasonality with an average concentration of 603 ± 462 ng/m^3 during winter and 184 ± 170 ng/m^3 during summer.

Sulfates present a moderate Pearson correlation with $NH_4{}^+$ and $NO_3{}^-$ (0.58 and 0.56 respectively), which indicates that they are influenced by regional sources of secondary aerosol formation and transport. To evaluate whether H_2SO_4 was neutralized by ammonia or not, the correlation between $NH_4{}^+$ and $SO_4{}^{2-}$ was examined showing an R^2 of 0.58, which indicates no neutralisation. However, the aforementioned correlation might be misleading, as $SO_4{}^{2-}$ can also have sea and crustal origin (Udisti et al., Citation2016).

Cl^- and Na^+ also present relatively high concentrations at the station, with average concentrations of 270 ± 255 and 230 ± 220 ng/m^3 respectively (Table 2); similar concentrations were reported by (Sakerin et al., 2019) at the same region. Cl^-, Na^+, K^+ and Mg^{2+} were correlated moderately (~ 0.6), while the average Na^+/Cl^- ratio was estimated as 1.1, which indicates that both ions originate from locally formed sea spray. According to reported results from other Russian high Arctic stations (e.g., HMO Tiksi), Cl depletion can also be important in the region (Popovicheva et al., Citation2019).

To estimate the anthropogenic origin of sulfates, the non-sea salt, non-crustal part of $SO_4{}^{2-}$ was calculated following the methodology described in (Becagli et al., Citation2012; Udisti et al., Citation2016). The concentrations of total (tot), sea-salt (ss) and non-sea salts (nss) Ca^{2+} and Na^+ were calculated using the following four equations:

$$_{tot}Na^+ = {}_{ss}Na^+ + {}_{nss}Na^+ \tag{5}$$

$$_{tot}Ca^{+2} = {}_{ss}Ca^{2+} + {}_{nss}Ca^{2+} \tag{6}$$

$$0.562 \times {}_{nss}Ca^{2+} = {}_{nss}Na^+ \tag{7}$$

$$_{ss}Ca^{2+} = 0.038 \times {}_{ss}Na^+ \tag{8}$$

where 0.562 represents the Na^+/Ca^{2+} weight-to-weight (w/w) ratio in the crust, and 0.038 is the Ca^{2+}/Na^+ w/w ratio in seawater.

$$ssSO_4{}^{2-} = 0.253 \times ssNa^+ \tag{9}$$

(accordingtow/wratioinseawater)

$$_{cr}SO_4{}^{2-} -= 0.590 \times {}_{nss}Ca^{2+} \tag{10}$$

(accordingtow/wratioinuppercrust)

The non-sea salt, non-crustal ($_{nss\text{-}ncr}SO_4{}^{2-}$) was calculated as the difference between $_{tot}SO_4{}^{2-}$ and $_{ss}SO_4{}^{2-}$ and $_{cr}SO_4{}^{2-}$. The ratio of $_{nss\text{-}ncr}SO_4{}^{2-}/{}_{tot}SO_4{}^{2-}$ was found higher than 0.8 during the cold season indicating anthropogenic origin of $SO_4{}^{2-}$, while during the warm season $_{nss\text{-}ncr}SO_4{}^{2-}$ was in most cases equal to zero, indicating that $SO_4{}^{2-}$ is mainly affected by natural sources.

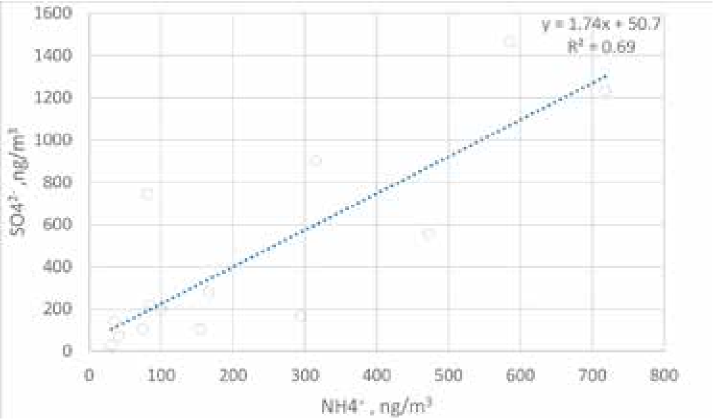

Fig. 7. Correlation between $_{nss\text{-}ncr}SO_4{}^{2-}$ and $NH_4{}^+$ for the cold season.

The correlation between $_{nss\text{-}ncr}SO_4{}^{2-}$ and $NH_4{}^+$ for the cold season is presented in Figure 7. The correlation coefficient was calculated equal to 0.70 indicating that H_2SO_4 is neutralized by NH_3. Considering that $_{nss\text{-}ncr}SO_4{}^{2-}/{}_{tot}SO_4{}^{2-}$ ratio is highly dependent on the season (close to unity during the cold season), it can be used as an indicator of the anthropogenic origin of the aerosol particles.

As regards to the observed elemental composition (Table 2), S presents the highest average concentration (151 ± 124 ng/m^3) followed by Na and Cl (90.7 ± 56.0 and 113 ± 78.0 ng/m^3) and Ca (93.5 ± 71.1 ng/m^3). The Na/Cl ratio was calculated to be almost 1 indicating the sea origin of those elements in combination with low Cl depletion (Cesari et al., Citation2016). Elements of crustal origin, such as Ca and Fe, present much higher concentrations during the warm season, due to dust resuspension and lower in wintertime, when snow cover does not allow this process.

The reconstructed PM_{10} mass was calculated for the warm (summer, autumn) and the cold (winter, spring) periods of the year. Mass reconstruction was based on the carbonaceous, ionic and elemental composition of the PM samples. The average reconstructed PM_{10} concentration for the cold season was calculated equal to 2.83 ± 2.20 μg/m^3 and 2.05 ± 1.81 μg/m^3 in the warm season. The average reconstructed PM_{10} mass concentration was 38% higher during the cold season of the year. PM_{10}

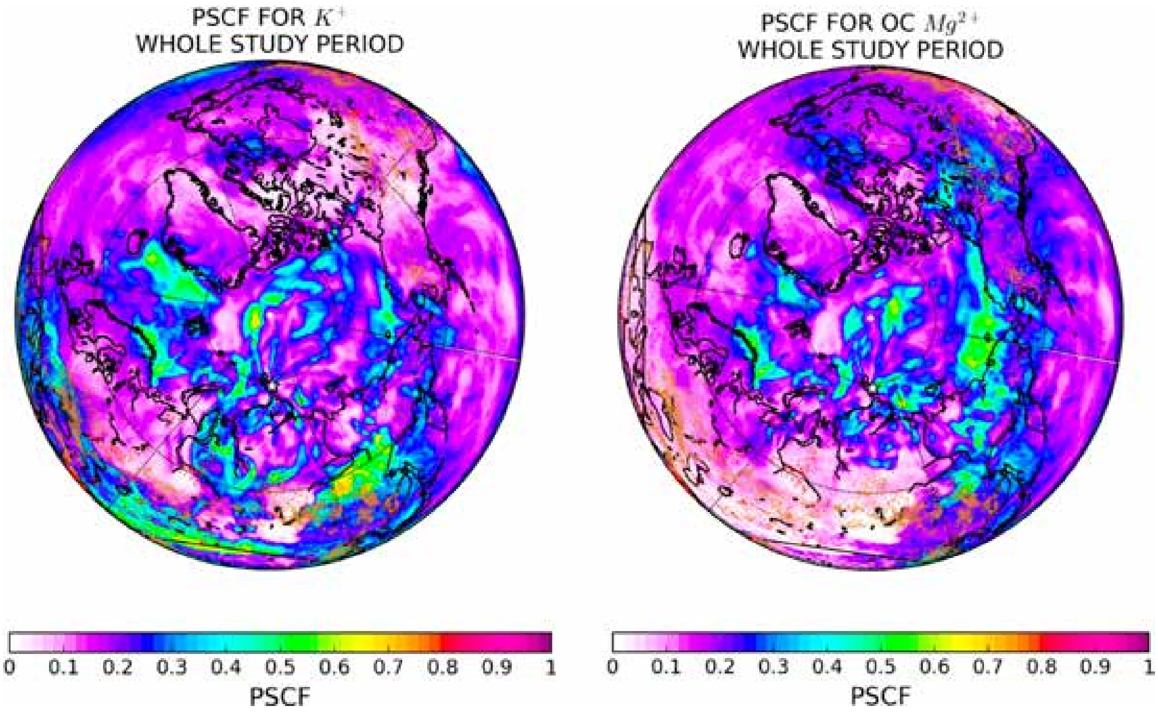

Fig. 8. PSCF analysis for K^+, Mg^{2+}, SO_4^{2-} and NH_4^+. The red dots in the map represent the gas flaring regions from (Global Gas Flaring Reduction Partnership (GGFR), http://www.worldbank.org/en/programs/gasflaringreduction) while the brown dots represent active forest fires from MODIS (Giglio et al., Citation2003).

concentrations were comparable with those reported in PM_{15} at Sevettijarvi (2.9 μg/m^3 in winter and 3.9 μg/m^3 in summer) (Laakso et al., Citation2003 and references within).

The PSCF analysis for K^+, Mg^{2+}, SO_4^{2-} and NH_4^+ is depicted in Figure 8. The source contribution analysis for SO_4^{2-} and NH_4^+ reveals that their main origin is rather continental similar to EC. Regarding the K^+ and Mg^{2+}, their main origin is sea related emissions, while it is apparent that their concentrations are also affected by forest fires.

4. SUMMARY

Chemical composition analysis of aerosols at the research station “Ice Base Cape Baranova” reveals respective levels and seasonality of the PM components. The average concentration of OC was estimated to be 677 ± 322 ng/m^3 and was dominant among other aerosol compounds with a maximum in winter (760 ± 398 ng/m^3). The average concentration of EC was 82 ± 70 ng/m^3, and it reached 142 ± 120 ng/m^3 in wintertime. High EC concentrations in winter and early spring were related with continental origin. Regarding EC and OC, gas flaring and wildfires regions were identified as the most important contributors of EC at the station.

The highest monthly averaged Absorption coefficients were observed in January (1.01 ± 0.70 Mm−1) and the lowest ones in April and October (0.39 ± 0.36 Mm−1). Absorption coefficient measurements were used together with the EC data to estimate the MAC for this Arctic site. MAC was calculated equal to 4.12 m2/g. Accordingly, the eBC variation shows the highest monthly averaged concentrations observed in January (245 ± 169 ng/m^3) and the lowest ones in April and October (94.6 ± 87.4 ng/ m^3), in agreement with the winter seasonal trends of eBC concentrations in other Arctic stations. PSCF analysis for continuous eBC measurements showed that air masses coming from the gas flaring regions of Russia are associated with the highest eBC concentrations. Other important source locations are the inhabited/industrial regions of Siberia, as well as north China and Kazakhstan.

For SO_4^{2-}, the seasonal patterns are very distinct, with very low transport during summer as seen by the respective footprint emission probabilities. Further analysis showed influence from anthropogenic sources in winter and from natural sources in summer. K^+ and Mg^{2+} concentrations originate from sea-salt in winter and from forest fires in summer.

The dominant ion during winter is SO_4^{2-} and has an average concentration of 390 ± 290 ng/m^3 for the study period. The average Na^+/Cl^- ratio was estimated as 1.1, which leads to the conclusion that Cl^- depletion is very low, and both ions have a distinct origin from the locally formed sea spray.

The ratio of $_{\text{nss-ncr}}SO_4^{2-}/_{\text{tot}}SO_4^{2-}$ was found higher than 0.8 during the cold season, indicating the anthropogenic origin of SO_4^{2-}, while during the warm season nss-ncrSO_4^{2-} is in most cases equal to zero indicating that SO_4^{2-} is mainly (but not exclusively) affected by natural sources. The nss-ncrSO_4^{2-}/totSO_4^{2-} ratio appears to be highly dependent on the season being very close to unity during the cold season, when the transportation of anthropogenic particles is dominant; this ratio can be used as an indicator of the anthropogenic origin of the aerosol particles.

The present study provides, for the first time, quantitative information about several PM components and their respective geographical location of the prevailing sources in a Russian high region, where measurements lack. The chemical characterization of aerosol samples collected in the Ice Cape Baranova station and the identification of the spatial origin of the species is important and will assist researchers in understanding the factors that affect the aerosol concentrations in he high Arctic.

Black Carbon Sources Constrained by Observations in the Russian High Arctic*

1. INTRODUCTION

Short-lived climate forcers are aerosols and gases that cause radiative forcing (1, 2) and have lifetimes of less than a few years. (3, 4) Light-absorbing aerosols are of particular interest because they have a warming effect that is strongest over highly reflective surfaces (e.g., clouds, snow, and ice). (5) Furthermore, their deposition on snow and ice decreases surface albedo, which can enhance melting (6, 7) and trigger surface warming. Most of the radiation absorption of accumulation-mode aerosol is due to black carbon (BC). (8) BC also influences cloud radiative properties. (9, 10) BC originates from incomplete combustion, e.g., of biomass or fossil fuels. (1, 11) Freshly emitted BC is hydrophobic but aging in the atmosphere changes its properties to a more-hydrophilic state. (12) It is an important constituent in Arctic Haze, a phenomenon that is primarily the result of long-range pollution transport from sources outside the Arctic. (5, 7, 13, 14) The majority of the Arctic BC originates from anthropogenic sources, especially industrial applications, residential combustion, and diesel transportation activities, (15) while other important sources include fires in boreal forests and agricultural regions especially from spring to fall. (16-18)

Near the surface, about 50% of the BC north of 60° N originates from Russia, (19) where emission inventory data are highly uncertain. (20) Emissions from flaring of gas associated with oil production are prone to particularly high uncertainty because both activity data and emission factors are largely lacking. According to the Global Gas Flaring Reduction Partnership (GGFR) (http://www.worldbank.org/en/programs/gasflaringreduction), nearly 50 billion m3 of gas are flared in Russia annually. The Russian flaring emissions in the Yamal and Khanty-Mansiysk regions are directly within the major low-altitude pathway of sub-Arctic air masses penetrating into the Arctic, (16) and thus, Stohl et al. (21) estimated that they contribute about 42% of the annual average BC surface concentrations in the Arctic.

However, limited measurements are available that would enable the constraining of this particular source of BC in the Russian Arctic. For instance, in the whole Russian territory north of 50° N, continuous measurements of equivalent BC (EBC) are performed only at Tiksi station (71.36° N; 128.53° E), (22, 23) which is far from the major industrial sources in Russia. Based on isotope measurements, one recent observational study (24) suggests that the contribution of gas flaring emissions to BC at Tiksi is lower than estimated by Stohl et al. (21) However, new bottom-up inventories (25, 26) contain gas-flaring emissions that are even higher than those used by Stohl et al. (19) For the clarification of the role of gas-flaring emissions, any EBC measurements from regions closer to the oil production facilities of Russia would be extremely valuable. In these regions, BC has been measured only with low time resolution during a few ship campaigns. (21, 27-29) However, to relate such measurements to particular source regions, measurements with high time resolution are necessary. In a comparison with the few available observations, modeled BC concentrations were found to be too low, (21) but a comprehensive analysis was not possible because of the low time resolution of these measurements.

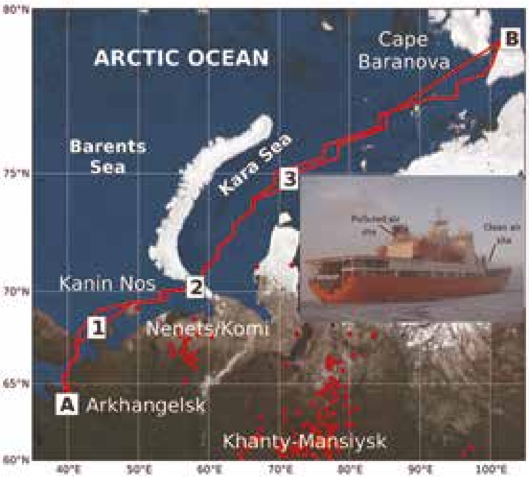

In the present study, we report highly time-resolved EBC concentrations measured during the "Sever-2015" expedition through the White Sea, Barents Sea, and Kara Sea in October 2015. We compare the EBC measurements recorded during the cruise with predicted BC concentrations simulated with a Lagrangian particle dispersion model (LPDM). Furthermore, we investigate and quantify the origin of the BC observed during the cruise using modeling results coupled with the most recent emission inventory for BC. This is done to assess how the oil and gas industrial emissions in high northern latitudes affect Arctic BC.

2. METHODOLOGY

2.1 Expedition and Analysis of Equivalent Black Carbon

The expedition "Sever-2015" was carried out onboard the research vessel "Akademik Treshnikov" of the Russian Arctic and Antarctic Research Institute from October 9 to 25, 2015. The ship is the modern vessel of RMRS (Russian Maritime Register of Shipping, class notation KM Arc7AUT2), and it uses three propulsion WÄRTSILÄ diesel four-stroke engines with 600 rpm. The ship track in the Arctic Ocean and the research vessel are shown in Figure S1, together with the main gas-flaring

---

* Olga B. Popovicheva,† Nikolaos Evangeliou, Konstantinos Eleftheriadis, Athina C. Kalogridis, Nikolay Sitnikov, Sabine Eckhardt, and Andreas Stohl // Environmental Science and Technology.2017: 51: c3871-3879 DOI 10.1021/acs.est.6b05832

facilities. The cruise started on October 10 from the port of Arkhangelsk (64.58° N, 40.50° E; point A on the map) and continued through the delta of the Dvina river toward the White Sea and Kanin Nos (point 1 in Figure S 1) in the Barents Sea. Next, it passed the Kara Strait (point 2 in Figure S1) and the Kara Sea until it reached the archipelago Severnaya Zemlya (79.35° N, 101.83° E; point B). After a stay of 2 days near the research station "Ice Base Cape Baranova" on the Bolshevik Island (from October 15 to 17 2015), the ship turned back. A storm forced the ship to moor in the Kara Sea (point 3 in Figure S1) from October 19 to 21 before it could continue its return journey to Arkhangelsk, where it arrived on October 25. Meteorological data (temperature, apparent wind speed, and direction) during the cruise were obtained from the Vaisala maritime observation system MAWS-420. Real wind direction and speed was estimated from the aforementioned data. Surface air temperature, pressure, and wind data are shown in Figure S 2, respectively.

Aerosol EBC concentrations were determined continuously using an aethalometer purposely designed by the Moscow State University (MSU) and Central Aerological Observatory (CAO) for ship campaigns. In this instrument, light attenuation caused by the particles depositing on a quartz fiber filter is measured at three wavelengths (450, 550, and 650 nm). The light-attenuation coefficient of the collected aerosol was calculated with the method of Hansen and Rosen. (30) EBC concentrations were determined continuously by converting the time-resolved light attenuation to the EBC mass corresponding to the same attenuation and characterized by a specific mean mass attenuation coefficient. This calibration parameter was derived during parallel long-term measurements against an AE33 aethalometer (Magee Scientific) that operates at the same three wavelengths (450, 550, and 650 nm).

Attenuation coefficient b_{atn} is defined as

$$b_{atn} = A\ (m^2)\cdot\delta\ ATN/V\ (m^3) \qquad (1)$$

where A is the filter exposed area, V is the volume of air sampled, and δATN is the light attenuation defined as follows:

$$\delta\ ATN = \ln(I_o/I) \qquad (2)$$

where I_o and I is the light intensity transmitted through unexposed and exposed arts of the filter, respectively. Good linear correlation between the aethalometer's attenuation coefficient batn and the EBC concentrations calculated with the AE33 aethalometer (at 660 nm) was achieved (R2 = 0.92; see Figure S3). This allowed the estimation of EBC mass concentrations using the regression slope and intercept between batn at 650 nm and EBC of the AE33 aethalometer at 660 nm:

$$EBC\ (ngm^{-3}) = 3.3 \times 10^5 \cdot A\ (m^2)\cdot\delta\ ATN/V\ (m^3) \qquad (3)$$

where 3.3 × 105 is the correction factor that includes the specific mass absorption coefficient for the MSU aethalometer calibrated against the AE33 aethalometer assuming the mass absorption cross-section (MAC) adopted by AE33 equal to 9.89 $m^2\ g^{-1}$. (31) The uncertainty of EBC measurements from both aethalometers depends on the accuracy of the MAC value used for the conversion of the light-absorption coefficient to mass concentration. The constant MAC value adopted here is an approximation, assuming a uniform state of mixing for BC in atmospheric aerosol. This can be considered a valid assumption in the case of background aerosol measurements performed in this study. Absolute uncertainties of the reported MAC values remain as high as 30–70% due to the lack of appropriate reference methods and calibration materials. (32)

The level of uncertainty (1-σ) of EBC measurements was 30 ng m^{-3} for a 6 min integration time. Aethalometer filters were changed manually at the latest when ATN values approached 70, but at most times, filters were changed at lower values. During rough and wet weather conditions, water droplets or sea spray affected the measurements adding higher noise to the recorded ATN signal. These short data periods were either excluded from the data set or, where possible, treated manually by establishing an adjusted baseline for the reference ATN values.

To identify the cleanest location on the vessel (i.e., the spot least influenced by the ship exhaust), particulate mass (PM) concentration was measured on all decks of the vessel using a TSI DustTrak 8530 monitor. The best site for ambient aerosol monitoring was identified to be at the foredeck, where the aethalometer was placed, while the spot most affected by the exhaust pipe was found at about 10 m on the upper bridge (Figure S 1). A second aethalometer of exactly the same type was therefore installed at this location to record potential impact from ship pollution. EBC concentrations from the two aethalometers were compared and the absence of contamination on the foredeck, where the aethalometer was placed (clean air site), was assured. When the apparent wind was blowing from the back of the vessel toward the clean air site on the foredeck, all aethalometer data were removed from further analysis. For instance, such contamination might have occurred when the ship moored near point 3 (Figure S1) during the storm event, and therefore, these measurements were removed from the data set.

2.2 Emissions and Modeling of Black Carbon

The concentrations of BC were simulated with version 10 of the flexible particle dispersion model (LPDM FLEXPART). (33, 34) The model was driven with operational meteorological analyses every 3 h from the European Centre for Medium-Range Weather Forecasts (ECMWF). The ECMWF data had 137 vertical levels and a horizontal resolution of 1° × 1°. Computational particles released from the measurement locations were tracked back in time in FLEXPART's "retroplume" mode. (35) Simulations extended over 30 days back in time, sufficient to include most aerosol emissions arriving at the station, given a typical BC lifetime (~1 week). This enabled the identification of where the measured BC came from and allowed the quantification of BC source contributions. The source contributions can also be displayed as a function of the time elapsed since the emission has occurred (i.e., "age"), which can be shown as "age spectrum" consisting of stacked bars, where a bar's color indicates the contribution of a certain age bin (0–1 days, 1–2 days...29–30 days) (see Figure 1b). FLEXPART simulations were performed every hour during the cruise, with particles released from small boxes covering the latitude and longitude ranges of the ship track during the hour. The FLEXPART retroplumes consist of an emission sensitivity (often also called source-receptor relationship), which yields a simulated concentration in

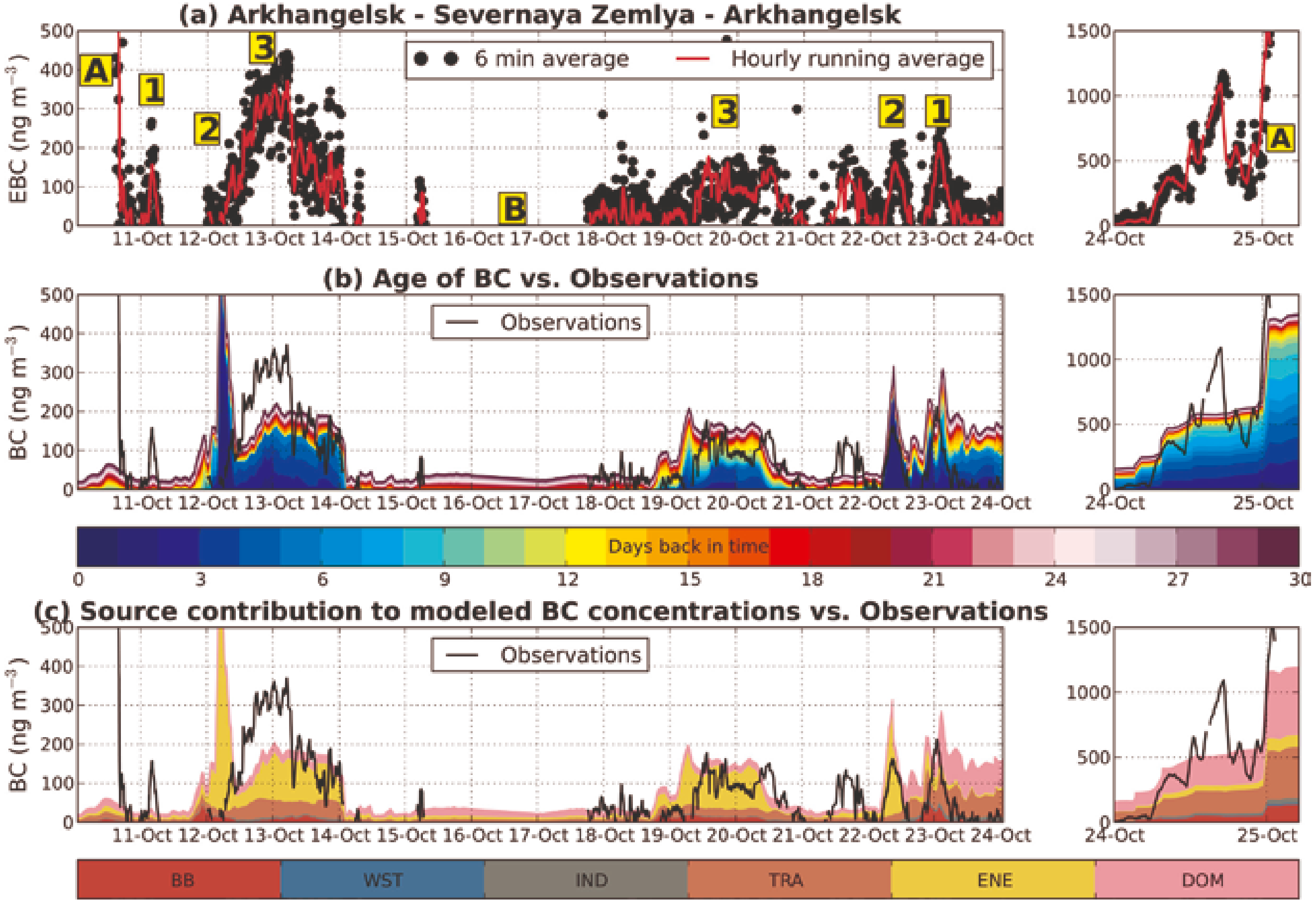

Figure 1. (a) Time series of equivalent black carbon (EBC) mass concentrations during the expedition cruise. Numbers and letters in red brackets show geographical names during the cruise according to Figure S1. (b) Age spectra of modeled BC (colors) from all possible sources showing the contribution of emissions each day back in time to the surface concentration of BC. Hourly means of measured BC concentrations are shown as a black line. (c) Contribution from different emission source types to the BC surface concentrations. The emission sources of biomass burning (BB); waste burning (WST); industrial combustion and processing (IND); surface transportation (TRA); power plants, energy conversion, and extraction (ENE); and residential and commercial (DOM) have been adopted from GFEDv3.1 and ECLIPSE inventories. (36, 37) Notice that the different scale used in all three panels from October 24th to the 25th, when measured and modeled concentrations were much higher than for the rest of the cruise. Flaring emissions are included in the energy sector (ENE).

the receptor box when multiplied with gridded emissions from an inventory.

Emission fluxes were taken from the "Evaluating the CLimate and Air Quality ImPacts of ShortlivEd Pollutants" (ECLIPSE) version 5 emission data set,36 which is available from the Web site of the International Institute for Applied Systems Analysis (IIASA) (http://www.iiasa.ac.at/web/home/research/ researchPrograms/air/Global_emissions.html). This inventory is appropriate for use in our study, as it accounts for BC emissions from gas flaring from the main emitting facilities located west of Yamal Peninsula (Komi and Nenets distinct) and in Khanty-Mansiysk (south of Yamal Peninsula).21 Biomass burning (BB) sources (namely forest, peat, savanna, woodland fires, and deforestation) were adopted from the Global Fire Emissions Database version 3 (GFED v3.1).[37] With regard to anthropogenic sources, it includes industrial combustion and processes sector (IND) emissions from combustion happening in industrial boilers as well as emissions from industrial production processes. Residential and commercial sector (DOM) includes emissions from combustion in heating and cooking stoves and boilers in households and public and commercial buildings like malls, hospitals, and schools. The waste treatment and disposal sector (WST) includes emissions from waste incineration and the treatment process. The transport sector (TRA) includes emissions from all land-based transport of goods, animals and persons on road networks as well as off-road activities, e.g., on railroads, agricultural and forest lands, and construction sites. Shipping in in-land waters and domestic aviation are also included in this sector, but international shipping and aviation are treated as separate sectors. Finally, energy production and distribution sector (ENE) includes emissions from combustion processes in power plants and generators and emission related to distribution of energy to consumers, as well as emissions from gas flaring in oil facilities.

For our simulations, we assumed that BC has a density of 2000 kg m^{-3} and follows a logarithmic size distribution with an aerodynamic mean diameter of 0.25 μm and a logarithmic standard deviation of 0.3. Each computational particle released in FLEXPART represents an aerosol population with a lognormal size distribution.34 This treatment of aerosol size distribution allows the simulation of several different types of particles, each with its own size distribution. Removal processes acting differently for the different particle sizes will then affect specific particle sizes. Assumed aerodynamic mean diameter and logarithmic standard deviation are used by FLEXPART's dry deposition scheme, which is based on the resistance analogy,[38] and they are consistent with those used in other transport models.[18,39] Below-cloud scavenging was determined based on the precipitation rate taken from ECMWF. The incloud scavenging was based on cloud liquid water and ice content, precipitation rate, and cloud depth from ECMWF.40 The FLEXPART user manual (available from http://www. flexpart.eu) provides more information on FLEXPART's removal parametrizations. All FLEXPART results for the cruise can be viewed interactively at http://niflheim.nilu.no/NikolaosPY/RusArctExp_2015.py.

3. RESULTS AND DISCUSSION

3.1 Onboard EBC Measurements

The EBC concentrations measured during the cruise are shown in Figure 1a. At the beginning of the expedition (October 10, 2015) when the ship was in or near the port of Arkhangelsk (White Sea), high values of EBC were measured (hourly values up to 700 ng m^{-3}), probably due to local pollution. Only after the ship passed the industrial area of the Dvina river delta (October 10, 2015 at 20:30), EBC dropped to below 100 ng m^{-3}. In the open White Sea, EBC was 40 ng m^{-3}, on average, but a small peak (~163 ng m^{-3}) was observed near the Kola Peninsula in the morning of October 11 (06:30). In the basin of the Barents Sea absorption was below the detection limit of the aethalometer, and only in the Pechora Sea (West of Kara Strait) on October 12 (06:30) did EBC concentrations rise above the minimum detection levels again, gradually increasing up to 153 ng m^{-3}. In the Kara Strait EBC was strongly enhanced (~220 ng m^{-3}); concentrations kept increasing in the Kara Sea up to a maximum of 360 ng m^{-3} (Figure 1a), in an area north of strong gas-flaring emissions (see Figure 1 in ref 21). Notice that at remote Arctic stations, measured EBC concentrations are much lower, typically only around 10 ng m^{-3} at this time of the year, (41) which can be considered the typical Arctic background. (42) Hence, EBC values observed in the Barents Sea were relatively close to the background concentrations observed in other parts of the Arctic, whereas in the Kara Sea, EBC concentrations were strongly enhanced compared to this level. It is worth to note that the measured EBC concentrations are comparable to those reported by Stohl et al. (21) of about 200–400 ng m^{-3} during a ship cruise in the Kara Sea in September of 2011.

In the morning of October 13 (07:30), when the ship was in the Eastern Kara Sea, EBC dropped to 100 ng m^{-3} and then varied between 50 and 220 ng m^{-3} until midnight of October 14 before decreasing toward minimum detectable limits until archipelago Severnaya Zemlya. On October 15 (02:50), the ship moored in the Shokalsky's passage near station "Ice Base Cape Baranova" on the Bolshevik Island (Figure S 1) until October 18, when the voyage back to Arkhangelsk started.

On the way back to Arkhangelsk, on the morning of October 18, we observed EBC concentrations reaching around 60 ng m^{-3} (Figure 1a). While these concentrations were lower than those observed on the way to the Bolshevik Island, they are still much higher than the Arctic background. From October 19 at 10:00 to October 21 at 22:00, the ship maneuvered in the central part of the Kara Sea searching for mooring stations. At that time BC varied to about 200 ng m^{-3}. However, due to frequent changes of the ship's course, the ship's exhaust might have been transported to the clean air site (see Figure S1) via complicated pathways. Therefore, enhanced EBC measurements during this period were excluded from further analysis. On October 21, when the vessel continued its voyage to Arkhangelsk, relatively high EBC concentrations were measured, while on October 22 at 18:00, no absorption could be measured. On October 23, the ship passed through the Kara Strait recording EBC concentrations of up to 250 ng m^{-3}. Measured EBC concentrations declined substantially in the Barents Sea until the ship reached the Kola Peninsula, where a small peak was recorded on October 24 at around 6:00. Next, EBC rapidly increased along the Dvina River in the White Sea with a maximum of about 1100 ng m^{-3} on October 24 and 25, 2015. When the ship arrived at the port of Arkhangelsk, EBC concentrations of 1500 ng m^{-3} were measured. Although we initially considered these high EBC concentrations close to the port of Arkhangelsk as local pollution, in the next section, we show that this was actually not the case.

3.2 Analysis of BC Sources Observed during the Expedition

Figure 1b shows the modeled concentrations color-coded according to their age since emission in contrast to the measurements, while in Figure 1c, the modeled concentrations are separated according to the different emission categories. It was already mentioned that the ECLIPSE inventory includes anthropogenic and biomass burning emission sources adopted from GFED v3.1. (36, 37) Flaring emissions dominate the emissions from the energy (ENE) sector south of the Barents and Kara Seas. Generally, the model captured periods with enhanced concentrations (e.g., in the Kara Sea during both the outward and return trip) and such with very low concentrations (e.g., in the Barents Sea) quite well. One exception is the first few hours of the cruise, when FLEXPART retroplumes showed that clean air masses from the Arctic reached the vessel in the port of Arkhangelsk. It is, however, very likely that the high measured EBC concentrations were caused exclusively by local pollution within the port, which cannot be captured by FLEXPART.

In the morning of October 12, FLEXPART strongly overestimated the measured BC concentrations (shortly before the ship passed through the Kara Strait), then underestimated them by about 50% and finally captured them almost exactly in the Kara Sea (October 13). As shown in Figure 1c, the modeled concentrations during this period had a large flaring contribution (ENE in Figure 1c). The measurements during this period thus enable us to constrain the rather uncertain gas-flaring emissions. Before the highest modeled BC peak on October 12, retroplumes arrived straight from the east, with very little influence from the continent. At the time of the model peak, however, the retroplume encountered the northern parts of a strong cyclone centered over the Urals during the previous days. As a consequence, the retroplume turned direction over the Nenets and Komi regions almost exactly where the ECLIPSE inventory places very high gas-flaring emissions, resulting in very high values of the footprint emis-

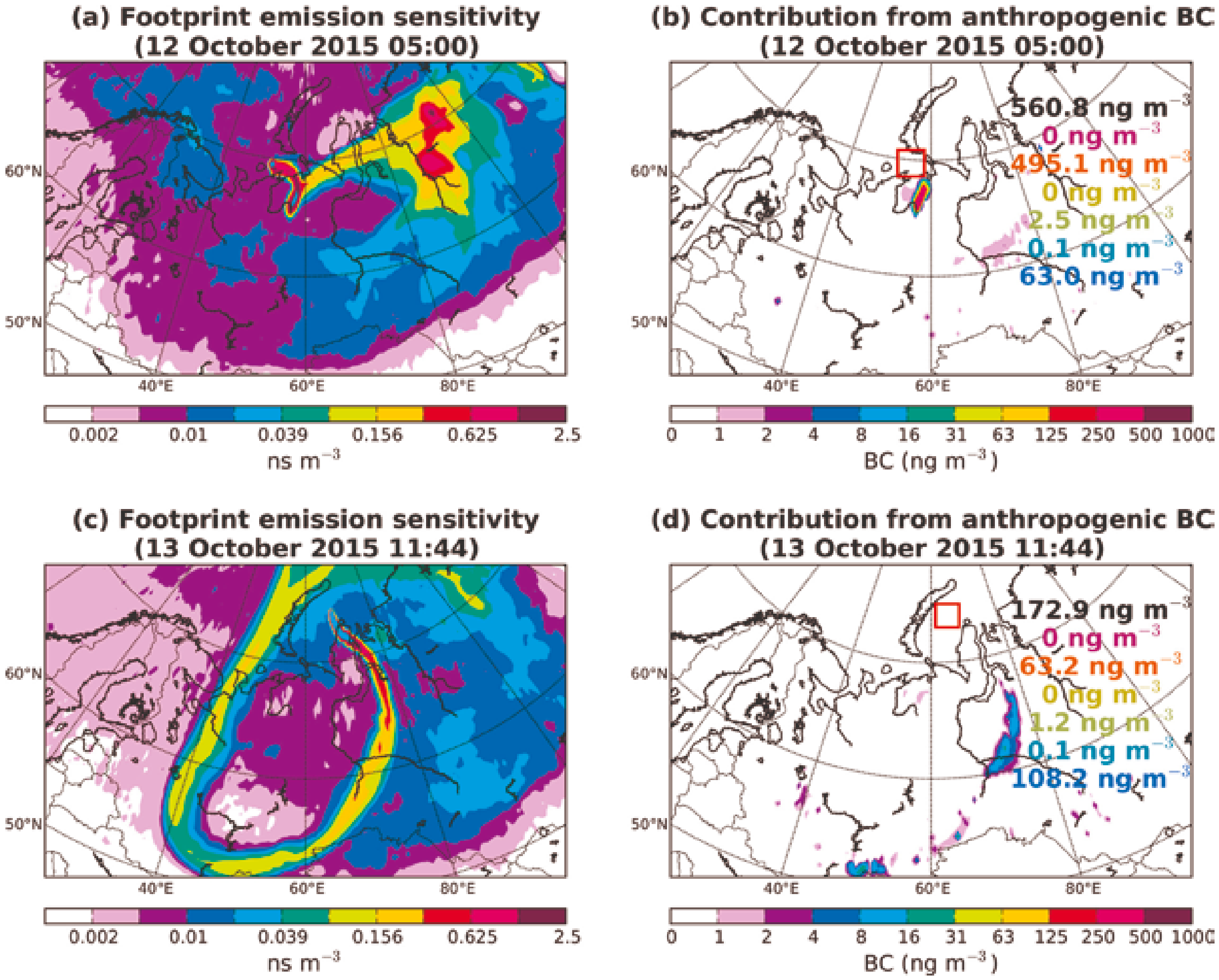

Figure 2. (a) Footprint emission sensitivity and (b) contribution from anthropogenic sources to surface BC concentrations on October 12, 2015 at 05:00. (c) Footprint emission sensitivity and (d) contribution from anthropogenic sources to surface BC concentrations on October 13, 2015 at 11:44. Values written in black report the simulated concentration of BC at the receptor (ship) for the same time period from all anthropogenic sources, while colored ones denote the continental contribution from anthropogenic sources. Magenta areas show contribution from South America, orange from Europe, yellow from Australia, green from North America, cyan from Africa, and blue from Asia

sion sensitivity (Figure 2a) and source contributions (Figure 1c). This complex situation prevailed only for about 3 h. After that, the retroplume circled the whole cyclone and this situation prevailed constantly for more than a day and during the entire passage of the Kara Sea (see Figures 2c and 3d). Based on the above analysis, it is likely that the modeled BC peak on October 12 is a result of the model not capturing the complex meteorological situation accurately enough. Even a small shift in the location of where the retroplume turned (Figure 2a) would have produced much smaller simulated BC concentrations. When the meteorological situation was more stable, the model captured the measured EBC concentrations rather well, especially on October 13, when gas flaring emissions from the Yamal and Khanty-Mansiysk region contributed strongly. This suggests that gas flaring emissions for this region in the ECLIPSE inventory are in the right order of magnitude, perhaps with a slight tendency toward overestimation in the Nenets and Komi regions.

The very small EBC values in the Severnaya Zemlya archipelago were also well captured by FLEXPART (Figure 1b). During this time, the retroplumes showed transport from the Arctic Ocean, with very little influence from land sources. Figure 3a,b depicts FLEXPART daily average emission sensitivities calculated when the vessel arrived to Severnaya Zemlya (October 14, 2015) and when it departed (October 18, 2015). Winds shifted on October 18, with retroplumes arriving again first from southerly directions and thus increasing the potential for BC uptake over the land. Indeed, both measured and modeled BC concentrations increased again on October 18.

On the way back, measured EBC concentrations in the Kara Sea were again captured quite accurately by FLEXPART. On October 19 to 20, BC originated mainly from the Russian gas flaring sites of Yamal and Khanty-Mansiysk, confirming that these emissions appear to be well-captured by the ECLIPSE inventory. From the afternoon on October 20, air arrived straight from the west and was not influenced anymore by sources on the continent. This was also the case on October 21, when air came from the north. Measurements also showed decreasing EBC concentrations from October 20 to 21 (from 135 ng m^{-3} on October 20 at 10:00 to near the detection limit on October 21 at 2:00).

On October 22, as the ship approached the Kara Strait, air arrived from the southwest and gas flaring emissions from the Nenets and Komi regions were sampled again, similar to the results from October 12. This time, the model overestimated the measured EBC concentrations only slightly. Nevertheless, together with the results

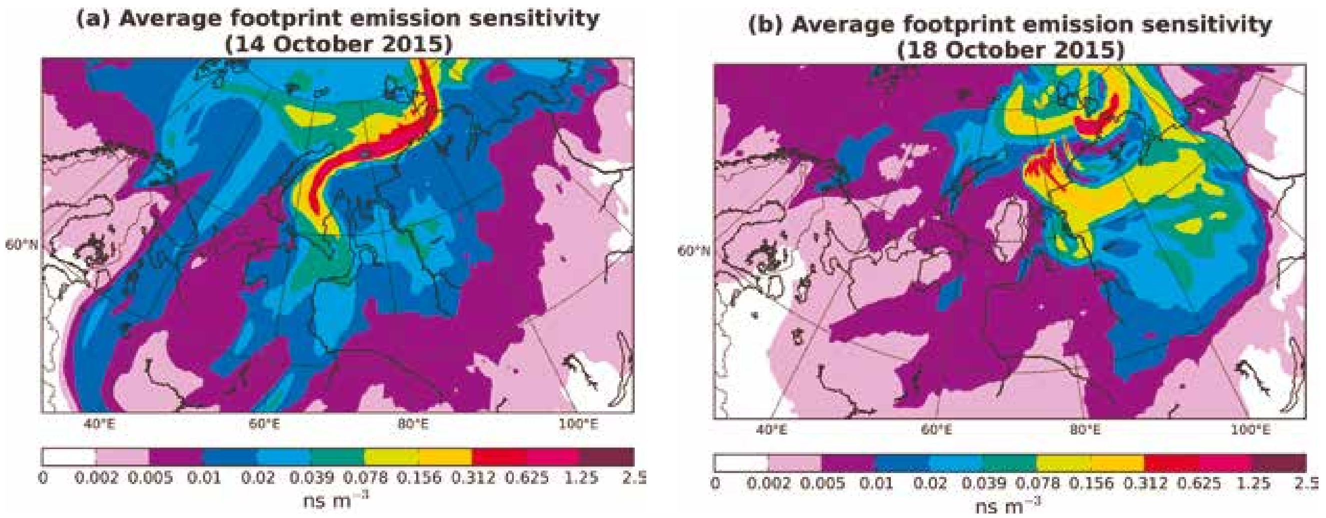

Figure 3. Daily average footprint emission sensitivities when the vessel (a) arrived (October 14, 2015) and (b) departed (October 18, 2015) from the "Ice Base Cape Baranova" station.

from the outward journey, this may suggest that flaring emissions in the Nenets and Komi regions are somewhat overestimated in the ECLIPSE inventory.

On October 24 to 25, measured EBC values in the White Sea reached more than 1000 ng m^{-3} and FLEXPART simulated similarly high BC values. The retroplumes at this time arrived from the southwest and brought polluted air masses mainly from Eastern Europe (Figure 4a). An example of the source contributions for October 25 at 00:00 is shown in Figures 4b and 5c. At that time, the modeled concentration of BC was 1310.5 ng m^{-3}, which is close to the observed values in the range from 696 to 1501 ng m^{-3}. About 10% (130.8 ng m^{-3}) originated from fires over Ukraine (Figure 4c), whereas about 90% originated from anthropogenic sources mainly in Central and Eastern Europe (Figure 4b). Excluding biomass burning, surface transportation contributed about 38%, residential and commercial combustion sources up to 41%, gas flaring contributed about 8%, and emissions from industrial combustion and processing contributed between 1–2%.

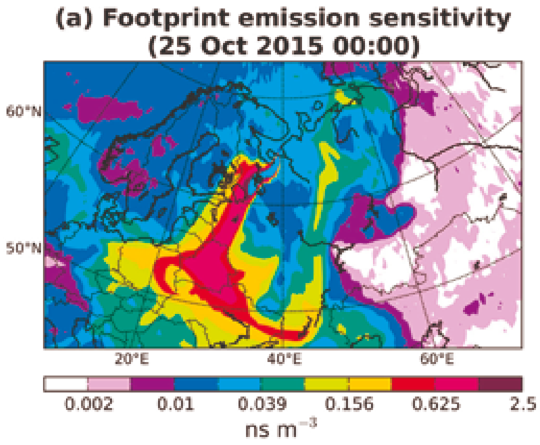

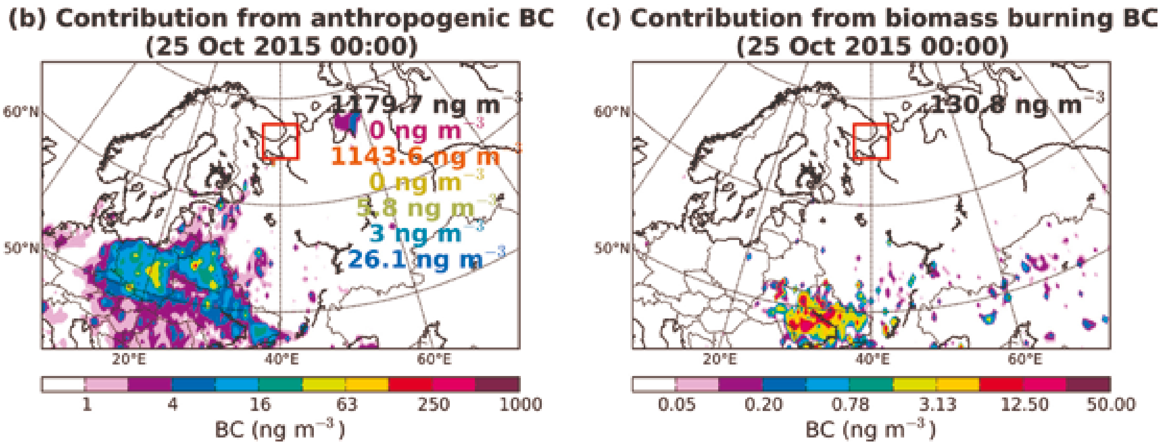

Figure 4. (a) Footprint emission sensitivity when the ship had passed the Dvina River and before arrival to the port of Arkhangelsk (October 25, 2015 at 00:00). (b) Contribution from anthropogenic sources and (c) biomass burning to the simulated surface concentration of BC at the same date and time. Black values show the concentration of BC at the receptor (ship) for the time period from all anthropogenic- and biomass-burning sources. Colored values denote continental contribution from anthropogenic sources; magenta areas show contribution from South America, orange from Europe, yellow from Australia, green from North America, cyan from Africa, and blue from Asia.

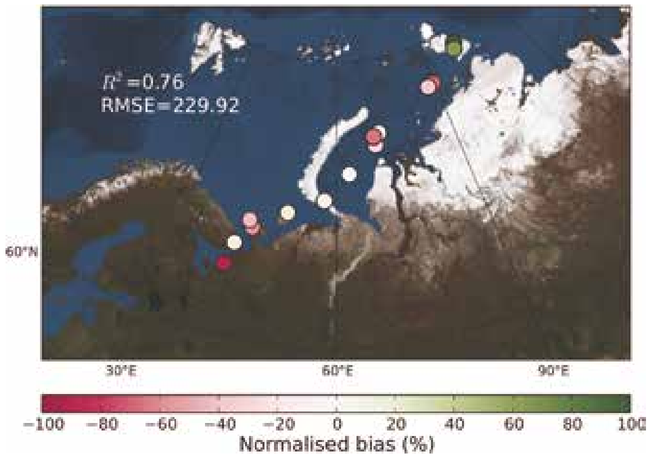

Figure 5. Distribution of normalized bias, i.e., modeled-observed over observed, for the measured EBC and the BC concentrations predicted by FLEXPART. The biases were calculated for the daily average concentrations and for the ship location at midnight of each day (00:00).

Figure 5 depicts calculated normalized bias for the daily average measured EBC and modeled BC concentrations along the ship track in the White, Barents, and Kara Seas. This statistic expresses the difference (model-observed) over the observed values. It is a useful indicator for assessing the models' performance because it avoids overinflating the observed range of values, especially at low concentrations, and it is used here to show the locations where modeled concentrations over- or underestimated the observations. The model is least biased when the gas-flaring sources contribute the most to surface concentrations of BC, namely in the Pechora Sea (west of Kara Sea), in the Kara Strait, and in the Kara Sea on the way to the Bolshevik Island, as well as in the middle of the Kara Sea (point 3 in Figure S1), and close to the port of Arkhangelsk on the way back to Arkhangelsk. The extremely low concentrations calculated by the model in the beginning of the cruise in contrast to the high EBC concentrations (≈700 ng m^{-3}) led to negative biases near the port of Arkhangelsk and in the industrial area of Dvina river delta. On the contrary, the lack of absorption in the aethalometer near the Bolshevik Island from October 15 to 17 resulted in significant overestimated BC concentrations predicted by the model and high positive biases (Figure 5).

The very good agreement (R2 = 0.76) between modeled and measured concentrations was confirmed by the root-mean-square error (RMSE). Whereas R2 is a relative measure of fit, RMSE is an absolute measure of fit. It can be interpreted as the standard deviation of the unexplained variance; hence it is in the same units as the response variable. Lower values of RMSE indicate better fit. RMSE is a good measure of how accurately the model predicts the response, and is the most important criterion for fit if the main purpose of the model is prediction. The RMSE, when all data were included, was estimated to be 230 ng m^{-3}. This high value is more or less expected here considering that the RMSE calculates the square error, hence it is very sensitive to larger errors. In the present case, if the points from the initial period of the cruise (Arkhangelsk and Dvina river industrial area) that were subject to local pollution are excluded, the RMSE falls to 85 ng m^{-3}, which is very low compared to the range of values observed during the cruise (0–1500 ng m^{-3}).

Overall, we found that the model had no systematic bias compared to the observations, which supports the validity of the ECLIPSE emission inventory for northern Russia. The good agreement, especially in the region where flaring emissions are important, suggests that flaring emissions are also captured quite well in this inventory. This is particularly true for the Yamal and Khanty-Mansiysk regions, whereas there may be some overestimation of flaring emissions in the Nenets and Komi regions. Local pollution cannot be captured by our model due to poor temporal and spatial resolution of the available operational wind fields or by the emission inventory used (available in 0.5° resolution). When local pollution was insignificant (e.g., in regions far from urban and industrial areas), emissions from residential and commercial combustion, as well as surface transportation, were also captured well.

Аэрозоль и эмиссия судовых силовых установок: исследования экспедиции «Север-2015»*

В настоящее время опасность антропогенных загрязнений Арктики становится все более очевидной. Климат Арктики особенно подвержен воздействию основной климатически-активной компоненты аэрозоля – черного углерода, являющегося продуктом горения ископаемого топлива и биомасс. Осаждение черного углерода на снег вызывает уменьшение альбедо подстилающей поверхности, ускорение таяния снега и льда. Несмотря на большую площадь территории Российской Арктики, в настоящее время исследования происхождения, эволюции и переноса природных и антропогенных аэрозолей крайне ограничены. Особенно это касается аэрозолей в эмиссиях хозяйственной и индустриальной деятельности при сжигании различных видов топлива, включая эмиссию транспортных средств.

Недостаток знаний о массовых, оптических и физико-химических характеристиках аэрозолей, их изменениях в процессе ближнего и дальнего переноса от локальных и региональных источников, особенно в зимний сезон, когда степень загрязнения Арктики повышается, создает большие неопределенности в понимании последствий влияния аэрозолей на температуру атмосферы, аэрозольный сток и скорость таяния снега в области вечной мерзлоты и снежно-ледяного покрова акваторий Северного Ледовитого океана. Проведение мобильных измерительных кампаний для оценки источников эмиссий, как, например, промышленных объектов, позволяет определить характерные свойства и трассеры техногенного влияния на состав аэрозоля в пограничном слое атмосферы.

Загрязнение окружающей среды Арктики эмиссиями силовых установок морских судов началось с момента появления паровых судов и продолжается до настоящего времени. Оценки Американского агентства окружающей среды (US Environmental Protection Agency, EPA) указывают на источник сжигания дизельного тяжелого мазутного топлива стационарными теплоэлектростанциями и двигателями транспортных средств как доминирующую эмиссию в регионах Российской Арктики (EPA, 2012. Report to congress on black carbon. Report Number EPA-450/D-12-001 prepared by U.S. Environmental Protection Agency, Washington DC). Сложный многокомпонентный состав аэрозолей был обнаружен в прибрежных районах Северного Ледовитого океана, где наряду с частицами сажи были выявлены обугленные частицы с высоким содержанием серы, типичные для эмиссии продуктов сжигания тяжелого мазутного топлива силовыми установками судов (Xie Z., Blum J.D., Utsunomiya S. et al. Summertime carbonaceous aerosols collected in the marine boundary layer of the Arctic Ocean // J. Geophys. Res. 2007. Vol. 112. D02306). Подобные частицы могут служить микромаркерами эмиссии двигателей морских судов (Popovicheva O., Kireeva E., Persiantseva N. et al. Microscopic characterization of individual particles from multicomponent ship exhaust // J. Environ. Monit. 2012. Vol. 14 (12). P. 3101–3110).

В ходе экспедиции «Север-2015» одной из задач научно-исследовательской группы МГУ–ААНИИ Росгидромета было изучение аэрозольного состава атмосферы и эмиссии судовых силовых установок на НЭС «Академик Трёшников» на переходе г. Архангельск – о. Большевик – г. Архангельск и организация мониторинга характеристик аэрозолей на НИС «Ледовая база “Мыс Баранова”». Экспедиция на НЭС «Академик Трёшников» стартовала 10 октября 2015 года из Архангельска. Судно прошло через дельту р. Двины – зону интенсивного судоходства и повышенного уровня антропогенных загрязнений. На следующие сутки судно пересекло Белое море и далее, через Баренцево море и Карские Ворота, достигло берегов острова Большевик архипелага Северная Земля 15 октября. Через два дня, по завершении намеченных научно-исследовательских и погрузо-разгрузочных работ на НИС, экспедиция отправилась в обратный путь. На этом маршруте

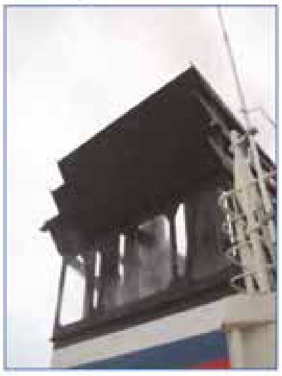

Ледокольные транспорты «Таймыр» и «Вайгач» в Карском море. Открытие архипелага Северная Земля. Е.В. Войшвилло. 1940 год (слева). Эмиссия силовой установки из выхлопной трубы НЭС «Академик Трёшников» (справа).

---

* О.Б. Поповичева, В.В. Мовчан, Н.М. Ситников, А.П. Макштас и В.Ю. Кустов //Российские полярные исследования, 2015;4, 14-16

Аэрозольные измерения PM, BC и отбор проб на борту НЭС «Академик Трёшников» в экспедиции «Север-2015».

Портативный аэталометр «Портаэталометр-1А» в кейсе с термостатом.

также проводились замеры эмиссии и изучение аэрозольного состава атмосферы.

Ранее возможность мобильного мониторинга аэрозолей на морских судах использовалась многими экспедициями, но обычно это делалось без учета возможных загрязнений, обусловленных собственной эмиссией данного судна (Stohl A.Z., Klimont, Eckhardt S. et al. Black carbon in the Arctic: the underestimated role of gas flaring and residential combustion emissions // Atmos. Chem. Phys. 2013. Vol.13. P. 8833–8855). Ряд измерительных кампаний был нацелен на определение коэффициента эмиссии и характеристик аэрозоля в продуктах сгорания непосредственно в выхлопной трубе дизельного двигателя судна.

В экспедиции «Север-2015» была поставлена задача оценки массовых, оптических и физико-химических характеристик аэрозолей в невозмущенном пограничном слое атмосферы и в слое атмосферы, загрязненном эмиссией газовыхлопной трубы судна. Оценка проводилась на основе измерений комплекса характеристик аэрозоля. Для выполнения этой задачи до начала рейса в порту Архангельск и во время рейса проводился мониторинг распределения полной массовой концентрации (PM) аэрозоля в различных частях судна: на носовых, кормовых и палубных надстройках. Экспериментальным путем была определена наиболее загрязненная продуктами сгорания область – она располагалась над надстройкой пункта управления полетами на палубе IV яруса на расстоянии порядка 10 м от оконечности выхлопной трубы, на высоте 15 м над судовой вертолетной площадкой. Здесь был установлен пост постоянных измерений вблизи основного источника эмиссии дизельного двигателя – газовыхлопной трубы силовой установки судна. Приборы для мониторинга и отбора проб аэрозоля в невозмущенном приводном слое атмосферы были установлены в носовой части судна.

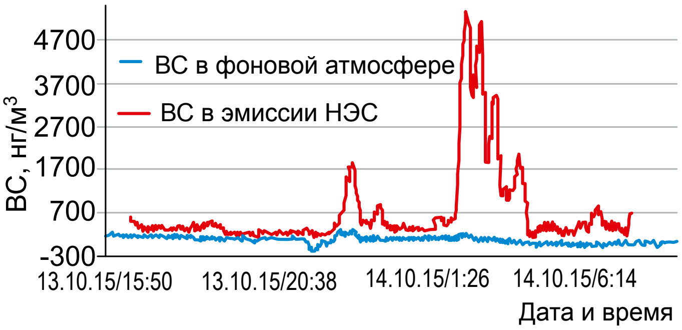

Для измерений полной массовой концентрации аэрозоля был использован лазерный нефелометр Dust Track 8530. Для измерения концентрации черного углерода, маркера локальных источников эмиссии судовых силовых установок и шлейфов дальнего переноса воздушных масс, была использована методика аэталометрических измерений массовой концентрации черного углерода (BC). Для этого специалистами Центральной аэрологической обсерватории (ЦАО) Росгидромета и Научно-исследовательского института ядерной физики МГУ (НИИЯФ МГУ) был разработан трехволновой портативный аэталометр «Портаэталометр-1А», предназначенный для измерений в реальном времени поглощательной способности частиц и спектральной зависимости при их осаждении на фильтрах в процессе прокачки воздуха. Для работ в Арктике аэталометр был оснащен специальным термостатом.

Калибровка аэталометра «Портаэталометр-1А» для определения массовой концентрации BC была произведена на базе новейших исследований аэрозольных технологий на станции ГСА «Демокритос» в г. Афины (Греция). Во время экспедиции «Север-2015», после выполнения соответствующей интеркалибрации, два аналогичных аэталометра использовались одновременно для определения массовой концентрации BC в чистом воздухе (в носовой части судна) и воздухе, наиболее загрязненном вследствие работы судового двигателя (вблизи трубы). Предварительные результаты одновременных измерений массовой концентрации BC во время прохождения судном Карского моря представлены на рисунке. Как видно из рисунка, фоновый аэрозоль характеризуется низкими значениями BC, составляющими в среднем порядка 89 нг/м^3. В то же время отчетливо проявляются высокие уровни локального загрязнения атмосферы эмиссией дизельного двигателя НЭС, достигающие максимальных значений при направлении ветра непосредственно на место расположения аэталометра в кормовой части, превышающих 5 мкг/м^3.

Регистрация данных общей концентрацией аэрозолей и массовой концентрацией BC в двух точках проводилась постоянно, за исключением времени на техобслуживание приборов (замена фильтров, смена флеш-карты с данными). Также специалистами-метеорологами научно-исследовательской группы НЭС проводилась непрерывная регистрация основных метеорологических характеристик.

С целью определения физико-химических характеристик аэрозолей в приводном слое атмосферы арктических морей была использована система отбора частиц с размером менее 10 мкм (PM10), созданная на базе аспиратора АПВ4 и сборников аэрозолей Airmetrix PM10. В ходе экспедиции был выполнен отбор проб аэрозолей в чистой атмосфере, во время прохождения районов повышенного судоходства и вблизи источника эмиссии дизельного двигателя судна. Периодически отбор аэрозолей проводился на металлические подложки с помощью двухкаскадного импактора с диаметром пропускания частиц PM10 на первой ступени и 630 нм на второй ступени.

16 октября 2015 года аэталометр «Портаэталометр-1А» был доставлен на НИС «Ледовая база “Мыс Баранова”» для проведения серий измерений в рамках программы мониторинга оптических свойств арктических аэрозолей и исследования их сезонной изменчивости. Прибор установлен в заранее выбранном и подготовленном месте, наименее подверженном локальному воздействию загрязнений, ассоциированных с функционированием объектов обеспечения жизнедеятельности станции (дизельная электростанция, камбуз и кают-компания, пути транспортного сообщения).

Учитывая калибровку, проведенную на уровне мировых стандартов, данные о массовой концентрации черного углерода на станции «Ледовая база “Мыс Баранова”» могут быть в будущем переданы непосредственно в мировую сеть мониторинга аэрозолей в рамках Arctic Monitoring and Assessment Programme (AMAP), в глобальные модели транспорта аэрозолей и дальнего переноса воздушных масс, а также для проведения сравнительных измерений уровней загрязнений на полярных станциях. Предполагается, что в дальнейшем такие приборы-аэталометры послужат основой для создания мобильной системы комплексного анализа аэрозольного состава атмосферы при проведении экспедиционных работ в удаленных районах, будут устанавливаться на передвижных платформах и беспилотных летательных аппаратах.

В заключение следует отметить, что значительная изменчивость массовой концентрации аэрозолей в фоновой и загрязненной атмосфере, их микроструктуры, состава, содержания органических, неорганических и ионных соединений существенно усложняет задачу анализа аэрозольной нагрузки атмосферы и оценки климатических последствий эмиссии. Аэрозоли горения могут служить трассером загрязнений, позволяющим идентифицировать источник эмиссии, если их характеристики определены в зависимости от вида топлива, условий и способа его сжигания. Учитывая вышесказанное, пробы аэрозоля, отобранные на НИС «Ледовая база “Мыс Баранова”», будут подвергнуты комплексной характеризации образцов частиц с использованием аналитического и химического оборудования лаборатории анализа аэрозолей НИИЯФ МГУ. Методами микроскопического анализа индивидуальных частиц в образцах проб будут идентифицированы микромаркеры дизельной эмиссии по наличию групп частиц сажи. При этом распространенность характерных групп определит степень загрязнения аэрозолей источниками дизельной эмиссии по сравнению с фоновым морским аэрозолями. Анализ содержания органических/неорганических и ионных компонентов в климатически активных и опасных аэрозольных составляющих загрязненной атмосферы определит влияние эмиссии судовых силовых установок. Кластерный анализ морфологии и состава индивидуальных частиц даст возможность оценить вклад дизельной эмиссии и шлейфов дальнего переноса воздушных масс в распространяемость и микроструктуру аэрозолей арктического региона.

КЛИМАТИЧЕСКИЙ ТРАССЕР – ЧЕРНЫЙ УГЛЕРОД

Siberian Arctic black carbon: gas flaring and wildfire impact*

1 INTRODUCTION

Global carbon pollution is annually produced by the burning of fossil fuel and biomass. Combustion emissions are increasingly recognized as an important source of chemically active aerosols. Black carbon (BC) originates from the incomplete combustion of fossil fuels and biomass burning; it is a short-lived climate forcer, absorbs incoming solar radiation and, therefore, is of high significance for the Arctic climate (Wang et al., 2011). The combined total effects of BC and sulfates cause an Arctic surface warming of +0.29 K, explaining approximately 20 % of the observed Arctic warming since the early 1980s (Ren et al., 2020). BC resides in the lowest atmospheric layer, affects aerosol–cloud interactions (Yun et al., 2013), and has a cloud and sea-ice feedback when deposited (Flanner, 2013), thus accelerating melting (Quinn et al., 2008).

Long-range transport to the Arctic carries, among other aerosol constituents, many tracers of anthropogenic and wildfire origin (Chang et al., 2011). Winiger et al. (2016) showed that BC in Arctic Scandinavia is predominantly linked to emissions in Europe. Over the whole Arctic region (north of 66°N), Russia contributes 62 % to surface BC (Zhu et al., 2020). Industrial and residential sources are responsible for the highest measured BC concentrations at Tiksi station (Siberian Arctic) (Popovicheva et al., 2019b). Stathopoulos et al. (2021) have demonstrated that the long-term impact of light-absorbing carbon in the high Arctic is 3 times higher in the cold period of the year compared to the warm period. There, fossil sources mostly prevail during the winter–spring season, while biomass burning sources dominate during low-BC-concentration periods in summer (Winiger et al., 2017). Although BC dominates light absorption by atmospheric aerosols, other carbonaceous aerosol species (brown carbon, BrC) represent an important fraction of light absorption in the UV and near-UV spectra, thus having an important role in the assessment of radiative forcing in the Arctic climate. Spectral dependence of the light absorption is generally described by the absorption Ångström exponent (AAE), which is typically used to differentiate between aerosol types (BC, BrC) and sources of BC (Sandradewi et al., 2008; Helin et al., 2021; Zotter et al., 2017).

Quantification of the particulate Arctic pollution is a serious problem worldwide; reliable source emission inventories are challenged, and regional contributions of BC sources in the Arctic are still inconclusive (Zhu et al., 2020). The global anthropogenic emission dataset ECLIPSEv6 (Evaluating the Climate and Air Quality Impacts of Short-lived Pollutants) using the GAINS model (Klimont et al., 2017) includes all major economic sectors, such as energy and industrial production, transport, residential combustion, agriculture, and waste, distinguishing between sector fuel technology, fuels and emission control options. The model predictions for the European gateway to the Arctic were greatly improved when the emission inventory from anthropogenic sources was updated by estimates of European BC emissions (Winiger et al., 2016).

Due to large size and continuous production, gas flaring of the oil industry is one of the highest BC emission sources (Ismail and Umukoro, 2012) with a strong environmental and climatic impact on the Arctic (Cho et al., 2019). Flaring in ECLIPSEv6 dominates BC emissions in the Arctic; models have found that flaring contributes 42 % to the annual mean BC surface concentrations in the Arctic (Stohl et al., 2013). However, because flares are difficult to measure, their particulate emissions and physicochemical properties are still underestimated (Conrad and Johnson, 2017; Popovicheva et al., 2019a). Currently, models are struggling to reproduce BC concentrations largely due to emission-related uncertainties in the Arctic region (Schacht et al., 2019). The observed annual mean contribution of fossil fuel combustion to the Arctic concentrations agrees within a factor of 2 (Qi and Wang, 2019).

High-latitude flaring emissions mainly originate from the North Sea, Norwegian Sea, the northeastern part of European Russia (Komi Republic) and western Siberia. The largest oil and gas producing regions of northwestern Siberia are located along the main low-level pathway of air masses entering the Arctic and thus make a disproportionally large contribution to the Arctic lower troposphere (Stohl, 2006). Eleftheriadis et al. (2009) and Tunved et al. (2013) identified these regions as a key source for the highest measured BC concentrations and sub-micrometer aerosol mass concentrations, respectively, at Zeppelin station. The impact of BC long-range transport from northwestern Siberia was also observed at Ice Base Cape Baranova station located on Severnaya Zemlya archipelago (eastern Siberia) (Manousakas et al., 2020). Accordingly, possible gas flaring impact was observed at Tiksi station (northeastern Siberia) despite the large distance of the station from the largest oil and gas producing regions (Winiger et al., 2017). To better understand and quantify the contribution of gas flaring to the Arctic environment, targeted aerosol and atmospheric composition measurements at the closest distance from the flaring facilities are needed. The present operating Eurasian Arctic stations are all too far away to allow for the assessment of how air masses are affected by gas flares or what the contribution from different source categories is (Stohl et al., 2013). Simulations combined with observations of BC at the proximity of the source

---

* Olga B. Popovicheva, Nikolaos Evangeliou, Vasilii O. Kobelev, Marina A. Chichaeva, Konstantinos Eleftheriadis, Asta Gregorič, and Nikolay S. Kasimov// Atmospheric Chemistry and Physics.2022;22:5983-6000
DOI: 10.5194/acp-22-5983-2022

regions (e.g., the plumes from gas flaring regions over the Kara Sea) provide a better constraint (Popovicheva et al., 2017). In addition, measurements of BC coupled with conditional probability simulations performed inside the oil and gas producing region of northwestern Siberia have successfully distinguished between multiple industrial and urban sources (Popovicheva et al., 2020).

Recent efforts have sought to develop a new Russian BC emission inventory (BCRUS) for the Siberian Arctic, based on activity data from local information, improved spatial distribution of BC emissions, and updated emission factors for oil and gas fields in northwestern Siberia (Huang et al., 2015). According to this, it was found that BC emissions from gas flaring account for 36 % of the total anthropogenic BC emissions over Russia. Residential BC emissions, transportation, industry and power plants contribute 25 %, 20 %, 13 % and 5.4 %, respectively. The emissions from gas flaring in BCRUS show a discrepancy more than 40 % higher than ECLIPSEv5. Using BCRUS, modeled surface BC at Zeppelin, Barrow and Alert stations were basically improved (Huang et al., 2015). The contribution of anthropogenic emissions in Russia to the annual total Arctic surface BC was calculated to be 56 %, with gas flaring from the Yamalo-Nenets Autonomous Okrug (YNAO), Khanty-Mansiysk Autonomous Okrug (KMAO) and Komi Republic being the main source (31 % of Arctic surface BC) (Zhu et al., 2020). However, due to the absence of BC inventories for industrial emissions and a denser observational network in the western Siberian High Arctic, the spatial distribution of BC sources is still associated with large uncertainties.

Agricultural fires in East Europe and North America are a major source of biomass burning in the Eurasian Arctic (Treffeisen et al., 2007; Stohl et al., 2006, 2007). Springtime fires in Siberia can double the North American Arctic background (Warneke et al., 2010). Long-term airborne observations of BC in northern Siberia have revealed a strong impact from forest fires in summer (Kozlov et al., 2016; Paris et al., 2009). Particulate BrC emitted by intensive wildfires has been measured in plumes transported for over 2 d (Forrister et al., 2015). In summer 2019, wildfire activity in Central and East Siberia occurred along the trans-Arctic transport pathway of Siberian biomass burning emissions resulting in enhanced aerosol lamina observed in western Canada (Johnson et al., 2021).

In 2019, a new aerosol station was developed by Moscow State University on Bely Island located in the Kara Sea (western Siberian Arctic) (https://peexhq.home.blog/2019/12/11/new-research-aerosol-stations-in-the-russian-arctic, last access: 1 April 2022) (Fig. 1). The region was chosen because it is close to the air pathway of large-scale emission plumes from populated industrial regions of Eurasia and Siberian wildfires to the Arctic. We present here the ground-based continuous BC (equivalent BC, EBC) measurements from August 2019 until November 2020 at the "Island Bely" station for the first time. The Arctic annual trends of BC are assessed, while the geospatial source origin of the air arriving at the station is identified using a Lagrangian particle dispersion model. Furthermore, the anthropogenic and biomass burning contributions to the modeled surface concentrations of BC are evaluated against measured BC concentrations at the station. Characterization of the pollution events in cold and warm periods separates the impact of gas flaring versus biomass burning. In addition, the spectrally resolved absorption measurements provide an opportunity for the characterization of BC sources. The present study assesses long-range transport of BC to the western Siberian Arctic from the main large-scale emission regions of the Eurasian continent using Lagrangian modeling coupled with continuous observations.

2. EXPERIMENTAL

2.1 Aerosol station Island Bely

Western Siberia is the world's largest gas flaring region with a leading oil and gas production industry (Fig. 1). YNAO is located north of the West Siberian Plain and covers a vast area of 769 000 km^2. More than 94 % of the region's economy is associated with industrial applications related to the extraction of fuels, their processing and transportation. Specifically, YNAO has the largest reserves of Russia's natural gas and oil; YNAO emissions of BC are the largest in the Russian territory (Vinogradova, 2015). The relative contributions from gas flaring to annual mean BC surface concentrations from all emission sources (surface transportation, industry, residential, biomass burning) exceed 70 % (Stohl et al., 2013).

Bely Island is located in the Kara Sea, north of the YNAO (Fig. 1). For the purpose of atmospheric composition observations and sampling at the Island Bely station, the aerosol pavilion has been built approximately half a kilometer to the southeast of the Roshydromet meteorological station continuously operating on the island (Fig. 1). There are no other anthropogenic constructions on the island. Thus, the major advantage of a newly developed research station is its long distance from any local anthropogenic sources. Previous research at Tiksi station has shown significant aerosol pollution from local sources (Popovicheva et al., 2019b), which is not the case at the Island Bely station. An aerosol sampling system was installed at the aerosol pavilion in May 2019. Three total suspended particle (TSP) inlets were installed approximately 1.5 m above the roof and 4 m above the ground. One is used for the real-time BC monitoring with air flow at 5 L min^{-1} and two for aerosol chemical characterization operating with 2.3 m^3 h^{-1} flow. The TSP inlet is equipped with an electric heating wire to prevent rimming and ice blocking of the system.

A model AE33 aethalometer (Magee Scientific, Aerosol d.o.o.) was used to measure the light attenuation caused by particles depositing on two filter spots at different flow rates (Drinovec et al., 2015) and at seven wavelengths from ultraviolet (370 nm) to infrared (950 nm). The "dual spot" technique is applied for real-time loading effect compensation. The light-absorbing content of carbonaceous aerosol at 880 nm is reported as equivalent black carbon concentration (EBC), which is determined for each time interval from the change in the light attenuation at a wavelength of 880 nm using a mass absorption cross-section of 7.7 m^2 g^{-1} and a filter multiple scattering parameter C of 1.57. Light-absorbing organic components (BrC) absorb light at shorter wavelengths more effectively than at 880 nm, which is observed as an increased AAE (Sandradewi et al., 2008; Grange et al., 2020; Helin et al., 2021). AAE was calculated using Eq. (1) for 470 nm and 950 nm wavelengths:

$$\mathrm{AEE} = \frac{\ln(\mathrm{babs}(470)/\mathrm{babas}(950))}{\ln\,(950/470)} \qquad (1)$$

where babs stands for the absorption coefficient at 470 and 950 nm. In order to avoid instrumental noise when calculating the AAE, the following data processing was implemented. The 1 min absorption coefficients for the whole period were averaged to 1 h. The dataset was filtered to periods when EBC exceeded 20 ng m^{-3} (sensitivity level at 1 h time resolution), and then the AAE was averaged to 3 h.

The aethalometer model (Sandradewi et al., 2008) is typically used for the source apportionment of EBC when measurements of absorption coefficient are performed by filter photometers. The model uses an a priori assumed pair of AAEs for traffic (AAETR) and biomass burning (AAEBB) to determine the contribution of both sources. Although the aethalometer model is an efficient tool for source apportionment of EBC in a well-mixed urban atmosphere where two sources with distinct aerosol optical properties prevail (fossil fuel from traffic and fresh biomass burning), the results can be affected when the characteristic optical properties of a specific source change over time. This is usually the case for wildfires where different burning modes (flaming or smoldering) and different types of wood can significantly influence BrC emissions and its chemical composition (Kalogridis et al., 2018b). Furthermore, chemical evolution after emissions and atmospheric aging (i.e., aerosol mixing state, particle morphology and size distribution) additionally influence aerosol absorption, which can be noticed especially for long-range-transported air masses (Cappa et al., 2016; Saleh et al., 2013; Romshoo et al., 2021). Forrister et al. (2015) have shown that BrC emitted from wildfires was highly unstable, with 6 % of BrC remaining above background levels after 2 d.

BC measurements at the Island Bely station were performed from 10 August 2019 to 30 November 2020 with a time resolution of 1 min. Basic meteorological parameters, such as temperature and wind speed and direction, were obtained every 3 h from a meteorological station located 500 m from the Island Bely station. Cleaning of 1 min time-resolved BC data was based on the definition of what can be considered as a peak: a strong fast increase in BC value a few times higher than previous value and then a similarly fast decrease. The analysis of meteorological parameters was complementary to check whether the wind originated from the sector corresponding to locations of diesel generators at the Roshydromet meteorological station (240–250° from the "Bely Island" station). In such cases, strong peaks of BC were removed from further analysis. The total duration of the peaks under the influence of local contamination varies from several minutes to 1–2 h per day and monthly. For instance, in January 2020, when wind blew from 240–250° for 24 h in total, large peaks corresponding to a fraction of 13 % of the data were removed. In July 2020, when wind originated from the same location for a total of 45 h, measurements corresponding to a fraction of 22 % of the data were removed. Lack of windy weather at Bely Island is a very rare event, only 0.7 % of the observation time; during such weather, peaks of BC were never observed.

2.2. Atmospheric transport model coupling with emissions

To investigate the possible origin of BC, the Lagrangian particle dispersion model FLEXPART (FLEXible PARTicle dispersion model) version 10.4 was used (Pisso et al., 2019). The model was driven by 3 h operational meteorological fields from the European Centre for Medium-Range Weather Forecasts (ECMWF) with

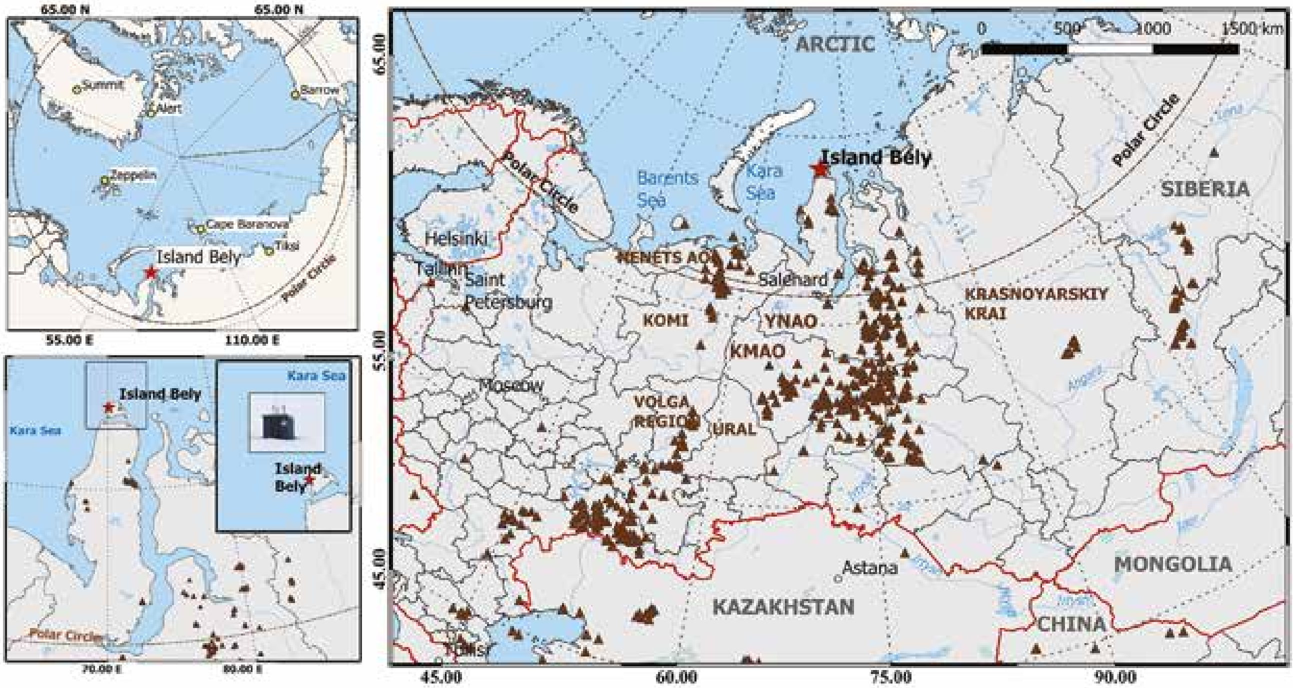

Figure 1. Top-left map shows the location of the newly established Island Bely aerosol station in contrast to other Arctic stations (Zeppelin, Alert, Barrow, Summit, Tiksi and Cape Baranova). Bottom-left map shows a zoomed-in version of the location of Bely Island in the Kara Sea, where the new station was developed (73°20′7.57″ N, 70°4′49.05″ E). The map on the right shows the Island Bely aerosol station in combination with the European part of Russia and western Siberia and the Yamalo-Nenets Autonomic Okrug (YNAO). Flares of oil and gas fields are shown for the year 2019 in brown triangles (adopted from https://skytruth.org/, last access: 1 April 2022).

137 vertical levels and a horizontal resolution of 1° × 1°. In FLEXPART, computational particles were released at heights of 0–100 m from the receptor (Island Bely station) and were tracked backward in time in FLEXPART's "retroplume" mode. Simulations extended over 30 d backward in time, sufficient to include most BC emissions arriving at the station given a typical BC lifetime of 1 week (Bond et al., 2013).

The tracking includes gravitational settling for spherical particles of the size observed. FLEXPART differs from trajectory models due to its ability to simulate dry and wet deposition of gases or aerosols (Grythe et al., 2017), turbulence (Cassiani et al., 2015), and unresolved mesoscale motions (Stohl et al., 2005), while it includes a deep convection scheme (Forster et al., 2007). For our simulations, we assumed that BC has a density of 1500 kg m^{-3} and follows a logarithmic size distribution with an aerodynamic mean diameter of 0.25 μm and a logarithmic standard deviation of 0.3 (Long et al., 2013).

FLEXPART simulations were performed every 3 h during the studied period. The FLEXPART output consists of a footprint emission sensitivity which results in a modeled concentration at the receptor when coupled with gridded emissions from an emission inventory. The emission sensitivity expresses the probability of any release occurring in each grid cell to reach the receptor. The source contributions to receptor BC were derived by combining each gridded emission sector (gas flaring, transportation, waste management, etc.) from an emission inventory with the footprint emission sensitivity. Calculations for anthropogenic sources (emission sectors are described below) and open biomass burning were performed separately. This enabled the identification of the exact origin of BC and allowed for the quantification of its source contribution. The modeled concentrations can also be displayed as a function of the time elapsed since the emission occurred (i.e., "age"), which can be shown as "age spectrum".

In this study, anthropogenic emission fluxes were adopted from the latest version (v6b) of the ECLIPSE (Evaluating the Climate and Air Quality Impacts of Short-lived Pollutants) dataset, an upgraded version of the previous version (Klimont et al., 2017). The inventory includes industrial combustion (IND) emissions from industrial boilers and industrial production processes. The energy production sector (ENE) includes emissions from combustion processes in power plants and generators. The residential and commercial sector (DOM) includes emissions from combustion in heating and cooking stoves and boilers in households and public and commercial buildings. The waste treatment and disposal sector (WST) resembles emissions from waste incineration and treatment. The transport sector (TRA) includes emissions from all land-based transport of goods, animals and persons on road networks and off-road activities. Emissions from shipping activities in in-land waters (SHP) is included as a separate sector. The gas flaring (FLR) sector includes emissions from oil and gas facilities. The methodology for obtaining emissions from FLR specifically over Russia has been improved in ECLIPSEv6 (Böttcher et al., 2021). Updates were based on new field-type-specific emission factors that were applied to Visible Infrared Imaging Radiometer Suite (VIIRS) observations of the flared gas volume at individual flaring locations. For comparison, BCRUS emissions for the FLR sector (Huang et al., 2015) were also used in this study.

Emissions from biomass burning (BB) were adopted from Copernicus Atmosphere Monitoring Services (CAMS) Global Fire Assimilation System (GFAS). CAMS GFAS assimilates fire radiative power (FRP) observations from satellite-based sensors converting the energy released during fire combustion into gas and aerosol daily fluxes (Di Giuseppe et al., 2016; Kaiser et al., 2012). Data are available globally on a regular grid with a horizontal resolution of 0.1° from 2003 to the present. FRP observations assimilated in GFAS are the NASA Terra MODIS and Aqua MODIS active fire products (http://modis-fire.umd.edu/, last access: 1 April 2022, Kaufman et al., 2003). FRP measures the heat power emitted by fires as a result of the combustion process and is directly related to the total biomass combusted (Wooster et al., 2005). Using land-use-dependent conversion factors, GFAS converts FRP into emission estimates for 44 smoke constituents (Kaiser et al., 2012), one of which is BC.

Biomass burning emissions were also adopted from the Global Fire Emission Dataset version 4.1 (GFEDv4.1). The product combines satellite information on fire activity and vegetation productivity to estimate gridded monthly burned area and fire emissions, as well as scalars that can be used to calculate higher-temporal-resolution emissions. All data are publicly available for use in large-scale atmospheric and biogeochemical studies and include (i) burned area (Giglio et al., 2013), (ii) burned area from "small" fires based on active fire detections outside the burned area maps detailed in Randerson et al. (2012) and updated in van der Werf et al. (2017), (iii) carbon and dry matter emissions from van der Werf et al. (2017), (iv) fractional contributions of various fire types to total emissions, and (v) list of emission factors to compute trace gas and aerosol emissions based on Akagi et al. (2011) and Andreae and Merlet (2001). The current version (v4) has a spatial resolution of 0.25° and is available from 1997 onwards.

In the present paper, several different configurations were used to calculate modeled surface BC concentrations at Island Bely station, namely ECLIPSEv6 with GFED4 (ECLIPSEv6-GFED4) and ECLIPSEv6 with CAMS (ECLIPSEv6-CAMS). The same two configurations were also used after substituting the FLR emissions in ECLIPSEv6 with those from BCRUS (Huang et al., 2015).

3 RESULTS AND DISCUSSION

3.1 Monthly climatology of black carbon

The climate at Bely Island is characterized by an average annual temperature of −8 °C, precipitation of 450 mm and stable snow coverage from October to May. Meteorology displays a large annual variability determined by alternating periods of the polar night and midnight sun. Median temperatures stay above 0 °C for 4 months each year between June and September. This period is also characterized by the highest-frequency occurrence of ocean air masses and the most stable wind speeds. A shift occurred in October with decreased solar insolation resulting in a temperature shift to below 0 °C. The cold month winds were primarily continental, with a low-frequency occurrence of ocean air masses.

The cycle of temperature and wind speed variations observed during the study period is shown in Fig. 2a and b. The period from 1 November 2019 to 1 April 2020,

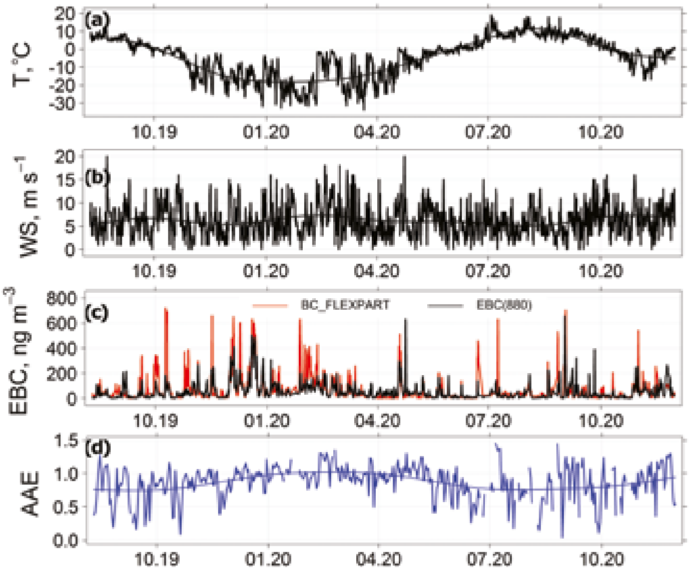

Figure 2. Meteorological conditions with respect to (a) mean temperature and (b) wind speed (data were smoothed to show long-term variations), (c) time-series of 24 h median EBC (black) and model BC using ECLIPSEv6-CAMS emissions (red), and (d) 24 h average absorption Ångström exponent (AAE) measured at Island Bely station from 10 August 2019 to 30 November 2020 (date format in mm.yy).

when temperatures dropped below −10 °C, as well as November 2020, is denoted as the “cold period”. The remaining period of our study, from 10 August to 31 October 2019, as well as from April to 1 November 2020, is considered as the “warm period”. Figure 2c illustrates the long-term time series of 24 h median EBC concentrations measured at a wavelength of 880 nm (EBC(880)) during the study period, with a median of 37 ± 64 ng m^{-3} (maximum: 520 ng m^{-3}; minimum: 6 ng m^{-3}). The polar frequency plot of wind speed and direction shows the maximum number of hours the wind was from northeast and southwest directions at around 5 m s^{-1} (Fig. 3a). BC concentration roses in Fig. 3 indicate the sources of the highest concentrations, which originated from the continent in both cold and warm periods.

Figure 4 illustrates a long-term time series of monthly EBC concentrations at the Island Bely station during the period from August 2019 to November 2020. The highest concentrations were observed from November to April and the lowest ones from June to August, in agreement with the typical seasonal trend of the Arctic aerosol concentrations (Stone et al., 2014). EBC monthly climatology during the study period is shown in Fig. 4a in terms of the median and upper and lower quartiles. For winter months, the maximum median EBC concentration was 165 ng m^{-3} observed in December 2019. The increase in the Arctic concentrations in winter, known as the Arctic haze, was more pronounced in November–December 2019 and January–March 2020. On average, concentrations in summer were about 10 times lower than those in winter, with a minimum median value of 30 ng m^{-3} in July 2020. Observations at the Island Bely station for the second year started from August 2020 and lasted until November 2020 to confirm the general annual trend of low summer and high winter BC concentrations. However, monthly median EBC in September 2020 demonstrated a value of 30.7 ng m^{-3}.

A similar annual trend was recorded in 2015–2016 at Tiksi station (coast of Laptev Sea), with high concentrations reaching 130 ng m^{-3} during winter–spring and low concentrations of about 20 ng m^{-3} observed from May to October (Popovicheva et al., 2019b). As shown by earlier studies at various polar stations, such as in Ny-Ålesund, Alert and Barrow, aerosols display Arctic haze peak concentrations during winter and early spring months (Stone et al., 2014). EBC during Arctic haze at both Island Bely and Tiksi stations are typically higher as compared to those observed at Alert (100 ± 65 ng m^{-3}), a station that has shown the largest concentrations among all polar stations (Sharma et al., 2004). The latter confirms previous findings from Eckhardt et al. (2015) and Winiger et al. (2017) that the Siberian Arctic is mainly polluted as a result of the influence from emissions occurring on the Eurasian continent.

Near-surface measurements allow for the evaluation of the capability of transport models to reproduce the distribution of BC in the Arctic based on different emission datasets (Schacht et al., 2019; Zhu et al., 2020). Figure 4a and Supplement Table S2 show observed and modeled BC monthly median mass concentrations at the Island

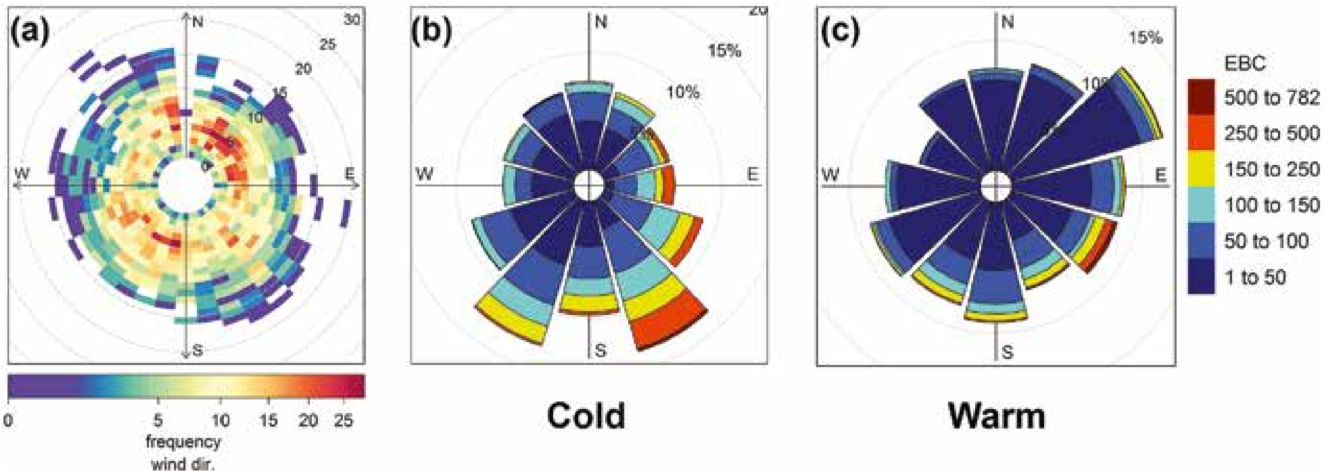

Figure 3 (a). Polar frequency plots of wind speed and direction. Each cell gives the total number of hours the wind was originating from a certain wind direction. The dashed circular grey lines show the wind speed (in m s^{-1}). Rose diagrams show EBC concentrations during the cold (b) and warm (c) periods.

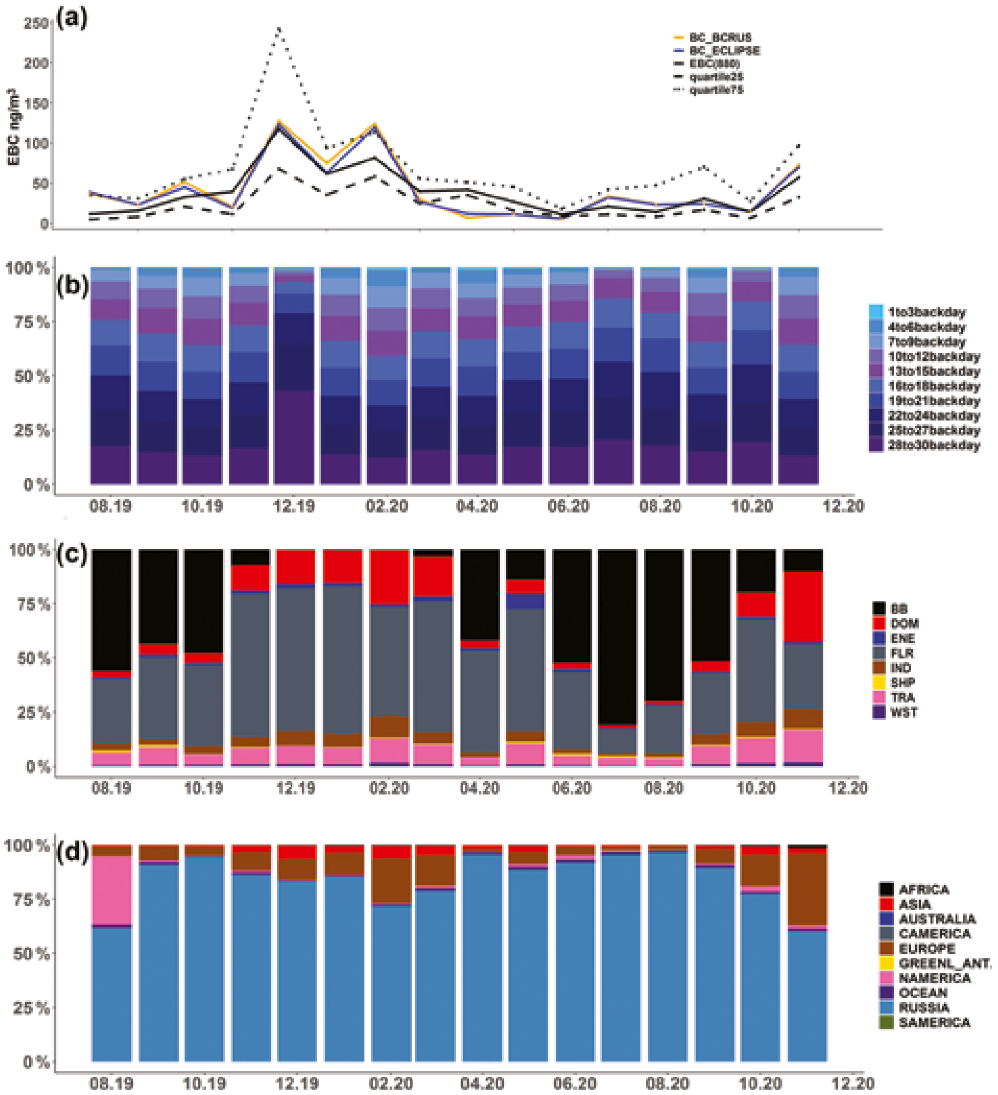

Figure 4(a). Monthly climatology of EBC at the Island Bely station depicting medians and 25th and 75th percentiles (dashed lines). Near-surface monthly median BC concentrations simulated with FLEXPART coupled to ECLIPSEv6-CAMS (steel blue) and ECLIPSEv6-BCRUS-CAMS (red) emissions are also shown. (b) Age spectrum of modeled BC from all possible sources showing the contribution of emissions from each day back in time to the surface concentration of BC. (c) Contribution from different emission source types to surface BC concentrations. The emission sources of biomass burning (BB) adopted from GFEDv4.1 and residential and commercial (DOM), power plants, energy conversion and extraction (ENE), gas flaring (FLR), industrial combustion and processing (IND), shipping (SHP), and transportation (TRA) adopted from ECLIPSEv6 were considered. (d) Continental spectrum showing the contribution from each continent or region to surface BC concentrations; 10 regions were considered, namely Africa, Asia, Australia, Central America, Europe, Greenland and Antarctica, North America, world ocean, Russia, and South America (see Supplement Fig. S3).

Bely station. The use of ECLIPSEv6 emissions caused overestimations of modeled BC concentrations of up to 46 % (February 2020). All simulated BC concentrations were found in the range between the 25th and 75th percentiles of measured EBC. Modeled BC is underestimated in March–May 2020, being 29 ng m^{-3} below the 25th percentile of EBC in April 2020. When FLR emissions in ECLIPSEv6 were substituted by BCRUS FLR, similar modeled BC monthly median concentrations were calculated, thus indicating that other sectorial emissions might make a large contribution to surface BC at the station.

Figure 4b shows the so-called “age spectrum” of modeled BC for the Island Bely station. In the cold period of high EBC concentrations, the longest age of more than 19 d back affects up to 60 % of the surface concentrations. In this time, due to the geographical proximity, Russia dominates. However, both Europe and Asia contribute around 20 % to the monthly averaged surface BC, with the largest contribution being in February 2019 and November 2020 (Fig. 4b, d). The most aged air masses (from 28 to 30 d back) contributed up to 50 %, arriving at the Island Bely station in December 2019, which is the month of the highest observed EBC concentrations during the study period. The impact of the closest regions with ages between 7 and 9 d is more significant in the winter months, while in the warm period, such short-term contributions become negligible. The calculated age and continental spectrum of BC obtained for the Island Bely station mainly denote the variability in air mass transport patterns in different seasons. In the cold season, the Siberian Arctic tends to force the air from south to north into the Arctic (Stohl, 2006), thus bringing

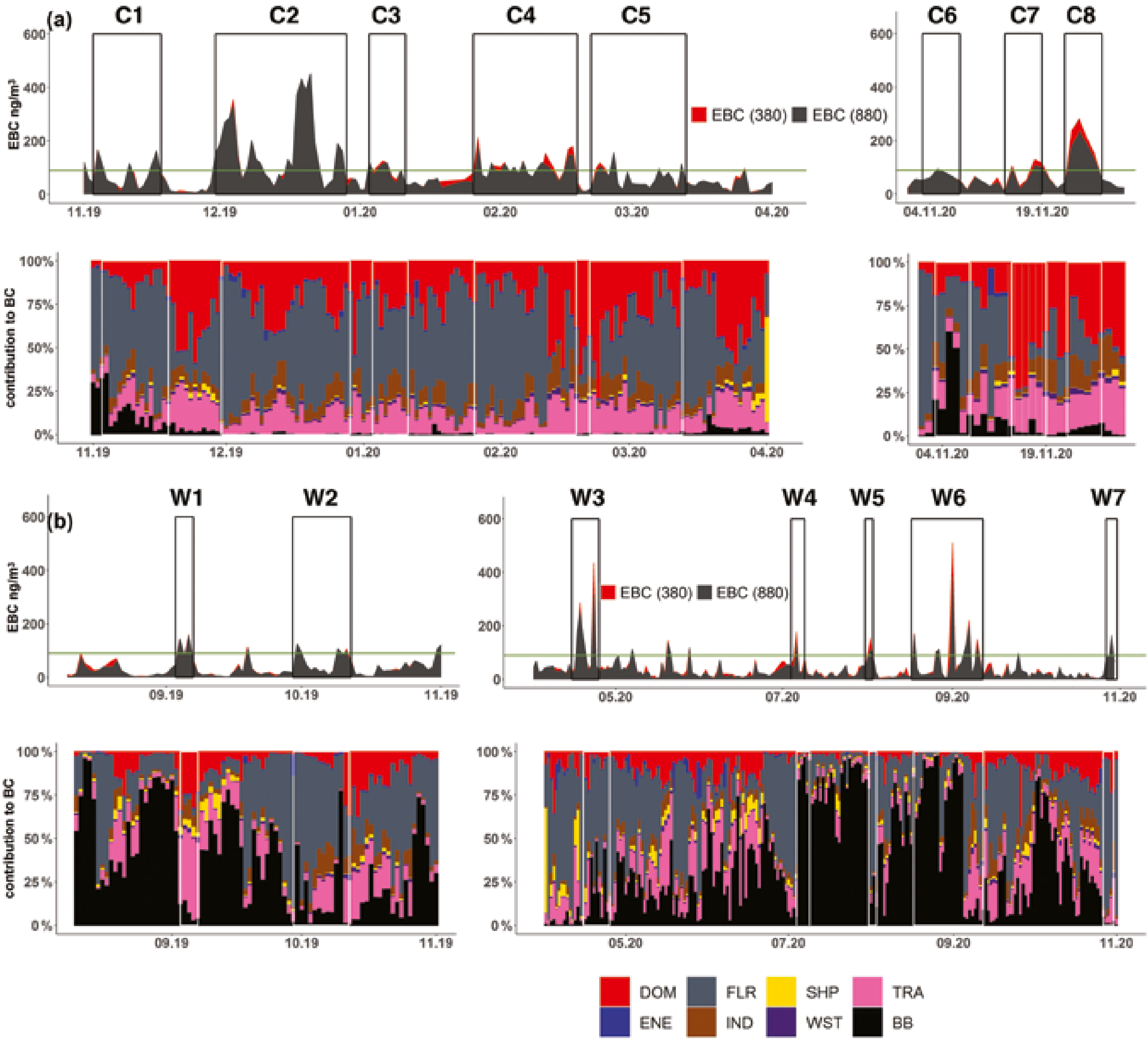

Figure 5. The 24 h median EBC concentrations measured at 880 nm (black) and 370 nm (red), as well as source contributions to surface BC from anthropogenic (DOM, ENE, FLR, IND, SHP, WST, TRA) and BB sources for (a) the cold and (b) the warm period. Pollution episodes were composed from the periodically repeated events of high EBC concentration. The straight green line indicates the pollution level of the 80th percentile.

more anthropogenic BC from highly populated regions.

Monthly averaged BC contributions from different sources simulated by FLEXPART using ECLIPSEv6 emissions are shown in Fig. 4c and Supplement Table S3. From November 2019 to March 2020 the FLR sector contributed 47 %–68 % (maximum in January 2020) to surface BC when air masses arrived at Bely through oil and gas extraction sites. February and November 2020 demonstrated the biggest non-gas flaring impact. More specifically, February 2020 coincides with the largest model overestimation (Fig. 4a), implying a likely misestimation of non-gas flaring emissions in ECLIPSEv6. From April 2020 the impact of FLR dropped significantly (Supplement Table S4), with a minimum of 12 % in June. Starting from April to October 2020, BB emissions played the biggest role in surface BC, contributing 81 % in July 2020. It is noteworthy that the impact of SHP emissions became quite perceptible in the warm period when the oceanic ice is absent in the Arctic and touristic cruises peak.

Emission sensitivities of surface BC presented over the whole Arctic (north of 66° N) have been also simulated using the same model (Zhu et al., 2020). Anthropogenic sources contributed 82 % of the annual BC, as estimated from the BCRUS emission dataset. Arctic BC originated predominantly from anthropogenic emissions in Russia (56 %), mainly FLR from YNAO, KMAO and Komi Republic (31 % of surface Arctic BC). In summer (July–August), open BB in Siberia, Alaska and Canada contributed 75 %. At Zeppelin, modeled BC (39.1 ng m^{-3} for annual mean) was reported to be 85 % higher than the observed value (21.1 ng m^{-3} for annual mean) (Zhu et al., 2020). At Tiksi, modeled BC was underestimated (74.4 ng m^{-3} for annual mean) by 40 % compared with observations (104.2 ng m^{-3} for annual mean) (Zhu et al., 2020). Annual (from September 2019 to August 2020) median modeled concentrations of BC using ECLIPSEv6, BCRUS and CAMS for the Island Bely station are shown in Supplement Table S2. We find that modeled

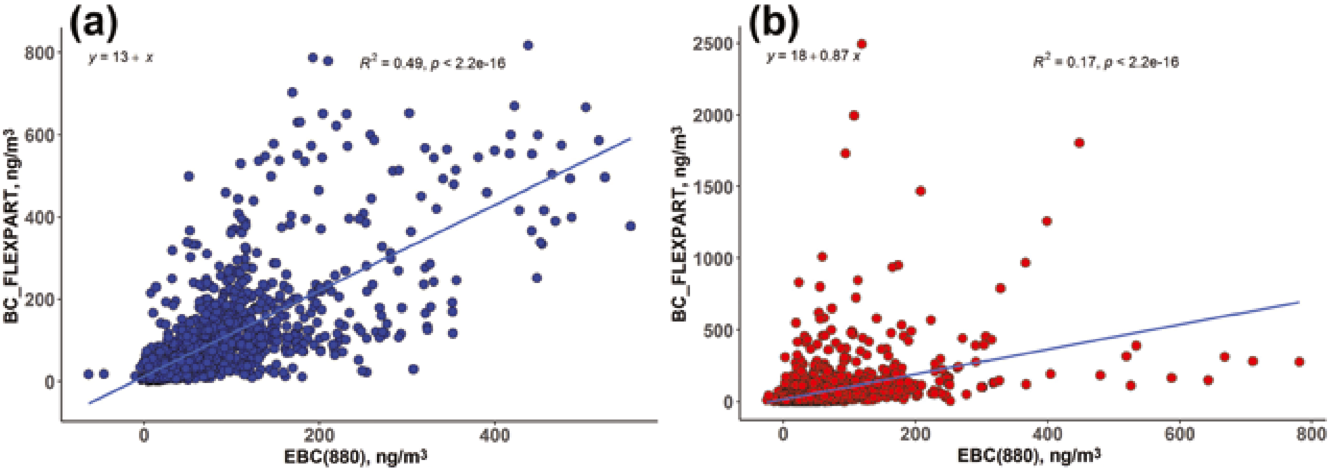

Figure 6. Scatterplots of 3 h median measured EBC(880) against modeled BC from FLEXPART for the (a) cold and (b) warm period. Solid line is the linear regression fit of the comparison between modeled and observed values.

BC (78.4 ng m^{-3} for annual mean) is 26 % higher than the observed value (61.8 ng m^{-3} for annual mean); the overestimation is much smaller than observed for other remote stations. Annual averaged contributions of anthropogenic emissions by ECLIPSEv6 and ECLIPSEv6 with flaring from BCRUS were equal to 76 % and 80 %, respectively, due to the difference in FLR emissions in the two datasets (Supplement Table S4).

3.2 Cold season pollution

Figure 5a shows EBC concentrations measured at the Island Bely station during the cold period from November 2019 to April 2020 and from 1 to 30 November 2020. The time series indicates that EBC undergoes the typical Arctic seasonal trend with higher concentrations in winter and early spring and lower in summer. Background pollutant concentrations at Arctic stations are generally very low without any detectable influence from local or regional sources (Eleftheriadis et al., 2004; Popovicheva et al., 2019b). We relate the Arctic background to the lowest 20th percentile of EBC data (10 ng m^{-3}). Long-term pollution episodes were assumed to be repeated events of high EBC concentration above the 80th percentiles (90 ng m^{-3}) that are clearly distinguishable from the background (Fig. 5a).

The aerosol optical properties with respect to absorption, presented as daily median AAE, are shown in Fig. 2d. The AAE for highly aged aerosols measured during periods of low BC was lower than 1 (reaching values as low as 0.2) and is mostly related to the aerosol size distribution (large particles) and internally mixed BC particles (Cappa et al., 2016). As shown by modeling studies (Virkkula, 2021), pure BC particles surrounded by non-absorbing coatings can have AAEs in the range from < 1 to 1.7, also depending on the morphology of the fractal aggregates (Romshoo et al., 2021). The AAE increased in periods of higher aerosol concentration levels in the cold period ranging from 0.6 to 1.35.

In many cases, when AAE exceeded 1 in the cold period, the pollution episodes could be identified as being influenced by BB. However, due to the mixing with background aerosol and aging processes, a large variability in AAE values might be observed at receptors of long-range-transported pollution, and AAE may not be representative of BB sources. Nevertheless, it can still be used as a qualitative parameter when extra information is available. Such events of increased AAE were rarely observed in our study, and the most prominent BB impact occurred during the pollution episodes C4, C7 and C8 when the impact of domestic sources was significant (Fig. 5a).

In general, FLEXPART coupled with ECLIPSEv6-CAMS emissions captures periods with both high and low concentrations relatively well (Fig. 2c). A good correlation between measurements and simulations, with a Pearson coefficient R of 0.7 and the root mean squared error (RMSE) of 89.2 ng m^{-3}, was obtained for the cold period (Fig. 6a). According to monthly median contributions to BC concentrations in the cold period, the impact of anthropogenic sources, namely FLR, DOM and TRA, dominated surface BC by 97.7 % (Fig. 4c).

Looking closely to specific episodes, during pollution episode C1, three events of high EBC concentrations were observed (Fig. 5a). On 5 November 2019, measured EBC reached 180 ng m^{-3}, while FLEXPART simulated similarly high BC values. Footprint emission sensitivities at this time showed that air masses originated from East and North Europe, passed south of European Russia, and then turned straight through West Siberia approaching Bely Island from the southeast (Fig. 7). The same air mass moved towards the large Russian FLR sources of YNAO, KMAO and Krasnoyarskiy Kray (see Fig. 1), causing up to a 71 % contribution to surface BC (Supplement Table S5).

On 12 November 2019, air masses arrived at Bely Island through the Yamal Peninsula after passing from the ocean (Supplement Fig. S1). The model strongly underestimated measured EBC concentrations by about 10 times (Fig. 7). We fail to provide a concrete explanation for this; a simplified hypothesis is that a number of flaring sites located at the Yamal Peninsula might have not been included in the emission database, but this certainly needs further research. In contrast, the model strongly overestimated measured EBC concentrations on 16 November 2019. At that time, air masses passed through remote regions of eastern Siberia and arrived through the gas flaring sites of Krasnoyarskiy Kray at the station (Fig. 7) causing an FLR contribution of 98.6 % to surface BC (Supplement Table S5). The reason might be the use of incorrect emission factors for BC at the FLR facilities of Krasnoyarskiy Kray in the adopted emissions because direct transport from

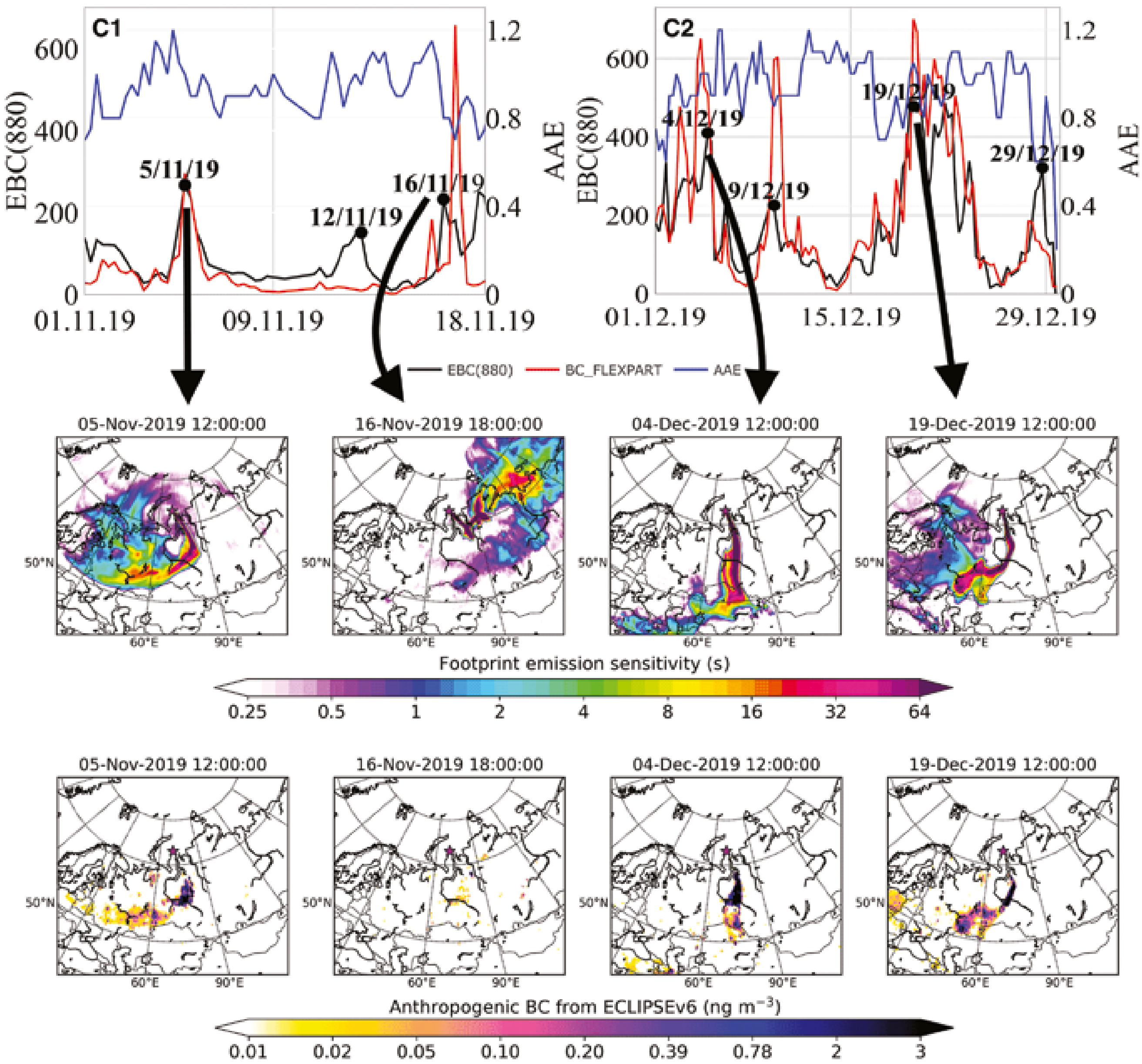

Figure 7. Examples of pollution episodes C1 and C2 observed in the cold period (see Fig. 5a), during which FLR contribution prevails. The 6 h median EBC(880) (black line), BC simulated with FLEXPART (red line) and AAE (blue line) (upper row) values. Footprint emission sensitivities in seconds showing the largest probability of emission origin (middle row). Spatial distribution of anthropogenic contribution (in ng m^{-3}) to surface BC at the Island Bely station (bottom row).

this region was observed. During 12 and 16 November 2019 the AAE was in the range from 0.7 to 1, which agrees with the expected optical properties for the FLR sources.

Pollution episode C2 in December 2019 gave the highest EBC concentrations observed during the whole cold period (Fig. 5a). On 4 December, EBC approached 400 ng m^{-3}, when air masses originated from Kazakhstan and the Russian gas flaring regions of KMAO and YNAO (Fig. 8). The maximum EBC concentration of approximately 500 ng m^{-3} with an AAE of 1.05 was observed on 19 December when air came from Europe, initially through the Russian oil and gas basins of Volga-Ural in the south of European Russia and then through KMAO and YNAO in western Siberia (Fig. 8). During the December pollution events, FLR contribution dominated, reaching 73 % on 19 December (Supplement Table S5).

The highest FLR contributions were observed during the pollution episodes C3–C6 (Supplement Table S5). Similar air mass transportation through either gas and oil fields of YNAO and KMAO in western Siberia or Komi and Nenets regions north of European Russia occurred in all of the events (Supplement Fig. S1).

In contrast to the aforementioned events, the pollution episode C7 was unrelated to FLR as air masses did not cross flaring regions (Fig. 8). On 16 November 2020, retroplumes confirm the origin of surface BC from Central and East Europe and the Kola Peninsula (Fig. 8). DOM and TRA hold the largest share of the source contribution with 73 % and 20 %, respectively (Supplement Table S5), while the model overestimated measured EBC. Episode C8 gave the biggest EBC (370) concentration which reached 346 ng m^{-3} and exceeded EBC(880) (133 ng m^{-3}) on 24 November 2020 (Supplement Table S5). At this time, air masses came to Bely Island directly from the most populated region of European Russia (Fig. 8). The contributions of DOM and TRA were 34 % and 23 %, respectively. AAE approached the highest value observed (1.3) during the study period. This might show a detectable impact of biomass burning in the classified DOM emissions. BC from wood burning contributes around 61 % of the total residential emissions, especially in areas where there is limited use of natural gas (Kalogridis et al., 2018a) and in forest regions (Huang et al., 2015). Note that the impact of IND emissions was the largest in episodes C7 and C8 as compared to the whole cold period (Supplement Table S5) due to industrial emissions from sites in central European Russia.

3.3. Warm season pollution

Figure 5b shows EBC concentrations measured at the Island Bely station during the warm period from 10 August to 31 October 2019 and from 1 April to 1 November 2020. It is immediately seen that BC in the warm period was mainly affected by Russian emissions (90 %) and only in October 2020 and August 2019 partly (~ 20 %) by European and North American emissions (Fig. 4). EBC concentrations rarely exceeded the 80th percentile that was set as the pollution criterion, while the duration of the warm period episodes was shorter.

Due to the mixing with background aerosol and aging processes, air masses influenced by BB events should be expected to have increased AAE as compared to the BC produced by fossil fuel. However, aging processes may induce a high variability in AAE in areas affected by long-range transport, and hence AAE may not be representative of a BB source. Pollution events were rarely observed in this season, and the most sufficient BB impact occurred during the pollution episodes W4, W7 and W8.

However, events characterized by higher AAE were observed more often, indicating that BB impact was more significant during the warm period, mainly during spring and summer (episodes W3, W4 and W6). A comparison between measured and modeled concentrations showed a poor correlation (R of 0.41 and RMSE of 121 ng m^{-3}) (Fig. 6). According to monthly median contributions to surface BC concentrations in the warm period, the impact of BB emissions was as high as 50 % (Fig. 4c). SHP emissions contributed about 1 % as a result of the increase in touristic activity in the Arctic and the more active use of the Northern Sea Route due to the Arctic ice retreat.

From the beginning of the study period in August 2019, large wildfires were observed in Siberia (Voronova et al., 2020). The latter resulted in a strong BB impact at the Island Bely station (Fig. 5b). However, during episode W1, EBC concentrations not caused by wildfire plumes reached approximately 200 ng m^{-3} (Fig. 5). During this time, air masses were transported from northern Europe (Supplement Fig. S1), and the main contribution to surface BC at the Island Bely station was due to TRA emissions (36 %, Supplement Table S5).

Episode W2 during October 2019 (Fig. 5) was characterized by EBC of 119 ng m^{-3}, while modeled BC was strongly overestimated (Supplement Fig. S1). The calculated BB contribution to the station's surface BC was 64 % (Supplement Table S5), and the hotspot BB sources were near the Pur River (YNAO), as recorded by CAMS (Supplement Fig. S1). The measured AAE does not indicate any contribution from BrC, as would be expected for BB sources, and observed AAE values were lower than 1 (Supplement Table S5). Note that the FIRMS active fire data analyses (https://firms.modaps.eosdis.nasa.gov/, last access: 1 April 2022) indicate that the fire spots were in the same grid cell as industrial facilities of an oil extraction field in the Purovsky region (YNAO). Thus, it might be that thermal anomalies from flaring facilities were mistakenly related to fires in CAMS. This hypothesis is reinforced by the fact that no wildfires were recorded by the local forest fire service (https://aviales.ru, last access: 1 April 2022) during October 2020 in western Siberia and Krasnoyarskiy Kray.

Pollution episode W3 is related to strong springtime wildfire activity that occurred in southern Siberia. The retroplumes on 18 and 23 April 2020 showed that the air originated from Central Asia, a large territory of southern Siberia and Krasnoyarskiy Kray, and arrived at Bely Island through western Siberia from the southeast (Supplement Fig. S1, Fig. 9). High footprint emission sensitivities coincided with the location of large wildfires resulting in BB contribution to surface BC at the station equal to 28 % (18 April 2020) and 19 % (23 April 2020). The most significant impact of wildfires was observed on 23 April 2020, when the 6 h median EBC concentration reached 700 ng m^{-3} with AAE ranging from 1.3 to 1.5, clearly indicating an elevated contribution of BrC (Supplement Table S5).

Wildfires occurred in northern Krasnoyarskiy Kray and Sakha Republic, Central Siberia, between April and November 2020 (https://aviales.ru/popup.aspx?news=6286, last access: 1 April 2022) that burned around 7 000 000 ha of forest. The pollution episode W4 on 7 July 2020 recorded a 6 h median EBC of 150 ng m^{-3} and an AAE of around 1.4, clearly indicating BB impact. The model captures this event well, providing the highest BB contribution exactly when observed, equal to 90 % (Supplement Table S5). Air masses arrived from the east and passed north of Krasnoyarskiy Kray where the large wildfires occurred (Fig. 9).

Unprecedented high wildfire-related BC concentrations were observed in September 2020 (pollution episode W6). EBC concentrations exceeded 5 and 20 times the 80th percentile of the measurements. Maximum 6 h median EBC reached 534 ng m^{-3} on 1 September 2020, and it was even higher than the largest Arctic haze concentration observed in December 2019 (Supplement Table S5). Increased AAE of around 1.4 revealed a strong BB impact. This event resulted from long-range transport of BC from the Eurasian continent during the intensive wildfires in western Siberia (Krasnoyarskiy Kray and Yakutia) (Fig. 9), where around 1 000 000 ha of forest was burned in August 2020. The contribution of BB to surface BC at the Island Bely station was as high as 95 %.

Despite the exclusive BB origin of the light-absorbing carbon measured at the Island Bely station, the AAE was much lower than the established value for fresh BB (close to 2) (Sandradewi et al., 2008) likely due to aging. This apparent reduction in the BrC contribution to absorption is in agreement with Forrister et al. (2015), who examined BrC concentrations and AAE from western US forest fires as a function of aging. Their results show that most of the BrC (~ 94 %) emitted from wildfires was lost within a day. Similar observations have been reported for long-range-transported North American smoke over the northeastern Atlantic (Zheng et al., 2020) and for trans-

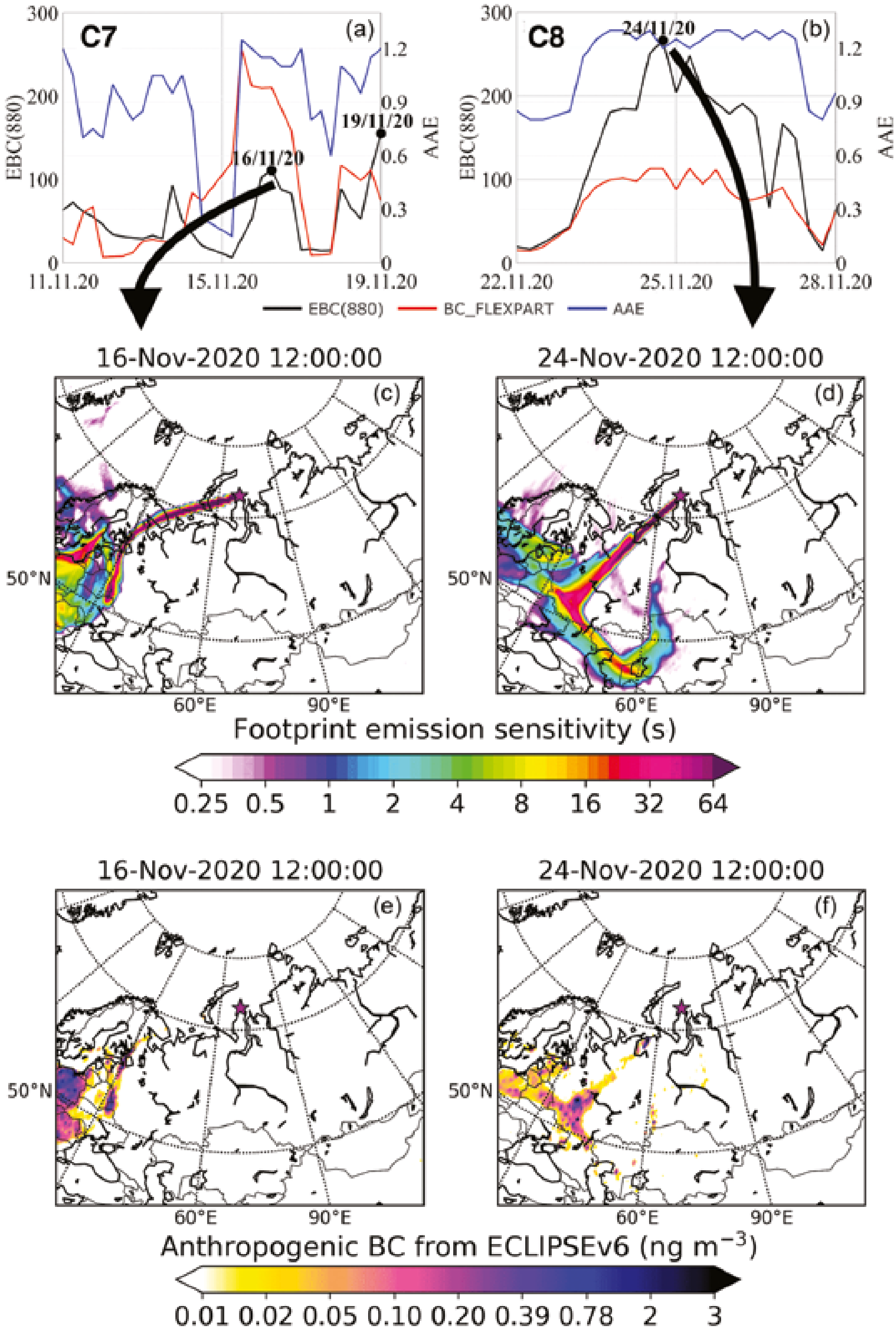

Figure 8. Examples of pollution episodes C7 and C8 observed in the cold period (see Fig. 5a), during which DOM and TRA contributions prevail. Time series of measured EBC, modeled BC and AAE (a, b), footprint emissions sensitivities (c, d), and anthropogenic contribution to surface BC (e, f) are shown.

ported Russian smoke over the Mediterranean (Diapouli et al., 2014).

The last pollution episode W7 was observed at the end of October 2020. Although it occurred in the warm period, it is rather related to Russian FLR and European TRA emissions (Supplement Table S5, Fig. 5b). At the end of October 2020 air masses came mainly from Europe, passing through the Yamal Peninsula.

4 CONCLUSIONS

The present paper aims at performing a quantitative analysis of the Arctic pollution via high-resolution measurements from a recently developed aerosol station at Bely Island (Kara Sea) combined with Lagrangian modeling. A consequent goal is to examine the impact of anthropogenic and natural sources to the high Arctic as a

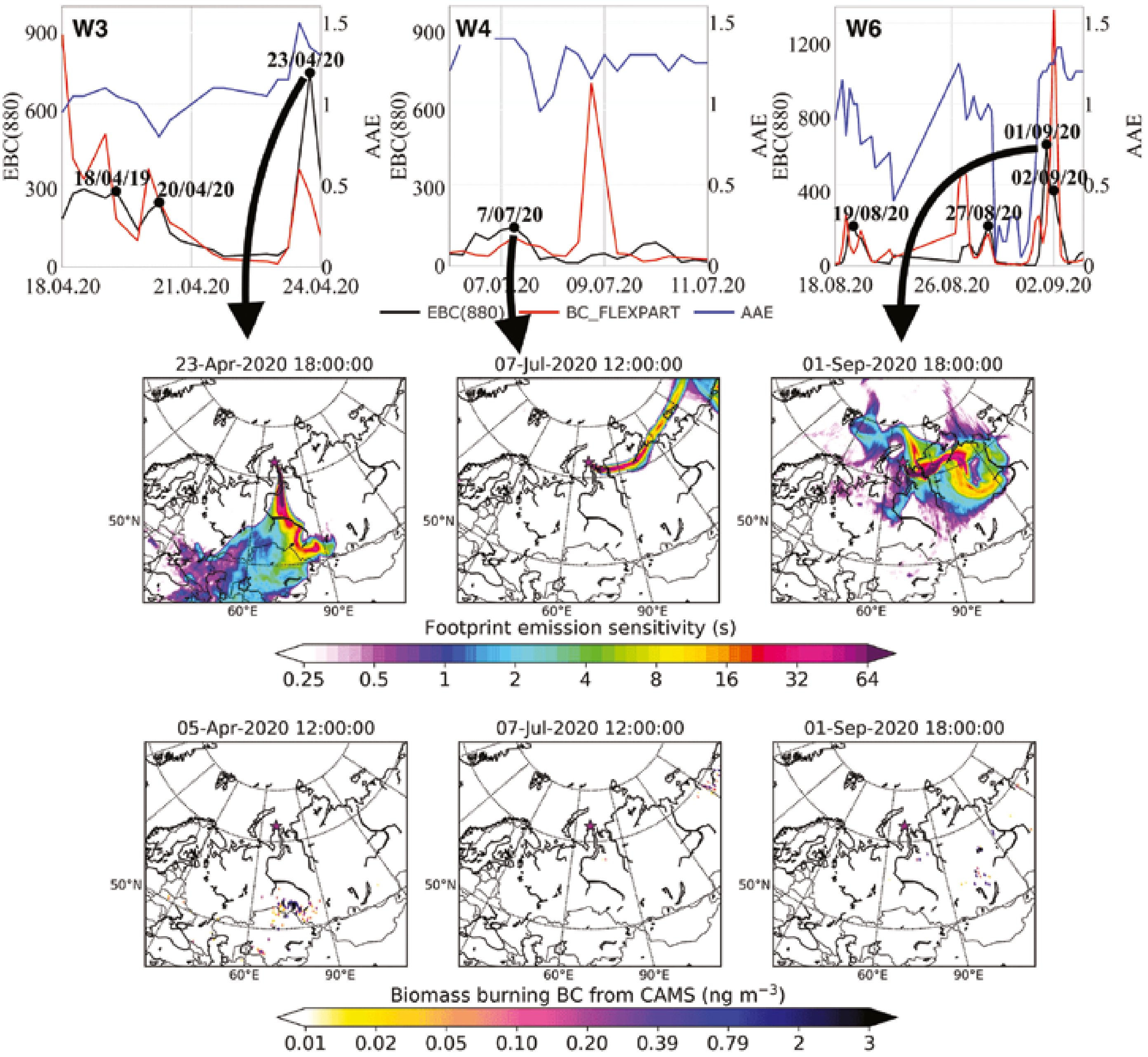

Figure 9. Examples of pollution episodes W3, W4 and W6 in the warm period (see Fig. 5b), during which BB contribution prevails. The figure has been arranged similar to Fig. 7 (time series of measured EBC, modeled BC and AAE, footprint emissions sensitivities and BB contribution to surface BC).

result of long-range transport. The main results can be summarized as follows.

- EBC monthly climatology is following the typical Arctic aerosol seasonal variation characterized by higher EBC concentrations in winter and lower in summer.
- AAE for aged BC larger than 1 indicates wildfire impact in the warm period, but mixing with gas flaring emissions from nearby regions was also observed.
- The recently upgraded ECLIPSEv6 emissions and ECLIPSEv6 coupled with FLR from BCRUS represent measured EBC accurately in the cold period. Annual average contributions of anthropogenic emissions to surface BC were 76 % and 80 % (50 % and 59 % from gas flaring) for each dataset, respectively.
- The most significant model overestimation was observed in February 2020 when air masses passed through non-gas-flaring regions. The largest underestimation occurred in April 2020 during the period of spring agriculture fires.
- Daily BB emissions from CAMS were more efficient in representing pollution episodes than monthly GFED4 emissions, and therefore they were mainly used here.
- Russian emissions dominate during the whole year; European and Asian ones contribute up to 20 % in the cold period. Pollution episodes with EBC concentrations above 90 ng m^{-3} occur in 18.5 % of the observation time. Monthly average FLR emissions dominate (98 %) any other emission sector.
- FLR and BB emissions contribute the largest share of EBC to the Island Bely station during the cold and warm period, respectively. This is consistent with previously reported source contributions to the Rus-

sian Arctic. When air is transported from Europe, other sources such as TRA become important. The same applies for SHP emissions that become important in summertime because of cruise activities and ice retreat.

- Emissions from gas and oil fields in western Siberia and northern European Russia cause the vast majority of the pollution episodes in the Arctic.
- A total of 15 pollution episodes with concentrations reaching close to 723 ng m^{-3} were detected. The duration of the cold pollution episodes is longer than of the warm period, and the median (up to 160 ng m^{-3}) and maximum EBC (up to 450 ng m^{-3}) concentrations are higher.

In conclusion, the significance of high-quality measurements at the Island Bely station is established in the present study because (i) the station is located along the main pathway of air masses entering the Arctic, and (ii) it is north of the world's largest gas flaring regions. The operation of the Island Bely station is an asset in source emission optimization because EBC measurements in the High Arctic are still rare.

DATA AVAILABILITY

All model data used in the present publication, together with all figures of footprint analysis and source contributions to surface BC, are openly available through the websites https://niflheim.nilu.no/NikolaosPY/Bely_2020_cams.py (Evangeliou, 2022a) and https://niflheim.nilu.no/NikolaosPY/Bely_2020_huang_cams.py (Evangeliou, 2022b). All raw model data can be obtained from the corresponding author upon request. The definitions of the regions and continents used in the current analysis are based on regional masks that can be seen in Supplement Fig. S3.

SUPPLEMENT

The supplement related to this article is available online at: https://doi.org/10.5194/acp-22-5983-2022-supplement.

Лесные пожары как источник черного углерода в арктике летом 2022 г.*

ВВЕДЕНИЕ

Характерное для современного глобального потепления распределение тенденций приповерхностной температуры и осадков на севере Евразии свидетельствует об ее определяющем вкладе в изменения климата Северного полушария [1]. Вариации крупномасштабной атмосферной циркуляции, сопровождающие изменения климата на севере Евразии, приводят к аномальной жаре, засухам и, как следствие, к сильным пожарам [1]. Отмечаются особенности формирования летней жары на европейской территории России в контексте общих изменений климата [2]. Лесные и сельскохозяйственные пожары, в которых ежегодно сгорают миллионы тонн биомассы, оказывают значительное влияние на радиационный баланс атмосферы, облачность и климатическую систему Северного полушария [3]. Дымовые эмиссии пожаров в бореальных лесах и лесах умеренных широт вносят существенный вклад в глобальный баланс углерода, являются источником климатически активных аэрозолей на региональном уровне [4]. Экологически опасные компоненты дымов в шлейфах пожаров могут распространяться на обширные территории. Зарегистрировано влияние широкомасштабного транспорта дымовых эмиссий из европейской России в Европу [5]. Шлейфы крупных лесных пожаров в Восточной Сибири привели к увеличению концентрации аэрозолей над озером Байкал [6], а перенесенные вдоль трансарктического пути – в западной Канаде [7]. В Японии наблюдалось ухудшение качества воздуха под действием дымов сибирских пожаров [8]. Растущая антропогенная нагрузка на окружающую среду и климатические изменения повышают уровень пожарной активности, что в результате наносит большой ущерб экономике регионов и здоровью населения [9].

При горении биомассы происходит образование многокомпонентных аэрозолей разного состава и свойств, зависящих от условий сжигания, вида растительности, влажности и минерализации почвы [10–12]. Открытое высокотемпературное пламенное горение является источником образования черного углерода (BC, black carbon), многообразные соединения органического углерода (OC, organic carbon) доминируют в продуктах пиролизного сжигания (тления) при низких температурах [13; 14]. Длительные наблюдения выявили значительное влияние верховых и низовых лесных пожаров на уровень концентрации черного углерода [15].

Арктический регион особенно подвержен воздействию крупномасштабных эмиссий антропогенных источников и лесных пожаров [16]. В зимне-весенний период из-за комбинации интенсивного дальнего переноса антропогенных эмиссий и температурной инверсии наблюдается явление арктической дымки, в теплые сезоны устойчивость атмосферы уменьшается, и концентрация аэрозолей падает [17]. Черный углерод в составе продуктов горения природных топлив и биомасс хорошо поглощает солнечное излучение, оказывает значительное воздействие на климат Арктики [18]. Рост концентрации черного углерода с начала 1980-х годов с учетом охлаждающей способности сульфатов привел к увеличению температуры поверхности на 0,29°C, что внесло значительный вклад в потепление региона [19]. В настоящее время черный углерод признан климатически значимым компонентом, вторым после углекислого газа [17]. Фракция высокомолекулярного OC, называемая коричневым углеродом (BrC, brown carbon), поглощает солнечное излучение в ультрафиолетовом диапазоне, внося значительный вклад в нагрев атмосферы региона.

В весенне-летние сезоны шлейфы пожаров достигают прибрежных районов российского сектора Арктики, где наблюдаются высокие концентрации BC – до 1,5 мкг/м^3 по сравнению с уровнем около 20 нг/м^3 в удаленных районах [20]. Весенние пожары в Сибири удваивают фоновый уровень загрязнений в арктическом регионе Северной Америки [21]. Сезонные циклы черного углерода, определенные в десяти полярных обсерваториях, продемонстрировали низкий уровень загрязнений летом, изредка нарушаемый переносом дымовых эмиссий пожаров с континента [22]. Значительная сезонная изменчивость наблюдалась на российских полярных станциях гидрометеорологической обсерватории Тикси (побережье Карского моря) и Ледовой базе «Мыс Баранова» (архипелаг Северная Земля, восточносибирский сектор Арктики) с максимумом концентрации черного углерода зимой 245 ± 169 нг/м^3 и низким фоновым уровнем 94,6 ± 84,7 нг/м^3 летом [23–25]. Сельскохозяйственные пожары в европейской России и на юге Сибири являются важным источником эмиссий и загрязнений Арктики [26]. Лесные пожары на территории Сибири случаются в весенние и летние месяцы с максимальным количеством площадей, охваченных пожарами во второй половине лета [9].

Аномально большие площади, пройденные огнем, и объемы эмиссий аэрозолей были зарегистрированы в Сибири в 2019 г. [9], когда от природных пожаров пострадали территории площадью 72,4 тыс. км^2, что составило 42% площадей природных пожаров в тот год на всей территории России. Причиной явились многодневная адвекция тепла и дефицит осадков, способствовавшие увеличению класса пожарной опасности и росту концентраций вредных газовых примесей и аэрозолей в атмосфере. Условия циркуляции, сопутствующие периодам силь-

---

* О. Б. Поповичева, М. А. Чичаева, Р. Г. Ковач, Н. С. Касимов, В. О. Кобелев, А. И. Синицкий//
Арктика: экология и экономика. 2023;13: с. 257-270
DOI: 10.25283/2223-4594-2023-2-257-270

ных пожаров, приводили как к ослаблению переноса черного углерода в Арктику летом 2010 г., когда траектории воздушных масс проходили в стороне от основных очагов пожаров и не обогащались эмиссиями горения; так и к увеличению концентрации черного углерода летом 2012 г., когда имел место перенос из районов крупномасштабных пожаров в Якутии [27].

Лето 2022 г., согласно сводкам Гидрометцентра России (https://meteoinfo.ru), оказалось засушливым и жарким, третьим в истории метеонаблюдений по достижению рекордных температур после 2021 и 2016 гг. Пожарная ситуация определила необходимость количественного анализа последствий переноса дымовых эмиссий в Арктику, позволяющего не только оценить уровень загрязнений и степень опасности их воздействия на окружающую среду, но и идентифицировать регионы наиболее значительных источников климатически активных аэрозольных компонентов атмосферы.

В 2019 г. на острове Белый, расположенном в Карском море, была установлена исследовательская полярная аэрозольная станция МГУ (https://peexhq.home.blog/2019/12/11/new-research-aerosol-stations-in-the-russian-arctic). Расположение станции на севере Ямало-Ненецкого автономного округа (ЯНАО) (рис. 1), на пути выноса крупномасштабных эмиссий из индустриальных регионов Западной Сибири, населенных и промышленных районов Европы и Азии предоставляет уникальную возможность для изучения аэрозольного состава атмосферы Арктики. В результате непрерывных измерений уровня загрязнений атмосферы черным углеродом был определен значительный вклад факельного сжигания газа в нефтегазодобывающих регионах Западной Сибири, Казахстана, Поволжья, Урала и Республики Коми, эмиссий транспортного и жилого секторов в холодный период года, а также сельскохозяйственных и лесных пожаров весной и летом [28].

Данная работа посвящена изучению аэрозольной нагрузки атмосферы по данным измерений, выполненных на инструментальном комплексе полярной аэрозольной станции «Остров Белый» летом 2022 г. Анализируются многократные эпизоды загрязнений в августе 2022 г., в которых концентрация черного углерода значительно превышала фоновый уровень, характерный для летнего периода. Измерения поглощающей способности аэрозолей в широком диапазоне солнечного излучения позволяют провести оценки влияния шлейфов лесных пожаров на аэрозольный состав атмосферы. На основе траекторного анализа переноса воздушных масс во время эпизодов загрязнений на острове Белый моделируется пространственное распределение источников черного углерода и определяются регионы источников пожарных эмиссий в августе 2022 г.

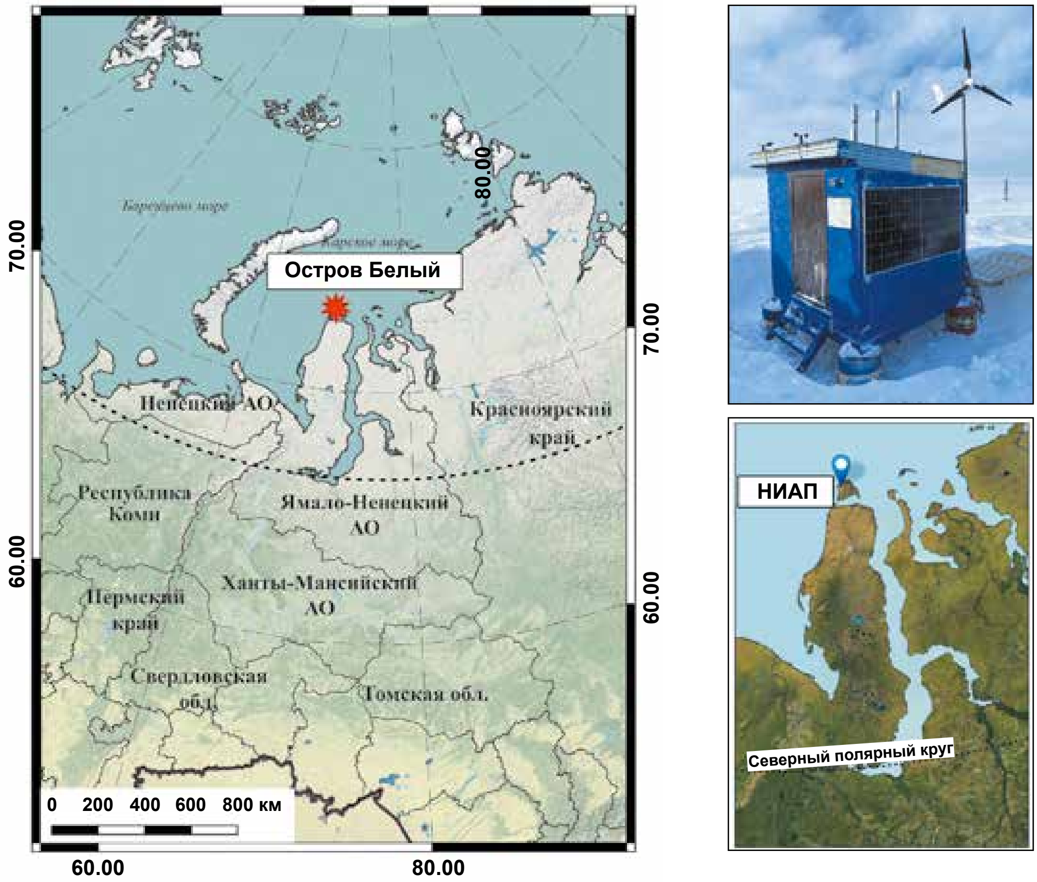

Рис. 1. Слева: расположение полярной станции МГУ «Остров Белый» на острове Белый (73°20'7,57"N, 70°4'49,05"E) в Карском море. Справа: павильон станции и его расположение на острове Белый (НИАП – научно-исследовательский аэрозольный пост). Составлено авторами на картографической основе ESRI Satellite https://server.arcgisonline.com
Fig. 1. On the left: location of the MSU polar station “Bely Island” on Bely Island (73°20'7.57"N, 70°4'49.05"E) in the Kara Sea. On the right: location of station pavilion on Bely Island (НИАП – scientific research aerosol post). Based on ESRI Satellite https://server. arcgisonline.com

ПРИРОДНЫЕ ПОЖАРЫ ЛЕТОМ 2022 г.

Июнь 2022 г. на территории России был умеренно теплым, на большей части страны зарегистрирована среднемесячная температура выше нормы на 2–3°С (https://meteoinfo.ru). Заметно теплее оказался июль 2022 г., превышение составило от 2 до 7°С. Август 2022 г. стал пятым самым теплым периодом в метеорологической летописи с 1891 г. Жаркая погода, державшаяся в центральных и северных районах в конце июля, с наступлением августа захватила практически всю европейскую территорию. В центральном районе европейской части страны температура воздуха достигала 30–35°С. Территории европейской России, а также Ханты-Мансийского автономного округа (ХМАО) и ЯНАО находились в области положительных температурных аномалий, среднемесячное отклонение составило 2–4°С (рис. 2). 12 августа в ХМАО и ЯНАО отклонение температур от среднемесячных достигло 12°С (https:// www.ventusky.com).

Атмосферное давление составило 1005–1010 Па над районами крайнего Севера, где расположился относительный барический минимум (https:// meteoinfo.ru) (рис. 3). В это время над континентальной частью наблюдались максимумы атмосферного давления до 1020 Па, определившие перемещение воздушных масс с континента в высокоширотные области Северного Ледовитого океана.

По данным модели GFS Американского национального управления по океану и атмосфере NOAA (https://www.ventusky.com), «на европейской территории России суммы атмосферных осадков за июнь и июль не достигли нормы, дефицит осадков составил –10...–40 мм», в августе 2022 г. территория европейской России и Западной Сибири находилась в области дефицита осадков от –10 до –100 мм. Температурные аномалии и засушливая погода повлекли за собой возникновение пожароопасной ситуации как в северных областях, так и на большей части площади европейской России.

По данным дистанционного мониторинга ФБУ «Авиалесоохрана» (https://aviales.ru/), август характеризуется максимальными числом и площадью пожаров, зарегистрированных в Западной Сибири: в ЯНАО – 11 628 га, в ХМАО – 349 525 га. Их площадь превысила территории, охваченные пожарами в июле, в три и два раза соответственно. В европейской России по площади, пройденной огнем, доминировали Республика Коми (24 730 га), Рязанская (24 416 га) и Нижегородская (7561 га) области. На территории ЯНАО в 2022 г. пик пожарной опасности пришелся на вторую половину июля и начало августа, когда было зарегистрировано 397 природных пожаров (https://aviales.ru/ popup.aspx?news=7551). Самый масштабный лесной пожар с 7 по 15 августа охватил 800 га. В ХМАО с начала пожароопасного сезона (с 22 апреля по 31 августа 2022 г.) было ликвидировано 432 лесных пожара. В европейской России лидерами по числу пожаров стали Республика Коми (443), Нижегородская (91) и Рязанская (50) области.

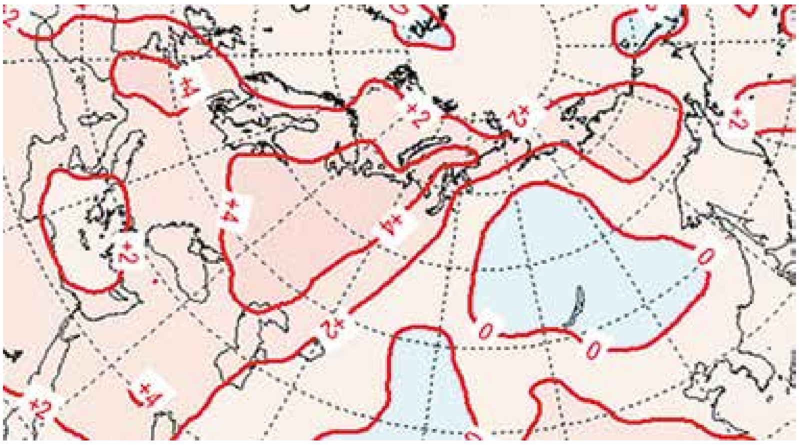

Рис. 2. Карта аномалий температуры воздуха на высоте 2 м над уровнем земли в августе 2022 г. Составлено авторами по данным https://meteoinfo.ru

Fig. 2. Map of air temperature anomalies at 2 m AGL in August 2022. Based on https:// meteoinfo.ru

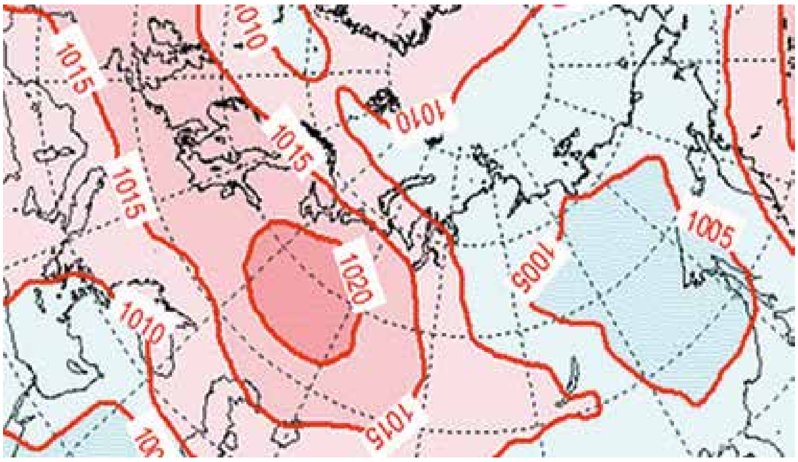

Рис. 3. Барическое поле на уровне моря в августе 2022 г. Составлено авторами по данным https://meteoinfo.ru

Fig. 3. Baric field at sea level in August 2022. Based on https://meteoinfo.ru

МЕТОДЫ ИЗМЕРЕНИЙ НА ОСТРОВЕ БЕЛЫЙ

Непрерывные измерения уровня концентрации черного углерода проводятся на базе полярной аэрозольной станции МГУ «Остров Белый» (см. рис. 1). Методика обработки данных учитывает местонахождение метеостанции им. М.В. Попова на юго-востоке от павильона станции, где работает дизельный генератор, являющийся единственным локальным источником загрязнения на острове. Главным преимуществом научно-исследовательского аэрозольного поста является его изоляция от антропогенных источников в отличие от гидрометеорологической обсерватории «Тикси», находящейся под воздействием выбросов близлежащего поселка Тикси [29]. Для обработки метеопараметров использовались данные с сайта погоды (https://rp5.ru/). Измерения черного углерода, проведенные при направлении ветра с метеостанции, исключались из анализа.

Система отбора проб аэрозолей в реальном времени специально разработана для суровых арктических условий, снабжена системой обогрева и защиты от сильных ветров. Аэталометр AE33 (Magee Scientific) измеряет поглощение света частицами, осаждающимися на фильтре при прокачке воздуха с разными скоростями потока [30], на семи длинах волн от ультрафиолетового (470 нм) до инфракрасного (950 нм) диапазонов с разрешением 1 мин. Поглощение на длине волны 880 нм пересчитывается в эквивалентную концентрацию черного углерода eBC(880) с массовым коэффициентом 7,7 м^2/г. Спектральная зависимость позволяет учесть увеличенное поглощение фракции высокомолекулярного органического углерода в ультрафиолетовом диапазоне излучения по сравнению с инфракрасным [31]. В данной работе разница между eBC(470) и eBC(880) является индикатором влияния лесных пожаров и обозначается DeltaC. Эта величина оказывается значительной в эмиссиях сжигания биомасс [32; 33].

Фоновые аэрозольные концентрации в Арктике определяются в отсутствие влияния локального и регионального загрязнения [29; 34]. Согласно исследованиям, проведенным в 2019–2020 гг., фоновая концентрация черного углерода на острове Белый составляет 10 нг/м^3. Длительные события, в течении которых концентрация eBC превышала пороговое значение, равное 80 перцентилям выборки (90 нг/м^3), были определены как эпизоды загрязнений [28].

Для исследования пространственной неоднородности распределения черного углерода применена методика построения розы загрязнений в полярных координатах направления и скорости ветра [35], что позволяет определить направление источника высоких концентраций для точки мониторинга [36].

Метод отнесения траекторий переноса воздушных масс к концентрации загрязнений в момент их прихода в точку наблюдений (concentration weight trajectories) [37] позволяет определить местонахож дение потенциальных источников. Концентрация Cij для каждой ячейки сетки (i, j) рассчитывается в соответствии с формулой

$$\ln(\bar{C}_{ij}) = \frac{1}{\sum_{k=1}^{N}\tau_{ijk}} \sum_{k=1}^{N} \ln(Ck)\tau_{ijk},$$

где i и j – широта и долгота ячейки; k – индекс траектории; N – общее число рассчитанных траекторий; C_k – концентрация, измеренная в момент прихода траектории k; τ_{ijk} – время пребывания траектории k в ячейке (i, j).

В данной работе региональное распределение источников черного углерода для острова Белый определялось путем соотношения обратных траекторий переноса воздушных масс за период наблюдений (август 2022 г.) к концентрации eBC в момент их прихода на станцию «Остров Белый». Рассчитан массив обратных траекторий переноса воздушных масс с шагом 1 ч и длительностью десять дней на высотах 250, 500 и 1000 м над уровнем земли (AGL) на основе модели HYSPLYT лаборатории «Air Resources Laboratory» [38] и архивных метеорологических данных GDAS (http://www.arl.noaa.gov/ ready) с пространственным разрешением 1° широты и 1° долготы. Статистическая обработка данных и визуализация результатов проводились с использованием языка программирования R (ПО RStudio), пакетов OpenAir, Plotly, ggplot2, карты построены посредством ГИС-пакета QGIS.

Информация об очагах пожаров получена из базы данных Fire Information for Resource Management System (FIRMS), созданной системой NASA/GSFC Earth Science Data Information System (ESDIS) (https://firms.modaps.eosdis.nasa.gov/map) спутникового зондирования термоактивных точек на поверхности земли. Для наблюдения шлейфов пожаров использовались космоснимки NASA Earth Observing System Data and Information System WORLDWIEW (https://worldview.earthdata.nasa.gov/). Расположение газовых факелов нефтегазодобывающего и перерабатывающего комплекса определялось по данным спутников MODIS и VIIRS о свечении объектов с температурой выше 1200°C, характерной для факельного сжигания газа (https://viirs.skytruth.org/ apps/heatmap/).

ОБСУЖДЕНИЕ РЕЗУЛЬТАТОВ

Эпизоды загрязнений черным углеродом в августе 2022 г.

Непрерывные измерения черного углерода в 2019–2020 гг. на полярной аэрозольной станции МГУ «Остров Белый» показали сезонную изменчивость, характеризующуюся высокими значениями с декабря по апрель (60 ± 92 нг/м^3) и минимальными в июне-сентябре (18 ± 72 нг/м^3) [28]. В среднем летом концентрации были в 10 раз ниже, чем зимой, редко наблюдались эпизоды загрязнений. Перенос дымовых эмиссий лесных пожаров в Красноярском крае и Якутии был зарегистрирован 7 июля и 1 сентября 2020 г. По среднесуточным данным максимум черного углерода (534 нг/м) наблюдался 1 сентября 2020 г., тогда он превысил арктический фон в 20 раз.

В июне и июле 2022 г. на станции «Остров Белый» наблюдались фоновые концентрации BC (15,8 ± 14,2 нг/м^3) за исключением периода с 3 по 8 июля, когда концентрация черного углерода превысила 150 нг/м^3. Временной ряд одночасовых усредненных концентраций черного углерода в августе 2022 г. представлен на рис. 4. Наблюдается большая варьируемость концентраций eBC(880) от 0,5 нг/м^3 до максимального значения 851 нг/м^3 12 августа в 09:00. Для сравнения с концентрациями черного углерода,

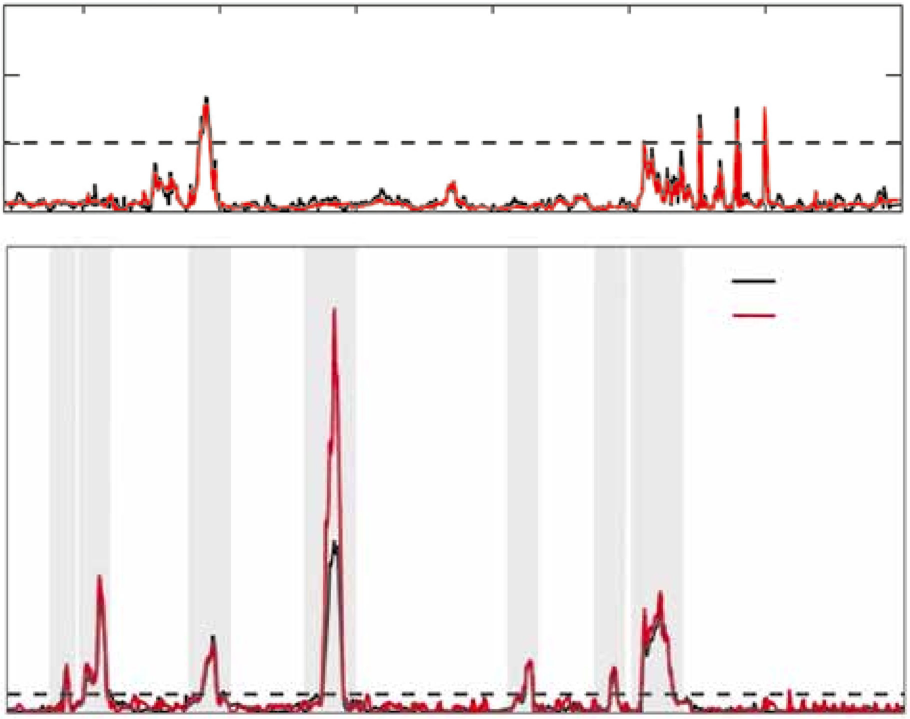

Рис. 4. Концентрации черного углерода на длинах волн 880 и 470 нм в июне и июле 2022 г. (а) и августе 2022 г. (б). Эпизоды, помеченные номерами, описаны в табл. 1. Пунктирной линией показано пороговое значение загрязнения 90 нг/м^3

Fig. 4. Black carbon concentrations at wavelengths of 880 and 470 nm in June and July 2022 (а), August 2022 (б). Episodes marked by numbers are described in Table 1. The dotted line indicates the pollution threshold of A pollution threshold of 90 ng/m^3

Таблица 1. Эпизоды загрязнений черным углеродом на станции «Остров Белый» в августе 2022 г. Максимальная концентрация eBCmax(880) на длине волны 880 нм, разница DeltaC между eBC(470) и eBC(880)

Эпизод	Дата, время	eBC$_{max}$(880), нг/м^3	DeltaC, нг/м^3
I	02.08.2022, 23:00 – 03.08.2022, 23:00	227	16
II	04.08.2022, 0:00 – 04.08.2022, 12:00	567	116
III	07.08.2022, 17:00 – 08.08.2022, 11:00	384	9
IV	11.08.2022, 16:00 – 12.08.2022, 14:00	851	1150
V	18.08.2022, 21:00 – 19.08.2022, 03:00	238	18
VI	21.08.2022, 19:00 – 22.08.2022, 23:00	345	44
VII	23.08.2022, 0:00 – 24.08.2022, 01:00	577	27

обусловленными действием пожаров в 2020 г., были рассчитаны среднесуточные значения eBC(880) летом 2022 г. Максимальное значение 390 нг/м^3 было достигнуто 12 августа 2022 г., что оказалось ниже значения 534 нг/м^3, зарегистрированного при рекордных пожарных эмиссиях 1 сентября 2020 г. В краткосрочных измерительных кампаниях были получены данные эпизода загрязнений на гидрометеорологической обсерватории «Тикси» с 3 по 7 июля 2015 г. Тогда была зарегистрирована концентрация 130 нг/м^3, что могло быть результатом переноса шлейфов крупномасштабных пожаров в Западной Сибири [29]. Исследования на полярной станции «Ледовая база Мыс Баранова» показали максимальное влияние (250 нг/м^3) в результате дальнего переноса воздушных масс из регионов пожаров в Евразии 5 августа 2016 г. [23].

Среднее значение eBC(880) в августе составило 68 ± 132 нг/м^3. Определены семь эпизодов загрязнения, длительность которых и максимальные концентрации представлены в табл. 1. Они чередуются с периодами фоновых концентраций на уровне 10 нг/м^3.

Отметим, что в эпизодах загрязнений концентрация eBC(470), измеренная в ультрафиолетовом диапазоне излучения, превышала eBC(880) в инфракрасном диапазоне, т. е. наблюдалась положительная разница в значениях DeltaC (см. табл. 1), что указывает на значительное влияние эмиссий лесных пожаров.

Роза ветров августа 2022 г. показывает, что примерно в 20% случаев наблюдались ветры юго-западного направления, частота встречаемости ветра в западном направлении составляет около 15%, восточные ветры практически не регистрировались, а частота встречаемости южных ветров составила 5–7% (рис. 5а).

Расчеты двумерной функции распределения концентрации eBC(880) в зависимости от скорости и направления ветра (рис. 5б) хорошо идентифицируют источники высоких концентраций черного углерода (более 450 нг/м^3) в южном и юго-западном направлениях. Именно в этих направлениях от острова Бе-

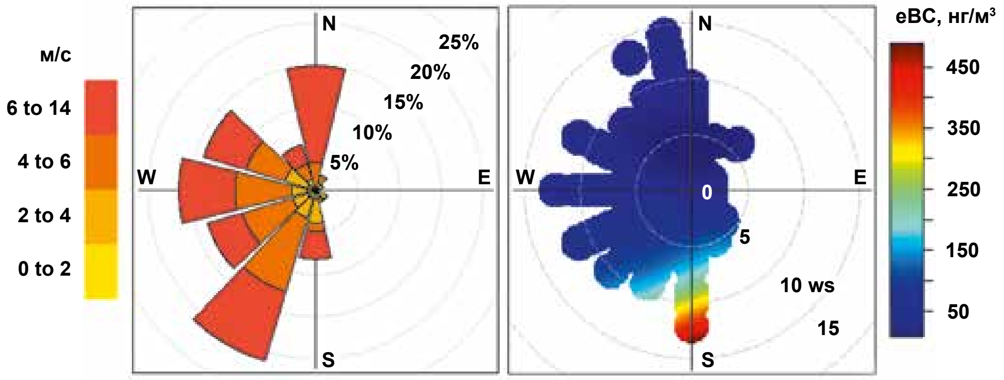

а *б*

Рис. 5. Роза ветров (а) и распределение черного углерода eBC(880) в зависимости от направления и скорости ветра (б) в августе 2022 г.

Fig. 5. Wind rose (a) and distribution of black carbon eBC(880) depending on wind direction and speed (б) in August 2022

лый находятся полуостров Ямал и континент, где в августе 2022 г. были зарегистрированы крупнейшие лесные пожары на площади суммарно 665 265 га (https:// avіales.ru/). При ветрах с севера и северо-запада, т. е. направления Северного Ледовитого океана, концентрации черного углерода были близки к фоновым – около 50 нг/м^3.

Перенос воздушных масс на острове Белый

Обратные траектории переноса воздушных масс для моментов наивысших концентраций семи эпизодов загрязнений показаны на рис. 6 и 7. Космические снимки позволяют увидеть шлейфы дымов пожаров в дни максимальных концентраций eBC, наблюдаемых на острове Белый. Во время эпизодов I–III воздушные массы приходили на остров Белый по северным территориям евразийского континента (рис. 6а–6в), огибая регионы ЯНАО и ХМАО над крупными очагами пожаров на границе ХМАО и ЯНАО. Во время эпизодов I–III воздушные массы проходили на острове Белый с северных территорий евразийского континента (рис. 6а–6в), огибая регионы ЯНАО и ХМАО над крупными очагами пожаров в Березовском и Советском районах, где согласно сводкам «Авиалесоохраны» на 28–29 июля 2022 г. зарегистрировано 18 и 23 лесных пожара соответственно, а площадь возгорания составила от 3028 до 4004 га (рис. 6а и 6б). 4 августа концентрация eBC(880) достигла наивысшего в этот период значения, равного 567 нм/м^3, а разница в поглощении в ультрафиолетовом диапазоне по сравнению с инфракрасным DeltaC составила 116 нг/м^3. Самые высокие концентрации черного углерода (851 нг/м^3), превышающие порог загрязнений практически в 10 раз, а фон – в 85 раз, были зарегистрированы в эпизоде IV, когда воздушные массы проходили в широтном направлении вдоль побережья Северного Ледовитого океана через Кольский полуостров, Республику Коми и ЯНАО (см. рис. 7). В ЯНАО по данным на 15 августа было семь природных пожаров на общей площади 5540 га, самый масштабный из них с площадью возгорания более 800 га. Тогда значение DeltaC достигло 1150 нг/м^3, продемонстрировав наивысшее значение индикатора влияния лесных пожаров на аэрозольный состав атмосферы.

Воздушные массы, прибывающие на разных высотах в точку наблюдений, могут иметь отличающиеся траектории движения. Для эпизода IV рассмотрен перенос воздушных масс на высотах 250, 500 и 1000 м (см. рис. 7б). Траектории приходили с запада и круто разворачивались над территорией Ненецкого автономного округа к северо-востоку в направлении острова Белый, что было связано с распределением барических полей 12 августа 2022 г., когда над океаном сформировалась область низкого давления, а над континентом – высокого (см. рис. 3). Поток воздушных масс проходил над севером европейской России к полуострову Ямал, далее он резко поворачивал над областями пожаров (см. рис. 7а). Траектории на высоте 250 и 500 м делали дополнительный изгиб над районами пожаров в ЯНАО, тогда как траектория на высоте 1000 м проходила вдали от этого района (см. рис. 7б).

Во второй половине августа перенос воздушных масс значительно изменился. Во время эпизодов загрязнения V–VII он проходил в основном над европейской Россией, включая степные районы Оренбургской, Саратовской и Челябинской областей (рис. 6г–6е). Во время прохождения воздушных масс над Мещерским и Окским биосферными заповедниками (Рязанская область) наблюдались крупномасштабные лесные пожары, охватившие площади до 25 000 га. Очаги пожаров также были зарегистрированы вдоль пути следования над северными районами Казахстана. К острову Белый воздушные массы прибывали из центральных районов страны, Республики Карелия и Мурманской области. 23 августа концентрация eBC(880) достигла максимума, равного 511 нм/м^3, а значение DeltaC составило 27 нг/м^3.

Самый длительный эпизод загрязнения VII случился с 23 по 24 августа, когда наблюдался перенос воздушных масс через территории Западной Сибири и Восточно-Европейской равнины (см. рис. 6е), более детально – с севера Красноярского края на юго-запад по направлению к северным территориям Казахстана и далее к Волгоградской и Саратовской областям, на северо-восток к острову Белый.

Распределение источников черного углерода для острова Белый определялось путем расчета концентраций eBC(880) для каждой ячейки пространственной сетки по формуле (1) за период наблюдений (август 2022 г.). Определены области, характеризующиеся концентрациями eBC выше порогового уровня загрязнений 90 нг/м^3, которые представляют регионы источников эмиссий черного углерода разной интенсивности (рис. 8). Источники самых высоких концентраций черного углерода на северных

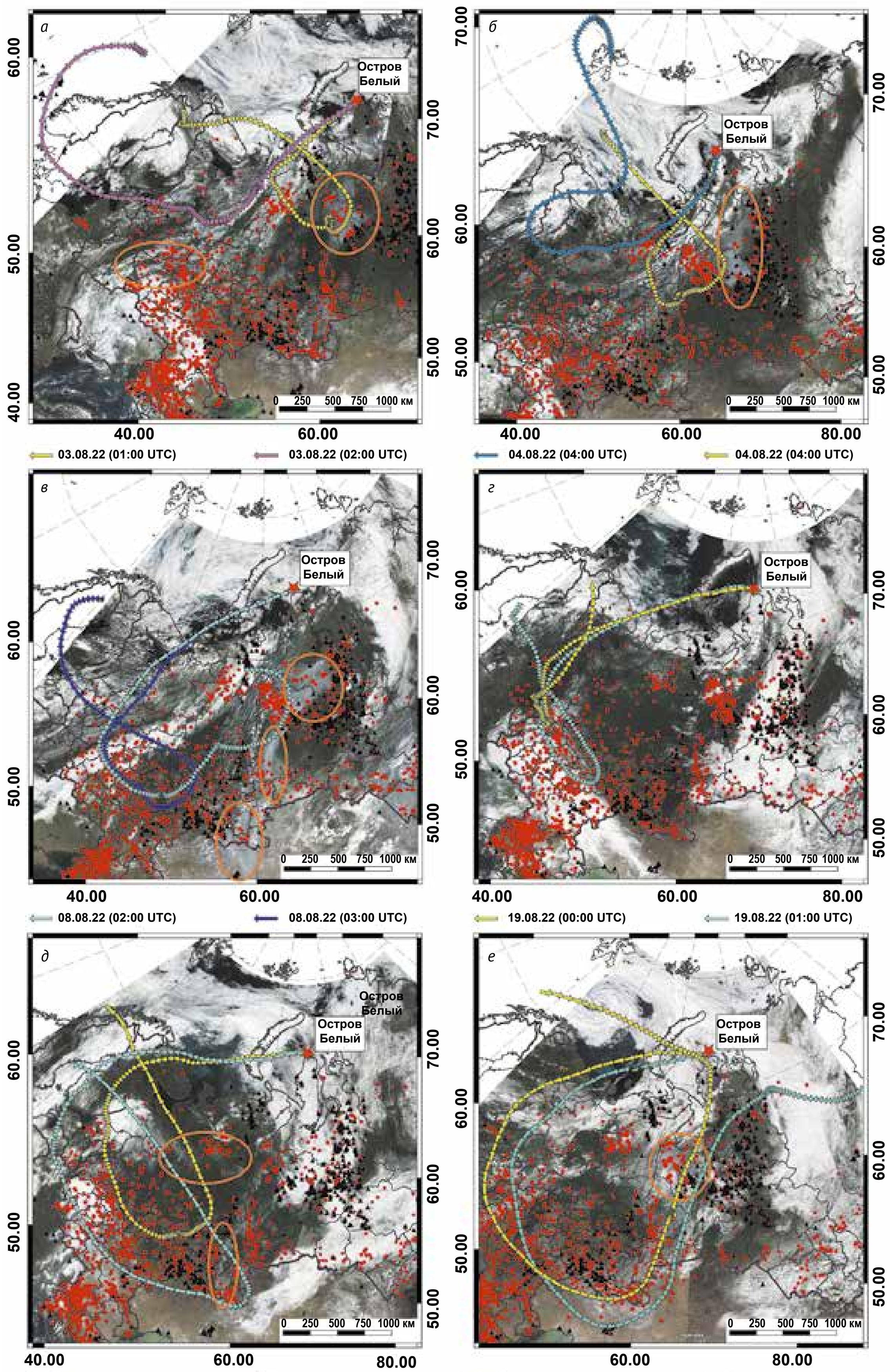

Рис.6. Обратныетраектории воздушных масс на высоте 500 м над уровнем моря во время эпизодов I (а), II (б), III (в), V (г), VI (д) и VII (е); указаны время и дата прихода на станцию «Остров Белый». Красными точками показаны пожары за десять дней прохождения воздушными массами территорий до острова Белый. Черными треугольниками показано расположение газовых факелов нефтяных и газовых месторождений (по данным https://skytruth.org/). Космоснимки соответствуют дате максимальной концентрации в каждом эпизоде, кругами указаны области дымовых шлейфов. Составлено авторами на основе спутниковых снимков MODIS Corrected Reflectance imagery https://worldview.earthdata.nasa.gov

Fig. 6. Air mass back trajectories at a height of 500 m AGL during episodes I (а), II (б), III (в), V (г), VI (д) and VII (е); the time and date of arrival at the station “Island Bely”. Red dots show fires during ten days of air masses passage over the territories to Bely Island. Black triangles show the location of gas flares of oil and gas fields (according to https://skytruth.org/). Space images correspond to the date of maximum concentration in each episode; circles indicate areas of smoke plumes. Based on MODIS Corrected Reflectance imagery https://worldview. earthdata.nasa.gov

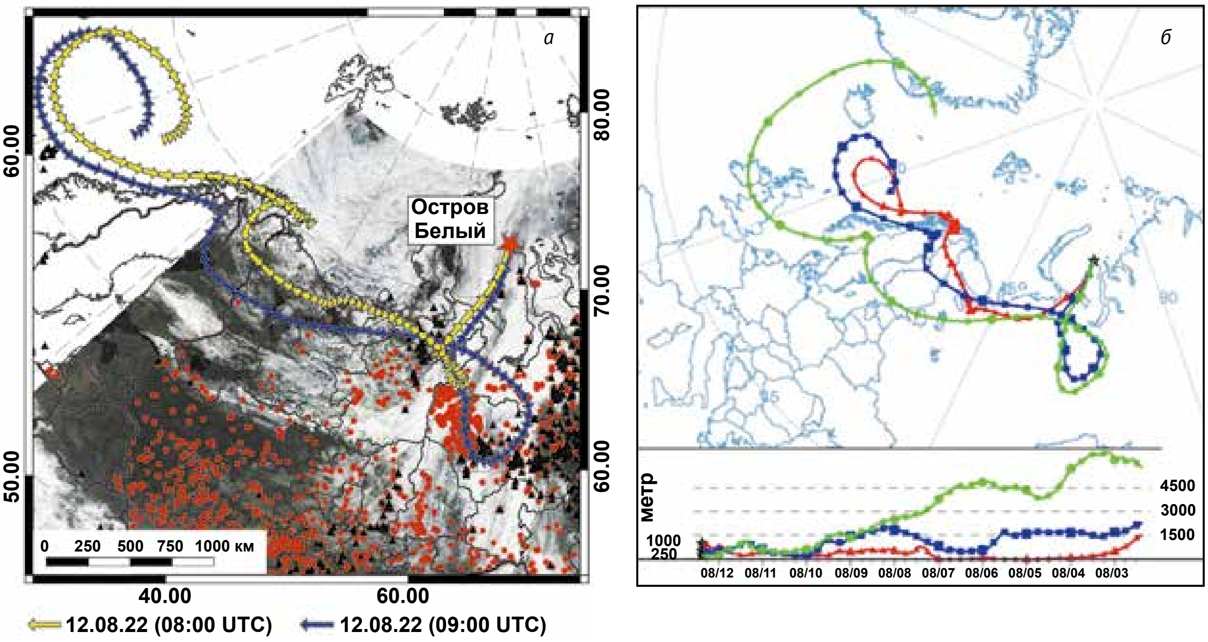

Рис. 7. Обратные траектории воздушных масс во время эпизода загрязнения IV на высоте 500 м AGL. Указаны время и дата прихода на станцию «Остров Белый». Составлено авторами на основе спутниковых снимков MODIS Corrected Reflectance imagery https://worldview.earthdata.nasa.gov (а) Обратные траектории в момент наблюдений 12 сентября 2022 г. в 9:00 на высотах 250 (зеленая), 500 (синяя) и 1000 м (красная) AGL. Составлено авторами на основе Arlmap HYSPLIT map background file https://www.ready.noaa.gov/HYSPLIT_util.php (б)

Fig. 7. Air mass back trajectories during pollution episode IV at 500 m AGL. The time and date of arrival at the station “Bely Island” are indicated. Based on satelite images MODIS Corrected Reflectance imagery https://worldview.earthdata.nasa.gov (a). Back trajectories at the time of observations on September 12, 2022 at 9:00 at altitudes of 250 (green), 500 (blue) and 1000 m (red) AGL. Based on Arlmap HYSPLIT map background file https://www.ready.noaa.gov/HYSPLIT_util.php (б)

Рис. 8. Региональное распределение источников черного углерода для острова Белый в августе 2022 г. Зоны, характеризующиеся концентрациями eBC выше порогового уровня загрязнений, оконтурены красной линией. Очаги пожаров в этих зонах показаны точками. Треугольниками помечены факелы нефтегазовых месторождений. Составлено авторами на картографической основе ESRI Standard map https://server.arcgisonline.com/ArcGIS/rest/services/World_Street_Map

Fig. 8. Regional distribution of black carbon sources for Bely Island in August 2022. Zones characterized by eBC concentrations above the threshold level of pollution are outlined by the red line. Dots show the fire centers in these zones. Triangles mark flares of oil and gas fields. Based on the ESRI Standard map https://server.arcgisonline.com/ArcGIS/rest/services/World_Street_Map

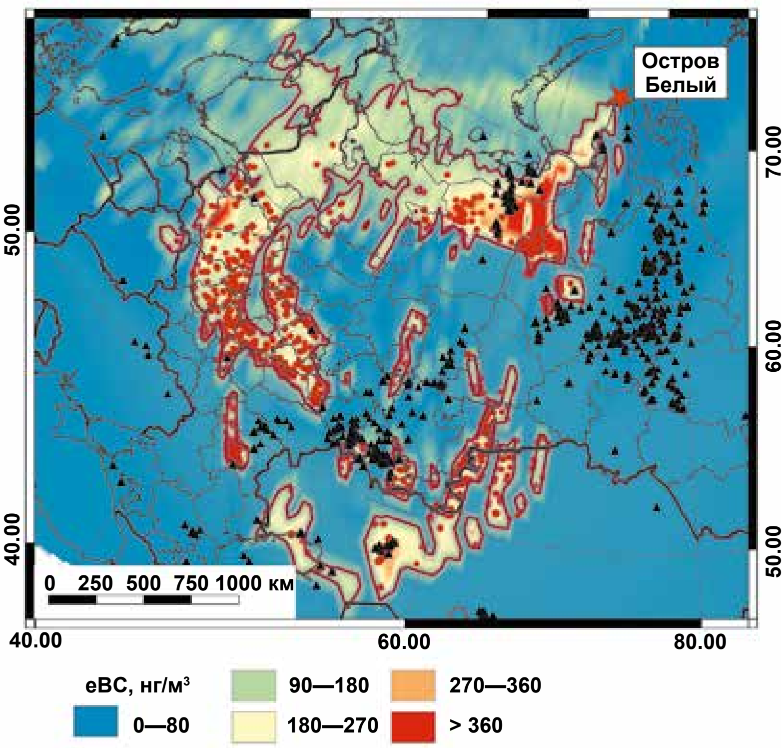

территориях России определены в ЯНАО и ХМАО, Ненецком автономном округе, в республиках Коми и Карелия, Архангельской и Мурманской областях. В центральных регионах европейской России выделяются Рязанская, Владимирская, Пензенская, Орловская и Смоленская области, республики Мордовия, Марий Эл и Татарстан. Самые удаленные регионы источников обнаружены на юге Урала (в Оренбургской и Челябинской областях) и в северных районах Казахстана.

Для определения регионов пожарных эмиссий на рис. 8 нанесены спутниковые данные о расположении термоактивных точек (пожаров) внутри зон, определяющих концентрации eBC выше 90 нг/м^3. Хорошо видны регионы высоких концентраций черного углерода и охваченные обширными пожарами. Дополнительно на карту рис. 8 нанесены данные о свечении объектов с температурой выше 1200°C, связанные с факелами нефтегазовых месторождений. Как видно, регионы источников арктических загрязнений черного углерода в Арктике и месторасположение крупнейших объектов топливно-энергетического комплекса не совпадают, еще раз указывая на доминирующую роль пожаров в августе 2022 г.

ЗАКЛЮЧЕНИЕ

Непрерывные измерения поглощающей способности аэрозолей в широком диапазоне солнечного излучения, выполненные на инструментальном комплексе полярной станции «Остров Белый», позволили определить уровень аэрозольного загрязнения на острове Белый летом 2022 г. В августе 2022 г. максимальные концентрации черного углерода в инфракрасном диапазоне достигали 851 нг/м^3, что в 85 раз превысило фоновые концентрации для арктического региона. Траекторный анализ показал, что воздушные массы переносили на остров Белый шлейфы пожаров, охвативших в результате рекордных температурных аномалий и засушливой погоды значительные территории европейской России и Западной Сибири. Вклад пожарных эмиссий в состав аэрозолей арктического региона подтвердился по повышенному поглощению в ультрафиолетовом диапазоне солнечного излучения в максимуме, превысившем черный углерод в инфракрасном диапазоне на 1150 нг/м^3. Моделирование методом отнесения траекторий переноса воздушных масс дало оценку вклада регионов ЯНАО и ХМАО, европейской России, юж ного Урала и северных районов Казахстана в загрязнение атмосферы западно-сибирского сектора российской Арктики.

Работа выполнена по программе развития Междисциплинарной научно-образовательной школы Московского государственного университета им. М. В. Ломоносова «Будущее планеты и глобальные изменения окружающей среды» при поддержке гранта РНФ № 22-17-00-102. Методология инфраструктуры аэрозольного комплекса на полярной станции «Остров Белый» развита в рамках проекта № 075-15-2021-938.

Климатический трассер – черный углерод на полярном круге

1. ВВЕДЕНИЕ

При сжигании углеводородного топлива и во время лесных пожаров в атмосферу выбрасываются мельчайшие аэрозольные частицы, В настоящее время вклад от сжигания природного ископаемого топлива в индустриальных установках, отопительных и транспортных системах, при горении биомасс в природных пожарах лесов и при сжигании биотоплива для отопления домов составляет порядка 25% от всей эмиссии аэрозолей с поверхности Земли [1]. Агломераты частиц в эмиссиях сжигания углеводородного топлива имеют размеры 0.1–0.5 мкм, состоят из первичных наночастиц диаметром 20–40 нм [2]. Физико-химические характеристики дыма пожаров существенно зависят от фазы тления или открытого горения [3, 4]. Микроструктура микрокристаллитов графита является причиной поглощения солнечного излучения в видимом диапазоне. Измеренную спектрофотометрическим методом [5, 6] концентрацию хорошо поглощающего аэрозоля в атмосфере называют black carbon (BC), отсюда в русском переводе появилось название «черный углерод».

Микрочастицы в продуктах сжигания являются опасным веществом для здоровья людей, особенно в районах интенсивного транспорта и индустриальной деятельности. Они адсорбируют вредные вещества и проникают в организм человека на клеточном уровне через дыхательные пути, вызывают и усиливают дыхательные, сердечно-сосудистые и аллергические заболевания [7].

Оценки глобальных климатических моделей прямого радиационного эффекта BC от всех источников сжигания топлива и биомасс достигают 2 Вт/м2, что лишь в два-три раза ниже парникового эффекта эмиссии диоксида углерода [8]. BC признан вторым после диоксида углерода короткоживущим климатическим трассером со временем жизни порядка недели. Предсказывается, что благодаря антропогенной эмиссии BC глобальный эффект ежегодного увеличения усредненной температуры поверхности Земли составляет 0.4K [9]. Показано значительное влияние дыма лесных пожаров Сибири на концентрацию и варьируемость в атмосфере черного углерода, достигающего 15% массы аэрозолей [10].

Арктический регион наиболее чувствителен к быстрым климатическим изменениям. Скорость роста температуры воздуха в Арктике превысила в два раза скорость увеличения глобальной средней температуры за последние 100 лет [9]. Явление загрязнения атмосферы Арктики, названное Арктической Дымкой, стало известным в 1950-е годы. Исследования, проведенные в последующие 20 лет показали [11], что наблюдаемая зимой дымка является следствием переноса воздушных масс из средних широт в Арктику [12].

Экосистема Арктики особенно подвержена сильному воздействию аэрозольной компоненты в эмиссиях источников сжигания природного топлива и биомасс. BC, осаждаясь на поверхности, способен изменять отражательную способность снега и льда, что приводит к раннему снеготаянию и сокращению площади арктических льдов. Оценивается, что эмиссия в Арктику с российских территорий составляет 10-15% от мировой эмиссии углеродосодержащих аэрозолей, более 50% эмитируется к северу от 60 с.ш. [13]. По модельным оценкам, сжигание попутного нефтяного газа (ПНГ) в факелах составляет основной источник антропогенных эмиссий BC Сибирского региона (36.2%), за которым следуют эмиссии жилищного фонда (25.0%), транспорта (20.3%), промышленности (13.1%) и теплоэлектростанций (5.4%) [14]. Вывод о значительном вкладе индустриальных эмиссий в высокую концентрацию черного углерода в акватории Карского моря подтвердился в морских экспедициях в периоды выноса воздушных масс из районов Ямало-Ненецкого и Ханта-Мансийского автономных округов [15, 16].

Однако оценка экологического состояния атмосферы и изменения природной среды в регионах российской Арктики сильно усложнены существующим недостатком знаний об источниках эмиссий, количестве и составе аэрозольных загрязнений, определяющих степень воздействия на экосистему Арктики. Утилизация ПНГ в факелах, как источник загрязнений воздуха, в нефтедобывающих регионах остается наименее изученной среди всех эмиссий при сжигании природного топлива как по полному количеству эмитированных продуктов, так и по фракции черного углерода [17]. Оценка последствий воздействия сжигания ПНГ в факелах на растительный покров проводится с помощью тепловых космических снимков [18] , на снежный покров – методами анализа концентраций загрязнений в окрестностях факела [19].

В Ямало-Ненецком автономном округе (ЯНАО) в настоящее время наблюдается повышение эффективности всех видов экономической деятельности, интенсификация производства нефтегазового комплекса, увеличение объемов используемых природных ресурсов. В округе открыто 235 месторождений углеводородного сырья, из которых 63 находится в промышленной разработке, работает 59 нефтегазовых предприятий. Согласно данных Ямалстата по состоянию на 01.01.2014 ежегодные выбросы вредных веществ от сжигания ПНГ в ЯНАО составляют более 732 тыс. тонн вредных веществ. Более половины всей эмиссии приходится на оксид углерода, более трети – на углеводороды и летучие органические соединения, остальную часть выбросов (5%) составляют твердые вещества, окислы азота, сернистого ангидрида. Однако оценок эмиссий черного углерода не производится. На Полярном круге находится город Салехард, где оценки степени загрязнения воздуха эмиссиями черного углерода ранее не проводились. Значительные территории субарктической и арктической зоны ЯНАО находятся за Полярным кругом,

---

* Кобелев В.О., Поповичева О.Б., Синицкий А.И. // Научный вестник Ямало-Ненецкого автономного округа. 2020;106:47-53 DOI: 10.26110/ARCTIC.2020.106.1.004

куда в зимне-весеннее время происходит преимущественный перенос воздушных масс. В июле 2019 года на Полярном круге случились самые интенсивные природные пожары, по данным Атмосферной службы мониторинга (CAMS) в 100 раз превышающие уровень ежегодно наблюдаемых пожаров.

Данная работа посвящена изучению степени загрязнения атмосферы ЯНАО продуктами сжигания природного топлива и биомасс, эмитируемыми в результате хозяйственной деятельности в городской среде, во время переноса шлейфов индустриальных эмиссий теплоэнергетического комплекса и интенсивных лесных пожаров на Полярном круге. Впервые проведены измерения вблизи г. Салехард, количественно определены концентрации черного углерода, степень воздействия эмиссий климатического трассера – черного углерода на состояние атмосферы на Полярном круге.

Объекты и методы исследования

Для исследования степени загрязнения атмосферы продуктами сжигания, эмитируемыми городскими, индустриальными источниками и лесными пожарами на Полярном круге, в 4-х км на юго-восток от города Салехард был организован научно-исследовательский аэрозольный пост (НИАП) (рис.1). Непрерывные измерения концентрации черного углерода производились при помощи аэталометра AE33 (Magee Scientific). Название “Aethalometer” является производным от греческого глагола ‘aethaloun’ (αεφαλουν), означает «почернеть от сажи». Аэталометрический метод основан на регистрации ослабления излучения видимого спектра собранными на фильтре аэрозольными частицами непосредственно в процессе их осаждения из воздушного потока. Аэталометр измеряет ослабление интенсивности света, проходящего через пятно на фильтрующей ленте (рис. 2), на семи длинах волн в диапазоне от инфракрасного до ультрафиолетового. В процессе измерений определяется величина ослабления ATN (attenuation) как $ATN=100*\ln(I_0/I)$, где I_0 – интенсивность падающего света, а I – интенсивность света, прошедшего через фильтр. Особенностью аэталометра AE33 является одновременное измерение по двум каналам с разными скоростями прокачки воздуха из одного и того же входного воздушного потока, что обеспечивает оценку нелинейности поглощения при высоких нагрузках на фильтре компенсационной поправкой поглощения света частицами. Массовая концентрация ВС вычисляется по изменению оптического поглощения на длине волны 880 нм, другие аэрозольные частицы (органические, минеральные) в данном диапазоне поглощают значительно меньше [20].

Измерения массовой концентрации ВС были проведены с апреля по август 2019 г., сопровождались сбором данных о метеорологических параметрах (направлении и скорости ветра) с метеорологического ресурса rp5.ru. Ежеминутные данные усреднялись в течение каждого часа. Произведено осреднение ВС для 3-х часовых интервалов метеоданных при каждом направлении ветра.

С 19 апреля по 7 августа 2019 года в 4-х км на юго-восток от города Салехард проводились непрерывные измерения оптических свойств аэрозолей. Определена высокая варьируемость концентрации черного углерода, от 3 до 688 нг/м^3. Анализ концентраций по секторам, определяемым расположением источников эмиссий аэрозолей горения различной

Рис. 1. Расположение НИАП измерений черного углерода вблизи г. Салехард

Рис. 2. Аэталометр АЕ33 для измерения концентрации черного углерода на Научно-исследовательском аэрозольном посту вблизи г. Салехард

Рис. 3. Пятна осажденных из атмосферы частиц на ленте аэталометра АЕ 33

степени интенсивности, выделил пять направлений: наиболее чистое юго-западное, наиболее загрязненный сектор – город Салехард, арктический сектор полуострова Ямал, крупнейший индустриальный комплекс ТЭК на востоке ЯНАО и индустриальный комплекс на юге ЯНАО и ХМАО.

На рис. 4-6 приведены диаграммы розы ветров и пространственные распределения концентрации ВС по секторам для трех периодов измерений; апреля – мая, июня и июля-августа. Совместный анализ направления ветра и концентрации ВС показал наиболее чистый сектор 1 (220-270 градусов) – юго-западное направление ЯНАО, Шурышкарский район, где отсутствуют объекты ТЭК и крупные населенные пункты. Значения ВС определены на самом низком уровне среди других секторов, в диапазоне от 3 до 95 нг/м^3. В среднем значение ВС в секторе 1 за апрель – май было 50 нг /м^3, в июне – 25 нг/м^3.

Самым загрязненным сектором 2 оказался сектор 280-340 градусов выноса городских эмиссий из г. Салехард, значение ВС за указанный период варьировались от 33 до 597 нг/м^3. Среднее значение в апреле – мае достигло161 нг/м^3, в июне – 156 нг/ м^3. Наблюдается 4-х кратное превышение средних концентрации ВС для самого загрязненного сектора городских эмиссий из г. Салехард относительно самого чистого сектора 1 Шурышкинского района ЯНАО.

Сектор 3 (350-50 градусов) – направление полуострова Ямал. Ближайший крупный объект ТЭК Новопортовское нефтяное месторождение находится на

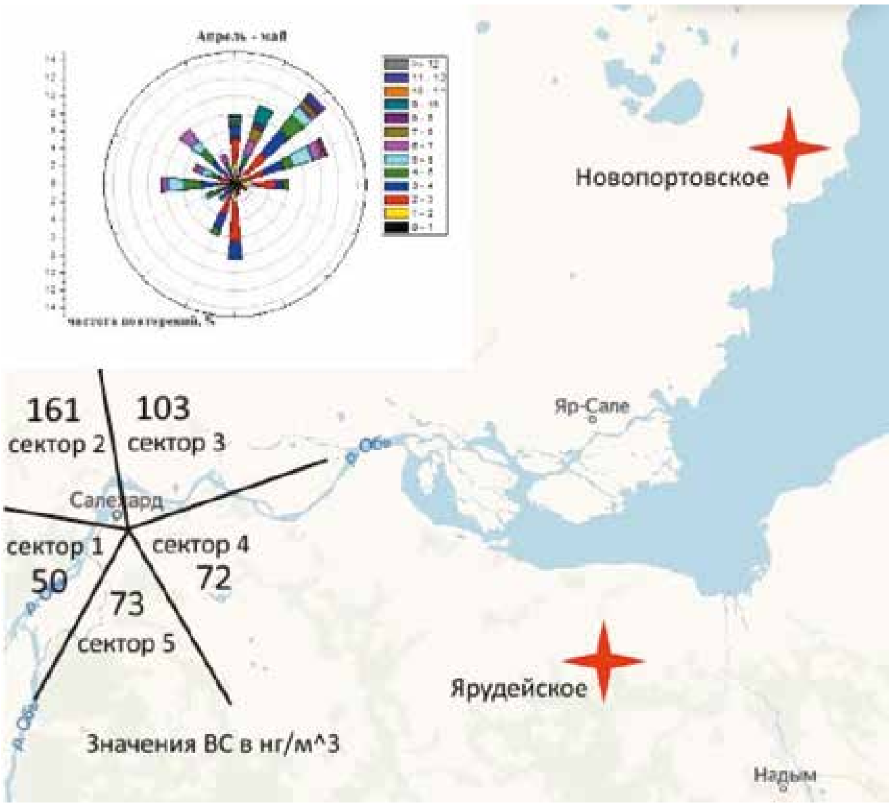

Рис. 4. Роза ветров (сверху, в таблице справа скорость ветра в м/с) и диаграмма распределения ВС по секторам (снизу) для апреля-мая 2019 г.

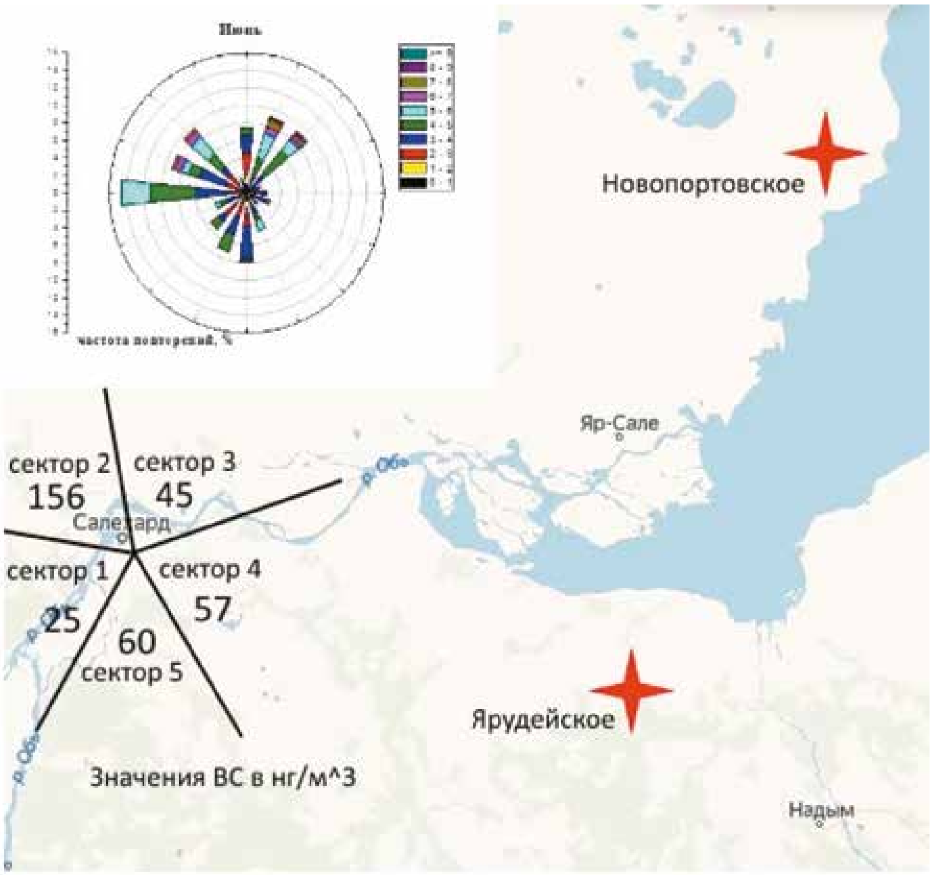

Рис. 5. Роза ветров (сверху, в таблице справа скорость ветра в м/с) и диаграмма распределения ВС по секторам (снизу) для июня 2019 г.

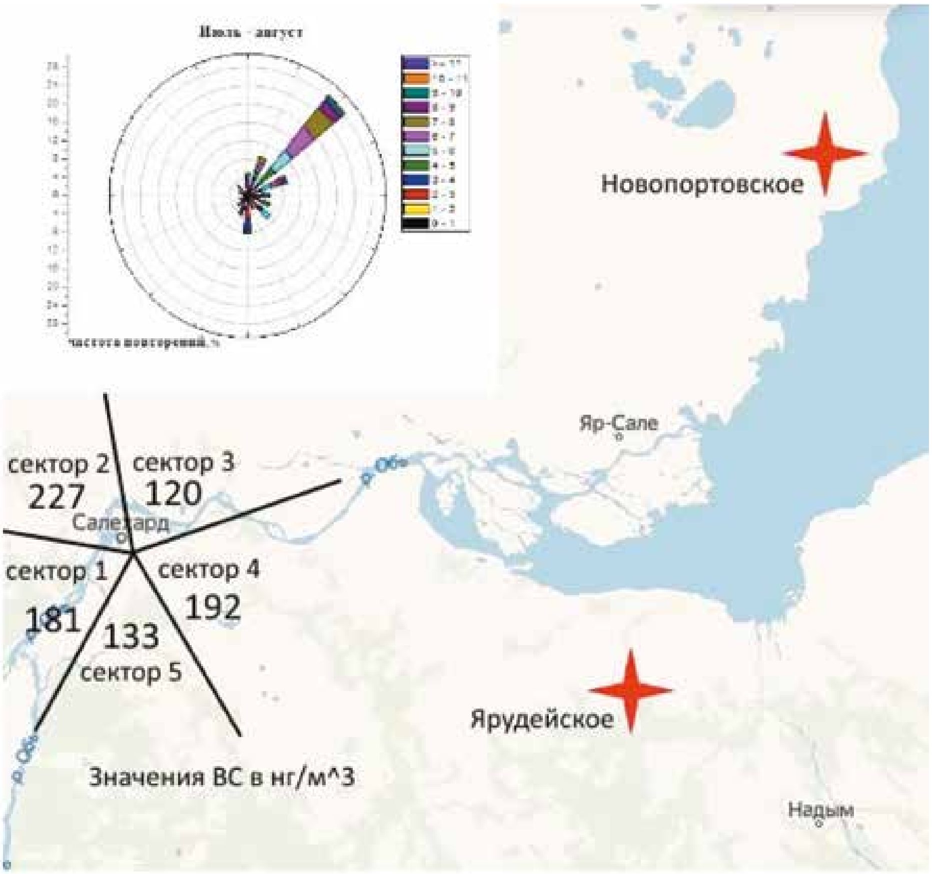

Рис. 6. Роза ветров (сверху, в таблице справа скорость ветра в м/с) и диаграмма распределения ВС по секторам (снизу) для июля-августа 2019 г.

удалении 280 км. Значения BC за указанный период варьировались от 25 до 244 нг/м^3. В апреле – мае и июне средние значения в секторе 3 наблюдались 103 и 45 нг/м^3.

Сектор 4 (60-150 градусов) – направление индустриальный ТЭК ЯНАО. Ближайший крупный объект ТЭК Ярудейское нефтяное месторождение находится на удалении 200 км. Значения BC варьировались в диапазоне от 17 до 203 нг/м^3. В апреле – мае и июне средние значения в секторе 4 наблюдались 72 и 57 нг/м^3.

Сектор 5 (160-210 градусов) – направление юг ЯНАО – ХМАО, крупные объекты ТЭК отсутствуют. Значения BC лежат в диапазоне от 11 до 145 нг/м^3. В апреле – мае и июне средние значения в секторе 5 наблюдались 73 и 60 нг/м^3.

По данным МЧС ЯНАО наиболее интенсивные пожары, охватившие площадь 200 га, наблюдались в июле – августе 2019 г. Как и ожидалось, продукты горения лесных массивов значительно увеличили наблюдаемые концентрации BC во всех секторах (рис.4 в). Площадь возгорания по состоянию на 31.07.2019 составляла 1839 га, на 30.06.2019 была 61 га. Среднемесячная концентрация увеличилась по всем направлениям и варьировалась от 14 до 688 нг/м^3. Выделились несколько эпизодов с пиковыми одночасовыми значениями BC: 3-5 июля – 688 нг м^3, 14-15 июля – 959 нг/м^3,17-18 июля – 1581 нг/м^3, 30-31 июля – 1205 нг/м^3 и 2-3 августа 440 нг/м^3, показывая беспрецедентно высокие для северного Полярного круга уровни загрязнения атмосферы в летний период. По сравнению с периодом отсутствия природных пожаров по всем секторам произошло увеличение концентрации BC от 1.5 до 5 раз, в чистом секторе 1 – в 7 раз.

ЗАКЛЮЧЕНИЕ

Впервые получены количественные данные о влиянии городских эмиссий, эмиссий теплоэнергетического комплекса и лесных пожаров на концентрацию климатического трассера – черного углерода на Полярном круге. Анализ данных вблизи г. Салехард показывает низкий уровень концентрации менее 25 нг/м^3 при направлении ветра с юго-запада, более чем в три раза в среднем увеличение концентрации при направлении ветра со стороны городского массива Салехарда, и периодическое увеличение при направлении ветра с юго западного направления, со стороны всего региона ЯНАО. Лесные пожары в июле 2019 г. на Полярном круге привели к возрастанию концентрации черного углерода в среднем в 7 раз по отношению к фоновым арктическим значениям.

Черный углерод городских эмиссий в Арктическом регионе по данным вблизи г. Салехарда*

1. ВВЕДЕНИЕ

Научные исследования глобальных процессов окружающей среды в Арктическом регноне – наиболее чувствительном к быстрым климатическим изменениям – особенно важны в настоящее время. Среди основных климатически активных аэрозольных компонентов атмосферы выделяется продукт горения природных топлив и биомасс – черный углерод (blackcarbon, BC), хорошопоглощающий солнечное излучение [1]. Его вклад в повышение температуры в Арктике, наблюдаемое с 1976 по 2007 г., составляет 1,09 ± 0,81 °С [2]. Осаждение черного углерода на снег вызывает уменьшение альбедо подстилающей поверхности и, следовательно, ускорение таяния снега и льда [3].

Черный углерод эмитируется и мелкодисперсной вдыхаемой фракции аэрозолей и влияет на здо ровье людей, вызывая ряд хронических легочных заболеваний [4]. Уровень загрязнения воздуха в Арктическом регионе, вызванный местными источниками выбросов продуктов сжигания, может значительно превышать стандарты качества воздуха, ухудшать состояние здоровья населения и экосистемы в целом [5]. Анализ аэрозольного состава атмосферы наиболее актуален для северных районов России, где наиболее токсичные [6] дизельные эмиссии транспортных систем определяют высокую степень загрязнения воздуха [7].

Исследования многолетних изменений арктического климата демонстрируют значительное влияние эмиссий черного углерода на состояние атмосферы Арктики. Зимой вследствие комбинации интенсивного дальнего переноса продуктов хозяйственной деятельности и температурной инверсии наблюдается арктическая дымка [3]. Весной при увеличении солнечной активности устойчивость атмосферы уменьшается, концентрация BCпадает, влияние локальных антропогенных источников становится более значительным, что определяет важность количественного анализа эмиссий загрязняющих веществ в прибрежных районах Арктики [8]. Длительные измерения черного углерода в континентальной части Российской Арктики на побережье моря Лаптевых [9, 10] подтвердили значительное воздействие на степень загрязнения атмосферы как дальнего переноса загрязнений, так и локальных источников в жилом секторе.

В настоящее время на российские территории выше 60° с.ш. приходится более 50% общемировой эмиссии черного углерода[11, 12]; среди источников доминируют горение биомассы в Сибири [12] и сжигание дизельного топлива стационарными источниками и транспортными системами [13]. Весной и летом в прибрежных районах Арктики регистрируются шлейфы природных пожаров, в которых наблюдаются высокие (до 1,5 мкг/м^3) концентрации BC по сравнению с минимальными(~20 нг/м^3)в удаленныхрайонах [14, 15]. В периоды воздействия шлейфов природных пожаров наблюдалось значительное ухудшение качества воздуха в городской среде [16, 17]. Для этих сезонов была рассчитана важней шая характеристика сибирских пожаров – индекс эмиссиичерногоуглерода(~0,52±0,07 г BC кг ‘)| 15].

С оценками индексов антропогенных эмиссий BC в Арктическом регионе ситуация значительно более неопределенная. На основе базы данных антропогенных эмиссий ECLIPSE4.0 и расчетов модели FLEXPART получены среднегодовые концентрации BC в северных районах Сибири (в Ненецком, Ямало-Ненецком (ЯНАО) и Ханты-Мансийском округах), которые варьируются в диапазоне 100–500 нг/м^3 [8]. Показано, что среди основных категорий эмиссий доминируют индустриальное сжигание попутного газа нефте- и газодобывающим топливно-энергетическим комплексом (ТЭК) и жилой сектор, вклады которых составляют 70–80 и 5–10% всех эмиссий соответственно. Вынос загрязнений из северных индустриальных районов в арктические моря приводит к возрастанию концентраций BC до 400 нг/м^3 в сравнении с уровнем в несколько нг/м^3 при направлении ветра с океана [8, 18].

Наиболее развитая на сегодня база данных российских эмиссий BCRUS у читывает спутниковые данные по наземному свечению, инвентаризацию дорожного транспорта, современные технологии сжигания и количество потребляемого топлива [19]. Модельные оценки в районах российского севера, проведенные на базе траекторной модели HYSPLYT и BCRUS, указывают на регион ЯНАО как на один из доминирующих по степени загрязнения окружающей среды черным углеродом [20]. Однако в силу отсутствия локальных данных о концентрациях BC в городах индексы эмиссий жилого сектора в базе BCRUS адаптировались на основе измеряемых в других странах с подобным уровнем жизни. Из за отсутствия официального реестра индустриаль ных и городских эмиссий и систематических изме рений черного углерода все самые современные модели оценивают пространственное распределение концентраций BC и уровень эмиссий городов лишь по порядку величины [5, 19, 20].

Единственная в настоящее время инвентаризация городских источников черного углерода, проведенная за полярным кругом, в г. Мурманске, основывается на разработанной методологии оценок индексов эмиссий автомобильного и внедорожного транспорта, судов и дизель-генераторов, использующих дизельное топливо [21]. Оценки городских эмиссий дали суммарные выбросы BC порядка 400 тыс. т за год [6], однако эта оценка не подтверждена натурными измерениями.

Салехард находится на полярном круге и представ.ляет собой типичный город севера России, не являющийся индустриальным центром. Население Салехарда составляет 50 тыс. чел. На его территории

---

* О.Б. Поповичева, В.О. Кобелев, А.И. Синицкий, Н.М. Ситников, М.А. Чичаева, А. Хансен // Оптика атмосферы п океана.2020; 33: 690-697 DOI: 10.15372 Л0020200905

нет крупных промышленных предприятий, которые могли бы дать весомый вклад в выбросы ВС в атмосферу. При этом, находясь в регионе ЯНАО, Салехард оказывается на пути выноса крупномасштабных эмиссий в Арктику [8]. Цель настоящей работы – определение эмиссий черного углерода в Салехарде в натурных измерениях. Эти данные важны как для оценки качества воздуха типичного города севера России, так и для количественных оценок вклада городов в инвентаризацию выбросов в Арктическом регионе.

1. МЕТОДЫ ИЗМЕРЕНИЙ И ОЦЕНОК

В апреле 2019 г. в 4 км от центра и в ~ 1 км от восточной окраины Салехарда (66°30’с.ш., 66°38’в.д.) был создан измерительный аэрозольный комплекс (ИАК) «Обдорск» (рис. 1). На втором этаже павильона был установлен аэталометр АЕ33 (Magee Scientific), забор воздуха осуществлялся снаружи устройством, предохраняющим последний от попадания воды. Работа АЕ33 основана на непрерывном отборе аэрозолей из атмосферы при раз ных скоростях потока воздуха н одновременном измерении ослабления излучения, проходящего через два фпльтра, а также через референс-филыр без прокачки воздуха [22]. Такой метод позволяет учесть нелинейность поглощения с увеличением нагрузки, возникающую при накоплении частиц на фильтре. Аэталометр АЕ33 обеспечивает измерение поглощения осажденными на фильтре частицами излучения на семи длинах волн в диапазоне от ультрафиолетового (370 нм) до инфракрасного (950 нм). Массовая концентрация черного углерода ВС$_{880}$ определяется по изменению ослабления излучения в инфракрасном диапазоне на λ = 880 нм с массовым коэффициентом поглощения 7,7 м^2/г. Именно в этом диапазоне хорошо поглощают продукты сжигания природного ископаемого топлива, в го время как органическая п минеральная аэрозольные составляющие – значительно меньше [23]. При сжи гании древесины и в дымах лесных пожаров значительно увеличивается поглощение на коротких длинах волн [24], которое определяет массовую концентрацию ВС$_{470}$ на λ= 470 нм. Разница между ВС$_{880}$ и ВС$_{470}$ служит маркерной оценкой вклада горения биомассы по сравнению со сжиганием природного топлива [25]. В настоящей работе значительная разница между измеренными концентрациями (ВС$_{470}$ – ВСдао) показывает вклад дымовых эмиссий по сравнению с городскими эмиссиям транспорта и ТЭК. Одновременно с измерениями аэталометром проводился сбор метеоданных (температура, направление и скорость ветра) с метеостанции ФГБУ «Гидрометцентр России» (http://www.meteomfo.ru/archive-pogoda/russia/moscow), находящейся на расстоянии 5 км от измерительного комплекса.

Для идентификации источников загрязнений широко используется метод определения направления выноса загрязнений [26]. В настоящей работе он применен на основе анализа данных одновременных измерений концентраций ВС, направления и скорости ветра в приближении «локального источника», действующего при удалении на 1–10 км [27|. Рассчитывается двумерная функция вероятности (Conditional probability function, CPF) попадания концентрации ВС в заданный диапазон значений при определенных направлениях и скоростях ветра по методу, описанному в [28]. Функция CPF определяется как отношение числа случаев регистрации концентрации ВС в некотором заданном диапазоне значений $n_{\theta,j}$ к числу $m_{\theta,j}$ всех измеренных концен

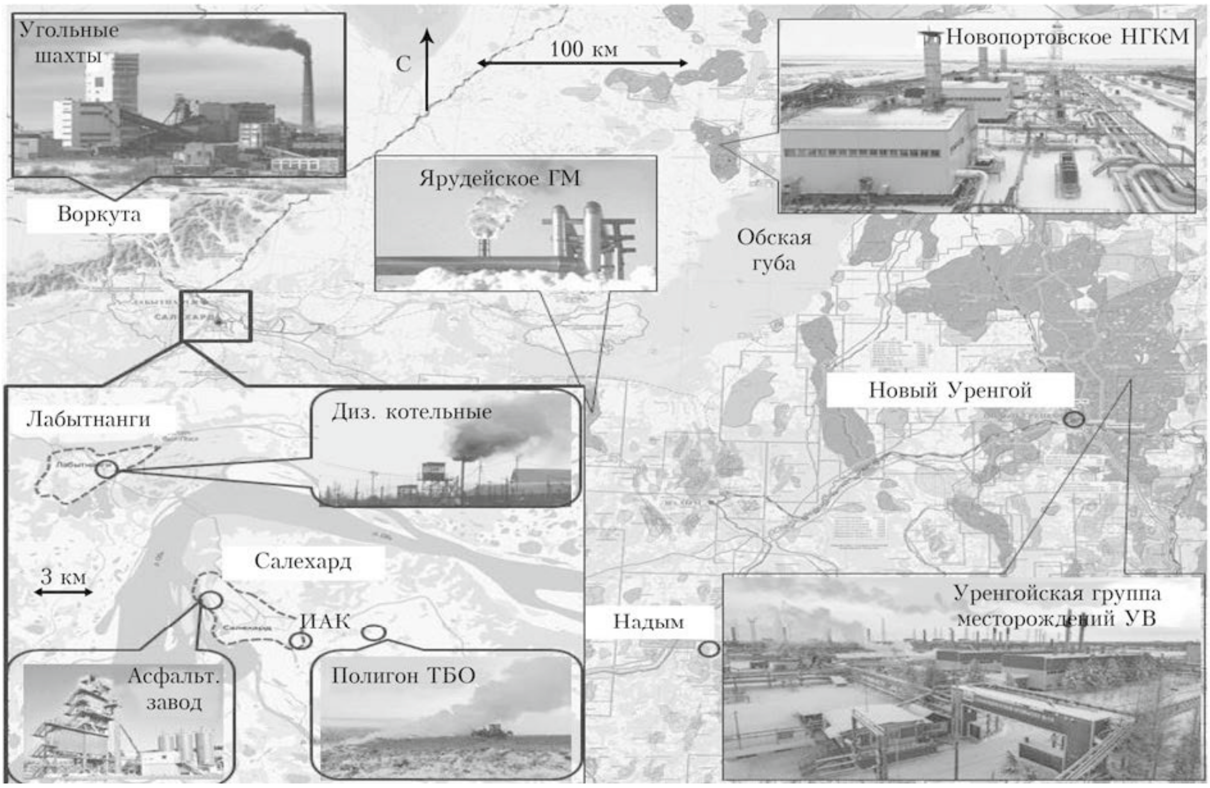

Рис. 1. Карта региона ЯНАО с крупнейшими нефте- и газодобывающими предприятиями. На вставке слева – Салехард, Лабытнанги и их окрестности; указано месторасположение измерительного аэрозольного комплекса и объектов хозяйственной деятельности

траций ВС при определенных направлении θ и скорости j ветра:

$$CPF = \frac{n_{\theta,j}}{m_{\theta,j}}$$

Высокие значения CPF идентифицируют направление нахождения источника эмиссий с концентрациями в заданном диапазоне измеряемых величин. Поскольку различные источники, в зависимости от месторасположения и интенсивности эмиссий, идентифицируются в разных диапазонах концентраций [28], весь диапазон измеренных концентраций делится на интервалы, в которых определяются направления потенциальных источников. С помощью этого метода можно идентифицировать и удаленные источники в случае, если в период измерений не происходило значительных изменений атмосферных фронтов [28].

Для определения направления прихода воздушных масс в период выноса городских эмиссий в точку наблюдения рассчитаны обратные траектории переноса воздушных масс по модели HYSPLIT с использованием архивных метеорологических данных GDAS [29] на сайте лаборатории воздушных ресурсов (http://www.arl.noaa.gov/ready). Проведены расчеты на высотах 50, 100, 250 и 500 м длительностью 72 ч. Обработка данных на разных высотах показала, что в указанное время воздушные массы приходили в точку наблюдения из одного и того же района исследования, что позволило далее ограничиться демонстрацией результатов расчетов для высоты 500 м.

С целью получения более детальной информации об источниках городских эмиссий и типе сжигаемого топлива был сделан запрос в Департамент городского хозяйства г. Салехарда, получены и обработаны: официальные данные по выбросам системы тепло- и энергоснабжения АО «Салехардэнерго» за 2018–2019 г. и информация о транспортной ин фраструктуре города. Представленные официальные данные основаны на расчетах валовых выбросов «углерода(сажи)», предполагающих индекс эмиссии углерода 1,5–3 г на килограмм топлива для разных групп стационарных дизельных установок, согласно ГОСТ Р56163-2014 «Метод расчета выбросов от стационарных дизельных установок». В расчетах эмиссий от сжигания газа применялась методика определения выбросов загрязняющих веществ в атмосферу при сжигании топлива в котлах производительностью менее 30 т пара в час.

2. РЕЗУЛЬТАТЫ И ОБСУЖДЕНИЕ

Измерения концентрации черного углерода на ИАК «Обдорск» были проведены с 19 апреля по 5 августа 2019 г. В этот интервал среднесуточная температура воздуха увеличилась с –6 °С в апреле до –17 °С в июле. В июне, согласно ресурсу пожаров ЕКС ЯНАО (https://karta.yanao.ru/eks. Forest_fires), в регионе были зарегистрированы природные пожары. Поэтому далее для оценок влияния техногенных источников был выбран период до начала природных пожаров, с 19 апреля по 1 июня 2019 г. Анализ розы ветров в этот период показал преимущественное северо-западное направление ветра при скорости до 12 м/с. При больших скоростях ветра усиливалось турбiулентное перемеи i и ван ие слоев атмосферы, наблюдались эпизоды самых низких концентраций ВС. Малая скорость ветра и безветренная погода приводили к накоплению загрязнений в месте наблюдения.

На рис. 2 (цв. вставка) приведены результаты расчетов двумерной функции вероятности CPF попадания концентрации ВС в заданный интервал процентилей, которые показывают, какой процент значений находится ниже определенного уровня. В интервале самых малых процентилей, до 10%, самая высокая вероятность определяется в юго-западном направлении (на Южный Урал). Столь низкая концентрация ВС (1,6–30 нг/м^3, в среднем ~15 нг/м^3) характерна для удаленных от каких-либо источников районов [10, 30] и принимается в настоящей работе как уровень арктического фона.

Источники эмиссий ВС с концентрациями в интервале процентилей 10–50% локализуются в восточном, южном и юго-западном направлениях (рис. 2). Карта расположения объектов хозяйственной деятельности (см. рис. 1) указывает на местонахождение в 3 км от ИАК в восточном направлении полигона твердых бытовых отходов (ТБО) и цементного завода. В южном и юго западном направлениях в окрестностях Салехарда на десятки километров нет ни населенных пунктов, ни каких-либо промышленных предприятий. Однако в том же направлении на расстоянии ~ 300 км находится самый большой нефтедобывающий район Ханты Мансийского автономного округа. Вероятно, ИАК регистрирует шлейф крупно масштабных эмиссий центральной и южной частей крупнейшей в мире западно-сибирской нефтеносной провинции. Подобная ситуация обнаружения удален ного источника методом CPF может наблюдаться в случае отсутствия резких границ атмосферных фронтов, изменяющих направление ветров, как описано в [28]. Более слабый потенциальный источник ВС с более низкой вероятностью определяется в северо-западном направлении, где в 360 км расиоложено Новопортовское нефтегазоконденсатное месторождение (НГКМ) (см. рис. 1).

Мощный источник эмиссий, с концентрациями в интервале больших процентилей (50–80%), располагается на северо-западе ИАК, в направлении Салехарда и Лабытнанги, находящегося на другом берегу р. Оби. Наибольшая вероятность (от 0,1 до 0,3) попадания концентраций ВС в диапазон 73–135 нг/ м^3 регистрируется в секторе направлений ветра 280– 340° (см. рис. 2), который далее определяется как сектор выноса городских эмиссий. Расчет обратных траекторий переноса воздушных масс показал, что в период, когда направление ветра регистрировалось из сектора выноса городских эмиссий, все дальние переносы в точку наблюдений проходплп через город из того же сектора (рис. 3).

Самый мощный источник эмиссий, с концентрациями в интервале процентилей 80–100%, определяется с максимальной вероятностью -0,8 на северо-востоке от ИАК. Карта объектов хозяйственной деятельности на рис. 1 указывает на расположение на расстоянии более 300 км от г. Салехарда крупнейших в ЯНАО месторождений углеводородов (Уренгойское, Ярудейское, Новопортовское). Центр города является источником самых высоких (до 424 нг/м^3)

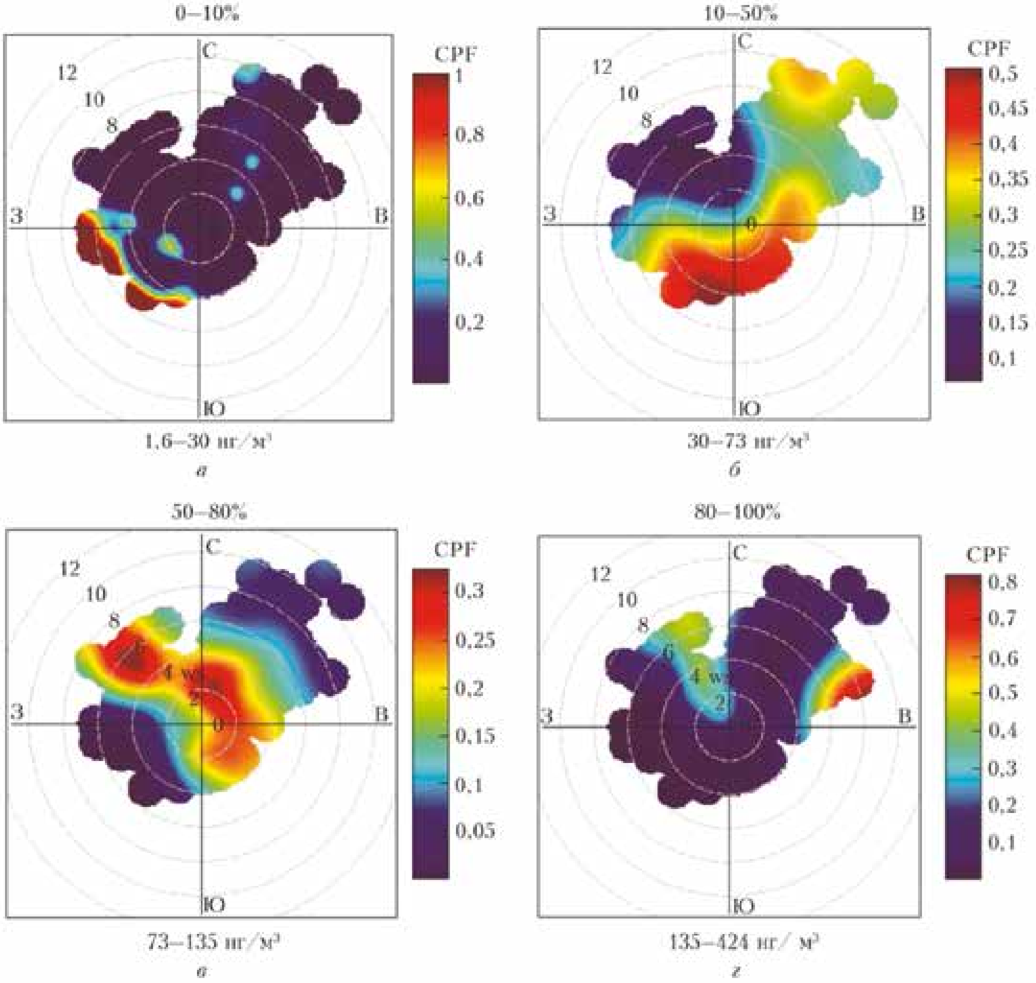

Рис. 2. Функция вероятностей (CPF)попадания концентрации ВС в заданный интервал значений в полярных координатах направления и скорости ветра (ws, м/с) в апреле – мае 2019 г. Над графиками указаны рассчитываемые интервалы процентелей концентраций ВС, внизу – соответствующие диапазоны концентраций ВС

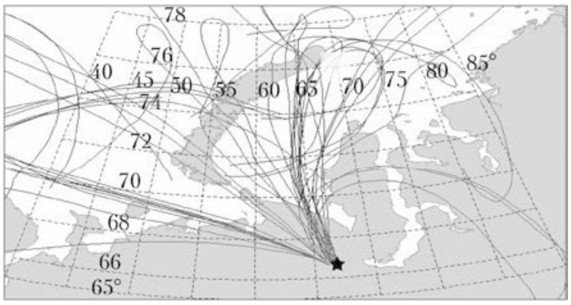

а

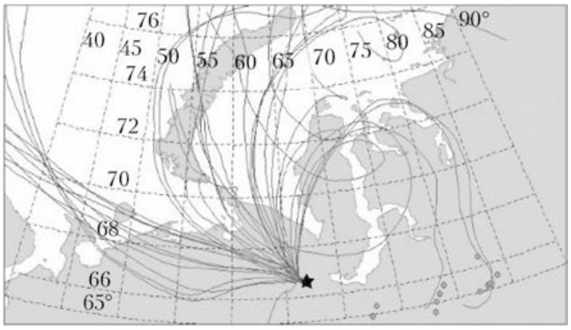

б

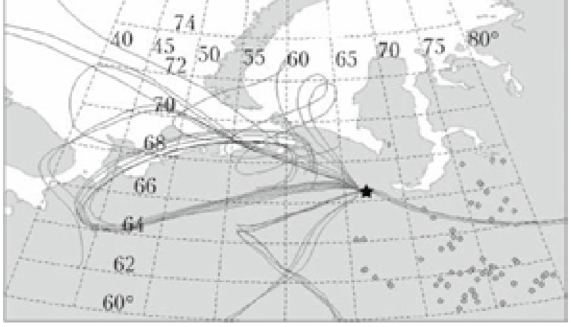

в

Рис. 3. Траектории воздушных масс, приходящих на ИАК в: период выноса городских эмиссий ВС в секторе направлений ветра 280–340°: а – апрель-май; б – июнь; в – июль 2019 г.; кружками отмечены области пожаров по ресурсу ЕКС ЯНАО концентраций BC, регистрируемых с вероятностью 0,4 на северо-востоке.

Результаты измерений массовых концентраций черного углерода на ИАК «Обдорск» в секторе выноса эмиссий Салехарда представлены на рис. 4. Таблица обобщает статистику за весь период измерений в выборке сектора городских эмиссий для средней, минимальной и максимальной концентраций BC. В апреле – мае концентрация BC_{880} варьировалась от 1,6 до 424 нг/м^3, периодически превышая арктический фон более чем в 15 раз, в эпизодах при малой скорости ветра. В некоторых эпизодах в апреле – мае, преимущественно при высоких концентрациях, наблюдалось увеличенное поглощение на к = 470 нм, приводившее к увеличению разности BC_{470} и BC_{880}, обусловленное сжиганием биомассы в жилом секторе н угля на угольных котельных г. Лабытнанги. Отметим, что такое превышение отсутствует в эмиссиях дизельных двигателей, генераторов и установок, использующих дизельное топливо [24]. Разница между BC_{880} и BC_{470}, указывающая на вклад сжигания биомассы и угля, достигла 80 нг/ м^3 1 мая и 77 нг/м^3 6 мая. В среднем концентрация BC в городских эмиссиях составила 133 + 80 нг/м^3. Для сравнения: среднемесячные концентрации BC в Томске (Западная Сибирь) с населением в– 10 раз больше, чем в Салехарде, в весенний (апрель – май) период составляют – 700 нг/м^3, что более чем в 5 раз выше уровня загрязнений черным углеродом атмосферы Салехарда [31]. Концентрация BC на фоновой станции в 70 км от г. Томска в гот же период – 400 нг/м^3.

Средняя, минимальная (min), максимальная (шах) концентрации BC, среднеквадратичная ошибка (а) и количество данных в выборке сектора городских эмиссий (Лт) за указанный период измерений на И Л К «Обдорск»

Период измерений	Концентрация BC средняя	min	max	σ	N
19.04 – 31.05	134	12	424	62	247
01.06 – 31.06	102	3	526	54	166
01.07 – 31.07	204	9	689	150	65

По официальным данным, основным городским источником эмиссий продуктов сжигания природного топлива (газа и дизельного топлива) в Салехарде является теплоэнергетическая система. В настоящее время на балансе АО «Салехардэнерго» находится 36 отопительных котельных и 3 центральных тепловых пункта. Основной вид топлива для котельных – природный газ с минимальной теплотой сгорания 7987 ккал/м^3. Суммарный валовый выброс углерода (сажи) в 2018 г. равен 5,874 тыс. т. Выбросы углерода (сажи) от объектов, работающих

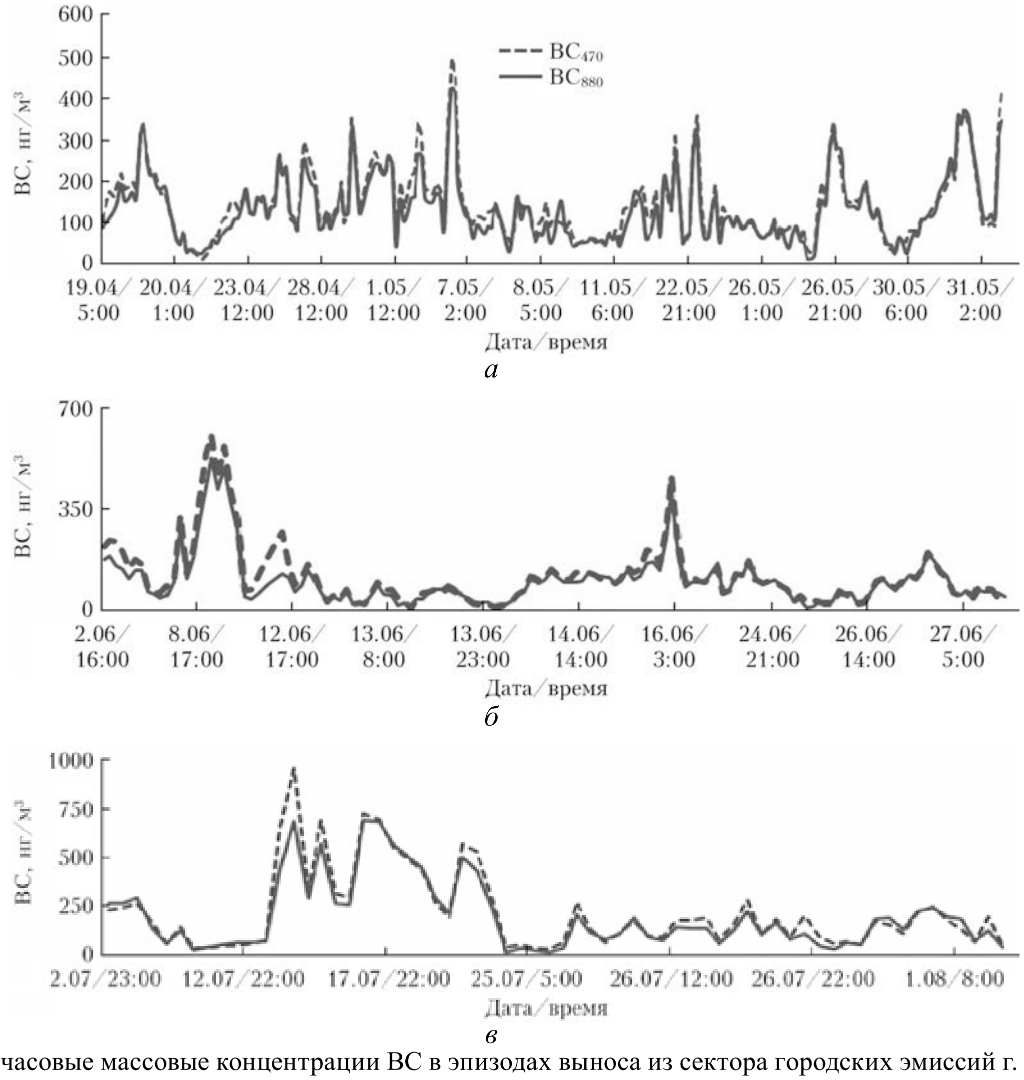

а

б

в

Рис. 4. Среднечасовые массовые концентрации BC в эпизодах выноса из сектора городских эмиссий г. Салехарда Поповичева О.Б., Кобелев В.О., Синицкий А.И. и др.

на газу, суммарно составили 0,065 тыс. г (всего 1,2% от общих выбросов), а на дизельном топливе (две дизельные электростанции, один аварийный дизель- генератор, автотранспортный цех) – 5,808 тыс. т (98,8%отобщихвыбросов). С сентября 2018 г. Салехардский энергоузел присоединен к электрическим сетям АО«Тюменьэнерго» (ЕЭС России), а электро станции ДЭС-1 и ДЭС-2 выведены из эксплуатации. Среди наиболее значительных источников эмиссий остались зоны г. Лабытнанги и пос. Харп, котельные на территории которых работают на угле и мазуте, а также асфальтовый завод в северной части Сале харда.

Весомый вклад в загрязнение атмосферы Сале харда вносит автомобильный транспорт, выбросы загрязняющих веществ которого за 2018 г. равны 0,395 тыс. т. Дизельное топливо и бензин – основные виды топлива, использующиеся для автомобильных перевозок, а также для обслуживания пассажирских и транспортных водных путей по р. Оби и Обской губе. По данным ОГИБДД УМВД, автомобильный парк Салехарда насчитывает 18191 транспортное средство (86% – легковые автомобили, остальное – автобусы и грузовой дизельный транспорт).

В июне на ПАК «Обдорск» концентрация ВС в секторе выноса эмиссий г. Салехарда в среднем составила 105±80нг/м^3, были зарегистрированы эпизоды максимальных BC_{880} до 526 нг/м^3 (см. рис. 4). Совместный анализ концентраций ВС и скорости ветра показал, что наибольшие значения ВС наблюдались в дни с низкой, порядка 1 м/с, скоростью ветра, способствующей накоплению загрязнений вблизи города. Наиболее длительный эпизод высоких концентраций черного углерода был заре гистрирован с 8 по 12 июня, когда разница между BC_{880} и BC_{470} – 78 нг/м^3, а 11 июня достигла 156 нг/м^3. Такое увеличение концентрации ВС на коротких длинах волн обусловлено влиянием дымовых эмиссий лесных пожаров, площадь которых в этот период, согласно ресурсу ЕКС, составляла от 0,3 до 4,2 км^2. Как показывают расчеты траекторий дальнего переноса в апреле – мае 2019г., воз душные массы, приходящие в место наблюдений с северо-востока, проходили через город (см. рис. 4). В период с 8 по 12 июня они пересекали район пожаров на северо-востоке от города.

В июле 2019 г. в северных районах Сибири наблюдались природные пожары, интенсивность которых в 100 раз превышала уровень ежегодно наблюдаемых пожаров (https: //atmosphere.copernicus. eu/ cams-monitors-rmprecedented-wildfires-arctic). Средняя июльская концентрация ВС, измеренная в секторе выноса эмиссий Салехарда, составила 350 + 120 нг/ м^3. Согласно ресурсу ЕКС ЯНАО с 14 по 25 июля в ЯНАО было зарегистрировано более 40 пожаров на суммарной площади ~ 1000 га. Именно в этот период на ИАК были зарегистрированы продолжительные максимумы ВС880 (до 690 нг/м^3) и BC_{470} (до 958 нг/ м^3) (см. рис. 4). Значения ВС470 превысили BCgso на рекордную величину – 264 нг/м^3, идентифицирующую вклад дымовых шлейфов из районов пожаров (см. рис. 3) в полную нагрузку атмосферы города эмиссиями продуктов горения биомассы.

ЗАКЛЮЧЕНИЕ

Салехард – типичный город Арктического региона, где среди источников значимой компоненты загрязненной атмосферы – черного углерода – доминируют теплоэнергетика и транспорт, использующие дизельное топливо, бензин и природный газ. На ИАК «Обдорск», установленном вблизи г. Салехарда, в апреле-августе 2019 г. быт проведен цикл измерений концентрации черного углерода. На северо-западе от ИАК в направлении Салехарда в интервале больших процентилей концентраций черного углерода (от 50 до 80%) определен сектор выноса городских эмиссий, подтвержденный расчетами траекторий переноса воздушных масс. Средние концентрации ВС в городских эмиссиях в апреле-мае и июне составили 113 и 105 нг/м^3 Оценки качества воздуха в городской среде показали, что в отдельных эпизодах концентрация ВС превышала арктический фон более чем в 30 раз. Во время ин тенсивных июльских пожаров средняя концентрация увеличилась до 350 нг/м^3. Было зарегистрировано рекордное значение – 264 нг/м^3 маркерной оценки вклада горения биомассы по сравнению со сжиганием природного топлива, указывающее на беспрецедентно высокое для Арктического региона загрязнение атмосферы в период природных пожаров.

Авторы благодарны Администрации г. Салехарда (Департамент городского хозяйства) за предоставленную информацию о возможных источниках загрязнения за 2018–2019 гг. и Программу комплексного развития транспортной инфраструктуры муниципального образования город Салехард Ямало-Ненецкого автономного округа на 2017–2025 гг.

Работа по установке комплекса и проведение измерений выполнены при поддержке гранта РФФИ № 18-0560084, анализ результатов аэталометрических измерений – гранта РНФ № 19 773004.

The effects of hygroscopicity on ice nucleation of fossil fuel combustion aerosols in mixed-phase clouds*

1. INTRODUCTION

Soot aerosols produced by incomplete combustion of fosSoot aerosols produced by incomplete combustion of fossil fuel and biomass containing black carbon (BC) and organic matter (OM) can absorb solar radiation, thereby changing vertical temperature profiles and decreasing surface radiation (Andreae and Gelencs´er, 2006). Combustion aerosols can also act as cloud condensation nuclei, causing indirect effects on clouds by decreasing the cloud droplet radius. This causes cooling which counteracts the warming by greenhouse gases. Combustion aerosols can also act as heterogeneous ice nuclei (IN) in mixed-phase clouds (e.g. Cozic et al., 2008), as well as in cirrus clouds (Koehler et al., 2009; Penner et al., 2009). Recent measurements of IN activity at −30 C and above water saturation for biomass-burning-generated particles show that IN number concentrations are elevated by at least a factor of 2–3 during biomass-burning episodes over those typical of background air (Prenni et al., 2012). The ice nucleation effects of fossil fuel combustion aerosols in mixed-phase clouds are very uncertain, which hinders the prediction of climate change. Due to the abundance of fossil fuel (ff) combustion aerosols, a small change in their ice nucleation ability can produce a large difference in indirect effects. Several studies have noted the sensitivity of aerosol forcing to ice nucleation in mixed-phase clouds (ohmann and Hoose, 2009; Storelvmo et al., 2008a, 2011; Yun and Penner, 2012).

During the lifetime of soot aerosols in the atmosphere their hygroscopicity can be altered through coating by sulfate and organics (Zhang et al., 2008; Petters and Kreidenweis, 2007; Gunthe et al., 2011). Several laboratory experiments have investigated the effect of coating on the ability of soot particles to nucleate ice (DeMott et al., 1999; Mohler et al., 2005; Friedman et al., 2011; Crawford et al., 2011). DeMott et al. (1999) conducted ice nucleation experiments on lamp black soot at 213–233K with sulfuric acid coating varying from zero to several weight percent. It was found that ice nucleation required the highest supersaturation at almost every temperature when the soot particle was treated with approximately one monolayer of sulfuric acid. However, the critical supersaturation required for ice formation was much lower when BC particles were treated with a multilayer equivalent coverage of sulfuric acid. Mohler et al. (2005) investigated ice nucleation of soot particles generated from a graphite spark generator (GSG) at 185–240 K, and found that internal mixtures of soot and sulfuric acid required higher supersaturation than that of uncoated soot to nucleate ice. The uncoated lamp black soot used by DeMott et al. (1999) and the GSG soot used by Mohler et al. (2005) have very different ice nucleation properties, with the uncoated GSG soot being a much more efficient ice nuclei (Kärcher et al., 2007). Friedman et al. (2011) found no heterogeneous ice nucleation below water saturation above their experimental detection limit (which was about 0.01–0.1% of the soot particle concentration, or about 10 L^{-1}) for both coated and uncoated soot particles generated from a mini-CAST Real Soot Generator at 253K and 243 K. Above water saturation, ice nucleation could have occurred for both coated and uncoated soot but could not be distinguished from droplet formation. Crawford et al. (2011) examined nucleation of ice at 210–235K for sulfuric-acid-coated soot particles generated from a CAST propane burner with various amounts of organic content. They found that uncoated soot particles with 30% organic mass content freeze before water saturation, and those with 80% and 90% organic mass content are inactive or freeze at water saturation, respectively. After coating by sulfuric acid, they all nucleated ice close to the homogeneous freezing conditions of sulphuric acid. These studies all lead to different conclusions about the effect of adding a soluble coating to soot. One possible reason for the differences in nucleation is the differences in the properties of the bare soot particles, for example, the organic content, porosity, surface area, etc. The amounts of sulfuric acid coating were also not quantified in most of these laboratory studies. This hinders the comparability among different laboratory studies, and also the applicability of the results to modeling studies. Nevertheless, these studies demonstrated that the addition of a soluble coating can alter the ice nucleation ability of soot particles, which most model studies of aerosol indirect effects (AIE) do not explicitly consider (e.g. Yun and Penner, 2012; Lohmann and Hoose, 2009; Storelvmo et al., 2011).

Here we adopt recent laboratory studies from Popovicheva et al. (2008b, 2010, 2011) and Koehler et al. (2009), which provide a link between sulfuric acid coating, hygroscopicity, and ice nucleation efficiencies, and develop a method of differentiating hydrophobic, hydrophilic, and hygroscopic particles and their ice nucleation in models. Coating or mixing with secondary organic matter may also change the particle hygroscopicity as was shown in laboratory simulations performed in Popovicheva et al. (2009) and Crawford et al. (2011), among others. However, it has been shown by Popovicheva et al. (2009) that with the same amount of coverage, the impact of organic acid on soot hygroscopicity is weaker than that from sulfuric acid. Also, our model currently does not follow organic functional groups. To do so would require a sophisticated organic chemistry/aerosol model that accounts for formation of secondary organic aerosols (as in, for example, Lin et al., 2012) as well as a better quantification of the role of different organic functional groups in ice formation. Thus, this study, which only considers the coating of soot by sulfuric acid, should be viewed as an exploratory step toward a more sophisticated treatment of ice nucleation.

Progress in characterizing soot hygroscopicity has been achieved by a systematic comparative analysis of the water uptake by soot particles of various physico-chemical properties and by the identification of water–soot interaction mechanisms in relation to the soot composition (Popovicheva et al., 2008a). Two mecha-

---

* Y. Yun, J. E. Penner, and O. Popovicheva // Atmospheric Chemistry and Physics. 2013; 13: 4339–4348
DOI: 10.5194/acp-13-4339-2013

nisms of water–soot interaction, namely, the bulk dissolution of water onto soot due to coverage by soluble compounds and the water molecule adsorption on surface active sites, were identified. The formation of a water film that extended over the surface at a relative humidity <80% was suggested as a quantification measure to separate soots with respect to their hygroscopicity (Popovicheva et al., 2008b). Hydrophobic soot which has a limited number of active sites never forms a film, while hydrophilic soot develops a water film on its oxidized surface. Water uptake on hygroscopic soot covered by soluble compounds is characterized by many layers of water uptake. Koehler et al. (2009) performed a series of experiments on well-characterized soot and linked the extent of soot hygroscopicity to its IN ability, based on Popovicheva et al. (2008b). The frozen fractions of hydrophobic, hydrophilic, and hygroscopic soot were measured at cirrus cloud temperatures (−40 C or less). In addition, Popovicheva et al. (2011) performed a series of laboratory experiments to identify the threshold amount of sulfate coating needed to transform hydrophobic to hydrophilic to hygroscopic soot.

Here we develop a method of differentiating hydrophobic, hydrophilic, and hygroscopic soot particles by the amount of sulfate deposited on the particles and treat their respective ice-nucleating properties in mixed-phase clouds in a model. The mixed-phase cloud treatment for hydrophobic, hydrophilic, and hygroscopic soot is developed by extending the observations by Koehler et al. (2009) to mixed-phase cloud temperatures using the Phillips et al. (2008) parameterization. Section 2 describes the 3-ffBC/OM (hydrophobic, hydrophilic and hygroscopic) soot scheme, which is implemented in place of a single-category scheme (1-ffBC/OM) (Wang et al., 2009) as well as our method of extending the Koehler et al. (2009) observations using the Phillips et al. (2008) parameterization. In section 3, we present the hydrophobic, hydrophilic and hygroscopic ffBC/OM aerosol fields, as well as the cloud water field and radiative forcing from the original and the new scheme. Section 3 also presents an updated total anthropogenic forcing with the new 3-ffBC/OM scheme. A discussion follows in Sect. 4.

2. METHODS

The 3-ffBC/OM scheme was implemented into the CAMIMPACT coupled aerosol transport model and general circulation model (Wang and Penner, 2010), as well as an offline radiation model. The coupled model (online simulation) provides the aerosol fields and meteorology fields for the offline model and is used to calculate the total anthropogenic forcing. The offline model reads the aerosol and meteorology fields and examines the cloud water fields and mixed-phase cloud anthropogenic forcing. Using the offline model ensures that a fixed amount of ffBC/OM aerosol enters the ice nucleation scheme, and that changes in the cloud field and radiation is solely from the treatment of hygroscopicity in the ice nucleation scheme.

2.1 Models

The University of Michigan IMPACT aerosol model has a detailed description of the formation of sulfate particles, their interaction with non-sulfate aerosols, dry deposition, and wet deposition (Herzog et al., 2004; Liu et al., 2005, Wang et al 2009). Pure sulfate aerosols are predicted to be in one of three modes (nucleation mode (radius<5 nm), Aitken mode (5 nm<radius<50 nm), and accumulation mode (radius >50nm)). Both the mass and number of pure sulfate aerosol for the three modes are predicted. The primary nonsulfate aerosol components included in the model are natural organic matter (NOM), fossil-fuel-burning black carbon and organic matter (ffBC/OM), biomass-burning black carbon and organic matter (bbBC/OM), aircraft BC (ABC), dust, and sea salt. Only the mass concentration is predicted for these non-sulfate aerosols although dust and sea salt are carried in 4 separate size bins. The number concentrations of these non-sulfate aerosols are calculated with assumed size distributions. Although BC and OM from fossil fuel burning and biomass burning are treated as distinct species in the model, they are assumed to be internally mixed (Liu et al., 2005). Carbonaceous aerosol (OM and BC) is currently represented by a single submicron size bin, which is the sum of three log-normal distributions with the geometric means and variances described in Penner et al. (1998). For fossil fuel BC and OM, the volume mean radius is 0.103 mum. Comparisons of the model-simulated BC profiles to data from Schwarz et al. (2008) were included in Koch et al. (2009). The mixing of sulfate with non-sulfate aerosols occurs through condensation of sulfuric acid onto the surface of non-sulfate aerosols, coagulation with pure sulfate aerosols, as well as aqueous formation of sulfuric acid in cloud droplets. The coated sulfate mass on each separate type of non-sulfate aerosol is separately predicted. Detailed descriptions of the aerosol microphysics can be found in Herzog et al. (2004).

The NCAR CAM3 model was updated to include a two-moment microphysics scheme for cloud liquid and ice (Wang and Penner, 2010). In mixed-phase clouds, the Phillips et al. (2008) parameterization (PH08) of deposition/condensation/immersion freezing was implemented (Yun and Penner, 2012). Phillips et al. (2008) has been updated to suppress deposition/condensation/immersion freezing by soot above −15 C (Phillips et al., 2013). We have compared the current parameterization with the revised Phillips et al. (2013) parameterization for soot aerosols, and found that the changes of ice number concentrations simulated in our model between the old and new versions of parameterization are generally within 10 %. The ice number concentration is lower with the new parameterization at warm temperature regions due to the suppression of soot ice nucleation. It is higher at cold temperature regions (where soot ice nucleation is not suppressed) due to the smaller baseline value of soot surface area. Comparison plots are shown in appendix A).The contact freezing parameterization is that of Young (1974), with the contact ice nuclei concentration fitted to that recommended by Young (1974). All aerosols are assumed to be interstitial for the calculation of ice nucleation in our model. In reality, particles might have entered the droplets either due to higher peak supersaturations at cloud base or due to collision scavenging, in which case the effect of hygroscopicity on ice nucleation may be overruled. However, we have estimated the fraction of hydrophobic and hydrophilic soot activated into cloud droplet to be about 15% in our model. That from hygroscopic soot is about 20 %. From the estimate by Hoose et al. (2008), the contribution of collision scavenging is at most about one-fifth of nucleation scavenging for BC and OM. Therefore, the effect of hygroscopicity still matters for the rest (about 80 %) of the soot particles.

The offline radiation model of Chen and Penner (2005) was extended to include mixed-phase clouds. The ice nucleation scheme in mixed-phase clouds is the same as that in the CAM-IMPACT model (Yun and Penner, 2012). In the offline radiation model, we predict the ice number concentration from nucleation using aerosol concentrations from an online calculation that are read-in. The ice/liquid number/ mass concentration change from contact freezing and the Bergeron–Findeisen process (the conversion of liquid to ice) was also implemented, due to its importance to radiative forcing (Storelvmo et al., 2008b). Other meteorology variables are fixed and no further processing of ice particles takes place (no sedimentation, coagulation, or precipitation formation).

2.2 3-ffBC/OM scheme

The differentiation between hydrophobic, hydrophilic, and hygroscopic ffBC/OM aerosols is based on the number of monolayers of sulfuric acid coating. Freshly emitted ffBC/OM particles are assumed to be hydrophobic. After each time step, the number of monolayers of sulfate coating (n_{coat}) is calculated and compared with threshold values. If $n_{coat} < 1$, the particle remains hydrophobic. If $1 \le n_{coat} < 3$, the particle is moved to the hydrophilic category. If $n_{coat} \ge 3$, the particle become hygroscopic. This is shown as a diagram in Fig. 1. The size distributions of the three ffBC/OM species prior to coating by sulfate (and water) are assumed fixed (see Penner et al., 1998). The accommodation coefficient for the condensation of sulfuric acid on hydrophobic and hydrophilic particles is set to 0.018 (Zhang and Zhang, 2005), while that for hygroscopic particles is 0.65, similar to sulfuric acid surfaces (Pöschl et al., 1998).

The PH08 parameterization was modified to treat the nucleation of ice in mixed-phase clouds by the 3-ffBC/OM categories. Ice nucleation was measured at −40°C as well as at a colder temperature (−51.5°C or −57°C) in Koehler et al. (2009). Due to the coexistence of liquid and ice, water saturation is assumed in mixed-phase clouds in our model. Therefore, we use the frozen fraction measured at −40°C at water saturation to adjust the PH08 parameterization in mixed-phase clouds. The uncertainty of the relative humidity w.r.t. water in Continuous Flow Diffusion Chamber (CFDC) is about 3% (P. R. DeMott, personal communication, 2012). This is an implicit artifact of detecting IN using any CFDC type device or any ice nucleation device presently available (P. R. DeMott, personal communication, 2012). By using the published value of the fraction of soot nucleated at 100%±3% RHw we are assuming that the measured values represent the averaged value from 97% to 103% RHw. The data published by Koehler et al. (2009) show that the true fractions could be higher or lower by approximately ±10 if the measured RHw differs by 3 %.

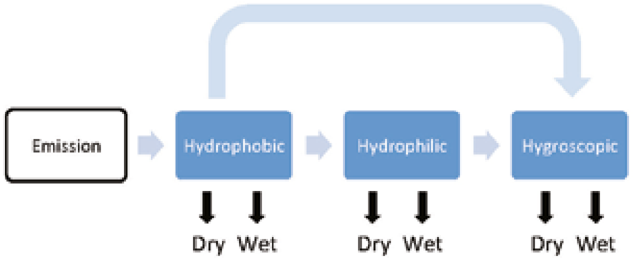

Fig. 1. Diagram showing the 3-ffBC/OM scheme. Hydrophobic, hydrophilic and hygroscopic BM/OM then enter into the ice nucleation scheme in mixed-phase clouds as shown in Fig. 2.

All of the soot samples used in Koehler (2009) studies were first characterized using three hygroscopicity categories, using the concept of quantification of water uptake (Popovicheva et al., 2008b). There are five different soot samples. Aircraft engine combustor (AEC) soot is the only soot sample characterized as hygroscopic, so it was chosen as the representative for hygroscopic soot in our study. Thermal soot (TS) is hydrophobic. Graphitized thermal soot (GTS) is produced by heating the TS soot to ≈300°C to remove any impurities from the surface and graphitize the structure, and it is extremely hydrophobic. We think that the soot emitted from fossil fuel combustion is likely to have impurities and unlikely to be extremely hydrophobic. Therefore TS was selected as the representative for hydrophobic soot for this study. Thermal oxidized soot (TOS) and TC1 soot (TC1 kerosene flame soot) are both characterized as hydrophilic. However, TC1 soot is typically composed of agglomerates of 20–50 nm particles, is highly microporous and is subject to swelling phenomenon. Therefore the hydrophilic properties of TC1 soot may not be solely explained by the surface properties. So TOS was selected as the representative for hydrophilic soot for this study. For hydrophobic and hydrophilic soot, we use the data for the 200 nm particles because this size is close to the volume mean diameter of the BC/OM particles in our model, which is 180 nm. There are only data for polydisperse particles at −40°C for hygroscopic soot. However, the frozen fractions of the polydisperse particles and 250 nm particles are similar at −57°C. So we assumed that differences between the size distribution between the polydisperse particles and our soot particles would not have a large impact on the freezing properties of hygroscopic particles. The frozen fraction of hydrophobic, hydrophilic, and hygroscopic soot measured at −40°C and at water saturation is 0.03 %, 2 %, and 3 %, respectively (Table 1 in Koehler et al., 2009), while that predicted by PH08 for the same conditions is 0.2 %. Therefore, we increased the PH08 frozen fraction by a factor of 10 for hydrophilic ffBC/OM, and reduced it by a factor of 0.15 for hydrophobic ffBC/OM. In doing so, we preserve the temperature dependence specified in PH08.

For hydrophobic and hydrophilic soot, heterogeneous freezing is the likely freezing mechanism in the Koehler et al. (2009) experiments due to the monotonic increase of frozen fraction with RHw, and the lack of correlation with the “Koop” line. Freezing for hygroscopic particles followed the Koop line for homogeneous freezing of pure dissolved solute at −40°C for a short distance near water saturation. However, the frozen fraction slightly above water saturation was far smaller than that predicted by a homogeneous freezing mechanism. Therefore, we made two assumptions to treat the freezing of hygroscopic particles at higher temperatures. The first is that these particles freeze homogeneously, so we exclude them as a heterogeneous IN. This is similar to the observation of internally mixed propane burner soot by Crawford et al. (2011). The second is that they freeze heterogeneously, and we scale the frozen fraction of PH08 by a factor of 15. This is similar to the observation of multilayer coated lamp black soot by DeMott et al. (1999). The ice nucleation ability as a

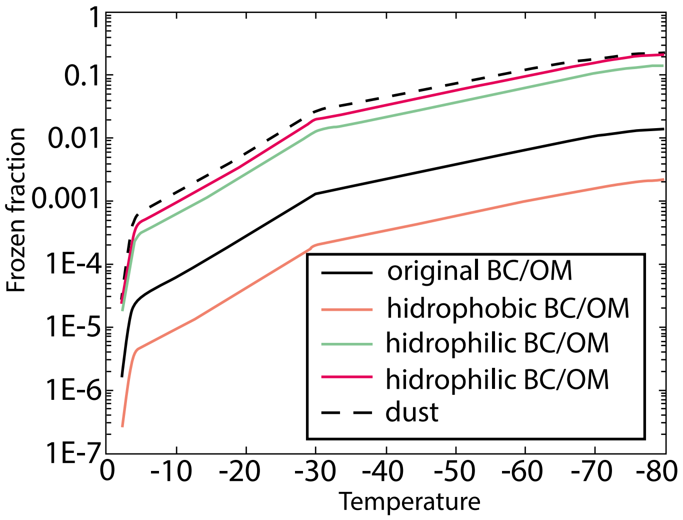

Fig. 2. Frozen fraction as a function of temperature for dust, BC/OM in the original 1-ffBC/OM scheme, and hydrophobic, hydrophilic, and hygroscopic BC/OM in the new 3-ffBC/OM scheme with hygroscopic soot particles as heterogeneous ice nuclei

function of temperature for dust, the ffBC/OM in the original 1-ffBC/OM scheme, and hydrophobic, hydrophilic, and hygroscopic soot in the 3-ffBC/OM scheme with hygroscopic soot as heterogeneous ice nuclei are shown in Fig. 2. The contact freezing treatment was kept the same as in the 1-ffBC/OM scheme, since we want to examine the effect of treating soot ice nucleation using the results of Koehler et al. (2009), whose measurement includes deposition/condensation/immersion freezing but no contact freezing. Contact freezing in our model is represented by the Young (1974) parameterization fitted to the observation of total number of contact ice nuclei measured by Blanchard (1957) (see Yun and Penner, 2012). This treatment makes the contribution from contact freezing to total ice nucleation very small (on the order of 1 %). The cirrus cloud ice nucleation scheme was kept unchanged in this paper; this may be inconsistent, but we want to focus on the effect in mixed-phase clouds.

2.3 Experiment setup

Table 1 shows the three offline simulations. In the 1BC simulation, the original PH08 scheme is used and the sum of hydrophobic, hydrophilic, and hygroscopic ffBC/OM is treated as one species. For each configuration, the model is run twice with present-day (PD) and pre-industrial (PI) aerosol fields. PI aerosol fields are only applied to ice nucleation in mixedphase clouds. The online model is run using the 3BC noSCO scheme with PD and PI emission files described in Penner et al. (2009). Aerosol direct effects as well as indirect effects on warm-phase and cirrus clouds are included in the online model.

Table 1. Offline simulations.

Schemes	Description
1BC	1-ffBC/OM scheme
3BC	SCO 3-ffBC/OM scheme and hygroscopic soot particles as heterogeneous ice nuclei
3BC_noSCO	3-ffBC/OM scheme and no hygroscopic soot particles as heterogeneous ice nuclei

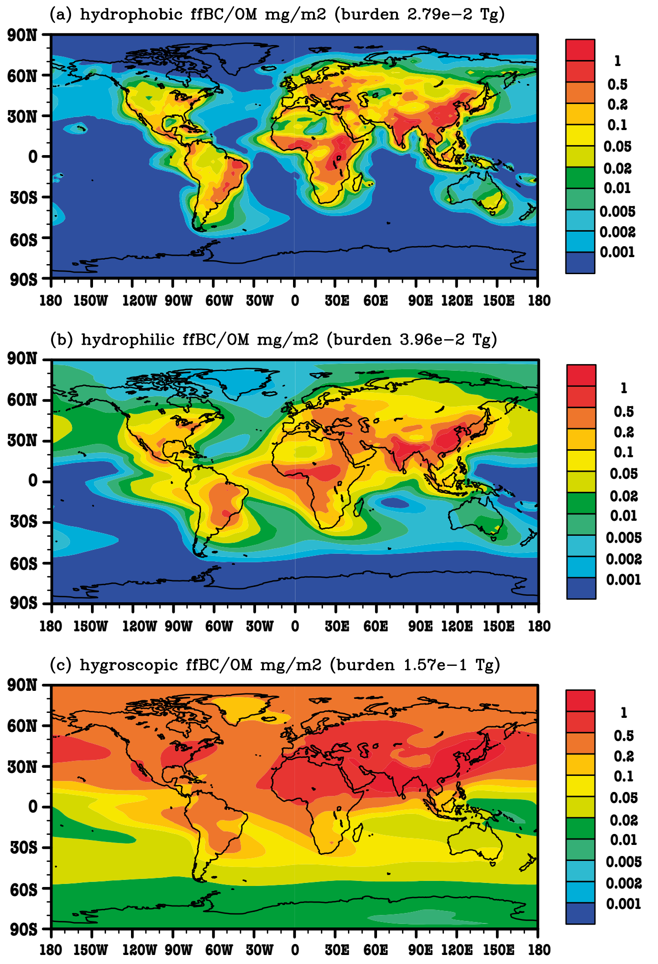

Fig. 3. PD annual average horizontal distribution of column-integrated hydrophobic (a), hydrophilic (b), and hygroscopic (c) ffBC/OM (mgm^{-2}).

3 RESULTS

3.1. Aerosol fields for hydrophobic, hydrophilic, and hygroscopic ffBC/OM

Figure 3 shows the PD horizontal distribution of columnintegrated hydrophobic, hydrophilic and hygroscopic ffBC/OM. Hydrophobic ffBC/OM is confined mainly to regions near emissions. Hydrophilic ffBC/OM is transported farther than hydrophobic ffBC/OM. Hygroscopic ffBC/OM is even more widespread. Table 2 shows the burden and lifetime for hydrophobic, hydrophilic, and hygroscopic soot using the 3-ffBC/OM scheme and the 1-ffBC/OM scheme. The majority of the ffBC/OM particles are hygroscopic, contributing 69.93% to the total ffBC/OM burden. Hydrophilic and hydrophobic ffBC/OM particles contribute 17.64% and 12.43 %, respectively. The aging process that transforms hydrophobic soot to hydrophilic and hygroscopic soot as a result of additional increases in sulfate coating is considered as a sink of the hydrophobic and hydrophilic soot particles, while the only sink of hygroscopic soot is via wet and dry deposition. Therefore hydrophobic soot particles have the shortest lifetime of 0.45 days. The lifetimes of the hydrophilic and hygroscopic ffBC/OM particles are 0.95 and 4.55 days, respectively. The lifetime of soot particles using the 3-ffBC/OM scheme is decreased compared to that in the 1-ffBC/OM scheme. This is mainly driven by the increased wet removal rate for the hygroscopic particles, since the sulfate coating thick-

Table 2. ffBC/OM burden and lifetime.

Schemes	Burden	Lifetime
Hydrophobic	0.0279	0.45
Hydrophilic	0.0396	0.95
Hygroscopic	0.157	4.55
3-ffBC/OM Total	0.225	3.68
1-ffBC/OM Total	0.233	3.88

ness is not diluted by newly emitted hydrophobic soot through the process of calculating an "averaged" coating thickness as in the 1-ffBC/OM scheme. As a result, the total fossil fuel combustion soot burden is smaller in the 3-ffBC/OM scheme (Table 2).

Figure 4 shows the change in the hydrophobic, hydrophilic, and hygroscopic ffBC/OM number concentrations from PI to PD due to anthropogenic emissions. Concentrations increase in most places due to higher PD emissions. However, the concentration of hydrophobic ffBC/OM is smaller for the PD in most places of the Northern Hemisphere (NH) (Fig. 4a), and the concentration of hydrophilic ffBC/OM is smaller for PD at NH high latitudes (Fig. 4b). This is because sulfate emissions increase significantly in the PD in the industrial regions in the NH and more readily coat the surface of the ffBC/OM particles. Therefore, the ffBC/OM particles become hygroscopic more easily and are less likely to remain hydrophilic and even less likely to remain hydrophobic.

3.2 Comparison of mixed-phase cloud water field and radiative forcing

Figure 5 shows the grid-mean ice number concentration (Ni) change from PI to PD in mixed-phase clouds using the offline model. There is a larger increase in Ni in the NH than in the Southern Hemisphere (SH) for all three experiments. The 1BC case shows increases of the order of $1\ L^{-1}$ throughout the mid-troposphere north of 30 N, while the 3BC noSCO case shows decreases north of 60 N, caused by the decrease of hydrophilic ffBC/OM (Fig. 4b). The 3BC SCO case shows much larger increases that also extend to the SH, due to the enhanced effect of hygroscopic ffBC/OM. In general, Ni increases from PI to PD predicted by the 3-ffBC/OM scheme are very different from those predicted by the 1-ffBC/OM scheme. However, the sign of the change depends strongly on the freezing ability of hygroscopic ffBC/OM. When hygroscopic ffBC/OM acts as a heterogeneous IN in mixed-phase clouds, there is a larger increase in Ni ; when hygroscopic ffBC/OM does not, there is a smaller overall increase.

An increase in Ni causes a net conversion of liquid to ice mass in mixed-phase clouds, as a result of the Bergeron–Findeisen process. Figure 6 shows the change in the liquid water mass mixing ratio in all 3 schemes from PI to PD. Liquid cloud mass mixing ratio decreases at most latitudes except north of 60°N in the 3BC noSCO scheme. The decrease is largest in the 3BC SCO case and smallest in the 3BC-noSCO case, consistent with the changes in N_i.

Table 3 shows the anthropogenic forcing in mixed-phase clouds from the three cases. Two aspects contribute to the anthropogenic ffBC/OM forcing. The first is the decrease of ice effective radius associated with the increase of Ni (Fig. 5). Smaller ice effective radius leads to more reflected solar radiation and less long-wave transmission, reducing the net incoming short-wave radiation as well as the net outgoing long-wave radiation at the top-of-the-atmosphere (TOA). Therefore, the anthropogenic short-wave (SW) forcing from this effect is negative, and the long-wave (LW) forcing is positive. The second aspect is the decrease of liquid water mass mixing ratio (Fig. 6). This results in a smaller liquid water path in the present-day, and therefore a reduced short-wave reflectivity and increased long-wave transmissivity. The result of this change is a positive SW forcing and a negative LW forcing. As shown in Table 3, the second effect dominates the sign of the SW and LW forcings.

The treatment of ffBC/OM with different freezing properties results in significant changes to the offline mixed-phasem cloud forcing (CF). When hygroscopic ffBC/OM particles are excluded as IN, there is a 35% decrease in the net anthropogenic forcing compared to the 1BC case. When hygroscopic ffBC/OM particles are included, there is an increase by a factor of 6, due to the large liquid water change in the 3BC SCO case. The two treatments for hygroscopic soot particles lead to a net offline mixed-phase anthropogenic forcing that varies by almost a factor of 10, from 0.111 to $1.059Wm^{-2}$.

The total anthropogenic forcing (including sulfate) using the 3BC scheme with the coupled model shows a positive net CF of $0.06Wm^{-2}$. The net whole-sky forcing is the same as the CF in the offline simulations because the aerosol and meteorology fields are fixed and no direct effect is included. That for the online model, however, includes all effects (e.g. nucleation of warm cloud, cirrus cloud, and direct effects as well as changes to the cloud fields that result from nucleation) and is $-2.45Wm^{-2}$. However, this number would be smaller if hygroscopic soot particles were allowed to act as IN in mixed-phase clouds in the online simulation. Based on a one-year simulation using the online model, the net whole-sky anthropogenic aerosol forcing for 3BC SCO case is $-1.28Wm^{-2}$.

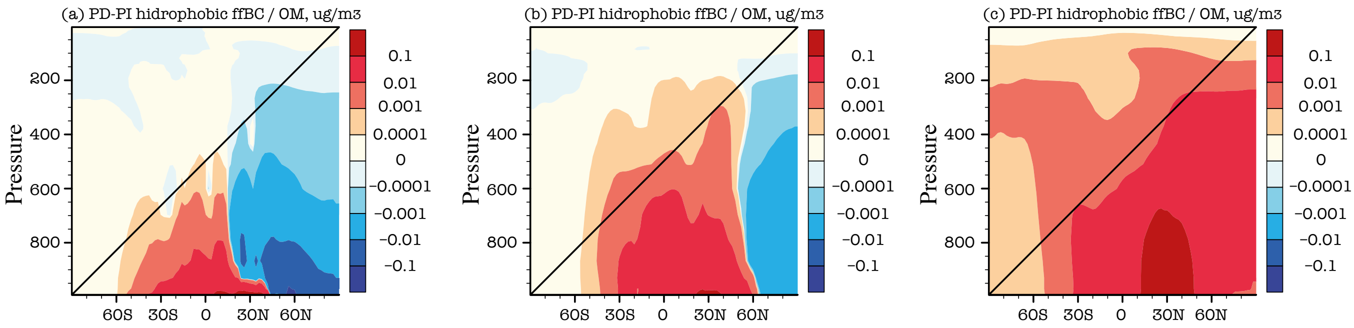

Fig. 4. PD–PI annual average changes of hydrophobic (a), hydrophilic (b), and hygroscopic (c) ffBC/OM (μgm^{-3}).

4 DISCUSSION

Anthropogenic aerosol emissions are thought to produce negative forcing through their indirect effect on warm clouds.

This could counteract the warming effect of greenhouse gases and thus has important implications for predicting climate change. However, there are large uncertainties associated with their effects in mixed-phase clouds, which hinders our ability to fully determine the effects of aerosols on climate. Our results show that the net effect of anthropogenic aerosols on mixed-phase clouds is a warming. This warming effect comes from the decrease of optical depth due to the Bergeron–Findeisen process. To estimate the importance of mixed-phase cloud forcing relative to other clouds, we removed the effect of the ADE (0.67Wm^{-2} estimated using the offline radiation model) from the online anthropogenic SWCF to estimate the forcing from only the AIE (1.61Wm^{-2}). As a result, the SW forcing in mixed-phase clouds contributes 867.33–68.7% of the anthropogenic SW forcing in all clouds, and the LW forcing contributes 860.32–2.12% (Table 3). The magnitude of the mixed-phase cloud forcing is very sensitive to whether the effect of hygroscopicity is considered, and how it is considered. It is larger when hygroscopic particles are included as IN due to the larger fraction of soot particles acting as ice nuclei. More laboratory experiments are needed to fully determine the freezing properties of hygroscopic ffBC/OM at mixed-phase cloud temperatures to reduce the range of uncertainty.

Table 3. Annual average anthropogenic cloud forcings (CF) and whole-sky forcings (Wm^{-2}). The line separates offline and online simulations. Offline forcings are for mixed-phase clouds, while online forcings include all effects: warm, mixed-phase, and cirrus clouds and direct effects.

	SWCF	LWCF	Net CF	Net Whole -Sky
1BC	0.188	−0.0173	0.171	0.171
3BC SCO	1.106	−0.0470	1.059	1.059
3BC noSCO	0.118	−0.007	0.111	0.111
3BC noSCO (online)	2.28	−2.22	0.06	−2.45

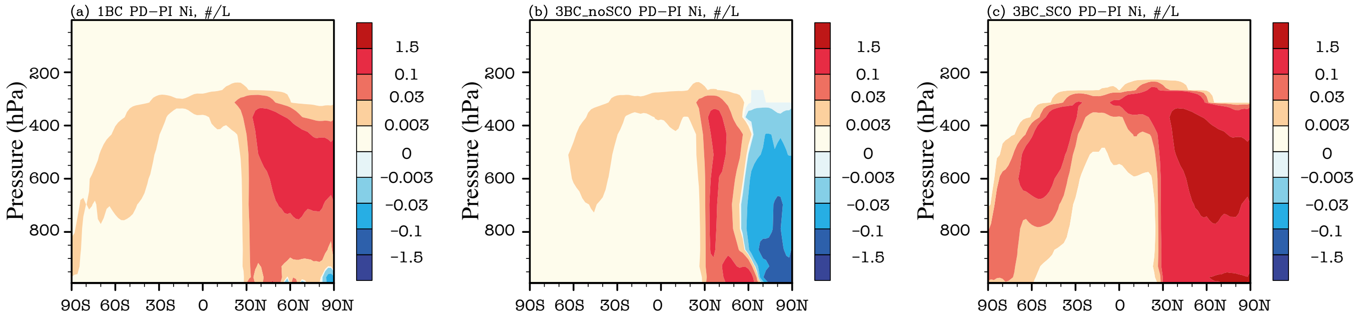

Fig. 5. PD–PI annual average changes of grid-mean ice number concentration in mixed-phase clouds from 1BC (a), 3BC noSCO (b) and 3BC SCO (c) simulations (# L^{-1}).

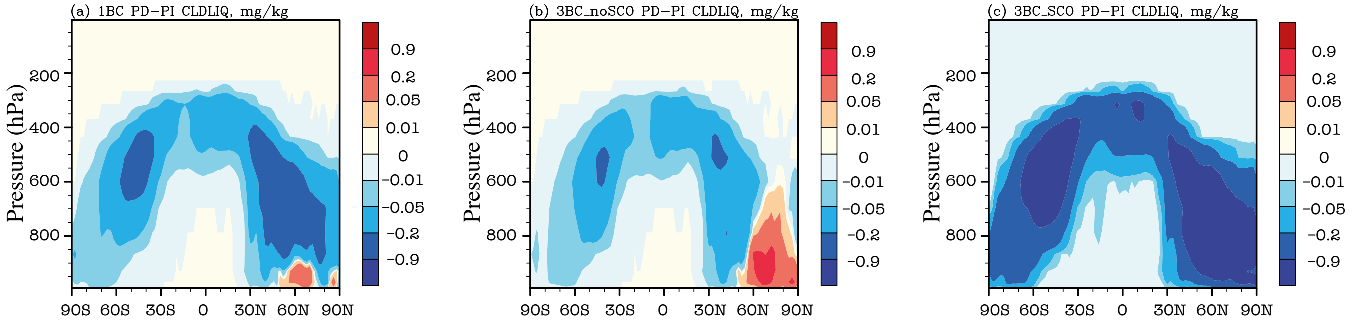

Fig. 6. PD–PI annual average changes of grid-mean liquid water mass mixing ratio (CLDLIQ) in mixed-phase clouds from 1BC (a), 3BC noSCO (b) and 3BC SCO (c) simulations (mg kg^{-1}).

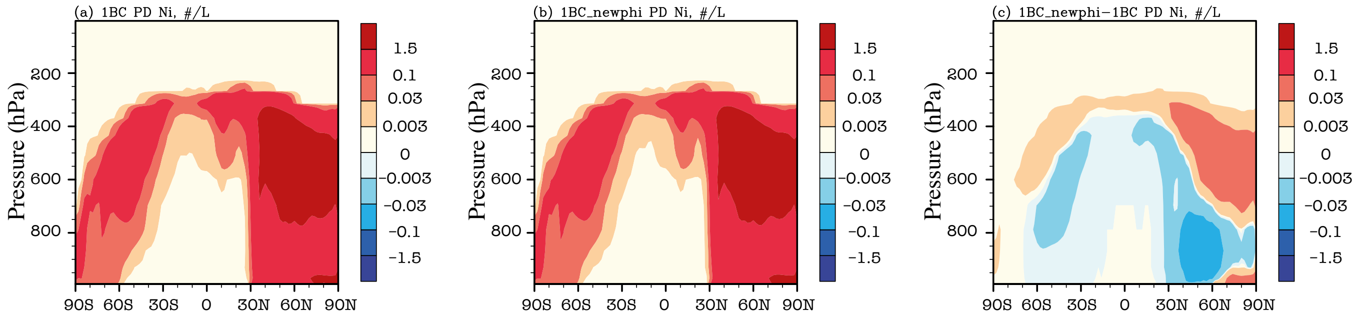

Fig. A1. Comparison of the simulated ice number concentration with (a) the original Phillips et al. (2008) scheme, (b) the new Phillips et al. (2013) schem, and (c) their differences.

Equal abundance of summertime natural and wintertime anthropogenic Arctic organic aerosols[*]

Organic aerosols (OAs) contribute to the Arctic aerosol mass near the surface[1–4] and affect the local climate through direct aerosol–radiation interactions and by altering the cloud properties[5,6]. OAs interact with other aerosol components[7–9], for example, black carbon or elemental carbon (EC) and sulfate, and can augment or offset their radiative forcing[10]. The Arctic OA indirect effect is estimated to be of a similar magnitude as that of the sulfate indirect effect, and much larger than the OA direct effect[11]. The magnitude of these effects depends on the OA physicochemical properties, sources and formation processes[12,13], which are not traceable by satellites[14], and hence surface observations are indispensable[15]. However, OAs have received little attention in the Polar Regions[16–18], mainly because of measurement challenges, and hence their complex composition and sources are poorly understood[19,20]. Nevertheless, an increasing abundance of natural OAs in a warming Arctic is expected[21] as a result of northward-expanding vegetation[22], intensifying boreal forest fires[23,24], decreasing sea-ice extent[25] and thawing permafrost[26,27]. Enhanced OA emissions are also expected from increasing local anthropogenic emissions, which include oil and gas exploration, and shipping activities28,29.

Attempts to model the Arctic OA concentrations have been limited, with typical under-predictions in winter and/or spring, when haze can be omnipresent and persistent[30–33]. The formation of secondary organic aerosols (SOAs) from anthropogenic or natural sources in different seasons is poorly represented[32,34]. Of 16 models deployed in a recent AeroCom evaluation of the simulated annual aerosol optical depth in Polar Regions[32], only 6 considered biogenic precursors, which can contribute to particle growth and so the size range of cloud condensation nuclei. Only in one of the models was methanesulfonic acid (MSA) considered, which resulted in an outlier Arctic aerosol optical depth in terms of both seasonal variability and year-long magnitude[32]. A recent study showed that natural OAs other than MSA may account for about half of the summertime Arctic OAs[33]. Biological emissions, often not considered in Arctic models, may be a missing source of ice-nucleating particles[2,35] that is possibly further enhanced with the thawing permafrost[36]. The contribution of anthropogenic emissions, for example, from gas flaring[37], to primary OA and SOA precursors is expected to vary substantially in space and time across the Arctic region but, unlike black carbon[38], has been largely overlooked. Long-term ambient measurements of the Arctic OA composition are critically needed to identify its main sources and therefore are a first step for subsequent implementation into models. However, available studies[3,39–41] are single-site, short-term[3,39] or campaign-based[39,40], and too infrequent to reveal seasonal patterns in the main sources of Arctic OAs[42]. Hence, Arctic aerosol source apportionment studies typically do not consider OAs[43,44], or are limited to a few primary markers (for example, levoglucosan from biomass burning or EC) and radiocarbon measurements[45,46]. Therefore, current efforts have so far been unable to provide an understanding of the sources and formation pathways of the pan-Arctic OAs in different seasons.

Determination of OA sources across the Arctic

Here we fill this critical knowledge gap by determining the spatial and seasonal distribution of individual OA classes (factors) across the Arctic (Fig. 1, Methods and Supplementary Text 1). This was achieved by offline aerosol mass spectrometer (AMS) measurements of nebulized aerosol water extracts[47] from filter samples (Methods and Supplementary Text 2), followed by multisite positive matrix factorization (PMF) for OA source apportionment in relative terms, and subsequent quantification using externally measured water-soluble organic carbon (WSOC; see Methods). Factor identification is aided by organic marker, major ion and EC measurements (Methods and Supplementary Text 3). Source apportionment (Methods and Supplementary Text 4) results are also combined with concentration-weighted trajectory (CWT) analysis48 to determine the geographical origin of the OA factors (Methods and Supplementary Text 5). We performed the analysis of 350 (bi-)weekly composite samples from filters collected at eight observatories across the Arctic (Fig. 1a) at roughly overlapping periods in 2014–2019 (Supplementary Table 1), yielding unique results of annual cycles which included the periods of winter darkness and summer daylight (Supplementary Table 2). Using this methodology, we determined the anthropogenic and natural sources that drive the mass of primary OAs and SOAs in the pan-Arctic region in both winter and summer. Our work is the first systematic, concerted and multiseason, multistation effort with advanced analysis techniques, which goes beyond intensive observation periods and case-study work20.

The total OA was found to be a major aerosol fraction that typically contributes 10–40% to the total particulate

---

[*] V. Moschos, K.Dzepina, D. Bhattu, H. Lamkaddam, R. Casotto, R. Daellenbach, F. Canonaco, P. Rai, W. Aas, S. Becagli, G. Calzolai, K. Eleftheriadis, C. E. Moffett, J. Schnelle-Kreis, M. Severi, S. Sharma, H. Skov, M. Vestenius, W. Zhang, H.Hakola, H. Hellén, L.Huang, J.-L. Jaffrezo, A. Massling, J. K. Nøjgaard, T. Petäjä, O.Popovicheva et al. //Nature Geoscience. 2022; 15: 196–202
DOI: 10.1038/s41561-021-00891-1

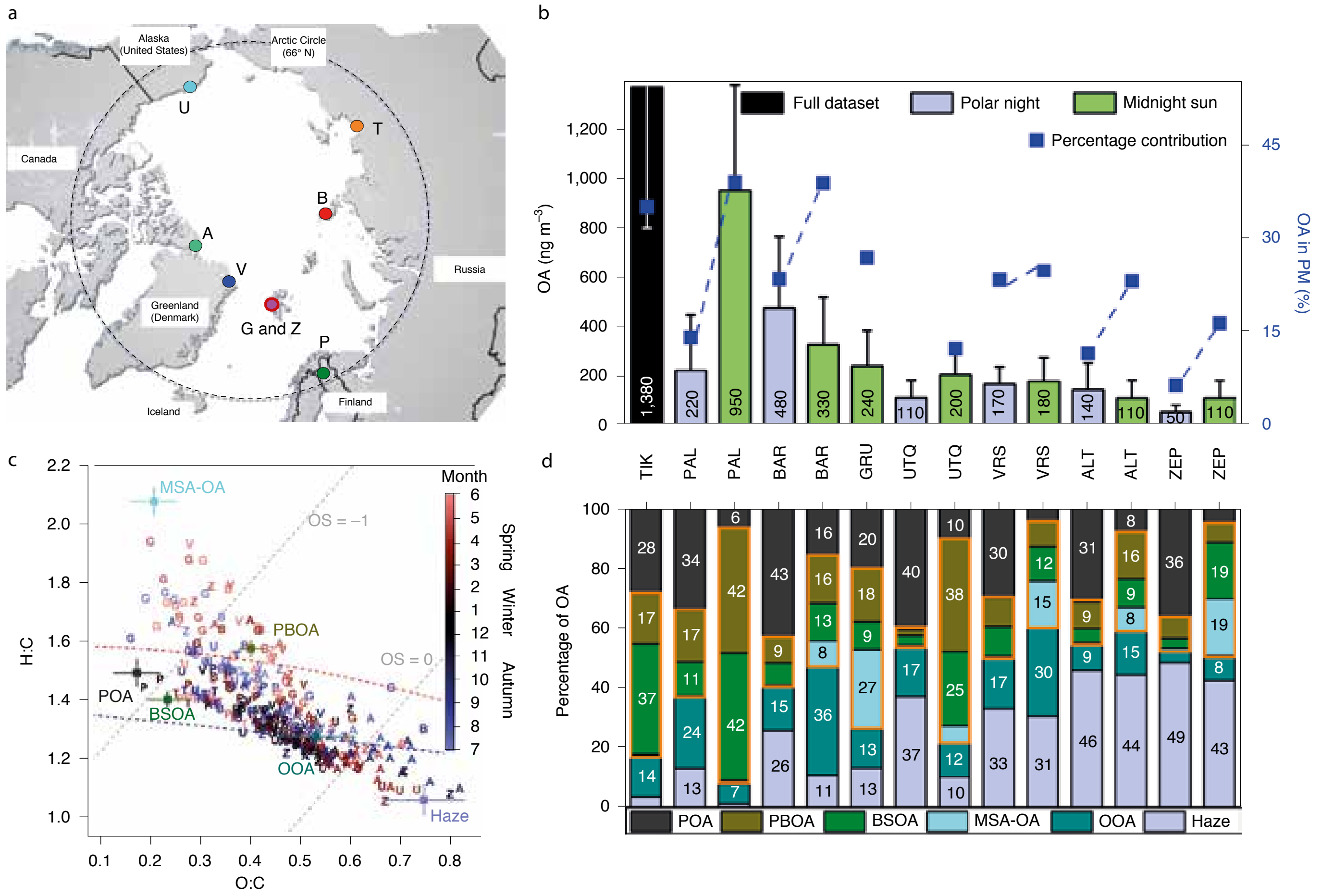

Fig. 1. Sites, OA factors and chemical characteristics. a, Arctic political map showing the aerosol filter sampling stations (Supplementary Text 1 and Supplementary Table 1). A, Alert; B, Cape Baranova; G, Gruvebadet; P, Pallas-Matorova; T, Tiksi; U, Utqiaġvik; V, Villum Research Station; Z, Zeppelin. Adapted from Hugo Ahlenius/GRID-Arendal (https://www.grida.no/resources/8378). b, Station-specific average total OA mass concentrations (whiskers are 1 standard deviation, s.d., corresponding to sample-to-sample variability) based on a statistical analysis of the water-soluble fraction to obtain factor recoveries (Supplementary Text 4) in the polar night (winter) versus midnight sun (summer) periods (Supplementary Table 2), sorted in descending order of the station annual average, and percent contribution to the particulate mass (including non-sea salt sulfate, nitrate, ammonium, EC and estimated sea salt63). The dashed blue lines connect winter and summer contributions at each station (no winter samples for G and T, and U winter samples were not analysed for ions). c, Van Krevelen plot as a tool for compositional differentiation among samples: atomic O:C ratio versus H:C ratio of the Arctic AMS-PMF-based factors (Supplementary Fig. 2), and individual PMF input bulk samples (colour coded by month: 1, January, through to 12, December). Red and blue dashed curves refer to the triangle reported by Ng et al.85. Grey dashed lines denote two example oxidation states (OS). Error bars correspond to 1 s.d. from a bootstrap analysis (Methods and Supplementary Text 4). d, Spatial distribution and seasonal variability in the average factor percentage contributions to total OA (water-soluble (Supplementary Fig. 7); entire time-series (Supplementary Fig. 10)). Factors are sorted from bottom (Haze) to top (POA) based on their onset (see Fig. 3), starting from late winter for Haze. Primary OAs, POA + PBOA (top). Orange outline, sum of natural-dominated OAs.

mass at the different stations (Fig. 1b; the dataset range is 3–65%), with higher relative contributions in the summer. Although only water-soluble

OA (WSOA) components were measured, the results represent the total OA by scaling the measurements by the water-soluble fraction of each factor (Methods and Supplementary Text 4). On average, WSOAs comprise 82 ± 4% of the total OA. Absolute OA concentrations were generally higher at the more continental stations,~1.4 µg m^{-3} in Tiksi (TIK), ~0.4 µg m^{-3} in Cape Baranova (BAR) and 0.2 µg m^{-3} and 1.0 µg m^{-3} in Pallas-Matorova (PAL) in winter and summer, respectively, whereas typical concentrations at the other stations were lower (0.1–0.2 µg m^{-3}). Figure 1c shows the O:C versus H:C ratios for all the samples measured by the AMS, which highlights the large variability in the OA chemical composition across stations and seasons. We determined six major OA factors (Methods and Supplementary Text 4, Supplementary Tables 3 and 4 and Supplementary Figs. 1–10). These include factors related to anthropogenic-dominated emissions, namely, oxygenated organic aerosol (OOA), Haze and primary-anthropogenic organic aerosol (POA), and to natural-dominated emissions, namely, MSA-related organic aerosol (MSA-OA), biogenic secondary organic aerosol (BSOA) and primary biological organic aerosol (PBOA). We could not relate any factor to fresh wildfire

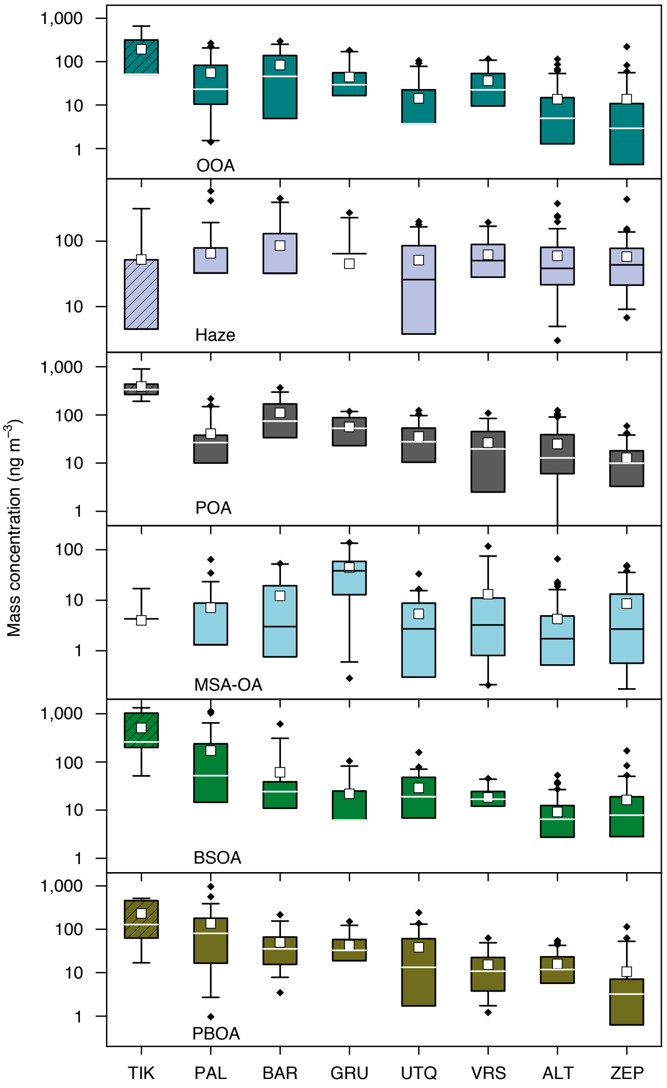

Fig. 2. Station-specific yearly mass concentration of speciated Arctic OAs. Absolute OA factor concentrations at the different stations shown as box-and-whisker plots. The stations appear in the same order as in Fig. 1b, whereas the factors appear in the same order as discussed in the main text. Note the different range of y-axis values for the different factors. The lower whiskers are missing if associated values are out of scale. Boxes for TIK are hatched to indicate incomplete (inter)annual coverage. For WSOAs, see Supplementary Fig. 8. Horizontal line and box, yearly median and interquartile range; squares and whiskers, yearly mean and range within the 5th and 95th percentiles; diamonds, outliers.

emissions in the spring or summer, probably because of multiple reasons such as the rapid aerosol ageing during transport49, emissions remaining aloft on ascent to the middle and/or upper troposphere (if they originate from North America and East and South Asia)[2,23,50] and/or because this source becomes important only during short-term events. The atomic O:C versus H:C ratios of the six major OA factors (Fig. 1c) and their relative contributions across stations and seasons (Fig. 1d) are very distinct, and show the large diversity in the sources that drive the OA mass in the Arctic region. In the following, we discuss characteristic features of the factors, their spatial (Fig. 2) and seasonal (Fig. 3) variabilities, as well as their major source regions (Fig. 4).

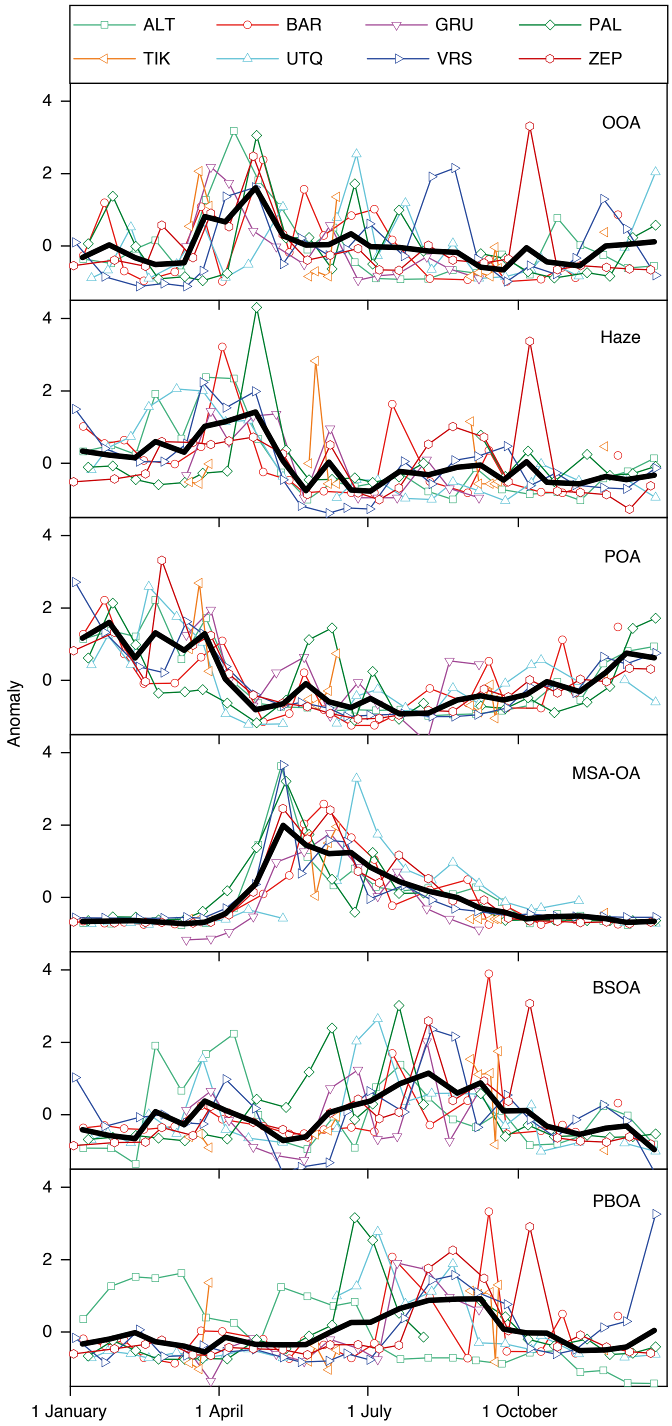

Fig. 3. Seasonal variability of speciated pan-Arctic OAs. Standardized annual cycles for each OA factor at the different stations. Bi-weekly averaged data from multiple years for each station are merged into a single annual cycle (the sum of individual station values in each panel equals zero). The y-axis values (anomalies) were calculated using the absolute mass concentration values as: (value – station average)/s.d. of station. The thick black lines indicate the average annual cycle of each factor over all the stations (note that here the sum of the yearly values in each panel is not equal to zero).

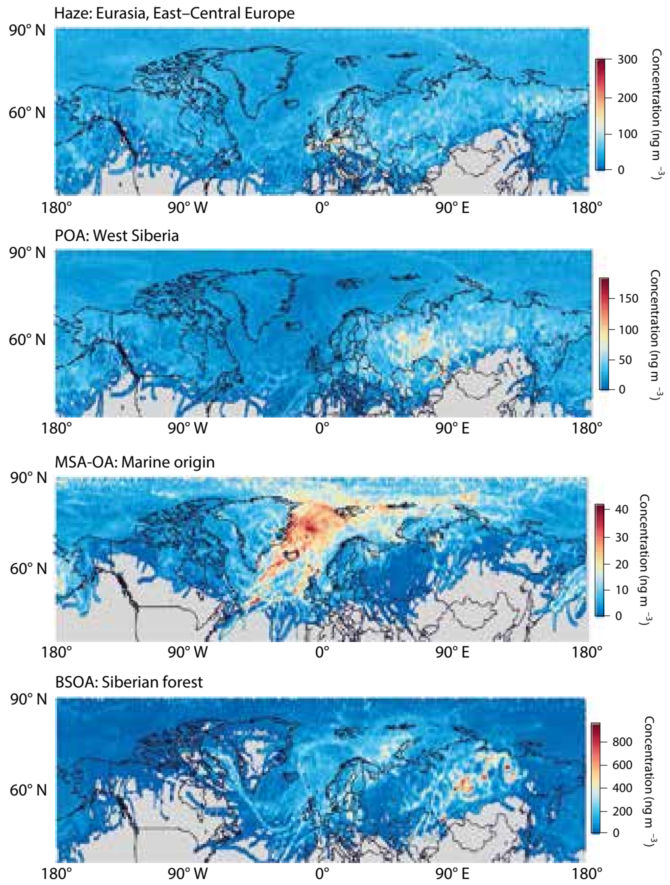

Fig. 4. Major source regions of long-range transported Arctic OA factors. Merged results from the CWT-based back-trajectory (BT analysis with ZeFir (Methods) at different Arctic stations (Supplementary Text 5 and Supplementary Fig. 11) showing long-term pan-Arctic hot spots of transported anthropogenic-dominated (Haze and POA) and natural-dominated (MSA-OA and BSOA) OA factors. The entire time series of each factor mass concentration at the different stations (time periods shown in Supplementary Table 1 and Supplementary Fig. 10) were used to create the maps (see Supplementary Text 5 for a discussion of the potential uncertainties in the source regions). The trajectories represent 5 days back in time for MSA-OA and (up to) 10 days for the other factors (Supplementary Text 5 and Supplementary Fig. 11). Colour scales indicate the water-soluble factor concentrations linked to the major source regions ('long-range' probability heat maps). The individual station results shown in Supplementary Fig. 11 were merged for each factor, except for POA, for which only six stations with winter data were considered here (no GRU and TIK), to indicate specific regions with intense gas-flaring activity during winter (for example, the Komi Republic, Khanty-Mansisk and Yamalo-Nenets autonomous districts in West Siberia). PBOA is expected to reside mainly in the coarse aerosol mode, and thus has a relatively short atmospheric lifetime (and hence more local and/or regional origins), and the formation of OOA might be linked to a prior accumulation of volatile organic compounds (thus probably not directly transported in the particle phase); therefore, the merged results for these factors are shown only in the Supplementary Information (Supplementary Fig. 11). The World Maps available with ZeFir are taken from Natural Earth Data.

Anthropogenic-dominated OA factors

The OOA factor (O:C ~0.5) contains large oxygenated fragment ions (Supplementary Table 5). Its time-series shows a pan-Arctic enhancement during and after polar sunrise (Fig. 3), which potentially links this factor to oxidation products of volatile organic compounds that have accumulated during the polar night and form SOAs in the spring[25,51–53]. In this regard, a strong decrease in volatile organic compound concentrations was reported at PAL for April54.

Although the OOA factor might be dominated by wintertime anthropogenic emissions, the contribution from natural sources during the summer cannot be excluded. The Haze factor contains more fragmented oxygenated ions (O:C ~0.75; Fig. 1c), builds up in late winter, peaks in spring (Fig. 3) and correlates with sulfate (Supplementary Table 6), similar to the profile and timing of the Arctic haze phenomenon[55]. Except for intermittent peaks at BAR, PAL and TIK, its yearly concentration is spatially homogeneous (Fig. 2), but with a certain temporally structured variability56 with the timing of the winter/spring peak occurring a few weeks later in time at most observatories as we move from west to east (Fig. 3), which indicates the effect of regional transport. This factor therefore becomes predominant in relative terms (Fig. 1d) at remote stations with lower OA loadings, that is, ~45% throughout the year at Alert (ALT) and Zeppelin (ZEP) (1st and 3rd quartiles, Q1–Q3 = 38–54%). Haze organics are associated with long-range atmospheric transport from Eurasia (Fig. 4). Therefore, the transport of pollutants from distant urbanized areas to remote environments contributes substantially to the formation of pan-Arctic SOAs (OOA and Haze; Q1–Q3 = 44–56% of the total OA during the polar night).

The POA factor is mainly composed of hydrocarbons (Supplementary Table 5) from primary anthropogenic emissions (O:C ~0.2), most probably related to gas flaring. POA has an H:C ratio of ~1.3 (Fig. 1c), lower than the H:C ratio (~1.8–1.9) of freshly emitted hydrocarbons detected at lower latitudes from traffic emissions[57,58], which suggests a high contribution from unsaturated hydrocarbons. This factor is ubiquitous under dark and cold conditions, and peaks in December–March (Fig. 3) with a typical median pan-Arctic contribution to the total OA of 35% during the polar night (Fig. 1d, Q1–Q3 = 28–42%). In winter, POA correlates strongly with EC (Supplementary Fig. 12), which is reported to be of fossil origin45,49. The POA:EC ratio of ~1.1 is similar to the respective organic carbon (OC):EC ratios from oil and gas extraction emission estimates59. We found West Siberian locations (Fig. 4) as a major potential source region of the POA in winter (mainly at ALT, BAR, PAL and ZEP; Supplementary Fig. 11), similar to those previously found for surface black carbon[42,60,61]. The presence of POA at Gruvebadet (GRU) and TIK in the summer (Figs. 1d and Fig. 2) might indicate a more local origin at urban-type Arctic settlements.

Natural-dominated OA factors

MSA-OA is characterized by the fragmentation pattern of MSA (for example, CH_3 and CH_3SO; Supplementary Table 5), which is produced from marine dimethylsulfide oxidation. It correlates strongly with MSA, which comprises on average 80% of the factor, as measured by ion

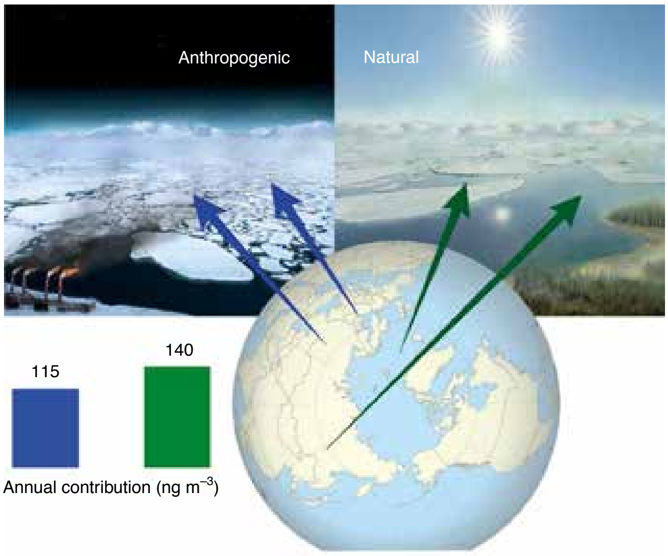

Fig. 5 Conceptual overview of anthropogenic-dominated versus natural-dominated Arctic OAs. A conceptual image of anthropogenic-dominated and natural-dominated emissions that drive the OA mass in the Arctic in winter and summer, respectively. The most important geographical source regions are indicated by the arrows. Bars show the entire-dataset average contributions of nearly equally contributing summed anthropogenic-dominated (blue) and summed natural-dominated (green) organic components. Credits: Helen Cawley for the landscape drawing; map made using Natural Earth.

chromatography (Supplementary Table 7). This factor consistently originates from marine regions (Fig. 4), and increases with solar radiation (Supplementary Fig. 14). The MSA-OA absolute concentrations (Fig. 2) and clear annual cycles (Fig. 3) are consistent among the stations, with much higher concentrations in May–June, the main season of phytoplankton blooms. The range of maximum concentrations at ALT and Utqiaġvik (UTQ) (~20–30 ng m^{-3}) is comparable to those of previous measurements of MSA from these stations by ion chromatography[62,63]. The highest weekly averaged MSA-OA levels, which exceed 100 ng m^{-3}, occur at GRU, Villum Research Station (VRS) and ZEP. Although at these stations MSA-OA is typically 22% (Q1–Q3 = 12–34 %) of the total OA during the midnight-sun period (Fig. 1d), this factor is neither the only nor the predominant natural OA component.

BSOA is linked to biogenic emissions, for example, mono- and/or sesquiterpenes and isoprene[64,65], from forests, tundra, lakes, wetlands carbohydrate-related AMS fragments typically linked to primary biological compounds (Supplementary Table 5), and with arabitol and mannitol[71] (R2 = 0.86; Supplementary Fig. 13), which are sugar-alcohols present in fungal spores and other biological matter. PBOA exhibits substantial concentration increases in July–September, to reach up to 1.0 µg m^{-3} at PAL (Fig. 2), and a distinct temporal evolution, peaking later than MSA-OA (Fig. 3). Similar to BSOA, PBOA exhibits higher relative contributions at lower latitude Arctic stations (~70° N), averaging one-third of the total OA at PAL and UTQ in the summer (Fig. 1d, Q1–Q3 = 26–47%). PBOA anticorrelates with the snow depth at PAL and VRS (where such data are available) and with the 30-year climate-normal average snowfall at UTQ (Supplementary Fig. 14). These findings indicate that maximum local biological activity is associated with the lack of snow covering the ground[72], which causes entrainment of PBOA into the air Implications of Arctic OA spatiotemporal variability Overall, the pan-Arctic OA composition and sources are not uniform. They are largely driven by the stations' latitude (and altitude; Supplementary Fig. 15), favourable conditions for long-range atmospheric transport and distance to anthropogenic and natural aerosol sources, as well as the presence of light and snow cover. We show that secondary Arctic OAs, separated into various distinct subtypes, typically dominate the OA mass, although the contribution of primary OAs from both natural and anthropogenic emissions is often equally important (Fig. 1d). This finding is in line with lower-latitude OA source apportionment studies12. The current and future abundance of condensable organics could be critical for the cloud condensation nuclei budget and cloud properties. In the Arctic winter, the sea-ice extent is at its maximum, low-level clouds have a pronounced warming effect and surface pollutants can become trapped close to the ground due to temperature inversion[55]. In this period, theland-surface OA sources are predominantly anthropogenic and linked to both primary emissions and secondary processes. The widespread Haze organics are dominated by aged anthropogenic-dominated emissions transported mainly from Eurasia, peak during polar sunrise and abruptly decrease in May. Under cold and dark conditions, all the stations are affected by OA emissions related to oil or gas extraction activities, mainly in West Siberia. The Arctic amplification of temperature increase[73,74] is more intense during winter[75], and may be affected by aerosols altering the cloud properties. Hence, the future evolution of anthropogenic-dominated wintertime Arctic OA should be monitored from a climate perspective, especially in response to the development of effective emission control measures at lower latitudes[11,29]. In the summer, the decreasing anthropogenic pollution is replaced by natural OA emissions, with similar absolute concentrations. These emissions include marine SOAs from dimethylsulfide oxidation and little-explored primary biological emissions and biogenic SOAs. These collectively contribute to an increased importance of natural OA in the summertime aerosol particle mass in the inner Arctic76. We found an overall nearly equal yearly abundance (Fig. 5) of summed anthropogenic-dominated OAs (average of 115 ngm^{-3}, Q1–Q3 = 20–100 ngm^{-3}; 95th percentile, 435 ngm^{-3}) and summed natural-dominated OAs (average of 140 ngm^{-3}, Q1–Q3 = 40–160 ngm^{-3}; 95th percentile, 445 ngm^{-3}). This indicates that the typically lower total aerosol volume/mass in the summer versus winter or spring77 is due to species other than the total OA, which exhibits less of a seasonal cycle across the Arctic (Supplementary Fig. 16). The effects of anthropogenic and natural organics on cloud condensation nuclei and ice-nucleating particles, and potentially on the Arctic climate, have been largely unexplored. The importance of considering land coverage and biosphere–atmosphere exchanges[78,79] for the response of natural Arctic OAs to warming is highlighted in Supplementary Fig. 14. A small increase in temperature results in a substantial (exponential) increase of BSOA, which identifies one of the potential feedback mechanisms in the Arctic. Also, extension of the ice-free season and expansion of snow-free areas80 may lead to enhanced airborne organics from biological activity and secondary marine emissions.

Currently, the Arctic system is in transition21, with long-range transported anthropogenic-dominated emissions (including sulfate) continuously decreasing due to better air quality regulations in the lower latitude regions. Meanwhile, natural emissions are expected to increase81,82, which probably enhances the magnitude and relative importance of the composition-dependent OA– cloud effect11. Our results provide the first understanding of the present-day year-long, pan-Arctic OA sources, which can be used for comparisons with past (for example, through ice-core archives83) and future measurements of these changing biogenic and anthropogenic emissions. Given practical difficulties in deploying multiple online AMS instruments for long time periods around the Arctic and the widespread availability of ambient filters, the measurement methodology and analysis techniques employed here are also applicable to emerging Arctic stations (for example, in far East Siberia84).

Online content

Any methods, additional references, Nature Research reporting summaries, source data, extended data, supplementary information, acknowledgements, peer review information; details of author contributions and competing interests; and statements of data and code availability are available at https://doi.org/10.1038/ s41561-021-00891-1.

3. ВЫСОКОШИРОТНЫЕ ИСТОЧНИКИ ПЫЛЕВЫХ И ОРГАНИЧЕСКИХ АЭРОЗОЛЕЙ

Newly identified climatically and environmentally significant high-latitude dust sources*

1. INTRODUCTION

Mineral dust is an essential and relevant climate and environmental variable with multiple socioeconomic effects on, e.g., weather and air quality, marine life, climate, and health (Creamean et al., 2013; Terradellas et al., 2015; Shepherd et al., 2016; Querol et al., 2019; Nemuc et al., 2020). Mineral dust is transported from local sources of high-latitude dust (HLD, ≥50° N and ≥40° S, Bullard et al., 2016), low-latitude dust (LLD, mostly 0–35° N), and the so-called "global dust belt" (GDB, Prospero et al., 2002), defined as extending into the Northern Hemisphere from the western coast of northern Africa over the Middle East (western Asia), central, and East Asia and southwestern North America (Ginoux et al., 2012), with only minor sources in the Southern Hemisphere (Prospero et al., 2002; Ginoux et al., 2012; Bullard et al., 2016; Terradellas et al., 2017). Dust is often associated with hot, subtropical deserts, but the importance of dust sources at the cold, high latitudes has recently increased (Arnalds et al., 2016; Bullard et al., 2016; Groot Zwaafting et al., 2016, 2017; Kavan et al., 2018, 2020a, b; Boy et al., 2019; Gassó and Torres, 2019; IPCC, 2019; Tobo et al., 2019; Bachelder et al., 2020; Cosentino et al., 2020; Ranjbar et al., 2021; Sanchez-Marroqin et al., 2020). Dust produced at high latitudes and in cold climates (Iceland, Greenland, Svalbard, Alaska, Canada, Antarctica, New Zealand, and Patagonia) can have regional and global significance (Bullard et al., 2016). Local HLD emissions are increasingly being recognized as driving the local climate, biological productivity, and air quality (Groot Zwaafting et al., 2016, 2017; Moroni et al., 2018; Crocchianti et al., 2021; Varga et al., 2021). HLD can induce significant direct (blocking sunlight) and indirect (clouds and cryosphere) radiative forcing (Kylling et al., 2018) on solar radiation fluxes and snow optical characteristics, strongly impacting Arctic amplification, including glacier melt (Boy et al., 2019).

HLD aerosols consist of a variety of different dust particle types with various particle sizes and shape distributions as well as physical, chemical, and optical properties that differ from the crustal dust of the Sahara or American deserts (Shepherd et al., 2016; Arnalds et al., 2016; Bachelder et al., 2020; Baldo et al., 2020; Crusius, 2021). Therefore, impacts on climate, environment, and human health can differ from those of LLD. For example, Icelandic dust is of volcanic desert origin, often dark, and has higher proportions of heavy metals than crustal dust (Arnalds et al., 2016). The IPCC special report (IPCC, 2019) recognizes dark dust aerosols as a short-lived climate forcer (SLCF) and light-absorbing aerosols connected to cryospheric changes. Light-absorbing HLD particles can induce direct effects on solar radiation fluxes as SLCF and snow optical characteristics impacting cryosphere melt via radiative feedback (Peltoniemi et al., 2015; Boy et al., 2019; Dagsson-Waldhauserová and Meinander, 2019, 2020; IPCC, 2019; Kylling et al., 2018). HLD significantly affects the formation and properties of clouds (Abbatt et al., 2019; Sanchez-Marroquin et al., 2020; Murray et al., 2021).

Dust is connected to climate change: historical dust (paleo dust) is not only a contributor to climate change, but is also a record of previous dust and climate conditions (Lamy et al., 2014; Lewandowski et al., 2020). Dust can significantly contribute to air pollution mortalities (Terradellas et al., 2015; Nemuc et al., 2020). Deposition at high latitudes can provide nutrients to the marine system; mineral and organic matter on glaciers, including natural and anthropogenic dust, can form cryoconite granules. Cryoconite, dust, and ice algae can reduce surface albedo and accelerate the melting of glaciers (Lutz et al., 2016; McCutcheon et al., 2021). Monitoring dust in remote, high-latitude areas has crucial value for climate change assessment and understanding the impacts of global warming on natural systems and socioeconomic sectors. Bullard et al. (2016) summarized natural HLD sources as covering over 500 000 km^2 and producing particulate matter of ca. 100 Mt dust per year.

Dust emissions respond to changes in wind speed, soil moisture, and other parameters affected by climate change; changes in land cover and surface properties by human activities can affect dust emissions (Kylling et al., 2018). The fundamental processes controlling aeolian dust emissions at high latitudes are essentially the same as in temperate

---

[*] Outi Meinander, Pavla Dagsson-Waldhauserova, Pavel Amosov, Elena Aseyeva, Cliff Atkins, Alexander Baklanov, Clarissa Baldo, Sarah L. Barr, Barbara Barzycka, Liane G. Benning, Bojan Cvetkovic, Polina Enchilik, Denis Frolov, Santiago Gassó, Konrad Kandler, Nikolay Kasimov, Jan Kavan, James King, Tatyana Koroleva, Viktoria Krupskaya, Markku Kulmala, Monika Kusiak, Hanna K. Lappalainen, Michał Laska, Jerome Lasne, Marek Lewandowski, Bartłomiej Luks, James B. McQuaid, Beatrice Moroni, Benjamin Murray, Ottmar Möhler, Adam Nawrot, Slobodan Nickovic, Norman T. O'Neill, Goran Pejanovic, Olga Popovicheva, et al. // Atmospheric Chemistry and Physics. 2022;22:11889-11930
https://doi.org/10.1016/j.catena.2023.107212

regions. However, there are other processes specific to or enhanced in cold regions. Low temperatures, humidity, strong winds, permafrost, and niveo-aeolian processes, which can affect the efficiency of dust emission and distribution of sediments, were listed in Bullard et al. (2016).

The modeling of emissions, transport, and deposition complemented with available observations can provide essential information related to dust's impact on the climate and environment at the high latitudes (IPCC, 2019). The locations and characteristics of local dust sources are two of the major observations documented for inputting information into numerical models to predict or simulate the HLD process from its emission to downwind deposition. In some cases, model results can indicate possible but not yet identified dust sources in the HLD regions. A general lack of observational and long-range transport modeling studies results in poor HLD monitoring and predicting. Models have predictive capacity and, without the observations, can constitute a source of information and indicate where more direct observations are needed. The first long-range transport modeling studies show that the main transport pathways from HLD sources clearly affect the High Arctic (>80° N) and European mainland (Baddock et al., 2017; Beckett et al., 2017; Đorđević et al., 2019; Groot Zwaafting et al., 2016, 2017; Moroni et al., 2018). The World Meteorological Organization Sand and Dust Storm Warning Advisory and Assessment System (WMO SDS-WAS) monitors and predicts dust storms from the world's major deserts (https://community.wmo.int/activity-areas/gaw-sand-and-dust-storm-warning-advisory-and-assessment-system-sds-was, last access: 17 August 2022), where HLD sources have recently been included in the SDS-WAS dust forecasts. Europe's largest desert is at a high latitude in Iceland (Arnalds et al., 2016), with dust transport observed over the North Atlantic to European countries (Ovadnevaite et al., 2009; Prospero et al., 2012; Beckett et al., 2017; Đorđević et al., 2019).

HLD is a short-lived climate forcer, air pollutant, and nutrient source, showing the need to identify the geographical extent and dust activity of the HLD sources (Arnalds et al., 2014, 2016; Dagsson-Waldhauserová et al., 2014, 2015; Terradellas et al., 2015; USGCRP, 2018; IPCC, 2019). Bullard et al. (2016) designed the first HLD map based on visibility and dust observations, combined with field and satellite observations of HLD storms, resulting in 129 locations described in 39 papers. Here, we compile and describe 64 HLD sources at the northern and southern high latitudes. This work's main aim is to

- i. identify new and previously unpublished HLD sources,
- ii. estimate the high-latitude land area with potential dust activity and calculate the source intensity (SI) for the identified sources,
- iii. provide model results on HLD emission, long-range transport, and deposition at various scales of time and space, and
- iv. specify key climatic and environmental impacts of HLD and related research questions, which could improve our understanding of HLD sources, with the help of literature surveys on clouds and climate feedback, atmospheric chemistry, marine environment, cryosphere, and cryosphere–atmosphere feedbacks.

We focus on high latitudes with natural dust sources and include some anthropogenic dust sources, such as road dust, when unpaved roads serve as a significant dust source. Direct emissions of volcanic eruptions and road dust formed via abrasion and wear of pavement or traction control materials are excluded. Identifying dust sources is the first step to understanding the HLD life cycle (dust emission, transport, and deposition). After that, impacts and feedback mechanisms can be identified and quantified as physical, chemical, and optical properties of dust from these source areas. Their properties during emission, transport, and deposition are needed to be characterized to allow a holistic understanding.

2. MATERIALS AND METHODS

2.1. Identification and characteristics of dust sources

Three topical workshops in Russia, Finland, and Iceland (Meinander et al., 2019a, b) on HLD were organized in 2019 to identify, describe, and assess new HLD sources (≥50° N and ≥40° S, according to Bullard et al., 2016, and including the Arctic as a subregion at ≥60° N). The HLD source map and observations on dust properties provided here are based on

- **i.** new field and satellite observations not described in published academic papers,
- **ii.** newly identified HLD source locations reported in the recent literature but not included in previous collections, and
- **iii.** updated observations on previously documented sources.

Each location was assessed to classify each source: category 1 refers to an active dust source with high ecological significance, category 2 to a semi-active source with moderate ecological significance, and category 3 to new sources with unknown activity and importance. Moreover, SI values for each HLD location at the northern and southern (Antarctica and Patagonia) high latitudes were quantified, and the potential land surface area for dust emissions in the northern, Arctic, and southern HLD regions was calculated (Sect. 2.2).

2.2 HLD from the UNCCD G-SDS-SBM

The Global Sand and Dust Storms Source Base Map (G-SDS-SBM), developed by the United Nations Convention to Combat Desertification (UNCCD) in collaboration with the United Nations Environment Programme (UNEP) and World Meteorological Organization (https://maps.unccd.int/sds/, last access: 17 August 2022; Vukovic, 2019, 2021), represents gridded values of SDS SI (values 0 to 1) at a resolution of 30 arcsec. The Source Base Map was developed by including the information on soil texture, bare land fraction, and NASA satellite Moderate-resolution Imaging Spectroradiometer Enhanced Vegetation Index, MODIS EVI, as well as the data on land cover, topsoil moisture, and temperature. Values of SI represent topsoil's potential to emit soil particles under windy conditions, assigning the highest values of SI to the most productive surfaces. SI values are derived under the assumption that they are exposed to the same velocity of surface wind. Input data, which change depending on the weather (and possibly human activities) for bare land fraction, moisture, and temperature data, are defined for 4 months (January, April, July, October – each month representing one season) by using extreme values. This was observed from 2014 to 2018, providing favorable conditions for surfaces to act as sources. Thus, sources that may appear during heat waves and drier conditions (or drought), when the surface at high latitude is unfrozen, snow-free, and more susceptible to wind erosion, are included in this map. Such weather extremes under climate change are becoming more frequent and are projected to increase (IPCC, 2013), justifying the source mapping approach using the information on extreme topsoil conditions. Using the maps produced for the four seasons, maximum and minimum values are determined for each grid point to explore the potential of high-latitude land surfaces to act as dust sources and their seasonality and to compare values of SI with marked locations of HLD sources.

2.3. Methods used to identify and study the dust sources

Various methods identified the HLD sources (Table 1), including direct observations and measurements, satellite data, emission, long-range transport, and deposition modeling and media, social media, and literature sources (e.g., web pages, conference abstracts). More details and literature references can be found in each source section. Dust emission, long-range transport, and deposition modeling calculations were made to study whether the HLD sources have local, regional, or global significance. Two well-established dust atmospheric models – SILAM and DREAM – were used to simulate the atmospheric dust process over high latitudes. Both models have been thoroughly evaluated for other deserts, where the accuracy of their results has been verified.

Estimates of the emission and deposition of global and Arctic dust were computed separately to assess Arctic dust's global impact using the SILAM model (Sofiev et al., 2015) – a global- to meso-scale atmospheric dispersion and chemistry model – applied for air quality and atmospheric composition modeling. The dust emission estimate is driven by the European Centre for Medium-Range Weather Forecasts (ECMWF) IFS meteorological model at a resolution of 0.1×0.1°. The computations were performed using ECMWF ERA5 meteorological reanalysis data for 2017 at a resolution of 0.5×0.5°. The dust emission model was validated against AERONET (AErosol RObotic NETwork, https://www.aeronet.com/, last access: 17 August 2022) aerosol optical density (AOD) data and provided unbiased results for the main dust emission areas. For Arctic areas, where dust does not contribute to the AOD as much, the simulated AOD from all aerosols is unbiased concerning the

Table 1. Methods used to identify and study the dust sources.

Method	Sources
Direct observation: photographs and visual observations	Marambio, Antarctic Peninsula, Schirmacher Oasis, East Antarctica McMurdo Sound/Ross Sea
Satellite images: Meteosat-11 images	Denmark, Sweden, Iceland
Instrumentation: SEM	Svalbard
Instrumentation: LOAC	James Ross Island
Instrumentation: SL-501 surface and snow albedo	Marambio, Antarctic Peninsula
Instrumentation: magnetic susceptibility upon heating, magnetic hysteresis parameters	Svalbard
Instrumentation: ICP-MS, AES-ICP, XRD, XRF	Russia (source nos. 2–5 of Fig. 1)
Instrumentation: high-performance liquid chromatography, potentiometry	Russia (source nos. 7–8 of Fig. 1)
Passive deposition samplers	James Ross Island
Snow samples	Svalbard (Hornsund, Pyramiden), Antarctica
Social media: Twitter account (@SanGasso) and hashtag (#highlatitudedust)	South America (Patagonia), Alaska, Greenland, Iceland
Literature sources	Denmark, Sweden
SILAM model	Arctic
DREAM model	Arctic, Antarctic

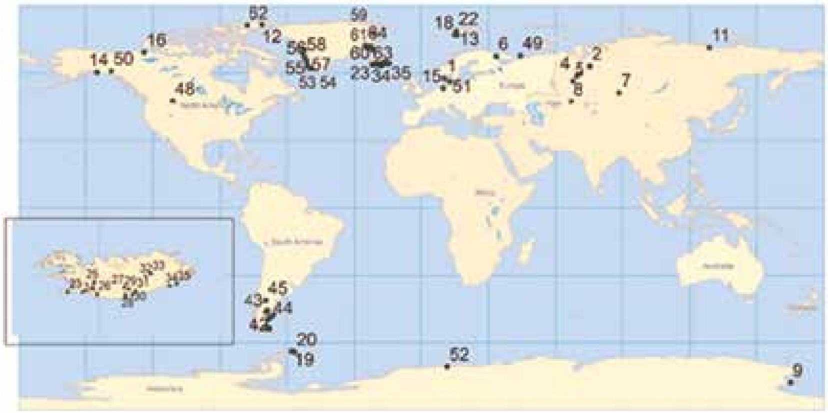

Figure 1. Map of the locations of the northern (north of 50° N) and southern (south of 40° S) high-latitude dust (HLD) sources identified and included in this study. The numbers are the identified 64 dust sources, as shown in Fig. 1.

measurements. While the simulation's relatively coarse resolution cannot capture the smaller point-like dust sources, it is still expected to give a good approximation of the overall patterns and magnitudes of dust emission and deposition. The SILAM results are presented in Sect. 3.3 (Fig. 4) and 3.4 (Figs. 12 and 15).

DREAM is a fully dynamic numerical prediction model for atmospheric dust dispersion originating from soil. The dust component of this system (Pejanovic et al., 2011; Nickovic et al., 2016) is online and driven by the atmospheric model Nonhydrostatic Mesoscale Model on E-Grid (Arakawa E-grid) (NMME) (Janjic et al., 2001). Dust concentration in the model is described with eight particle bins, with radii ranging from 0.18 to 9 µm. DREAM-ICELAND is the model version to predict dust transport emitted from Iceland's largest European dust sources (Cvetkovic et al., 2021). The size distribution of particles in the model is specified according to in situ measurements in the Icelandic hotspots. The model horizontal resolution of ~3.5 km is sufficiently fine to resolve the Icelandic dust sources' rather heterogeneous and small-scale character. As the first operational numerical HLD model in the international community, DREAM-ICELAND is used daily, having predicted Icelandic dust since April 2018. DREAM results are included in Sect. 3.4 (Figs. 8 and 11) and 3.6 (Fig. 16) and as a supplementary animation (available through a link in the Supplement).

3 RESULTS AND DISCUSSION

3.1 Locations of the HLD sources

Sixty-four HLD sources at northern and southern high latitudes (Fig. 1) were identified. In the northern HLD region are 49 locations (47 locations ≥50° N and 2 >47° N) in Alaska, Canada, Denmark, Greenland, Iceland, Svalbard, Sweden, and Russia, of which 35 are in the Arctic HLD subregion (≥60° N). In the southern HLD region (≥40° S), 15 sources were identified in Antarctica and Patagonia, South America. The sources included the boreal, remote, rural, mountain, marine and coastal Arctic and Antarctic, river sediments, mining, unpaved roads, soils (Podzols, Retisols, Gleysols, Phaeozems, and Stagnosols; USS Working Group WRB, 2015), and glacial dust. The observational periods for these locations varied from days or weeks to multiple years and included data from ground-based measurements, remote sensing data, and modeling results. Results on the calculated SI and areas of high-latitude surface land with higher (SI ≥0.5), very high (SI ≥0.7), and the highest (SI ≥0.9) potentials for dust emission are shown in Sect. 3.2. Observations and characteristics of the identified dust sources in our collection (Fig. 1) are presented in Sect. 3.4 and Tables S1–S7 in the Supplement (including the contemporary classification for each source into categories 1–3, based on the currently available observations, in Table S1, satellite observations on new HLD sources in Iceland in Table S2, observations on new HLD sources in Greenland and Canada in Table S3, SI values for each source in Tables S4 and S5, including latitude and longitude, and results from Russian HLD sources in Tables S6–S7).

3.2 SI from UNCCD G-SDS-SBM

Figure 2 presents the G-SDS-SBM SI values (maximum and minimum) for the northern HLD region. The northern HLD region includes the area north of latitude 50° N and the Arctic region (as a subregion of the HLD region) north of 60° N. HLD sources show extreme seasonal characteristics, with some exceptions. The sources appear and disappear (or change SI values) seasonally or appear (or increase SI values) only during favorable extreme weather conditions. Figure 3 shows G-SDS-SBM SI values for the southern HLD region (south of 40° S) without values for Antarctica since G-SDS-SBM does not include areas south of 60° S. Tables S4 and S5 give the values of

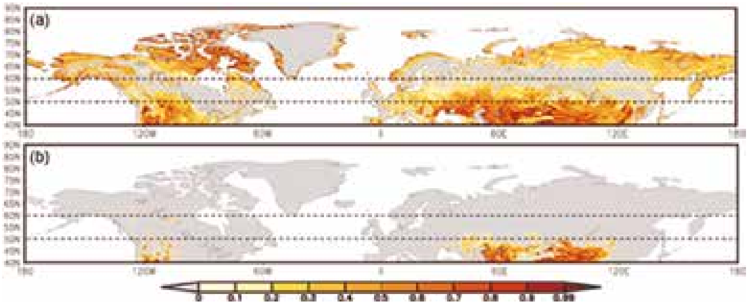

Figure 2. UNCCD Global Sand and Dust Storms Source Base Map (G-SDS-SBM) for annual maximum (a) and minimum (b) SI for the northern HLD region and Arctic subregion (north of 50 and 60° N, respectively, marked with dashed lines).

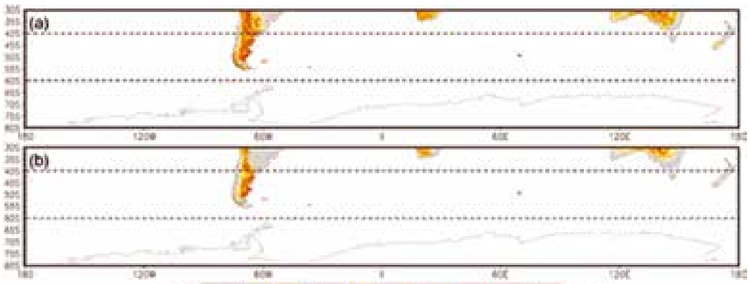

Figure 3. UNCCD G-SDS-SBM for annual maximum (a) and minimum (b) SI for the southern HLD region (south of 40° S) without Antarctica (south of 60° S), marked with dashed lines.

Table 2. Relevant surfaces for the northern HLD and Arctic regions: surface of total area of the region, surface of land area within the region (km2 and % of the total surface), and total surface (km2 and % of the land surface) of areas with SI values above thresholds (0.5 for surfaces with at least "higher" dust emission potential, 0.7 for surfaces with at least "high" dust emission potential, and 0.9 for surfaces with the "highest" dust emission potential) in maximum (max) and minimum (min) seasonal values; values are derived from UNCCD G-SDS-SBM.

Northern HLD region (north of 50° N)

Total area (km^2)	Land area (km^2)	Land area (%)
64 392 015	34 695 710	54

	Max		Min	
	Surface area (km^2)	Surface area (%)	Surface area (km^2)	Surface area (%)
SI ≥ 0.5	1 364 799	3.9	1916	0.006
SI ≥ 0.6	803 372	2.3	1053	0.003
SI ≥ 0.7	509 965	1.5	718	0.002
SI ≥ 0.8	342 913	1.0	562	0.002
SI ≥ 0.9	233 336	0.7	451	0.001

Arctic region (north of 60° N)

Total area (km^2)	Land area (km^2)	Land area (%)
36 876 709	18 853 826	51

	Max		Min	
	Surface area (km^2)	Surface area (%)	Surface area (km^2)	Surface area (%)
SI ≥ 0.5	1 035 059	5.5	515	0.003
SI ≥ 0.6	665 082	3.5	350	0.002
SI ≥ 0.7	440 804	2.3	297	0.002
SI ≥ 0.8	303 521	1.6	264	0.001
SI ≥ 0.9	208 701	1.1	217	0.001

SI for specific locations marked in Fig. 1. Further analysis consists of assessing the areal coverage of sources, with different thresholds for SI values in absolute values (km^2) and the percentage they occupy concerning the total land surface area in the defined HLD regions.

The total surface area of dust sources with a higher potential for dust emission (SI ≥0.5) over the northern HLD region (north of 50° N) is 3.9 % of the total land surface (1 364 799 km^2). The area with a very high potential for dust emission (SI ≥0.7) is 1.5 % (509 965 km^2). The area with the highest dust emission potential (SI ≥0.9) is 0.7 % of the total land area (233 336 km^2) (Table 2). In the Arctic region (north of 60° N) – the subregion of the northern HLD area – dust sources with a higher potential for dust emission (SI ≥0.5) are 5.5 % of the total land surface (1 035 059 km^2). The area with a very high potential for dust emission (SI ≥0.7) is 2.3 % (440 804 km^2). The area with the highest dust emission potential (SI ≥0.9) is 1.1 % (208 701 km^2). The surface of dust-productive areas with minimum seasonal SI values in the northern HLD region is about 3 orders of magnitude smaller than the maximum, meaning the northern HLD sources greatly depend on weather conditions. Maximum surfaces contain dust-productive regions that are defined under the most favorable weather conditions for soil exposure to wind erosion (including extreme weather). All sources defined here are not necessarily active every year or in the same period, meaning these surfaces can seasonally or occasionally (under severe weather) appear as dust sources.

For the southern HLD region (40–60° S, area without Antarctica), the land surface is only 2 % of the total surface area (Table 3). The surface area of dust sources with SI ≥0.5 is 22.6 % of the total land surface (309 520 km^2). The area with SI ≥0.7 is 4.5 % (61 527 km^2). The area with the highest dust emission potential (SI ≥0.9) is 0.6 % (8630 km^2). The surface areas for minimum SI values above these thresholds are 2 to 3 times smaller than the surfaces for maximum SI values compared to the difference in the northern HLD region. This means that soil surface conditions in the southern HLD region are favorable for dust emission over the whole year. Especially in locations of HLD markers, SI maximum and minimum values do not change over most locations or decrease by 0.1 or 0.2, except for one location (no. 38), which has SI values changing from 0.9 to 0 at the location of an HLD marker.

3.3 Emission and deposition of global and Arctic dust

The SILAM model estimated the total emission of annual dust and its deposition (data for 2017) onto snow-covered land, frozen sea, and total sea surfaces (frozen and non-frozen) (Fig. 4). The computations were also performed for Arctic dust and total global dust, with results for overall dust (diameter less than 30 µm) and fine dust (diameter less than 2.5 µm) separately (Fig. 15 of Sect. 3.5). Based on the model, the total emission of Arctic dust equals approximately 1.0 % of the globe's total dust emission. The deposition of Arctic dust onto

Table 3. Relevant surfaces for the southern HLD region: surface of the total area of the region, surface of land area within the region (km^2 and % of the total surface), and total surface (km^2 and % of the land surface) of areas with SI values above thresholds (0.5 for surfaces with at least "higher" dust emission potential, 0.7 for surfaces with at least "high" dust emission potential, and 0.9 for surfaces with the "highest" dust emission potential) in maximum (max) and minimum (min) seasonal values; values are derived from UNCCD G-SDS-SBM.

<table>
<tr><th colspan="5">Southern HLD region (south of 40° S)</th></tr>
<tr><td>Total area (km^2)</td><td colspan="2">Land area (km^2)</td><td colspan="2">Land area (%)</td></tr>
<tr><td>61 435 208</td><td colspan="2">1 367 987</td><td colspan="2">2</td></tr>
<tr><td></td><td colspan="2">Max</td><td colspan="2">Min</td></tr>
<tr><td></td><td>Surface area (km^2)</td><td>Surface area (%)</td><td>Surface area (km^2)</td><td>Surface area (%)</td></tr>
<tr><td>SI≥ 0.5</td><td>309 520</td><td>22.6</td><td>186 266</td><td>13.616</td></tr>
<tr><td>SI≥ 0.6</td><td>151 480</td><td>11.1</td><td>81 522</td><td>5.959</td></tr>
<tr><td>SI≥ 0.7</td><td>615 27</td><td>4.5</td><td>29 256</td><td>2.139</td></tr>
<tr><td>SI≥ 0.8</td><td>25 416</td><td>1.9</td><td>10 842</td><td>0.793</td></tr>
<tr><td>SI≥ 0.9</td><td>8630</td><td>0.6</td><td>2747</td><td>0.201</td></tr>
</table>

snow- and ice-covered surfaces equals about 19 % of the total dust deposition onto these areas and about 57 % of the deposition onto the areas explicitly located in the Arctic region. For fine dust, the corresponding figures are 7 % and 22 %. Compared to the deposition of black carbon (anthropogenic sources and wildfires combined; Fig. 15 of Sect. 3.5) onto snow and ice, the deposition of fine Arctic dust is about 70 % higher globally and around 580 % higher in the Arctic regions. While these figures provide a general quantification of the deposited amounts, detailed calculations of the thermal and optical properties of dust and black carbon deposited on snow would be required to compare the deposited substances' net impacts on the climate.

3.4 The identified dust sources

Observations of the identified 64 dust sources in our collection (Fig. 1) are presented and discussed in alphabetical order as follows: (1) Alaska (source nos. 14 and 50 in Fig. 1); (2) Antarctica (nos. 9, 19, 20, and 52); (3) Canada (no. 2, 16, 48, and 62); (4) Denmark and Sweden (nos. 1, 15, and 51); (5) Greenland (nos. 53–61 and 64); (6) Iceland (nos. 23–45); (7) Russia (nos. 2–11); (8) South America and Patagonia (nos. 17, 21, 46, 47, 49, 52, and 63); (9) Svalbard (no. 13, 18, and 22). Dust events originating simultaneously from Greenland, Iceland, and North America are demonstrated as a supplementary animation (available through a link in the Supplement). The numbers are the identified 64 dust sources shown in Fig. 1. Additional information, including latitude, longitude, and SI values, can be found in the Supplement (Tables S1–S4).

3.4.1 Alaska, Copper River Valley, USA

Alaskan dust sources were identified over a century ago (Tarr and Martin, 1913). However, limited satellite detection due to abundant cloud cover and an isolated location resulted in sparse information on this region (Crusius et al., 2011). The main identified sources are piedmont glaciers (Malaspina, Bering), resuspension of ash from past eruptions (Hadley et al., 2004), and major rivers carrying glacial sediment (Copper, Yukon, Tanana, and Alsek) (Gassó, 2020a, b; 2021a, b). Resuspension of glacial dust transported by these rivers can be abundant, often triggering air quality alerts by the Alaska Department of the Environment (USGCRP, 2018). The largest and most active of such dust sources is the Copper River (Fig. 5), estimated to transport 69 Mt of suspended sediment annually (Brabets, 1997). Transported sediment is deposited on the Copper River Delta, an alluvial floodplain covering an area of 2800 km^2. When conditions allow, sediment is resuspended, resulting in dust plumes that can extend hundreds of kilometers over the Gulf of Alaska. Dust events, often lasting several days or weeks (Schroth et al., 2017), are most common in late summer and fall, when the river discharge and snow cover are at their minimum and high wind speeds are commonplace

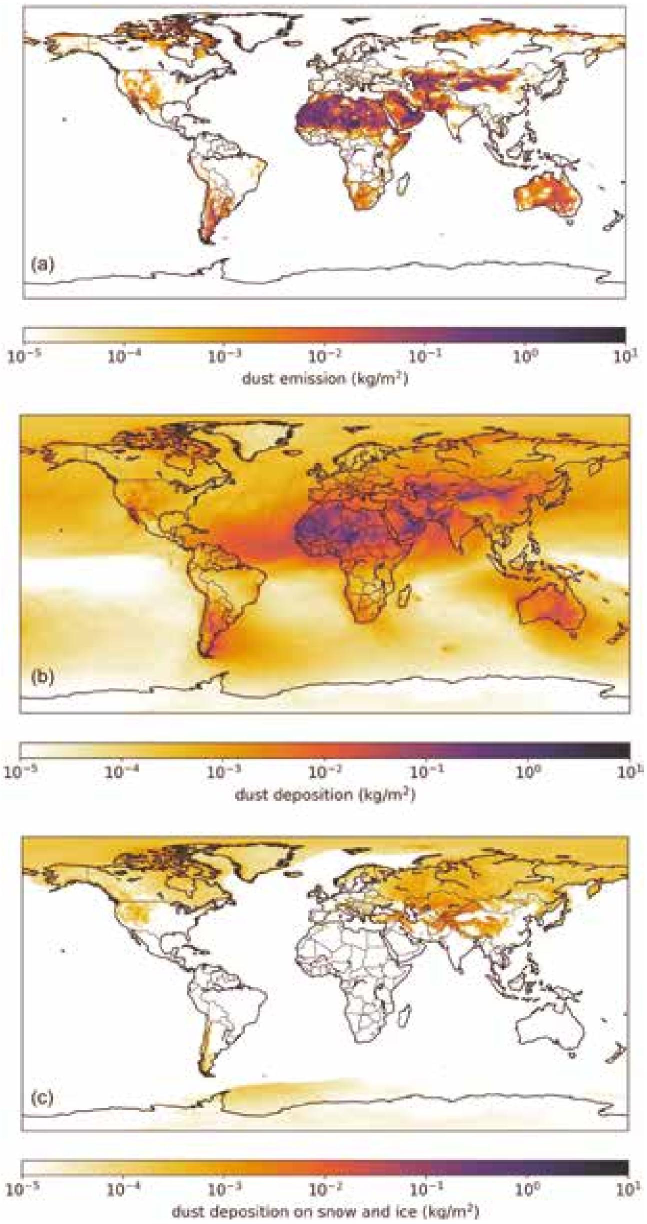

Figure 4. SILAM emission and deposition modeling results of dust emission (a), dust deposition (b), and dust deposition on snow and ice (c) (kg per m^2).

(Crusius, 2021). However, these occurrences have been observed year-round (Gassó, 2021a; January 2021). Dust reaches the open waters beyond the continental shelf and the influence of coastal sediments (Crusius et al., 2017). Thus, it has been proposed that dust from coastal sources such as the Copper River Delta can be an important source of bioavailable iron in the Gulf of Alaska (Crusius et al., 2011; Crusius, 2021; Schroth et al., 2017). Further work is also needed to investigate the relative importance of dust emissions from Alaska and East Asia (Bishop et al., 2002) in other areas. Also, dust from this region may initiate ice production in supercooled clouds, which is crucial for climate feedback (Murray et al., 2021). Regarding the magnitude and seasonal variability of emissions of sources in southern Alaska, a few dedicated studies have focused on dust from the Copper River Delta (Crusius et al., 2017; Schroth et al., 2017; Crusius, 2021). However, to our knowledge, no dust activity and source characterization have been carried out along the coast of the Gulf of Alaska. Moreover, resuspended road dust is a major air quality issue throughout Alaska.

3.4.2 Antarctica

James Ross Island, Ulu Peninsula

The northern part of James Ross Island – Ulu Peninsula – represents one of Antarctica's largest ice-free areas (312 km^2). Its bare surface, consisting mainly of weathered sedimentary rocks, is an active HLD source (Kavan et al., 2018). Suspended sediments originate from outside the local fluvial systems based on the elemental ratios of and (Kavan et al., 2017). The wind speed threshold of 10 m s−1 is needed for activating local dust sources, with most of the particles captured (by mass) in size bins between 2.5 and 10 µm. Mean (median) mass concentrations of the PM10 were 6.4±1.4 (3.9±1) µg m$^{-3,}$ while the PM2.5 was 3.1±1 (2.3±0.9) µg m^{-3} for the whole measurement period from January to March 2018. Mean PM10 values are comparable to background stations in northern Europe. The highest daily aerosol concentration was 57 µg m^{-3} for PM10, with hourly PM10 with >100 µg m^{-3}. Higher aerosol concentration occurs in late austral summer, when the soil water content in the upper soil layer is significantly lower than in early summer. Long-range transport of dust originating in Patagonia was observed during aerosol measurements (Kavan et al., 2018). A higher proportion of long-range-transported dust was found in snow pits on higher elevated glaciers compared to a higher proportion of locally transported dust in lower elevated glaciers (Kavan et al., 2020b). Kňažková et al. (2020) identified a redistribution of mineral material within the HLD source area in Abernethy Flats, impacting the local microtopography.

Marambio, Antarctic Peninsula

Marambio Base (64°14′ S, 56°37′ W; 198 m a.s.l.) on Marambio island, Graham Land, Antarctic Peninsula, is a member of the Global Atmosphere Watch (GAW) program of the WMO, with personnel available year-round. This region has ice-free areas and cold desert soils (Cryosols) that can be seasonally susceptible to wind erosion and weathering. The removal of fine materials occurs mainly by wind action. The Finnish–Argentinian co-operative research in Marambio includes measurements of ozone, solar irradiance, aerosols, and ultraviolet (UV) albedo (Aun et al., 2020). The UV Biometer Model 501 from Solar Light Co. (SL501) UV albedo data of 2013–2017 in Marambio were used to analyze the effects of local HLD on measured snow UV albedo and solar UV irradiance and differences in simulated UV irradiances (Meinander et al., 2018; data not presented here). For validating the UV albedo data, surface photos were taken regularly. The surface photos and UV albedo measurements show that local dust can be detected on the snow and ice. Also, the optical dome of the SL-501 sensor was found to be sandblasted by the windblown dust when returning to Finland for maintenance. These findings suggest that, in Marambio, local dust can decrease surface snow/ice albedo, possibly enhance the cryosphere melt, and contribute to warming in the Antarctic Peninsula due to the ice-albedo feedback mechanism.

McMurdo Sound, Antarctica

The McMurdo Sound area of the Ross Sea region is widely recognized as the dustiest place in Antarctica, where locally sourced aeolian accumulation is up to 2 to 3 orders of magnitude above global background and dust fallout rates for the continent (Chewings et al., 2014; Winton et al., 2014). The area includes the McMurdo Dry Valleys (MDVs), the largest ice-free area (4800 km^2) in Antarctica. The MDVs have high but extremely variable fluxes of locally derived aeolian sand (e.g., Speirs et al., 2008; Lancaster et al., 2010; Gillies et al., 2013; Diaz et al., 2020) and common aeolian landforms. This has led to the assumption that the MDVs are a significant regional

Figure 5. Satellite image (left) of the Copper River region and photo (right) taken at the Copper River Delta on the same day (14 October 2019). The common occurrence of clouds prevents direct viewing of the dust in suspension, illustrating the difficulty in observing dust activity from space. (Satellite image from NASA Worldview; photo by Sarah Barr.)

dust source (e.g., Bullard, 2016). Some modeling studies suggest the MDVs could supply large volumes of dust to a wide area of the Southern Ocean (e.g., Bhattachan et al., 2015). However, field-based observations show that very little sediment is transported out of the MDVs (Ayling and McGowan, 2006; Atkins and Dunbar, 2009; Chewings et al., 2014; Murray et al., 2013) because the valleys have already been extensively winnowed into a well-developed deflation surface and large coastal piedmont glaciers form a topographic barrier, preventing aeolian sediment from escaping. The dominant source of aeolian sediment in the McMurdo Sound area is the debris-covered surface of the McMurdo Ice Shelf (1500 km^2), with minor contributions from local ice-free headlands. This ice shelf is unusual because it has high surface ablation and a continuously replenishing supply of fine-grained sediment advected from the seafloor. The sediment is blown off the ice shelf by frequent intense southerly wind events, forming a visible sediment plume onto coastal sea ice. Within a few kilometers of the ice shelf, accumulation rates on sea ice are up to 55 g m^{-2} yr^{-1}, reducing rapidly downwind to an average of 1.14 g m^{-2} yr^{-1}, equating to 0.6 kt yr^{-1} of aeolian sediment entering McMurdo Sound annually (Atkins and Dunbar, 2009; Chewings et al., 2014). Some sediment is transported at least 120 km from the source and could travel much farther, contributing iron-rich dust to the Ross Sea (Winton et al., 2014). Coastal areas and lowland parts of the MDVs are on the threshold of climatically driven change with observed increases in ablation and seasonal meltwater flow incising into permafrost (Fountain et al., 2014), suggesting that the dust potential of McMurdo Sound and the MDVs could rapidly change. The MDVs (4800 km^2) are estimated to best fit Category 3 (source with unknown activity, Table S1). The McMurdo Ice Shelf "debris bands" are estimated to best fit Category 2 (moderately active source).

Schirmacher Oasis, East Antarctica

Schirmacher Oasis (70°45′30" S, 11°38′40" E) is approximately 80 km from the coast of the Lazarev Sea, Queen Maud Land, East Antarctica. The oasis is an ice-free area of over 35 km^2 with typically hillocky relief. The oasis and surrounding area have been explored since the early 1960s. However, no systematic studies of dust on local ice and snow have been done. Most of this region's dust is assumed to be formed with the soils blown in the air because of strong winds. Human activity produces some of the dust in this region: the oasis shelters four bases, which use diesel oil and petrol to supply heat and transport operations. Two airports are nearby, which operate during the summer – lasting from late November to late February. In December 2019, we collected the snow samples on 11 sites near the local ice roads, bases, and airports. These data will contribute to our future study.

3.4.3 Canada

Lake Hazen, Ellesmere Island

Evidence of dust activity in Canada has been reported, e.g., in the prairie, crater lake, and river valley environments (e.g., Wheaton and Chakravarti, 1990; Neuman, 1990; Wheaton, 1992; Hugenholtz and Wolfe, 2010; Fox et al., 2012). Satellite observations of HLD events over water are relatively common (see, for example, Bullard et al., 2016). Whether directly concerning explicit plume remote sensing or indirectly regarding plume deposition, the detection of such events has remained largely unreported. Ranjbar et al. (2021) recently reported detecting a drainage-flow-induced dust plume over (frozen) Lake Hazen, Nunavut, Canada, using a variety of remote sensing techniques (Lake Hazen is the Arctic's largest lake, by volume, at 81.8° N latitude in the northernmost portion of Ellesmere Island). shows a true-color georeferenced RGB MODIS-Terra image acquired on 19 May 2014 at 19:50 UT (15:50 EDT) over Lake Hazen. The authors employed MISR stereoscopy, CALIOP, and CloudSat vertical profiling as well as MODIS thermal IR techniques to identify and characterize the plume as it crossed over a complex springtime terrain of snow, ice, and embedded dust. While limited by the lack of dedicated dust remote sensing algorithms over snow and ice terrain, the plume characterization boded well for developing systematic, satellite-based, HLD detection approaches using current and future generations of aerosol and cloud remote sensing platforms.

Kluane Lake, Yukon

Within the St. Elias mountain range at the northern end of the Pacific Coast Range on the continental side of the Yukon Territory lies the Kluane Lake region (KLR), which contains Łhù'ààn Mân' (Kluane Lake) (no. 50 in

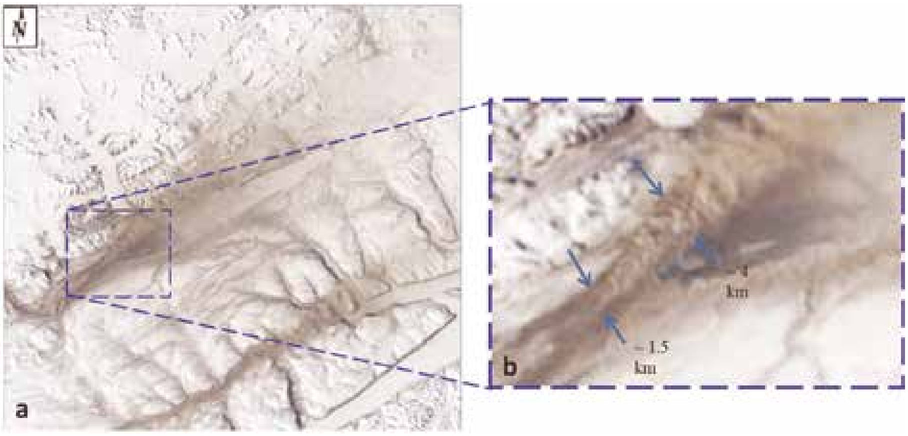

Figure 6. MODIS Terra satellite image on 19 May 2014 at 19:50 UTC (a). True-color image: MODIS channels 1 (620–670 nm), 3 (459–479 nm), and 4 (545–565 nm) were loaded into the RGB channels of the display. (b) The sub-image is a zoom of the most discernible part of the plume (outlined by the blue broken-line square).

Fig. 1). The lake is fed primarily from the meltwater of the Kaskawulsh glacier down the (formally the Slims River) and snowmelt from the surrounding regions in the springtime. This seasonal discharge has, in recent history, been known to be highly variable as the glacier terminates at the fork of two distinct watersheds – one draining into the Bering Strait through the Yukon River and the other into the Gulf of Alaska – supplying the two watersheds’ inconstant ratios. In 2016, most of the glacier’s discharge was diverted to the Gulf of Alaska in an intense discharge event, dramatically decreasing the Łhù’aÌaÌn Mân’s water levels and increasing the dust emission potential from the (Shugar et al., 2017). This drastic change makes the KLR an excellent natural laboratory for investigating the impact of proglacial hydrology on dust emission potential under past and future climates. Research was conducted in the early 1970s in this same valley as a comprehensive set of dust flux measurements as part of several publications (Nickling, 1978; Nickling and Brazel, 1985). Nickling (1978) concluded that there is a dynamic relationship between soil moisture (driven by precipitation and nighttime radiation insolation) and wind, resulting in periodicity of dust emissions from the valley in all but the mornings throughout the snow-free seasons. Within a more recent study by Bachelder et al. (2020), soil and aerosol samples were collected within the delta, where air quality thresholds were exceeded, indicating a negative impact on local air quality throughout May. Notably, daily particle size distributions of PM10 were very fine (mode of 3.25 µm) compared to those measured at more well-characterized, LLD sources. Moreover, mineralogy and elemental composition of ambient PM10 were found to be enriched in trace elements (e.g., As and Pb) compared to dust deposition, bulk soil samples, and fine soil fractions ($d<53$ µm). Finally, through a comparison of the elemental composition of PM10, dust deposition, and fine and bulk soil fractions as well as meteorological factors measured, Bachelder et al. (2020) propose that the primary mechanisms for dust emissions from are the rupture of clay coatings on particles and the release of resident fine particulate matter.

3.4.4 Denmark and Sweden

In Denmark, large areas with severe wind erosion have been documented (Kuhlman, 1960). Published literature on the activity of dust sources in Denmark is rare; some documentation is only in Danish. On 23 April 2019, a dust plume from Denmark’s western coast, with dust plumes from Sweden’s 12 km-long Mellbystrand around the mouth of the Lagan River (no. 51 in Fig. 1) and Poland could be observed in Meteosat-11 Dust RGB and Natural Colour images: 23 April 12:30 UTC. These dust plumes were observed to travel to the North Sea (Kerkmann et al., 2019). The source in Denmark appears to be from Holmsland Dunes (no. 15 in Fig. 1). Other potential dust sources in Denmark include, e.g., Råbjerg Mile (no. 1 in Fig. 1), the largest moving dune in northern Europe with an area of around 2 km^2 (Doody et al., 2004), located between Skagen and Frederikshavn. Råbjerg Mile moves at approximately 15 m yr^{-1} due to wind and has moved around 1.5 km further east in the last 110 years. The drifting sand is not considered to be transported very far. In general, dust storms in Denmark are considered small, and locally based dust storms can be expected when farmers prepare the arable soils in spring, creating dust in case of a very dry month of April. In Tilviden, flying sand took over (after Frederik II cut the oak trees for building ships in 1600). Also, a regional soil and sand event in Denmark, reportedly common in April, was recently documented between Mejrup and Holtebro on 6 April 2021 (Television Midtvest, 2021; not identified in Fig. 1; coordinates are estimated as 56°23′ N, 8°41′ E). This location between Mejrup and Holtebro remains to be marked as a potential dust source for future observations. The event was observed over roadways in several parts of the region, reducing visibility due to a long period without rain and with strong winds for >24 h, causing the soil to blow off the harrowed fields.

3.4.5 Greenland

Greenland’s ice-free areas have long been identified as locally important dust sources (Hobbs, 1942), with dust storms described as reaching >100 m high (Dijkmans and Törnqvist, 1991). These storms can cause the darkening of the Greenland Ice Sheet by deposition, which may affect albedo and rates of ice melt (Wientjes et al., 2011; McCutcheon et al., 2021). Potential dust source areas in Greenland are mapped in the recently issued global dust atlas by Vukovic (2021) (UNCCD, 2021). Dust input to soils and lakes may also have substantial ecological impacts (Anderson et al., 2017). Bullard and Mockford (2018) investigated the seasonal and decadal variability of dust emissions in southwestern Greenland and presented the first long-term assessment of dust emissions. Dust emissions occur all year but peak in spring and early fall. The evidence linking increased dust emissions to preceding jökulhlaup (a type of glacial outburst flood) events is inconclusive, requiring further exploration. The decadal record confirmed that dust-storm magnitude may have increased from 1985 to the 1990s (Bullard and Mockford, 2018). Amino et al. (2020) also showed that dust deposition on the southeastern dome in Greenland has increased in recent decades. They link this increase to dust emissions in coastal Greenland, where snow cover is decreasing. However, further work is needed to characterize the magnitude of dust events at the source and how their emissions are changing. Bullard and Mockford (2018) also presented preferential dust-event pathways from Kangerlussuaq, indicating that most events travel toward the Davis Strait and the Labrador Sea, where the dust might impact the boundary layer of mixed-phase clouds (Murray et al., 2021).

Modern satellite remote sensing methods can detect dust storm events in Greenland’s different valleys and coastal areas. The new HLD sources identified in this study based on satellite observations are in Table S3. Figure 7 illustrates one such dust storm episode on the Nuussuaq Peninsula, Greenland, on 1 October 2020 (Markuse, 2020, containing modified Copernicus Sentinel data (2020), originally posted to Flickr by Pierre Markuse at https://flickr.com/photos/24998770@N07/50447335522, reviewed on: 25 October 2020 by FlickreviewR 2, and licensed under the terms of the cc-by-2.0.2020). One example of DREAM regional-scale modeling of atmospheric transport of dust from Greenland potential dust sources is demonstrated in Fig. 8 (supplementary animation available through a link in the Supplement), where the DREAM circumpolar prediction experiment example shows the predicted surface dust concentration for 4 November 2013 and Icelandic volcanic desert dust reaching Greenland, as discussed, e.g., in Meinander et al. (2016).

Figure 7. HLD storm on the Nuussuaq Peninsula, Greenland – 1 October 2020 (Markuse, 2020).

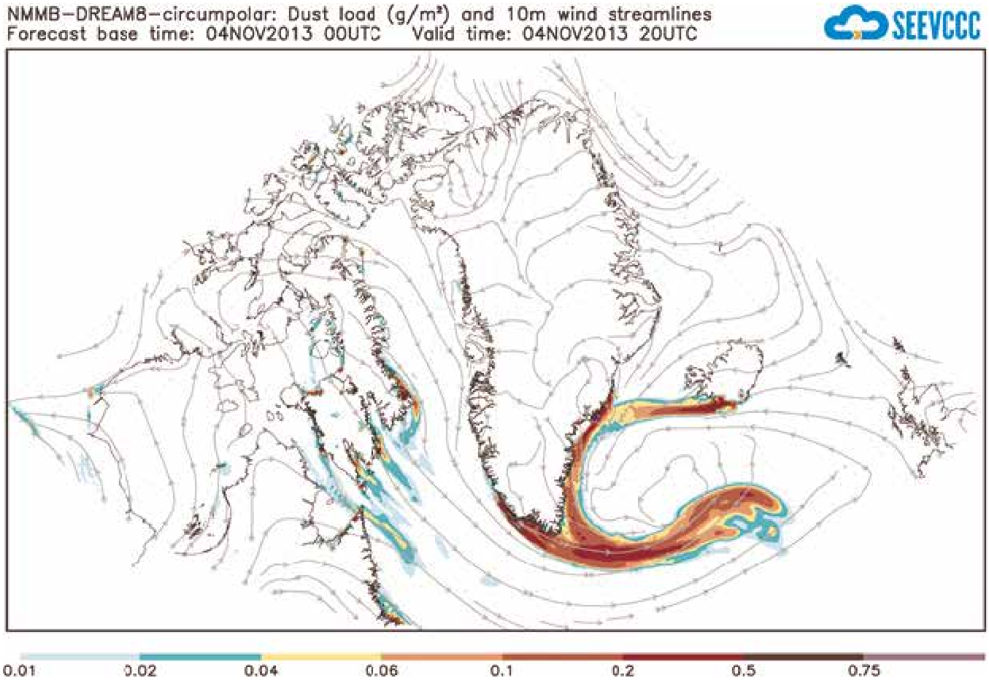

Figure 8. DREAM model-predicted dust load for 4 November 2013 (supplementary animation available through a link in the Supplement).

3.4.6 Iceland

Iceland has been recognized for a while as a potentially important dust source. In our collection, 13 new sources in Iceland were included (Table S2) compared to previous sources, in which eight Icelandic dust hotspots were identified (Arnalds et al., 2016). Sandkluftavatn, Kleifarvatn, Skafta jökulhlaup deposits, and other areas have also been found to produce large amounts of dust (Dagsson-Waldhauserová et al., 2019). In recent years, increased dust activity has been reported in Flosaskard and Vonaskard (Gunnarsson et al., 2021). These dust hotspots cover almost 500 km^2, while deserts are over 45 000 km^2 (Arnalds et al., 2016). Most of the dust hotspots are near glaciers: glacial floodplains, old lakes, jökulhlaup deposit areas, or sandy beaches. Glaciofluvial plains receive a massive amount of unconsolidated silty material during the melting of nearby glacial regions.

New dust sources with the number of events are identified here and presented based on satellite image observations from 2002 to 2011 (Table S2), suggesting that Iceland's entire southern coast could be considered one source. However, previous results on Icelandic dust suggest that nearby locations may have different particle characteristics (Fig. 9). Therefore, each source must be studied independently. For example, the grain size distribution curves of the samples from Dyngjusandur, Hagavatn, Landeyjarsandur, Maelifellsandur, Myrdahlsandur, and Sandkluftavatn showed generally unimodal distributions with a rather diverse character (average diameters ranging from 19.8 to 97.7 µm, Fig. 9). Richards-Thomas et al. (2021) identified a range in particle diameter be-

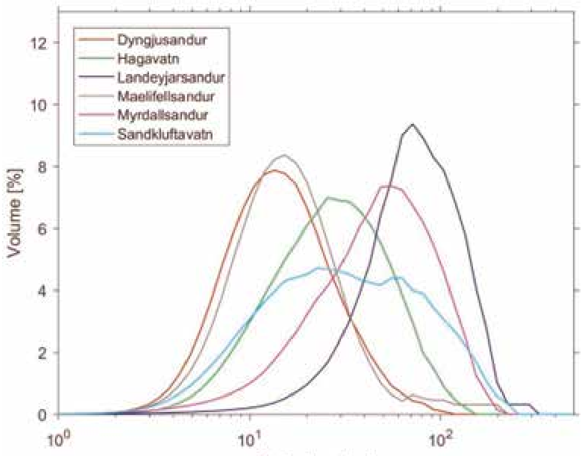

Figure 9. Grain size distributions of samples from Icelandic source areas (redrawn from Varga et al., 2021).

tween 0.4 and 89 µm, with the medians (d50) of the distributions from 12 to 25 µm. Some hotspot particles are bimodal with peaks at 2 and 30 µm and a more significant proportion of the sample within the silt-size range.

Icelandic dust particles have different shapes, lower densities, higher porosity, increased roughness, and darker colors than other desert dust (Butwin et al., 2020; Richards-Thomas et al., 2021). Those greater than 20 µm retain the volcanic morphological properties of fresh volcanic ash. Dust and fresh volcanic ash particles less than 20 µm are crystalline and blocky. Icelandic dust particles contain amorphous glass, large internal voids, and copious dust coats comprised of nano-scale flakes. The amorphous basaltic material is mostly aluminosilicate glass ranging from 8 wt % (Hagavatn hotspot) to 60 wt %–90 wt %, with relatively high total Fe with a higher Fe solubility and magnetite fraction than LLD (10 wt %–13 wt %, Baldo et al., 2020). PM10 concentrations measured during severe Icelandic dust storms well exceeded 7000 µg m^{-3} (Dagsson-Waldhauserová et al., 2014, 2015; Mockford et al., 2018). Submicron particles contribute with high proportions (>50 %) to PM10 mass concentrations and number concentrations (Dagsson-Waldhauserová et al., 2014, 2016, 2019). Aeolian transport of 11 t of dust over a 1 m transect was measured during the severe dust/ash storm in 2010, when grains >2 mm were uplifted (Arnalds et al., 2013).

As well as differences in Icelandic dust sources, the chemical composition of the aircraft-collected Icelandic dust particles has a different chemical signature than, e.g., airborne Saharan dust particles transported to Barbados (Sanchez-Marroquin et al., 2020). This difference can be observed in Fig. 10a and b, where the chemical composition of most Icelandic dust particles falls in a different area of the chemical composition ternary diagram than the Saharan dust particles from Barbados. One of the most prominent differences between these types of dust is Ti's presence in ~30 % of the Icelandic dust particles, while this element is almost absent in the Saharan dust particles and dust collected elsewhere and shown in Fig. 10c. Furthermore, the chemical composition of the aircraft-collected Icelandic dust is consistent with surface scooped samples of dust or volcanic ash from Iceland. Moreover, a droplet freezing-based assay confirmed that the sampled Icelandic dust has a high ice nucleation ability and can influence the radiative and lifetime properties of clouds containing water and ice.

No direct observations or measurements of the new sources were available. Instead, two model computations are presented for Iceland because of the lack of observations and complexity of the AOD interpretation in polar and subpolar regions. Without high uncertainty of direct measurements, the importance of the HLD modeling rises; models validated over better-observed regions may become an important or primary source of information. Results using the DREAM model, with a horizontal resolution of `~3.5 km, were used here to resolve the heterogeneous and small-scale character of the Icelandic dust sources (Fig. 11). As the first operational numerical HLD model, DREAM-ICELAND predicted the Icelandic dust for the example case of 18 September 2020 (Fig. 11).

In Fig. 12, dust emissions in Iceland are presented in 3-month periods for March 2020–August 2021. The modeled results clearly show the seasonal nature of the dust sources. The summer season (June–August) appears to be the strongest dust season. However, there are also dust emissions in wintertime with snow-covered land surfaces, according to observations of dust events during snowfall (e.g., Dagsson-Waldhauserová et al., 2015). The 2021 summer season in these modeled emission results appears in the same locations as summer 2020 but with more severe emissions in the highlands in 2021, agreeing with the field observations in Vatnajökull National Park during the HiLDA measurement campaign in the 2021 season (https://gomera.geo.tu-darmstadt.de/wordpress/, last access: 17 August 2022), where the most severe dust events were measured

.

3.4.7 Russia

The Russian Arctic and sub-Arctic are the most relevant regions connected to the HLD sources. In these territories, atmospheric dust is produced due to burning gas (Novy Urengoy is called the gas capital of Russia) and forest fires (especially in Siberia; see MODIS or Senti-

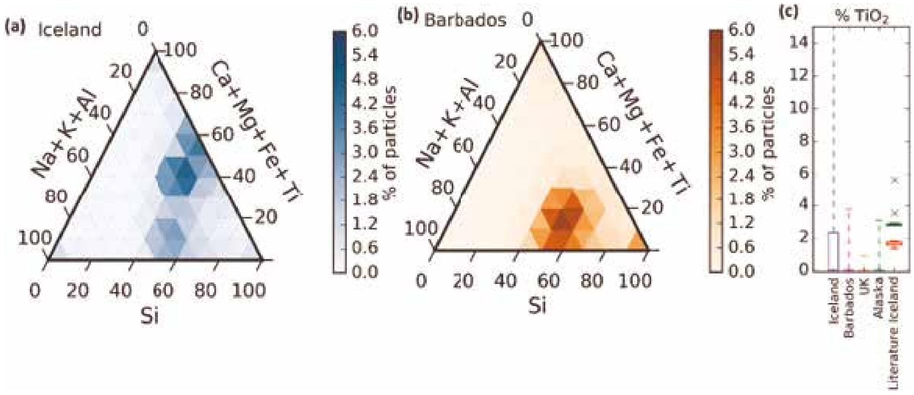

Figure 10. Ternary graphs of the chemical composition of Icelandic dust particles (a) and Saharan dust particles collected in Barbados (b). Each graph contains a heat map with the percentage of dust particles in each sample compositional bin. The chemical composition of each aerosol has been recalculated from the weight percentages given by the SEM software, excluding elements that are not Si, Al, Fe, Mg, Ca, Na, K, Ti, Mn, and P. (c) The box represents particles in the Q3 percentile of the percentage of the composition of Ti in all the dust particles in each sample (Icelandic dust, Saharan dust collected in Barbados, dust collected in the UK, and dust collected in Alaska). The whiskers represent the composition of all particles between the median plus and minus 2 standard deviations. The data have been compared to the Ti weight percentage of different Icelandic dust and ash samples from the literature. (Figure extracted from the Supplement of Sanchez-Marroquin et al., 2020.)

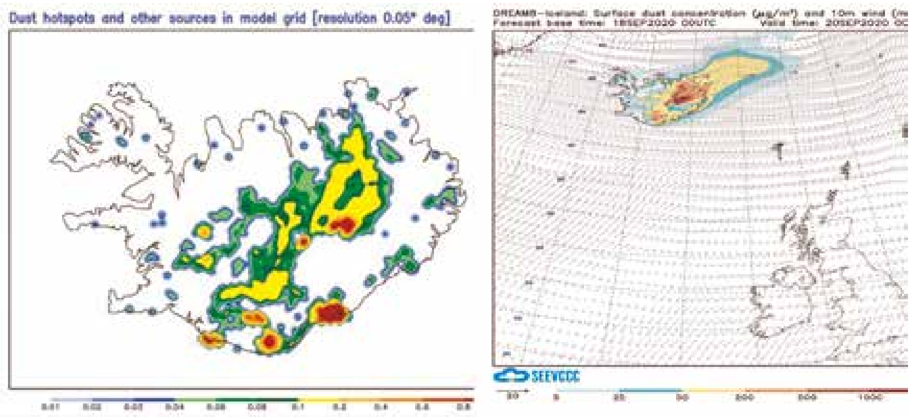

Figure 11. Left panel: dust sources in the DREAM-ICELAND model grid with areas vulnerable to erosion and containing hotspots (Arnalds et al., 2016). Right panel: an example of the operational Icelandic dust surface concentration forecast for 18 September 2020 (available at the Republic Hydrometeorological Service of Serbia site, http://www.seevccc.rs/?p=8, last access: 17 August 2022).

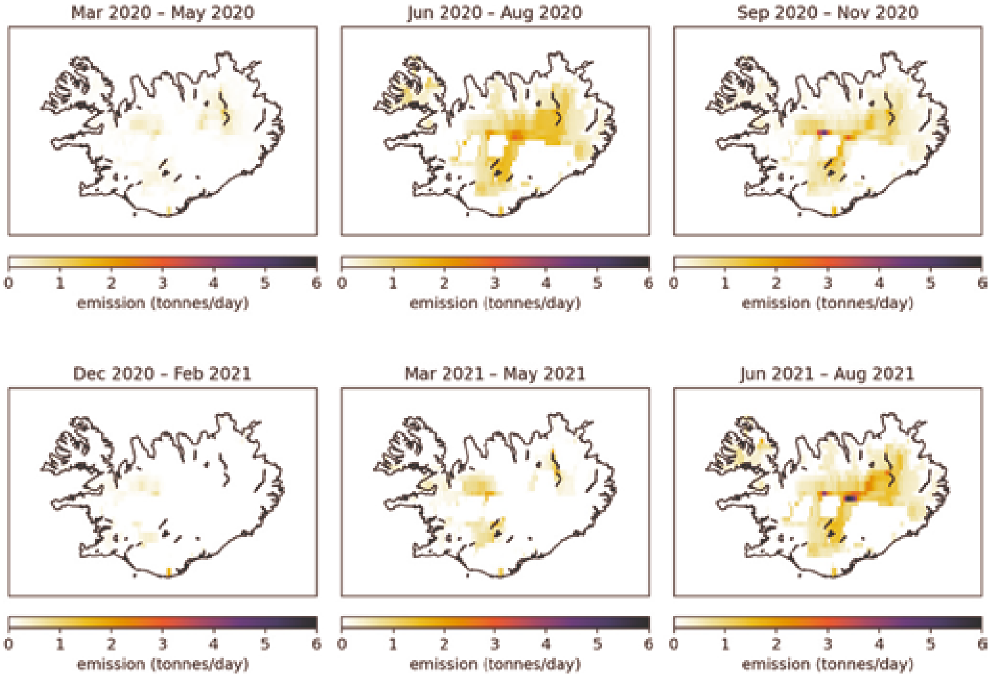

Figure 12. SILAM-modeled dust emissions (tonnes per day) in Iceland for 3-month periods in March 2020–August 2021.

nel images for Novy Urengoy on 3–8 August 2021) and dusting of abandoned and non-reclaimed heaps. Wind erosion is followed by vegetation destruction from gas and oil extraction, especially in Western Siberia. Some Russian sources included in our collection (e.g., nos. 7 and 8 of Fig. 1) could be identified as dust sources on the periphery of HLD and LLD source regions. Source no. 7 of Fig. 1 is the Altai Mountains. Some parts of these territories are covered by permafrost, where winter lasts for 5–6 months. From October, in lower mountains (less than 1000 m a.s.l.), and from September, in higher mountains (more than 1500 m a.s.l.), a stable snow cover persists. The mean daily air temperature during winter within the lower, middle, and higher mountains is −21, −29, and below −30 °C, respectively. Source no. 8 is in Central Kazakhstan. From late December to early March, a stable snow cover from 5 to 30 cm occurs within plains and up to 50 cm within hollows. Periods of snow cover and thaw correspond to transitions of the mean daily temperature of air through 0 °C, which, on average, are 7 November and 23 March ± 10–12 d. From early January to late February, the air's mean daily temperature can be as low as −20 °C. The Soil Atlas of the Northern Circumpolar Region (https://esdac.jrc.ec.europa.eu/content/soilatlas-northern-circumpolar-region, last access: 30 May 2022) covers all land surfaces in Eurasia and North America above the latitude of 50° N. Thus, these territories are considered high latitude.

Western Siberia, Altai Mountains, and Central Kazakhstan

In the most widespread undisturbed soils (Gleysols, Phaeozems, Podzols, Retisols, and Stagnosols) in Western Siberia (Semenkov et al., 2015a, b) – the largest plain in the world – mineralogical and elemental composition (Table S6) were studied using X-ray diffractometry, X-ray fluorescence spectrometry, ICP-MS, ICP-AES, and content of total organic carbon (TOC), as reported in detail in Semenkov et al. (2019), Semenkov and Koroleva (2019), and Semenkov and Yakushev (2019). At location nos. 7 and 8 of Fig. 1 (Table 4), the concentrations of N-containing substances, pH values, dust content, and dust deposition rate were measured in snow in

Table 4. Major ions (mg L^{-1}), pH value, dust content (mg m^{-2} in snow), and deposition rate (mg m^{-2} d^{-1}) during winter at HLD source nos. 7 and 8 in Fig. 1.

HLD no.	M	SD	Me	Min	Max	N
No. 7						
Dust content (mg m^{-2})	316	439	112	0	1542	30
NH_4^+ mg L^{-1}	0.75	0.98	0.30	0	3.60	43
NO_2^- mg L^{-1}	0.015	0.019	0.008	0	0.08	107
NO_3^- mg L^{-1}	2.3	3.4	1.4	0	20.4	118
pH	6.6	0.8	6.7	4.1	8.4	129
No. 8						
Dust deposition rate (mg m^{-2} d^{-1})	1.67	1.67	1.08	0.05	6.6	38
NH_4^+ mg L^{-1}	0.20	0.009	0.10	0	1.34	682
NO_2^- mg L^{-1}	0.027	0.007	0	0	0.61	127
NO_3^- mg L^{-1}	0.47	0.02	0.19	0	3.93	697
pH	6.1	0.02	6.1	4.6	8.0	585

M – mean, Max – maximum, Me – median, Min – minimum, N – number of observations, SD – standard deviation.

winter from 2009 to 2019 (Koroleva et al., 2016, 2017; Semenkov et al., 2021; Sharapova et al., 2020).

Murmansk region: Apatity, Kirovsk, Kovdor

Large amounts of displaced rock have been breaking the balance of geological emissions of gas and dust from mining, dumps, and tailing pits (e.g., Csavina et al., 2012). Over 150 Mt of industrial wastes are disposed of in the Murmansk region annually, reaching about 8 Gt (Table S7). The dusting of processing tailing is one of the main sources of air pollution resulting from suspended matters near the mining enterprises. About 30 % of all suspended matter is released from the mining enterprises into the atmosphere due to wind-induced dusting of beaches and slopes of tailing dumps. Elevated concentrations of suspended matter are registered every summer in Apatity's atmosphere. Dust storms from technogenic dust sources of the mining industry on the Kola Peninsula are presented, e.g., in Baklanov and Rigina (1998), Baklanov et al. (2012), and Amosov and Baklanov (2015).

Tiksi

Aerosol characterization was performed at the Hydrometeorological Observatory (HMO) Tiksi (71.36° N, 128.53° E) on the coast of the Laptev Sea in Northern Siberia from 2014 to 2016 (Popovicheva et al., 2019). FTIR analyses of functionalities and ionic and elemental components provided insight into the dust-source-influenced and season-dependent composition of Eastern Siberian Arctic aerosols. Analysis of wind and aerosol pollutant roses, with long-range transport analysis, helped identify the dust sources at Tiksi, demonstrating impacts from lower latitudes or local emissions from the adjacent urban Tiksi area. In warm periods, Na^+, Cl^-, K^+, and Mg^{2+} are found to be the major ions in the sea-salt aerosols, which are ubiquitous in the marine boundary

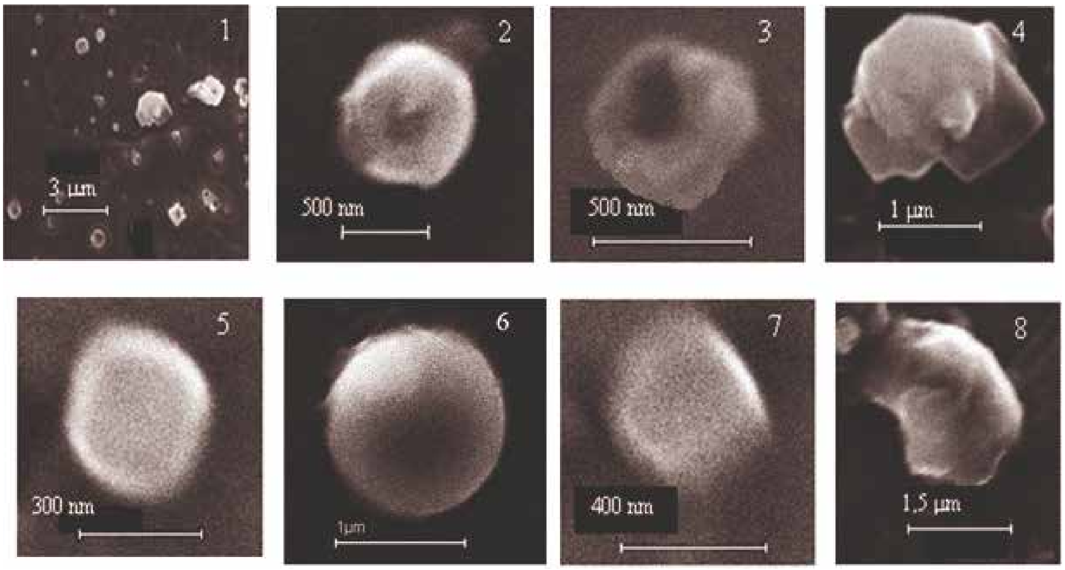

Figure 13(1). Panorama and representative micrographs of natural background aerosols at HMO Tiksi; (2) reacted sea salt NaCl in Group Na-rich; (3) reacted sylvite KCl and (4) sylvinite (nNaCl+mKCl) in Group K-rich; (5) an organic particle in Group Organic; (6) Fe and Ca aluminosilicate in Groups Al and Si-rich; (7) particle in Group Fe-rich and (8) CaCO3 in Group Ca-rich of natural aerosols on 27 September 2014. New unpublished results of the Popovicheva et al. (2019) investigation.

layer, significantly impacting the dust concentrations in the coastal region. However, Cl^- and K^+ could also originate from biomass burning during the warm period. Ammonium is mainly produced by the soil and emissions from biota and the ocean, commonly found in the form of (NH4)2SO4 and NH4Cl. Like sulfates, ammonium is influenced by regional sources of secondary aerosol formation and transport. Bands of CO (at 871 cm^{-1}) and NH (3247 cm^{-1}) indicate the dominance of dust carbonates in the natural inorganic aerosol. Also, S, Fe, Na, Al, Si, Ca, Cl, K, Ti, Mn, Co, Cu, Zn, Ga, Sr, Ba, Hg, and Pb were detected in the background dust, with sulfur displaying the highest concentration, followed by Fe, Na, and Al.

According to individual particle analyses by scanning electron microscopy (SEM) with energy-dispersive X-ray analysis (EDX), SEM-EDX, during the summer and fall, when the wind comes from the southwest and air masses arrive from the ocean, aerosol particles demonstrate a large variability in shapes, sizes, and composition (Fig. 13.1). Elemental composition is characterized by a dominant weight percentage of C, K, Na, Cl, O, and Fe. The distribution of elements over particles is heterogeneous, with greater amounts of Cl, K, and Na than C and O in around 50 % of particles, indicating that background aerosols contain soil, salts, minerals, and carbonaceous compounds. Group Na-rich with dominant Na and Cl is the most abundant at 32.5 %, originating from sea spray near the ocean (Fig. 13.2). The other particles contain small amounts of K, Ca, and Mg, from seawater impurities, as well as S, gained through acid displacement.

The second-most abundant group of individual particles is Group K-rich at 28.8 %, dominated by K and Cl, which are not of marine origin because the concentration of non-sea-salt (NSS) K^+ ions significantly exceeds K's possible concentration in sea-salt aerosol (SSA). Instead, Group K-rich particles are of natural mineral sylvite (KCl), transformed from genuine ones because the average weight ratio of was found to be equal to 3.3 – significantly higher than 1.1 – in sylvite (Fig. 13.3). KCl is water-soluble and may react in a polluted atmosphere. The variation of wt % of K versus Cl shows the lack of Cl compared to genuine sylvite and the formation of complex chemical compounds KxCly with various K and Cl atomic ratios. A representative micrograph of particles in Group K-rich demonstrates the reacted sylvite in Fig. 13.3, with slight damage by an electronic beam that can prove the presence of nitrates that were easily evaporated during EDX analyses. Parts of Groups Na-rich and K-rich, 20 % and 5 %, respectively, contain Na, Cl, and K and are assumed to be particles comprised of natural sylvite from alternative layers of halite and sylvite (nNaCl+mKCl) (Fig. 13.4). They have distinctive mineral shapes and are stable regarding evaporation by an electron beam. About 14.8 % of individual particles composed of Group Organic are made up almost exclusively of C and O. These particles are roughly spherical- or liquid-like-shaped (Fig. 13.5): around half contain only C and O, probably secondary organic aerosol from the biogenic source; the other half come from the seawater of the Arctic Ocean, as demonstrated by trace amounts of Na, Cl, and Mg. The oxidation of volatile organic compounds, humic-like substances (HULIS) in the marine environment, perhaps contributes to observed organic matter.

Finally, a few biogenic particles such as pollen, spores, algae, bacteria, and plant or insect remnants are found in natural aerosols, indicated by the specific shape and presence of K, S, Si, and Cl with C. The remaining groups – Fe-rich (14.4 %), Ca-rich (6.4 %), and Al-, Si-rich (3 %) – are representative of atmospheric dust derived from the Earth's crustal surface. Dust particles have solid irregular shapes of round and euhedral morphology. Analyses of the soil sample taken near the CAF showed stony material with minimal fertile ground cover. EDX analyses demonstrated 27.7 and 9.8 wt % of Si and Al, 46 and 10.6 wt % of O and Fe, respectively, and 3.5 wt % of K in various Fe, K aluminosilicates containing small additives (less than 1.7 wt %) of Na and Mg. Since the tiny dust of stony soil may be easily dispersed into the atmosphere by wind, we assume that Group Al, which is Si-rich, and around half of Group Fe-rich, are composed of Fe, K aluminosilicates (Fig. 13.6). Group Fe-rich containing Fe, Ni, Ca, and Si is composed of soil particles of iron–nickel ore (Fig. 13.7). Finally, Ca carbonates and sulfates with Ca, C, S, and O are found in Group Ca-rich (Fig. 13.8) according to the observations of Ca^{2+}, CO, and SO ions described above. With aluminosilicates, they are most likely windblown dust.

3.4.8 South America and Patagonia

Extending from 39 to 54° S, with an area of 600 000 km^2, dust activity (Fig. 14) from this large desert remains largely unknown. Some basic facts must be formally assessed, such as the locations of sources and geomorphological features associated with dust as well as the seasonality and frequency of the dust's activity. At present, limited surveys of dust activity (Crespi-Abril et al., 2017; Gaiero et al., 2003; Gassó and Torres, 2019) and case studies of individual sources exist (Gassó et al., 2010; Gassó and Stein, 2007; Johnson et al., 2011). Recently, a list of dust activities and sources in Tierra del Fuego (Cosentino et al., 2020) was published. Generally, dust sources in Patagonia are at topographic lows, and the river valleys (e.g., the Deseado and Santa Cruz rivers) (Coronato et al., 2017; Hernández et al., 2008) are associated with the late Holocene para-glacial environments. The most active modern source of dust is the drying of Colhué Huapi Lake (CHL) in central Patagonia (45.5° S, 68° W) (Montes et al., 2017) – a shallow lake with variable water levels exposed to intense evapotranspiration. An anthropogenic component appears to be linked to intense farming, oil prospection, and water supply to urban centers (Gaitán et al., 2009; Hernández et al., 2008; Mazzonia and Vazquez, 2009; Del Valle et al., 1998). CHL has been steadily shrinking (Llanos et al., 2016) and was dried up by the summer of 2020. Consequently, dust activity originating in CHL has increased with frequent blowouts large enough to be easily detected from space (Gassó and Torres, 2019).

Overall, satellite detection in the Patagonia region remains challenging. There are several difficulties in surveying dust activity in the area: obstructed views from space because of cloudiness, nighttime dust activity, and sparse population. Also, except for a few sources, the lack of recurrence in dust emission is a general feature of the desert: sources that were active during one season do not reactivate until two or three seasons later. A comprehensive and dedicated survey combining surface and space-based detection networks is needed for a better understanding.

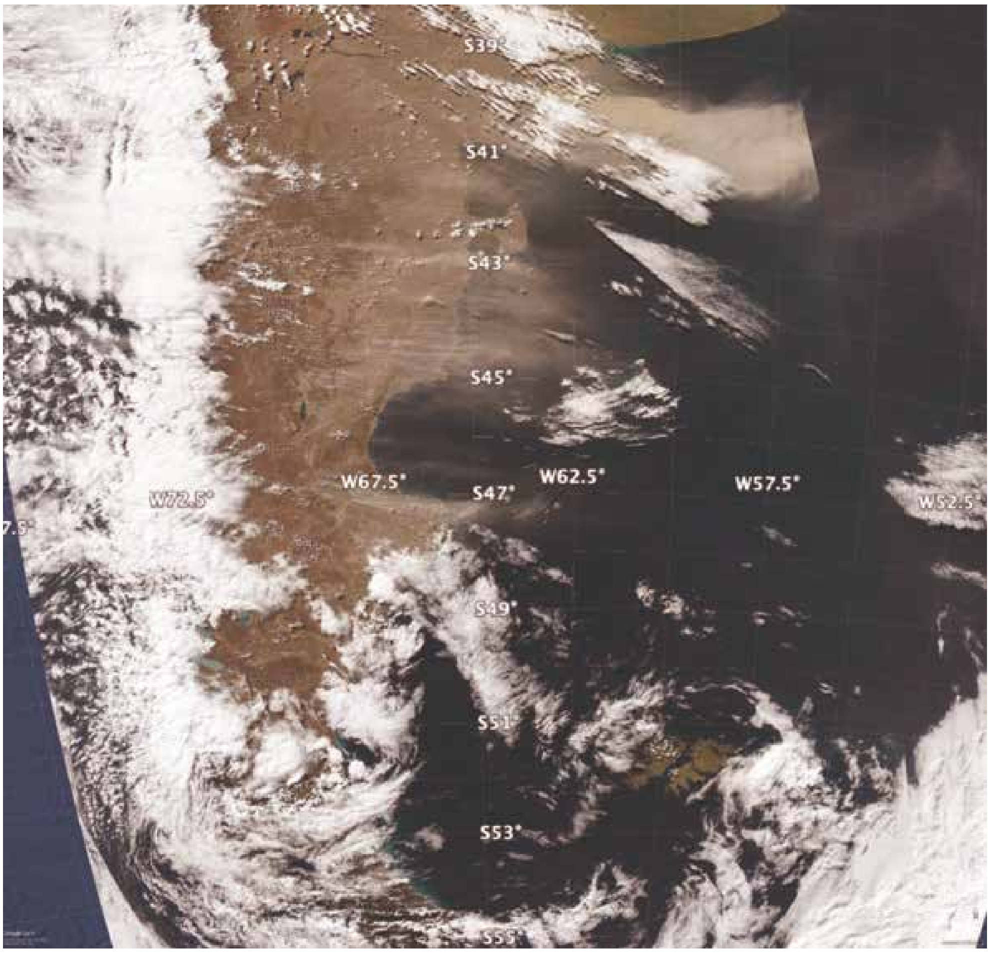

Figure 14. A dust event spanning the northern and central sections of the Patagonian Desert (+1000 km) on 28 March 2009. Events this large occur about once every 1 to 3 years. This event is typical in that it was triggered by the passage of a powerful low-pressure center commonly found at these high latitudes. Also, this event is singular in that a large portion of it is cloudless, enabling a direct view from space (most dust activity in Patagonia occurs under cloudy conditions). The thick dust cloud in the upper right corner is from an area used for cattle farming, which was undergoing a drought, whereas the active sources further south can be considered more naturally occurring with less anthropogenic interference. Source: NASA's Worldview interface image processed with Google Earth.

3.4.9 Svalbard

Evidence of the presence and activity of dust sources in Svalbard is only recent and quite rare. However, for example, dust storms in Longyearbyen are reported as a regular feature in fall. Dörnbrack et al. (2010) documented and characterized a strong dust storm in the Adventdalen valley – the center of Spitsbergen – in May 2004, using airborne lidar observations and mesoscale numerical modeling. In the same area, near Longyearbyen, dust emissions from an active coal mine were documented by Khan et al. (2017). Kandler et al. (2020) also reported Svalbard measurements in Longyearbyen in September 2017, with high iron and chlorite-like contributions in dust.

The accelerated ablation of Svalbard's glaciers (Schuler et al., 2020) and the increasing melt rate of permafrost are causing accelerated growth in periglacial and proglacial areas. The significance of the morphogenetic processes of deflation, denudation, and sediment transport on slopes and in river channels in glaciers' marginal zones is increasing (Zwoliński et al., 2013). Thus, these areas have become potential sources of dust and, as such, have been investigated for the physical and chemical properties of their sediments, regardless of the documented occurrences of the dust events these areas have experienced.

Fluvial, glaciofluvial, and weathering deposits at five different sites on the coastal plains near the Ny-Ålesund research station (78.92481° N, 11.92474° E), northwestern Spitsbergen, were investigated (Moroni et al., 2018). The mineralogical assemblage is characterized by dolomite, calcite, quartz, albite, and sheet silicates (vermiculite, muscovite, clinochlore) in variable amounts along with monazite, zircon, apatite, barite, iron sulfate, Fe, Ti, Cu, and Zn ores as accessory minerals. With a weight fraction of 4 % to 53 % of particles smaller than 100 µm, these deposits should be considered a valid dust source. However, the contribution is influenced by the modest extension of bare soils (less than 4 km^2) and the brief duration of the area's driest summer. The composition of the aerosols collected at the Gruvebadet lab near Ny-Ålesund during the summer–fall period reveals the presence of such a local dust component (Moroni et al., 2016, 2018). Further evidence of local dust sources in the Ny-Ålesund area and Brøgger Peninsula also results from the annual snowpack's chemical composition (Gallet et al., 2018; Jacobi et al., 2019). The contribution of local dust sources at this site is of secondary importance compared to that of long-range transport (Moroni et al., 2015, 2016, 2018; Conca et al., 2019).

A similar study was conducted on the loose sediment deposits in the neighborhood of the Polish Polar Station Hornsund (77.00180° N, 15.54057° E), southwestern Spitsbergen, where a belt of nearshore plains consisting of marine terraces and nival moraine bars, with bare surfaces available for mineral dust uplift from late spring, widely outcrop (Zwolinski et al., 2013). The mineralogical assemblage consists of quartz, alkali feldspar, plagioclase, dark mica, and chlorite, with zircon, apatite, monazite, iron sulfide, and iron ore as accessory minerals. The same assemblage was found in the aerosols and snow cover collected at the base station and the surrounding glaciers in the same period. This fact, along with the significant proportion of particles smaller than 50 µm in the loose sediment deposits, supports the prevalence of the local dust source in the melting season. Further evaluation of the impact of local dust sources was obtained from analyzing shallow and deep cores from different glaciers in the Hornsund area (Lewandowski et al., 2020; Spolaor et al., 2021). The results suggest that, for Spitsbergen glaciers with the summit close to (Ny-Ålesund) or below (Hornsund) the equilibrium line, the summer dust deposition from the local sources is predominant, affecting the glacier ice's chemical composition. However, the dating of monazite grains and the presence of magnetite and iron sulfide (magnetic susceptibility and SEM data, Lewandowski et al., 2020) also suggest the existence of regional wind transport from Nordaustlandet and Edgeøya, respectively. Further, a long-range component from northern Europe, Siberia, and, to a limited extent, Greenland, Iceland, and Alaska was also evident (Moroni et al., 2018; Crocchianti et al., 2021).

Recent estimations of dust load in central and southern Svalbard from different sources range from 4 g up to 4–5 kg m^{-2} (Rymer, 2018; Rymer et al., 2022), with the highest values in the Ebba Valley due to frequent dust storms in this area (Strzelecki and Long, 2020). Kavan et al. (2020a) found a negative correlation between deposition rate and altitude at Pyramiden (78.71060° N, 16.46059° E; western coast of Petuniabukta) and Ariekammen (77.00035° N, 15.53674° E; Hornsund area). The pattern was clear up to the altitude of approximately 300 m a.s.l., suggesting the influence of local sources in the lower levels of the atmosphere and long-range transport at higher altitudes. The lower values of the deposition rates found at Ariekammen were ascribed to the more maritime climate of the Hornsund region.

3.5 Climatic and environmental impacts of HLD

Climatic and environmental impacts of HLD on clouds and climate feedback, atmospheric chemistry, the marine environment, and cryosphere–atmosphere feedback (Fig. 15) were investigated with the help of topical literature surveys (Sect. 3.5.1–3.5.4). Direct radiative forcing of HLD (blocking sunlight) and comparison of dust and black carbon as SLCF in the cryosphere are included in the cryosphere–atmosphere feedback section.

The amounts of dust emission and deposition (Mt) of annual global and Arctic dust (data for 2017), as compared to anthropogenic and wildfire black carbon (Fig. 15), were studied using the SILAM model (Sofiev et al., 2015). The results of black carbon emissions presented in Fig. 15 were based on the Copernicus Atmosphere Monitoring Service (CAMS) global emission inventory version 4.2 and black carbon originating from wildfires from the SILAM IS4FIRES fire emission model, equaling 5 % of the total primary fire particulate matter (PM) emissions of the model. The IS4FIRES model is based on fires observed by the MODIS instrument on board the Terra and Aqua satellites.

3.5.1 Impacts of HLD on atmospheric chemistry

Icelandic dust, a specific HLD of volcanic origin, is constantly resuspended from the deserts. Regarding atmospheric chemistry, the most substantial impact comes from the particles in the 0.002 to 10 µm range, as they can be carried over more considerable distances (Finlayson-Pitts and Pitts, 1999). The Icelandic dust in the troposphere is not as addressed as the impact of desert dust. This HLD is very likely a long-range transporting carrier for many species adsorbed on its surface, which can act as a sink of trace gases and a subsequent platform for transferring taken-up species. Along with transport, adsorbed species may undergo different heterogeneous reactions that can lead to secondary compound formation. Such processes can influence the reactivity and balance of atmospheric species. Optical, hygroscopic, and, more generally, physicochemical properties of the HLD can change due to surface processes, implying atmospheric trace gases due to heterogeneous interactions (Usher et al., 2003). The consequences can be starkly different depending on the nature of atmospheric trace gases interacting with HLD. This section aims to illustrate the diversity of interactions between HLD and atmospheric trace gases to emphasize the various impacts of these aerosols on atmospheric physics and chemistry. In the case of ozone, if the direct heterogeneous interaction with dust does not play a major role in the atmospheric concentration decrease in the primary compound, surface processes are triggered, affecting the atmospheric budget of ozone. In the case of NO_2, heterogeneous processes on dust can significantly lead to HONO species forming, with direct impacts on gas-phase atmospheric reactivity. In the case of SO_2, beyond a complex reaction pathway, the heterogeneous process dually affects the budget of the taken-up species and the chemical and physical properties of the dust surface.

If the heterogeneous reaction of NO_2 with various types of atmospheric particles, e.g., salts, soot, mineral dust, and proxies, was addressed in the literature (George et al., 2015), the interaction of NO_2 with volcanic particles, typical HLD desert dust, under atmospheric conditions, has only been studied by Romanias et al. (2020). They explore the possible formation of a short-lifetime key atmospheric species, considered a trigger of numerous atmospheric processes: HONO, a precursor of OH radicals in the atmosphere. To that end, NO_2 uptake on Icelandic HLD is explored under various and contrasting atmospheric conditions. Despite the relatively close volcanic regions where the selected samples originate, uptake coefficients of NO_2 contrasted significantly with the dust location due to magmatic and morphological differences among samples. This point confirms that, concerning heterogeneous atmospheric chemistry, sample behavior can dramatically deviate from one class of dust to another, with physical and chemical characterizations of the samples remaining key intrinsic descriptors. Nonetheless, volcanic dust appears as effective NO_2 scavengers from the atmosphere. The interaction of NO_2 with

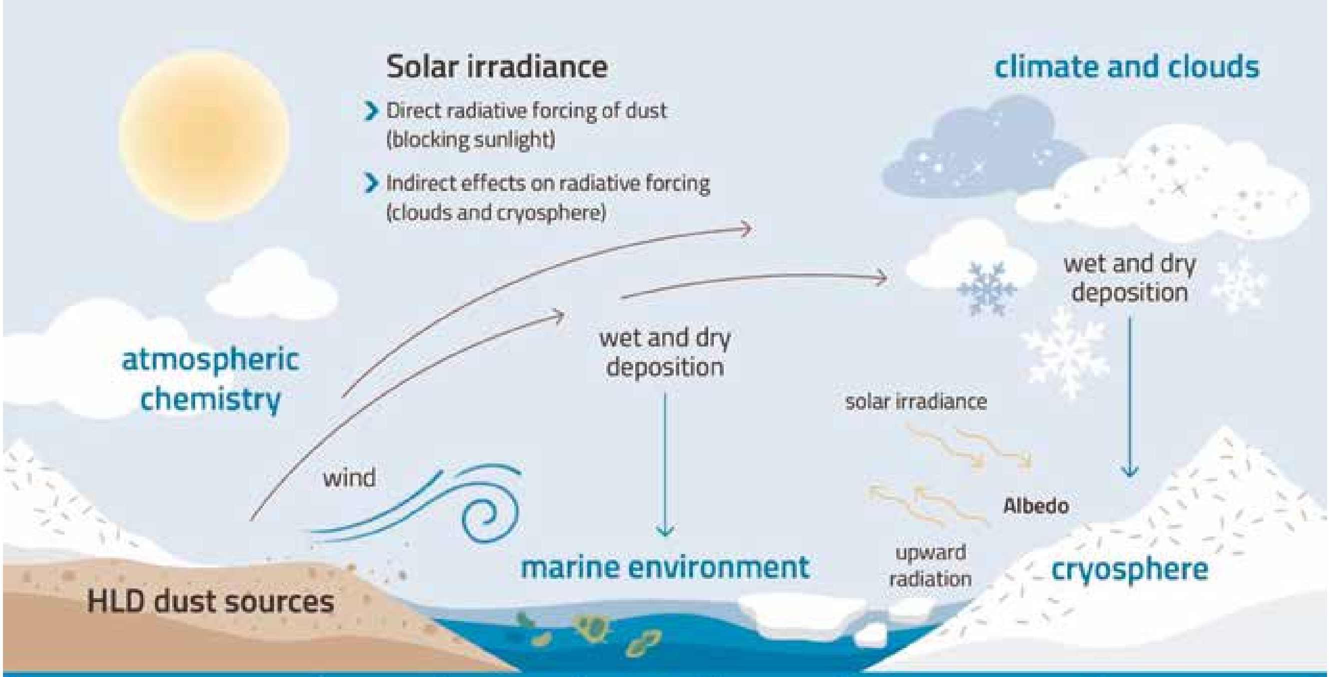

FLUX (MEGATONNES)	GLOBAL DUST < 30 µm	GLOBAL DUST < 2.5 µm	ARCTIC DUST < 30 µm	ARCTIC DUST < 2.5 µm	ANTHROPOGENIC BLACK CARBON (CAMS global emissions v4.2)	WILDFIRE BLACK CARBON (5 % of fire PM emissions)
Total emission	3000	160	30	1.6	4.6	1.9
Deposition on snow	32	5.2	4	0.21	0.18	0.029
Deposition on sea ice	5.5	0.59	3	0.17	0.009	0.008
Deposition on Arctic snow	7.6	1.1	4	0.19	0.027	0.013
Deposition on Arctic Sea ice	4.7	0.52	3	0.17	0.0055	0.0074
Deposition on sea surface	500	86	15	1.0	1.7	0.9
Deposition on Arctic Sea surface	21	2.4	12	0.68	0.035	0.063

Figure 15. Climatic and environmental impacts of HLD include direct radiative forcing (blocking sunlight), indirect radiative forcing (clouds and cryosphere), as well as effects on atmospheric chemistry and the marine environment. The amounts of dust emission and deposition (Mt) of global and Arctic dust, as compared to black carbon, were estimated using the SILAM model (Sofiev et al., 2015). The black carbon emissions are based on the CAMS global anthropogenic emission dataset v4.2, and the wildfire black carbon emissions are based on the IS4FIRES fire emission model, equaling 5 % of the total primary fire PM emissions of the model.

HLD is evidenced as a source of NO and, more interestingly, HONO, with kinetics and formation yields highly dependent on relative humidity. Higher HONO formation yields on volcanic samples are observed for relative humidity (RH) values exceeding 30 % RH. Heterogeneous construction of HONO from NO_2 interaction with Icelandic dust is estimated as atmospherically significant under volcanic eruptions or, more frequently in Iceland, during typical volcanic dust storms. This leads to HONO formation rates of up to 10 pptV h^{-1}, which can significantly influence the regional atmosphere's oxidative capacity. The experimental determination of NO_2 uptake coefficient γ allows inclusion of such processes in atmospheric modeling, improving their representativeness.

A transient uptake of SO_2 – an initially important uptake of SO_2 that is progressively reduced – leads to low steady-state uptake coefficients of SO2 after several hours of exposure in the ranges of 10^{-9} to 10^{-8}. The surface coverages were in the range of 1014–1016 molec. cm^{-2} using the total surface area or the geometric surface area of aerosols, respectively (Urupina et al., 2019). Zhu et al. (2020) estimated that around 43 % more volcanic sulfur is removed from the stratosphere within months due to SO_2 heterogeneous chemistry on volcanic particles than without. Concomitantly with SO_2 uptake, sulfites and sulfates are monitored on the surface of volcanic dust, with sulfates being the final oxidation product, attesting to SO_2 surface reaction. Through surface hydroxyl groups, the dust surface's chemical composition plays a crucial role in converting SO_2 to sulfites, as evidenced experimentally using lab-scale but atmospherically relevant experimental setups (Urupina et al., 2019). This provides original insights into the kinetics and mechanism of SO_2 uptake and the transformation on volcanic material under simulated atmospheric conditions, bringing an accurate perspective on SO_2 heterogeneous sinks in the atmosphere on the HLD surface. The model simulations of Zhu et al. (2020) suggested that the transformation of SO_2 on such particles plays a key role in the stratosphere's sulfate content. Interestingly, this transformation and accumulation of sulfates on the surface of particles could turn the unreactive ozone material reactive, especially in the stratosphere, where volcanic particles have longevity.

The case of SO_2 uptake points to the aging of the HLD surface with subsequent impacts on its chemical (e.g., hygroscopicity) and physical (e.g., optical) properties. Changes in hygroscopic properties can correlate with HLD's erratic behavior to act as cloud- or ice-nucleating particles, depending on their interactions with atmospheric gases. Similarly, sulfate and sulfuric acid's high surface coverage for volcanic dust, as reported by Urupina et al. (2019), questions the variability of the HLD refractive index and the impact on remote sensing of fresh versus aged dust.

3.5.2 Impacts of HLD on clouds and cloud-climate feedback

Clouds across the mid and high latitudes are of first-order importance. Climate and HLDs may play a first-order but highly uncertain role in defining their properties through the initiation of ice formation. Clouds frequently persist in a supercooled state. However, even a few droplets converting to ice crystals through heterogeneous freezing can lead to microphysical processes that dramatically reduce a cloud's liquid water content, reducing its albedo and exposing the surface underneath (Murray et al., 2021; Tan and Storelvmo, 2019). Only a small subset of atmospheric aerosol can nucleate ice; concentrations of around only one ice-nucleating particle (INP) per liter of air active at the cloud temperature can dramatically alter cloud albedo. In contrast, the concentrations of aerosol particles capable of serving as cloud condensation nuclei (CCN) are orders of magnitude larger. Hence, dust particles at the high latitudes will rarely exist in high enough concentrations to dramatically impact cloud droplet numbers by providing additional CCN. However, HLD has been shown to serve as an effective INP in sufficient concentrations to potentially impact mixed-phase clouds (Sanchez-Marroquin et al., 2020). Ice formation's role in climate projections depends on the clouds' locations. In the following paragraphs, we discuss two distinct classes of clouds that may be influenced by HLD particles serving as INPs.

For boundary layer clouds over oceans between approximately 45 and 70°, the amount of ice versus supercooled water, as well as albedo, is critical for the global climate (Vergara-Temprado et al., 2018; Bodas-Salcedo et al., 2014). These clouds are where substantial solar insolation exists, and the contrast between a high-albedo cloud and a dark ocean surface is significant. Hence, these clouds are implicated in the cloud-phase feedback, where water replaces ice, increasing their albedo as the world warms with increased carbon dioxide (Storelvmo et al., 2015). This feedback's uncertainty is very high, with the temperature rise associated with a doubling of carbon dioxide, rising from around 4 K to well above 5 K simply by increasing the amount of supercooled water in clouds in the current climate (Frey and Kay, 2018). Hence, understanding the sources of INPs at the high latitudes, including HLDs, is critical to understanding these climate-relevant issues (Murray et al., 2021).

The second group of clouds is those occurring at high latitudes. For example, in the central Arctic, mixed-phase clouds play a critical role in the local Arctic climate and the phenomenon of Arctic amplification. In a corollary to the cloud-phase feedback, water replacing ice leads to more downward longwave radiation, resulting in positive feedback (i.e., amplification) (Tan et al., 2016). Hence, the phase of clouds and therefore the INP population in clouds in the present Arctic atmosphere are key to defining this feedback's strength. Moreover, any changes in the INP population with a changing climate may also provide feedback on cloud properties (Murray et al., 2021).

Given the apparent importance of INPs in defining cloud properties and climate feedback, surprisingly little is known about the ice-nucleating properties of HLDs. Mineral dust from low-latitude sources is one of the most important types of atmospheric INPs in clouds below approximately −15 °C around the globe because of its relatively high ice-nucleating activity and abundance in the atmosphere (Murray et al., 2012). A handful of papers have also identified HLDs as significant contributors to the Arctic's INP population (Irish et al., 2019; Sanchez-Marroquin et al., 2020; Tobo et al., 2019; Šantl-Temkiv et al., 2019). HLDs may differ in their ice-nucleating ability from LLDs for several reasons. Firstly, the HLDs from glacial valleys, for example, are often richer in primary minerals (olivines, pyroxenes, feldspars, and amphiboles) and less rich in clays compared to LLDs. This is crucial because K-rich feldspars are known for their exceptional ice-nucleating ability, whereas clays are much less active (Harrison et al., 2019; Atkinson et al., 2013). Secondly, the most prominent LLD sources, like those in Africa, are abiotic (Price et al., 2018), whereas it has been found that HLDs can be associated with highly effective biogenic ice-nucleating material (Tobo et al., 2019; Šantl-Temkiv et al., 2019). The inclusion of biological ice-nucleating material, which can be ice-active at temperatures much higher than −15 °C, may mean that these dust sources have a disproportionately greater impact on cloud glaciation and climate than their low-latitude counterparts. Much more research is needed to define and understand the ice-nucleating ability of these HLD sources.

3.5.3 Impacts of HLD on the marine environment

Mineral dust particles are a source of essential nutrients such as P and Fe to the ocean ecosystems (e.g., Jickells et al., 2005; Mahowald et al., 2005; Stockdale et al., 2016). Dust deposition onto the ocean's surface can stimulate primary productivity and enhance carbon uptake, indirectly affecting the climate (e.g., Jickells and Moore, 2015; Mahowald, 2011). The extent of these impacts primarily depends on the dust deposition fluxes, their chemical properties, and the nutrients of (co)limitation patterns in the ocean waters (e.g., Boyd et al., 2007, 2010; Kanakidou et al., 2018; Mills et al., 2004; Moore et al., 2013; Shi et al., 2012; Stockdale et al., 2016). The Arctic Ocean is often nitrogen-limited (von Friesen and Riemann, 2020).

The aerosol fractional Fe solubility (%) is defined as the ratio of dissolved Fe (in the filtrate, which has passed through 0.2 or 0.45 µm pore size filters) to the total Fe in the bulk aerosol (e.g., Meskhidze et al., 2019; Shi et al., 2012). This is typically used to indicate the fraction of Fe, which is likely to be bio-accessible for marine ecosystems (Meskhidze et al., 2019).

Sub-Arctic oceans are Fe-limited or seasonally Fe-limited. Fe limits primary productivity in the sub-Arctic Pacific Ocean (Martin and Fitzwater, 1988). The atmospheric Fe deposition in the Gulf of Alaska is dominated by dust transported from glacial sediments from the Gulf of Alaska coastline (Crusius et al., 2011), with relatively high fractional Fe solubility – around 1.4 % (Schroth et al., 2017). Although the upwelling of deep water is the major source of dissolved Fe, the atmospheric flux of dissolved Fe to the Gulf of Alaska's surface water is comparable to the Fe flux from eddies of coastal origin (Crusius et al., 2011). The magnitude of glacial dust's deposition to the Gulf of Alaska varies significantly depending on the regional weather conditions. However, the extent of its impacts is still unclear (Schroth et al., 2017). Currently, the spatial resolution of global dust models is too low to accurately reproduce Alaskan dust flux, generated by anomalous offshore winds and channeled through mountains (Crusius, 2021). Recently, Crusius (2021) determined dissolved Fe inventories based on time series of dissolved Fe and particulate Fe concentrations from Ocean Station Papa in the central Gulf of Alaska, including measurements from September 1997 to February 1999. The analysis showed 33 %–70 % increases in dissolved Fe inventories between September and February of successive years. These increases were possibly linked to dust fluxes from the Alaskan coastline – known to occur mostly in fall (Crusius et al., 2011; Schroth et al., 2017). These new results support the importance of atmospheric Fe's contribution, although more work is needed to confirm the sources of dissolved Fe in the Gulf of Alaska.

The sub-Arctic North Atlantic Ocean is seasonally Fe-limited (Nielsdóttir et al., 2009; Ryan-Keogh et al., 2013). Natural dust from Iceland largely contributes to the atmospheric dust deposition in the North Atlantic Ocean (Bullard, 2016). Icelandic dust originates from volcanic sediments and has a relatively high total Fe content – about 10 % (e.g., Arnalds et al., 2014; Baldo et al., 2020). The estimated total Fe deposition from Icelandic dust to the ocean's surface is 0.56–1.38 Mt yr−1 (Arnalds et al., 2014). The initial Fe solubility observed in dust samples from Icelandic dust hotspots ranges from 0.08 % to 0.6 % – comparable to that of mineral dust from low-latitude regions such as northern Africa, while the fractional Fe solubility at low pH (i.e., 2) is significantly higher than typical LLD (up to 30 %) (Baldo et al., 2020). Achterberg et al. (2018) argued that deepwater mixing is the dominant source of Fe in the sub-Arctic North Atlantic Ocean's surface water, which is up to 10 times higher than the Fe supply by atmospheric Fe deposition. However, during the 2010 eruption of the Icelandic volcano Eyjafjallajökull, Achterberg et al. (2013) observed elevated dissolved Fe concentration and nitrate depletion in the Iceland Basin, followed by an early spring bloom. They measured an initial fractional Fe solubility of 0.04 %–0.14 % for Icelandic ash, which is below or towards the lower end of the range of values estimated for Icelandic dust (0.08 %–0.6 %) (Baldo et al., 2020). High deposition flux (Arnalds et al., 2016) and higher Fe solubility of Icelandic dust (Baldo et al., 2020) suggest that they may impact Fe biogeochemistry and primary productivity in the surface ocean. However, more research is needed to confirm this.

The Southern Ocean is known to be Fe-limited (Moore et al., 2013). Major atmospheric dust sources include, for example, Australia, southern South America, and southern Africa (e.g., Ito and Kok, 2017). Contribution from local sources in Antarctica is also observed (e.g., Chewings et al., 2014; Winton et al., 2014, 2016b). Winton et al. (2016a) reported a background fractional Fe solubility from Antarctic dust sources of 0.7 % – similar to the upper limit of Fe solubilities observed in Icelandic dust (Baldo et al., 2020). However, mineral dust originating from glacial sediments from the Gulf of Alaska coastline showed higher Fe solubilities (1.4 %) (Schroth et al., 2017) – likely due to the different mineralogy and Fe speciation in the samples. The various methods used to determine the fractional Fe solubility in these studies may also contribute to this difference (Perron et al., 2020).

Although the upwelling of deep water is a major source of dissolved Fe, the atmospheric deposition of dissolved Fe can locally contribute to the phytoplankton bloom (Winton et al., 2014). However, evidence exists that increased dust flux enhanced primary production in the Southern Ocean in the last glacial age (Martínez-García et al., 2014). The Ross Sea is a continental shelf region around Antarctica and a highly biologically productive area in the Southern Ocean, which has important implications for global carbon sequestration (e.g., Arrigo et al., 2008; Arrigo and Van Dijken, 2007). In the Ross Sea, an additional Fe supply is required to sustain the intense phytoplankton bloom during the austral summer (Tagliabue and Arrigo, 2005). Measurements conducted on snow pits and surface snow samples showed that local Antarctic dust contributes to Fe deposition. However, this contribution is only a minor component of the total Fe supply to the Ross Sea, with most being supplied by the upwelling of deep water (Winton et al., 2014, 2016a, b).

In the polar regions, atmospheric dust is mostly delivered to the sea ice, where melting and freezing cycles (ice processing) can enhance the formation of relatively more soluble phases of Fe oxide–hydroxide minerals such as ferrihydrite. This formation can increase the flux of atmospheric dissolved Fe to the ocean (Raiswell et al., 2016).

3.5.4 HLD impacts on the cryosphere and cryosphere–atmosphere feedback

The cryosphere is the frozen water part of the Earth system, including sea, lake, and river ice, snow cover, glaciers, ice caps, and ice sheets, and permafrost and frozen ground. These components play a crucial role in the Earth's climate (IPCC, 2019). Temperatures in fragile areas, such as the pristine polar regions, have been increasing at twice the global average; the highest increase in the temperature on the coldest days – up to 3 times the rate of global warming – is projected for the Arctic (IPCC, 2021). Warming in vulnerable cold climate land areas causes glacier retreat, permafrost thaw, and a decrease in snow cover extent (IPCC, 2019). Consequently, potential HLD sources, such as glacial sediments, can increase (e.g., Nagatsuka et al., 2021). When dust is long-range-transported and wet- or dry-deposited or windblown from local dust sources, the ice and snow albedo decreases and influences glacier melt (e.g., Boy et al., 2019) via the positive ice-albedo feedback mechanism (AMAP, 2015; Flanner et al., 2007; Gardner and Sharp, 2010; IPCC, 2019). Cryospheric melt processes are controlled by many environmental factors (IPCC, 2019), such as solar irradiance, ambient temperature, and precipitation (e.g., Meinander et al., 2013, 2014; Mori et al., 2019). Kylling et al. (2018) used dust load estimates from Groot Zwaaftink et al. (2016) (using an LLD complex refractive index for HLD) to quantify the mineral dust instantaneous radiative forcing (IRF) in the Arctic for 2012. They found that the annual-mean top-of-the-atmosphere IRF (0.225 W m^{-2}) had the largest contributions from dust transported from Asia south of 60° N and Africa; HLD (>60° N) sources contributed about 39 % to the top-of-the-atmosphere IRF. However, HLD had a larger impact (1 to 2 orders of magnitude) on IRF per emitted kilogram of dust than low-latitude sources. They also reported that mineral dust deposited on snow accounted for nearly all the bottom-of-the-atmosphere IRF (0.135 W m^{-2}), with over half caused by dust from high-latitude sources north of 60° N.

For snow and ice (glacier) surface radiation balance, the net energy flux EN is due to differences between downward (↓) and upward (↑) non-thermal shortwave (SW) and thermal longwave (LW) radiative fluxes. This is most critically influenced by the surface characteristics of the bi-hemispherical reflectance (BHR), i.e., albedo (Manninen et al., 2021). Therefore, melt is also controlled by dark impurities in snow and ice (IPCC, 2019). Black carbon (BC) is, climactically, the most significant and best-studied dark light-absorbing aerosol particle in snow (e.g., Bond et al., 2013; Dang et al., 2017; Evangeliou et al., 2018; Flanner et al., 2007; Forsström et al., 2013; Mori et al., 2019; Meinander et al., 2020a, b). Radiation-transfer (RT) calculations indicate that seemingly small amounts of BC in snow, on the order of 10–100 parts per billion by mass (ppb), decrease its albedo by 1 %–5 % (Hadley and Kirchtetter, 2012). BC has been shown to enhance snowmelt (AMAP, 2015; Bond et al., 2013; IPCC, 2019). Other light-absorbing particles include organic carbon (OC, including brown carbon – BrC) and dust. Also, blooms of pigmented glacier ice algae can lower ice albedo and accelerate surface melting (McCutcheon et al., 2021), showing a direct link between mineral phosphorus in surface ice and glacier ice algal biomass. This indicates that nutrients from mineral dust likely drive glacier ice algal growth, identifying mineral dust as a secondary control on ice sheet melting. Some Icelandic dust sources have particles almost as black as black carbon by the reflectivity properties when measured as bulk material or on snow and ice surfaces (Peltoniemi et al., 2015). Unlike BC, Icelandic dust has been shown to melt snow quicker in small amounts and to insulate and prevent melt in larger amounts (e.g., Dragosics et al., 2015; Möller et al., 2016; Boy et al., 2019). Changes related to permafrost thaw and snowmelt and ice melt, including disappearing glaciers, rising sea levels, and drinking water shortages, are among the most serious global threats (IPCC, 2019). Water availability is vital in regions where crops depend most on snowmelt water resources (Qin et al., 2020). Snow is also essential in the catchment areas (i.e., areas supplying watercourses) and for many snow-dependent organisms, including plants, animals, and microbes (Zhu et al., 2019). Melt can also run hydroelectric power plants that supply electricity (e.g., Lappalainen et al., 2022). This all highlights the importance of investigations and continuous assessment of the temporal and spatial significance and contribution of different light-absorbing impurities in enhancing or initiating cryospheric melt in the changing climate.

3.6. Understanding the HLD sources

The HLD results are further discussed from the perspective of HLD SI values, comparison to available HLD information on the various regions, geological perspective on sources, focusing on a gap identified in HLD observations for the central part of the East European Plain and dust particle properties, and local HLD sources and long-range transport of dust with the focus on results from the observations in Svalbard and Antarctica.

3.6.1. SI values

Most of the HLD study sites agree with UNCCD G-SDS-SBM SI values of the highest dust-productive areas, identifying an environment from a given location within a distance of ≤0.1°. Surfaces with higher maximum SI include a significant portion of the land surface in HLD regions. In the southern HLD region, an annual change in SI exists. However, approximately half the dust-productive surface stays exposed to wind erosion during the year. In the northern HLD region, SI intensity varies significantly with the weather. High values of SI may not always coincide with high surface winds, meaning high values may exist but not necessarily result in a dust storm. In case emissions occur, dust may remain undetected because of the absence of ground observations over most of the HLD region and frequent cloud cover over airborne dust, obscuring remotely sensed imagery.

Based on the SI values, the East Greenland sources in this study (nos. 58–64 in Fig. 1) are seasonal, meaning their SI minimum value is zero. Conversely, the West Greenland sources are not necessarily seasonal since their SI minimum values are somewhat reduced (but not to zero). However, the term "seasonal" regarding the SI values means that the soil surface conditions are suitable for dust emissions, although that does not mean emissions will happen. Similarly, the seasonality of all sources in this collection can be further studied.

When the newly identified sources are close together, this might indicate that they are part of the larger dust source area, like South Iceland, West Greenland, or East Greenland. The discovered sources could be considered to represent the hotspot locations, i.e., the most emissive or active locations, of those dust-productive areas. Simultaneously, however, the land surface and soil composition can be very complex and spatially variable and the identification of single sources justified until the source characteristics and particle properties have been characterized in more detail. For example, Icelandic sources have shown that each source, even proximate ones, may have different particle size distributions and optical properties. The results (Fig. 2) suggest two northern HLD belts. The first HLD belt would extend at 50–58° N in Eurasia and 50–55° N in Canada and the second dust belt at >60° N in Eurasia and >58° N in Canada, with a "no-dust" belt between the HLD and LLD belts (except for British Columbia).

Uncertainties about the detected locations of the HLD sources and G-SDS-SBM SI values arise from the methodology for determining HLD source locations. These locations are ad hoc location sources from satellite images of dust plumes; other kinds of airborne dust observations may introduce some errors in location estimation compared to on-site land surface monitoring and the precision of available data locations. The resolution of

G-SDS-SBM may be too coarse for small-scale source areas (in this case, the representative grid point value shows a reduced SI value since it represents the whole grid box). However, the in-point (at location) values are also given maximum values in the area around the given location (one point distance: 30 arcsec, 0.1°, 0.5°, and 1° distance). Values of SI above 0.9 have topsoil potential for SDS production in the top 10 % of grid boxes, with some emission potential in G-SDS-SBM (or in the top 10 % of most dust-productive surfaces globally in case of favorable weather conditions), above 0.8 in the top 20 %, above 0.7 in the top 30 %, and so forth. Factors reducing source function value or topsoil dust productivity are sparse vegetation, coarser soil texture, higher moisture, and temperatures near the freezing point. Uncertainties in the methodology for deriving G-SDS-SBM arise from the quality and resolution of available global datasets and the determination of thresholds for EVI in defining bare land fraction (primarily for brown grassland, which may appear as potential dust sources but with lower productivity). Surfaces with low SI values in favorable conditions for dust emission, in case of high winds, may produce some blowing dust events; sources with higher values of SI may generate dust storms. Real dust production from sources depends on high winds occurring while SI is high.

Forty-nine locations were in the northern HLD region (47 according to the HLD definition by Bullard et al., 2016, except for 2: nos. 8 and 48, with latitudes 47.7 and 47.6° N, respectively), while 15 were in the southern HLD region, including 4 south of 60° S, where the values of SI are not provided. In the northern HLD region, higher dust-productive potential (SI 0.5) has 17 of 49 marked locations at the HLD source marking the exact location. Also, 38 sites are where a distance from a mark point (D) is equal to or less than 0.1° (Supplement Table S4). Very high dust productivity, with SI 0.7, has 33 locations within D 0.1° and 42 and 46 within 0.5 and 1°, respectively. The highest dust-productive potential, with SI 0.9°, has 27 locations within D 0.1° and 39 and 44 within 0.5 and 1°, respectively. One point has the highest SI value with less than 0.5° and five less than 0.9° away when considering the largest environment of the HLD source mark. Three HLD source region marks are in the sea, so their source values are marked as −99 (undefined). In the southern HLD region, 11 locations are considered (situated between 40 and 60° S). Seven sources have very high dust productivity with SI 0.7 where the HLD source marker is; three more have SI 0.7° in the area of the source marker with D 0.1°. The highest dust-productive potential, with SI 0.9°, has seven sources in the area with the source marker with D 0.1° and three more in the area with D 0.5°. The source maximum and minimum intensities in these southern HLD regions differ much less than in the northern HLD region.

As a summary, our modeling results on the spatial distribution of the dust sources (Fig. 2) showed evidence supporting a northern HLD belt, defined as the area north of 50° N, where we distinguish the following HLD-source areas: (a) "transitional HLD-source area", which extends at latitudes 50–58° N in Eurasia and 50–55° N in Canada, and (b) "cold HLD-source area", which includes areas north of 60° N in Eurasia and north of 58° N in Canada, with currently a "no-dust source" area between the HLD and LLD belts (except for British Columbia).

3.6.2 Comparison of various regions

For the HLD sources identified and included in our collection, the available information varied from detailed characterizations to the first satellite observations, waiting to be complemented with measurement data. Model output of dust transport can provide valuable additional information. The sources are at the northern and southern high latitudes and include a variety of environments. Particle properties, such as particle size distributions, have been determined for only some of the identified HLD sources. For example, our study's many Iceland southern coast sources have not had any characterization done. Previous results on the known sources in Iceland's southern coast region show that the particle size distributions vary substantially from location to location. No assumptions can be made based on characterization in one place.

For Iceland seasonality, the correlation of SILAM modeled and measured PM10 and PM2.5 total aerosol concentration in Iceland is low, especially in 2018, which can mainly be explained by the measurement locations being far from the source locations and showing the effects of road dust rather than long-range-transported dust. Also, the Reykjavik and Akureyri dust inventories are unrepresentative due to the challenge of fitting the modeled long-range-transported dust emissions 695 to the measurement data within the 0.1° model resolution. Near Reykjavik, dust emissions, e.g., from Landeyjasandur, may contribute to the measured dust concentrations. However, the 0.1° resolution of the model is too scarce to simulate them.

The ends of summer and fall (October) are the seasons for dust activity in Greenland. For example, on 19 October 2021, there was significant dust activity in West Greenland: several glacial valleys emitted dust along the 700 km-long coast. During that dust event was a good Sentinel overpass showing a long narrow valley with a great deal of haze (dust) suspended (appearing as fuzziness in the image) (Gassó, 2021b). As far as we know, no previous observations for this source exist. Greenland's HLD sources (nos. 53–58 of Fig. 1) from its western coast are considered new and identified here using satellite observations. Currently, further knowledge on the recurrence and area of the emission source is lacking. It is probable that these Greenland HLD sources from the western coast have been unidentified due to frequent cloudy conditions. The representation of dust sources in modeling approaches requires information on the location, soil characteristics, and temporal changes. A detailed specification of the geographic distribution of potential dust sources and their physical (e.g., particle size distribution, optics) and mineralogical/chemical (e.g., mineral fractions, chemical composition) properties is critical to accurately parameterize dust emission's potential in numerical dust models. Various methods exist to detect new sources; remote sensing is one of the most powerful tools, as demonstrated on Iceland's southern coast and Greenland's western and eastern coasts.

The central part of the East European Plain, with the wide occurrence of silty soils derived from loess-like sediments and reduced natural vegetation, is a potential aeolian dust source (Bullard et al., 2011; Sweeney and Manson, 2013). However, this region currently lacks observations on dust lifting and transport. Therefore, this region was not included in our collection of HLD sources. The gap for observations in the central part of the East

European Plain for potential HLD source updates is filled here with new data in Figs. S1–S4 on the partitioning of elements among the five particle size fractions separated from the natural soils of a rural area 100 km southwest of Moscow (Fig. S1). The study area (55°12′–55°13′ N, 36°21′–36°22′ E) belongs to the southeastern part of the Smolensk–Moscow Upland (314 m a.s.l.), representing a marginal area of the Middle Pleistocene (MIS 6) glaciation with moraine topography modified by post-glacial erosional and fluvial processes. The major soil reference group is Retisol (IUSS Working Group WRB, 2015), developed on the loess-like loam. About 50 % of the soils in the interfluve area were subjected to arable farming. A new and unpublished independent dataset on 33 elements in topsoil horizons was obtained with a higher-accuracy ICP-MS/AES analysis (compared to the DC-ARC-AES dataset of Samonova and Aseyeva, 2020).

Additional dust sources with massive dust storms causing severe traffic disruption have been documented outside the dust belt at higher latitudes. These sources were mainly arable fields, such as those in Germany and Poland, as well as Montana and Washington State (in the US) (Hojan et al., 2019).

3.6.3 A geological perspective on HLD sources and particle properties

Dust sources involve very different formations and geological environments, each leaving its own imprint on the sediments. Thus, the geomorphological, sedimentological, petrological, and geochemical study of the loose sedimentary formations in the source areas provides information on the origin and provenance of dust when it is transported out or far away. These types of studies – quite typical for Saharan dust – are not so well-established in the case of HLD sources. These territories are not all easily accessible. Even when they are, the time may not coincide with the dust production and/or dust emission period, which may be one reason for this missing source area characterization.

Geomorphological studies cover a wide range of subjects and topics, from characterizing specific dust sources (e.g., Arnalds et al., 2016; Bullard and Mockford, 2018; Bertran et al., 2021) to analyzing processes (e.g., Bullard and Austin, 2011; Hedding et al., 2015; Wolfe, 2020) to landform evolution (Heindel et al., 2017). Sedimentological studies on dust sources focus on the particles' morphological characteristics and textural details of the loose sediment formations. The size, shape, and surface characteristics of the particles result from morphogenetic processes. As such, these particles say a great deal about the source areas. Furthermore, the particles' size and shape influence their lifting and transport capacity and, finally, the distance they can reach from their site of origin. This applies to the studies of the properties of volcaniclastic dust sources in Iceland (e.g., Butwin et al., 2020; Richards-Thomas et al., 2021). From the petrological and geochemical perspective, the panorama is even wider and more varied. Save a few (e.g., Baratoux et al., 2011; Moroni et al., 2018), most studies are not aimed at studying dust sources but comprise different targets involving the parental soils (e.g., Antcibor et al., 2014; Brédoire et al., 2016). While providing information on the (possible) source areas for dust, these latter studies are not explicitly aimed at studying dust sources, so they are not functional for that purpose. Specific survey and sampling activities by a team of experts would be required to address all aspects of dust sources and properties adequately. Thus, obtaining a database as rich and articulated as possible on the particles' physicochemical properties within dust would be feasible, providing the ability to predict dust behavior within the aerosols and understand medium- and long-range transport phenomena present. A further aspect regarding dust sources and properties is the evolution of the particles' physicochemical properties due to the lifting and transport mechanisms. The aerosols must be sampled in different places at different distances from the source. However, this approach is complicated by the air masses mixing during transport, requiring a deep investigation of air mass back-trajectories. Conversely, treating the soils in the lab by re-suspending and sampling them using impactors at well-defined cut-off size ranges can be very advantageous. Such work has been carried out on Australian soils and southern African soils (Gili et al., 2021) to study the dust sources in Antarctica, which is now underway in Iceland (Beatrice Moroni, personal communication, 2021).

3.6.4 Local HLD sources versus long-range-transported dust: discussing Svalbard and Antarctica

The same areas of dust lifting can also be deposition sites when particles leaving their respective source regions are deposited there after prolonged transport pathways. The extent of the contribution of local and long-range sources may vary during the year depending on the type of atmospheric circulation and state of the exposed surfaces, particularly the presence of bare deglaciated soils. Such is the case of Svalbard, where the local dust sources prevail over the long-range ones, especially in summer; the contrary occurs in the rest of the year (Moroni et al., 2016; Spolaor et al., 2021). Conversely, and always in Spitsbergen, the types of contributions – local and long-range – may also depend on the altitude due to the stratified structure of the lower atmosphere frequently found at high latitudes (e.g., Moroni et al., 2015; Kavan et al., 2020a).

Investigating the physicochemical properties, and possibly estimating their contributions at different times of the year, is key to identifying the source regions of dust. For example, in Spitsbergen's case, the potential source contribution function (PSCF) analysis of aerosol samples taken in Ny-Ålesund clearly identified four different HLD sources in Eurasia, Greenland, Arctic–Alaska, and Iceland (Crocchianti et al., 2021). Conversely, chemical–mineralogical investigation and single-particle analysis recognized and estimated Icelandic dust's contribution to Ny-Ålesund (Moroni et al., 2018).

Kandler et al. (2020) collected dry dust deposition near sources in northwestern Africa and central Asia, on Svalbard, and at three locations of the African outflow region and studied particle sizes and composition. Their results showed low temporal variation in estimated optical properties for each site but considerable differences among the African, central Asian, and Arctic regions. An insignificant difference was found between the K-feldspar relative abundances, indicating comparable ice nucleation abilities. The mixing state between calcium and iron compounds differed for near-source and transport regimes, potentially and partially due to size-sorting effects. Thus, in certain situations (high acid availability, limited time), atmospheric processing of the dust is ex-

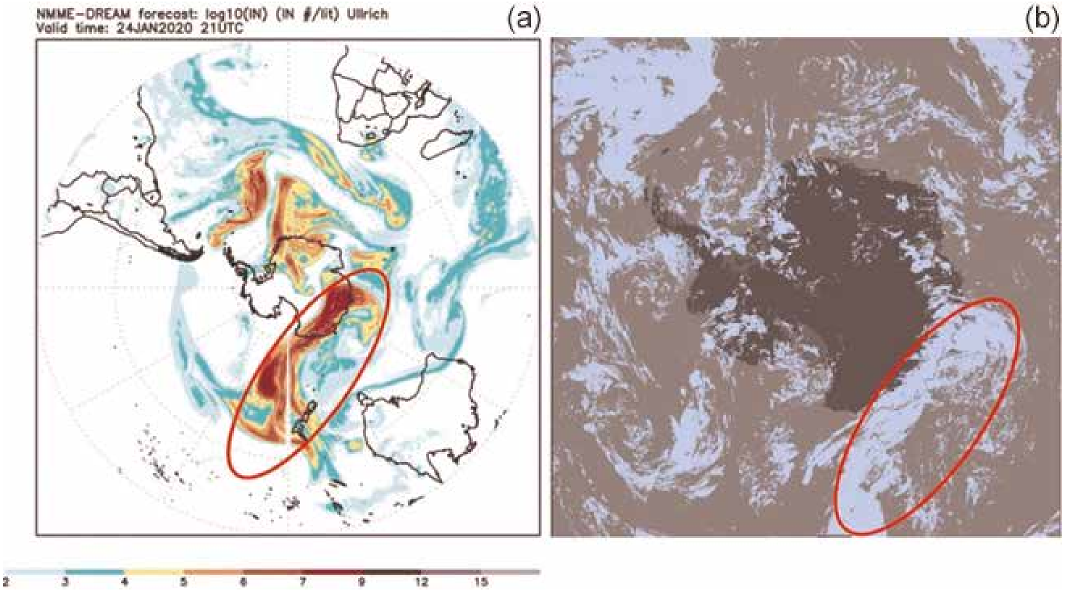

Figure 16. Global NMMB DREAM model experiments over Australia and the South Pole. Model dust load for 22 January 2020 (a). NASA MODIS ice cloud phase for 24 January 2020 (b).

pected to lead to less iron solubility for near-source dust (for central Asian ones) than for transported ones (particularly those of Sahelian origin).

In the southern part, under certain meteorological conditions, dust from lower latitudes can be transported far toward polar regions. Such was the case when a massive dust storm formed over Australia on 22 January 2020. Two days later, dust moved southward, covering a large part of Antarctica's eastern coast. The RHMSS global version of the DREAM model with incorporated ice nucleation parameterization due to dust (Nickovic et al., 2016) predicted the formation of cold clouds over the Antarctic. This ice cloud phase was also documented by NASA satellite observations (Fig. 16). The simulation was part of a WMO SDS-WAS initiative to include dust impacts on high latitudes in its agenda to better understand the role of mineral dust as a climate factor at high latitudes.

The MDVs were previously assumed to be a significant regional source of dust (e.g., Bullard, 2016). New observations show otherwise. Instead, the McMurdo Ice Shelf's (sometimes called the McMurdo debris bands) debris-covered surface is the major dust source. In this study, more details are provided to underline the importance and estimates of the size of the areas. The MDVs (4800 km^2) were estimated to fit Category 3 best. Despite active local aeolian sediment transport with many annual occurrences, they are an insignificant source or exporter of dust regionally, thus having only a small but poorly known climatic or environmental significance. The MDVs are changing quickly with increased ablation, meltwater, and permafrost incision, so their importance regarding dust generation may change in the near future. The McMurdo Ice Shelf "debris bands" fit Category 2 best. Although it is only about 1500 km^2, the McMurdo Ice Shelf is clearly the region's largest and most important dust source – active with a continuous supply of new sediment for export and exposed to frequent strong winds (with many events during the year), although few have been documented. The aeolian sediment impacts sea ice albedo (not directly measured) and marine sedimentation, contributing enough dissolved Fe to potentially support up to 15 % of primary productivity in the southwestern Ross Sea (Winton et al., 2014).

Ice core studies from Antarctica ice sheets show that Antarctica receives long-range dust transport from Australia, South America, southern Africa, and New Zealand (e.g., Bullard, 2016). However, several studies around coastal areas have shown that, locally, Antarctic-sourced dust accumulation rates are at least 2 orders of magnitude higher than that recorded from the polar plateau or global dust models (Chewings et al., 2014; Winton et al., 2014).

4 CONCLUSIONS AND OUTLOOK

This study aimed to identify new HLD sources with the focus on their potential climatic and environmental impacts. A literature survey on impacts and model calculations on emission, transport, and deposition were made to investigate the local, regional, and global significance of the HLD sources. We identified 64 new HLD sources. We estimated that, at the high latitudes, the land area with higher (SI $\geq$0.5), very high (SI $\geq$0.7), and the highest potential (SI $\geq$0.9) for dust emission covers >1 670 000, >560 000, and >240 000 km^2, respectively. These estimations agree with the first HLD sources' estimate of an area of >500 000 km^2 by Bullard et al. (2016), which mainly included the sources with a very high potential for dust emission, as classified in this study. Our study shows that active sources cover a significantly larger area, confirmed by over 60 new HLD sources with evidence of their dust activity, which is not limited to dry areas. The potential HLD emission areas need proof of observed and identified HLD emission sources.

Our modeling results on spatial distribution of the dust sources showed evidence supporting a northern high-latitude dust (HLD) belt, defined as the area north of 50° N, with a "transitional HLD-source area", extending at latitudes 50–58° N in Eurasia and 50–55° N in Canada, and a "cold HLD-source area", including areas north of 60° N in Eurasia and north of 58° N in Canada, with currently a "no-dust source" area between the HLD and LLD belt, except for British Columbia. Using the SILAM global atmospheric transport model, we estimated that 1.0 % of the global dust emission originated from the high-latitude regions. About 57 % of the dust deposition on snow and the ice-covered Arctic regions came from HLD sources.

Our update provides crucial information on the extent of active HLD sources and their locations. Active HLD sources as essential sources of aerosols that directly and indirectly affect climate and the environment in remote regions are often poorly understood and predicted. HLD is likely a significant source of atmospheric iron deposition in the Southern Ocean encircling Antarctica. More research is needed to quantify the deposition flux of HLD and nutrient (Fe, P, and trace metals such as Co) content and solubility, which can then be fed to ocean biogeochemical models to quantify their impact on ocean biogeochemistry. HLD is also an active INP, changing cloud properties, and HLD has severe consequences when deposited within the cryosphere. However, more studies are needed for HLD from different regions. For example, northern Asian HLD sources are assumed to be numerous but are difficult to access and gain information from. This points to the following main action items for monitoring dust at high latitudes.

- Firstly, the work on HLD sources needs a multidisciplinary combination of field, laboratory, and experimental work, remote sensing, and emission, transport, and deposition modeling. An increase in observational and modeling studies improves HLD monitoring and predicting.
- Secondly, the activity of the currently identified active sources should be followed and reevaluated in the coming years and decades.
- Thirdly, research gaps and future research directions essentially include finding, identifying, and characterizing new dust sources. As soon as there is evidence of finding a new HLD source, it should be included in the list of dust sources and be subject to further study.
- Fourthly, the role of different types of road dust in the Arctic could be separately assessed using a standard methodology.

In Arctic communities, road dust as a signature of non-exhaust traffic dust formed via the abrasion and wearing down of pavement, traction control materials, vehicle brakes, and tires is a common concern (e.g., Kupiainen et al., 2016; Nordic Council of Ministers, 2017). This paper excluded this type of road dust and only included significant anthropogenic road dust sources where unpaved roads are a substantial dust source. Unpaved areas of parking lots, storage areas, road shoulders, roadside lawn dust, and winter's effects could be considered too. During winter's cold and wet conditions, dust accumulates in snow and ice and the humid road surface texture. As snow and ice melt and street surfaces dry up in spring, high amounts of dust become available for suspension. For example, in Finland, north of 60° N, a major anthropogenic dust source comes from sand and gravel uptake for building purposes from ridges formed during the Ice Age. These nonrenewable ridges cover 1.5 million hectares. Since 1960, it has been estimated that approximately 40 million $t\,yr^{-1}$ has been utilized (Fig. 211 of Wahlström et al., 1996). These open-sand areas are visible in aircraft photos and satellite images. In Finland, long-range-transported LLD contributes to the dust amounts too (e.g., Meinander et al., 2021). Another health-significant anthropogenic springtime dust source is wintertime pavement traction sanding (Kuhns et al., 2010; Kupiainen, 2007; Stojiljkovic et al., 2019). These springtime dust events are annual but local throughout the country. In comparison, the Moscow metropolitan area (55°45′ N, 37°37′ E) is one of the most significant sources of dust at latitudes above 50° N, where dust's impact can extend over several hundred kilometers (Adzhiev et al., 2017). Moscow's road dust is mainly generated on paved roads, but roadside soils also contribute (Kasimov et al., 2020). Most often, unsealed soils are covered with lawns and are widespread in parks and recreational and industrial zones characterized by heavy pollution, a mixed upper horizon, and a high degree of soil cover heterogeneity.

This paper aimed to contribute beyond the state of the art of HLD sources by focusing on collecting and providing information on the geographical distribution of dust-productive soils and potential dust sources. This is some of the most important information that is currently lacking but that is necessary to perform successful long-range transport and deposition modeling. The information on the geographical distribution of dust-productive soils needs evidence and verification of detected dust events and is insufficient alone. Therefore, the paper focused on identifying new dust sources, clarifying their climatic and environmental importance, and using emission, long-range transport, and deposition modeling to study where the potential impact areas of the HLD sources are. Our results suggest that future HLD studies should include and update sources within the HLD belt defined here, i.e., at 50–58° N in Eurasia and 50–55° N in Canada and at >60° N in Eurasia and >58° N in Canada, as well as sources on the periphery of these regions, especially if sources are highly elevated (Wang et al., 2016).

Icelandic sources have shown that each source, even if nearby, may have different particle size distributions and optical properties. A detailed specification of the geographic distribution of potential dust-productive soils, verified dust sources, and their physical (e.g., particle size distribution, optics) and mineralogical/chemical (e.g., mineral fractions, chemical composition) properties can contribute to the various topics: predicting dust forecasts (e.g., health protection warnings during extreme events); long-range emission, transport, and deposition modeling; dust monitoring control; understanding extreme and rare events; Arctic protection; aviation control; health; tourist boards; assessing climate, environment, and air quality (e.g., Arctic Council Arctic Monitoring and Assessment Programme, AMAP, and Intergovernmental Panel on Climate Change, IPCC, reports); implementing HLD in calculations on direct and indirect radiative forcing, including cloud formation, cryospheric effects, and modeling the impacts. The new observations in this study improved the representation of HLD sources for various approaches and applications related to the observed current, previous, and future environmental changes at high latitudes.

In summary, establishing continuous monitoring of HLD sources and their future changes is key to understanding the climatic and environmental effects at high latitudes, especially in the Arctic. Climate change causes permafrost thaw, decreases snow cover duration, and increases drought, glacial melt, and heatwave intensity and frequency – all leading to increasing the frequency of topsoil conditions favorable for dust emission (increasing soil's exposure to wind erosion) and the probability of dust storms. Although dust originates from natural soils, dust sources are also influenced by human activities, e.g., when deforestation and land management in cold regions lead to ecosystem collapse and desertification (Prospero et al., 2012; Arnalds, 2015). Dust storms from agricultural fields (as reported, e.g., in Poland) can reach distances of over 300 km, drastically reducing visibility and resulting in hundreds of car accidents and fatalities (Hojan et al., 2019). Whether natural or anthropogenic, wildfires can result from new dust sources also (Miller et al., 2012). Hence, human actions can positively and negatively influence HLD and its effects. To understand and assess the temporal activity changes in HLD sources and the multiple impacts of HLD on the Earth systems over time, continuous monitoring and regular updates on locations, particle properties, and activities of current and new HLD sources are needed

.

DATA AVAILABILITY

Data are mostly included in this article or are available on request via personal communication.

Mass spectrometric analysis of unprecedented high levels of carbonaceous aerosol particles long-range transported from wildfires in the Siberian Arctic*

1 INTRODUCTION

The Arctic is a particularly vulnerable region regarding the effects of global warming, with atmospheric temperatures increasing at 2 to 3 times the global average rate; this phenomenon is referred to as Arctic amplification (IPCC, 2013; Schmale et al., 2021). In addition to carbon dioxide and other greenhouse gases, particulate matter (PM) emissions transported to the Arctic region also contribute to the rapid warming. Black carbon (BC) is emitted by fossil fuel combustion and biomass burning and is linked to the light absorption of the atmosphere as well as of snow or ice surfaces. Long-range transport to the Arctic carries BC and other tracers of anthropogenic and wildfire origin (Bond et al., 2013; Manousakas et al., 2022; Matsui et al., 2022; Moschos et al., 2022; Stohl et al., 2013). Beyond BC, wildfires are a major source of volatile organic compounds (VOCs), primary organic aerosol (POA), and brown carbon (BrC), which can act as a strong absorber of solar radiation at ultraviolet (UV) and visible wavelengths (Farley et al., 2022; Forrister et al., 2015; Fleming et al., 2020).

The frequency and size of wildfire events have increased during recent decades, and the trend is expected to continue due to global warming and the associated rise in extreme weather events (Abatzoglou et al., 2019; Kharuk et al., 2021). As wildfires in the northern regions increase, the long-range transport of wildfire plumes from central Siberia to Arctic regions can become more common, increasing the impact of carbonaceous aerosols in the Arctic on radiative forcing (Calì Quaglia et al., 2022; Yue et al., 2022). Siberian wildfire plumes may even reach densely populated regions in Europe or East Asia (Ikeda and Tanimoto, 2015; Semoutnikova et al., 2018); this is associated with a significantly increased risk of mortality as well as respiratory and cardiovascular diseases of the exposed population (Chen et al., 2021). Although northern boreal regions like Siberia are predicted to be impacted the most by increasing wildfire intensity, studies investigating organic aerosol emissions, especially from Siberia, are scarce (Flannigan et al., 2009).

In addition to individual fuel properties, combustion conditions largely affect the emission composition. Low combustion efficiency with a flameless burning (smoldering) generates aerosols rich in organic matter (OM) (Kalogridis et al., 2018), resembling the composition of the biomass by intense release of phenolic building blocks from lignin, cellulose, and hemicellulose (Simoneit, 2002) and containing tarlike BrC with Angström absorption exponents (AAEs) significantly larger than unity (Chakrabarty et al., 2010). Under flaming conditions, the overall organic aerosol content is reduced; soot carbon, related to elemental carbon (EC), and parent polycyclic aromatic hydrocarbons (PAHs) become more substantial aerosol constituents; and the AAE shifts to unity (Popovicheva et al., 2016, 2015).

Atmospheric aging reactions under the influence of, e.g., UV radiation, ozone, NOx , or SOx , transform organic vapors and OM by, e.g., photolysis and hydroxyl and nitrate radical reactions (Peng et al., 2021; Surratt et al., 2008; Forrister et al., 2015). In homogeneous gas-phase reactions, organic vapors may be oxidized and condense as secondary organic aerosol (SOA) on existing particles or even form new particles (nucleation). Moreover, heterogeneous reactions between atmospheric oxidants and particle constituents may increase the molecular complexity of primary aerosols in the atmosphere, which is associated with higher functionalization, an increase in heteroatom content (O, N, S), and oligomer formation. Additionally, reactions between individual constituents of the particle phase complete the ongoing complex multiphase chemistry (Schneider et al., 2022; Pardo et al., 2022; Lin et al., 2015; Chacon-Madrid and Donahue, 2011). For biomass burning, atmospheric aging may promote the formation of chromophores and thus BrC but may also lead to a degradation of chromophores by photochemistry with increasing atmospheric lifetime (Fleming et al., 2020; Forrister et al., 2015).

Wildfires may rapidly increase the level of particulate matter (PM) to a range that atmospheric oxidant concentrations become insufficient to uniformly process the wildfire aerosol, leading to differences in atmospheric processing of plume centers and the plume periphery (Hodshire et al., 2021). For example, OH radicals, the main oxidant under photochemical conditions, may already be consumed at the periphery of the plume, so enhanced photobleaching was observed at the plume edges relative to the core (Lee et al., 2020), along with faster photochemistry (Palm et al., 2021). Furthermore, other photosensitive atmospheric oxidants, such as NO3 radicals, may be protected by the plume optical depth and become relevant for the chemistry in the plume center (Decker et al., 2021). Consequently, the product spectrum of atmospheric processing differs from aging of biomass burning aerosol at typical ambient conditions. Additionally, the net appearance of OM in wildfire plumes during aging becomes dilution driven as high near-source aerosol concentrations release adsorbed

---

* Eric Schneider, Hendryk Czech, Olga Popovicheva, Marina Chichaeva, Vasily Kobelev, Nikolay Kasimov, Tatiana Minkina, Christopher Paul Rüger, and Ralf Zimmermann // Atmospheric Chemistry and Physics. 2024; 24: 553–576 DOI: 10.5194/acp-22-11889-2022

and absorbed vapors during atmospheric transport (Palm et al., 2020), on the one hand counteracting the known significant net increase of OM mass for a wide range of biomass burning aerosol aging (Ortega et al., 2013) but on the other hand forming secondary organic aerosol (Fang et al., 2021; Li et al., 2020). As aerosol concentrations at the plume periphery are lower than in the center, they undergo more intense aging (Hodshire et al., 2021). Quantification of transported wildfire aerosol and its molecular characterization during aging may improve the understanding of the impacts on the sensitive Arctic ecosystem and related effects on climate.

Siberian wildfires are a major source of climate-relevant species emitted at northern latitudes (Lavoué et al., 2000). Yakutia in eastern Siberia is known to be prone to largescale wildfires (Tomshin and Solovyev, 2018) owing to the combination of hot summers with temperatures up to 40 ◦C; low humidity in the atmosphere and pedosphere; and the phenomenon of dry thunderstorms, which have been estimated to account for more than half of the fire causes. As such, lightning ignites dry biomass, while strong wind accelerate the spread of the fire (Narita et al., 2021). On 4 August 2021, strong smoke enveloped large areas of western Siberia, namely Yamalo-Nenets Autonomous Okrug (YNAO) and Khanty-Mansysky Autonomous Okrug (KMAO) (NUR24.RU, 2021).

In our study, intensively high concentrations of OC and EC were observed in Nadym and on Bely Island, located in the north of western Siberia, during August 2021, according to filter samples collected at both locations. Backward air mass trajectories and satellite images indicated large-scale wildfires in Yakutia as the main source. Multi-wavelength thermal–optical carbon analysis with photoionization mass spectrometry and ultra-high-resolution mass spectrometry with complementary ionization techniques confirm the origin of the observed high OC and EC concentrations and provide an advanced chemical characterization of Arctic pollution associated with aerosol emissions from vast Siberian fires and differences in atmospheric aging of the plume center and plume periphery.

2. EXPERIMENTAL SECTION

2.1. Sampling sites

One part of the sampling campaign was carried out in Nadym from 5 to 12 August 2021. A total suspended particle (TSP) sampling system was operated in an area far from roads and residential sectors, with a flow rate of 70 L min−1 and variable duration of 3–12 h to achieve comparable filter loadings of the nine resulting samples. Quartz fiber filters (QFFs; 47 mm, QM-A 1851047, Whatman, USA) were used to collect PM samples, after 6 h of pretreatment at 600 ◦C.

The second sampling system was operated at the pavilion of the research aerosol station Island Bely installed for the purpose of addressing pollution in the western Siberian Arctic (Popovicheva et al., 2023, 2022). The TSP inlet was installed approximately 1.5 m above the roof and 4 m above the ground for filter sampling (see Popovicheva et al., 2022, for details). Three QFFs were collected by weekly sampling, starting on 31 July 2021 and ending on 21 August 2021, with a sampling flow rate of 2.3 m−3 h−1. A more detailed overview of the sampling parameters as well as an indepth discussion of the study area and typical PM emissions sources can be found in Sect. S1 in the Supplement.

2.2. Air mass transportation

To evaluate the impact of air mass transportation and smoke plume origin, 240 h backward trajectories (BWTs) were generated using the NOAA HYSPLIT model of the Air Resources Laboratory (Stein et al., 2015) and archive data from the National Center for Environmental Prediction's Global Data Assimilation System with the coordinate resolution equal to 1◦ × 1◦ latitude and longitude and an input height of 500 m above ground. Additional BWT calculations with input heights of 10, 100, 250, and 500 m are presented in Fig. S1.

Data on the occurrence of fires were obtained from the Fire Information for Resource Management System (FIRMS) operated by NASA's Earth Science Data and Information System (ESDIS) (https://firms.modaps.eosdis.nasa.gov/map, last access: 3 April 2023) at GSFC based on satellite observations which register open flaming. This work uses data arrays on the spatial location of fire centers from the Moderate Resolution Imaging Spectroradiometer (MODIS). The satellite images of smoke plumes in the sampling days were obtained from https://worldview.earthdata.nasa.gov (last access: 3 April 2023). Fire activity is shown in 10 d back from a day of BWT analyses (Fig. 2).

The Ozone Mapping and Profiling Suite (OMPS) aerosol index information was obtained from the Goddard Earth Sciences Data and Information Services Center (GES DISC) based on satellite instrumentation that measures the radiance scattered by the limb of the atmosphere. The OMPS aerosol index is based on the normalized radiance of the 340 and 378.5 nm wavelengths (Torres, 2019).

2.3. Analytical instrumentation

2.3.1. Fourier-transform ion cyclotron resonance mass spectrometry (FT-ICR MS)

Ultra-high-resolution FT-ICR MS measurements were carried out on a solariX (Bruker Daltonik, Bremen, Germany) equipped with a 7 T superconducting magnet and an InfinityCell©. A detailed description of the extraction procedure as well as the settings for each ionization technique can be found in Sect. S2. Shortly, filter extracts were analyzed in positive and negative mode electrospray ionization (ESI), as well as positive-mode atmospheric pressure photoionization (APPI; Kr, 10/10.6 eV) with a direct-infusion ion source setup (Bruker Daltonik, API ion source). For each measurement, 400 scans were collected in the range of m/z 150–1000 with a resulting resolving power > 310 000 at m/z 400 and mass accuracy below 1 ppm.

2.3.2. Multi-wavelength thermal–optical carbon analysis coupled to resonance-enhanced multiphoton ionization time-of-flight mass spectrometry (TOCA-REMPI-TOFMS)

For direct analysis of filter samples, a thermal–optical carbon analyzer (TOCA; Model 2001, DRI, US) coupled to time-offlight mass spectrometry (TOFMS) was used with resonanceenhanced multiphoton ionization (REMPI). Organic and elemental carbon (OC, EC) were determined according to the IMPROVE_A protocol (Chow et al., 2007) for the separation of pyrolytic OC from EC. Precisions of the carbon analysis are sample dependent and range between 2 % and 6 % for TC and 5 % and 10 % of the split between OC and EC, according to the manufacturer. In addition to 635 nm, the TOCA was further retrofitted with six laser diodes, emitting light in the visible UV and near-infrared (NIR) spectral range at 405, 445, 532, 780, 808, and 980 nm (Chen et al., 2015). The multi-wavelength TOCA was used to determine the Angström absorption exponent (AAE), which is defined for a wavelength pair λ_1/λ_2 by

$$\mathrm{AAE}(\mathrm{ATN}\lambda) = -\frac{\ln \frac{\mathrm{ATN}_1}{\mathrm{ATN}_2}}{\ln \frac{\lambda_2}{\lambda_1}} \qquad (1)$$

with ATN being the light attenuation. In this study, the wavelength pair of 405 and 808 nm was used to calculate the AAE (AAE405/808), representing the exclusive absorption of BC in NIR and the lower visible UV range with absorption of both BrC and BC. ATN was derived from the ratio of the laser transmittance (LT) of the untreated filter sample before TOCA to the LT at the end of the TOCA so that refractive particle constituents are still retained. In order to account for filter loading effects on ATN, the empirical correction from Chow et al. (2021) was applied. The uncertainty of the AAE determination was derived from error propagation of the LT measurement, which has a precision of 8 % at 405 and 808 nm (Chen et al., 2015). Thus, the final uncertainty of the AAE405/808 calculation is within ± 15 % at 95 % confidence.

A small fraction of evolving particulate matter during IMPROVE_A is bypassed from the carbon quantification by a modified quartz tubing behind the oven of the TOCA and reaches a REMPI-TOF-MS through a heated transfer capillary (Grabowsky et al., 2011). REMPI refers to a selective ionization technique for aromatic compounds and predominantly yields molecular ions (Streibel and Zimmermann, 2014). A more detailed description of REMPI can be found in Sect. S2.3.

2.4 Mass spectrometric and statistical data analysis

External mass calibration of the FT-ICR MS was performed using arginine oligomers covering the entire mass range. An internal calibration of each mass spectrum was performed by characteristic and commonly abundant peaks from a self-generated calibration list (CHOx and CHNOx class compounds, manually verified), achieving sub-parts per million mass accuracies. Raw data were peak picked (cutoff: S/N = 6) and exported with Bruker Data Analysis 5.1 (Bruker Daltonik, Bremen, Germany). The exported mass spectra were processed by self-written MATLAB algorithms and routines combined in a graphical user interface named CERES Processing (Rüger et al., 2017). After careful investigation and taking into account attribution boundaries from the literature, the following restrictions were deployed for elemental composition assignment in the range of 150–1000 m/z: CcHhNnOoSs Nana; $5 \le c \le 60$, $5 \le h \le 100$, $n \le 3$, $o \le 20$, $s \le 1$ (ESI+: $na \le 1$) with a maximum error of 1 ppm (Tang et al., 2020; Schneider et al., 2022). Additional restrictions were applied for the H/C ratio (0.4–2.4), O/C ratio (0–1.4), and double-bond equivalents (DBEs; 0–28). The assignment of radical cations was allowed for APPI. Equations used for the calculation of molecular properties can be found in Sect. S2.4.

Principal component analysis (PCA) and hierarchical clus-ter analysis (HCA) were performed by the MATLAB R2021b Statistics Toolbox (MathWorks, Inc., MA). HCA was per formed with the following settings: unweighted average distance (UPGMA), cosine distance metric, maximum number of clusters set to five, and absolute intensities normalized by power transformation. Prior to PCA, sum parameters were standardized to a mean of 0 and standard deviation of 1.

Calculation of relative sum formula intensities is done by the L1 norm (normalization to total ion current, TIC) of all assigned elemental compositions of the respective sample.

3 RESULTS AND DISCUSSION

3.1 Air mass transportation to Nadym and Bely Island

Figures 2 and S2 present backward trajectories (BWTs) for air mass transport at times corresponding to sample collection in Nadym and on Bely Island throughout the sampling campaigns using the HYSPLIT simulation data. We present this analysis first, as it provides useful information for analysis of aerosol chemistry discussed in later sections. Extremely high smoke intensity was initially observed in Nadym on 5–6 August 2021 when samples N01 and N02 were collected (Table S1). Air masses that arrived on those days in Nadym from the NE and NNE directions passed the wildfire areas in Krasnoyarsk Krai (Figs. 1, S2, and S3). As observed from satellite images, they brought a wide and dense smoke plume that covered YNAO, KMAO, Yakutia, Krasnoyarsk Krai, and Irkutsk Oblast. On 7 August 2021 when samples N03, N04, and N05 were collected, BWTs arrived in Nadym from the NE direction. Subsequently, they passed through Yakutia, which had the largest density of detected fires, then Irkutsk Oblast and Krasnoyarsk Krai, before turning to YNAO (Fig. 2).

On 8 August 2021, the smoke plume area narrowed and almost localized over the territory of Krasnoyarsk Krai. When samples N07 and N08 were collected, the OMPS aerosol index in Nadym had declined from > 5 to < 0.625. Finally, air masses changed their direction, and

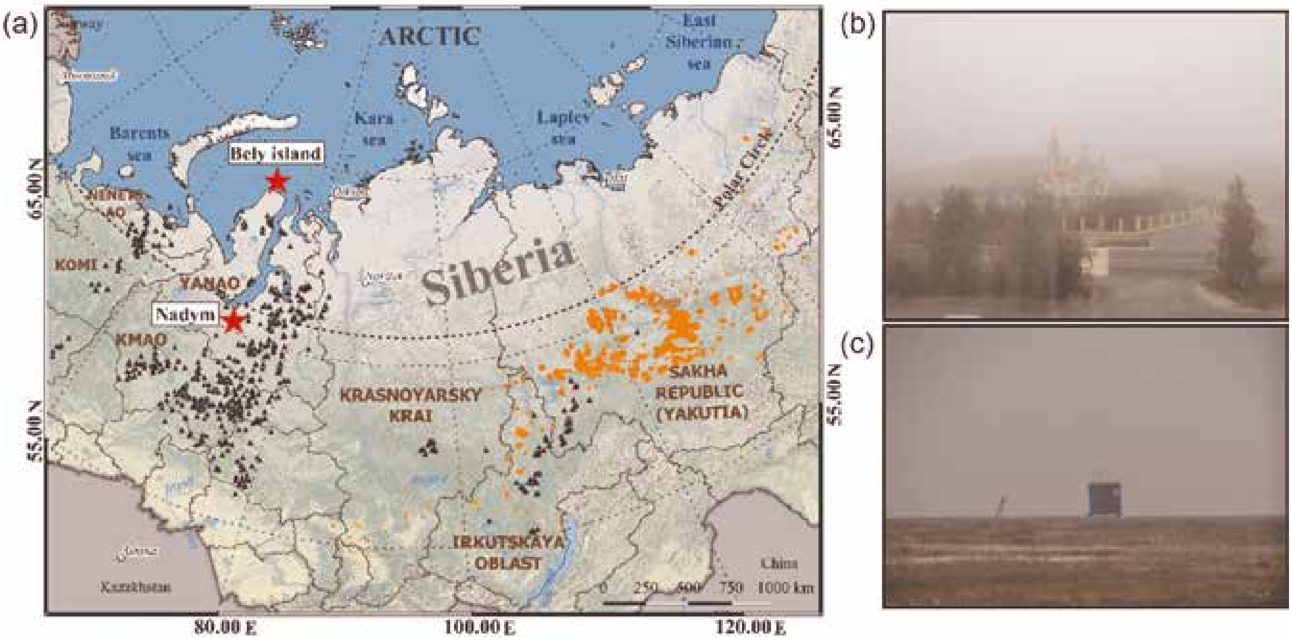

Figure 1. Location of Bely Island (73◦2017.5711 N,70◦4149.0511 E) and Nadym (65◦3210011 N, 72◦3110011 E) in Yamalo-Nenets Autonomous Okrug (YNAO) (western Siberia) (a). The map was created using the open-source geographic information system QGIS (https://qgis.org/en/site, last access: 3 April 2023) with ESRI physical imagery (https://server.arcgisonline.com/ArcGIS/rest/services/World_Physical_Map/MapServer/ tile/%7Bz%7D/%7By%7D/%7Bx%7D&zmax=20&zmin=0, last access: 3 April 2023) as the base layer. Moreover, the open-source Natural_Earth_quick_start package was used to add a layer of natural and cultural boundaries and polygons from ESRI shapefile storage. VIIRS and MODIS active fire data for August 2021 have been downloaded from https://firms.modaps.eosdis.nasa.gov/ (last access: 3 April 2023), shown in orange. Flares of oil and gas fields are indicated for 2020 as black triangles (https://skytruth.org/, last update 2023). Photo of Nadym (b; https://nur24.ru/news/ecologia/smog-ot-pozharov-v-yakutii-polnostyu-okutal-yamal-foto-video, last access: 3 April 2023) and Island Bely station during the smoke event (c; photo taken by the authors).

on 9 August 2021 they arrived in Nadym from the NW and NNW. They brought clean Arctic air with an OMPS aerosol index below 0.625 from the White, Barents, and Kara seas. The clean Arctic background for BC was previously determined from the 20th percentile of 1.5 years of continuous monitoring, which accounted for 10 ng m^{-3}. Background pollutant concentrations in Arctic stations are generally very low without any detectable influence from local or regional sources (Eleftheriadis et al., 2004; Popovicheva et al., 2019). Conversely, episodes of pollution were defined by the 80th percentile, accounting for 90 ng $^{m-3}$ (Popovicheva et al., 2022).

Air mass trajectories and satellite images reveal that the wildfire plume that has strongly impacted Nadym also reached further north into the Arctic and brought deep smoke into Bely Island during the same period from 5 to 7 August 2021. In contrast to the plume arriving in Nadym, the northern part of the evolving wildfire plume was first transported north from its origin for several days and moved around over the Arctic Ocean before a change in wind direction transported the plume westward. The OMPS aerosol index (Fig. S3) suggests that the periphery (lower OMPS aerosol index, approx. 1.85, yellow) of the Yakutian wildfire plume was transported to Bely Island, in contrast to the plume center aerosol transported to Nadym (higher OMPS aerosol index, > 5, red). This may have led to a gradient in photochemical processing of the plume, i.e., a lower extent of atmospheric processing by OH radicals, with the northern section containing more atmospherically aged aerosol and the southern section more fresh wildfire emissions, which were picked up on the way westward.

3.2 Carbonaceous aerosol in Nadym and on Bely Island

Long-range transport of a wildfire plume from Yakutia caused high carbon concentrations in ambient PM in Nadym from 5 to 7 August 2021 (samples N01–N07) (Fig. 3). For sample N04, concentrations of organic carbon (OC) and elemental carbon (EC) approached a maximum of 100 and 40 µg m−3, respectively (Table S1). On 8 August 2021, OC and EC dropped to 5.4 and 1.7 µg m−3 for sample N08, respectively. On 9 August 2021 transport of clean Arctic air masses decreased OC and EC down to 0.7 µg m−3 and 0.1 µg m−3 for N09, respectively, while on 12 August 2021, 3.7 µg m^{-3} of OC and 1.2 µg m−3 of EC were obtained for N10 (Fig. 3). Regarding the distribution of the individual carbon fractions, no significant difference between the samples could be determined apart from a significantly higher contribution of EC2 in sample N10 (two-sided Grubbs test, significance level of 0.05), collected when smoke has almost disappeared (Table S1). EC2 has been associated with soot particles from internal combustion engines and indicates that local emissions, e.g., from road traffic, contributed significantly to the carbonaceous aerosol. A generally substantial contribution of pyrolytic OC (OCpyro) is an indication

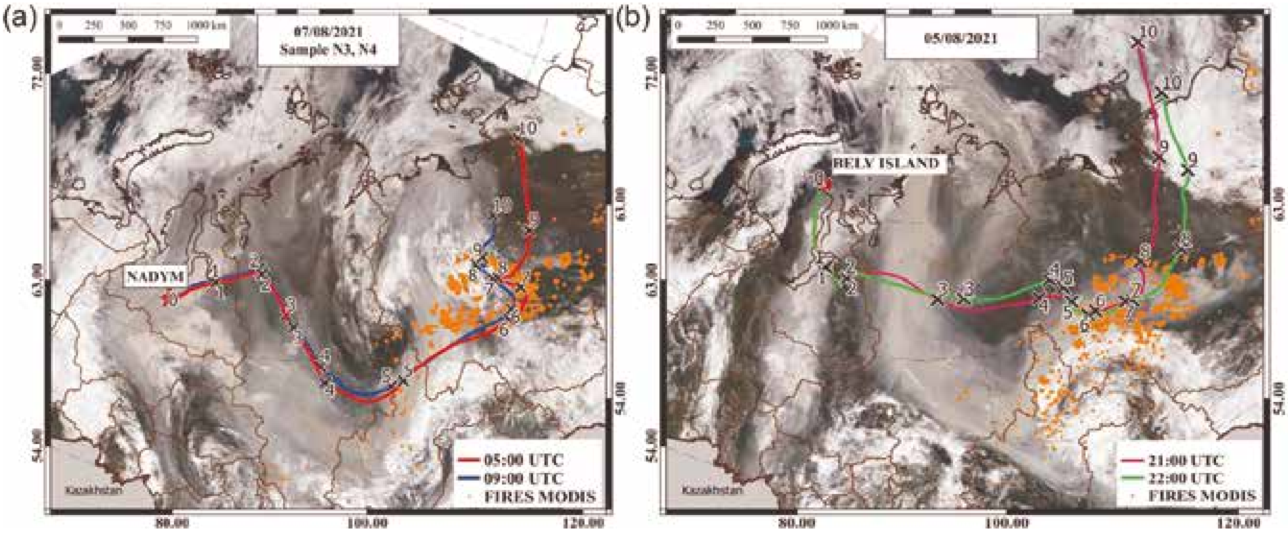

Figure 2. Backward trajectories with indications of transport time (days back indicated by crosses) and satellite images of smoke plume on the day of peaking concentrations of carbonaceous aerosols in Nadym on 7 August 2021 (a) and on Bely Island on 5 August 2021 (b). The dates of sample completion for N03 and N04 from Nadym and B01 from Bely Island are presented. The maps were created using the opensource geographic information system QGIS (https://qgis.org/en/site, last access: 3 April 2023) with satellite imagery from 7 and 8 August 2021 (https://worldview.earthdata.nasa.gov, last access: 3 April 2023) with the TERRA MODIS fire anomaly layer and the MODIS-corrected reflectance true color imagery as the base layer (MODIS Science Team, 2017d, c, b, a). The open-source Natural_Earth_quick_start package was used to add a layer of natural and cultural boundaries and polygons from ESRI shapefile storage. Backward trajectories were calculated using HYSPLIT software (https://www.ready.noaa.gov/HYSPLIT.php, last access: 3 April 2023).

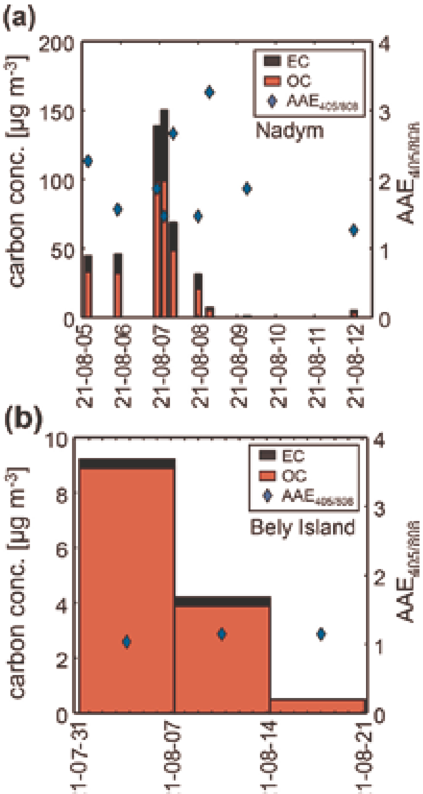

Figure 3. Carbon concentrations and Angström absorption exponent (AAE405/808 nm) in Nadym (a) and on Bely Island (b) measured by a multi-wavelength thermal–optical carbon analyzer (TOCA). Sampling conditions as well as EC and OC values, divided into individual fractions based on the IMPROVE_A protocol, are listed in Table S1.

of the presence of biomass burning (BB) and secondary organic aerosol (SOA) (Grabowsky et al., 2011; Cheng et al., 2011). In the week from 31 July 2021 to 6 August 2021 (sample B01, Bely Island) when the wildfire plume arrived in Nadym, concentrations of OC and EC at Bely Island reached the highest weekly averages of 8.9 and 0.3 µg m^{-3}, respectively, and declined in 2 subsequent weeks to 3.9 (B02) and 0.5 µg m^{-3} (B03) of OC and 0.3 (B02) and < 0.05 µg m^{-3} (B03) of EC (Table S1). PM of Bely Island was substantially affected by the wildfire emissions in Yakutia (Fig. 2), as was Nadym, but lower concentrations of carbonaceous aerosol particles were observed as only the periphery of the plume with lower aerosol concentrations was transported to Bely Island (Fig. S3).

The wavelength dependence of light absorption in the UV– Vis to near-infrared range is described by the AAE. While BC shows an AAE close to unity, BrC has a stronger increase in absorption towards lower wavelengths in the visible and UV range with AAE significantly larger than unity (Andreae and Gelencsér, 2006). Regarding biomass burning, spectral absorption obtained throughout the near-ultraviolet to near-infrared spectral region and high Angström absorption exponents (AAEs) up to 4.4 are found for smoke from smoldering combustion of pine debris in the wavelength regions from 370 to 670 nm. In contrast, open flaming smoke from pine combustion shows a low AAE of around 1, also typical for high-temperature fossil fuel combustion, while mixed fires emit particles absorbing light with the intermediate AAE characteristics (Popovicheva and Kozlov, 2020).

For N01–N05, AAEs for the wavelength pair of 405 and 808 nm (AAE405/808) were observed in the range of 1.5 to 3.3 (Fig. 3), showing the presence of significant amounts of BrC. Although there was no distinct relation

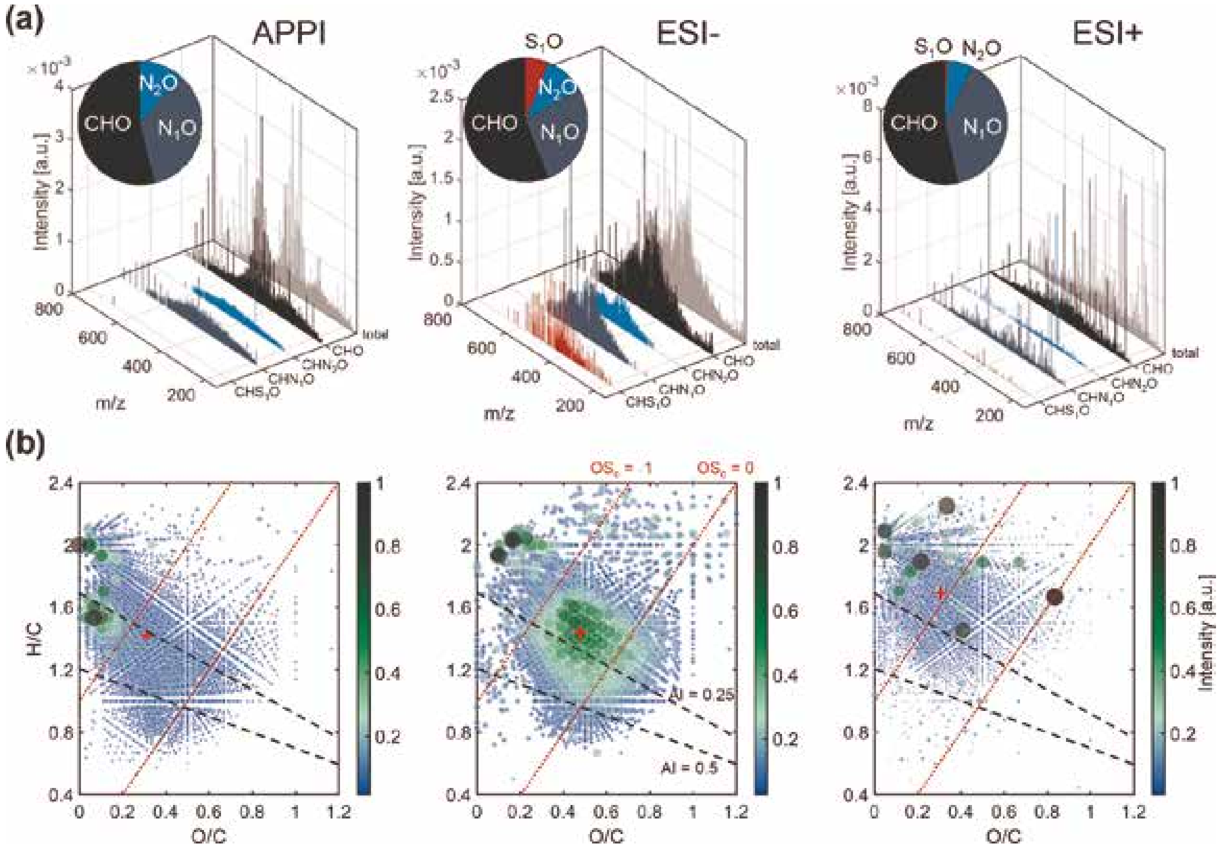

Figure 4. FT-ICR MS data overview. (a) Averaged and normalized assigned elemental composition mass spectra of wildfire-plume-impacted samples in Nadym (N01–N05) in three ionization techniques (left to right: APPI, ESI−, and ESI+), with inserts of relative abundance pie charts of the four main compound classes. (b) Van Krevelen diagrams with average-intensity-weighted H/C and O/C ratios marked in red. The dotted lines indicate the limits of the average carbon oxidation state (OSC; red) and modified aromaticity index (AI; black).

of AAE405/808 to concentrations of OC or EC, a moderate correlation coefficient of 0.59 was obtained between AAE405/808 and the ratio of OC to EC (Fig. S4). This correlation indicates the contribution of aerosols from smoldering biomass burning, which is known to result in lower amounts of EC and BC but higher releases of BrC than flaming biomass burning (Cheng et al., 2011; Chen et al., 2006; Popovicheva et al., 2016). For N09, a moderately high AAE405/808 of 1.9 was observed, which may be caused by a still-significant relative biomass burning contribution to overall low OC and EC concentrations. After the wildfire plume left Nadym, the lowest AAE405/808 of 1.3 (N10) among all samples from Nadym was observed, pointing towards dominating aerosol emissions from fossil fuel combustion associated with a higher contribution of BC (Helin et al., 2021).

At Bely Island, the weekly average of AAE405/808 of 1.0 for sample B01 (31 July to 6 August 2021) was not affected by BrC in the wildfire plume during the highest concentrations of OC and EC. In the subsequent 2 weeks with lower OC and EC concentrations, an AAE405/808 of 1.2 was obtained, which is, however, not significantly different from 1 considering the associated measurement uncertainty of ± 0.5. Since lower aerosol concentrations from the periphery of the Yakutian wildfire plume reached Bely Island, it can be assumed that the wildfire aerosol has been more intensively processed during atmospheric transportation. Atmospheric aging may form BrC (Al-Abadleh, 2021), but, particularly toward longer photochemical ages, the phenomenon of photobleaching and whitening of BrC by atmospheric oxidants becomes dominant, decomposing chromophores and consequently decreasing AAE (Fang et al., 2021; Schnitzler et al., 2022) caused by a higher ratio of atmospheric oxidants to BB aerosols.

In Salekhard approximately 350 km west from Nadym and 800 km south from Bely Island, equivalent black carbon (eBC) was continuously measured during the summer of 2018, revealing an average concentration of (350 ± 120) ng m^{-3} (Popovicheva et al., 2020). Although EC and BC are determined by different measurement principles, they are highly correlated, appear in a similar concentration range, and essentially represent graphitized carbon (Wat son and Chow, 2002; Andreae and Gelencsér, 2006; Chow et al., 2021), thus enabling inter-comparison estimates. The observed concentrations of EC in Nadym during 5 to 7 August 2021 exceeded the BC concentrations in Salekhard by 2 orders of magnitude. Furthermore, even compared to the highest average levels for July and August from 2003 to 2017 of fine particulate matter (PM2.5), primary OM, and BC caused by transported wildfire aerosol to YNAO (Yasunari et al., 2021), carbonaceous aerosol concentrations observed in Nadym in our study remain significantly high. At Bely Island, 10 times higher concentrations of OC and EC were observed compared to averages of organic aerosol and BC during summertime (Moschos et al., 2022;

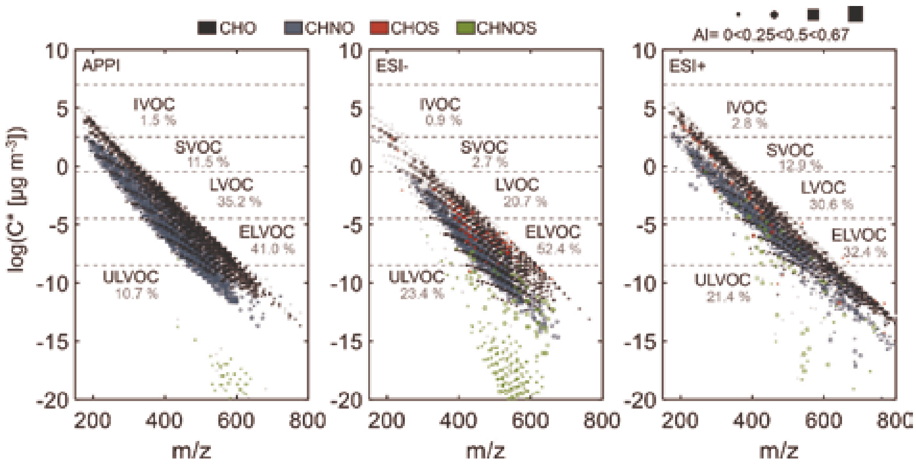

Figure 5. Saturation vapor pressure (C*) versus m/z plot for unique compounds from averaged wildfire-impacted samples (N01–N05), separated by compound class (black: CHO, blue: CHNO, red: CHOS, green: CHNOS). Compounds abundant after strong wildfire impact (samples N08–N10) are in grey. The aromaticity index is indicated by the dot shape and size. The relative number of compounds per volatility class is listed below each volatility class label.

Popovicheva et al., 2022). Therefore, our results indicate unprecedented high concentrations of long-range-transported wildfire aerosol to the Arctic with different aging conditions between the two sampling sites.

3.3. PM bulk composition by APPI and ESI FT-ICR MS

All filter sample extracts analyzed by FT-ICR MS were measured with three atmospheric pressure ionization techniques: ESI+, ESI−, and APPI (+). A detailed discussion of the selectivity and sensitivity of each ionization technique can be found in Sect. S3.

Principal component analysis (PCA) based on FT-ICR MS average elemental compositions as well as other sum parameters, e.g., DBE, AI, H/C, and O/C (Table S3, Fig. S6), shows a clear grouping of samples N01 to N02 and N03 to N05 with a divergence of N07 and strong separation of N08 to N10. For chemical comparison of the FT-ICR MS data, samples are combined and classified based on the PCA results, previously discussed air mass trajectories, and the EC and OC concentrations. For Nadym, samples N01 to N05 are combined to form one dataset representing the strongest wildfire plume impact causing high OC and EC concentrations (Figs. 3 and S2). In contrast, samples N08 to N10 had the lowest concentrations of OC and EC. N09 was chosen as a reference for the absence of a wildfire impact, termed “ambient aerosol” for Nadym. The apparently different chemical composition of sample N07, indicating the influence of regional gas flaring, is separately addressed in Sect. 3.6. For Bely Island, sample B01 is selected for comparison with the Nadym dataset, as it represents the strongest wildfire impact at this location and additionally covers a similar time period (31 July to 7 August 2021) to the Nadym wildfire-plumeimpacted samples (N01 to N05, 5 to 7 August 2021). Samples B02 and B03 represent a declining wildfire aerosol influence and ambient aerosol at Bely Island, respectively.

For the wildfire-plume-impacted samples (N01–N05), 1108 compounds are common between all ionization techniques (Fig. S5), but most compounds are uniquely identified by a single ionization technique. Notably, ESI+ and APPI share the highest number of common elemental compositions (1361), while ESI+ and ESI− share the lowest number (553) of two ionization techniques. In general, almost every compound detected in any ionization mode is part of a homologous series spanning several CH2 units in the range of often 20 or more carbon atoms (Fig. S7). Other homologous series, including, e.g., methoxy groups, are also observed. The Van Krevelen diagrams (Fig. 4b) show complex fingerprints, with changing highest-intensity regions for each ionization technique. The lipid region (H/C > 2, low O/C, low aromaticity, low carbon oxidation state) is highly abundant, as well as lignin-like structures (medium H/C, medium O/C, AI < 0.5, and OSC 0 to −1). In ESI, highly oxidized compounds with sugar-like structures (high O/C, low aromaticity, high OSC) and highly oxidized molecules with high unsaturation (HUHOMs) are observed additionally. This highlights the need for different ionization techniques to achieve a broad coverage of the chemical space, as has been shown before, e.g., for biomass burning tar balls from wildfires (Brege et al., 2021). Saturation vapor pressure is a parameter used to characterize SOA (Donahue et al., 2011, 2012). Observed compounds in the wildfire plume show low to very low volatility as a result of high oxygen contents, and other heteroelements (N, S), gained by atmospheric aging during long-range transpor or maintained due to reduced photochemical processing. The majority of compounds is found in the lowto ultra-lowvolatility area, but there is a difference when comparing individual compound classes.

3.4. Compound class characterization of PM in Nadym

3.4.1. CHO

Mass spectra of identified elemental compositions (Fig. 4a) show a broad distribution over the whole mass range (approx. 200–800 Da) of the highest abundant (rel. intensity) compound class. The relative intensity distribution of the oxygen number shows a high degree of oxidation (Fig. S8), with ESI− showing the highest average oxygen number of 9.6 oxygen atoms per molecule (Table S3). This is an indicator of acidic functional groups, e.g., hydroxyl (R-OH) or carboxylic acids (R-COOH), which are efficiently ionized by ESI− and lead to the sensitive detection of highly oxidized compounds. High oxygen content is also reflected in a low volatility, which is observed for the wildfire-plume-impacted samples (Fig. 5).

Van Krevelen (VK) plots (Fig. 4B) show a wide distribution over several structure regions, including the lipid-, phenol-, and carbohydrate-like regions, as well as oxidized aromatic compounds. All of them are known from the literature to be regions of products of biomass burning and atmospheric aging of BB emissions (refer to BB VK). They are not found in PM samples from Nadym (N08–N10) collected after the plume has passed (Fig. S10). ESI− in particular shows intense distribution of signals in the center of the VK plot (medium H/C and O/C), while in each polarity the lipid region of low-oxidized compounds is highly populated. Both regions show no high abundant peaks after 8 August 2021, indicating no significant contribution of fresh biomass burning emissions to ambient PM. Typical elemental compositions of BB markers are found in the wildfire-plume-affected PM samples from Nadym: levoglucosan and its isomeric anhydrosugars, resin acids, methoxyphenols, and lipids. Figure S9 shows semi-quantitative time trends (normalized to the sampling volume) of six biomass burning marker elemental compositions, including elemental compositions of known cellulose and lignin degradation products. The thermal degradation of cellulose structures leads to the formation of the anhydrosugar levoglucosan as well as minor amounts of its isomers galactosan and mannosan. Coniferyl alcohol is a gymnosperm lignin degradation product found, e.g., in pine wood smoke (Simoneit et al., 1993). 7-Oxodehydroabietic acid is emitted from the burning of gymnosperm plants, e.g., Scots pine and larch, which are the dominant forest types in Yakutia (Kharuk et al., 2021). Nonacosene and nonacosanol are biomarkers emitted from higher plant waxes (Simoneit and Elias, 2000). A clear, similar trend is visible for each marker compound, as the abundance increased with a maximum on 7 August 2021 (N04), followed by a slow decrease to 0 towards the end of the observed wildfire plume impact (9 August 2021). Finally, some peaks are detected in the lower VK space with $H/C < 0.7$ and $0.2 < O/C < 1.5$, particularly in mass spectra of APPI and ESI−. This has been assigned to HU-HOMs, which are produced from the photooxidation of larger PAHs on soot particles, thus indicating heterogeneous processing of wildfire aerosol particles. The formation of HU-HOM changes the polarity of soot particles from hydrophobic to hydrophilic and therefore affects the uptake of water and cloud formation (Li et al., 2022).

The maximum carbonyl ratio (MCR) is a tool used to predict the possible maximum of carbonyl groups in molecules, based on the identification of elemental compositions (Y. Zhang et al., 2021). The applied ionization techniques display differences in the distribution of relative intensity into the five defined MCR areas (Table S4). ESI+ data indicate that there are manifold combinations of oxygencontaining functional groups including not only carbonyl but also single-bound oxygen as found in hydroxyl (R-OH), hydroperoxyl (R-OOH) or ether (R-O-R), which is part of this organic aerosol, as there is a relatively even distribution of compounds for each MCR limit. Comparing the wildfireplume-affected samples (N01 to N07) with after-plume samples (N08–N10), it is apparent that the distribution of the MCR of samples N08–N10 is shifted to lower MCR, indicating a stronger influence of products from oxidative atmospheric aging. This trend is observed for all applied ionization techniques and may be explained by the lower concentrations of VOCs and thus lower reactivity towards atmospheric oxidants, which lead to more oxidized aging products due to a higher ratio of oxidants to organic carbon compared to dense wildfire plumes.

3.4.2. CHNO

Wildfires, particularly under flaming conditions, are known to emit reactive nitrogen species like nitrogen oxides (NOx) and nitrous acid (HONO) (Peng et al., 2021; Lindaas et al., 2021). These short-lived compounds may consequently be converted to long-lived peroxyacetyl nitrate (PAN), nitric acid (HNO3), organic nitrates, or other organic nitrogencontaining compounds (Peng et al., 2021).

PAN and NOx . take part in atmospheric aging reactions, forming organic aerosol molecules containing the elements oxygen and nitrogen. The most common functional groups are nitrate, nitro, and nitrooxy moieties. Nitrogen-containing compounds are also a relevant portion of BrC due to their potential light-absorbing properties, especially in combination with aromatic ring systems (e.g., nitrophenol derivatives) (Fleming et al., 2020).

The CHON class is the second-most abundant class by intensity but has the highest number of detected compounds in PM affected by wildfires in Nadym, with molecules commonly containing one or two nitrogen atoms. Most compounds of the CHON class show a high degree of oxidation, comparable to the CHO class, with the same shift to a lower oxygen number for ESI+ (Fig. S8). Notably, the oxygen distribution of the ESI− data shows the maximum at nine oxygen atoms, independent of the nitrogen number. An O/N ratio ≥ 3 is the limit for the potential presence of an organic nitrate group, but as the elemental compositions show a high degree of oxidation (O/N » 3), the detection of hydrocarbons with only nitrate groups is rather unlikely.

Nitroorganics are a relevant species regarding their lightabsorption properties and their role in BrC (Salvador et al., 2021). More likely, the majority of compounds detected by ESI and APPI contains more than one functional group, and therefore no clear identifications solely based on the O/N ratio are possible. On the other hand, compounds with an $O/N < 3$ can be identified as potential nitro compounds, which are frequently detected here by ESI+ (998) and APPI (390).

ESI+ also detects a number of compounds with more or equal amounts of nitrogen compared to oxygen. These compounds could be assigned to alkaloid-like structures or other moieties that include nitrogen-containing heterocyclic compounds (Laskin et al., 2009), which are preferably released under low-temperature and oxygen-poor combustion conditions (Ren and Zhao, 2015).

3.4.3. Sulfur-containing compounds (CHOS/ CHNOS)

Sulfur is, to some degree, a part of biomass, e.g., as disulfide bonds or in certain amino acids, and compounds containing sulfur are therefore emitted by biomass burning. Second, e.g., organosulfates are markers for secondary organic aerosol formation with reactions of precursors with anthropogenic pollutants, including sulfates, dimethyl sulfide, and other sulfur-containing nucleophiles like $SO2$ (He et al., 2014; Ye et al., 2021). Additionally, marine biogenic emissions of reduced sulfur compounds are a major source of dimethyl sulfide (DMS), carbon disulfide ($CS2$), and their oxidation product carbonyl sulfide (OCS) (Qu et al., 2021; Lennartz et al., 2017). The presence of nitrogen in the precursor, as well as the high abundance of NOx , may also lead to the formation of nitrooxy-organosulfates (He et al., 2014). CHOS compounds, observed almost exclusively by ESI−, display 4 to 11 oxygen atoms (Fig. S8) as well as low DBE values, indicating long-chain aliphatic structures with one sulfate group and additional oxygen-containing groups. Identical sum formulae have previously been observed in aerosol samples from Chinese megacities (Wang et al., 2016), as well as the ozonolysis of isoprene SOA in the presence of acidic sulfate aerosol (Riva et al., 2016). For example, the $CHO6S1$ class is dominated by one homologous series (DBE = 2) reaching from $C5H10O6S1$ (198.01981 Da) to $C35H64O6S1$ (612.44236 Da), including several sum formulae known from the literature, with a proposed terpene origin and the structure of an aliphatic chain with one sulfate, hydroxyl, and carbonyl group each (Riva et al., 2016). Only a few compounds display higher DBE values (DBE = 7), indicating the minor abundance of aromatic precursors. Some of these CHOS compounds are also found in the Nadym PM samples after the plume has passed (N08–N10) but less often and only at higher molecular weights. This may be explained by an independent source of acidic sulfate aerosols, e.g., originating from sea spray or marine emission sources (M. Zhang et al., 2021), leading to the formation of the observed compounds through reactions with biogenic emitted terpenes, e.g., via the epoxide pathway, as well as the presence of other sulfurcontaining functional groups, apart from sulfates, like sulfides or thiophenes.

Nitrooxy-organosulfates are also observed in the wildfireplume-impacted samples (N01–N05) but with a lower relative intensity compared to CHOS compounds (Fig. S11). These compounds are, for example, a product of the combination of two aging reactions adding a nitrate (or nitrooxy) and a sulfate group to one molecule. The sum formulae of one exemplary compound $C10H17N1O7S1$ are suggested to contain one nitrate and one sulfate group, within several isomers, and were also identified in aerosol samples from Shanghai and nighttime oxidation experiments of monoterpenes under acidic conditions (Wang et al., 2016; Surratt et al., 2008). In addition, the sulfur content in CHNOS compounds can also be in the form of sulfides, sulfones, sulfur in ring systems, or other functional groups (Ditto et al., 2021). Detected CHNOS compounds in the main plume are almost exclusively comprised of ELVOC or ULVOC. Similar results for low-volatility CHNOS compounds in aerosol over agricultural fields were linked to a biogenic origin with formation based on sulfate addition to epoxide CHON precursors (Vandergrift et al., 2022).

3.4.4. Reduced compounds (CH/CHN)

Pure hydrocarbons are only detected by APPI due to the poor ionization efficiency of non-polar molecules with ESI, as well as the good ionization efficiency of photoionization for most hydrocarbons (Kauppila et al., 2017). It is expected that hydrocarbons are not found in high abundance in an aged, long-range-transported wildfire plume, as oxidation reactions lead to the transformation of pure hydrocarbons or non-oxygen-containing species. Nevertheless, due to the plume optical thickness protecting hydrocarbons from photolysis and general oxidant deficits, some hydrocarbons are observed, including an extensive homologous series of alkenes from C15 to C33. (DBE = 1) as well as higher aromatic structures potentially identified as alkylated (aromatic) ring systems (DBE = 6–9).

Reduced nitrogen compounds are only found in ESI+, which indicates amine, pyridine, or other basic aromatic nitrogen moieties in the detected molecules. They are found in the moderate DBE range of 4–8, so the occurrence of aromatic structures is possible. Proposed alkaloid structures, in the same DBE range, also containing two or more nitrogen atoms in one molecule, are a known product of incomplete biomass burning, e.g., due to high concentrations in ponderosa pine foliage and thermal stability of these compounds (Laskin et al., 2009).

3.5 Carbohydrate, lignin, and resinoic acid thermal degradation products in PM of Nadym

The REMPI mass spectra from OC fractions OC1 and OC2 were combined to form OC1–2 (Fig. 6), which is dominated by thermal desorption, and OC3 and OC4 to form OC3– 4, showing a shift towards smaller molecular masses due to thermal decomposition of larger chemical structures as a complementary approach to FT-ICR MS. As discussed in Sect. 3.4.1 regarding CHO species, BB releases monomers from the decomposition of the biopolymers cellulose, hemicellulose, and lignin, which are commonly used as BB markers. However, the detection of lignans, such as tetrahydro- 3,4-divanillylfuran, suggests that phenolic dimers and larger thermal lignin fragments are also emitted (Oros and Si- moneit, 2001). Those larger fragments resist the temperatures in OC1–2 but decompose in situ to monomers in OC3– 4, which indirectly allows for BB identification. Previous studies have described REMPI mass spectra from the pyrolysis of cellulose, softwood-derived lignin (Grabowsky et al., 2011), several types of biomass (Fendt et al., 2012; Fendt et al., 2013), and SOA from ozonolysis of β-pinene (Diab et al., 2015). Due to the highly oxidized nature of cellulose and SOA, thermal decomposition is similar and complicates the assignment of the mass spectrometric pattern.

All samples which are strongly affected by the wildfire plume exhibit a minimum uncentered correlation coefficient of 0.94. This is in agreement with the similar air mass tra jectories to Nadym arriving from 5 to 7 August 2021, while the similarity to the background days is only 0.71 on average. During pyrolysis of low-volatility oxygenated compounds, oxygenated aromatic species are formed, such as phenol (m/z 94), cresol (m/z 108), benzofuran (m/z 118), and naphthols (m/z 144, m/z 158). Hence, most abundant peaks mainly belong to m/z found in OC3 of cellulose and SOA. The pyrolysis yield of lignin-derived species depends on the type of biomass: gymnosperm, angiosperm, or grasses. Although central Yakutia is largely covered by coniferous plants like larch and pine (Kharuk et al., 2021), m/z of syringol-type methoxyphenols (syringaldehyde, m/z 182; allylsyringol, m/z 194; sinapyaldehyde, m/z 208) from angiosperm can be detected next to guaiacoltype methoxyphenols from gymnosperm (guaiacol, m/z 124; methylguaiacol, m/z 138; eugenol, m/z 164; coniferyl alcohol, m/z 180). Moreover, hydroxyphenols from the decomposition of

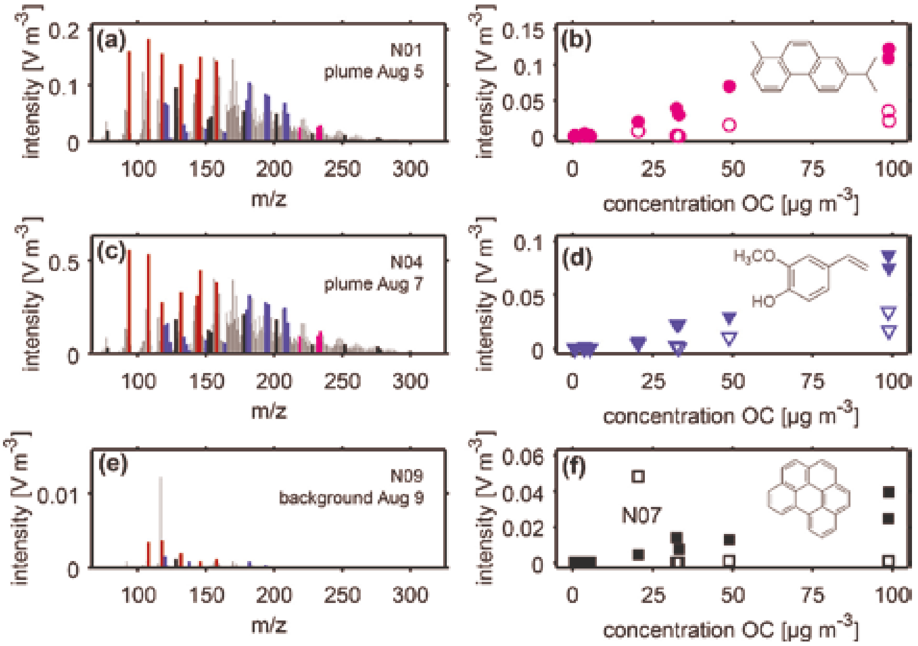

Figure 6. REMPI mass spectra, normalized to the sampling volume, of OC3–4 from Nadym samples N01 (a) and N04 (c) with elevated OC and EC concentrations as well as N09 as a reference for PM without wildfire impact (e). The different colors indicate decomposition products typical for coniferous plants (magenta), cellulose/SOA (red), and lignin (blue) as well as parent PAH (black). Correlations of (b) m/z 234 (e.g., retene), (d) m/z 150 (e.g., vinylguaiacol), and (f) m/z 276 (e.g., benzo[g,h,i]perylene) in OC1–2 (open symbols) and OC3–4 (filled symbols) to OC.

less lignified plants or plant material (B. Simoneit, 2002) are present in the REMPI mass spectra (vinylphenol, m/z 120; dimethylphenol, m/z 122; cinnamic alcohol, m/z 134; anisaldehyde, m/z 136).

In addition to monoaromatic compounds, polycyclic aromatic hydrocarbons and their derivatives are present in the sample or formed in situ. Retene or 1-methyl-7-isopropyl phenanthrene refers to an established marker for the combustion of coniferous biomass (Ramdahl, 1983). It is formed from the thermal degradation of diterpenoids with abietane skeleton. For pine and Siberian larch, most abundant diterpenoids are abietic acid and isopimaric acid as well as levopimaric and palustric acid, respectively (Bardyshev et al., 1970). Their thermal degradation depends on the individual combustion conditions and involves successive dehydrogenation, dealkylation, and decarboxylation, finally resulting in an aromatization of one to three six rings. Consequently, a broad product spectrum is obtained with retene as the most likely reaction product (Standley and Simoneit, 1994; Marchand-Geneste and Carpy, 2003), which has recently been investigated with TOCA-REMPI-TOFMS for spruce logwood and brown coal briquette combustion (Martens et al., 2023). Despite being an alkylated PAH, retene gives a relatively low yield of the molecular ion and partially fragments during REMPI, causing dehydrogenation and demethylation to m/z 232 and m/z 219, respectively. In OC3–4, retene (m/z 234) is formed in situ from earlier thermal degradation products of diterpenoids, such as dehydroabietic acid or simonellite, and highly correlates with the total OC concentrations in Nadym (Fig. 6b), giving evidence for a dominating OC source of burning coniferous biomass. In OC1–2, containing retene, which is truly in the sample, a correlation can also be observed. However, intensities of m/z 234 in OC1–2 are apparently lower than for OC3–4. Primary retene (RETprim), which has been formed during combustion and is detected in OC1–2, is associated with more efficient combustion than pyrolytic retene (RETpyr), which is formed from the pyrolysis of diterpenoids and their alteration products and is detected in OC3–4. Hence, the ratio of primary retene to total retene (RETtot) in OC may provide a metric for the combustion efficiency of coniferous biomass, similar to the modified combustion efficiency based on CO and CO_2 (Yokelson et al., 1996), which is further evaluated in Sect. S4.

According to RETprim/RETtot close to 0, samples N01– N02 (6 August 2021) contain biomass burning aerosol, e.g., originating from fires under smoldering conditions (Fig. 6). From 7 August 2021 to the morning of 8 August 2021 (N03– N07), the fires became more intense and changed to more flaming conditions, suggested by increased OC and EC concentrations, lower ratios of OC to EC that are typical for higher combustion efficiency, and RETprim/RETtot between 0.15 and 0.26; on these days, the main plume by means of the highest aerosol concentrations arrived in Nadym. During the reference days with typical background concentrations, 1 to 3 orders of magnitude lower intensities for RETpyr and no RETprim were detected, indicating low biomass burning activity. The same approach could be principally used for lignin-derived methoxyphenols, such as vinylguaiacol (m/z 150) (Fig. 6d), but it will be more affected by the dilution because of their higher volatility. Beyond methoxyphenols and retene, REMPI is particularly sensitive to PAH (Streibel and Zimmermann, 2014). In OC3–4, twoto four-ring PAHs (m/z 128, m/z 154, m/z 166, m/z 178, m/z 202, m/z 228) are formed by pyrolysis, but larger PAHs with five or more aromatic rings (m/z 252, m/z 276, m/z 278, m/z 300, m/z 302) are divided between OC1–2 and OC3–4 (Diab et al., 2015). For m/z 276, representing six-ring PAHs like benzo[g,h,i]perylene or indeno[c,d]pyrene, a good correlation can also be observed with OC (Fig. 6f). However, in OC vs m/z 276 of OC1–2, an outlier emerged, belonging to sample N07. The impact of regional gas flaring and associated emission of

PAH is separately discussed in Sect. 3.6.

To estimate the influence of the wildfire plume on ambient particle composition and concentration, a REMPI spectrum of OC3–4 from sample N09 (9 August 2021) with OC and EC concentrations below 1 µg m^{-3}, typical for the Arctic region average (Yasunari et al., 2021), is shown (Fig. 6e). More than 2 orders of magnitude lower intensities were found for lignin-related m/z and 1 order of magnitude lower intensities for aromatics formed from pyrolysis of low-volatility oxygenated compounds. Due to the absence of RETpyr, we conclude that those ions belong to pyrolysis of SOA rather than fragments of carbohydrates. The base peak at m/z 117, however, belongs to indole, which has a 32–40 higher photoionization cross section at 266 nm than toluene (Gehm et al., 2018) and results from the pyrolysis of bioaerosol components, such as proteins (Fuentes et al., 2010), which emphasizes the higher contribution of the natural background to the PM composition in Nadym.

3.6. Impact of gas flaring on PM composition in Nadym

In addition to long-range-transported wildfire emissions, gas flaring from open excess-gas burning at oil and gas fields is one of the major sources of black carbon (BC) emis- sions in the Siberian Arctic (Popovicheva et al., 2022, 2017; Stohl et al., 2013). Sample N07 was not apparent in OC and EC compared to the other wildfire-plume-impacted samples (N05 and N08) collected on the days before and afterward but differed in chemical composition. Backward air mass trajectories for sample N07 show the transport of air masses through the region south of Nadym, where many oil and gas fields are located (Fig. S2). A unique pattern of compounds is observed in both APPI-FT-ICR MS and TOCAREMPI MS, with each ionization technique being sensitive to the detection of aromatic hydrocarbon compounds due to the favorable photoionization properties of aromatic ring structures (Gehm et al., 2018; Huba et al., 2016). When excess gaseous organic compounds are burned in a gas flare, incomplete combustion can lead, among others, to the formation of aromatic hydrocarbons in a large range of molecular sizes, from benzene to aromatic soot precursors with large condensed ring structures in various structural combinations and sizes (Slavinskaya and Frank, 2009; T. Zhang et al., 2021; Senkan, 1996). Figure 7a shows a comparison of averaged samples impacted by the wildfire plume (N01–N05) and sample N07 APPI data, highlighting unique, condensed aromatic compounds (AI > 0.67), with up to 40 carbon atoms, exclusively observed in N07. Due to their pyrogenic formation, no pronounced alkylation is observed in these compounds, which is a key factor for the differentiation to condensed aromatic structures, e.g., found in petroleum (Fig. 7b). By calculating the slope of the planar limit and the ratio of core to methylated species intensity (C0/C0 + C1) in the sample N07 (Fig. 7b, Table S5), the pyrogenic origin (slope: 0.81, C0/C0 + C1: 0.7–0.8) is confirmed (Yunker et al., 2002; Cho et al., 2011). A slope of the planar limit from 0.75 to 1 indicates the addition of benzene rings linearly or nonlinearly to a core structure, and a maximum of intensity for each DBE value at C0 is associated with combustion emissions (Laflamme and Hites, 1978).

As pointed out in Sect. 3.5, markers of BB in the TOCAREMPI mass spectrum of OC34 strongly correlate with the total content of OC. However, for m/z of PAH,

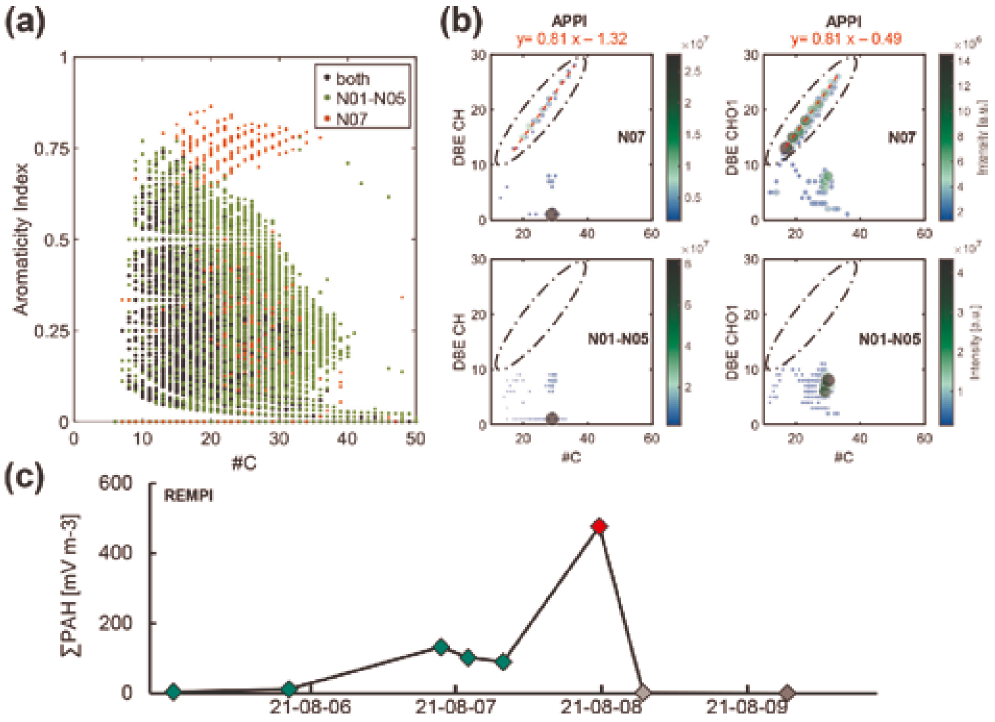

Figure 7. (a) Aromaticity index (AI) versus carbon number plot of sum formulae (APPI) observed uniquely in the wildfire-impacted samples in Nadym (N01–N05, green), in sample N07 additionally impacted by gas flaring (red), or both datasets (black). (b) Double-bond equivalent (DBE) versus carbon number plot of CH (left) and CHO1 (right) compound classes for main plume (bottom) and N07 (top) with the linear equation of the planar limit indicated in red. (c) Time trend of summed intensities of parent-PAH-related m/z (128, 152, 178, 202, 228, 252, 276, 278, 300, and 302) detected by TOCA-REMPI-TOFMS in OC1–2.

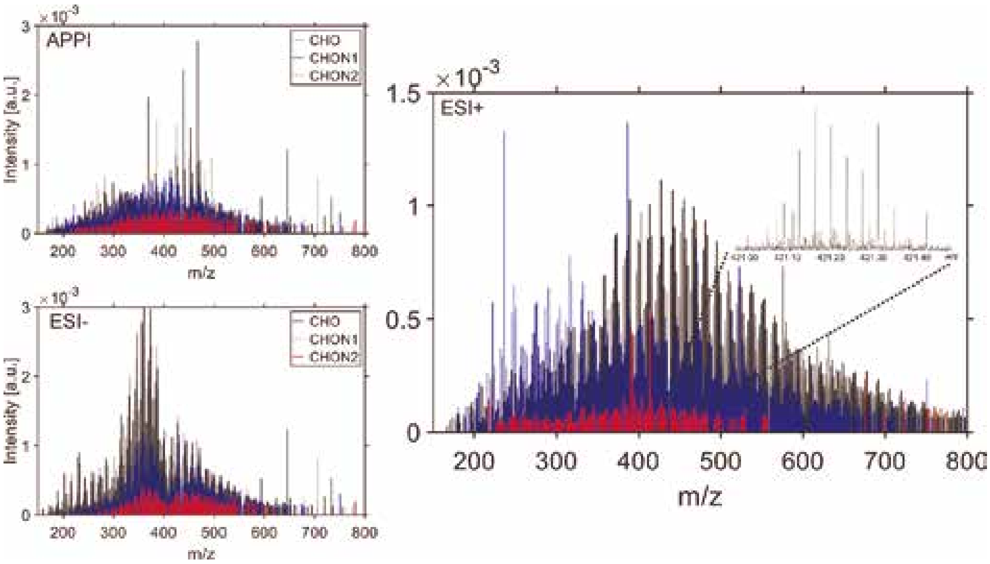

Figure 8. TIC normalized mass spectra of assigned CHO (black), CHON1 (blue), and CHON2 (red) elemental compositions identified in the wildfire-affected PM sampled at Bely Island, collected by APPI and ESI during the period during which wildfire aerosol arrived in Nadym. Zoomed-in representation of one nominal mass of the ESI+ spectrum, highlighting the molecular complexity of oxygenated compounds at m/z 421.

such as m/z 276 representing six-ring PAHs, sample N07 of 8 August 2021 deviates from this correlation (Fig. 6f). In the REMPI mass spectrum of OC12, minor fragments at m/z 118, 132, and 146 from low-temperature pyrolysis of carbohydrates and SOA are visible, but larger parent PAHs dominate the mass spectrum of N07 in contrast to wildfire plume sample N03 (Fig. S12) and support the findings from APPIFT-ICR MS.

Despite apparent differences in air mass trajectories of sample N07, containing PM from long-range-transported wildfire plume, from N05 or N08, the mass spectrometric analyses suggest the presence of a high-temperature combustion aerosol, such as from gas flaring, which was added to the chemical PM signature of biomass burning and aged organic aerosol. Both wildfire and gas flaring can be regarded as the most significant contributors to PM in northern Siberia.

3.7 Chemical characterization of PM from Bely Island

FT-ICR MS data of wildfire plume that affect PM on Bely Island, collected during the same period of high PM levels in Nadym (sample B01, 31 July to 6 August 2021), show a similar or even higher complexity than the PM in Nadym as well as partly different chemical composition. Figure 8 shows mass spectra of the three most abundant compound classes in the range of m/z 150–800 in APPI and ESI, with APPI showing approximately the same number of identified sum formulae (5231), ESI− showing a lower number (3553), and ESI+ showing even more identified formulae (7361) in PM on Bely Island (B01) compared to the composition of PM in Nadym averaged from 5 to 8 August 2021 (N01 to N07). When comparing the spectra of Fig. 8 with data from Nadym (Fig. S13), differences in the chemical composition become apparent.

The most pronounced region in the APPI spectrum of Nadym PM samples affected by wildfire plume (N01–N07) is m/z 400–500, containing high intensities of CHO1– CHO4 compounds with moderate aromaticity (DBE 5–10). This section is less abundant in the mass spectrum from PM of Bely Island (B01), but the lower m/z region compounds (200–350 Da), including CHO5–CHO7, are more pronounced. The same shift to a higher degree of oxidation can be observed in the ESI+ data of the PM samples from Bely Island. The CHO8–CHO14 compounds compile the broad signal distribution of the CHO class at m/z 400– 800 in the PM samples from Bely Island, while the ESI+ spectrum of Nadym PM samples is characterized by single intense signals of, e.g., marker compound masses like levoglucosan, which is not identified on Bely Island, and a more equal distribution of the remaining majority of signals.

The lower abundance of biomass burning marker compounds in PM samples from Bely Island could be attributed to more pronounced aging and SOA formation of the air masses reaching the Arctic region, reducing the amount of primary biomass burning markers.

In the REMPI mass spectra of OC3–4, BB-related thermal fragments discussed in Sect. 3.5 are clearly visible for the weekly samples from 31 July to 7 August 2021 (B01) and from 7 to 14 August 2021 (B02) (Fig. S14a and b). However, compared to a main plume sample from Nadym (N05) (Fig. S14d), these samples from Bely show distinct higher m/z in OC3–4, possibly due to the formation of larger, chemically different or more stable structures. The ratio of RETpyr to OC in B01 and B02 is 30 % to 50 % lower than in sample N05 but still confirms the significant contribution of BB aerosol. In the sample after the plume event from 14 to 21 August 2021 (B03), both overall and BB-related thermal fragments disappeared in the REMPI mass spectrum, while N-containing thermal fragments from the degradation of bioaerosol components, such as from proteins, increased in relative abundance at m/z 117 (indole) and m/z 131 (methylindole) (Fig. 139C) (Fuentes et al., 2010).

When comparing sum parameters determined from the elemental composition assignment of both datasets (Tables 1, S3, S6, and S7), a trend resulting from an increased photochemical age is visible. All ionization techniques show that the samples collected on Bely Island are more oxidized and less aromatic with a higher saturation vapor pressure, as well as higher average O/C and O/N

Table 1. Sum parameter trends comparing wildfire plume datasets from Nadym and Bely Island of the same period (31 July to 7 August 2021; "<": increase, "≈": steady, ">": decrease).

	Nadym		**Bely Island**	**Nadym**		**Bely Island**	**Nadym**		**Bely Island**
AI < 0.25 [% int.]	55.60	<	66.45	69.22	<	75.96	86.09	<	88.56
AI > 0.5 [% int.]	6.83	>	4.48	2.71	<	3.40	0.87	<	2.12
DBE	8.07	>	7.09	7.70	>	6.75	5.28	<	6.01
OSC	−0.80	<	−0.61	−0.50	<	−0.32	−1.09	<	−0.78
log(C*)	−5.41	<	−5.19	−8.01	<	−4.99	−5.49	≈	−5.87
O/C	0.31	<	0.42	0.48	<	0.54	0.30	<	0.40
O/N	5.78	<	6.65	6.66	<	8.39	4.70	<	6.83
CHO [% int.]	47.12	<	48.10	44.05	<	64.70	45.96	<	51.40
CHNO [% int.]	47.76	>	44.10	36.71	>	28.60	47.38	>	45.30

ratios. The relative CHO intensity is increased, while the other relative intensities are decreased. AAE values are also decreased, indicating degradation of chromophores by photobleaching (Liu et al., 2021). This behavior indicates more intense atmospheric aging, especially by reactions adding oxygen to the organic aerosol molecules, but not nitrogen or sulfur. This is contrary to observations made for the evolution of emissions from a boreal forest fire in Lac La Loche (Canada), where an increase in nitrogenand also sulfur-containing compounds was observed (Ditto et al., 2021). The lower concentrations from the wildfire plume periphery result in a higher ratio of atmospheric oxidants to reactive aerosol constituents. Furthermore, the more remote location of Bely Island compared to Nadym determines a lower mixing with reactive gases from anthropogenic emissions (e.g., NOx and SOx). Therefore, the PM composition in Bely Island shows a picture of more intensively oxidized organic matter with a lower content of N- and S-containing compounds compared to PM from Nadym. For a molecular insight into the differences in PM composition in Nadym and on Bely Island, the intersect of both datasets in each ionization technique is determined (Fig. 9a). The compound class distribution of each section gives an overview of the chemical composition unique to each sampling location. A large fraction of sum formulae is present in both datasets, which is explained by the almost-identical source of the PM emissions. Nevertheless, a high number of compounds is uniquely abundant in one of the two datasets.

The m/z unique to Nadym PM contains a disproportionate number of nitrogen-containing compounds (CHNO), while the PM sample from Bely Island contains more CHO compounds (except for APPI) relative to CHON compounds.

Van Krevelen plots of all applied ionization techniques reveal a clearly visible difference in the fingerprint of unique organic compounds (Fig. 9). Peaks only detected in the Nadym PM are in the low to medium O/C range, with a H/C ratio larger than 1.2 and an average OSC < −1. On the other hand, unique peaks in PM of Bely Island show a much higher O/C range, with abundant average OSC in the range of −1 to 0, as well as abundant low O/C and low H/C compounds. The number of unique nitrogen-containing compounds is almost identical for both sites, but the relative nitrogen number distribution is shifted to lower (or 0) nitrogen numbers for PM of Bely Island. An opposite trend is observed for the oxygen number distribution. The unique peaks detected in PM from Bely Island show a much higher degree of oxygenation (maximum at 13 oxygen atoms), whereas most of the unique peaks in Nadym PM samples contain less than 6 oxygen atoms. The overlap of both datasets is observed in between both oxygen number distributions.

These characteristic differences between wildfire plume PM in Nadym and on Bely Island agree with the previously discussed more intensive atmospheric aging of the organic aerosol in wildfire PM collected on Bely Island compared to the relatively fresh aerosol collected in Nadym.

3.8 Elucidation the origin of individual elemental compositions by hierarchical clustering

Hierarchical cluster analysis is applied to better understand which compounds of the tens of thousands of identified elemental compositions are the most relevant for the characterization and differentiation of the observed sample origins (wildfire plumes sampled in Nadym and on Bely Island, mixing of plume with gas flaring emissions, and samples after the wildfire plume had passed). Considering all elemental compositions, including both [M+H] and [M+Na] adducts that are found in ESI+ datasets, HCA (with a maximum number of clusters set to five) is performed to sort each elemental composition into a separate cluster (average silhouette value = 0.40) (Merder et al., 2021). The resulting clustergram (Fig. S15) shows the grouping of samples with a known similar origin into the same clusters. In order to highlight molecules related to different sample origins, the elemental composition clustering results are summarized into five main clusters. The chemical characteristics of the results are visualized in Van Krevelen space and compound class distribution plots (Fig. 10).

The analysis of elemental compositions by HCA emphasizes the dominating influence of wildfire emissions on the complex chemical composition of the detected organic aerosol species. Compounds present in the ambient aerosol samples are also observed as a constant background in the PM samples affected by wildfires at

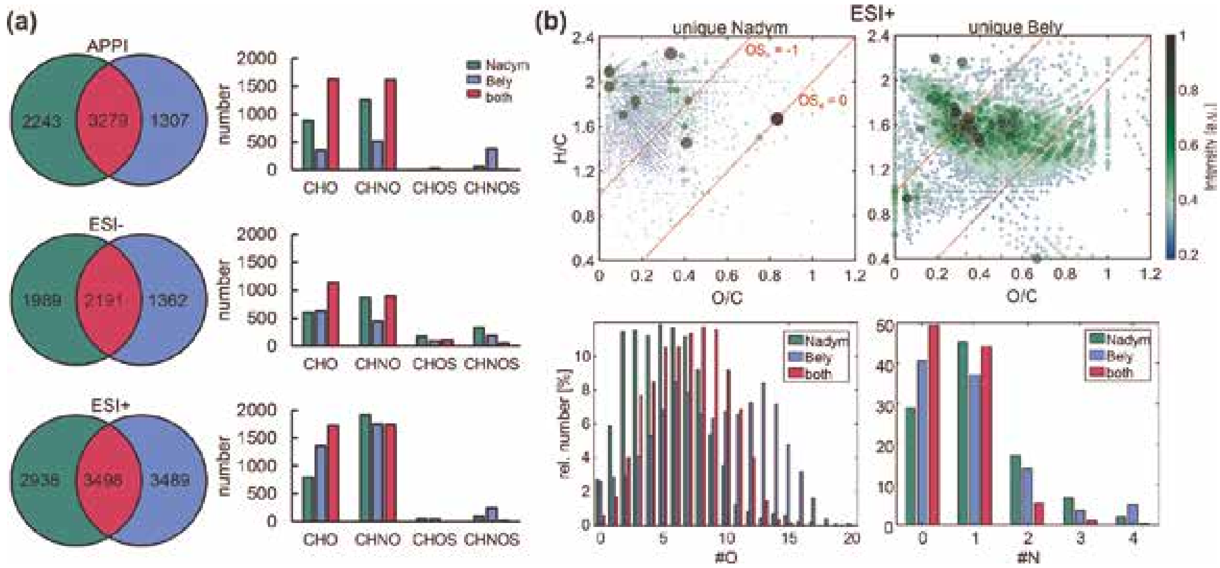

Figure 9. **(a)** Venn diagram with sum formula numbers (left) and relative intensity compound class distributions (right) of Nadym main plume (green) and Bely Island (blue) wildfire aerosol datasets. **(b)** Van Krevelen plot of unique compounds (ESI+) identified in Nadym and on Bely Island PM samples and relative number distribution of oxygen- and nitrogen-containing compounds for unique and shared (magenta) elemental compositions.

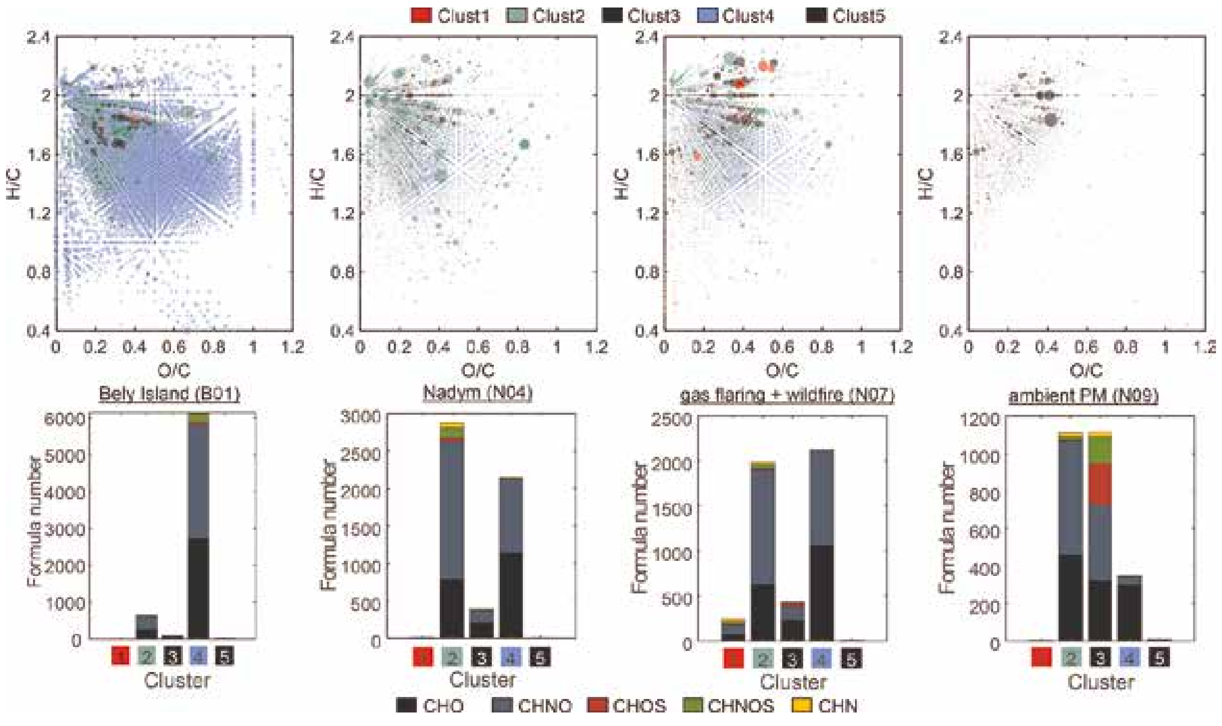

Figure 10. Visualization of hierarchical cluster analysis (HCA) results based on all elemental compositions detected in ESI+, with the number of clusters set to five. Van Krevelen (VK) plots of four exemplary samples and bar plots of the compound class distribution in each cluster. The colors in the VK plot indicate the cluster assignment of each elemental composition, with dot size indicating the intensity of each compound. Cluster 4 (blue) is associated with aged wildfire compounds, cluster 2 (green) is associated with fresher wildfire aerosol, cluster 1 (red) is associated with gas flaring, and cluster 3 and cluster 5 (black) are associated with ambient PM without a contribution of wildfires on Bely Island and in Nadym, respectively.

both sampling sites. The clustering in combination with knowledge of the respective dominating emission sources for each sample allows for a deeper discussion of the identified clusters.

Compounds of cluster 4 are detected with high abundance (intensity and number) in the wildfire-affected PM on Bely Island but are also, less dominating, present in the Nadym PM samples with wildfire influence (Fig. S16). The VK plot (Fig. 10) shows a broad distribution of compounds with O/C ratios up to unity. The complex pattern shown by these compounds is in line with the previous finding of intensively aged biomass burning aerosol arriving at Bely Island from 31 July to 6 August 2021. Cluster 2 contains typical compounds present in wildfire-affected PM sampled in Nadym, which are rarely present in PM on Bely Island with and without wildfire influence. The pattern shown by compounds in this cluster is less distributed over the VK space, with lower O/C ratios and higher H/C ratios, compared to the SOA compounds in cluster 4. This suggests less intense atmospheric aging of the wildfire plume arriving in Nadym from 5 to 8 August 2021; thus PM in Nadym was still substantial and had a clear signature of fresh biomass burning emissions. In addition to the fresh biomass burning emissions, aged aerosol species (cluster 4) are also detected. The detection of both aged and fresh biomass burning emissions agrees with the observation of higher aerosol absorption in the part of the wildfire plume transported to Nadym than that transported to Bely Island. A high wildfire plume density suppresses photochemistry inside of the plume due to light absorption, lower OH radical production, and a lower ratio of atmospheric oxidants to reactive aerosol species. Therefore, cluster 2 and 4 contain similar numbers of sum formulae in PM samples affected by wildfire aerosol in Nadym but substantially more sum formulae in cluster 4 in PM samples affected by wildfires on Bely Island.

The impact of gas flaring on sample N07 is clearly represented by compounds in cluster 1 (red), as it is the only sample where cluster 1 is significantly populated. Compounds of this cluster are found in the highly aromatic, low-O/C-ratio region of the VK space, as has previously been discussed for the gas-flaring-impacted sample. Compounds from typical concentration levels in Nadym and on Bely Island, termed ambient aerosol samples (N08–N10 and B03), are grouped into clusters 3 and 5, respectively. Cluster 5 makes its highest contribution to the Bely sample without wildfire impact, while compounds from cluster 3 are found in most PM samples of Nadym with the highest relative contribution after the wildfire plume had passed the site.

4 CONCLUSIONS

Our study shows the long-range transportation of wildfire plume over different trajectories and provides insights into the chemical composition of aged air pollutants in the Siberian Arctic. Due to PM sampling in Nadym and on Bely Island in the north of western Siberia at the same time, it was possible to observe the different atmospheric fates of the plume periphery and center aerosol at similar atmospheric residence times and transport distances. First, back-trajectory analysis with in-depth chemical characterization of the organic compounds through complementary mass spectrometric techniques revealed a complex organic mixture of primary and secondary organic aerosols at both sites and confirmed the dominant biomass burning source for samples N01 to N07. In situ detection of resinoic acids and alteration products as pyrolytic retene in relation to primary retene specified the biomass to coniferous vegetation and possibly provides an additional indication of the combustion efficiency in biomass burning. Furthermore, the additional influence of regional gas flaring on sample N07 could be underlined from its contribution of larger PAHs to the PM burden, which may serve as a criterion to separate contributions to the Arctic PM burden by wildfire from anthropogenic combustion emissions. After the plume passed Nadym, neither the molecular signature of BB nor gas flaring was found in samples N08 to N10, with up to 1 order of magnitude lower concentrations of OC and EC compared to samples N01 to N07.

During the main plume period at both sites, CHO and CHON were the dominating compound classes observed in ultra-high-resolution mass spectra by all ionization techniques, with especially nitrogen-containing compounds being of interest due to their effect on the light-absorbing properties of aerosols. Nevertheless, both sites showed distinct differences in their more detailed chemical properties. PM samples from Bely Island were more oxidized with a higher oxidation state but lower aromaticity than PM samples from Nadym. The biomass burning aerosol arriving at Bely Island was identified as originating from the plume periphery of lower concentration; thus it underwent more intense atmospheric aging than the center plume transported to Nadym, despite similar physical plume ages. Finally, hierarchical clustering of the ultra-high-resolution mass spectra from ESI+ could sort the detected sum formulae and deconvolute the chemical composition according to contributing aerosol sources.

The long-range transport of a wildfire plume from central Siberia was observed as an intense event of carbonaceous aerosol influx to the vulnerable Arctic ecosystem. Typical ambient concentrations of OC and EC in Nadym and on Bely Island were exceeded by 1 to 2 orders of magnitude. Moreover, AAE405/808 from 1.5 to 3.3 suggested the presence of BrC in Nadym, but the weekly average of AAE405/808 over a similar period on Bely Island accounted for 1–1.2, indicating more intense atmospheric aging and degradation of BrC chromophores from the same wildfire plume.

Despite the known impact of wildfire plumes on the Arctic aerosol composition, the investigated PM samples from Nadym and Bely Island describe a long-range-transport event with unprecedented high concentrations of carbonaceous aerosol. Detailed chemical characterization of aged wildfire aerosol emissions provides insights into biomass burning and atmospheric processes and may improve our understanding of interactions between the biosphere and atmosphere as well as consequences on the Arctic ecosystem and climate.

Code and data availability. Code to analyze all data and generate all figures is available from the first author upon request. Geographical information for the creation of maps was downloaded from QGIS (https://qgis.org/en/site/, QGIS, 2023). VIIRS and MODIS data were downloaded from NASA Earthdata (https://www.earthdata.nasa.gov/, NASA, 2023). Oil and gas flare location data were downloaded from SkyTruth (https://skytruth.org/, SkyTruth, 2023).

Полициклические ароматические углеводороды в снежном покрове Ямало-Ненецкого автономного округа как индикаторы влияния источников техногенных эмиссий*

ВВЕДЕНИЕ

Север Западной Сибири является одним из индустриально-развитых регионов. На территории Ямало-Ненецкого автономного округа (ЯНАО) добывается 85 % российского и 20 % мирового природного газа [1]. Ежегодные выбросы вредных веществ от стационарных и передвижных источников в ЯНАО составляют 856 тыс. тонн [1], поэтому уровень техногенного воздействия при освоении недр является определяющим в формировании экологической обстановки на всей территории округа. Комплексные геоэкологические исследования севера Западной Сибири в пределах ЯНАО показали сильный и умеренный уровни загрязнения углеводородами и тяжелыми металлами в локальном масштабе вблизи скважин и объектов промысловой инфраструктуры [2]. Характеристики снежного покрова вблизи объектов топливно-энергетического комплекса (ТЭК) и транспортных магистралей отличаются от удаленного малонаселенного арктического района Ямала увеличением степени закисления от нейтрального до слабокислого и кислого [3, 4].

Полициклические ароматические углеводороды (ПАУ) – класс органических соединений, состоящих из двух или более сконденсированных бензольных колец; они относятся к стойким органическим загрязняющим веществам, определяющим геохимические маркеры загрязнений [5]. ПАУ подразделяются на пирогенные, образовавшиеся в результате неполного сгорания ископаемых топлив и биомасс, и петрогенные нефтяного происхождения, а также образующиеся в диагенетических процессах (перилен). Они обладают высокой устойчивостью, токсичными, мутагенными и канцерогенными свойствами [5], что определяет актуальность исследований их распространения в окружающей среде.

Пирогенные ПАУ накапливаются в нижних слоях атмосферы в составе мелкодисперсных аэрозолей, в наземные экосистемы они поступают в результате сухого и мокрого осаждения при доминировании последнего [6]. От локальных источников (хозяйственных объектов, автомагистралей) аэрозольные эмиссии выпадают на расстоянии сотни метров [7]. Вблизи крупных городов и промышленных районов повышенный уровень ПАУ формируется на территориях в радиусе от 10 до 50 км [8–10]. В составе аэрозолей ПАУ могут переносится воздушными массами на сотни и тысячи километров от источника эмиссии [11]. Для 4-ядерных ПАУ фотоокислительная деградация на поверхности частиц аэрозолей происходит более интенсивно по сравнению с 5–6-ядерными [12], что приводит к накоплению высокомолекулярных полиаренов в снежном покрове при увеличении дальности переноса от источников эмиссий.

Исследования загрязнений окружающей среды продуктами антропогенной деятельности показали увеличенные концентрации органических компонентов в снежном покрове Арктики, возможно, связанные с более быстрыми климатическими изменениями в этом регионе в глобальном масштабе [13]. Высокие концентрации ПАУ характеризуют загрязнения проб снега в поселках, вблизи автодорог и промышленных предприятий на архипелаге Шпицберген [14]. Следовые количества ПАУ наблюдаются в удаленных районах высокоширотной Арктики, на Баренцево-Карском шельфе и хребте Менделеева в центральной части Северного Ледовитого океана [15].

Соотношение концентраций различных ПАУ в окружающей среде указывает на их происхождение [16]. Показатель суммарного содержания неалкилированных ПАУ широко используется для оценки уровня антропогенной загрязненности экосистемы [17]. Анализ профилей незамещенных полиаренов или их производных позволяет сравнивать источники поступления ПАУ [18]. Рассчитывают и индикаторные показатели ПАУ с разным числом ядер для оценки вклада пирогенных и петрогенных источников, в том числе автомобильного транспорта, отопительных систем, установок сжигания мусора, угля и переработки нефти [19].

По оценкам [20], до 30 % всех промышленных выбросов загрязняющих веществ в атмосферу приходится на нефтегазовый сектор экономики. Эмиссии сжигания попутного нефтяного газа (ПНГ) на российских территориях превышают все другие нефтедобывающие регионы мира; по объему сжигания ПНГ лидируют индустриальные регионы Центральной и Западной Сибири [21]. Распространение сконденсированных на аэрозолях канцерогенных и экологически опасных соединений на большие расстояния приводит к загрязнению снежного покрова, почвы и поражению растительных сообществ [22]. Однако из-за значительной изменчивости состава нефти и технологических условий сжигания на факельных установках физико-химические свойства

---

* Ю.А. Завгородняя, О.Б. Поповичева, В.О. Кобелев, Д.П. Стародымова, В.П. Шевченко, Н.С. Касимов// Проблемы Арктики и Антарктики, 2021; 67: 261-279
DOI: 10.30758/0555-2648-2021-67-3-261-279

эмиссий остаются наименее изученными среди всех источников эмиссий горения природных топлив [23]. Аэрозольное загрязнение снежного покрова нефтегазовыми факелами остается предметом актуальных научных исследований [24]. Аэрозольный состав атмосферы Арктического региона особо чувствителен к переносу крупномасштабных эмиссий от сжигания природного газа и ПНГ [25], что ставит актуальную задачу анализа концентраций ПАУ, поступающих с техногенными выбросами и накапливающихся в твердой фракции снега, а также оценки вклада индустриальных источников в состав ПАУ на основе характерных индикаторных показателей.

Данная работа посвящена анализу содержания и состава ПАУ в твердофазной фракции снежного покрова ЯНАО вблизи зон действия техногенных источников и на удалении от них. Задачами исследования являлись поиск количественных закономерностей и взаимосвязей между концентрациями ПАУ, локальными и региональными источниками, а также определение индикаторных показателей влияния эмиссий факельных установок сжигания попутного нефтяного газа объектов ТЭК.

ОБЪЕКТ И МЕТОДЫ ИССЛЕДОВАНИЙ

Исследования загрязнения снежного покрова проводились в субарктических и арктических районах ЯНАО. Климат этой территории характеризуется среднегодовой температурой –8 °С и количеством осадков 450 мм, устойчивым снежным покровом с октября по май. Отбор проб снега проводился в апреле 2018 и 2019 гг., в период максимального снегонакопления перед началом таяния. Была отобрана 51 проба снега, все пробы пронумерованы по меридиану с севера на юг и нанесены на карту (рис. 1). Координаты и описание представлены в табл. 1. Выбирались места различной интенсивности техногенного воздействия локальных и региональных источников, а именно:

– вблизи факельных установок сжигания попутного нефтяного газа на разном удалении от установок (150 и 300 м, 1 и 1,5 км) (GF1–GF4);

– вблизи факельных установок сжигания попутного нефтяного газа крупнейших объектов ТЭК центральных районов ЯНАО, расположенных южнее и восточнее Ямальского полуострова и реки Оби (пробы Yar1-2, Yar3-4; NUr1-2; Gub1-5; GF1-4, TSale1-2);

– вблизи автодорог (пробы Gub5 – 20 м от полотна, Gub3-4 – 100 м от дороги);

– в 20–30 км от городов Ноябрьск (Nbr1-2) и Новый Уренгой (NUr1-2), в черте города Надым (Ndm1-4), в 2–3 км от поселков Правохеттинский (PHet1-2) и Ягельный (Yag1-2), где значительно смешанное влияние пирогенных эмиссий антропогенного генезиса, нефтедобывающих установок, комплексов подготовки газа и компрессорных станций, бытовых отопительных систем населенных пунктов, транспортных сетей, свалок твердых коммунальных отходов (ТКО);

– в удаленном от техногенных выбросов арктическом районе, на территории полуострова Ямал (Ya1, Ya2, Ya6) и острова Белый (проба iBely), а также вблизи порта Сабетта (Ya3), поселков Тадибеяха (Ya4) и Бованенково (Ya5), где недавно началась разработка газовых месторождений.

Местонахождения объектов ТЭК в период 2018–2019 гг. были определены по спутниковым данным аномального свечения в видимом и инфракрасном диапазоне, получаемым с использованием радиометра VIIRS информационной системой FIRMS [26] (см. рис. 1).

Пробы снега отбирали из прямоугольных шурфов площадью 150–1000 см2 на всю глубину, исключая нижние 2–3 см на контакте с почвенным покровом, с помощью предварительно отмытого совка из химически стойкого полимерного материала. Во избежание загрязнения проб отбор производился с подветренной стороны в комбинезонах из безворсового материала и в полиэтиленовых перчатках. Методика отбора снега из шурфа обеспечивает получение пробы большого объема, что особенно важно в условиях низкой концентрации твердых частиц в удаленных районах [27], и была неоднократно опробована в природных зонах тайги и тундры [28–30]. Для количественных оценок и идентификации источников эмиссии более надежные результаты дает определение ПАУ в осадочном веществе [16].

Из пробы снега удаляли фрагменты высших растений, затем снег помещали в предварительно отмытые полимерные баки и доставляли в лабораторию. Из пробы талой воды отбирали при перемешивании аликвотные части объемом 1–2 л, которые фильтровали под вакуумом через предварительно взвешенные ядерные лавсановые фильтры с диаметром пор 0,45 мкм для дальнейшего определения концентрации твердых частиц (С) и через предварительно прокаленные кварцевые фильтры Whatman QMA для изучения состава ПАУ. Таяние при комнатной температуре и последующая фильтрация позволили избежать значительных потерь компонентов твердой фракции проб снега [31].

Экстракцию ПАУ из высушенных кварцевых фильтров с осадком проводили хлороформом с использованием системы ускоренной автоматической экстракции субкритическими растворителями ASE 200 (Dionex). Растворитель отгоняли под вакуумом на роторном испарителе, концентрируя пробу до конечного объема 0,025–0,05 мл. Количественное определение ПАУ проводили после растворения пробы в ацетонитриле методом обратнофазной хроматографии высокого давления на жидкостном хроматографе Agilent 1260 (Agilent Technologies, USA) с флюориметрическим детектором и системой обработки данных ChemStation, HPChem; колонка – Zorbax Extend-C18, 5мкм, 4,6×150 мм, элюент – ацетонитрил-вода. В качестве стандарта использовали комплект аттестованных растворов ПАУ в ацетонитриле СОП 0118-03 ER-PAH. Погрешность метода составляет 15 %.

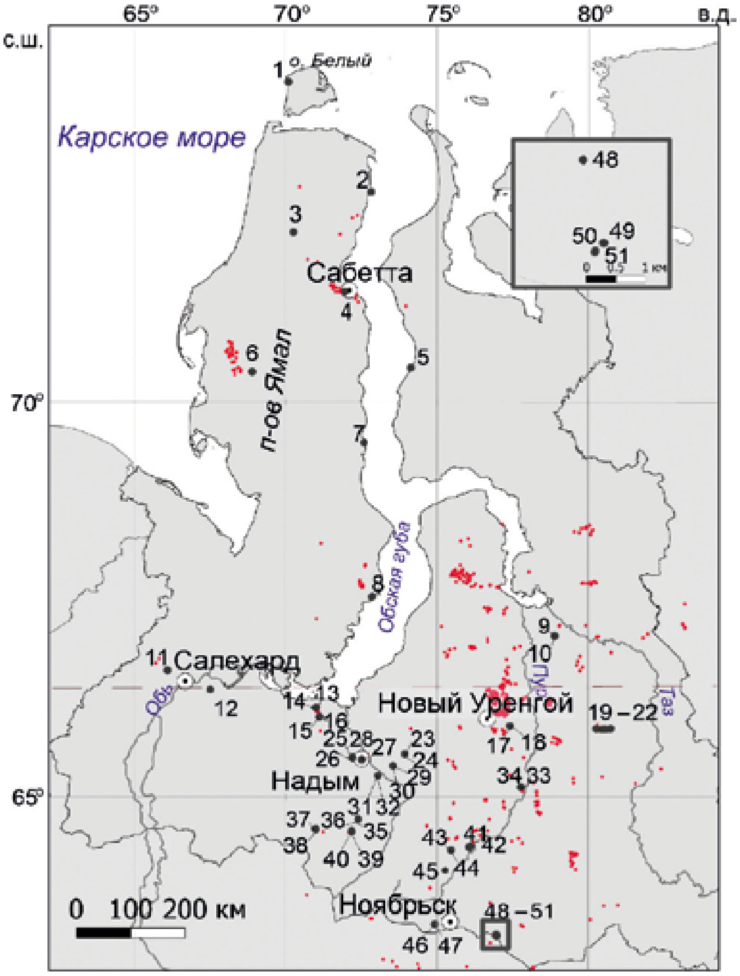

Рис. 1. Карта отбора проб снежного покрова на территории ЯНАО. Номера точек отбора со- ответствуют приведенным в табл. 1. Красными точками обозначены факелы сжигания при- родного газа на объектах ТЭК

Fig. 1. Map of snowpack sampling on the YNAO territory. The sampling point numbers correspond to Table 1. The red dots denote the natural gas flares at fuel and energy facilities

Во взвеси снега определялось суммарное содержание десяти индивидуальных ПАУ: 3-ядерных – фенантрена, антрацена; 4-ядерных – флуорантена, пирена, бенз(а)антрацена, хризена; 5-ядерных – бенз(b)флуорантена, бенз(k)флуорантена, бенз(а)пирен и 6-ядерных ç бенз(ghi)перилена. Количественное определение содержания 2–3-ядерных ПАУ с молекулярной массой меньше 178 не проводилось из-за крайне низкого их содержания в пробах. Рассчитывалось суммарное содержание высокомолекулярных (ВМ) 5–6-ядерных и низкомолекулярных (НМ) 3–4-ядерных ПАУ. Проведен сравнительный анализ профилей ПАУ (процентного содержания каждого индивидуального соединения от суммы всех ПАУ) для проб, отобранных вблизи определенных источников, а также в удаленных малонаселенных районах. Для анализа подобия проб твердой фракции снежного покрова по составу использован кластерный анализ, где мерой сходства служила величина (1 – r), где r – коэффициент корреляции Пирсона, а расстояние между кластерами вычислялось методом минимума дисперсии с помощью алгоритма Уорда.

РЕЗУЛЬТАТЫ И ОБСУЖДЕНИЕ

Суммарное содержание ПАУ

Проведенный анализ состава снежного покрова на территории ЯНАО позволяет оценить уровень загрязнений, накапливающихся в субарктических и арктических районах под действием индустриальных выбросов и смешанных пирогенных эмиссий антропогенного генезиса. Концентрации твердых частиц C в талой воде (твердой фракции снега), характеризующие количество взвешенного вещества в местах отбора проб, изменялись от 0,2 до 28 мг/л (см. табл.). Значительное превышение C в 10 и более раз относительно среднего наблюдается только для наиболее загрязненных мест отбора, расположенных рядом с факельными установками на объектах ТЭК в пробах GF2 и GF3 и на расстоянии менее 20 м от автомагистрали (Gub5).

На полуострове Ямал с низким уровнем техногенной нагрузки (кроме Ya3 и Ya5) НМ ПАУ оказались ниже чувствительности метода определения, а ВМ ПАУ обнаружены при концентрациях 0,28 нг/мг (см. табл.). В районах, расположенных южнее и

Таблица. Концентрации твердой фракции снега и состав ПАУ (НМ – низкомолекулярных и ВМ – высокомолекулярных) в снеге различных районов ЯНАО

Tabl. Concentration of the solid fraction and PAH composition (high and low-molecular weight) in the snowpack of different YNAO regions

№ станции	Обозначение	No	Eo	Расстояние до источника, км	, С тв мг/л	НМ ПАУ, нг/ мг	ВМ ПАУ, нг/мг		
				Населенный пункт	Дорога	Месторождение			
1	iBely	73,34	70,09	Сабетта , 255	–	Южно-Тамбейское , 270	1,0	0,0	0,23
2	Ya1	72,25	72,83	Сабетта, 105	–	Южно-Тамбейское, 150	0,2	0,0	1,4
3	Ya2	71,84	70,25	Сабетта, 90	–	Южно-Тамбейское, 105	0,7	0,0	0,8
4	Ya3	71,22	71,95	Сабетта, 6	1	Южно-Тамбейское, 6	1,1	3,9	1,5
5	Ya4	70,39	74,14	Тадибеяха, 0,5	–	Южно-Тамбейское, 120	0,2	0,0	0,6
6	Ya5	70,34	68,88	Бованенково, 0,16	2,5	Бованенковское, 10	1,0	1,7	0,7
7	Ya6	69,54	72,59	Сабетта, 190	–	Южно-Тамбейское, 212	0,5	0,3	0,7
9	Taz1	67,17	78,90	Тазовский, 32	0,5	Заполярное, 41	0,3	10,8	5,5
10	Taz2	67,17	78,90	Тазовский, 32	0,5	Заполярное, 41	0,4	13,3	7,0
11	Harp	66,72	66,08	Харп, 13	0,2	Ярудейское, 230	0,5	0,6	1,5
12	Slh	66,47	67,49	Салехард, 16	0,2	Ярудейское, 165	0,3	0,8	4,5
13	Yar1	66,23	71,00	Надым, 100	0,3	Ярудейское, 3,5	1,5	5,3	1,7
14	Yar2	66,23	71,00	Надым, 100	0,3	Ярудейское, 3,5	1,0	3,7	1,0
15	Yar3	66,11	71,11	Надым, 100	0,3	Ярудейское, 10	1,1	3,5	0,8
16	Yar4	66,11	71,11	Надым, 100	0,3	Ярудейское, 10	0,8	7,1	1,3
17	NUr1	65,98	77,42	Новый Уренгой, 32	1,1	Ново-Уренгойское, 8	0,4	17,0	4,7
18	NUr2	65,98	77,41	Новый Уренгой, 32	1,1	Ново-Уренгойское, 8	0,6	11,9	5,1
23	Pang1	65,60	73,94	Пангоды, 37	0,5	Медвежье, 40	0,8	8,0	1,7
24	Pang2	65,60	73,94	Пангоды, 37	0,5	Медвежье, 40	0,5	10,1	1,5
25	Ndm1	65,55	72,20	Надым, 15	0,5	Ярудейское, 72	0,6	4,2	3,4
26	Ndm2	65,55	72,20	Надым, 15	0,5	Ярудейское, 72	1,4	0,5	1,8
27	Ndm3	65,53	72,51	Надым, 0,1	0,1	Ярудейское, 95	1,0	11,2	4,6
28	Ndm4	65,52	72,51	Надым, 0,5	0,5	Ярудейское, 95	1,6	3,1	1,6
29	PHet1	65,44	73,55	Правохеттинский, 3	0,5	Ново-Уренгойское, 146	1,0	7,2	0,8
30	PHet2	65,44	73,55	Правохеттинский, 3	0,6	Ново-Уренгойское, 146	0,6	9,6	1,4
32	Ndm6	65,30	73,06	Надым, 35	0,8	Ярудейское, 134	0,6	15,3	4,4
33	TSale1	65,14	77,78	Тарко-Сале, 25	0,8	Западно-Таркосалинское, 5,8	0,7	6,6	4,2
34	TSale2	65,14	77,78	Тарко-Сале, 25	0,8	Западно-Таркосалинское, 5,8	0,8	3,2	2,3
35	Yag1	64,69	72,38	Ягельный, 2	1	Средне-Хулымское, 58	0,7	6,6	2,7
36	Yag2	64,69	72,38	Ягельный, 2	1	Средне-Хулымское, 58	0,5	21,5	4,9
37	Long1	64,55	70,99	Лонгюган, 26	0,5	Средне-Хулымское, 12	0,8	18,6	5,0
38	Long2	64,55	70,99	Лонгюган, 26	0,5	Средне-Хулымское, 12	0,5	26,6	4,4
39	Yag3	64,52	72,17	Ягельный, 23	0,5	Средне-Хулымское, 44	0,6	12,8	4,6
40	Yag4	64,52	72,17	Ягельный, 23	0,5	Средне-Хулымское, 44	0,4	11,6	3,3
41	Gub1	64,30	76,11	Губкинский, 23	0,5	Аркатойский, 0,5	1,0	18,2	3,8
42	Gub2	64,30	76,11	Губкинский, 23	0,5	Аркатойский, 0,4	1,0	4,5	4,1
43	Gub3	64,29	76,06	Губкинский, 26	0,1	Аркатойский, 3,5	0,9	12,1	3,8
44	Gub4	64,29	76,06	Губкинский, 26	0,1	Аркатойский, 3,5	2,3	4,7	1,4
45	Gub5	64,25	75,47	Губкинский, 50	0,02	Аркатойский у, 21	28,0	4,4	1,9
46	Nbr1	63,15	74,92	Ноябрьск, 24	0,5	Новогодний, 92	0,8	10,1	4,7
47	Nbr2	63,15	74,92	Ноябрьск, 24	0,5	Новогодний, 92	0,9	7,6	5,5
48	GF4	63,00	76,33	Ноябрьск, 75	0,3	Факел ПНГ, 1,5	1,2	87,8	56,8
49	GF1	62,97	76,33	Ноябрьск, 75	1,1	Факел ПНГ, 0,1	1,4	10,7	4,9
50	GF2	62,97	76,33	Ноябрьск, 75	1,2	Факел ПНГ, 0,015	20,0	225	124
51	GF3	62,97	76,33	Ноябрьск, 75	1,2	Факел ПНГ, 0,03	13,8	53,9	41,9

восточнее Ямальского полуострова и р. Оби, твердая фракция снега обогащена НМ ПАУ, что указывает на высокий вклад локальных источников и ближнего переноса [16].

Суммарное содержание ПАУ в твердой фракции снежного покрова отражает влияние техногенных источников. Общим признаком проб, отобранных в малонаселенной арктической зоне на полуострове Ямал (Ya1-2, Ya4,6) и острове Белый (iBely), является относительно невысокое содержание ПАУ(0,3–1,4 нг/мг). В районах разработки новых газовых месторождений: вблизи порта Сабетта (Ya3) и поселка Бованенково (Ya5) – содержание ПАУ повышается до 2–5 нг/мг. Подобные величины наблюдались также в зонах антропогенного влияния городов: Харп (Harp), Салехард (Slh) и Надым (Ndm1, Ndm2,4). Высокие, более 15 нг/мг, значения были зафиксированы вблизи автомобильных дорог (Gub3, Ndm3), полигона ТБО (Yag2) и компрессорной станции (Ndm6).

Распределение полей аэрозольного загрязнения снежного покрова вокруг нефтегазовых факелов определяется турбулентным режимом ветра в этой области [24]. Самым высоким содержанием (350 нг/мг) характеризуется проба GF1, отобранная на расстоянии менее 100 м от факельной установки сжигания ПНГ. На расстоянии более 1 км от того же объекта в пробе GF4 содержание ПАУ падает до 144 нг/мг. Σ10ПАУ на расстоянии 3,5–10 км от месторождений Западно-Таркосалинского (TSale1,2) и Ярудейского (Yar1,4) варьируется в диапазоне 5–10 нг/мг. На сходном расстоянии от Ново-Уренгойского (NUr1,2) и Средне-Хулымского (Long1,2) месторождений содержание ПАУ в 2–3 раза выше из-за разницы в преобладающем направлении ветра в месте отбора. Тазовский район оказывается в зоне влияния атмосферного переноса эмиссий крупного газового месторождения Заполярное, расположенного на 41 км южнее, что приводит к накоплению ПАУ до 20 нг/мг в пробах Taz1,2 (см. табл.).

Состав ПАУ

Процентное содержание индивидуальных соединений от суммы всех ПАУ вблизи источников эмиссий определяет их профиль (рис. 2). Профиль ПАУ проб GF2, GF3 и GF4, отобранных вблизи факельных установок, выражается в высокой доле пирена (25–30 %), бенз(ghi)перилена (20–25 %), бенз(а)пирена (5 %) при относительно низком содержании фенантрена и флуорантена (рис. 2а). Такой состав ПАУ характерен для источников бытовых пирогенных эмиссий [17, 32].

В пробах Gub3-5, отобранных рядом с автодорогами Сургут–Салехард и Муравленко–Губкинский и находящихся на больших расстояниях (26–50 км) от месторождения Губкинское, снижается доля бенз(ghi)перилена и повышается доля бенз(b) флуорантена (рис. 2б). Доминирование фенантрена в твердой фазе транспортных выхлопов характерно для бензиновых и дизельных двигателей [18]. Высокое содер-

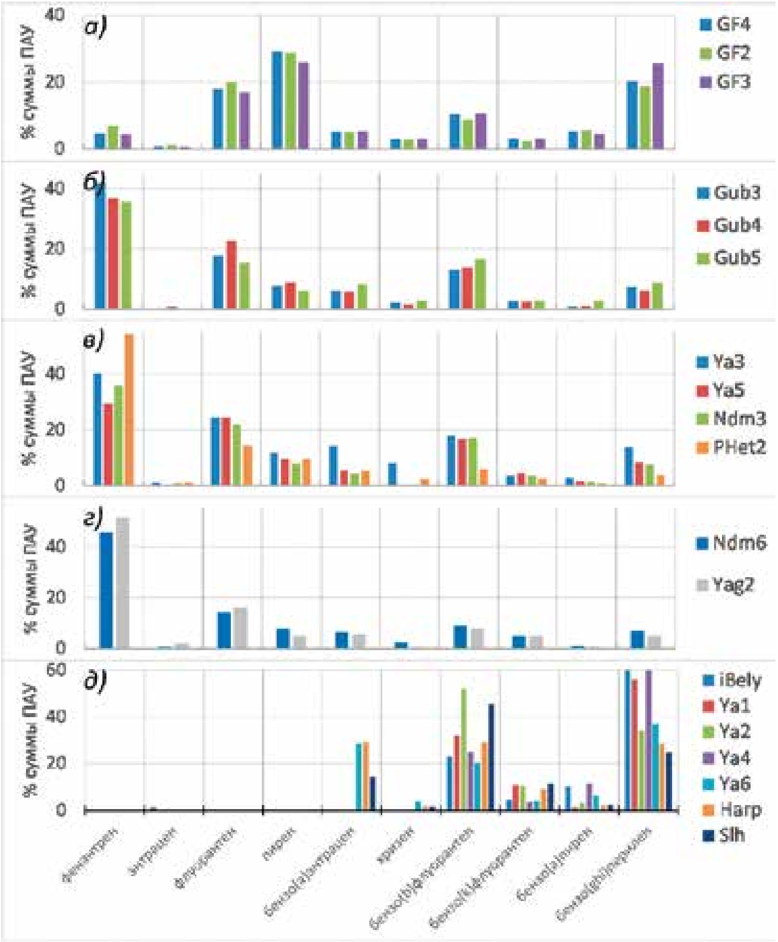

Рис. 2. Состав ПАУ твердой фракции снежного покрова.
а) – в зоне интенсивного действия факелов сжигания газа; *б)* – рядом с автодорогами Сургут–Салехард и Муравленко–Губкинский; *в)* – около населенных пунктов Надым, Правохеттинский, Сабетта, Бова- ненково; *г)* – около компрессорной станции и полигона ТКО; *д)* – на о. Белый, полуострове Ямал и на территории Обской губы

Fig. 2. PAH profiles of the snowpack solid fraction. *а)* in the region of gas flare impact; *б)* near Surgut-Salekhard and Muravlenko-Gubkinsky highways; *в)* near Nadym, Pravokhetinsky, Sabetta, Bovanenkovo settlements, *г)* near a compressor station and solid waste landfill, and д) on Bely island, Yamal Peninsula and Ob Bay territory

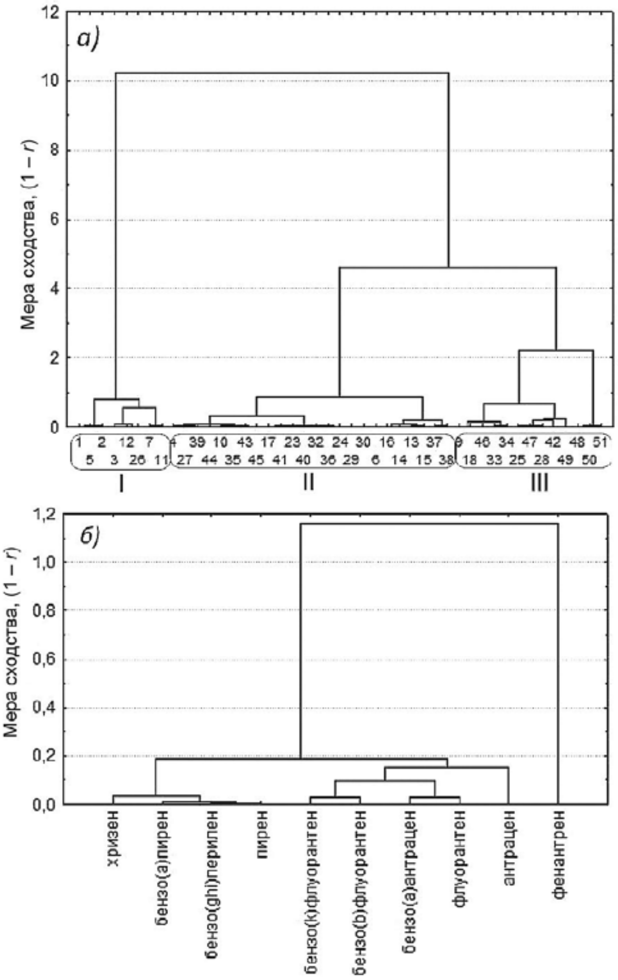

Рис. 3. Группировки ПАУ по результатам кластерного анализа индивидуальных соединений, мера сходства корреляционного анализа (1 – r) с кластеризацией а) состава ПАУ по местам пробоотбора и б) индивидуальных ПАУ. Классификация мест пробоотбора: I — удаленные от источников, II — находящиеся под влиянием многих источников техногенных эмиссий, III — под влиянием факельных эмиссий. Цифры на оси х означают номера мест отбора, указанных в табл. 1

Fig. 3. PAH grouping based on cluster analysis, linkage distance of cluster analysis based on a) PAH composition in snow sampling sites, I — remote from sources, II) mixed impact of numerous technogenic emissions, and III) under gas flaring emissions (the numbers on the axis x denote sites of sampling indicated in Tabl.1, and б) individual PAHs.

жание фенантрена и флуорантена, а также преобладание среди ВМ ПАУ бенз(b)флуорантена типично для выхлопов автомобильного транспорта и выбросов мазутных котельных [16]. Подобный профиль ПАУ определен на расстояниях порядка 100 км от Ярудейского (Ndm3) и Ново-Уренгойского месторождений (Phet2), где кроме дальнего переноса влияют эмиссии близкорасположенных поселков, что выражается в повышенном вкладе в состав ПАУ таких соединений, как флуорантен и пирен (рис. 2в). В городах одним из основных источников полиаренов является транспорт, но его влияние диагностируется слабее из-за наличия значительного количества городских эмиссий, включая отопительные системы различной крупности. Для городских территорий характерна высокая неоднородность накопления загрязнений в снеге, подобно полученным для пробы Ndm3, отобранной в г. Надым (рис. 2в), где на состав ПАУ влияет наличие множественных смешанных источников загрязнения. Высокое содержание фенантрена может определяться не только транспортной активностью, но и работой дизельных генераторов и сжиганием бытовых отходов [33].

Появление в составе ПАУ высоких концентраций фенантрена и антрацена характерно для мест отбора проб Ya3 и Ya5 рядом с недавно освоенным Южно-Тайбейским газовым и Бованенковским газоконденсатным месторождениями (рис. 2в). Эти пробы характеризуются увеличенной индустриальной нагрузкой на фоне общего низкого уровня загрязнения снежного покрова района и близостью населенных пунктов. Рядом с компрессорной станцией Ndm6 и полигоном ТКО Yag2 получено наиболее заметное преобладание фенантрена – до 50 % от суммы ПАУ (рис. 2г).

В зоне с низким уровнем техногенной нагрузки характерно практически полное отсутствие 3и 4-ядерных ПАУ (рис. 2д). Содержание высокомолекулярных ПАУ в местах отбора проб на острове Белый и на полуострове Ямал (кроме Ya3 и Ya5) составляет 70–100 % преимущественно за счет вклада бенз(b)флуорантена и бенз(ghi) перилена. Общими признаками для этих мест является удаленность от источников интенсивных эмиссий хозяйственной деятельности центрального района ЯНАО и объектов ТЭК. Высокое содержание бенз(ghi)перилена в снеге для территорий, отдаленных от техногенных источников полиаренов, отмечено в работах [34, 35]. 4-ядерные ПАУ бенз(а)антрацен и хризен присутствуют в пробах Harp и Slh, расположенных ближе к индустриальным территориям Обской губы (рис. 2д).

Характерные особенности ПАУ в твердой фракции снежного покрова определяются результатами кластерного анализа (рис. 3). По составу ПАУ все места отбора объединяются в три кластера: в первом (I) группируются отобранные в удаленных малонаселенных районах, второй (II) включает места, находящиеся под влиянием смешанных пирогенных эмиссий антропогенного генезиса, источниками которых могут являться сжигание угля и мазута в котлах мелких и крупных отопительных систем, выхлопы автотранспорта, выбросы работающих генераторов и компрессорных станций, сжигание древесины и бытового мусора в жилом секторе (рис. 3а). Остальные места отбора представляют третий (III) кластер наиболее заметного влияния факельных эмиссий в районах высокой техногенной нагрузки, расположенных южнее и восточнее Ямальского полуострова и реки Оби, где наблюдается более высокая плотность объектов ТЭК (см. рис. 1). При проведении анализа по индивидуальным ПАУ в кластер объединяются пирен, бенз(ghi) перилен и бенз(а)пирен, концентрации которых в снеге в зоне действия факельных эмиссий максимальны (рис. 3б). Бензфлуорантен и флуорантен объединяются в другой кластер, что указывает на их поступление из источников, отличных от выбросов факелов. Наименее связанным с другими ПАУ оказался фенантрен, на концентрацию которого может влиять не только тип источника, но и процессы трансформации.

Показателем значительного влияния эмиссий факельных установок, определяющим группу (1), является доминирование 4-ядерных при относительно невысоком содержании 3-ядерных полиаренов (рис. 4). При ослаблении факельных эмиссий по мере удаления от объектов ТЭК наблюдается изменение относительного содержания суммы ПАУ. Для группы (2) с заметным влиянием факельных эмиссий в составе ПАУ наблюдается высокая доля 4-ядерных соединений. К этой группе относятся пробы, отобранные на расстоянии 1–12 км от Ново-Уренгойского, Западно-Таркосалинского, Средне-Хулымского и Аркатойского газоконденсатных месторождений. На загрязненность проб Ya3 и Ya5 на полуострове Ямал влияют эмиссии Бованенковского и Южно-Тамбейского месторождений. Для группы (3) определяется слабое влияние факельных эмиссий объектов ТЭК, при этом в накоплении ПАУ играет роль дальний перенос, что выражается в снижении доли 4-ядерных полиаренов по сравнению с 5, 6-ядерными. Среди проб этой же группы находятся Taz1 и Taz2, отобранные на расстоянии 41 км от месторождения Заполярное. Места отбора группы (4), отнесенные к зоне влияния смешанных антропогенных эмиссий, объединяет доминирование в твердых выпадениях 3-ядерных ПАУ. Для слабого техногенного воздействия преимущественно в удаленных арктических регионах для группы (5) характерна высокая, вплоть до 100 %, доля высокомолекулярных 5, 6-ядерных ПАУ. Таким образом, суммарное содержание и состав ПАУ в твердой фракции снежных проб двухлетнего отбора, проведенного на различных расстояниях от объектов нефтегазодобывающего комплекса, у автодорог, вблизи населенных пунктов и в удаленных арктических районах, отражают геопространственное распределение техногенных эмиссий.

ИНДИКАТОРНЫЕ ПОКАЗАТЕЛИ ПАУ

Проведенный поиск количественных закономерностей и взаимосвязей между концентрациями индивидуальных ПАУ дает возможность определить индикаторные показатели. В расчетах индикаторных показателей ПАУ используют разные соотношения НМ и ВМ ПАУ и для полиаренов с разным числом колец [9, 10, 16, 19]. Среди НМ ПАУ отношение концентраций 4-ядерных флуорантен к пирену является более чувствительным индикатором источника поступления полиаренов в индустриальных районах по сравнению с отношением 3-ядерных изомеров фенантрена к антрацену, так как пара флуорантен и пирен более стабильна в широком диапазоне концентраций в аэрозольных эмиссиях различных источников [17]. Величины индексов для пирогенных источников определяются типом сжигаемого топлива [19]. Так, отношение бенз(а)пирена

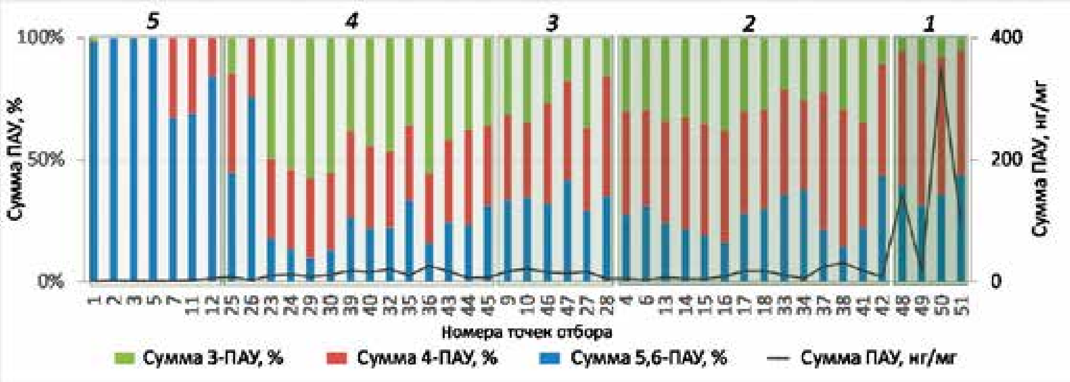

Рис. 4. Вклад суммы 3-, 4- и 5-, 6-ядерных ПАУ в их суммарное содержание: 1) влияние фа- кельных выбросов; 2) заметное влияние факельных выбросов; 3) слабое влияние факельных выбросов; 4) влияние смешанных эмиссий и 5) слабое техногенное воздействие. Кривой от- мечена сумма ПАУ (нг/мг) твердой фракции снега

Fig. 4. Percentage contribution of the sum of 3, 4 and 5, 6-nucleus PAHs to the total content of PAHs in snow sampled at sites 1) near gas flares; under 2) a noticeable impact of gas flare emissions and 3) weak impact of flare emissions as well as under 4) mixed source impact and 5) weak technogenic impact. The line presents the sum of PAHs

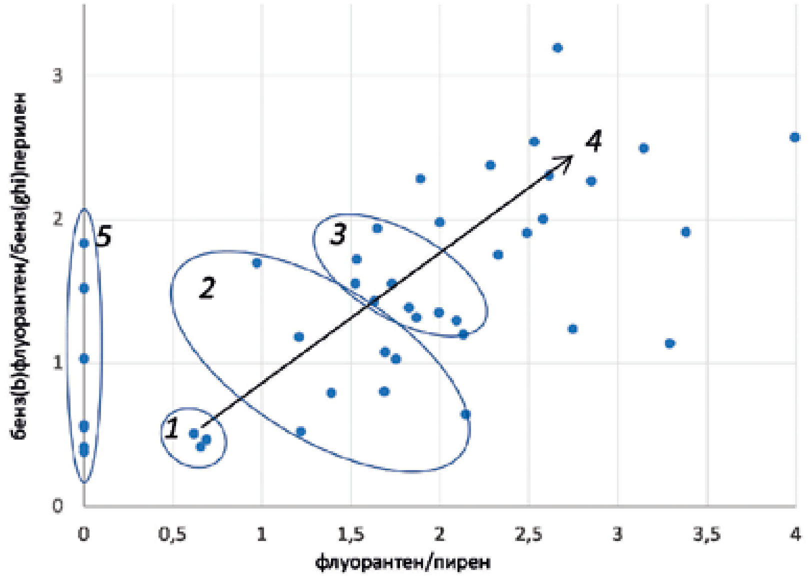

Рис. 5. Индикаторные показатели ПАУ в пробах твердой фракции снега, отобранных в местах: 1) влияния факельных выбросов; 2) заметного влияния факельных выбросов; 3) слабого влияния факельных выбросов; 4) смешанного воздействия и 5) слабого техногенного воздействия. Стрелкой показано изменение индикаторных показателей при снижении вклада факельных эмиссий

Fig. 5. Diagnostic indicators of PAHs in snow showing 1) the impact of gas flaring; 2) noticeable impact of gas flaring; 3) weak impact of gas flaring; 4) mixed source impact, and 5) weak technogenic impact. The arrow shows the indicator change with a decrease in flare emissions contribution

к бенз(g,h,i)перилену ниже 0,6 указывает на выбросы автотранспорта, а выше 0,6 – на стационарные источники [19].

Поскольку в профиле состава ПАУ снежного покрова под влиянием факельных эмиссий доминируют пирен и бенз(ghi)перилен, они используются в качестве соединений, определяющих характерные для данного источника соотношения НМ и ВМ ПАУ. Для определения индикаторных показателей, которые наилучшим образом описывают изменения состава ПАУ в твердой фракции снега при снижении вклада факельных эмиссий, рассчитывали отношения разных ВМ ПАУ. Наилучшая корреляция была получена для бинарных индикаторных показателей: отношения флуорантена к пирену и бенз(b)флуорантена к бенз(ghi)перилену. Были выделены группы, для которых состав полиаренов определяется степенью влияния источника факельного сжигания (рис. 5). Оба индикаторных соотношения имеют низкие значения ~ 0,6 вблизи факельных установок объектов ТЭК (группа 1). При ослаблении влияния факельных эмиссий (группа 2) и увеличении расстояния до месторождения и объектов ТЭК отношение флуорантена к пирену повышается до значений порядка 1 за счет вклада других пирогенных источников поступления ПАУ. Одновременно для высокомолекулярных ПАУ в составе снега снижается доля бенз(ghi)перилена, а отношение бенз(b)флуорантена к бенз(ghi)перилену повышается. В местах, отнесенных к области влияния смешанных эмиссий (группа 4), величины обоих индикаторных соотношений превышают 2.

ЗАКЛЮЧЕНИЕ

Для центральных районов ЯНАО содержание и состав ПАУ в твердой фракции снежного покрова определяются наличием загрязнения, сформированного действием источников техногенных эмиссий, в том числе эмиссий факельного сжигания попутного газа. Высокая плотность источников приводит к накоплению преимущественно низкомолекулярных ПАУ. Влияние выбросов факельных установок отличается от других типов эмиссий преобладанием пирена, бенз(ghi)перилена и бенз(a)пирена, суммарное содержание ПАУ в твердой фракции снега вблизи источника увеличивается до 350 нг/мг. Отношения флуорантена к пирену и бенз(b)флуорантена к бенз(ghi) перилену при значениях 0,6 идентифицируют влияние эмиссий факельных установок сжигания попутного газа. По мере удаления от объектов ТЭК и приближения к автодорогам и населенным пунктам повышается доля бенз(b)флуорантена, фенантрена и флуорантена. При ослаблении влияния факельных эмиссий наблюдается изменение относительного содержания суммы ПАУ, снижается доля 4-ядерных полиаренов по сравнению с 5-, 6-ядерными. Отношение флуорантена к пирену и бенз(b)флуорантена к бенз(ghi)перилену в местах влияния смешанных эмиссий превышает 2. Снежный покров удаленных арктических районов находится под воздействием переноса техногенных эмиссий. Состав ПАУ на территории полуострова Ямал и острове Белый характеризуется низким, не более 2 нг/мг, суммарным содержанием ПАУ, профиль которого представлен высокомолекулярными 5–6-ядерными полиаренами. Появление в составе твердой фракции снега 3-, 4-ядерных ПАУ в районах освоения новых месторождений зоны указывает на повышенный уровень техногенной нагрузки. Полученные результаты могут быть использованы в качестве значимых показателей возрастающего влияния развивающихся объектов ТЭК на экологию арктической части Западной Сибири.

Конфликт интересов. Авторы заявляют об отсутствии конфликта интересов. Competing interests. The authors have no competing interests. Финансирование. Работа выполнена при финансовой поддержке РФФИ в рамках проекта № 18-05-60-084, а также в рамках Программы развития Междисциплинарной научно-образовательной школы Московского государственного университета имени М.В. Ломоносова «Будущее планеты и глобальные изменения окружающей среды».

Funding. The work was carried out with the financial support of RFFI in the framework of project No. 18-05-60-084. The study was carried out as part of the Development Program of the Interdisciplinary Scientific and Educational School of Moscow State University “The Future of the Planet and Global Environmental Changes”.

Благодарности. Авторы выражают благодарность канд. геол.-минерал. наук А.Н. Новигатскому (Институт океанологии им. П.П. Ширшова РАН) за обучение методике отбора проб.

Acknowledgments. The authors thank A.N. Novigatsky (P.P. Shirshov Institute of Oceanology, Russian Academy of Sciences) for providing a method for snow cover sampling.

4. ВОДНЫЕ ПОТОКИ В РЕЧНЫХ БАССЕЙНАХ

Catchment and in-channel sources in three large Eurasian Arctic rivers: Combining monitoring, remote sensing and modelling data to construct Ob', Yenisey and Lena rivers sediment budget*

1. INTRODUCTION

Rivers are major conduits of particulate matter, metal, and carbon from land to coastal seas. They transport large quantities of water and constituents (Reid and Dunne, 2005). Sediments supplied into the river network and the subsequent movement of particles from source to sink are determined by a complex of natural and anthropogenic processes that change over time and are irregularly distributed in the river basin (Trimble, 1999, Wilcock, 2009, Parsons, 2012). The essential part for quantitative description of these processes is the definition of a sediment budget, which is one of the most important parameters of a watershed's erosion and deposition (Hoffmann et al., 2007, Cavalli et al., 2013). In a simplified way, the annual sediment flux (t year^{-1}) can be calculated from the contributions of watershed erosion (soil loss) and channel erosion:

$$W_w + W_{ch} + W_{gullies} + W_{other} = \\ = W_{wd} + W_{chd} + (W_{susp} + W_{bed}), \qquad (1)$$

W_w– Watershed erosion, which includes hillslope and rill, both rainfall and snowmelt ($W_{rainfall} + W_{snowmelt}$), $W_{gullies}$ – gully erosion, W_{ch} – channel erosion, W_{wd} – Deposition within the watershed, W_{chd} – deposition in the channel (including reservoirs), ($W_{susp} + W_{bed}$) – bed and suspended load in the river mouth, W_{other} – other possible sources of sediments that were not included in this study.

This balance approach provides a conceptual background to understand links between erosion and deposition on the catchment scale (Alekseevskii et al., 2012). As far as sediment generation is related to a wide range of processes, the catchment and channel erosion are not exceptional sources of bed and suspended load, combined in this form by the general component of the secondary sources W_{othe}. In particular conditions, within small catchments, gully erosion $W_{gullies}$ (Bartley et al., 2004), input from external point sources (e.g. construction sites, industrial or sewage effluent) or landslides (Chen and Lai, 2005) can generate the dominant part of the total sediment yield from a catchment. On global and large catchment scales, the relative importance of channel sources has been accepted (Dedkov and Gusarov, 2006, Kronvang et al., 2013). On a global scale, according to recent studies (Borrelli et al., 2017) that take into account soil protection methods based on a detailed (250 × 250 m) grid, total soil erosion was estimated at 17-18 · 10^9 t year^{-1}. The empirical estimates of global suspended load into the ocean and large endorheic regions are estimated as 15-20 · 109 t year^{-1} (Milliman, 2010), from which over 50 % is trapped in reservoirs (Vörösmarty et al., 2003) and a significant part is stored in catchment buffer zones (Sidorchuk, 2018).

Catchment sediment budget includes both channel gully and soil (sheet and rill) erosion, as well in-channel and overbank sinks and storage and the resulting bed load and suspended sediment load exported from the catchment. This explains its complexity. Sediment budgets are mainly done for small rivers (Trimble, 1999; Ollivier et al., 2011; Kronvang et al., 2013). The simple and most widely-used approach is based on entirely annual gross erosion W_w in the catchment (Tena and Batalla, 2013) which is used to estimate the sediment delivery ratio (SDR) as a percentage relationship between annual sediment yield $W_{susp} + W_{bed}$. The SDR concept neglects other sources besides W_w which influence suspended and bed load (Ferro and Minacapilli, 1995).

Other studies mostly rely on continuous measurements of sediment transport at the outlet gauging station versus a mixing model approach (Hughes et al., 2021) such as sediment fingerprinting (Collins and Walling, 2007), and integrated techniques (Bomer et al., 2019) which rely both on modelling (Van Rompaey et al., 2001; Bartley et al., 2004; de Vente and Poesen, 2005) and in situ quantifications (Kronvang et al., 2013; Chalov et al., 2017) of individual sediment sources. They provide a very broad range of estimates. Based on sediment-discharge curves (Dedkov and Gusarov, 2006) channel erosion W_{ch} contribution to total erosion ($W_w + W_{ch}$) was estimated as 10.4 ± 1.5 % for lowland rivers of the Russian plain, 4.9 ± 0.9 % for low mountains rivers, and 4.0 ± 0.8 % for middle altitudes rivers. The main disadvantage of these estimates is the lack of actual verification of the estimates, which is also based on broad assumptions. Indirect methods (fingerprinting) for identifying sediments composition and sources for the Great Britain rivers suggests that on average about 85–95 % of sediment flux are related to catchment processes (gully and soil erosion), and only 5–15 % accounts for channel erosion, but in some cases, the impact of channel erosion can be >40 % (Walling and Collins, 2005).

The data on large rivers sediment provenance is mostly based on regional empirical evidences that also sug-

---

*Sergey Chalov, Viktor Ivanov // Catena // https://doi.org/10.1016/j.catena.2023.107212 https://www.sciencedirect.com/science/article/abs/pii/S034181622300303X?via gest the importance of in-channel sources (both channel erosion and in-channel and overbank sinks and storage). Sediment budget components calculated for the Rhine (Frings et al., 2014) demonstrated 8 % sediment load increase over the downstream part of the river due to channel erosion. In the Amazon river, where the sediment runoff was estimated at 1240 Mt year^{-1}, over 2070 Mt year^{-1} is stored at the floodplain section of the river and 1570 Mt year^{-1} is contributed due to channel erosion (Dunne et al., 1998). Kesel et al. (1992) estimated bank erosion and in-channel and overbank sinks impact on total sediment yield for the Mississippi river. To determine fluvial sediment deposition rates, dated by Pb-210 and Cs-137 geochronology pushcores are used (Hinderer, 2012) and corresponding data is limited to particular river reaches.

There is no single broad understanding of the sediment budget of large river watersheds and the knowledge of sediment provenance in catchments remains to be an important fundamental problem. This gap is especially large at the Northern rivers which are poorly monitored, and the existing estimates of river flux are characterized by high uncertainty both in term of water (Lappalainen et al., 2018), sediment (Chalov et al., 2017) and chemicals (Raymond et al., 2007). For the Northern rivers in general, it is hampered by short data records, lack of seasonally explicit sampling, and methodological drawbacks in long-term monitoring (Krengel et al., 2018). Recent monitoring campaigns led to major revisions of flux estimates of sediment export (McClelland et al., 2016). Since 2018, the monitoring campaign ArcticFlux (Vihma et al., 2019) has been sampling the four largest Siberian rivers (Ob', Yenisey, Lena and Kolyma) multiple times per year at the most downstream river cross-section selected as unaffected by river mouth processes (tides, surges etc.). GIS databases and remote sensing data additionally expand capabilities to assess contribution of catchment and channel erosion. In particular, the revised universal soil loss (RUSLE-based) models have been applied for Polar regions both at regional (Borrelli et al., 2017, Fabre et al., 2019) and local (Pietroń et al., 2017, Maltsev and Ivanov, 2022) scales. Considering that these models predominantly built upon parameters that result from experiments conducted in the United States, their application to a non-plot-level and in areas outside the range of the original estimates requires specific accuracy assessments. Various successful applications and verifications of RUSLE-based models at the global level including Polar regions (Borrelli et al., 2017) point them as a legitimate approach to narrow the current gap of knowledge regarding soil erosion estimates in the North. Remote sensing proved to become an ultimate source of data related to planform changes contribution to sediment transport over extended reaches of large Northern rivers (Gautier et al., 2021, Chalov et al., 2021a).

In particular, in this study we aim at (1) understanding fluvial export from the studied rivers and (2) estimating catchment and channel erosion based on GIS methodology with an accounting of their accuracy. Finally, (3) we estimate a catchment sediment budget to conclude about partitioning between catchment and in-channel erosion and impacts of sediment sinks and storage on the total sediment export by the Ob', Yenisey and Lena rivers.

2. MATERIAL AND METHODS

2.1. Study catchments

Ob', Yenisey and Lena rivers represent three of the largest river systems located in Russia that together cover over 14 % of the total territory of Eurasia (Vihma et al., 2019) (fig. 1). Yenisey is the largest river of the Arctic Ocean and Russia in term of water discharge, with about 620 cubic kilometers annually. The Ob' river is the longest river in the region with the largest catchment area, whereas Lena is famous for the largest Arctic delta with an area of about 32 000 km^2 (Chalov et al., 2021a). These catchments include humid and arid lands, and cover both large industrial and mining centers as well as most rarely populated areas of the World (Table 1). The morphology of all three rivers is relatively undisturbed (Alekseevskii et al., 2012). For the Ob' and Lena downstream the wide braided sandy floodplains are typical, whereas the Yenisey channel is significantly different from the Ob' and the Lena and along its main stem forms stable, relatively strait, single with rocky, coble-boulders banks. Based on the confinement ratio (length of confined channel reaches per river length) the rivers are grouped in the following order: Lena–Yenisey–Ob' (Chalov et al., 2018). Reservoir construction lead to increased riverbed erosion at the downstream sections of the Ob' River (with incision rates up to 1 m during 50 years after dam construction) (Magritsky, 2010).

Table 1. Ob', Yenisey and Lena river characteristics.

River	Large dams in the river watershed (>higher than 15 m)		Population		Land use (%)		Percent of the unconfined rivers (from (Chalov et al., 2018)
	Number in the catchment	Density (per square km^2 of river catchment)	Largest cities located along river main channel (population)	Average population density (human per km^2 in the subcatchments)	Forest and natural shrubs main	Agricultural lands	
Lena	1	$4 \cdot 10^{-7}$	Yakutsk (306 thousand)	<1–3	20–80	< 5	36
Ob'	3	$1 \cdot 10^{-6}$	Novosibirsk(1.6 million), Surgut (347 thousand), Nizhnevartovsk (270 thousand).	<1–25	10–60	0–80	100
Yenisey	8	$3 \cdot 10^{-6}$	Krasnoyarsk (1.1 million)	<1–10	60–80	5–20	41

Catchment erosion from Eq. (1) was calculated as:

$$W_W = W_{rainfall} + W_{snowmelt} + W_{gullies} \qquad (2)$$

2.2. Catchment erosion

The calculations of hillslope and rill rainfall soil erosion $W_{rainfall}$ ($tha^{-1} y^{-1}$) in this work is based on the RUSLE erosion model (Renard et al., 1997). The digital elevation model GMTED 2010 (Danielson and Gesch, 2011) with a spatial resolution of 250 m was used. The RUSLE equation for rainfall erosion estimates (Panagos et al., 2015a) catchment erosion erosion (W_W, $tha^{-1}year^{-1}$), through combining the rainfall erosivity factor R (MJ mm^{-1} ha^{-1} $year^{-1}$), soil erodibility factor K (t ha h ha^{-1} MJ^{-1} mm^{-1}), topography factor LS (Dimensionless) and land cover factor C (Dimensionless) (Eq. (3)). The P-factor in the USLE (Wischmeier and Smith, 1978) and RUSLE (Renard et al., 1997) models represents support practices in the territories. In addition, methods of crop cultivation take into account some default soil support practices. In other words C and P factors are inextricably linked (Panagos et al., 2015b). Thus in our study the influence of the P factor was implemented into the C factor (Table 2).

$$W_{rainfall} = RKLSC \qquad (3)$$

To calculate hillslope and rill snowmelt erosion the model by Larionov-Krasnov was used (Larionov and Krasnov, 1997). The equation was developed in Russia based on a large spatially distributed dataset of coefficients. Modifications include an improved set of equations for determining topographic factors, calculating and mapping a rainfall erosivity index, as well as adaptation of land use factors and soil protection techniques specific to the Russian agricultural system (Belyaev et al., 2005). This model modifies the classical USLE (Wischmeier and Smith, 1978) by using soil loss experimental and field data. The approach of snowmelt erosion calculation is based on the assumption that snowmelt routine H and soil erodibility factor K play an important role in the snowmelt erosion process. Here factors of K, H and hill slope (I) compile the LST factor (Eq. (4b)). The land cover factor CT is also taken into account (Eq. (4a)):

$$W_{snowmelt} = LST\ CT \qquad (4a)$$

$$LST = f(H, K, L)\ f(I) \qquad (4b)$$

Where f() – is a specific morphometric operation that is described in Table 3 and developed by (Larionov and Krasnov, 1997) realized for GIS Mapinfo 10.0.

The model provides estimates of snowmelt soil losses, which can then be exported to various GIS tools for visual presentation and manipulation with other spatial data. The model has been validated on few locations, also within the Yenisey river watershed in Krasnoyarsk forest-steppe (Golubev et al., 2021), within Lena River watershed (Maltsev and Ivanov, 2022). Even though the model is considered as the simplest empirical approach, e.g. it does not contain the depth of seasonal soil freezing, it has been shown to be a relatively reliable tool for non-agricultural landscapes even compared to more complex physically-based models tested within territory of Siberia (Rumyantseva and Bobrovitskaya, 2010, Sukhanovsky and Pruschik, 2019, Golubev et al., 2021). As far as discussed by Belyaev et al. (2005), equation (4a) is unsuitable for estimating total erosion rates in arable regions where deep rilling and ephemeral gully erosion occurs, thus we applied the model mostly for the downstream sections of the Ob', Yenisey and Lena rivers located below reservoirs, where agriculture is limited. Table 3 presents parametrization of the snowmelt erosion model (Eq. (4a), (4b)). All calculations were done in Mapinfo pro 17.0.

Estimation of the particular parameters was done based on a combination of various approaches and specifically discussed in Ivanov and Chalov (2021). As the RUSLE equation provides estimates of annual soil loss (), for each subcatchment of the river system we used Eq. (5) to estimate the volume of eroded land.

$$w_W = W_W \cdot 0.0001 \cdot F \qquad (5)$$

where W_W– mean values of catchment erosion (t $ha^{-1}year^{-1}$), F – catchment area (m^2), w_W – catchment erosion rates for watershed (t $year^{-1}$).

The calculation of gully erosion requires specific studies which have not been done for the Polar regions

Table 2. RUSLE (Eq. (3)) parameters and datasets used in the study.

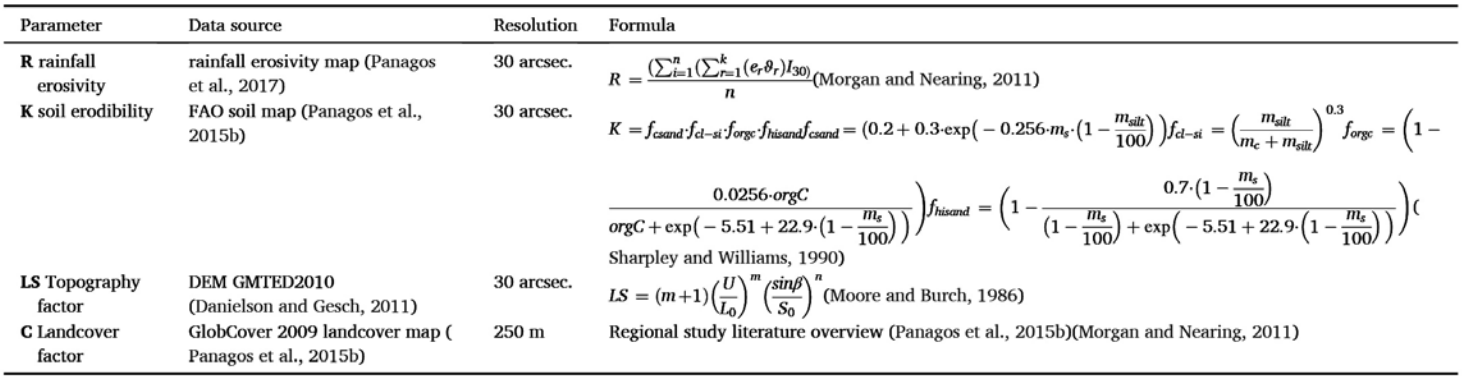

Parameter	Data source	Resolution	Formula
R rainfall erosivity	rainfall erosivity map (Panagos et al., 2017)	30 arcsec.	$R = \frac{(\sum_{i=1}^{n}(\sum_{r=1}^{k}(e_r\vartheta_r)I_{30})}{n}$(Morgan and Nearing, 2011)
K soil erodibility	FAO soil map (Panagos et al., 2015b)	30 arcsec.	$K = f_{csand} \cdot f_{cl-si} \cdot f_{orgc} \cdot f_{hisand} f_{csand} = (0.2 + 0.3 \cdot \exp(-0.256 \cdot m_s \cdot (1 - \frac{m_{silt}}{100}))f_{cl-si} = \left(\frac{m_{silt}}{m_c + m_{silt}}\right)^{0.3} f_{orgc} = \left(1 - \frac{0.0256 \cdot orgC}{orgC + \exp(-5.51 + 22.9 \cdot (1 - \frac{m_s}{100}))}\right) f_{hisand} = \left(1 - \frac{0.7 \cdot (1 - \frac{m_s}{100})}{(1 - \frac{m_s}{100}) + \exp\left(-5.51 + 22.9 \cdot \left(1 - \frac{m_s}{100}\right)\right)}\right)($ Sharpley and Williams, 1990)
LS Topography factor	DEM GMTED2010 (Danielson and Gesch, 2011)	30 arcsec.	$LS = (m+1)\left(\frac{U}{L_0}\right)^m \left(\frac{\sin\beta}{S_0}\right)^n$ (Moore and Burch, 1986)
C Landcover factor	GlobCover 2009 landcover map (Panagos et al., 2015b)	250 m	Regional study literature overview (Panagos et al., 2015b)(Morgan and Nearing, 2011)

R) er – rain drops energy (MJ mm−1 ha−1 year−1); – precipitation, mm; – max intensity of rain during 30 min, n – time, year; K) fcsand –coefficient of erodibility of soils with a high content of coarse-grained and fine-grained sand; fcl-si – the coefficient for soils with a high content of silt and clay; forgc – coefficient reflecting the effect of organic matter content; fhisand – the reducing coefficient for sandy soil; ms – sand fraction percentage, %; msilt – silt fraction percentage, %; mc – clay fraction percentage, %; orgC – organic carbon percentage, %. LS) U – the upper catchment area, is related to the width of flow, m^2/m; L0,S0 – length and slope of the standard Wischmeyer-Smith runoff platform (22.1 m and 0.09°); β – the steepness of slopes.; m = 0.4 and n = 1.3.

Table 3. Parameters and datasets of Eq. (5) used in the study.

Parameter	Data source	Resolution	Formula
LS_T Topography factor	DEM GMTED2010 (Danielson and Gesch, 2011)	30 arcsec.	$LS_T = 22.1^{-p_k} \cdot \Phi^{p_k} \cdot (K \cdot l)^{p_k} \frac{18.62 \sin arctg(0.01 \cdot I)}{1 + 10^{0.53 - 0.015 \cdot l \cdot I}} + 0.065 p = 0.2 + 2.067 \cdot (p_o - 0.2)(k \cdot l)^{-0.15} K^{0.45} I_t = \frac{48.27 \sin acrtg(0.01 I)}{1 + 10^{0.339 - 0.06 I}}$
H Snowmelt routine	Manual interpolation of gauging stations data [Larionov et al., 1998] [Krasnov et al., 2001]	–	$H = (H_{mz} + H_{oc}) k_{ck} k_{ek}$
K soil erodibility	FAO soil map (Panagos et al., 2015b)	30 arcsec.	$K = (16.67 \cdot 10^{-6} \cdot (f \cdot (100 - e))^{1.14})(12 - a) + 0.25 \cdot (b - 2) + 0.193 \cdot (4 - z)) \cdot s$ $f = (0.005 + 0.001\ mm) + (0.01 - 0.005\ mm) + (0.05 - 0.01\ mm) + (0.25 - 0.05\ mm) \cdot (0.1 - 0.05\ mm)$
τ Landcover factor	GlobCover 2009 landcover map (Panagos et al., 2015b)	250 m	Regional study data (Larionov et al., 1998) (Krasnov et al., 2001)

I – slope steepness, *l* – slope length, *M; H_{mz}* - maximum water reserves in snow, *mm; H_{oc}* - precipitation during the snowmelt, *mm; k_{ck}* - slope runoff coefficient during snowmelt (Larionov and Krasnov, 1997)*; k_{ek}* - slope exposure coefficient (Larionov and Krasnov, 1997)*; f* – percentage of particles with diameter of 0,1–0,001 *mm, %; e* - percentage of particles with diameter of *< 0,001 mm, %; a* - humus percentage, *%; b* - soil structure class (Larionov and Krasnov, 1997)*; z* - soil water permeability class (Larionov and Krasnov, 1997)*; s* - coefficient of soil erodibility reduction due to stony and gravelly soil (Larionov and Krasnov, 1997),*Φ, p_0* и *p*- empirical coefficients (Larionov and Krasnov, 1997).

with the exceptions of local reaches (Sidorchuk, 2019). The estimates of gully erosion are limited to the southern areas where this phenomena is widely developed across steppe zones of Yenisey and Ob' catchments (Kasimov et al., 2019). Due to this fact, we rely on the data published on the generalized map of gully erosion in Russia which describes 6 classes of gully densities – <0.011 km/ km^2; 0.011–0.2 km/km^2; 0.021–0.1 km/km^2; 0.11–0.5 km/ km^2; 0.51–1.3 km/km^2; >1.3 km/km^2 (Kovalev and Nikolaskaya, 2009). The mountainous areas are excluded from estimates. We digitized this map within the borders of the studied catchments to estimate average gully density in the Ob' catchment as 0.015 km^1 km^{-2}, 0.005 km^1 km^{-2} in the Yenisey catchment and 0.01 km^1 km^{-2} in the Lena catchment. The average rate of annual gully erosion Wgullies (Mt year^{-1}) is the product of total density of gullies Fgullies:

$$W_{\text{gullies}} = \frac{\text{Fgullies} \bullet \text{F} \bullet \text{w} \bullet \rho}{\tau} \tag{6}$$

where W_{gullies} is the average rate of annual gully erosion (Mt year^{-1}), Fgullies – total gully density (km^1 km^{-2}), F –

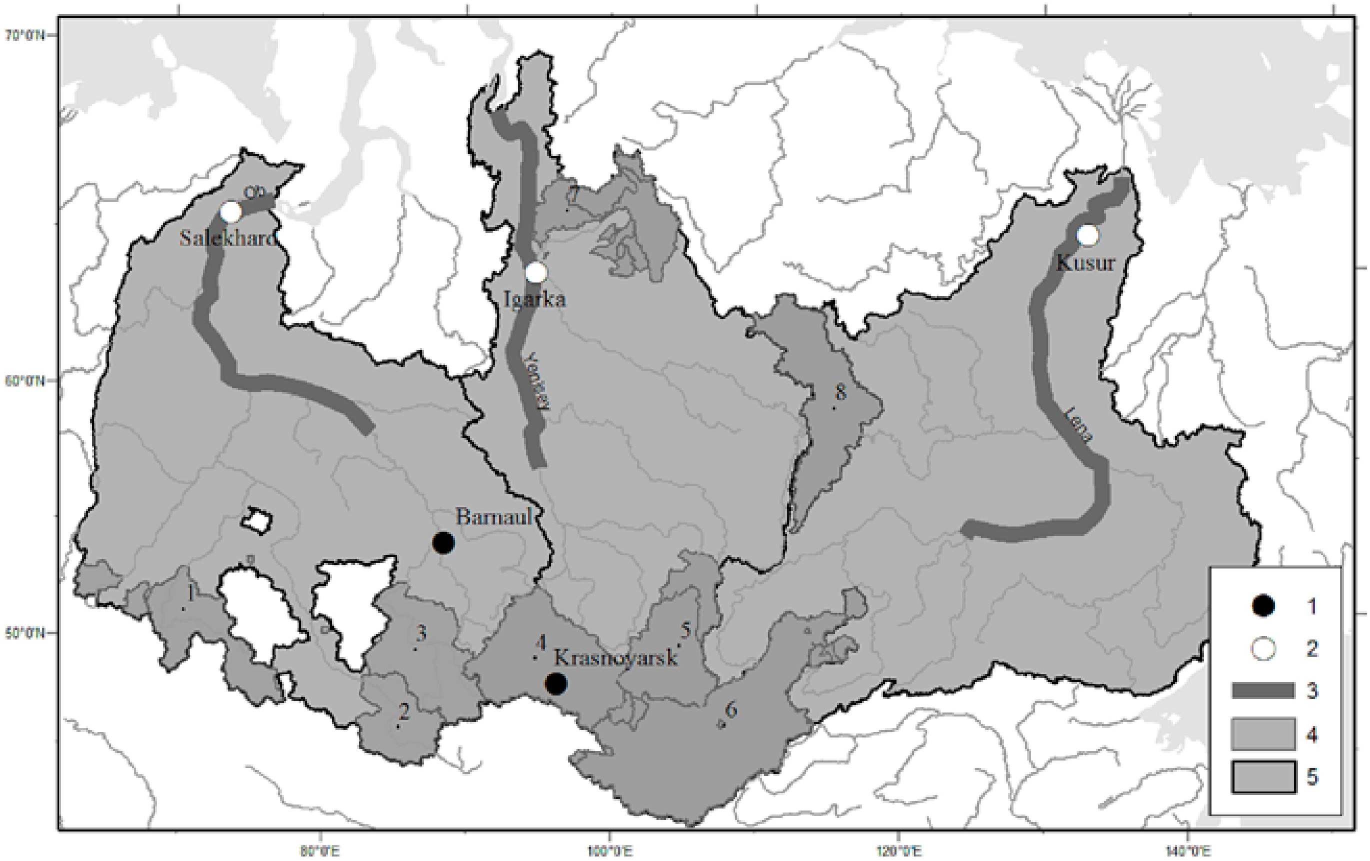

Fig. 1. Ob', Yenisey and Lena river catchments. Where 1 – Soil erosion gauging stations, 2 – River mouths, sediment gauging stations, 3 – Channel erosion calculation area, 4 – Reservoirs watershed, areas which was excluded from calculations, 5 – River watersheds, area of watershed erosion calculation. * Reservoirs watersheds: 1. - Sergeevsk reservoir, 2. -Shulbinsk reservoir, 3. - Novosibirsk reservoir, 4. - Krasnoyarsk reservoir, 5.- Angara cascade, 6. - Irkuts reservoir + Baikal lake, 7. - Kureika reservoir, 8. - Vilui reservoir.

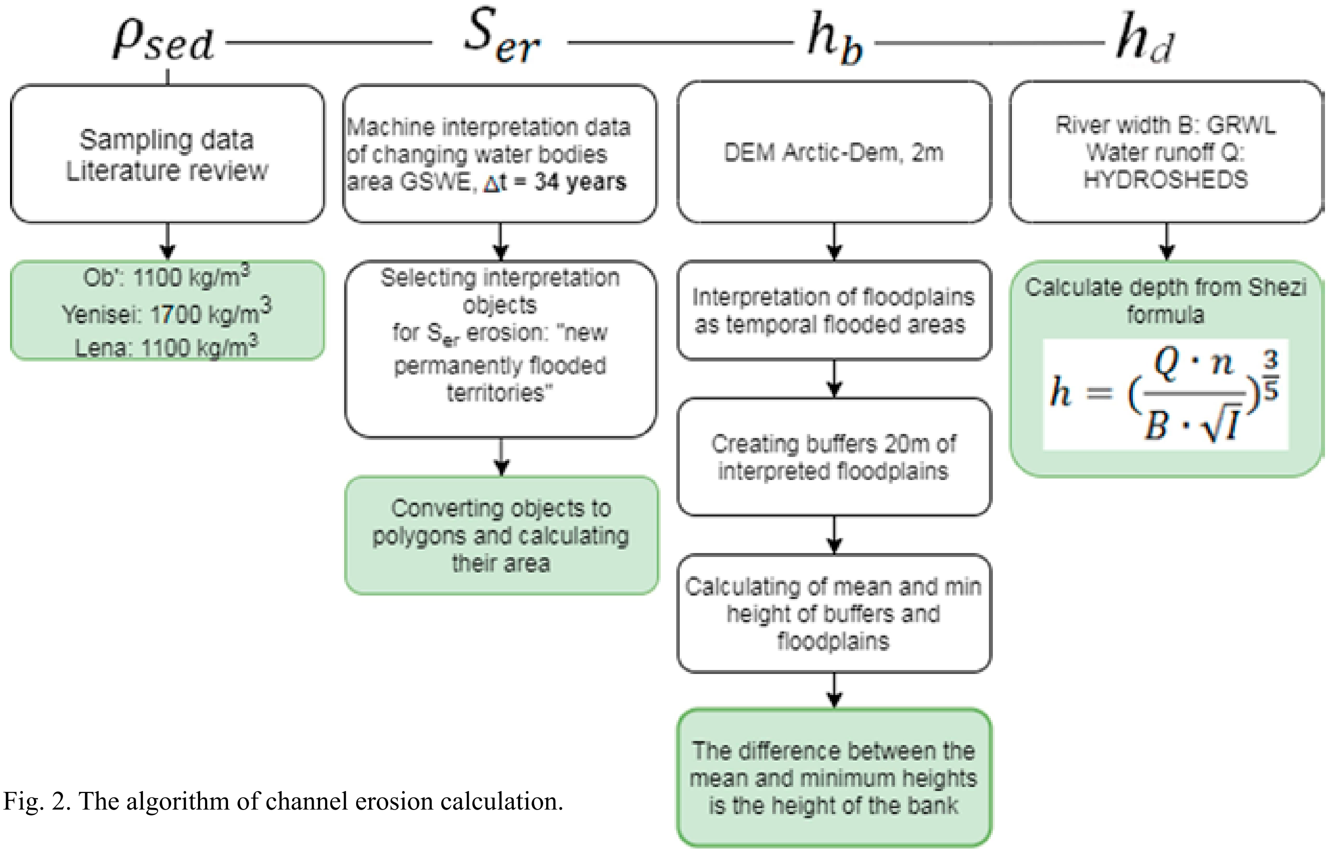

Fig. 2. The algorithm of channel erosion calculation.

watershed area (km^2), w – average cross-sectional area of gullies which is taken as a world average of 3.7 m^2 (Vanmaercke et al., 2016), ρ – average dry bulk soil density equals 1500 kg m^{-3} (Karaushev, 1977), τ – mean time of gullies development, taken as 120 years (Wilkinson et al., 2005).

2.3. Channel erosion

Contribution of sediments from in-channel sources is arguably the least understood and least quantified sediment budget component. Here, we rely on estimates of bank erosion which is considered to be the major source of sediments compared to channel bed erosion. To determine stream bank erosion contribution, we used detailed historical analysis of riverbeds from available satellite images to assess the Ob', Yenisey, and Lena rivers planform changes. Channel erosion was measured as bank retreat along studied rivers based on the GSWE automatic image interpretation dataset (Pekel et al., 2016) which provides global data of location and persistence of surface water and its changes from 1984 to 2016. For each year there are 14–22 space images (raster layers) which characterize periods of different water flow. In our research the "Water Transitions map" layer was used which provides estimate of long-term water history through identifying transitions between permanent water, seasonal water and land classes between the first and the last year. "The Water Transitions map" raster has 10 values that describe the evolution of water pixel state from 1984 to 2016: "New permanent" water surfaces (i.e. conversion of a no water place into a permanent water place.), "Unchanging permanent" water surfaces, "Lost permanent" (i.e. conversion of a permanent water place into a no water place), "New seasonal" (i.e. conversion of a no water place into a seasonal water place), "Unchanging seasonal", "Lost seasonal" (i.e. conversion of a seasonal water place into a no water place), "Conversion of permanent water into seasonal water", "Conversion of seasonal water into permanent water", "Ephemeral permanent water" (i.e. no water places replaced by permanent water that subsequently disappeared within the observation period), "Ephemeral seasonal" water (i.e. no water places replaced by seasonal water that subsequently disappeared within the observation period) (Pekel et al., 2016).

Mainly water surface area changes due to water balance fluctuations, but in the regional context of river channels, channel erosion can be described as a new permanent water body adjacent to the modern river channel. In our study channel erosion area was attributed to the "Conversion of seasonal water into permanent water" and "New permanent water surfaces" which is adjusted to the "Unchanging permanent water surfaces" of modern river channel and its braids that have a width >90–150 m in the low water period (that is 3–5 pixels of width of the GSWE resolution of 30 m). Thus we compute total erosion of the floodplain (including main channel and islands of the main course and its braids) as a general parameter named as channel erosion area.

The bank height (above average iced low flow period water level hb) was obtained from Arctic DEM digital elevation model with a resolution of 2 m (Morin et al., 2016). The bank height calculation was made in ArcGIS (ESRI, 2011) using "buffer" and "zonal statistics" tools. For each group of adjusted pixels (channel erosion area) with mean square of 0.05 km^2 a buffer zone of 15 m radius was created from which maximum and mean value of absolute height was calculated using Arctic DEM data. The difference between maximum and minimum of each buffer zone can be described as the difference of the low flow period level of the river and the present bank and floodplain height. Thus, 15,252 values of bank height were obtained for the Lena river study area, 15,763 for the Ob', and 2830 for the Yenisey River. Average annual

Table 4. Data and methods to calculate channel erosion used in this study.

Parameter	Data source	Resolution	Formula
S_{er} Eroded area	Data for automatic interpretation of satellite images for the search of GSWE water bodies (Dethier et al., 2020)	30 m	Areas of channel erosion – objects of the GSWE categories: “2-Not permanently flooded”, “7-periodically flooded areas “that have become” permanently flooded”
h_b bank height	DEM ArcticDEM (Morin et al., 2016)	2 m	$h_b = h_{fl} - h_{wat}$
h_d Mean river depth	GIS databases of slopes and discharges HYDROAtlas (Linke et al., 2019)Global data of river widths GRWL (Allen and Pavelsky 2018)	3 arcsec.	$Q = \omega \cdot C \cdot \sqrt{RI}, C = \frac{1}{n} h^{\frac{1}{6}},$ $h_d = \left(\frac{Q \cdot n}{B \cdot \sqrt{I}}\right)^{\frac{3}{5}};$
Sediment density	Literature overview, field measurements	Constant	1100 kg m^{-3} – for Ob’ and Lena 1700 kg m^{-3} – for Yenisey

ρ – density of bank sediments, kg m^{-3}; Δt – the time lag between satellite images, sec, for GSWE data it is 34 years (1984–2018); h_b – bank height, m, h_{fl} – absolute floodplain(bank) height, m; h_{wat} - absolute low water period water level, m; h_d – mean river depth, m; Q –water discharge, m^3 sec^{-1}; ω – crosssection square, m^2; C – Shezi coefficient, $m^{0,5}$ sec^{-1}; R – hydraulic radius,m; that is similar as river width B, I – slope, n – roughness coefficient.

water level exceeds average iced low flow period water level on 1–4 m, but to avoid larger failures it was concerned only to keep in mind this uncertainty. In addition, there are some uncertainties due to near bank canopy, which can increase bank height by several meters, which were checked manually.

The average depth of the river hd was estimated using 1D Shezi formula based on the data obtained from global databases HYDROAtlas (Linke et al., 2019) and GRWL (Allen and Pavelsky, 2018) under average annual flow conditions. Data of mean annual discharge and water slope was obtained from HYDROAtlas with mean resolution approximately of 4 km. Data of mean river width was obtained from GRWL with mean resolution approximately of 3 km. The Manning’s roughness coefficient is assumed as constant for all rivers as 0.045 (Baryshnikov, 1990). Totally, 627 values of mean depth were calculated for the Lena river of 1800 km, 452 values for the 1500 km of Yenisey river, and 226 for the 1680 km of the Ob’ river (Fig. 3).

River bank sediments density were assumed constant as 1100 kg m^{-3} for the Lena and Ob’ sandy river sediments, and 1700 kg m^{-3} for the Yenisey sandy-gravel sediments (Karaushev, 1977). These values were taken based on our field experiments (4–6 samples of river sediments for each river near cites, in Salekhard for the Ob’, Igarka for the Yenisey, Yakutsk for the Lena). These data are similar to the values on sediment grain sizes mentioned by (Slavina et al., 1981, Chalov et al., 1994, Shepelev, 1999).

The final formula of channel erosion calculation is presented below (Eq. (7)). The full algorithm of data processing is presented in Fig. 2.

$$W_{ch} = \frac{S_{er} \cdot \rho_{sed} \cdot (h_b + h_d)}{\Delta t}, \quad (7)$$

With ρ_{sed} – riverbank sediments density (kg/m^3), Δt – time gap between satellite images (y), S_{er} – eroded area from satellite data (m^2); h_b – bank height (m), h_d – mean river depth (m) – from global GIS databases with simple calculations (Table 3).

The channel erosion contribution was estimated for the downstream sections of each river system main streams. For the Lena river the reach from Kusur to Malykan settlements (1800 km from the mouth) was considered, for the Ob’ from the delta to the town Alexandrovskoye in the Tomsk region (1678 km from the mouth), for the Yenisey - from the delta to the town Yartsevo at the confluence with the Kas river (1501 km from the mouth). All formulas, input data and sources to calculate channel erosion is shown in Table 4.

2.4. Sediment export

Sediment export (Wsusp + Wbed) was estimated using long-term observations at the gauging stations located at the outlets of the selected rivers: Salekhard for the Ob’, Igarka for the Yenisey, and Kusur for the Lena. The series of observations for these rivers covered 78 years from 1938 to 2016 in case of Ob’ and Lena rivers. For the Yeniseythe

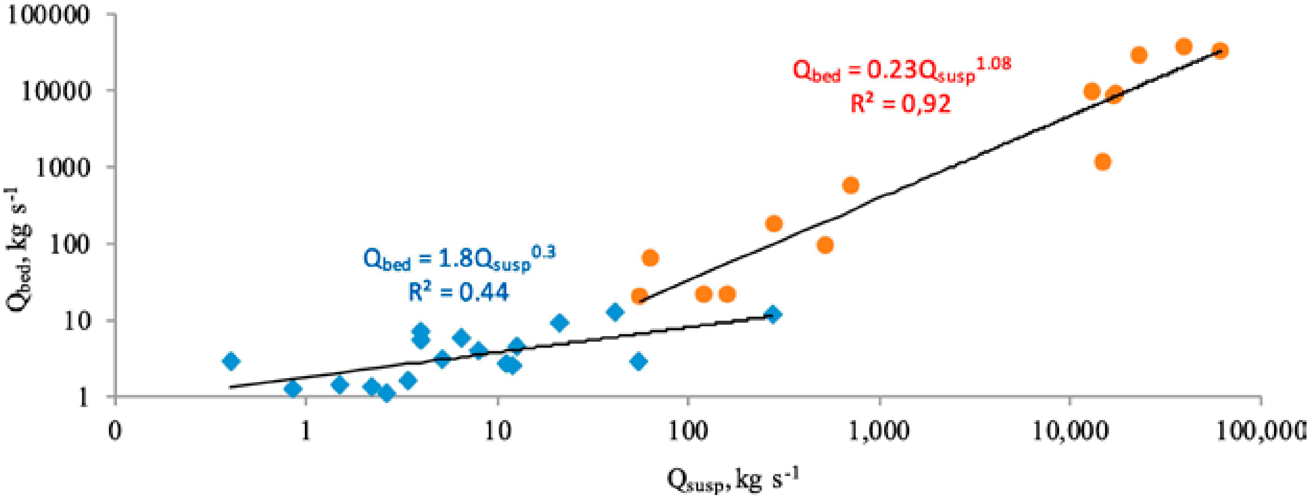

Fig. 3. The ratio Qbed = f(Qsusp) for medium (blue dots) and large sandy rivers (red dots) of Russia (based on dataset (Alekseevsky, 1990, Alexeevsky et al., 2013). (For interpretation of the references to colour in this figure legend, the reader is referred to the web version of this article.)

average annual sediment runoff was estimated for the period from 1992 to 2016 (24 years) which reflects the actual sediment yield after the dramatic changes of sediment runoff due to reservoirs construction in the upstream area of the Yenisey and Angara rivers (Magritsky, 2010). To calculate bed load Qbed we used the empirical model (Eq. (8)) proposed by Turowski et al. (2010) which is based on measured suspended load transport rates Qsusp:

$$Q_{bed} = \begin{cases} aQ_{susp}{}^{b}, Q_{susp} \le \left(\frac{a}{c}\right)^{1/(d-b)} \\ cQ_{susp}{}^{d}, Q_{susp} > \left(\frac{a}{c}\right)^{1/(d-b)} \end{cases}. \quad (8)$$

where Q_{susp} and Q_{bed} are in kg s^{-1}. We analyzed the dataset developed by (Alekseevsky, 1990, Alexeevsky et al., 2013) for Russian rivers to obtain the empirical coefficients a,b,c,d, for medium sized (average discharge below 428 $m^3\ s^{-1}$) and large rivers of Russia and China (water discharge in the range from 900 to 28 900 $m^3\ s^{-1}$) (Fig. 3). The largest river presented in the dataset include Northern Dvina, Ob', Lena, Yangtze and Yellow. Based on the obtained graph (Fig. 5) we further used the description of the median trend as an empirical equation to estimate bedload Q_{bed} from suspended load Q_{susp} at the Ob', Yenisey and Lena river (Eq. (9)):

$$Q_{bed} = 0.23Q_{susp}1.08 \quad (9)$$

Where R2− coefficient of determination between values and linear trend approximation.

2.5. Sediment deposition

The components of Eq. (1) related to sediment deposition and are not subjected to modelling and monitoring over large catchments, but can be estimated using (Eq. (10)) as a difference between gross erosion (catchment and channel) and sediment export.

$$W_{wd} + W_{chd} = W_{w} + W_{ch} + W_{gullies} - (W_{susp} + W_{bed}), \quad (10)$$

For areas upstream of reservoirs gross erosion was equal to W_w of its watersheds. This assumption is based on the sediment storage in the largest reservoirs of the world (Vörösmarty et al., 2003) which states that reservoirs retain over 90 % of sediments. In the Ob' river catchment the area upstream from reservoirs is 592000 km^2 or 22 % of the whole Ob' watershed; in the Yenisey the area upstream from Krasnoyarsk and Angara watershed (1200000 km^2 or 46 % of Yenisey watershed) was also not considered; in the Lena river catchment erosion was not considered for the relatively small upstream part of the watershed (148000 km^2 which is 6 % of the catchment) which is located upstream from few existing dams. All the calculations of the budget are done on yearly basis, which is the only plausible way to compile quantitative assessment of sediment budget components at the scale of the selected large rivers. This is important also to get comparable results between catchment and channel erosion considering large time lags and delivery periods within the vast territories.

Finally, we estimated a catchment scaling factor (which is opposite to traditional sediment delivery ratio

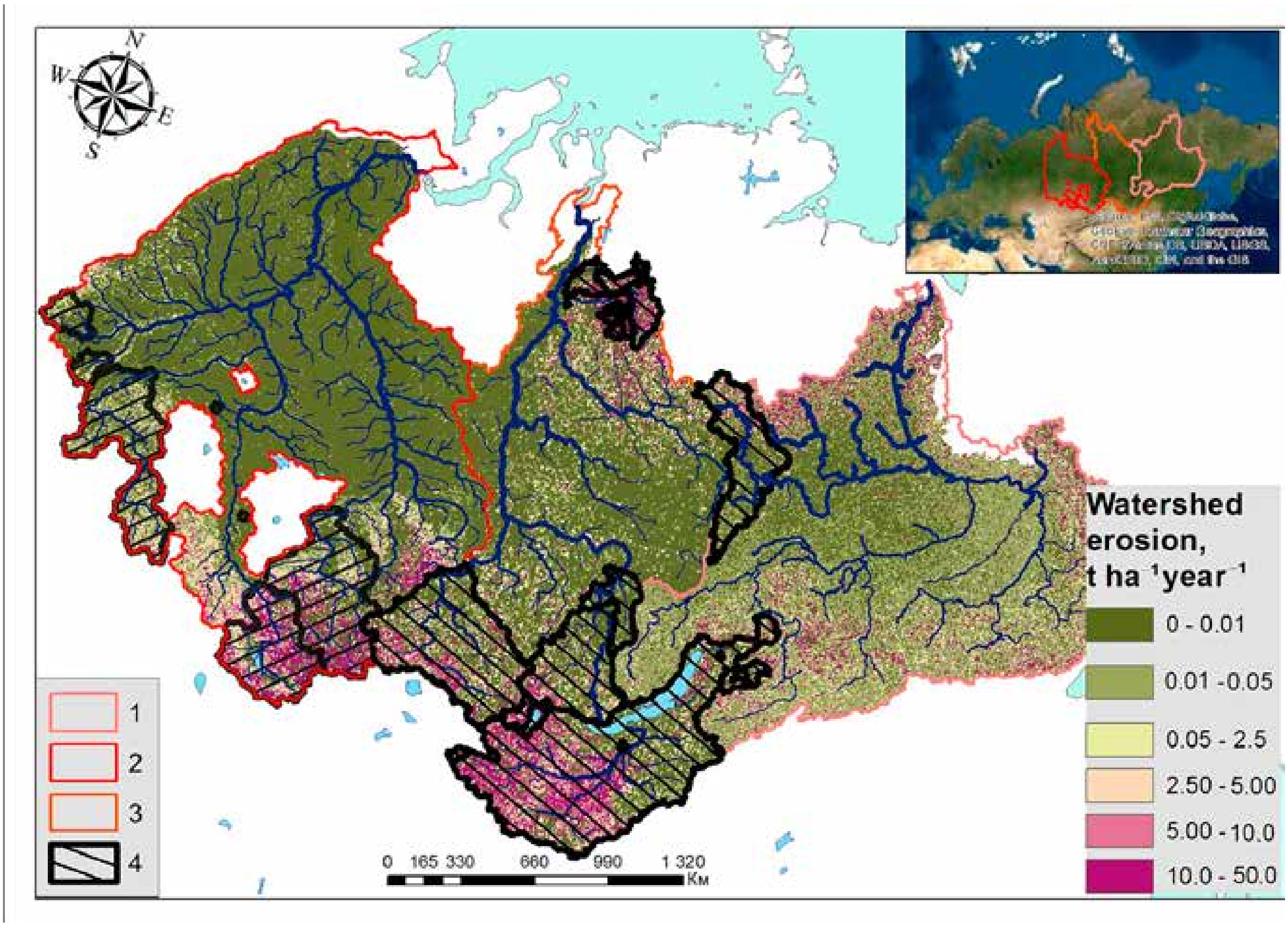

Fig. 4. Total Catchment soil erosion. Where 1 – Lena Watershed, 2 – Ob' watershed, 3 –Yenisey watershed, 4 – Reservoirs watershed, areas which were excluded from the calculations.

Table 5a. Estimates of catchment rain,snow melting and total erosion rates within the three studied river watersheds as mean annual values per hectare.

	Latitude	t ha^{-1} year^{-1}								
		Lena			Ob’			Yenisey		
		Rain	Snowmelt	Total	Rain	Snowmelt	Total	Rain	Snowmelt	Total
1	45–50				30.9	0.68	31.6	4.4	4.65	9.05
2	50–55	3.35	0.63	3.98	6.64	0.30	6.94	1.42	3.89	5.31
3	55–60	3.20	1.26	4.46	0.25	0.06	0.31	0.26	1.03	1.29
4	60–65	1.64	0.64	2.28	0.004	0.08	0.08	0.17	1.00	1.17
5	65–70	5.52	0.98	6.50	0.002	0.85	0.86	2.09	0.00	2.09
	∑	3.43	0.88	4.31	7.56	0.39	7.95	1.67	2.11	3.78

Table 5b. Estimates of catchment rain,snow melting and total erosion rates within the three studied river watersheds in unites of mass fluxes of latitude bands.

	Latitude	Mt year^{-1}								
		Lena			Ob’			Yenisey		
		Rain	Snowmelt	Total	Rain	Snowmelt	Total	Rain	Snowmelt	Total
1	45–50				762.5	17.8	861	127.8	137	267
2	50–55	384	78	433	459.5	23.8	564	105.8	296	403
3	55–60	285	115	371	28	6.8	35	12.8	60	75
4	60–65	74	31	76	0.00	3.8	4	8.8	64	75
5	65–70	19	10	0	0.00	6.8	7	59.8	0	62
	∑	762	234	880	1250	59	1471	315	557	882

(SDR) (Eq. (11b)) (Chen and Lai, 2005) and illustrates exceedance ratio of the sediment production over sediment export from the catchment (Eq. (11a)):

$$K_{red} = \frac{W_w + W_{ch}}{(W_{susp} + W_{bed})} \qquad (11a)$$

$SDR = 1/K_{red}$ (11b)

3. RESULTS

3.1. Catchment erosion

Average area-specific catchment erosion for Ob’ was estimated at 7.95 t ha^{-1}y^{-1}, for Yenisey at 3.78 t ha^{-1}y^{-1}, for the Lena it was estimated at 4.31 t ha^{-1}y^{-1}. The average for the three catchments was estimated at 5.34 t ha^{-1}y^{-1}. The spatial distribution of the catchment erosion contribution over the Arctic area is prone to longitudinal variations (Fig. 4). We found a significant decline in the estimates of soil erosion rates for croplands to forests and other forms of semi-natural vegetation (Table 5a and Table 5b). The predicted average soil erosion over 45–50° N is more than four times higher than the overall soil erosion rate for the Ob’ river (31.6 t ha−1 year−1 versus 7.95 t ha−1 year−1respectively) and three times higher for the Yenisey river (9.05 t ha−1 year−1 versus 3.78 t ha−1 year−1respectively). For the catchment sediment budget it is important that these areas (45–50° N) are considered as the blank areas (Fryirs et al., 2007) as far as sediment movement here is impeded by major dams and is not delivered to the downstream channel network. This significantly reduces the total contribution of catchment sources to the downstream area.

The applied Eq. (6) suggests that 20.7 Mt year^{-1} are transported by gully erosion within the Ob’ River, 5.9 Mt year^{-1} in the Yenisey River catchment and 11.5 Mt year^{-1} within Lena River catchment. If taking into account only areas below reservoirs, following the approach developed for the catchment erosion, the values will be reduced to 16.2, 3.2 and 10.8 Mt year^{-1}, respectively.

3.2. Channel erosion

The analyzed GSWE satellite images database show consistent planform changes that occurred along the Ob’, Yenisey and Lena between 1984 and 2018. Additionally, the DEM-based calculation revealed averaged morphological features of the rivers. The average value of bank height for the Lena is 7.5 m, 4.3 m for the Ob’, 9.8 m for the Yenisey. The distribution of bank height for each river was visualized as a map (Fig. 6). Based on our calculations mean depth of the Lena equals 2.9 m, 1.6 m along the Ob’ river downstream reach, and 8 m for the Yenisey river.

Lateral migration along the entire study reach was assessed in detail continuously and at the reach scale. The total channel erosion of the Ob’ from the mouth to the Alexandrovskoye town in the Tomsk region (1680 km from the mouth) was estimated as 151 Mt year^{-1}. The calculated gross input of sediments from channel erosion within the downstream 1500 km of the Yenisey river is estimated as 15.9 Mt year^{-1}. For the Lena river channel erosion along the downstream 1800 km causes 338 Mt year^{-1} of sediments annually delivered to the river system due to bank retreat (Fig. 7).

3.3. Sediment budget and deposition processes

A sediment budget, explaining production, fate and export of sediment, was calculated for the Ob’, Yenisey and Lena catchments. According to the data used in our calculations, both soil erosion and in-channel sediment production was considered as a static process under present hydroclimatic conditions. Estimating catchment erosion with the revised universal soil loss equation (RU-

Table 6a. Integrated sediment budget assessment for the entire Ob', Yenisey and Lena rivers.

Sediment budget, $1 \cdot 10^6$ t year^{-1}						K_{red}
River	Erosion			Sediment export	Deposition	
	Channel	Catchment	Catchment + channel			
Ob'	151	1471	1622	58.2	1564	27.9
Yenisey	15.9	882	898	32.5	865	27.6
Lena	338	880	1218	38.6	1179	31.6

Table 6b. Integrated sediment budget assessment for lower Ob', Yenisey and Lena rivers areas below the major reservoirs.

Sediment budget, $1 \cdot 10^6$ t year^{-1}						K_{red}
River	Erosion			Sediment export	Deposition	
	Channel	Catchment	Catchment + channel			
Ob'	151	230	381	58.2	323	6.55
Yenisey	15.9	107	123	32.5	90	3.78
Lena	338	845	1183	38.6	1144	30.6

SLE) for each pixel of the DEM resulted in estimates of sediment production across various catchment compartments.

In this research, we have calculated separately the sediment budget of whole catchments (Table 6a) and only for lower parts of the catchments below the largest reservoirs (Table 6b). The volume of sediment produced at the catchment located below the largest reservoirs, and also considering the low rates of catchment sediment delivery rates for large river watersheds (Ferro and Minacapilli, 1995, Borselli et al., 2008, Sidorchuk, 2018), the results (Table 6b) suggests the importance of channel erosion as major sediment source.

The integrated sediment budget for the entire catchment (Table 6a) shows that in the Ob' river watershed over 1564 Mt year^{-1} of sediments are deposited due to retention by reservoirs, in sinks within the watershed, or as in-channel and overbank deposition. Similar numbers indicate that 865 Mt year^{-1} of the total sediments produced on hillslopes and in channels are deposited within Yenisey fluvial system, and 1179 Mt year^{-1} in the Lena river. The established sediment budget for all three rivers (Table 6a) clearly shows huge discrepancies between sediment origin and export, the fact emphasizes the importance of gross deposition in the catchment.

The sediment budget of the lower segments of the catchments (below reservoirs) (Table 6b) indicate that 323 Mt year^{-1}, 90 Mt year^{-1} and 1144 Mt year^{-1} of sediments are currently stored in the lower segments of Ob', Yenisey and Lena catchments respectively (Fig. 8). For the lower part of Yenisey catchment the total watershed erosion is estimated as Ww = 107 Mt year^{-1}, whereas this number is significantly lower than theoretically available to be exported from the catchment due to the capturing by reservoirs and lakes (882 Mt year^{-1}). In particular, the Baikal Lake watershed which is one the most erosion-prone territories in the Yenisey catchment (Karthe et al., 2019, Chalov et al., 2021a), over half of the gross catchment erosion (387 Mt year^{-1}) is completely trapped by Baikal lake. As a result, only 12 % of the total soil erosion Ww is available in the downstream sections of the rivers. Similarly, for the Ob' catchment area, the total catchment erosion was estimated at Ww = 1471 Mt year–1, from which over 85 % is trapped by the upstream reservoirs mainly Novosibirsk reservoir on the Ob' and Shulbinsk reservoir on the Irtysh (Fig. 1). In other words, around 15 % of the gross soil erosion products (151 Mt year^{-1}) theoretically can reach downstream sections and be exported out of the river catchment. Similarly, in the Lena watershed the catchment erosion was estimated as

Table 7. Comparison of different estimates of soil erosion for the studied reach by various authors.

Rainfall erosion t ha^{-1} year^{-1}	RUSLE	Altai research Institute of agriculture gauging station in Barnaul***	Field measurements by [Golubev, 2022] in Krasnoyarsk
* sparse vegetation	1.17	1.7	–
** croplands	11.4	14.5	–
melting erosion t ha^{-1} year^{-1}	Larionov-Krasnov model	Altai research Institute of agriculture gauging station ***	
* sparse vegetation	1	–	–
** croplands	10	–	12 – 21.6

* RUSLE input parameters: LS = 1.375; K = 0.18 (Vorony-Calcic CHERNOZEMS); R = 300 MJ mm^{-1} ha^{-1} year^{-1}; C = 0.165 (GlobCover 2009: №20 Mosaic cropland).

** RUSLE input parameters: LS = 1.375; K = 0.18 (Vorony-Calcic CHERNOZEMS); R = 300 MJ mm^{-1} ha^{-1} year^{-1}; C = 0.017 (GlobCover 2009: №100 Grassland).

*** For soil erosion study sides with area of 631.5 ha, located on the slope of the southwestern exposure with a drain line length of 1800 with crops of perennial grasses and without crops (Volnov et al., 2017).

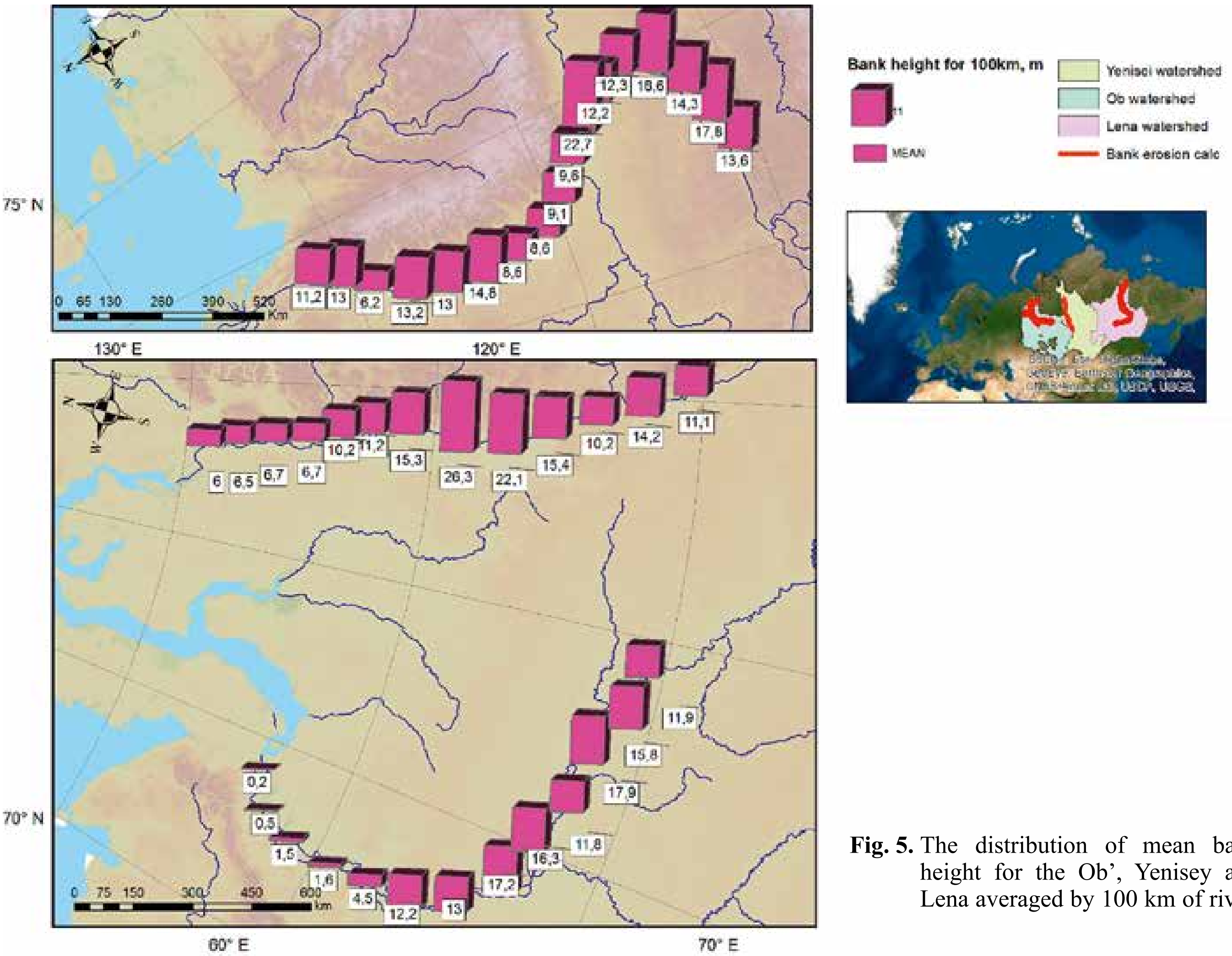

Fig. 5. The distribution of mean bank height for the Ob', Yenisey and Lena averaged by 100 km of river.

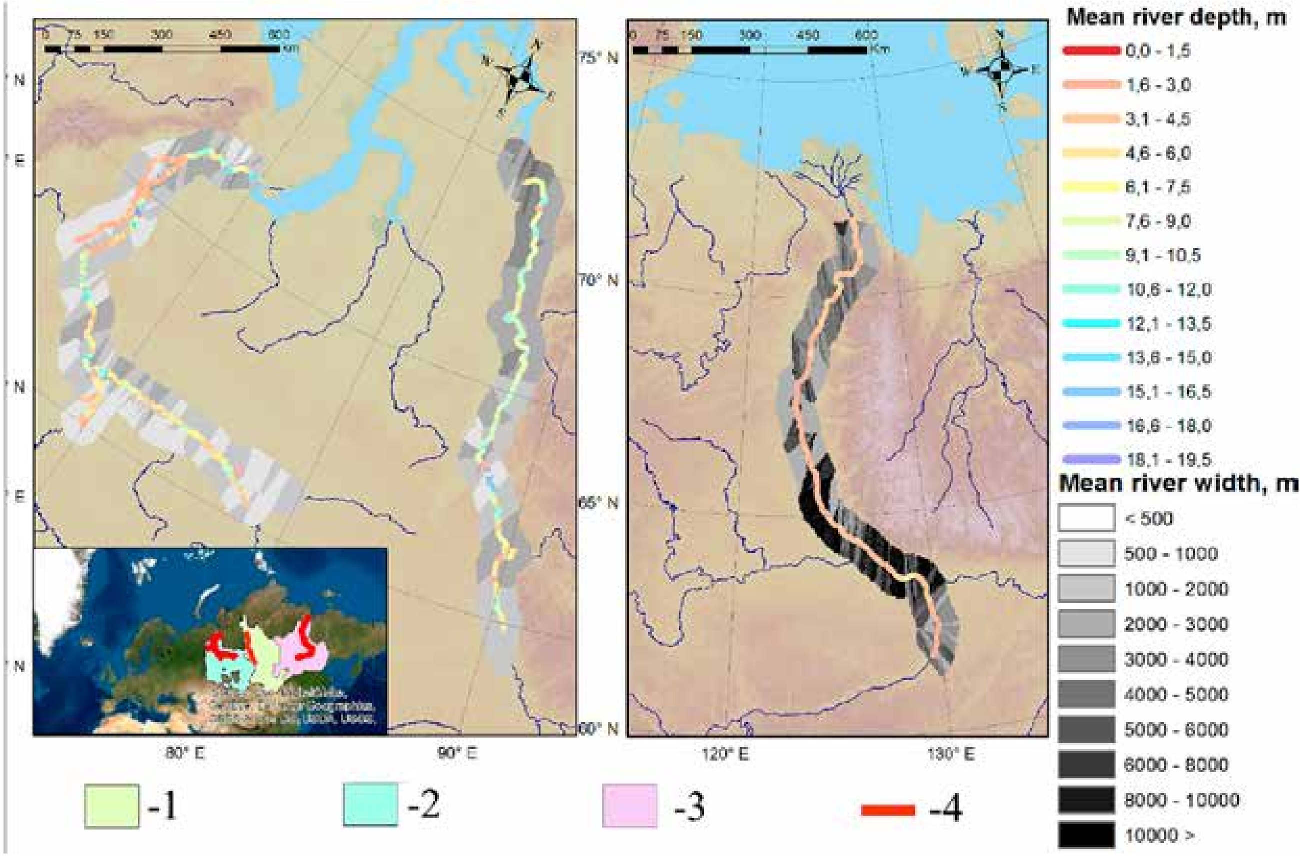

Fig. 6. The distribution of mean depth and mean width for the Ob', Yenisey and Lena averaged by 4 km of river. 1 – Yenisey watershed, 2 – Ob' watershed, 3 – Lena watershed, 4 – Channel erosion calculation area.

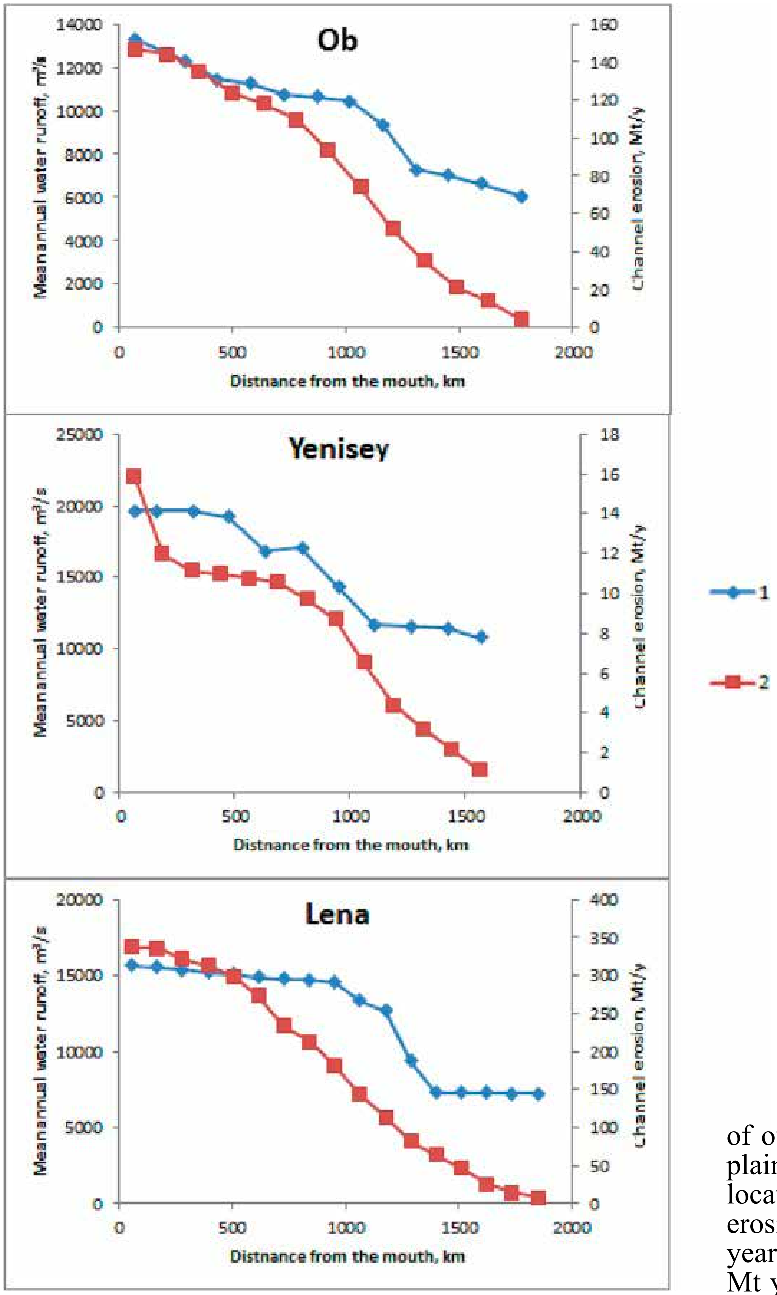

Fig. 7. Spatial distribution of cumulative channel erosion volume along the studied rivers, 1 – Annual mean water discharge, m^3 sec^{-1}, 2 – Channel erosion rates Mt year^{-1}.

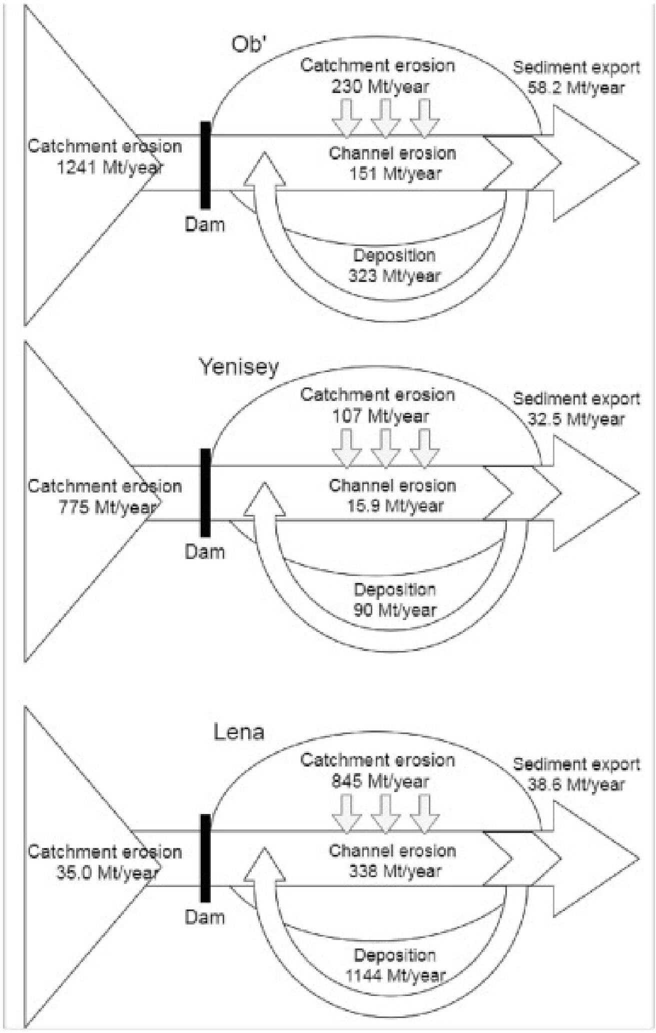

Fig. 8. Sediment budget of Ob, Yenisey and Lena rivers.

880 Mt year^{-1}. The largest reservoir here is located on the Vilui River which drains relatively stable territory, the gross erosion products that unavailable for downstream export due to reservoirs is 96 %.

3.4. Sediment runoff scaling factor

For the Ob' catchment, the scaling factor (Kred) (Table 6a) equals 27.9, for the Yenisey – 27.6, and for the Lena river – 31.6. These values, calculated by Eq. (11b) as SDR, indicate that on average only 4 % of sediment produced over Yenisey and Ob' watersheds, and 3 % of sediment produced over Lena watershed are available for the export if accounting the area upstream major reservoirs as blank areas. Considering catchment areas below major reservoirs, the Kred for the Ob' equals 6.55, for the Yenisey 3.78, for the Lena 30.6 (Table 6b). The large increase of the dimensionless Kred and absolute values of over Lena river compared to Ob' and Yenisey is explained by relatively small portion of the catchment area located upstream from reservoirs. Here, gross catchment erosion and channel erosion, both, produce only 35 Mt year^{-1} compared to the gross catchment erosion of 880 Mt year^{-1} in the Lena catchment. This data suggests the smallest impact of the dams in the relatively undisturbed Lena basin on the watershed-wide sediment budget compared to other large Arctic rivers.

4. DISCUSSION

4.1. Accuracy and uncertainties of sediment budget components estimate

Estimating of sediment budgets in such remote and data-scarce areas is associated with substantial uncertainty in the terms of both modelling and monitoring. Insufficient concurrent record or lack of data, separate methods used for different sediment budget components assessment, at present cannot be incorporated into the assessment of uncertainty. Below we provided discussion mostly related to comparative estimates of our results.

The catchment erosion components and are based on RUSLE-based models. In order to evaluate the performance of RUSLE model for catchment erosion estimates, multiple operations aiming to obtain insights about the validity of the modelling predictions were performed. Firstly, we compared the estimates with the ones provided by independent RUSLE-based assessments. The most detailed RUSLE simulation data is given by Borrelli et al. (2017) under global erosion modeling using a low resolution (compared to our approach) DEM who also verified the results by Global Assessment of Land Degradation and Improvement (GLADA) which is based on the analysis of NDVI indices (Bai et al., 2008). These numbers stress the accuracy of the RUSLE-based estimates of soil erosion for sparse vegetation and perennial grasses up to 50 % and in the range from 20 % to 50 % for the croplands. The average estimate of rainfall soil erosion by Borrelli et al. (2017) are 1 t ha−1 year−1 and 1.1 t ha−1 year−1, for Yenisey and Lena catchments, respectively, which is of the same magnitude (20–30 % difference) from average values obtained by our RUSLE model (Fig. 6).

Additionally, the measured soil erosion rates at the erosion plots from the locations across the studied catchment were superimposed to the estimates of our RUSLE model. In total, six soil erosion plots, located on different soil types and slopes, were identified. The experimental data of the Altai Research Institute of Agriculture soil erosion gauge with slope steepness of 2° to 4° (Volnov et al., 2017) (Ob’ catchment area, near Barnaul city) agreed fairly well with our model data. Here the measured soil erosion rates ranged from 1.7 (perennial grasses) to 14.5 t ha^{-1} year^{-1} (plowed soil and 13.4 t ha^{-1} year^{-1} (croplands) (Table 7). Similarly, the simulated values ranged from 0.5 to 1 t ha^{-1} year^{-1} and 1–2 t ha^{-1} year^{-1} (sparse vegetation by GlobCover 2009 (Bontemps et al., 2011)) to 11.4 t ha^{-1} year^{-1} (croplands by GlobCover 2009).

Some experimental data of snowmelt erosion was processed by Golubev (2022) for watershed Busim near Krasnoyark city. Field measurements of snowmelt erosion were estimated using surface level measurements. For croplands this method gives values of 12–21.6 t ha^{-1} year^{-1}, for the same sites the Larionov-Krasnov model calculated 10 t ha^{-1} year^{-1}.

The comparison of observational data on soil erosion at runoff plots and RUSLE/Larionov-Krasnov model data is presented in Supplementary Material 1, 2, 3.

Snowmelt erosion can play a significant role in the sediment budget for boreal watersheds (Litvin, 2002), but the models which can be used for these areas were not yet tested widely and might lead to huge uncertainties (SHI et al., 2020). Meltwater is responsible for 30 % of the catchment gross erosion in the forest-steppe part of the Angara river watershed (Bazhenova, 1982). The intensity of snowmelt and rainfall erosion estimated in in-situ experiments on the right bank of the Lower Volga identified significant rainfall erosion over snowmelt erosion (Surmach, 1976). Similar results were obtained by Tanasiyenko, 2003, Evseeva, 2009. Snowmelt and rainfall soil erosion for the forest-steppe and steppes of Western Siberia (Litvin, 2002) croplands were estimated at 4.5 to 8.1 t ha^{-1} year^{-1} and 17.1 t ha^{-1} year^{-1}, respectively. Such values of rain soil erosion are comparable to the RUSLE calculations. The RUSLE model gives a value of rain soil erosion of 11.4 t ha−1 year−1 for the plowed area in this area. Finally, the application of snowmelt module developed at MSU (Golosov et al., 2018) to the Lena river catchment indicated that 39 % of gross erosion is due to snow melting (Shynbergenov and Yermolaev, 2017).

Accuracy of channel erosion estimates was based on comparing the eroded area detected by the GSWE automatic image interpretation data (Pekel et al., 2016) with digitized images. For that we used manually digitized active-channel polygon for each series of satellite images of the middle and lower Ob’ (Kurakova and Chalov, 2019) which describes the portion of water surface constituted by wetted channels and adjacent bare or partially vegetated bars (Mandarino et al., 2019). The automatically and manually defined areas were in high agreement with differences in polygon areas up to 10.5 %. Additionally, estimates of bank height were verified by ADCP water discharge measurements done in 2019–2020 under ArcticFLUX monitoring at Salekhard (Ob’ river), Igarka (Yenisey river) and Yakutsk (Lena river) (https://sediment.ru/projects.html#arcticflux). The accuracy of the average depth under annual water discharges lay within 20 % of the monitored values. In Supplementary Material 4 there are illustrations of the comparison of automatically and manually defined channel erosion areas for four sample sites.

4.2. Main features of large rivers sediment budget

The results presented in this paper provide useful information about the sources of suspended sediment transported by Ob’, Yenisey and Lena rivers and its differences. Our data reveals higher catchment erosion in the Ob’ river (1471 Mt year^{-1}) compared to the estimated erosion in Lena river (880 Mt year^{-1}) and Yenisey catchment (882 Mt year^{-1}). This is mostly explained by the agricultural lowland area distribution within the Ob catchment compared to plateaus prevailing in the Yenisey catchment. Even larger differences are observed in the channel erosion sediment production which was estimated to be much higher along the Ob’ river (151 Mt year^{-1}) and Lena (338 Mt year^{-1}) downstream reaches compared to Yenisey (15.9 Mt year^{-1}). The specific channel erosion rates (per channel network kilometer), which by definition discard the effect of the watershed area, varied widely across rivers. Values ranged from 10.6 t km^{-1} year^{-1} for the Yenisey stream channel to 94 t km^{-1} year^{-1} for the Ob’ river and 187 t km^{-1} year^{-1} for the Lena stream channel. This is caused by different geomorphologic processes on different channel types, while the wide floodplain sandy anabranching channel of the Ob’ and the Lena is characterized by large-scale planform changes which contribute significantly to sediment transport. The mostly confined meandering Yenisey channel produces small amounts of in-channel sediments. It is interesting to note, that the differences between Ob’ and Lena are not in large agreement with unconfined channel distribution (Table 1), while the Lena river network has a large portion of confined channels compared to the Ob’ River. Channel erosion processes are controlled by distribution of channel patterns along the river which explains increase or decrease of in-channel contribution to sediment transport at certain river reaches, mostly associated with braided (anabranching channels) and wide floodplains. The more alluvial Ob’ river produces smaller amounts of sediments compared to the Lena river due to smaller height of banks (7.5 > 4.3 m). This is connected with that the significant calculated part of Ob’ channel is lying in the wetlands of the West-Siberian lowlands, where the height of the river banks is low. The study reach of the Lena River also covers mountain channels of the upstream and middle catchment.

Another possible driver of differences between the intensity of channel erosion is seasonal discharge seasonality. Bar-full discharge and bankfull discharge which range from the level that submerges barren bars and the top of the water level before overbank submersion when thermal and fluvial erosion begins has different frequencies. At the Lena River it lasts about 40 days a year (Hasholt et al., 2006, Gautier et al., 2021), and less than 30 days at the Ob' and Yenisey (Shiklomanov et al., 2021). This can be partly explained by the varying impact of dam regulation, which is much lower in the Lena River. Additionally, long-term river discharge changes related to more frequent high floods coupled with repeated flood peaks in the summer are considered as the driver of the increasing erosion in the middle and lower Lena (Gautier et al., 2021). Even though this seasonality is an important driver of the sediment budget, we excluded it from our analyses because observed variability of annual magnitudes of sediment budget components across large rivers are stronger than seasonal changes of sediment yield, so that the conclusions regarding watershed-wide sediment budget based on the annual values from these case studies are thought to be credible.

Another driver which explains increase of in-channel erosion along the Lena River, is the distribution of permafrost and associated thermos-erosional phenomena which enhance channel migration. Almost the entire Lena basin (approximately 78–93 %) is located within the permafrost zone. Various types of permafrost exist in the Lena basin, including sporadic, or isolated permafrost in the source regions, and discontinuous and continuous permafrost in downstream regions (Strauss et al., 2021). Here the thawing of the permafrost is considered as the main driver of erosion (Magritsky et al., 2018, Chalov et al., 2021a). Unfrozen sediments (taliks) underlie the main channel of the Lena River due to warming of the large water mass (Rachold et al., 1996). In the middle and lower reaches of the Lena River, the talik occupies only 10–15 % of the total area of the channel. It is in this narrow strip in the core zone of the interflow that the most intense channel changes are localized, without capturing the entire channel as a whole (Chalov, 2021). The permafrost and talik are almost absent within Yenisey and Ob' rivers (Strauss et al., 2021) and thus partly explain lower values of in-channel erosion of these rivers compared to Lena.

The results of this study suggests that the majority of eroded (produced) sediment is stored in colluvial deposits in dry valley bottoms, on slopes and on plateaus. This in general confirms the conceptual vision on large river systems (Lu et al., 2005) as sink areas. The fluvial systems which are sediment sources and have a positive balance between particle detachment and particle subsidence (Kred < 2) are typical for small catchments in the upper part of the study areas, mostly heavily disturbed by agricultural activities and are described both in the upper Ob', Yenisey (in particular within Mongolia, see (Onda et al., 2007, Pietroń et al., 2017) and Lena catchment (Chalov and Tsyplenkov, 2017). As far as these sediments are further trapped by the large reservoirs downstream, the fluvial system in the downstream part of the river systems is a sediment sink. The existence of the wide sink areas were also reported for the three large continent-wide drainage systems in different climatic conditions based on the most extended available data (including hollow seismics and sediment cores), i.e. the Amazon, the Ganges–Brahmaputra, and the Rhine Basins (Hinderer, 2012). According to Dunne et al. (1998), only 23 % of the maximum load at the transition from erosion to fluvial transfer are reaching the mouth of the Amazon River, and sediment storage in channels and floodplains of the Bengal plain of the Ganges–Brahmaputra is about 30 % of the river load (Goodbred and Kuehl, 1999). The differences in these numbers (over 20 % compared to 3–5 % in our study for the large Arctic rivers) is explained by the fact that a significant portion of catchment erosion considered in our study is stored in abundant watershed sinks such as swamps and lakes, as well as lithological complexes that prevent soil erosion.

The predicted proportion of gully erosion compared to RUSLE-based estimate of catchment erosion varies from 1.2 % (Lena River) to 7 % (Ob' River) if considering areas below reservoirs or from 0.6 % to 1.2 % for the whole catchment. These estimates confirm that gully erosion can be assumed to be negligible on most part of the territory due to small anthropogenic disturbances over the area. Even at the most disturbed upper part of the catchment, within Selenga River (upper part of Yenisey catchment), gully erosion generated less than 10 % of the total sediment yield from the catchment (Theuring et al., 2015, Kasimov et al., 2019).

Our results also suggest that bank erosion is an important source in the sediment export, especially for the Lena and Ob' rivers (up to 90 %). The volume of bank erosion in the lower reaches of these rivers is 3-13 times larger than the sediment export. For the middle reach of the Ob' (downstream the confluence with the Vakh) and the downstream Ob' reaches, lower Irtysh below Gornopravdinsk, channel erosion was estimated to contribute 151 Mt year^{-1} against 58.2 Mt year^{-1} of sediment exported to the sea. For the Lena river, bank erosion was calculated to cause 338 Mt year^{-1} of sediments delivered into the channel downstream, and the sediment export is 38.6 Mt year^{-1}. Considering that all these sediments are delivered to the river, their relative contribution to sediment load is evident. As evidenced by the detailed bank erosion monitoring studies for the similar environment in the Northern lowland rivers (Kronvang et al., 2013), net bank erosion may act as the major sediment source (over 90 %). This is opposite to the Southern rivers (e.g. Yellow River, Nile and other reported by (Gao et al., 2011, Syvitski and Kettner, 2011) where catchment erosion dominates over sediment budget and explains the few orders of magnitude shift in sediment yield during Anthropocene.

We also compared our estimates of bank erosion with the data on bed degradation below reservoirs which might induce significant impact on basin-wide sediment budget (Tena and Batalla, 2013). Below the Novosibirsk reservoir which is reported to have the most pronounced effect on sediment load over the Arctic large rivers (Magritsky et al., 2018), the bed degradation in the 26 km reach was estimated to be 1.3 m between 1960 and 1973 (Alexeevsky et al., 2013, Kurakova and Chalov, 2019). Accounting average dry bulk soil density ρ as 1800 kg/m^3, river width on this reach as 1000 m, we estimated bed degradation contribution to sediment yield as 4.4 Mt year^{-1}, which is about 3 %, compared to bank erosion in the Middle and lower Ob' as shown above. Considering that the period from 1960 to 1973 refers to most active bed degradation after dam construction, we conclude that bank erosion significantly dominates over bed erosion in the studied rivers and confirm validity of the presented approach.

The importance of channel erosion to the in-channel budget of the Ob', Yenisey and Lena rivers was evidenced by remote sensing data (Chalov and Prokopeva, 2021, Chalov et al., 2021a) and geomorphic reconstructions (Tananaev, 2016). Sediment grain classes analyses (Chalov and Efimov, 2021) also suggest that channel erosion delivers significant portions of fine sediments (less than 62 μm) which contribute to transit sediment flow (suspended or bed load). At the same time as revealed by the study on fifty-year dynamics of the Lena River islands (Gautier et al., 2021), mean total erosion area is larger than mean total depositional area across the anabranching channel of the Middle Lena river. A relatively low percentage is exported out of the catchment, while a significant portion of the sediment delivered from the channel erosion is stored within the channel and floodplains. Such a large attenuation of sediment in river channels and on floodplains is also evidenced by the data on up to 40 % decrease in suspended sediment load during high water events along braided channel reaches (Chalov et al., 2021b). The conditions of a longitudinal decrease in suspended-sediment concentration along the braided reach of the Lena River are characterized by high water discharges (>20,000 $m^3 s^{-1}$) and are associated with sediment deposition on the riffles surface and floodplain areas.

The calculated values of sediment deposition (Table 6a) generally reflect the existing empirical data on actual proportion of sediments redeposited in Vilui reservoir on the Lena tributary Vilui (Velinkin et al., 2012), Angara (the main tributary of Yenisei) River reservoirs (Stupin, 2010), and Novosibirsk reservoir of the Ob' river (Khabidov et al., 2011). In particular, during 50 years the storage capacity of Novosibirsk reservoir decreased approximately by 1.02 km^3, which equals 22.4 Mt $year^{-1}$, considering a sediment bulk density of 1110 kg m^{-3} (Karaushev, 1977). Compared to total catchment erosion upstream from the Novosibirsk reservoir (924 Mt $year^{-1}$), it can be considered that only 2.43 % of gross erosion is stored within in-channel sinks in the upper part of large catchments. The remaining significant part of the estimated eroded material is stored within catchment depositional surfaces (sheet deposition zone, alluvial fans etc.), which is confirmed by Maltsev and Ivanov (2022) who estimated the sediment deposition within an upper small catchment of the Lena watershed in the range from 96 % to 98 % of gross erosion. The study conducted in the Selenga catchment (Yenisey watershed) demonstrated (Onda et al., 2007) that after a single rainfall event over 93 % of gross erosion is trapped along hillslopes.

The role of sediment deposition was reviewed by Dedkov (2004) who indicated an increase of sediment yield with larger catchments area. Total suspended sediment yield increases downstream faster than the basin area for rivers with undisturbed or slightly disturbed basins. Rivers with intensively cultivated basins are also characterized by an increase in total suspended sediment yield downstream, but this increase is slower than the increase in basin area and the specific suspended sediment yield therefore decreases downstream (Dedkov and Gusarov, 2006). Understanding of such large and poorly monitored systems as Ob', Yenisey and Lena is still in its infancy, in particular with regard to the quantification of particular contribution of the sediment budget to sediment export. The present study estimates the annual magnitudes of sediment budget components and their relative values and may stimulate more integrated studies on the entire routing system in the future.

5. CONCLUSIONS

For the first time, a multi-level assessment of the main components of the sediment budget was done for the large river watersheds of Ob', Yenisey and Lena which cover over 14 % of the Eurasia continent. The components included soil erosion, channel erosion, sediment discharge, and sediment storage (floodplain and channel).

1. The volume of soil erosion significantly exceeds channel erosion. For the Ob' catchment erosion was estimated at 1471 Mt $year^{-1}$ (or 230 Mt $year^{-1}$ without catchments upstream of the main reservoirs), while the channel erosion of the lower course (a section of 1,680 km from the mouth) was estimated to be only 151 Mt y^{-1}. The catchment erosion of the Yenisey was estimated at 882 Mt y^{-1} (107 Mt $year^{-1}$ without catchments upstream of the main reservoirs), and the channel erosion as 15.9 Mt y^{-1} in the area from the delta to the Yartsevo, the town at the confluence of the Kas and the Yenisey (1501 km from the mouth). For the Lena total catchment erosion was estimated at 880 Mt ye^{-1} (or 845 Mt $year^{-1}$ without reservoirs catchments), the channel erosion as 338 Mt $year^{-1}$ (1800 km of downstream from the delta to Malykan settlement).
2. Sediment budget calculations indicate that only a small portion of the total sediment input leaves the major catchments of Arctic drainage basin. Under present hydro-climatic conditions 96–97 % is stored in various buffer zones of the catchment and river network.

Our presented method yields a novel picture on the large rivers sediment budget components over the basin-wide scale of the Arctic. The conclusion presented here should be in future added by detailed geomorphological reconstructions and in-channel monitoring datasets of sediment budget using sediment load measurements.

Reemission of inorganic pollution from permafrost – a freshwater hydrochemistry study in the lower Kolyma basin (North-East Siberia)*

1. INTRODUCTION

Permafrost loss has been observed widely in the Northern Hemisphere since the second half of 20th century (Streletskiy et al., 2015) and it has impacted markedly both terrestrial and aquatic environments (Mann et al., 2022; Vonk et al., 2015). Further significant changes are predicted in permafrost environments during the 21st century (Smith et al., 2022; Streletskiy et al., 2021; Teufel & Sushama, 2019) as the climate warms (Overland et al., 2014, 2017). Such changes will be both vertical and horizontal, resulting in deeper active layers (Abramov et al., 2021), shrinking permafrost extent, and the retreat of its respective zones (Lim et al., 2019; Streletskiy, 2021). The progressing permafrost degradation leads to important and lasting changes in geomorphological processes (Rudy et al., 2017; Tananaev & Lotsari, 2022), hydrological phenomena (Rudy et al., 2017; Suzuki et al., 2021) and biogeochemical cycles (Grosse et al., 2016; Mann et al., 2012; Vonk et al., 2015).

Among permafrost regions in the Northern Hemisphere especially the north-eastern Siberia have experienced dynamic environmental changes induced by climate change (Nitzbon et al., 2020). Recent climate-induced increases in thaw propagation have triggered changes in local relief in the Yedoma uplands, including soil subsidence (Günther et al., 2015), activation of thermokarst and thermoerosion processes (Grigoriev et al., 2009; Morgenstern et al., 2021), and the expansion of pond and thermokarst lake areas (Nitze et al., 2017; Veremeeva et al., 2021). In large rivers, an increase in runoff is both expected and already observed: in the Kolyma, mean annual discharge has increased over the 2010–2020 by 27.7% (94.6–120.7 km^3 year^{-1}) compared with a baseline period of 1971–2000 (Mann et al., 2022). At the same time, this increase followed period of water runoff decline due to impact of reservoirs located on the Kolyma main stem: at the lowest gauging station Kolymskoe the average discharge decreased from 3790 m3 s-1 during 1977–1980 to 3090 m^3 s^{-1} during 1991–1997. Mann et al. (2022) estimated also an increase of 50% (±25%) in Kolyma's mean annual runoff by 2100, in line with climate projections. Climate warming resulted also in an increase in Kolyma's sediment transport rates from 20 to 100 t km^{-2} year^{-1} in 1941–2000 (Chalov et al., 2018), which can be also attributed to mining impact (Walling & Fang, 2003) or changes due to permafrost thaw (Chalov et al., 2021).

Hydrochemical changes in permafrost regions are increasingly probable, leading to both temporary and permanent hazards to the surface water quality in the Arctic (Brubaker et al., 2012; Gunnarsdo'ttir et al., 2019). Permafrost active layer deepening and the formation of new thermokarst lakes, taliks and drainage pathways (Dzhamalov & Safronova, 2018; in't Zandt et al., 2020; Tananaev & Lotsari, 2022) all lead to changes in the migration of chemical compounds (Frey & Mcclelland, 2009; Monhonval et al., 2021) both horizontally and vertically (Ji et al., 2021; Tananaev et al., 2021). The newly formed drainage pathways may leach chemical compounds from layers previously disconnected from groundwater flow (Ji et al., 2021; Lim et al., 2019). Thermoerosion phenomena lead to intense erosion and thaw slump formation. Such phenomena impact the fluvial transport of suspended sediment and chemical compounds along the main hydrological pathways, to the estuaries and the ocean (Chalov et al., 2018; Frey & Mcclelland, 2009; Kokelj et al., 2013; Toohey et al., 2016). Both natural and anthropogenic chemical compounds may become mobilised from permafrost into surface waters (Kosek et al., 2019; Lehmann-Konera et al., 2018), and the anthropogenic compounds may be of both local and long-range-transport origin (Potapowicz et al., 2019; Szopin'ska et al., 2016).

The studies on the hydrochemical impacts of climate change in Siberian Arctic rivers have focused mainly on the organic carbon (OC) transport, including the dissolved OC (DOC), suspended particulate OC (POC) and riverbed sediment OC (SOC) (e.g., Holmes et al., 2012; Jong et al., 2023; Mann et al., 2012; Wild et al., 2019). Mann et al. (2022) stated that permafrost-derived OC additions will significantly enhance inland OC turnover over the upcoming decades; however, the fate of OC is uncertain due to additional transformation factors (Keskitalo et al., 2022). In the large rivers, OC occurs mainly as DOC: for Kolyma, the dissolved share has been calculated by Mann et al. (2022) as 80% (and similar by Jong et al., 2022; Keskitalo et al., 2022). Keskitalo et al. (2022) claim, based on isotopic evidence, that POC in Kolyma is more affected by the legacy Yedoma-derived OC than DOC, and Wild et al. (2019) confirm that POC in the large Siberian rivers may originate from the direct erosion of the old Yedoma layers. In rivers, they claim the DOC to be mainly from slow leaching of soil. Bröder et al. (2020) also remark that Kolyma transports more suspended POC at higher discharges. Finally, Mann et al. (2022) suggest that the OC flux and total export will rapidly increase due to climate change and permafrost degradation.

Compared to the research on OC sources, with respect to permafrost thaw, the recognition of inorganic elements, including heavy metals, is relatively poor and limited to selected elements (Ji et al., 2021; Lim et al., 2019). Systematic research on the potential accumulation of heavy metals in permafrost has only been conducted on mercury (Wang et al., 2022). Therefore, we present a study on the possible release of contaminants from permafrost

---

* Danuta Szumin'ska, Krystyna Kozioł, Sergey R. Chalov, Vasilii A. Efimov, Marcin Frankowski, Sara Lehmann-Konera, Zaneta Polkowska // Land Degradation and Development
https://doi.org/10.1002/ldr.4866
https://onlinelibrary.wiley.com/doi/10.1002/ldr.4866

into freshwater. Our objective was to perform a detailed hydrochemical assessment of permafrost thaw impact on the dissolved inorganic chemicals occurrence in the lower Kolyma River basin. We investigate this question in various freshwater environments: thermokarst lakes, permafrost ice, permafrost thaw creeks, and in watercourses representing various proportions of permafrost thaw supply.

2. METHODS

2.1. Study area and sampling

The study region is located in the lower Kolyma watershed (Figure 1) in a transitional zone between boreal forest (northern taiga) in the south and tundra ecosystems in the northern Yakutia. Kolyma is one of the largest pan-Arctic watersheds with a total area of 653,000 km^2, a total river length of 2129 km, and annual water discharge of 109 ± 7 km^3 (Holmes et al., 2012), fully underlain by continuous permafrost (Mann et al., 2012). The Arctic coastal lowlands of northeastern Yakutia constitute vast accumulative plains formed mostly by the Late Pleistocene until the beginning of late glacial warming, Yedoma Ice Complex, characterised by a high ice and organic matter content (Abramov et al., 2021). Yedoma deposits are a combination of aeolian, colluvial, nival and alluvial deposition and simultaneous ground ice accumulation accumulated under periglacial conditions in nonglaciated regions (Strauss et al., 2017). Along the Kolyma river, massive outcrops of permafrost are located, including the largest inland Duvanny Yar Yedoma ice complex (Murton et al., 2015). Permafrost thickness in the area reached 500–600 m, and the ice wedges at the Duvanny yar can reach 30 m. The sediments of the Duvanny Yar are eroded rapidly by the Kolyma River leading to permafrost cliff degradation several metres per year (Supporting information S1, Figures S1 and S2). Mineralogical composition of Yedoma sediments in Duvanny Yar included 1.3%–8.5% of the heavy mineral (pyroxene, hornblende, pyrope, pyrite, magnetite, and individual grains of apatite, goethite, and siderite), and prevalence of the light minerals (mainly quartz – up to 50% of grains, feldspars, illite, chlorite and clay minerals, dolomite, and occasionally calcite; Shmelev et al., 2021), which provides a plentiful source of migrating cations, especially Na^+, K^+, Ca^{2+}, Mg^{2+}, Fe^{2+} and Fe^{3+}, but also of anions bicarbonate, sulphate (from pyrite oxidation), phosphate, chloride and fluoride. These minerals contain also manganese, barium, zinc, lithium, chromium, cobalt, vanadium and various forms of Al and Si.

In the area, mean annual ground temperatures (MAGT) before the 1990s were of –8 to –11°C within the tundra and –7 to –8 °C in the taiga (Yershov et al., 1991). The very high ice content (up to 95% by volume) of Yedoma deposits in the Kolyma lowland (Strauss et al., 2021) makes them extremely vulnerable to climate warming. In 2000–2016 (Ran et al., 2022), MAGT in the studied region increased significantly against the former century due to climate warming, and now ranged from –8 to –4°C. Mean annual air temperature (MAAT) in Cherskii (68.75° N, 161.28° E, 28 m asl) increased from –12°C in the 1960s to –10°C in the 2000s, with a positive trend of 0.0472 °C per year (Sakai et al., 2016).

MAAT in Cherskii in the year of sampling (2021) amounted to –9.8°C and was lower than the MAAT in the years 2006–2021 (–8.9°C) (Supporting information S1, Table S2). However, the maxi mum air temperature in 2021 was the highest in the years 2006–2021 (tmax = 33.4°C) and it occurred directly before our sampling (Supporting information S1, Table S2, Figure S3). In the study area, the minimum air temperature ranged from –40.2 to –49.7°C and in 2006–2021 was observed in January, February or December. The maximum air temperature was observed in June–August, ranging 25.9–33.4°C (Supporting information S1, Table S2). The mean monthly air temperature was higher than 0°C from May to September (in 2006–2021) (Supporting information S1, Figure S4).

Samples have been collected between 19th and 22nd July 2001 (28 in total). River waters were collected in the four cross sections of Kolyma (Cherskii, samples K11–K13; Yermolovo, K21–K23; Duvanny Yar, K31–K33, K31b-K33b; Kolymskoye, K4), and in the mouth sections of the Anyui (A1, A2) and Omolon (O1) tributaries. In addition, a meltwater creek and ice were sampled from a permafrost cliff located at Duvanny Yar (P1-P3), and lake waters were collected from two thermokarst lakes (L11–L15, L21–L24) (Figure 1, a detailed description in Supporting information S1, Table S1). The Kolyma river samples were taken at the middle depth of three vertical profiles in the channel cross sections, except of Kolyma upstream of the permafrost cliff, where only one sample (from the middle of the channel) was collected. Water samples were pumped out with a filterless submersible 12 V pump (details in Chalov et al., 2022). In both lakes, samples were taken along a vertical profile located above the deepest point of the lake. Among the sample sites, direct permafrost influence was expected at the permafrost cliff, in Lakes 1 and 2 and in Kolyma cross section K3 (directly below permafrost cliff).

2.2. Analytical methods

All water samples, collected into 1 L HDPE bottles, were filtered through 0.7-µm-pore-size glass fibre filters (Whatman GFF, precombusted in 400°C, 24 h). This means that the analysis involved both the dissolved fraction and part of the colloidal matter in the sampled waters; however, for simplicity we will refer to it from here on as the dissolved fraction. Samples were kept in cool storage (+4°C) and analysed approximately 2 months since collection time. Specific electric conductivity (SpC), pH and dissolved oxygen (DO) were measured in K^+, Ca^{2+} and Mg^{2+}) were determined using Dionex ICS 3000 (Dionex, USA), calibrated with dilutions of a 1000 mg L^{-1} single-ion standard solutions. Analytical accuracy was checked with the TraceCERT® Multi Anion Standard 1 for IC (69734-100ML) and Multi Cation Standard 1 for IC (91286-100ML) (all solutions by Merck Life Science). Bicarbonate was determined by titration with HCl to pH = 4.3.

Elemental analysis was performed in acidified (with high-purity nitric acid, Suprapur, Merck Life Science) filtrate using inductively coupled plasma optical emission spectrometry (ICP-OES 9820, Shimadzu, Japan) for Be, P, S and Ti. Inductively coupled plasma mass spectrometry (ICP-MS 2030, Shimadzu, Japan) was applied for Ag, Al, As, Ba, Bi, Cd, Co, Cr, Cu, Fe, Li, Mn, Mo, Ni, Pb, Sb, Se, Si, Sr, V and Zn. For calibration of the ICP-MS, the ICP IV multielement standard (Merck Life Sciences) and single-element standards of As, Be, Sb, Se, Mo, and V (Sigma-Aldrich, USA) were used. Single-element 1000 mg L^{-1} standards (Sigma-Aldrich, USA)were

FIGURE 1. Location of the study area and sampling sites. Please note that all K-symbol samples come from Kolyma river cross sections. [Colour figure can be viewed at wileyonlinelibrary.com]

applied for the ICPOES. Internal standards controlling for the MS signal were solutions of Sc, Rh, Tb and Ge in suprapure 1% HNO_3 (Merck). Accuracy of the analysis was checked with Sigma-Aldrich CRMs (certified reference materials) Trace Metals ICP-Sample 1 and Trace Metals ICP-Sample 2, with 98%–104% recoveries. High-concentration samples were diluted with Milli-Q water (Direct 8 Purification System Water, Merck Life Sciences, France). All metals, non-metals and metalloids concentrations measured have been corrected for a procedural blank value if it exceeded the method limit of quantification (LOQ); in all other determinations, the blank correction was not required. The details of all measurement conditions and QA/QC parameters, including method LOQ, are given in the Supporting information S1, Table S3.

2.3. Statistical methods

Cluster analysis was performed using Statistica version 13 (TIBCO Software Inc.) on a selection of variables listing elemental, ionic and DOC concentrations, with the selection criterion that only variables with 33% or fewer values <LOQ (or below blank) were taken into account to avoid artifacts in grouping. Prior to cluster analysis, values <LOQ (or below blank) were re-

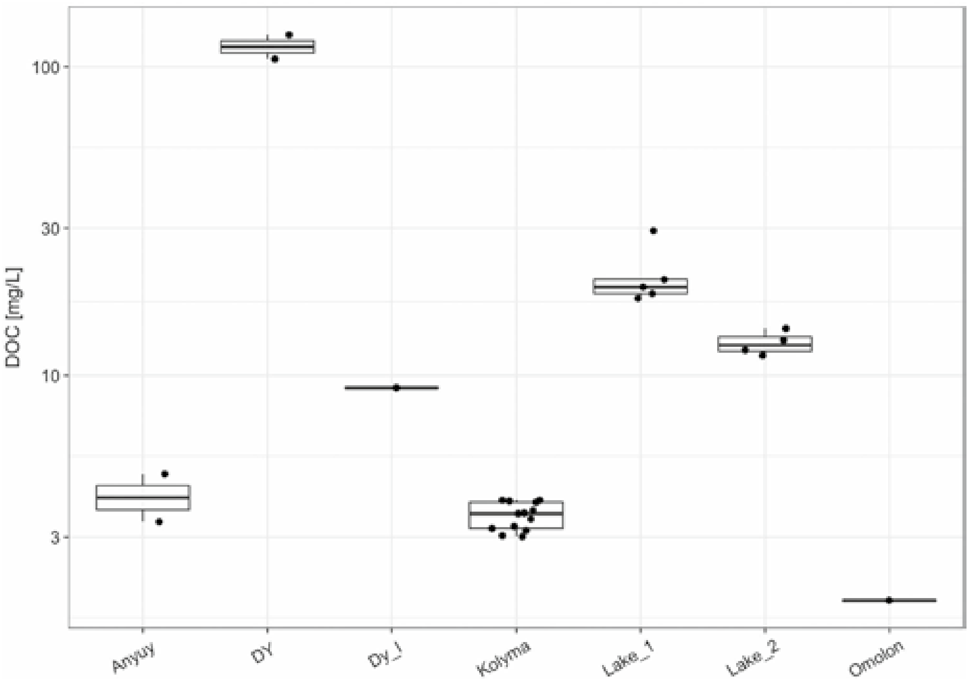

FIGURE 2. A dissolved organic carbon (DOC) concentration box-plot grouped by the water bodies sampled: Anyui, Kolyma and Omolon are river names; DY, permafrost-fed creeks draining a Yedoma cliff at Duvanny Yar; Dy_I, ice collected from Yedoma at the same site; Lake_1, the thermokarst lake close to Cherskii; Lake_2, a thermokarst lake at Duvanny Yar. Please note the logarithmic scale of DOC concentration.

placed by half LOQ (or blank, whichever was higher). All data were standardised (z-transformed) within variables. Clustering was performed using Ward's method and squared Euclidean distance. This analysis may be cross-compared with the principal component analysis presented in Supporting information S1.

Enrichment factors (EFs) relative to average concentration of elements in the suspended sediment of World rivers (after Viers et al., 2009) have also been calculated and are provided in Table S4 (Supporting information S1).

3. RESULTS

3.1. Electric conductivity, pH and DOC

SpC in the collected samples exhibited a wide range of values, from <50 µS cm^{-1} in Lake 2 to 1405 µS cm^{-1} in a sample from permafrostfed creek P2 (Supporting information S2). Conductivities in the Kolyma water ranged 125–165 µS cm^{-1}, and 65–69 µS cm^{-1} in its tributaries Anyui and Omolon. Finally, both Lakes 1 and 2 showed SpCs <100 µS cm-1, except the bottom layers of Lake 1 with a steep incline in SpC values, reaching 318 µS cm^{-1} near the bottom. Both lakes were thermically stratified, with much cooler water near the bottom (especially Lake 1, changing from 15 to 16°C at the surface to rv5°C near the bottom). The pH in studied fresh waters ranged between 6.74 and 7.84. The lowest pH values were found in Lake 2 and in Lake 2 (the waters deeper than 2 m) (Supporting information S2). The bottom layers of Lake 1 were also strongly depleted in oxygen (as documented in the field with a saturation drop from 90% to 7% DO between the depths 2 and 4 m; however, Lake 2 also noted a drop in DO concentrations from 99% at 1.5 m depth to 27.5% at 4 m depth: Supporting information S2). This was confirmed by the precipitation of iron hydroxide in the collected samples.

DOC concentration showed consistent values within each one sample type, while it differed widely between the various water bodies. Particularly high DOC concentrations (max = 127 mg L^{-1}) were found in the permafrost-fed creeks at Duvanny Yar (Figure 2).

3.2. Major ions

Bicarbonate, sulphate and chloride were the predominant anions in sampled waters. Bicarbonate, which is the main ion in the collected samples, reaching 422 mg L^{-1} in P2. Phosphate, nitrate, nitrite and bromide have only been detected in a few samples each, therefore they are not presented in graphs (Figure 3). The highest dissolved solid concentrations have been found in Yedoma-fed creeks (>350 mg L^{-1} of bicarbonate and >90 mg L^{-1} of chloride and sulphate both), and sulphate was relatively high in most Kolyma river samples. Among cations, calcium was predominant, at the average level of 13.4 mg L^{-1} in the Kolyma river, while magnesium was usually second, exceeding Ca^{2+} only in P2 sample at 74.2 mg L^{-1} in the permafrost cliff creeks (DY; Figure 4). Permafrost-fed creeks exhibited relatively high concentrations (approx. 50 mg L^{-1} or more) of all three cations: Ca^{2+}, Mg^{2+} and Na^{+} (Figure 4). If the ionic water type is defined, using the (mval) concentrations of major ions amounting to at least 20% of the anion or cation total, three groups of objects emerge (Supporting information S2): (1) thermokarst lakes and permafrost ice represented the HCO_3–Ca–Mg water type; (2) in the rivers, water types varied between HCO_3–SO_4–Ca–Mg, HCO_3–SO_4–Mg–Ca, SO_4–HCO_3–Ca–Na–Mg, SO_4–HCO_3–Ca–Mg, Ca–Mg–HCO_3–SO_4 and Ca–Mg–Na–HCO_3–SO_4; (3) permafrost creeks were of Mg–Ca–Na–HCO_3–Cl–SO_4 type.

3.3. Metals, metalloids and non-metals

Elemental concentrations exhibited a large variability (Figure 5), with maxima typically found in P1–P2 (DY) samples (Be, Co, Sb, Se, Sr, V), in the lower layers of lake waters (As, Cd, Cu, Fe, Mn, Ni, Si, Zn) or in single samples from Kolyma river (Ba, Li, Mo). Only Al showed the highest concentration in permafrost ice (sample P3). Multiple heavy metals showed much higher concentrations in permafrost creeks and ice (As 1.24–4.23 µg L^{-1}, Cu 1.82–11.4 µg L^{-1}, Co 0.57–3.99 µg L^{-1}, Mn 122–1300 µg L^{-1}, µg L^{-1} Ni 3.36–16.5 µg L^{-1}) than in Kolyma and its tributaries

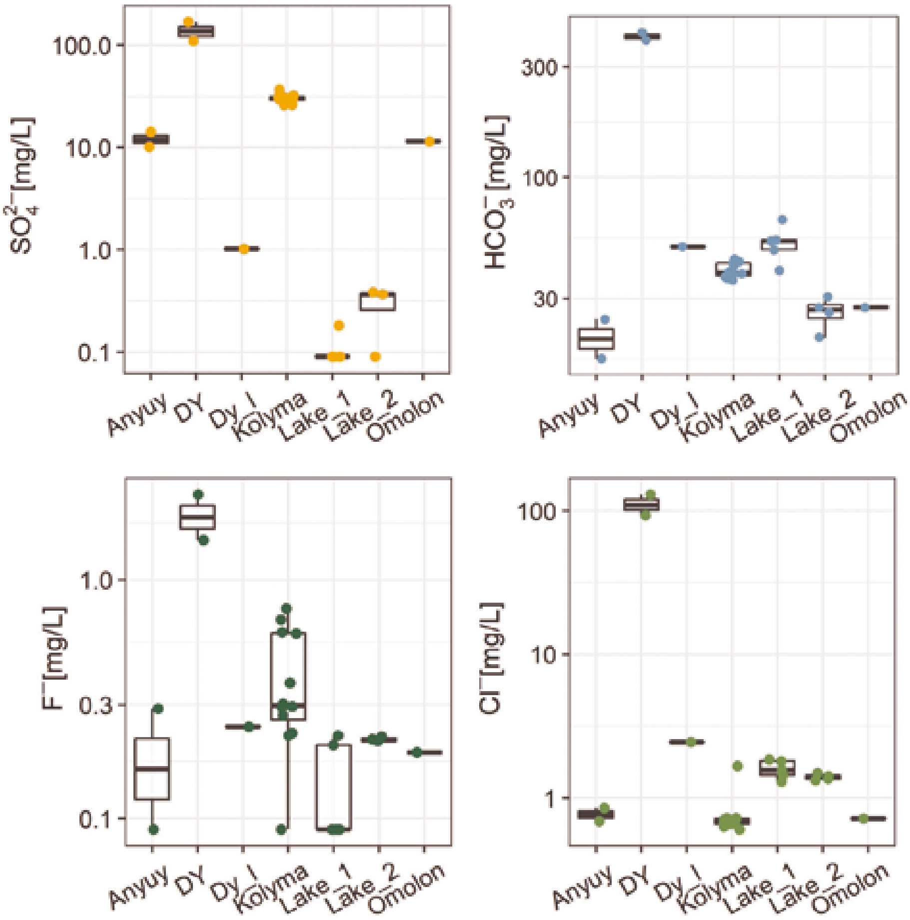

FIGURE 3. Major anions in the Kolyma region freshwaters. Nitrite, nitrate, bromide and phosphate, detected only in a few samples, are not shown. See Supporting information S2 for a full data table and Figure 2 caption for site symbols. [Colour figure can be viewed at wileyonlinelibrary.com]

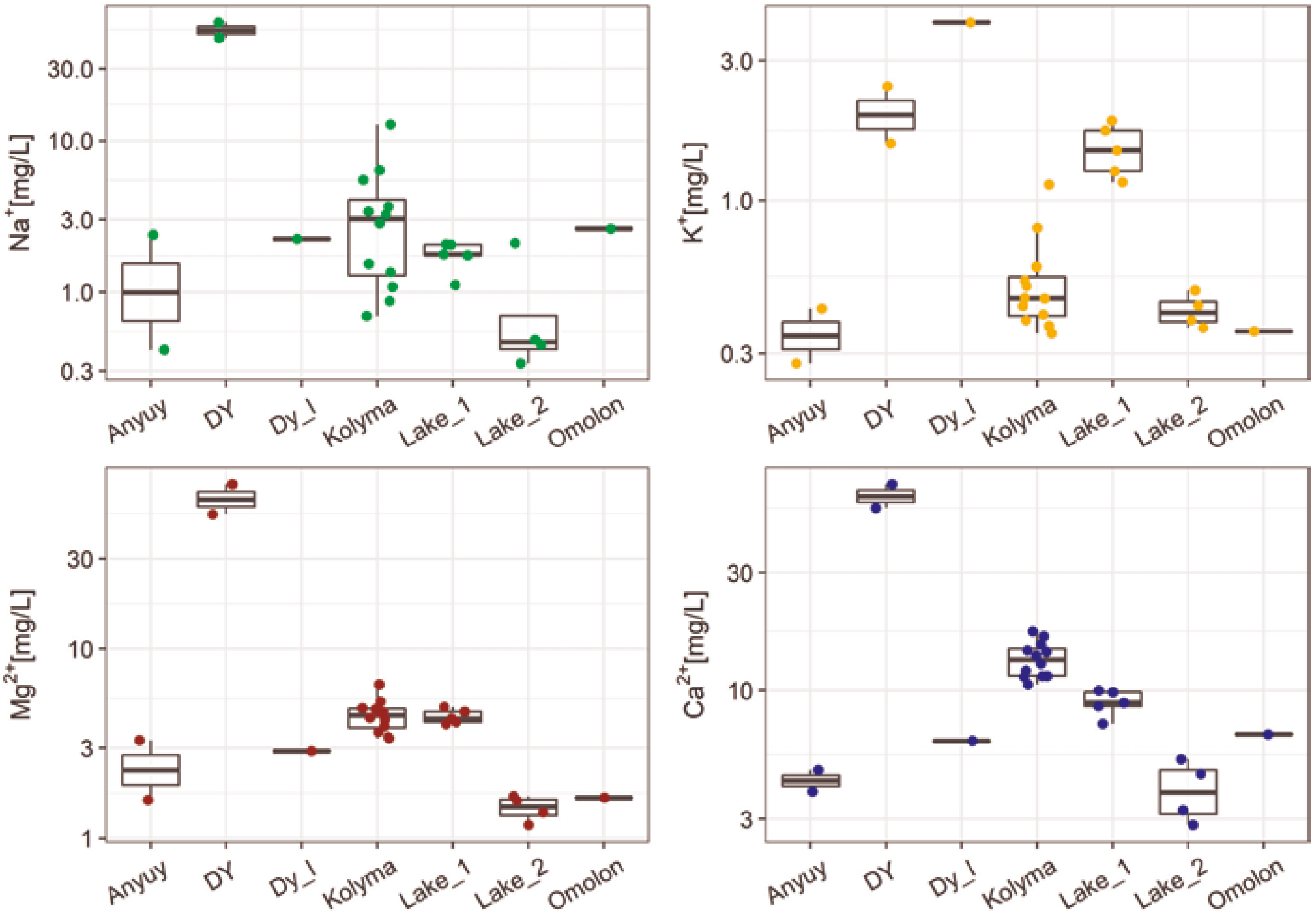

FIGURE 4. Major cations concentrations in freshwater samples from the lower Kolyma basin. Sampling sites named as in Figure 2. [Colour figure can be viewed at wileyonlinelibrary.com]

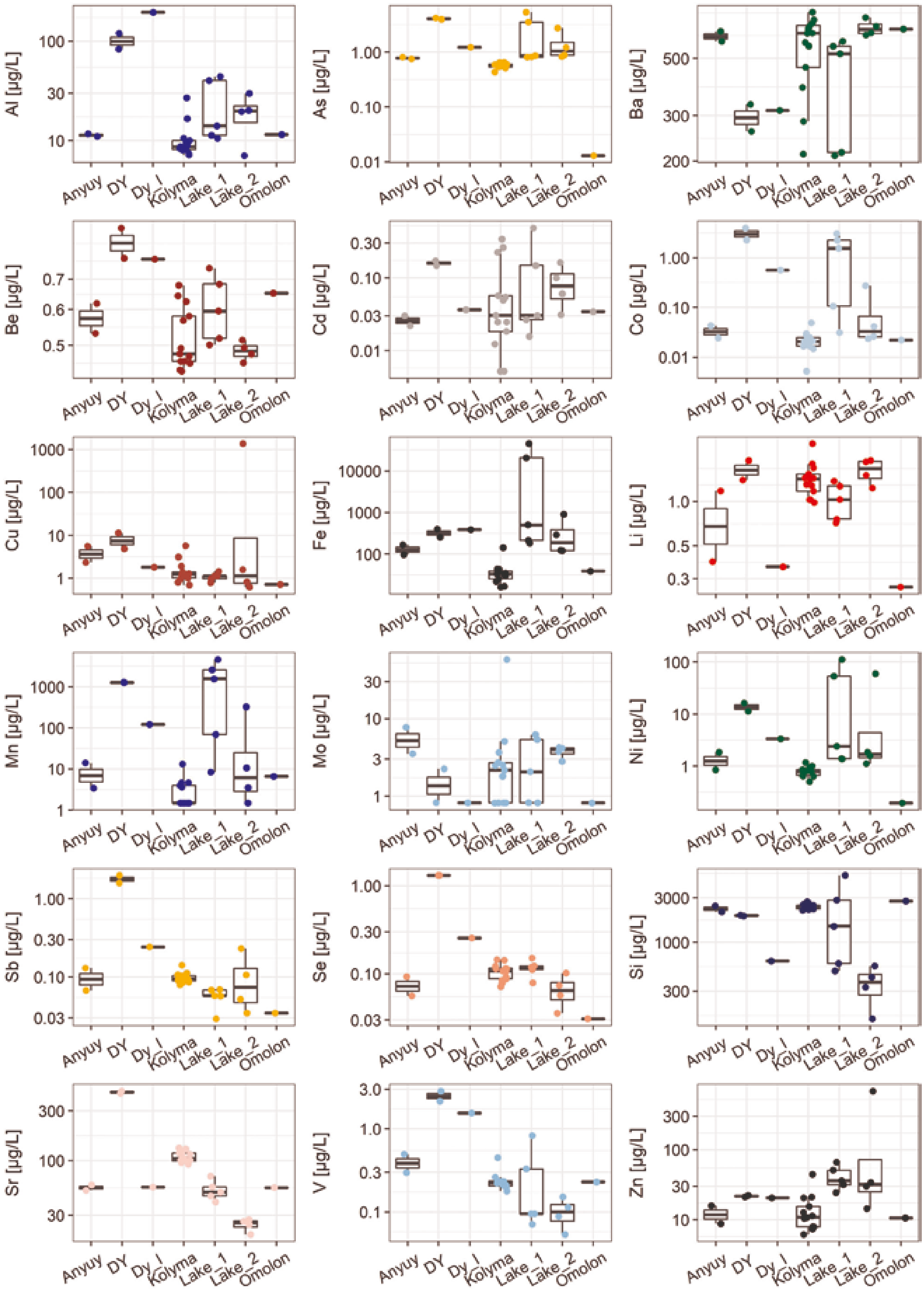

FIGURE 5. Elemental concentrations in the collected samples. Note the logarithmic scale of concentrations. Boxplots show quartiles and full range without outliers, points show all data. Sampling sites marked as in Figure 2. [Colour figure can be viewed at wileyonlinelibrary.com]

(As 0.22–0.81 μg L^{-1}, Cu 0.70–5.72 μg L^{-1}, Co 0.01–0.05 μg L^{-1}, Mn 0.61–14.1 μg L^{-1}, Ni 0.2–1.87 μg L^{-1}; Supporting information S2). Permafrost samples (creeks and ice) also contained metal that was not typically found in other samples: Ti (15.7–30.3 μg L^{-1}). In the lakes, several metals concentrations increased with water depth: Fe, Mn, Ni and Zn concentrations did so in both lakes; Al, K, Sr in Lake 1, and Cu, Pb, Sb in Lake 2. The only instance of an opposite direction of change was Mo, Na and Sb in Lake 1. The highest concentrations of selected elements in this study were observed in lake bottom waters, for example (Cu) = 1370 μg L^{-1}, (Mn) = 4610 μg L^{-1}, and (Zn) = 687 μg L^{-1}. Bottom lake waters, permafrost creeks and ice were also enriched with phosphorus (up to 34.7 μg L^{-1} in Lake 2, up to 512 μg L^{-1} in creeks and 43.3 μg L^{-1} in ice) (Supporting information S2).

Enrichment factors (EF) of all the collected samples indicate moderate or higher enrichment in heavy metals (As, Cd, Co, Cu, Mn, Ni, Pb and Zn). The highest EFs in the dataset were found in lake bottom waters for As, Co (L1), Cu (L2), Mn, Ni, Pb (L2) and Zn (L2) (Supporting information S1, Table S4). Permafrost creeks showed a significant enrichment in Co, Mn, Ni, Cd, and moderate enrichment in Cu and Pb. Permafrost ice presented significant enrichment in Zn (which is generally high in all samples compared with the worldwide mean dissolved concentration of Zn). Furthermore, the concentration level of Cd was higher in lake waters and in a few samples from the Kolyma river in the K3 cross section. In that particular cross section, the enrichment in Cd was higher in the mid-stream (samples K31 and K32) than in the river bottom waters (K31b, K32b), testifying to the limited mixing of dissolved elements in the vertical profile of the river, suggesting their local supply

3.4. Cluster analysis

To explore the patterns in elemental and ionic constituent concentrations, together with DOC, we performed cluster analysis. Grouping variables (Figure 6a), at the

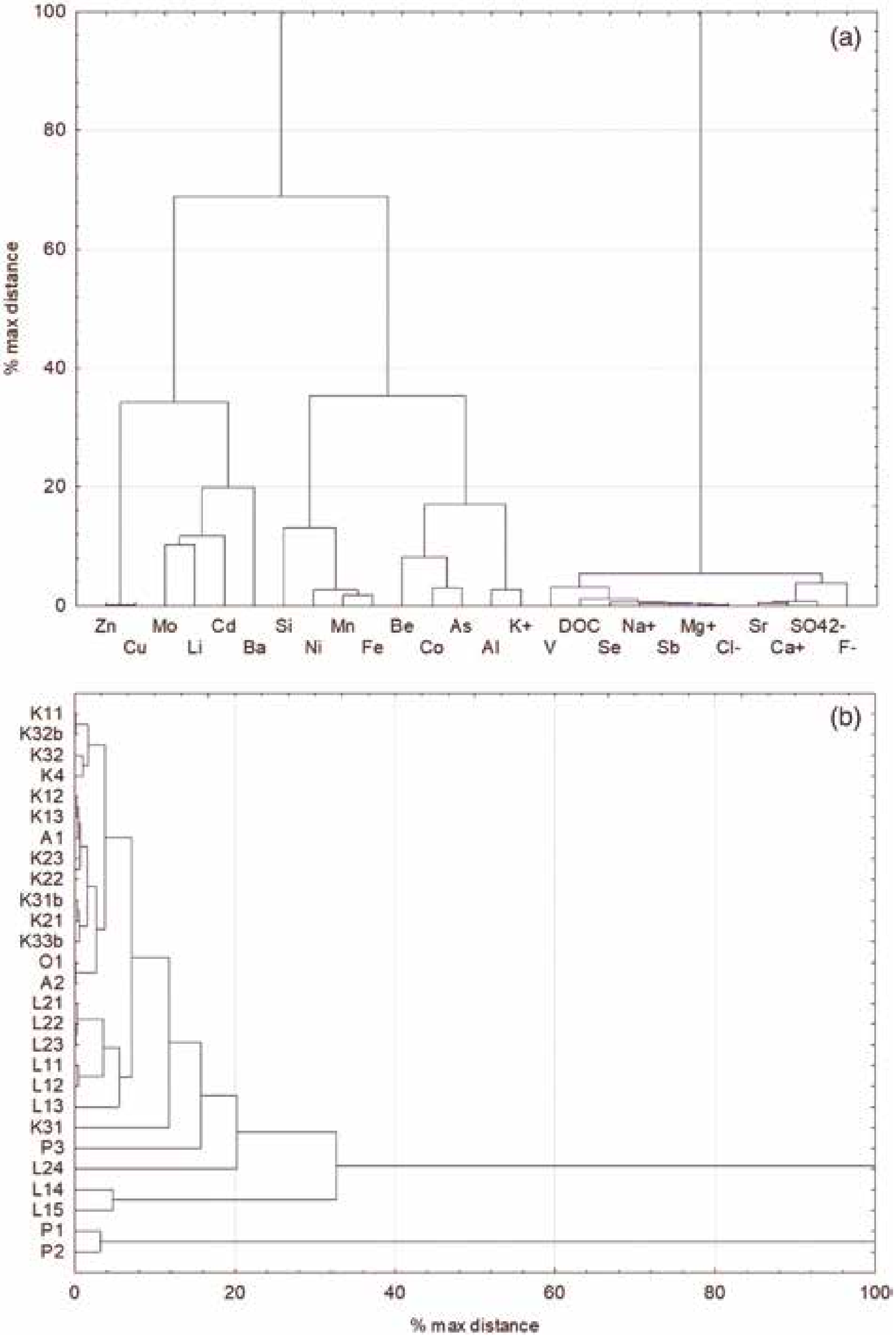

FIGURE 6. Cluster analysis results for all collected samples:
(a) clustering variables;
(b) grouping samples (objects). [Colour figure can be viewed at wileyonlinelibrary.com]

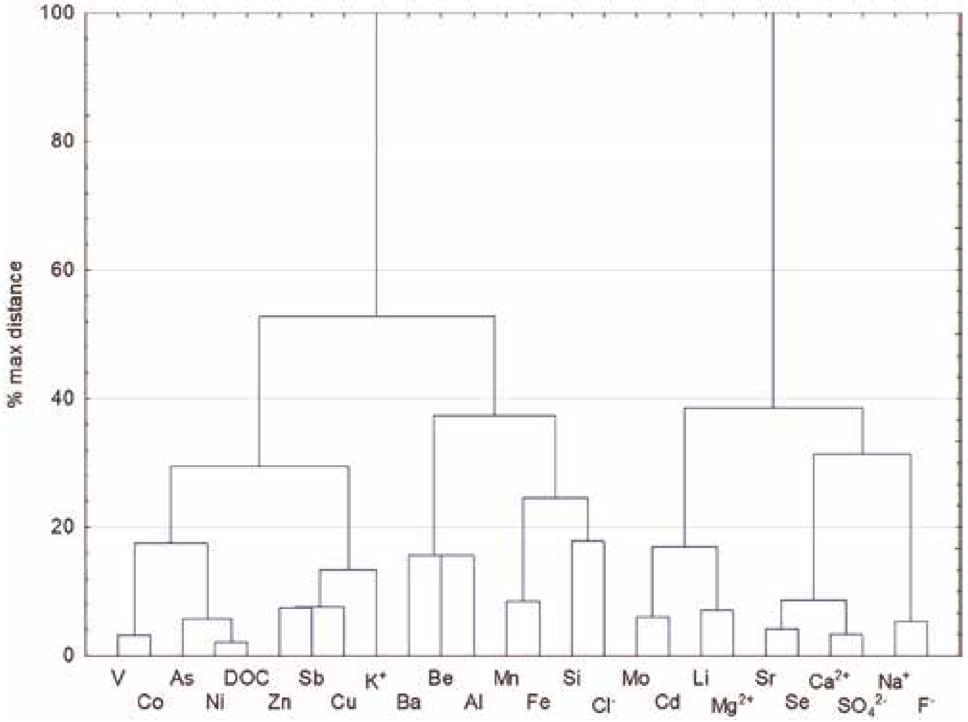

FIGURE 7. Results of the cluster analysis performed on river samples data alone (Kolyma, Anyui and Omolon). [Colour figure can be viewed at wileyonlinelibrary.com]

33% maximum distance level, yielded 5 clusters: C1 (Zn & Cu), C2 (Mo, Li, Cd & Ba), C3 (Si, Ni, Mn & Fe), C4 (Be, Co, As, Al and K+), and C5 (V, DOC, Se, Sb, Sr and all other ions).

At the 67% level, C1 and C2 form one cluster together, and another is formed by C3 and C4, joined. Grouping samples (Figure 6b), on the other hand, resulted in three distinct clusters at the 33% maximum distance level: P1 & P2; L14 & L15; and all other samples. Notably, permafrost ice P3 was classified as relatively similar to the samples from the bottom of Lake 2 and one Kolyma river sample (K31). The variables distinguishing Lake 2 and the P3 ice from other samples were the concentrations of DOC, Al, Co, As, Mn, Ni, Fe, Zn, while the variables setting the permafrost creeks P1 and P2 apart were the concentrations of Si, Sr, Sb, V and the ions Na^+, Mg^{2+}, F^-, and SO_4^{2-} (cf. Figures S5 and S6, Supporting information S1).

An additional cluster analysis (Figure 7), performed for river waters alone (Kolyma, Omolon and Anyui), yielded two clusters at 67% maximum distance level. Cluster c1 contained a wide selection of elements, two ionic constituents and DOC (V, Co, As, Ni, Zn, Sb, Cu, DOC and K^+, Ba, Be, Al, Fe, Si, Mn, Cl^-); and c2 joined Mo, Cd, Li, Sr, Se and almost all inorganic ions. Around 33% maximum distance, the c1 cluster divided into c1a (V, Co, As, Ni and DOC), c1b (Zn, Sb, Cu, and K^+), c1c (Ba, Be and Al) and c1d (Mn, Fe, Si and Cl^-), and cluster c2 was composed also of two sub-clusters: c2a (Mo, Cd, Li & Mg^{2+}) and c2b (Sr, Se, Ca^{2+}, SO_4^{2-}, Na^+ and F^-)

4. DISCUSSION

In this work, we have determined DOC and metals, metalloids an inorganic ions, in dissolved fraction (including smaller colloidal dispersal), thus gaining insight into the mobile phases of those constituents in the hydrochemical landscape of Kolyma river catchment and two isolated thermokarst lakes. As DOC may form complexes with metals and metalloids, and it has been previously described in the literature on Kolyma, we compare it first to those studies.

4.1. DOC in permafrost-affected aquatic environment

Among the studied samples, the permafrost creeks differ from river waters by the high content of DOC, major cations and anions, and selected metals and metalloids, including heavy metals. In this work, we found DOC concentrations of 106–127 mg L^{-1} in permafrostrelated streams and 3.0–3.9 mg L^{-1} in the Kolyma, leading to the questions about the DOC (and TOC) fate in the future Kolyma catchment. Similar DOC values of 154–336 mg L^{-1} and 103.4 mg L^{-1}, for creeks draining the permafrost cliff at Duvanny Yar, were obtained by Vonk et al. (2013) and Jong et al. (2023), respectively, and the concentrations of POC in the same samples amounted to 6700–9240 mg L^{-1}, eclipsing the DOC contribution. This is also consistent with the additionally sampled POC in P1 and P2 samples of ours, amounting to 8500 and 12,000 mg L^{-1}, respectively – (methods are reported in the Supporting information S1). The total discharge of the permafrost-fed creeks draining the cliff during the sampling period was estimated at 0.01 m3 s^{-1} with total sediment inflow exceeding 5 kg s^{-1} due to high sediment concentrations, emphasising high possible impacts on river hydrochemistry.

On the other hand, Jong et al. (2023) obtained DOC concentrations (2.76–4.97 mg L^{-1}) at approximately double the POC concentrations (1.49–2.73 mg L^{-1}) for Kolyma below Duvanny Yar, and similar results for Maly and Bolshoy Anyui (3.16–4.43 mg L^{-1} and 1.29–1.7 mg L^{-1}, respectively). In our research, thermokarst lakes were studied also, with DOC concentrations similar to a small stream studied by Jong et al. (2023), representing soil leaching and active layer drainage ([DOC] = 21.5 mg L^{-1}). Furthermore, the DOC concentration in a permafrost ice sample collected by us amounted to 9.13 mg L^{-1} which was approximately 11 times less than the concentrations in the creeks draining the permafrost cliff. Such contrasts lead to the question whether thawing permafrost will contribute to higher DOC and POC loads in the Kolyma river, and by how much. Despite the stark difference in the DOC concentrations in the source and recipient, as studied by us, it is not straightforward to interpret that all permafrost thaw water will be directly discharged into the large river, since hydrological studies indicate that permafrost thaw will also increase the water storage capacity in soils in the region (Suzuki et al., 2021). Furthermore, various layers of permafrost ice may have different OC concentrations, or else there is an enrichment processes between the ice source and the permafrost creek as a throughput. The extra rv90% of DOC in permafrost creeks (beyond the concentration in ice) may originate both from permafrost active layer (i.e., relatively recent atmospheric deposition and microbial processes) and the exclusion of various organic compounds during groundwater freeze. POC from the ice may also be a source of DOC in thaw waters; this is consistent with incubation experiments by Keskitalo et al. (2022) who claim that in the summer, POC in the Kolyma degraded rapidly (as did DOC). By following the conclusions of Keskitalo et al. (2022), we can interpret that the permafrost-released DOC was likely metabolised rather quickly and thus contributed to additional greenhouse gas fluxes (which is also consistent with the more general assessment of McFarlane et al., 2022), while the POC, following Jong et al.'s (2023) conclusions from the same area, was transferred in majority into a sink in riverbed sediments. In this study, we consider whether this OC promotes or hinders metal and metalloid export from permafrost into the Kolyma river. Indeed from the cluster analysis results it appears that DOC is co-transported out of permafrost with V, Sb and Se, besides the mobile ionic forms of Na, Mg and Cl (Figure 6a), while in the rivers it is rather co-transported with V, As, Co and Ni (Figure 7), indicating its potential role in supporting heavymetal transfer in the river, potentially transferring them into the aquatic ecosystem.

4.2. Inorganic elements in the changing permafrost environment

Our results indicate a wide variability in predominant inorganic components and their quantitites in the water bodies of the Kolyma river and its surroundings. While Kolyma has not been subject to inorganic geochemical studies before, the other large Siberian rivers have been shown to be influenced by catchment factors (land use, mining, large river dams >15 m) and climate change with respect to suspended transport of elements (Chalov et al., 2018). An anthropogenic enrichment in Pb, Zn, Cd and Cu has been suggested there. In further studies, a climate-induced enhanced mobilisation of selected elements was highlighted (Frey & Mcclelland, 2009; Gabysheva et al., 2022; Holmes et al., 2012; Soromotin et al., 2022). In the case of Kolyma, a potential impact of climate change was signalled for the suspended sediment load in the recent decades, and mining impact was also observed (Chalov et al., 2018, 2021).

The data presented here show the hydrochemical patterns of different waters in an environment shaped by permafrost seasonal and long-term changes. The ionic composition of all sampled waters is likely impacted by both suprapermafrost waters and an inflow of deeper, intra- and subpermafrost waters; especially the permafrost creeks P1 and P2 are likely connected to unfrozen groundwater (Cochand et al., 2019).

In the collected permafrost ice, a contrastingly high level of aluminium concentration has been noted as compared to the other samples; a relatively high concentration of Al was also found in the permafrost creeks and the sampled lakes. Aluminium co-occurs with K+, Be, but also with Co and As, frequently classified as heavy metals. Arsenic occurred at elevated (against other samples) concentrations in the lake bottom waters of this study. In the lake waters, permafrost creeks and permafrost ice, we found also elevated concentrations of other heavy metals (Co, Mn, Ni, Zn, Cu and Sb). Zinc, copper and cadmium showed elevated values also in the Kolyma, while the bottom layer waters of the thermokarst Lake 2 exhibited also a very high concentration of Pb. The cluster analysis of our data has shown similarities in the water chemistry between the permafrost ice sample (P3), the bottom layer of water in Lake 2 and a sample from Kolyma below Duvanny Yar (K31, sampled mid-depth away from the cliff side, where the main river current flows), which suggests the influence of legacy permafrost thaw upon the Kolyma river in this cross section. At the same time, the connection between the other lake samples and the samples from the permafrost creeks suggests a general permafrost water influence over the lakes, although it is probably a combined influence of the active layer drainage and deeper talik-type waters.

Such combined evidence leads to a tentative conclusion from our research that permafrost thaw may be a source of heavy metals remobilisation, yet the potential scale of such a phenomenon may only be assessed at this point from the limited published data. For example, Monhonval et al. (2021) characterised the chemical composition of Yedoma waters, by exploring the mineral element stock in sediments of the Yedoma. They found a relatively high concentration for Si, followed by Al, Fe, K, Ca, Ti, Mn, Zr, Sr and Zn. Moreover, the stock of Al and Fe (598 ± 213 and 288 ± 104 Gt) was at the same order of magnitude as the OC stock (327–466 Gt). Our surface water and ice samples from the Kolyma watershed exhibited similarly high concentrations of Si and Fe, as well as Al, K, Sr, Zn and additionally Ba. The cluster analysis of all the collected samples shows that in cluster C2, the elements Si and Fe were grouped together with Ni and Mn (Figure 6a). However, in river waters they correlated with Ba, Be, Al, Be, Mn and chlorides (cluster c1c and c1d, Figure 7). All these clusters may be connected to the Yedoma source, including suprapermafrost waters of the active layer, which are flowing intensely into the thermokarst lakes and rivers. Ji et al. (2021) studied elements in permafrost soils and concluded that Mn, Ca, Mg, Al and Ti showed the highest mobility from soil to suprapermafrost water and further into the ponds and flowing waters. Furthermore, they considered Mn a proxy for predicting the processes occurring in the active layer during summer–autumn thaw. We found an extremely high enrichment of Mn in permafrost creeks and lake waters; however, we also found in the same water bodies a higher concentration of the other heavy metals. Such enrichment in heavy metals, together with Fe in that shallow waters, may confirm their connection with the processes of chemical denudation of the active layer during seasonal thaw, leaching weathering products from there. Alekseev et al. (2003) found downward migration of Fe in the active layer in Kolyma Lowland due to weathering of chlorite. Conversely, the long-term research in the Yukon River basin (1982–2014) underlain by discontinuous permafrost shows a relationship between the deepening of permafrost active layer and significant increases in the Ca, Mg and Na annual flux in the Yukon River and its tributary Tanana, and in the SO_4 and P annual flux in the Yukon (Toohey et al., 2016). The authors described increased active layer expansion, weathering and sulphide oxidation due to permafrost degradation throughout the studied basin, all likely to occur in the Kolyma catchment also. Frey and Mcclelland (2009) forecast also a significant increase in the concentrations of major ions due to permafrost degradation and lowering water tables (except for nitrate in Siberia). In the studied samples from the Kolyma watershed, clusters C5 and c1c-d, c2 (in the all sample and river sample analysis, respectively; Figures 6a and 7) indicate the likely influence of rock weathering on water composition. The visible division within the c2 cluster into c2a (Mo, Cd, Li and Mg^{2+}) and c2b (Sr, Se, Ca^{2+}, SO_4^2, Na^+ and F^-) may represent two separate water supply factors, namely the shallow and deep groundwater flow, respectively (cf. Douglas et al., 2013 on the deep unfrozen water composition and Kabata-Pendias & Pendias, 2001, on the high mobility of Mo, Cd and Mg in oxidising conditions). An extra contribution to the total sulphate load in the rivers may also result from the wet deposition connected to wildfires, which have influenced considerably the deposition of sulphur (and nitrogen) compounds in the regions of Siberia and the Russian Far East (Berezin et al., 2013). On the other hand, the lower contribution of Ca^{2+} in thermokarst lake waters may result, according to Monhonval et al. (2021), from the leaching of soluble elements such as Ca during former thaw periods.

Among heavy metals (besides mercury, which was not subject of this study), As and Cd are sometimes mentioned as posing a new hazard due to permafrost thaw (Zhang et al., 2021). In this study, a potential source of those is the erosion of a permafrost cliff, given the significant enrichment of Cd in both lakes and the crossection of Kolyma near Duvanny Yar, and of As in lake 2 (located in a Yedoma plain above the cliff). The supply of Cd may be connected to the drainage of mixed suprapermafrost water, which may include atmospheric deposition and deeper water bringing weathering products. With the active layer deepening, atmospheric pollutants deposited in the past, which have been excluded from the freeze–thaw cycle for a time (Ji et al., 2021), may be remobilised (Edwards et al., 2021; Li et al., 2020; Lim et al., 2019; Rubino et al., 2016). The notable increase in heavy metals concentrations in deep lake waters indicate the likely source of these elements in permafrost thaw, talik water or enhanced mobility of suprapermafrost water eluting them from soil. Importantly, it is not only in the Lake 1 near the Cherskii research station and the settlement which experienced the elevated concentrations of these metals in the bottom waters, but also further from any human activity in the Lake 2, showing that such contamination is probably irrelevant of local infrastructure. The high concentration of As and Cd may also be connected to the redox conditions in either lake, since Lake 1 bottom waters were almost entirely deprived of DO (the lake was also described to contain high methane concentrations by Stepanenko et al., 2011; Walter et al., 2006) and Lake 2 bottom waters were also significantly depleted in DO (cf. Supporting information S2). In nearneutral pH, such as in our study, the oxidated phases of Fe, Al and Mn are typically hydrated oxides and hydroxides, forming colloidal dispersion and capable of adsorbing significant loads of heavy metals, thus only in the deeper waters of lakes with reducing conditions would these metals be abundant in the dissolved phase. In the studied freshwaters, it was evident that thermokarst lakes form at least temporary traps for heavy metals connected to one or several types of permafrost influence. Thermokarst lakes form one of the more dynamic elements of the continental permafrost landscape, and their mass emergence is among the more frequently observed impacts of climate change in the Northern Hemisphere (in't Zandt et al., 2020; Karlsson et al., 2012; Plug et al., 2008), including the Kolyma region (Veremeeva et al., 2021). Due to the dynamically increasing number of thermokarst lakes, and their predicted drainage with the advancing climate change and deepening active layer, the sedimentation in these lakes and the biogeochemical processes happening in them (in't Zandt et al., 2020) will likely be of high importance in studies of continental permafrost areas.

The described hydrochemical patterns including the water bodies of different status in hydrological system may be discussed also in terms of geochemical barriers related to permafrost environment. According to Perel'man (1986), geochemical barriers are connected with the sharp changes in physical or/and chemical conditions, which cause changes in transport conditions and result in a substantial accumulation of elements. In permafrost affected regions (rv25% land areas of the World), these sharp changes are connected with the border between seasonally unfrozen active layer and perennially frozen ground. Both the permanent changes (e.g., the development of new taliks, changes from continuous permafrost to discontinuous), as well seasonal freeze–thaw of active layer, may lead to changes in oxidation/reduction conditions, which may change quality and quantity of soluble elements in water. Therefore, despite the basic geochemical barrier connected with the border of the active layer, or more precisely with the transitional zone resulting from the Holocene climate fluctuations (Shur et al., 2005), the second-order geochemical barriers are determined by changes in hydration conditions and temperature of the active layer. Frequent changes in these conditions, common in the active layer, favour the concentration of Fe, Mn Co by the oxidising barrier and additionally Cu, Zn, Cd, Ni, Tl, Pb by the reducing hydrogen sulphide barrier (e.g., in the bottom layers of lakes in this study) (Perel'man, 1986). The observed differences in inorganic chemistry between the river waters, the lakes and all permafrost waters show a possible influence of oxidation condition in river waters, resulting in decreasing Al concentration, and increasing Si, Ba and Li content, due to Al oxidation and desorption of other elements from complexes in the clay minerals. Simultaneously with the enhanced migration of chemicals due to permafrost thaw, and active layer deepening (Gabysheva et al., 2022; Soromotin et al., 2022), element sinks may occur in lakes or low-energy flow paths in permafrost basins. Furthermore, Chalov et al. (2017) found that wetland-dominated conditions decreased considerably (by 42%–68%) the suspended and bed-load transport of elements in the Selenga delta waters. Therefore, in the studied permafrost aquatic geochemical system we can expect a temporal sedimentation and precipitation of elements in the lakes, and also a remobilisation of elements into flowing waters due to progressive increasing of flow network density, and co-occurrence of deepening supra-permafrost water pathways.

Finally, it should be noted that dissolved elements are the most mobile in flowing waters. Therefore, their share in the transport of elements may be increasing in the total load along the river/oceanic transitional zone due to the higher losses of suspended load and bed load into the delta environments (Chalov et al., 2017, 2021; Lisitsyn, 1995). Therefore, the dissolved elements calculation is important to further the comprehensive understanding of the changing Arctic rivers impact on marine environment.

5. CONCLUSIONS

In our study of the dissolved inorganic chemistry in the lower Kolyma basin, we found that the ionic HCO_3–Ca–Mg water type was prevalent (representing both lakes and permafrost ice), and the river and permafrost creek waters had also a significant admixture of sulphate. The highest concentrations of DOC (9.13–127 mg L^{-1}) were found in permafrost ice, permafrost creeks and thermokarst lakes, that is, the water bodies connected to permafrost thaw. Among the collected water samples, a few heavy metals were detected at higher concentrations in permafrost-related samples than elsewhere, that is, As, Cd, Co, Fe, Mn, Ni and V. The correlation between DOC and As, V, Co and Ni concentrations in the river waters may indicate the DOC promoting their transport there. The occasionally detected Cr, Pb and Ti were also typically associated with the permafrost-related origin of a sample. The highest concentrations of most of the studied elements were found in the lake bottom waters, suggesting that thermokarst lakes act as local traps for elements, including heavy metals, especially due to the reducing conditions allowing them to remain in the mobile phase there. Therefore, we conclude that important insights may be gained through further studies of the dissolved elements in permafrost catchments, especially on the weathering processes contributing to water chemistry. In thermokarst lakes, further knowledge may be gained through studies on the processes trapping heavy metals into sediments and remobilising them into water.

The impact of changes in permafrost regions, occurring due to climate change, needs to be considered with respect to both the remobilisation from older permafrost (of OC and other chemical components) and the interference with newly deposited anthropogenic contaminants. Such impacts are likely to be complex and modified by the local sedimentation processes in the local watercourses and lakes. The further forecasted climate change may result in the formation of new flow pathways for dissolved chemicals migrating between supra-, intra- and subpermafrost waters. Further research into the concentration of dissolved and particulate phases in permafrost thaw and active layer waters is warranted to diminish the uncertainties related to this field of knowledge or to estimate the total load of for example, heavy metals in the permafrost regions, available for remobilisation.

Microbial sulfate reduction (MSR) as nature-based solution (NBS) to mine drainage: Contrasting North European seasonal and catchment conditions*

1. INTRODUCTION

Microbial sulfate reduction (MSR) has increasingly been investigated for its potential to immobilize metals and reduce their bioavailability while also increasing the pH of acid mine drainage (AMD; e.g., Nielsen et al., 2018). The process involves microbes (bacteria and archaea) converting sulfate into sulfide that together with toxic dissolved metals precipitate into less mobile forms. Laboratory bioreactor experiments on MSR show a metal retention of 70% or more under favorable conditions (e.g., Sinharoy et al., 2020; Zhang & Wang, 2016). The activity depends on several factors, such as (bioavailable) carbon and sulfate supply, oxygen level, pH, and temperature (Xu & Chen, 2020). MSR has also been observed in the field at certain locations and time periods, for example, in individual wetlands or near tailing deposits at particular points of time (Mandernack et al., 2000; Praharaj & Fortin, 2004). Recently, Fischer, Jarsjö, et al. (2022) additionally showed evidence of ongoing and considerable MSR in multiple locations (so-called “hot spots”) within an AMD-impacted catchment (Imetjoki, Northern Sweden), which is essential if MSR is to be used as an effective mitigation solution for spatially extensive mining sites and their downstream regions. However, large knowledge gaps remain regarding catchment-scale MSR in freshwater systems, where specific catchment and seasonal conditions could differ substantially from site to site. It is therefore not known to what extent MSR more generally could provide a basis for viable bioremediation, for instance, as part of nature-based solutions for sites impacted by (acid) mine drainage across the world. This includes the Arctic, which counts as one of the world’s larger mining regions with numerous examples of largescale mine drainage development, and where cold conditions and pronounced seasonality may hamper the activity of freshwater sulfur-reducing microbes (SRM).

Current evidence shows that point locations which are relatively favorable for MSR contain soil and sediments with sufficiently high organic matter content to support the metabolism of SRM, and that they are associated with wetlands, lakes, or groundwater systems that prolong hydrological residence times and the general contact time for SRM (Hampton et al., 2019; Lindström et al., 2005). Such characteristics are found in the Imetjoki catchment where relatively high catchment-scale MSR was detected through a summer (August) field campaign (Fischer, Jarsjö, et al., 2022). Here, we hypothesize that in contrast, low-MSR catchments should have relatively limited vegetation/forest cover and steep topography that limits the number of lakes and wetlands as well as reduces residence times and therefore also SRM contact times. A northern European example of this is the Khibiny region in northwestern Russia where an active apatite mining complex is located (Efimov et al., 2019). The Khibiny catchments have been increasingly industrialized and polluted as a result of more than 90 years of ore extraction (Malinovsky et al., 2002).

Apart from impacts on MSR by regional topography and land cover conditions, it is reasonable to assume that MSR is impacted by the seasonality of hydroclimatic conditions. For instance, laboratory experiments generally show increased microbial activity with higher temperatures (e.g., Pellerin et al., 2020) although steady-state batch tests have shown that cold-tolerant bacteria may successfully reduce metal concentrations (Nielsen et al., 2018; Virpiranta et al., 2019). Field studies in temperate climates show indications of locally increased MSR during warmer summer periods (e.g., Praharaj & Fortin, 2004) although there are also reports on potentially high MSR levels during the winter (e.g., Björkvald et al., 2009; Fortin et al., 2000). Colder regions furthermore have a strong seasonal effect in runoff generation (e.g., frozen conditions vs. spring flood), implying that the mixing of water from different landscape compartments differs greatly over the year. This, together with annual fluctuations of water temperature, fundamentally changes the ambient conditions for SRM, supporting our working hypothesis that large-scale MSR values should vary over a hydrological year. A better understanding of the magnitude of such potential large-scale seasonal variations would be desirable in assessments of the overall effectiveness of MSR as a suitable mitigation solution. For the Arctic, for example, the suitability would most likely be related to whether or not the measures would be efficient for only a few favorable months per year.

The degree of MSR detected in water samples from catchments can be calculated using the isotopic fractionation model developed by Fischer, Jarsjö, et al. (2022). The method is based on the fact that sulfur isotope composition (of δ34S in SO42−) in surface water shows a distinct signal from SRM preferentially taking up 32S during sulfur reduction while leaving 34S in the remaining sulfate. To quantify for the first time the large-scale MSR sensitivity to contrasting catchment and seasonal conditions, we apply the isotopic fractionation model by Fischer, Jarsjö, et al. (2022) onto two major cold-climate mining-impacted regions: the Imetjoki catchment in northern Sweden containing the abandoned Nautanen copper mines (where ambient conditions were shown to be favorable for MSR during summer) and the actively mined Khibiny catchments on the Kola Peninsula, Russia. Specifically, we aim to quantify the large-scale MSR under (a) contrasting catchment conditions (i.e., spatial characteristics) of Imetjoki and Khibiny, and (b) contrasting seasonal conditions (i.e., temporal character-

---

* Sandra Fischer, Carl-Magnus Mörth, Gunhild Rosqvist, Sergey R. Chalov, Vasiliy Efimov, and Jerker Jarsjö // Water Resources Research
https://agupubs.onlinelibrary.wiley.com/doi/full/10.1029/2021WR031777

istics) in Imetjoki, extending snapshot observations of high MSR in late summer (Fischer, Jarsjö, et al., 2022) with observations during less-favorable snowmelt conditions in spring. & Kashulin, 2010; Dinu et al., 2020). The Khibiny mountain valleys (Figure 1e) are characterized by sandy till deposits and a forest-tundra ecosystem, while the higher plateaus (with mountain peaks up to 1000 m above the Umbozero and Imandra Lakes) hold mostly weathered rocks and Arctic tundra (Pereverzev, 2010). The average annual temperature for the Khibiny massif was −0.59°C between 1993 and 2017 according to the data from the Climatic Research Unit (CRU) at the University of East Anglia described by Harris et al. (2014; see Supporting Information S1 on details). For the same time period, the annual average precipitation was 715 mm/yr and annual average actual evapotranspiration was 290 mm/yr (based on CRU data and same calculation procedure as for the Imetjoki catchment). About 210 days per year were snow covered between 1998 and 2007 (Callaghan et al., 2011). The southwestern part of the Khibiny massif is drained by the Belaya River that has a catchment area of 142 km^2 and an average annual discharge of 1900 l/s (ID 22 in Figure 1; derived from CRU data following the water balance calculation steps of Fischer et al., 2020) before reaching the Imandra Lake. Furthermore, the Belaya River (main branch) starts at the outlet of the Bolshoy Vudyavr Lake gathering tributary inflows from the Yuksporiok, Saamsky, and Vudyavriok sub-catchments (Figure 1e). The southeastern part of the massif is drained by the Vuonnemiok Stream with an annual average discharge of 1300 l/s (ID 25 in Figure 1; based on water balance calculations) that empties in the Umbozero Lake. Kirovsk City is the main settlement in the Khibiny massif where there are five apatite-nepheline ore deposits (Figure 1e) that have been actively mined since the 1930s. They are now owned by the company PhosAgro. The mining activity has led to elevated surface water concentrations of strontium (Sr) and aluminum (Al), as well as copper (Cu), zink (Zn), nickel (Ni), and chromium (Cr) in the Yuksporiok and Vuonnemiok basins (Efimov et al., 2019; Malinovsky et al., 2002). The Kola Peninsula also hosts several Cu-Ni ore smelters that have for decades emitted large volumes of sulfur dioxide into the air resulting in acid rain and high sulfur and metal atmospheric deposition (Moiseenko & Bazova, 2016).

2.2. Field Campaigns and Analyses

Surface water sampling and measurement campaigns were conducted in the Imetjoki catchment in the spring (end of May during snowmelt) and in the late summer (end of August) of 2017. Apart from element concentrations and general water quality parameters (e.g., pH, dissolved organic carbon, etc.; presented in Fischer et al., 2020), sulfur isotopes ($\delta^{34}S_{SO4}$ values in SO_4^{2-}) were measured. In total, 11 locations were sampled for sulfur isotopes and sulfur concentrations in the spring and 13 locations were sampled in the summer (the latter used here for comparison, being presented in Fischer, Jarsjö, et al., 2022). Nine sampling locations were common for both campaigns. The sampling locations were distributed over the upstream areas (undisturbed by mining; IDs 1–2 in Figure 1), the mining site itself (directly affected by AMD; IDs 3–9), and downstream of the mining site (IDs 10–12, 14). Two adjacent rivers were also sampled for reference (IDs 13, 15). The same sampling and analysis procedures were followed in both the spring and summer campaigns as described in Fischer, Jarsjö, et al. (2022), making the results directly comparable. The sulfur isotopic composition was determined from collecting 2L water samples that were dripped through ion exchange resin columns to collect the sulfate in water and for easier transportation to the laboratory. Instrumental analyses were carried out with an elemental analyzer (CarloErba NC2500) coupled to a stable isotope ratio mass spectrometer (Finnigan Thermo Delta plus; analytical accuracy was ±0.2‰) at the laboratories of the Department of Geological Sciences at Stockholm University. Sulfur isotopes are reported in parts per million (‰) through the δ-notation relative to the Vienna-Canyon Diablo Troilite (V-CDT) standard:

$$\delta_{sample}\,(‰) = \left(\frac{R_{sample}}{R_{standard}} - 1\right) 1000 \qquad (1)$$

where R represents the $^{34}S/^{32}S$ retio

Surface water was sampled from rivers draining the Khibiny massif in late August in 2017 using an equivalent sampling strategy as the one performed in the Imetjoki catchment (following Fischer et al., 2020; Fischer et al., 2022). More specifically, the Belaya catchment and Vuonnemiok catchments were sampled within three zones: the upstream areas unaffected by the mining sites (IDs 16–19, 23 in Figure 1), the mining areas comprising the mine effluents (IDs 20–21, 24), and the downstream areas (IDs 22 and 25). An additional sample was collected from the Umba River (ID 26; draining the Umbozero Lake catchment), which corresponds to about 30 km downstream of the Vuonnemiok catchment.

2.3. Isotopic Fractionation and Mixing Scheme

Both the Imetjoki and Khibiny catchments were assumed to have two major sulfur isotopic end-members: sulfur from atmospheric deposition (δ_{dep}; composed of sulfur from both sea spray and fossil fuel emissions) and geogenic sulfur from weathered bedrock (δ_{rock}). This allowed us to apply the sulfur isotopic fractionation and mixing scheme developed by Fischer, Jarsjö, et al. (2022) to quantify MSR and its variation within each site. The quantifications are made based on stream water samples from which net MSR values are estimated. These MSR values reflect net (downstream) impacts of local MSR along the sub-catchment's flow paths, some of which may support considerable MSR (e.g., flow paths through wetlands or deep groundwater), whereas other may not support MSR or have negligible MSR only (e.g., fast macropore flow through upper soil layers or water from melting snow). In summary, the method compares stream water field measurements (representing potential post-MSR conditions) with theoretical predictions derived from sulfur end-member mixing (representing initial or pre-MSR conditions). Deviations between these two are assumed to be due to MSR. Although other microbial processes apart from MSR could contribute to isotopic deviations, they either represent only smaller/negligible fractionation (e.g., assimilatory sulfate reduction; Sharp, 2017) or they can be registered only when sulfur concentrations are much higher (e.g., sulfur disproportionation in marine/laboratory environments; Böttcher et al., 2005) than in our study environments. A theoretical stream water sample (δ_{sample}) is then in the considered conservative case composed of proportional fractions of each

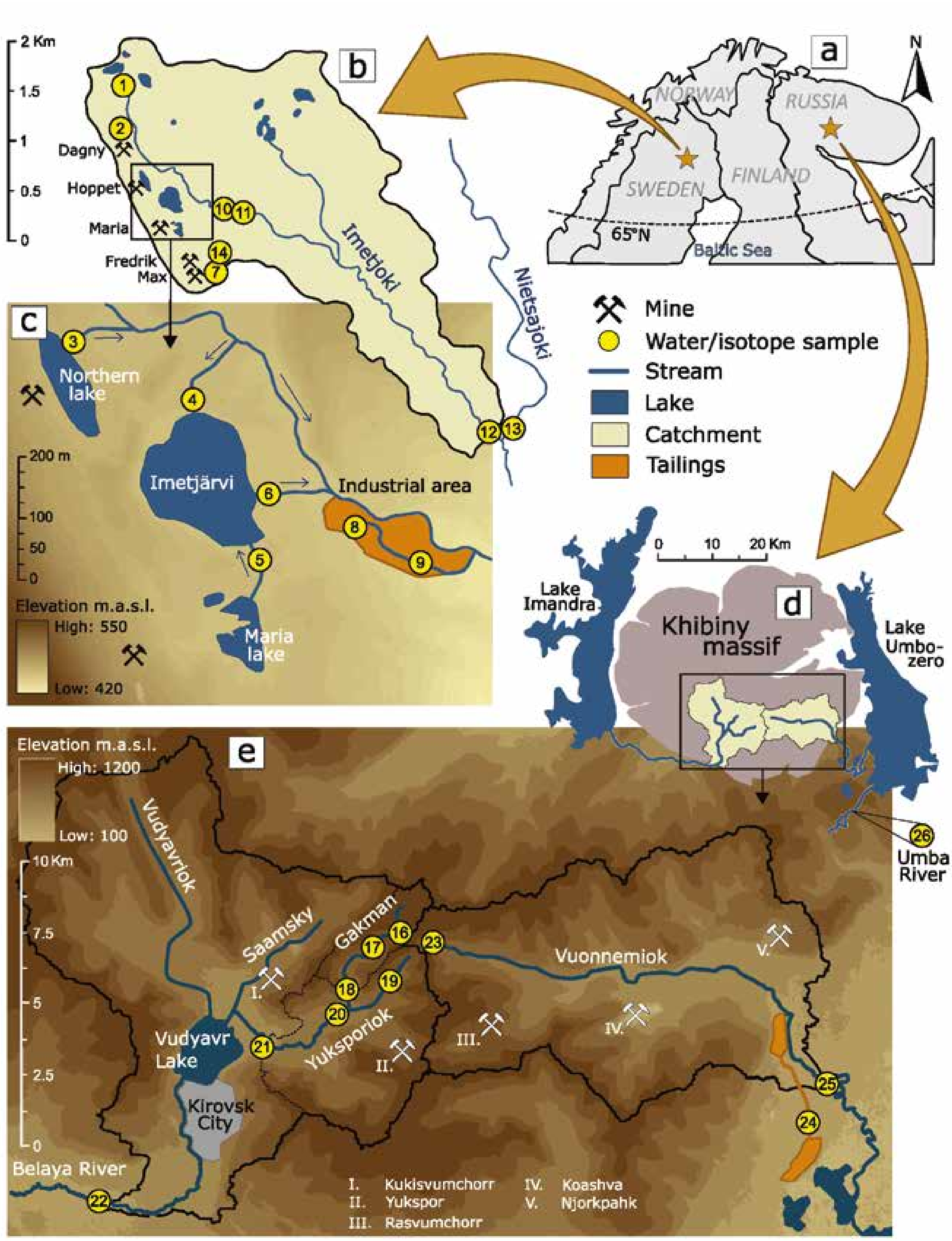

Figure 1. Map showing (a) the location of the two mining areas in northern Fennoscandia, namely (b) the Imetjoki catchment, including (c) the abandoned Nautanen copper mines and (d) the Khibiny massif with (e) the two investigated catchments Belaya and Vuonnemiok. ID 15 (reference Lina River) is not shown in the map and is located 5 km east of the Imetjoki catchment (see Fischer et al., 2020 for coordinates).

end-member (f_{dep} and frock, respectively) according to the principle of mass balance:

$$\delta_{sample} = \delta_{dep} f_{dep} + \delta_{rock} f_{rock} \tag{2}$$

so that $f_{dep} + f_{rock} = 1$. This theoretical mixing was quantified by applying a Monte Carlo simulation (as similarly executed in, e.g., Samborska et al., 2013), where end-member parameter values were randomly sampled from their independently observed regional parameter distributions (obtained, e.g., from a literature review, see below) to create 10,000 different theoretical initial conditions (i.e., the assumed stream water isotopic composition before MSR). A Rayleigh fractionation model was then applied to calculate the residual fraction of sulfur concentration after reduction (f_{red}). The model is based on the initial isotopic composition of the stream water (δ_0; here represented by the 10,000 theoretical predictions of δ_{sample}) and the residual isotopic composition in the stream water (δ_R; represented by the observed isotopic value of stream water δ_{stream}), according to:

$$\delta_R = \left(\frac{0{,}001\delta_0 + 1}{0{,}001\varepsilon\,(1 - f_{red}) + 1} \right) 1000 \tag{3}$$

where ε represents the isotopic enrichment factor. This Rayleigh model (Equation 3) was developed from a standard Rayleigh model (Mariotti et al., 1981) by Druhan & Maher (2017) to better represent isotope fractionation processes in water mixtures subject to different travel times – such as the case for a stream water sample in a catchment, where travel times will differ between different flow pathways within the catchment. Further, MSR was assumed to be equally likely at both end-members as well as the point of mixing; this was in order to conserve pre-MSR end-member fractions to post-MSR conditions. MSR was finally quantified as the percentage of reduced sulfur concentration, that is, MSR = $100(1 - f_{red})$. Estimates of end-member parameter values (δ_{dep}, δ_{rock}, and the sulfur concentration of atmospheric deposition, c_{dep}) as well as the enrichment factor (ε) were derived from a synthesis of regional observations and previously reported literature values.

To better quantify the median and average Monte Carlo outputs when MSR values were close to 0%, we have modified the analysis methodology presented in Fischer, Jarsjö, et al. (2022) where a theoretical model output below 0% was truncated (since MSR cannot physically be lower than 0%). This truncation becomes problematic for the current study because we consider average values relatively close to 0% and get both positive and negative random errors of which only the negative random errors will be truncated following the rule. This leads to an overestimation of MSR values derived from the resulting ensemble statistics, and to keep the output unbiased, we omitted the truncation rule.

3. RESULTS

3.1. Regional Data Synthesis

Regional sulfur isotopic end-member data (c_{dep}, δ_{dep}, and δ_{rock}) for the Kola Peninsula and northern Sweden are summarized in Table 1. The Kola Peninsula showed a higher average annual c_{dep} compared to northern Sweden. It is likely the result of nearby smelter emissions of sulfur dioxide (Forsius et al., 2010; Reimann et al., 1997), while also the higher δ_{dep} has been attributed to the processing of high sulfide ores, which were transported from the Norilsk mine in northcentral Russia to Kola smelters (de Caritat et al., 1997). No data were found on the specific δ_{rock} value of sulfide bedrock in Khibiny. We argue that since the Khibiny bedrock is of magmatic origin (Kogarko, 2018) – as is the bedrock in the Imetjoki catchment – sulfide minerals in Khibiny would most likely also have δ_{rock} values close to 0‰ justifying the use of the isotopic data set for Imetjoki also for the Khibiny catchments (Table 1). A reasonable range for the enrichment factor (ε) in shallow groundwater and surface waters was assumed to be −33 to −1‰, considering that most studies report values between −20‰ and −10‰ (Knöller et al., 2004; Robertson & Schiff, 1994; Wu et al., 2011), while some estimates reach as low as −33‰ (Massmann et al., 2003) and as high as −1‰ (Xia et al., 2017).

3.2. Surface Water Measurements

The measurement campaigns in the Imetjoki catchment in the spring (May) and summer (August) of 2017 revealed high surface water concentrations (15–5,000 µg/L) of Cu, Zn, and Cd at and downstream of the mining site, where the dissolved organic carbon (DOC) ranged between 1.3 and 11.6 mg/L and pH-levels were between 3.3 and 7.1 (Fischer et al., 2020). No systematic differences in concentrations could be seen between the seasons except for DOC, which were higher in all samples (on average 30%) from the summer compared to the spring. The measured sulfur isotope composition (δ_{stream}) and total sulfur (S) concentrations (c_{stream}) are plotted in Figure 2a together with a so-called "theoretical mixing line," which shows a hypothetic proportional mixing between the two end-members without the influence of MSR. The mixing line is defined through corresponding average regional values for each end-member (Table 1) where the gray area conveys the ±1 standard deviation range. Overall, δ_{stream} values measured in the spring (May) in Imetjoki (hollow circles; Figure 2a) lie closer to the theoretical mixing line than δstream measured in the summer (August). This is further illustrated in Figure 2b where the highest difference in δ_{stream} between spring and summer was seen in the Imetjärvi Lake inlet (ID 4; +2.8‰) and the Northern Lake outlet (ID 3; +2.5‰). The samples from the Northern Lake, Downstream 1, and Maria Lake sites (IDs 3, 5, and 10) all show an increase in c_{stream} by 60%–70% over the summer, while the values for the stream in the lower Industrial area (ID 9) only increased by 11% (i.e., from 20.5 mg/L in the spring to 22.8 mg/L in the summer; Table S2 in Supporting Information S1). The only decrease in cstream was detected in samples from the small brook in the upper Industrial area (ID 8) where the concentration decreased from 48 to 17 mg/L over the summer.

The surface waters within the Khibiny catchments showed clearly higher metal concentrations (3–24 µg/L for Cu, Zn, and Cr) close to the mining areas compared to the concentrations in the upstream areas unaffected by mining (with average concentrations of 0.2–0.7 µg/L for Cu, Zn, and Cr; see Table S6–S7 in Supporting Information S1 and Fischer, Mörth et al. (2022) for full analysis results). DOC levels were generally low in upstream areas (~1 mg/L) and increased only slightly (1.7–3.2 mg/L) in the mining-impacted and down-

Table 1. Regional Data Synthesis Over Sulfur (SSO4) Concentration in Atmospheric Deposition (cdep), Sulfur Isotopic Composition (δ34SSO4) in Atmospheric Deposition (δdep), and Sulfur Isotopic Composition (δ34S) in Bedrock (δrock) in Northern Sweden and on the Kola Peninsula

Parameter		Median	Mean	Std Dev	Min	Max	Data source*
c_{dep}(mg/L)	N. Sweden	0.48	0.57	0.32	0.13	1.7	Observed annual cdep between 1982 and 2017 from 11 locations in northern Sweden, also used in calculations presented in Fischer, Jarsjö, et al. (2022). cdep is composed of 9% sea spray and 91% of fossil fuel combustion.
	Kola Peninsula	0.90	1.42	1.5	0.11	10.2	Observed annual cdep between 1990 and 2017 from 13 locations on or in the vicinity of the Kola Peninsula (Arctic Monitoring and Assessment Programme, 2006; EBAS, 2021; Malinovsky et al., 2002; Reimann et al., 1997; Äyräs et al., 1995). cdep is composed of 8% sea spray and 92% of fossil fuel combustion.
δ_{dep}(‰)	N. Sweden	+5.4	+5.3	0.69	+3.8	+7.0	Reported values of $\delta_{34}S_{SO4}$ in samples of snow and precipitation from the Kalix River Basin, which encompasses the Imetjoki stream, between 1990 and 1991 (Ingri et al., 1997), also used in Fischer, Jarsjö, et al. (2022).
	Kola Peninsula	+6.6	+6.9	1.07	+4.3	+8.7	Reported values of δ34SSO4 in epiphytic moss samples (Hylocomium splendens and Pleurozium schreberi) from the Kola Peninsula during the summer 1994 (de Caritat et al., 1997). Since epiphytic mosses rely foremost on air for moisture and nutrients, they provide long-term average sulfur isotopic values close to the isotopic composition of atmospheric deposition with only minor (<1–2‰) isotopic fractionation (assimilation) during the uptake in the plant (Liu et al., 2009; Migaszewski et al., 2010; Xiao et al., 2015).
δ_{rock}(‰)	N. Sweden & Kola Peninsula	−0.60	−0.54	1.0	−3.4	+3.3	Reported $\delta_{34}S$ values for sulfide minerals of magmatic origin (pyrite-chalcopyrite deposits) at the copper mine Aitik in northern Sweden (Yngström et al., 1986) as also used in Fischer, Jarsjö, et al. (2022). Due to the magmatic origin of the Khibiny massif, sulfide minerals are likely to also have isotopic values close to 0‰, which justify using the values reported by Yngström et al. (1986) also for the Khibiny data set

Note.* See details in Text S2 in Supporting Information 1.

stream areas. The pH ranged between 6.8 and 10.6 for all Khibiny samples and all measured (total) sulfur concentrations occurred in the form of sulfate. All of the measured δstream values in Khibiny are falling either on or within 1 standard deviation from the theoretical mixing line (Figure 2c), which indicates that end-member mixing alone (with no/little isotopic fractionation) explains most of the spread in the values. Compared to the wide spread in sulfur isotopic data within the Imetjoki catchment, the Khibiny values formed two clear clusters; all upstream sampling points (IDs 16–19, 23) grouped toward the top-left corner with a small range in both δ_{stream} and c_{stream}, displaying a clear signal from the atmospheric deposition end-member, while results from the mining impacted sampling points (IDs 20, 21, and 24) grouped in the lower right corner in a similarly narrow range, likely portraying the bedrock end-member (see detailed results in Table S6–S7 in Supporting Information S1). The Yuksporiok 3 data (ID 21) represent a 3-day average value from which the corresponding coefficients of variation (CVs) were 0.22 and 0.14 for δ_{stream} and c_{stream}, respectively. A clear mining-impacted signal was derived from the downstream Vuonnemiok 3 sampling point (ID 25), while samples from the Umba River (ID 26) and Belaya River (ID 22) show a mix of the two end-members, however still within 1 standard deviation from the mixing line.

3.3. Calculated MSR in the Imetjoki and Khibiny Catchments

The Monte Carlo simulations for sampling points within the Imetjoki catchment resulted in an overall interquartile range between 10% and 37% MSR for both the spring and summer with the catchment-scale median MSR being 19% (mean: 27%; see full output details in Table S3–S4 in Supporting Information S1). A clear difference can be seen between the seasons (Figure 3), where the Monte Carlo MSR outputs in the spring (yellow probability density distributions) lie closer to the 0% line compared to the MSR distributions in the summer (purple density distributions). For locations sampled in both seasons, the difference in catchment-scale MSR was 9% units over the summer (i.e., 14% median MSR in the spring and 23% in the summer; Figure 3). The highest increase in MSR was detected at the Northern Lake outlet (from a median of 5% in spring to 24% in summer) and the Imetjärvi inlet (from 4% to 20%, respectively), which is also shown in Figure 2b where these two sampling points (IDs 3 and 4) had the highest increase in measured isotopic value from spring to summer. The smallest seasonal change was found in samples representing the Industrial area (ID 9), where high median MSR was found both in the spring (32%) and in the summer (34%).

The samples from the Khibiny catchments show an interquartile range of MSR values between 0% and 15% with a catchment-scale median MSR value of 7% for Yuksporiok (mean: 16%) and as low as 2% for Vuonnemiok (mean: 7%; see full output details in Table S5 in Supporting Information S1). The highest MSR (14%) in Khibiny was found in the Belaya River (ID 22), which may be impacted by potential MSR in the Vudyavr Lake and the other two (unmonitored) tributaries (Vudyavriok and Saamsky; Figure 1). However, the estimation for this location is uncertain as it may be biased from a potential release of additional sulfur from Kirovsk City, for example, as municipal wastewater having another and here unaccounted for isotopic signal.

4. DISCUSSION

4.1. Catchment Conditions Affecting Natural MSR

The Imetjoki and Khibiny catchments share similar climatic features (e.g., temperature and number of days with snow coverage), and the sulfur concentrations of their water systems show overlapping ranges. However, we found that catchment-scale median MSR values in Imetjoki (summer season) were about 18% units higher than the catchment-scale median MSR values in Khibiny during the same summer season (23% MSR vs. 5%). This supports our working hypothesis that some fundamental conditions are more favorable for MSR in the Imetjoki catchment compared to the Khibiny catchments. For instance, organic material was more abundant in the Imetjoki stream water most likely due to its forest cover, yielding higher DOC concentrations from decomposing vegetation. Direct effects of an increase in organic matter concentration on natural MSR have previously been observed in southern Finland (Bomberg et al., 2015), where organic material was added to acidic water in flooded mine shafts to induce MSR, which over the course of 15 years successfully increased the pH and decreased the metal concentrations. Although stream water DOC concentrations reflect the general supply of organic matter in the catchment, the available fraction of DOC for SRM is usually much smaller than the stream water concentrations since SRMs require already degraded organic matter (e.g., low molecular weight substrates; Muyzer & Stams, 2008), which means that the type of organic matter is also important to MSR (Berggren et al., 2007; van Hees et al., 2005). Furthermore,

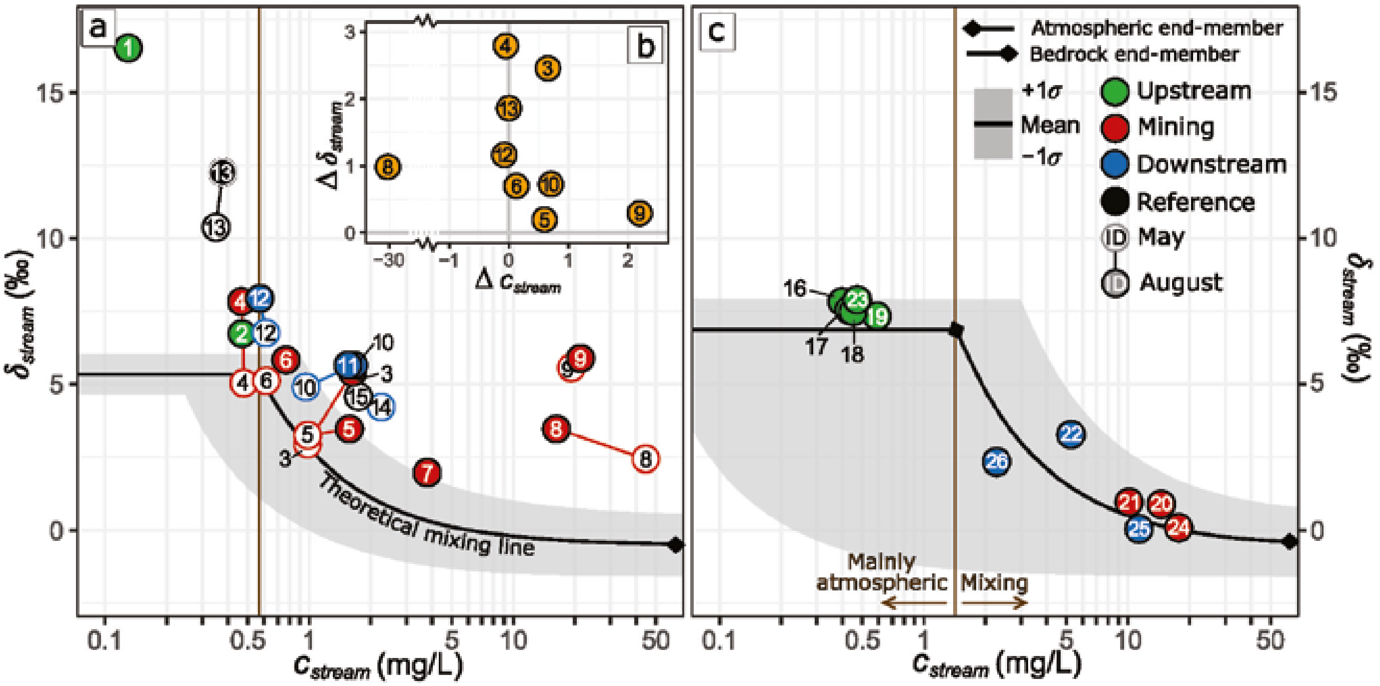

Figure 2. Measured stream water δ34SSO4 values (δstream) and total sulfur (S) concentration (cstream) for (a) the Imetjoki catchment and (b) corresponding seasonal difference between August and May and (c) Khibiny catchments. The theoretical mixing line represents proportional mixing of two average end-members based on the regional data synthesis in Table 1, where the gray area covers the respective ±1 standard deviation (σ) for each end-member. The regional mean sulfur (SSO4) concentration in atmospheric deposition (cdep) for each site is illustrated with a vertical line at 0.57 mg/L for the Imetjoki catchment and at 1.42 mg/L for the Khibiny catchments.

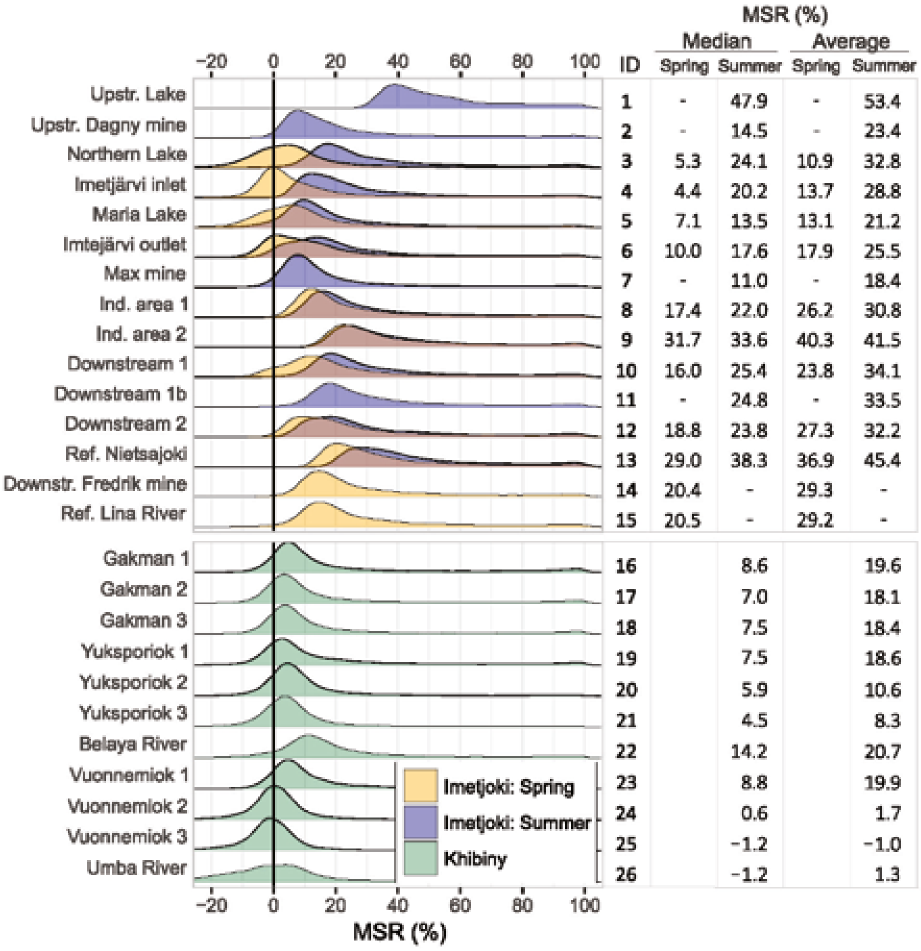

	MSR (%)			
	Median		Average	
ID	Spring	Summer	Spring	Summer
1	-	47.9	-	53.4
2	-	14.5	-	23.4
3	5.3	24.1	10.9	32.8
4	4.4	20.2	13.7	28.8
5	7.1	13.5	13.1	21.2
6	10.0	17.6	17.9	25.5
7	-	11.0	-	18.4
8	17.4	22.0	26.2	30.8
9	31.7	33.6	40.3	41.5
10	16.0	25.4	23.8	34.1
11	-	24.8	-	33.5
12	18.8	23.8	27.3	32.2
13	29.0	38.3	36.9	45.4
14	20.4	-	29.3	-
15	20.5	-	29.2	-
16		8.6		19.6
17		7.0		18.1
18		7.5		18.4
19		7.5		18.6
20		5.9		10.6
21		4.5		8.3
22		14.2		20.7
23		8.8		19.9
24		0.6		1.7
25		-1.2		-1.0
26		-1.2		1.3

Figure 3. Probability density distributions from the Monte Carlo simulations for calculated microbial sulfate reduction (MSR) for the Imetjoki (upper panel) and Khibiny (lower panel) catchments. MSR distributions in the Imetjoki catchment also reflect the two seasonal conditions from the spring (yellow density distributions) and the summer (blue density distributions).

the anoxic environments required for MSR (Pester et al., 2012) as well as relatively slow residence times allowing for longer exposure to SRM (Nelson et al., 2009) are likely present at multiple "hot spot" locations within the Imetjoki catchment, which contains 11 small lakes and has about 16% of its total area covered by peatlands (SGU, 2020). High $\delta^{34}S$ values in wetland-dominated sub-catchments (relative to other sub-catchments) have previously also been attributed to MSR (Björkvald et al., 2009). Notably, although most surface waters were only slightly acidic (pH 5.7–7.1), a few locations within the Imetjoki catchment displayed high metal concentrations and/or strongly acidic water (pH 3.3–4.8), which are potentially harmful to SRM (Xu & Chen, 2020). These strongly acidic waters were nonetheless associated with nonnegligible MSR levels. For example, the Industrial area (ID 8) had in the spring a pH of 3.3 and a Cu concentration of 5,000 µg/L and still showed a median MSR of 17%. An explanation could be that the local stream network has developed acid-tolerant SRM, considering that mine drainage from the Nautanen mines has been developed during a long time over the past 110 years, reaching a condition that can be described as nearly a steady state with regard to the considerable downstream pollution transport (Fischer et al., 2020).

The water from Belaya and Vuonnemiok catchments of Khibiny on the other hand showed low median MSR values (5%), which is consistent with the prevailing high alpine environments characterized by bare rocks and snow fields remaining over the summer, and the fact that they have been increasingly industrialized over the last century (Moiseenko et al., 2009). Both these factors contribute to the sparse forest cover of the Khibiny catchments, occurring only in the lower valleys outside of built areas, yielding generally low DOC concentrations (1–3 mg/L), as measured within the catchments in 2017. Furthermore, the high alpine environment spanning elevations between 100 and 1,200 m above sea level is characterized by steep slopes and a thin soil layer, which contributes to relatively fast throughflow of precipitation (i.e., shorter hydrological residence times). For instance, the Gakman sub-catchment (6.2 km^2; IDs 16–18) has a slope of 0.07 m/m, while the Imetjoki catchment (6.6 km^2) has a slope of 0.03 m/m. Whereas the Gakman sub-catchment in Khibiny on average had relatively similar pH (6.8–7.4) as Imetjoki, the Yuksporiok mining area in Khibiny (IDs 20–21) had highly basic pH (10.2– 10.6), which potentially is another factor that can limit the MSR values. Conclusive evidence regarding how much (high) pH may limit natural MSR seem however still to be lacking, since some studies have shown the presence of considerable SRM in alkaline waters, for example, up to pH 9.8 in mine shafts in southern Finland (Bomberg et al., 2015) and in mine tailings with pH up to 9.3 in New Zealand (Chappell & Craw, 2003).

4.2. Seasonal Conditions Affecting Natural MSR

The presented results regarding impacts of seasonality show that the catchment-scale MSR values under spring conditions with ongoing snowmelt were lower (14%) compared to MSR values under summer conditions (23%). This difference suggests that there is a summer "boost" in the activity of SRM. For instance, between early spring (May) and summer (August), the average catchment-wide water temperatures rose from 3.8 to 11.5°C, which is more favorable even for cold-tolerating bacteria (Virpiranta et al., 2019). However, the isolated effect of temperature (and the seasonal changes of it) on field-scale MSR is difficult to determine since multiple factors are likely interacting (Khan et al., 2019; Praharaj & Fortin, 2004). Two such factors that showed pronounced seasonality in Imetjoki are DOC, which increased on average with 30% over the summer (Fischer et al., 2020), and sulfur concentrations, which increased with 26% (Figure 2b; excluding ID 8 that decreased by almost 3 times). This also means that sites in warmer climates with usually increasing summer bioproductivity and DOC turnover would likely enable even higher such "boosting."

Another potentially influential factor is that the sampled spring stream water represents a mixture of groundwater-dominated baseflow and more surficial flows including meltwater. The latter may remain on top of or near the soil surface since the ground would still be frozen during spring, hindering infiltration and groundwater recharge. MSR along meltwater flow paths may therefore be negligible, implying that the associated flows would be isotopically characterized by sulfur from atmospheric deposition in contrast to the groundwater-dominated baseflow, which potentially can be affected by MSR. Hence, a key issue for understanding the mechanisms behind seasonal changes in net MSR is then to assess the dilution caused by meltwater as given by the relative fractions of meltwater and baseflow in the sampled stream water. Thorough investigations by Laudon et al. (2007) showed that meltwater percentages during the spring flood ranged between 10% and 30% of the total water volume in stream water in forested catchments of northern Sweden. This implies that even during the here considered spring campaign at Imetjoki, most (70%–90%) of the sampled stream water volumes are likely to have originated from flow paths with potentially active MSR. Considering a hypothetical case in which the meltwater presence is at the high end of the range (30%), recognizing that the meltwater should have an isotopic composition relatively similar to the composition of the atmospheric deposition (because of the essentially lacking MSR in meltwater), mass balance considerations then allow the estimation of the isotopic composition of the remaining 70% of the sample originating from baseflow as well as the associated MSR value. Results for instance showed that compared to downstream net MSR values (including snowmelt impacts) of 16–19% (at IDs 10 and 12; Figure 3), the MSR in the baseflow component would be somewhat higher, namely 18–23%. This is however not as high as the downstream MSR values observed during the summer campaign (24–25; at IDs 10 and 12; Figure 3), implying that snowmelt impacts only partially can explain the differences in MSR values between spring and summer. Snowmelt impacts will however likely vary from location to location as well as from region to region and may therefore need further attention in future studies.

Apart from above-discussed systematic differences between the MSR values in spring and in summer, we note that locally high MSR values can occur (also) during the spring season. For instance, the MSR value was 30%during spring at ID 9. Observations of relatively high MSR (before onset of dilution of meltwater) were similarly observed at the Krycklan catchment in northern Sweden (e.g., Björkvald et al., 2009) and at Lake Mjösjön in central Sweden where winter ice-coverage gave a gradual decrease in lake water oxygen levels and by that favored MSR (e.g., Andersson et al., 1992).

4.3. Implications – MSR as a Nature-Based Solution to Mine Drainage Under Ambient Changes

The present study supports previous cold region studies (e.g., Fischer, Jarsjö, et al., 2022) in detecting high MSR values locally (30%–40% under natural conditions). We additionally found novel evidence of a more general presence of MSR over different seasons even under the considered cold (Arctic) conditions, which indicates that there is large potential for using MSR as part of nature-based solutions to mitigate adverse impacts of (acid) mine drainage in the Arctic and elsewhere. For instance, this can be obtained through managing and taking advantage of favorable MSR conditions in (constructed) wetland and lake systems. Enhancement measures could be carried out by adding organic material in sedimentation ponds or mining shafts (e.g., Bomberg et al., 2015) utilizing already existing structures to provide prolonged residence times and possible anaerobic bottom layers.

The Arctic is currently subject to considerable climate-driven shifts in the carbon cycle that are projected to continue in the foreseeable future. There is notably an observed trend of increasing DOC values in streams (Guo et al., 2007), which is favorable for MSR (Bomberg et al., 2015), and will therefore probably act to enhance MSR over vast regions. Conversely, the increasing number of snowand ice-free days (e.g., Box et al., 2019) will increase vertical fluxes of water and oxygen in upper soil layers, which in turn may decrease MSR in some locations by removing associated pockets of anaerobic conditions (e.g., see similar discussion in Palomo et al., 2013). Unless such MSR-driven changes and their impact on the retention of metals and other substances along their transport pathways are recognized and understood, they may – if detected through downstream monitoring – be misinterpreted as changes in metal mobilization. For instance, increased retention by (neglected) MSR may be at risk of being misinterpreted as decreased source zone mobilization of metals. The metal mobilization (e.g., at mining waste heaps) is notably also expected to be impacted by ongoing hydroclimatic changes although through quite different processes (e.g., Hotton et al., 2020; Jarsjö et al., 2020; Shrestha et al., 2020). A key challenge in understanding the role of MSR in mitigation solutions to (acid) mine drainage is therefore to consider how it may impact the balance between mobilization and retention under conditions of future ambient changes.

5. CONCLUSIONS

We here interpret and compare the results from multiple stream water measurements in two major Arctic mining regions, allowing us for the first time to quantify net impacts of catchment conditions and seasonality on largescale MSR. This reflects a combination of multiple drivers and large-scale processes that, for example, are difficult to reproduce in laboratory experiments. Specifically, we conclude that:

1. A likely range of catchment-scale MSR values in the Arctic is ~5%–20% during the summer season with catchments located in vegetated terrain containing wetlands, lakes, or voluminous groundwater systems that allow longer reaction times for SRM being more likely to show median MSR values of around ~20%.
2. Local values of MSR can be as high as ~40% at hot spot conditions, for example, near lakes, indicating large potential for using MSR as part of nature-based solutions to mitigate adverse impacts of (acid) mine drainage.
3. Evidence of persistent field-scale MSR over different seasons in the Arctic indicate that microbial processes and their interactions with the environment may be more persistent than previously anticipated.

The present results showing widespread and persistent MSR even under cold conditions call for more detailed investigations regarding potential field-scale correlations between MSR and individual landscape and hydroclimatic characteristics (e.g., DOC, water temperature, ice cover, vegetation, and slope), which, for example, can be supported by the here utilized isotopic fractionation and mixing scheme.

DATA AVAILABILITY STATEMENT

The resulting data sets from the field measurement campaign in Khibiny 2017 are available through Zenodo at https://doi.org/10.5281/zenodo.6448039.

5. ВОДНЫЕ ПОТОКИ В РЕЧНЫХ БАССЕЙНАХ

Новые данные о трансформации стока воды и наносов в дельте реки Лены по итогам экспедиционных измерений в августе 2022 г.*

ВВЕДЕНИЕ

Дельта р. Лены – крупнейшая в стране по площади и числу рукавов, она уникальна по своему строению и истории образования, по своей экологической ценности и другим характеристикам [1–5]. Дельта расположена в Российской Арктике, быстро теплеющей и «теряющей» морские льды, в криолитозоне с отступающей мерзлотой, в устье второй по водоносности реки России, сток и режим которой с конца 1980-х гг. значимо меняется [6]. Все это создает условия для серьезных и нарастающих местных гидролого-морфологических изменений, влияющих на русловые процессы и распределение стока между русловыми системами, на характер продольной (между вершиной и морским краем дельты) трансформации речного стока наносов, растворенных веществ и тепловой энергии, на состояние прибрежной арктической морской акватории, судоходство и в целом на экологические условия и обитателей дельты. Эти нарушения, как и сама дельта, по-прежнему известны недостаточно, хотя в сравнении с другими арктическими дельтами степень ее гидрологической изученности несравнимо выше [1, 2, 5–13]. Стоковые посты и гидрометрические створы в дельте не функционируют с 2007 г.; комплексные гидрологические экспедиции проводились довольно давно; с 2022 г. заморожено российско-германское сотрудничество. Поэтому проведенные в августе 2022 г. гидрологические исследования не только были своевременны, но и стали источником новых знаний о современном гидрологическом состоянии южной части дельты Лены. Целью исследований было изучение распределения стока воды и наносов Лены между дельтовыми рукавами, продольных и по глубине изменений мутности воды и роли в них местных гидролого-морфологических процессов, определение гранулометрического и химического состава наносов, донных и береговых отложений, получение натурных опорных сведений для дешифрирования спутниковых снимков. В задачи представленного исследования также вошел детальный сравнительный анализ полученных во время экспедиции данных и результатов их лабораторной и камеральной обработки с материалами ранее проводившихся похожих исследований.

ДАННЫЕ И МЕТОДИКИ

Полевые гидрологические исследования проводились в восточном и среднем секторах дельты р. Лены с 10 по 16 августа 2022 г. (рис. 1). Крайней восточной и одновременно крайней южной точкой района работ был южный берег зал. Неёлова (к северу от пгт Тикси; с координатами 71,75° с. ш. и 128,86° в. д.), крайней западной точкой – гидроствор на Оленёкской протоке, в 3 км ниже впадения в нее Булкурской протоки (72,31° с. ш. и 126,07° в. д.), крайней северной точкой – створ на Большой Туматской протоке (72,71° с. ш.). Общая протяженность маршрута работ «на воде» составила около 530 км. В числе исследованных водных объектов были зал. Неёлова, концевой участок Главного русла р. Лены, Быковская, Оленёкская, Булкурская, Большая и Малая Туматская и Арынская (в истоке) протоки (прим. авторов статьи – в действительности это типичные дельтовые рукава, согласно теоретическим положениям отечественной устьевой гидрологии [4]), а также протоки, огибающие о. Самойловский, и ряд др. Особо следует выделить главный дельтовый узел разветвления у о. Столб. Полевой отряд базировался на о. Самойловский – на базе научно-исследовательской станции (НИС) «Остров Самойловский» Института нефтегазовой геологии и геофизики им. А.А. Трофимука СО РАН.

Полевые выезды выполнялись на моторном катере. Во время них, во-первых, были обустроены на о. Самойловский и о. Арга-Билир-Арыта водомерные посты, оборудованные датчиками уровня воды серии ERG-TP-01 (создатель – биологический факультет МГУ имени М.В. Ломоносова). На них осуществлялся непрерывный мониторинг температуры и уровня воды (в условной системе высот). В Оленёкской протоке, восточнее о. Самойловский, была установлена авторская зонд-ловушка (патент № 201927 от 29.05.2020 г.) для сбора взвешенных наносов на трех глубинных горизонтах. Во-вторых, были измерены 25 расходов воды и скоростей течения – с помощью акустического доплеровского профилографа течений (АДПТ) RioGrande, двумя-тремя проходами и с соблюдением для одного узла или вдоль рукава правила «синхронности измерений» [4]. Расхождение между расходами воды разных проходов было допустимым по РД 52.08.767-2012

---

* Д.В. Магрицкий, С.Р. Чалов, Е.Ж. Гармаев, К.Н. Прокопьева, Е.А. Крастынь
Проблемы Арктики и Антарктики
https://doi.org/10.30758/0555-2648-2023-69-2-171-190
https://www.aaresearch.science/jour/article/view/529

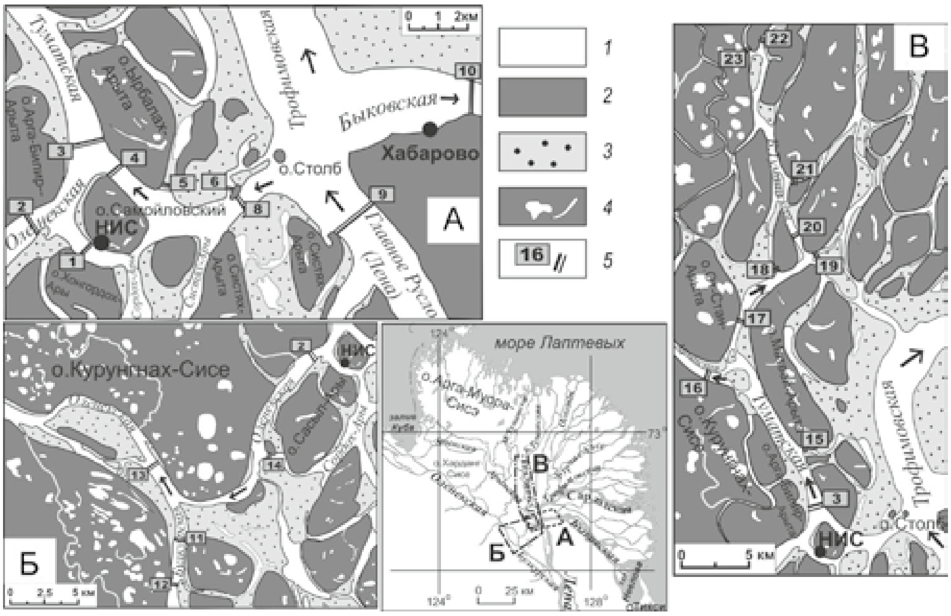

Рис. 1. Картосхема участков дельты р. Лены, где в августе 2022 г. проводились гидрологические работы.
1 – акватория (в межень и на врезках А, Б и В); 2 – острова; 3 – обсыхающие (при низких уровнях) разновысотные пески; 4 – термокарстовые и старичные озера на островах, а на песках – это заполненные водой понижения; 5 – местоположение и номера расходных гидростворов

Fig. 1. Map of the August 2022 hydrological survey sites in the Lena River Delta.
1 – water area (at low water conditions and insets А, Б, В); 2 – islands;
3 – drying out (during low water levels) sands; 4 – thermokarst and oxbow island lakes, water filled downgrades;
5 – water discharge measurement sites and their numbers

[14] (±10 % между проходами и ±5 % от среднего) на большинстве гидростворов. Несколько расходов признаны либо ничтожно малыми (створы № 6 и 7 на малых протоках у истока Оленёкской протоки (см. рис. 1, врезка А)), либо неверными из-за сильного влияния гидролого-морфологических факторов (одно измерение в устье Булкурской протоки и несколько измерений в малых протоках в системе Туматской протоки). В-третьих, проведены 58 измерений оптической мутности воды при помощи турбидиметра HACH 2100p. В самых глубоких местах на створах взяты пробы воды – погружной помпой, из поверхностного, придонного и среднего горизонтов. Вода забиралась в подготовленные емкости объемом 1 или 5 л. В-четвертых, пробоотборником типа ковш Ван-Вина отобраны донные отложения, а на термоэрозионных берегах – образцы грунта. Вес отбираемой пробы около 0,5 кг. Всего было взято 30 образцов грунтов. В-пятых, во время маршрутов наносились на карту участки термоэрозионных берегов. Эхолотом GARMIN измерялись глубины по фарватеру.

На НИС «Остров Самойловский» пробы воды с содержащимися в них наносами фильтровались через вакуумную установку Millipore и мембранные фильтры с размером пор 0,45 мкм производства Владипор (Россия) и Millipore (Франция). Грунты, донные отложения, фильтры Владипор с уловленными взвесями высушивались в сушильном шкафу при температуре 105 °C – 2 ч для фильтров и 8–24 ч для грунтов. Фильтры взвешивались на электронных аналитических весах с точностью до 0,0001 г. По массе осевших на фильтре наносов и объему пробы рассчитывалась весовая мутность. Сопоставление данных по весовой (S, мг/л) и оптической (T, NTU) мутности позволило обосновать эмпирическую зависимость вида:

$$S = 1{,}33 \cdot T - 2{,}45$$

(коэффициент достоверности связи r2 = 0,88). (1)

Также обосновывалась зависимость между измеренной поверхностной мутностью и значениями спектральной яркости на снимке Landsat 8.

Донные грунты были просиотованы через сита размерами: >10 мм, 5–10 мм, 2–5 мм, 1–2 мм, 0,5–1 мм, 0,25–0,5 мм, 0,1–0,25 мм и <0,1 мм. После – рассчитывался средневзвешенный диаметр отложений. Береговые грунты сжигались в муфельной печи при температуре 550 градусов в течение 1 ч для установления доли органики (торфа) в них. Часть проб воды, наносов и грунтов, фильтрата (после фильтрование через фильтры Millipore) была отвезена в Москву для расширенного анализа – на химический состав и гранулометрический (для мелких взвесей) – в лабораториях МГУ им. М.В. Ломоносова. Последний определялся методом лазерной дифракции на лазерном гранулометре Fritsch Analysette 22. Каждое определение состояло из трех-пяти измерений, результаты которых усреднялись.

Расчет распределения расходов воды (Q, м^3/с) в узлах разветвлений и соединений выполнялся с опорой на водно-балансовые решения. Расход взвешенных наносов в гидростворах определялся пересчетом величины рассеяния частицами взвесей ультразвукового сигнала, излучаемого АДПТ в водный поток, в мутность [15]. Для этого вначале была построена единая зависимость между фактическими мутностями воды, полученными в ходе измерений (на трех глубинных горизонтах на вертикали, на каждом гидростворе), и величинами обратного рассеяния на эхограмме (в точках отбора пробы воды). По этой зависимости величины обратного рассеяния в каждой ячейке эхограммы были пересчитаны в мутность воды и представлены в виде изолиний мутности в поперечном створе. В программном комплексе (ПК) ASET [16] по этим и другим данным, включая скорости течения и расходы воды, гранулометрический состав взвесей, рассчитывался расход взвешенных наносов (R, кг/с). Для экстраполяции скоростей в приповерхностном и придонном слоях использована логарифмическая зависимость, а для экстраполяции мутности – закон Великанова–Рауза. В ходе расчетов выяснилось, что ПК ASET учитывает только крупные (руслообразующие) взвеси и, следовательно, выдает заниженный расход наносов. Но это тоже важный методический результат.

ГИДРОЛОГИЧЕСКИЕ И МЕТЕОРОЛОГИЧЕСКИЕ УСЛОВИЯ ВО ВРЕМЯ ПОЛЕВЫХ РАБОТ

В среднемноголетнем масштабе погода в дельте р. Лены отличается суровостью и неустойчивостью из-за особенностей местонахождения района – в Арктике, на границе обширной суши и ледовитого моря, в устье крупнейшей реки. Обычно август (наряду с июлем) характеризуется самыми высокими температурами воздуха – +8…+9 °С на метеостанции (МС) Тикси – и началом ее быстрого снижения примерно с середины месяца, наибольшим количеством осадков и почти сплошной облачностью (ясных дней в среднем пять), ветреной погодой (штилевых дней четыре) с преобладанием северных ветров [17]. Далее по повторяемости следуют Ю, ЮЗ и З ветры.

Во время экспедиции бóльшую часть времени преобладал антициклональный тип погоды, с переменной облачностью – от 25–75 % 11, 13 и 15–16 августа до 100 % 12 и 14 августа (рис. 2б). Осадки прошли 12 августа; сильное усиление ветра отмечено 14 августа – со средней скоростью 8–10 м/с и порывами до 12–13 м/с, со сменой направления на восточное, т. е. вдоль Быковской и Оленёкской проток. Это резко усилило волнение в этих рукавах и ограничило работу «на воде». В остальные дни господствовали ветра северных румбов, со скоростью 2–5 м/с, не мешавшие работе. Температурный фон был благоприятным: с 11 по 13 августа температура воздуха понизилась с 11,8 до 7,6 °С (полярная станция (п. ст.) Хабарово), а к 16 августа вновь выросла – до 13,2 °С (см. рис. 2а). В течение суток диапазон колебаний составлял 5–9 °С; на метеостанции Тикси он немного меньше.

Экспедиционный выезд пришелся на летне-осенний сезон паводков и послепаводочного снижения уровня воды. В низовьях и особенно в дельте р. Лены паводки распластанные, в среднем их четыре [18]. В 2022 г. пик весеннего половодья наблюдался на постах Кюсюр и п. ст. Хабарово в первых числах июня, а его окончание – во второй половине июля (см. рис. 2в, г). К сожалению, Росгидромет не приводит данные наблюдений за июль. Половодье сменилось паводочной волной, спад которой пришелся как раз на экспедиционные работы; в третьей декаде августа пришла вторая паводочная волна. Во время экспедиции, с 11 по 16 августа, уровень снизился почти на 40 см, как по данным измерений на посту Хабарово (были любезно предоставлены наблюдателями), так и по логгерам, установленным участниками экспе-

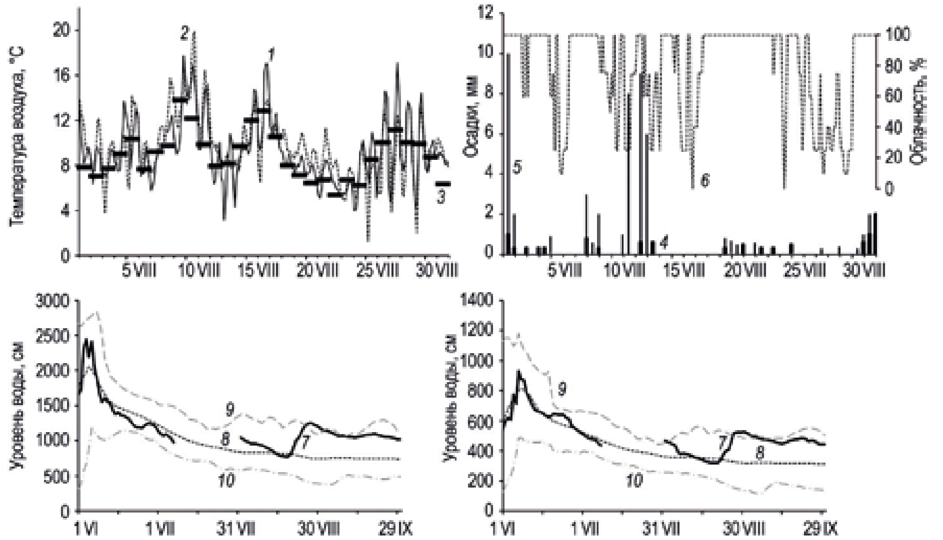

Рис. 2. Гидрометеорологические условия летом 2022 г. по данным наблюдений на пунктах Росгидромета и экспедиционных измерений: а – температура воздуха в августе на постах о. Столб (1, по срокам), Тикси (2, по срокам) и по данным реанализа ERA5 (3, вся дельта и с осреднением за сутки); б – суточный слой осадков (4 – о. Столб, 5 – Тикси) и облачность (6 – о. Столб); в, г – среднесуточные уровни воды на постах Кюсюр (в) и Хабарово (г): 7 – летом 2022 г., 8, 9, 10 – осредненные, максимальные и минимальные за 1991–2020 гг.

Fig. 2. Hydrometeorological conditions in the summer of 2022 based on Roshydromet and field data: a – August temperature from the “Stolb island” gauging station (1, air temperature measurements), Tiksi gauging station (2, air temperature measurements) and based on ERA5 reanalysis (3, the entire delta, daily); б – daily precipitation (4 – Stolb island, 5 – Tiksi) and cloudiness (6 – Stolb island); в, г – average daily water level from Kusur (в) and Khabarovo (г) gauging stations: 7 – summer 2022, 8, 9, 10 – average, maximum and minimum water levels from 1991 to 2020

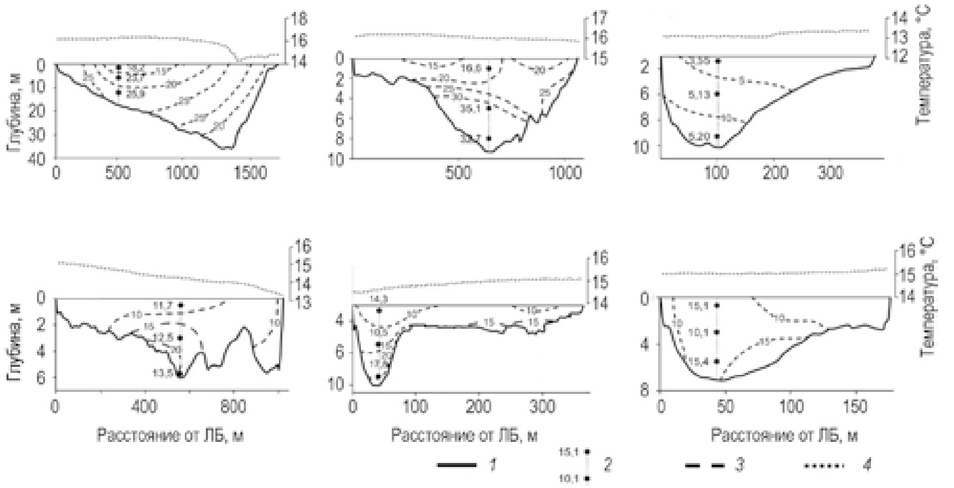

Рис. 3. Поперечные профили гидростворов с линией дна (1), значениями измеренной на вер- тикалях весовой мутности (2), изолиниями равной мутности (3) и кривой изменения припо- верхностной температуры воды (4). Створы: а — Главное русло (створ Л-9), б — Туматская протока (створ Л-3), в — Булкурская протока (створ Л-12), г — Оленёкская протока (створ Л-13), д — Арынская протока (створ Л-16), е — Туматская протока (створ Л-22)

Fig. 3. Hydrological site transverse profiles and their bottom line (1), measured SSC (2), isolines of equal SSC (3), based on SSC echograms, and surface water temperature curve (4). Transverse profiles: a — Main channel (L-9), б — Tumatskaya branch (L-3), в — Bulkurskaya branch (L-12), г — Olenekskaya branch (L-13), д — Arynskaya branch (L-16), e — Tumatskaya branch (L-22)

диции. 13 и, особенно, 14 августа флуктуации уровня резко выросли из-за усиления ветра. В целом хорошо видно, что гидрологические условия соответствовали средним многолетним (см. рис. 2в, г).

Во всех пунктах температура воды превышала температуру воздуха на 4–7 °С; внутрисуточная изменчивость находилась в диапазоне 0,5 °С. Во время экспедиции температура воды (по логгерам) вначале снизилась с 16,5–16,8 °С (с 11–12 августа) до 15 °С (14–15 августа) и вновь немного выросла (на 0,2–0,4 °С) в остальные дни. Запаздывание, по сравнению с колебаниями температуры воздуха, составило 1–2 суток. Различия в температурах воды у о. Самойловский и п. ст. Хабарово оказались незначительными, тогда как, по измерениям температурным датчиком АДПТ, температура воды по ширине потока и между гидрометрическими створами сильно разнилась. Самые холодные воды обнаружены в Булкурской протоке – 13,0–13,5 °С (рис. 3). В Главном русле у правого берега выявлен шлейф холодных вод шириной почти 0,4 км, который, по-видимому, тянется от поста Кюсюр и формируется водами водотоков, стекающих с Верхоянского горного массива [6]. Наоборот, на посту Хабарово (на Быковской протоке) такой зоны нет, что соответствует выводу из [6]. В Оленёкской протоке, от левого берега к правому, т. е. к едомным массивам с тающими многолетнемерзлыми породами (ММП), температура воды уменьшается на 2 °С.

СКОРОСТНОЕ ПОЛЕ ПОТОКА И РАСПРЕДЕЛЕНИЕ СТОКА ВОДЫ В ДЕЛЬТЕ

Во время экспедиции на 25 гидрометрических створах несколькими проходами были измерены расходы воды (см. рис. 1, таблица). 12 августа измерения выполнялись вокруг о. Самойловский и в главном дельтовом узле разветвления – у о. Столб; 13 августа – на верхнем участке Оленёкской протоки и в Булкурской протоке; 15 августа – в верхней части системы Туматской протоки, 16 августа – вновь к югу от о. Самойловский. Полученный массив данных позволил изучить современную ситуацию с рассредоточением стока Лены в привершинной части дельты, частично – по длине Оленёкской и Туматской проток.

О распределении стока в дельте Лены научное сообщество знает по-прежнему мало. И это несмотря на то, что дельта Лены одна из немногих в Арктике, где измерения расходов воды на постоянной основе все же проводились [13, 19]. В 1950 г. в истоке Быковской протоки был открыт стоковый пост о. Столб (сейчас это полярная станция им. Ю.А. Хабарова) и гидроствор на Главном русле. С 1973 г. Тиксинский ЦГМС начал проводить эпизодические, а с 1977 г. систематические измерения Q в истоках проток Трофимовской, Туматской и Оленёкской – на закрепленных гидростворах. Но после 2007 г. все стационарные измерения Q прекратились. Помимо сетевого мониторинга, большой объем измерений Q выполнен во время экспедиций, причем на большем числе водотоков и створов [1, 2, 7, 9, 20]: 1) в 1976–1987 гг. гидрографической партией Тиксинского ЦГМС, 2) в 1979–1981 и 1994–1995 гг. Лабораторией русловых процессов и эрозии почв МГУ им. М.В. Ломоносова, 3) в отдельные годы с 2001 по 2016 г. в рамках российско-германского сотрудничества – силами ААНИИ, СПбГУ и др. Последнее крупное обобщение всех имеющихся (стационарных и экспедиционных) данных по Q в рукавах дельты Лены опубликовано в [6] – в виде соответствующей таблицы перехода от расходов и уровней воды на посту Кюсюр к Q в главных дельтовых рукавах. Там же дан анализ устойчивости этого распределения в многолетнем и сезонном временных масштабах. Предыдущие обобщения содержатся в публикациях [1, 2, 7, 11, 12, 18, 19], среди которых выделяются работы [1, 7] со сведениями по распределению стока для максимального числа рукавов и узлов (разветвления и соединения). О расходах воды в рукавах, где гидрометрические измерения не проводились, можно составить приблизительное представление на основе альтернативных данных, полученных по гидролого-морфологическим зависимостям [7], на базе концепции гидрографических порядков [21] и по результатам численных гидродинамических расчетов [22].

При обработке и анализе данных измерений в августе 2022 г. прежде всего необходимо было соотнести распределение Q между рукавами с расходами воды на посту Кюсюр. Это замыкающий створ на р. Лене, который находится перед входом реки в «Ленскую трубу» и в 145 км выше вершины дельты (у о. Тит-Ары), в 315 км от устья Быковской протоки [6]. За август 2022 г. имелись лишь среднесуточные уровни на посту Кюсюр, импортированные с сайта «Информационная система по водным ресурсам и водному хозяйству бассейнов рек России» [23]. Они были пересчитаны в среднесуточные Q по кривой расходов воды (КР). КР не обеспечена данными за теплый сезон год начиная с 2012 г. (они не публикуются), тогда как реальные измерения Q не проводятся еще раньше – с 2003 г. [24]. В то же время, согласно [18, 19], КР для поста Кюсюр характеризуется хорошей многолетней устойчивостью. В итоге получилось, что с 10 по 16 августа 2022 г. Q на посту Кюсюр снизился примерно с 35200 до 28000 м^3/с. Различие с данными ArcticGRO [25] составило 3–4,5 %.

В итоге на концевом участке Главного русла – на месте бывшего гидрометрического створа «4,7 км выше о. Столб» – измеренный 12 августа расход воды составил ~93–94,7 % расхода в Кюсюре (с учетом времени добегания), тогда как, по данным работы [6], он должен быть 96,2 %. То есть объем оттока воды из Главного русла (между вершиной дельты и о. Столб) в левобережные протоки (включая протоку Булкурскую) и пойму оказался во время экспедиции выше. Это несоответствие подтверждают также данные по Булкурской протоке: по [6] ее доля ≤ 0,50 %, а по измерениям 13 августа она составила 0,53 % (см. таблицу). Свидетельствует ли это об уменьшении роли Главного русла? С одной стороны, по данным промеров в Главном русле с 1982 по 2009 г., в гидростворе наблюдалось постепенное повышение отметок дна [1], способное снижать пропускную способность русла и расходы в нем [4]. С другой, по данным многолетних наблюдений на гидростворе «4,7 км выше о. Столб», обнаружен многолетний рост доли стока Главного русла с интенсивностью ~0,9 %/10 лет [6], который усилился после экстремально высокого половодья В 1989 г. (Qmax = 220 тыс. м^3/с). Можно лишь предположить, что единичные данные 2022 г. не могут служить надежным доказательством первой версии.

У о. Столб сток Главного русла распределяется между совместным входом в Оленёкскую и Туматскую протоки (на запад), Трофимовской (на север) и Быковской (на восток) протоками (см. рис. 1). Далее протока Оленёкская, ниже отделения от нее Туматской протоки, на протяжении 26 км принимает слева воды Лены, стекающие с поймы и через протоки, включая протоку Булкурскую. По измерениям 12 и 13 августа доли проток Быковской, Трофимовской, Туматской и Оленёкской (ниже впадения Булкурской) составили, в сравнении с водностью на посту Кюсюр, примерно 24,9–25,5, 58–59,2, 6 и 6,6 %. Разница с расчетными данными из [6] оказалась минимальной – менее 0,3 % (за исключением 3 % у протоки Трофимовской, сток которой получен по разности). То есть опубликованное в [6] распределение по-прежнему актуально!

Особая новизна работ в 2022 г. – в получении данных о рассредоточении стока в районе о. Самойловский и в системе Туматской протоки (см. рис. 1, таблицу). Согласно им, в питании Оленёкской протоки огромную роль играет протока, огибающая о. Сасыл-Ары с юго-востока (створ № 14). Доля Арынской протоки равна ~55 % Q в истоке Туматской протоки, а в [7] она равна 59 % (при расходе у Кюсюра 35 000 м^3/с). В конце маршрута в Большой Туматской протоке осталось ~24,2 % первоначального стока (створ № 22), тогда как в [1] для этого участка дается ~20 %, но при существенно больших Q в истоке Туматской протоки.

Режим скоростей течения воды функционально связан с расходами воды, морфологическим строением русла и уклонами водной поверхности, которые ближе к морю выполаживаются. Средние скорости течений варьировали во время измерений расходов воды от 0,20–0,60 до 0,92 м/с (в Главном русле), максимальные – от 0,50–1,50 до 2,96 м/с (см. таблицу). Наименьшие скорости – 0,01–0,06 м/с – измерены в Булкурской протоке, а также в нескольких небольших поперечных или почти осохших протоках

ЗАКОНОМЕРНОСТИ ПРОСТРАНСТВЕННОЙ ИЗМЕНЧИВОСТИ МУТНОСТИ РЕЧНЫХ ВОД И ВЗВЕШЕННЫХ НАНОСОВ

Изучение взвесей в речном потоке решало как геохимические, так и гидрологические задачи. Первая гидрологическая задача связана с оценкой вклада местных эрозионных и аккумулятивных процессов в трансформацию стока наносов Лены на его пути от вершины (ВД) к морскому краю дельты (МКД). Как известно, в устьях часть принесенных реками наносов осаждается [4, 26, 27]. Первый участок активной аккумуляции (в условиях гидравлического подпора) – это устьевой, включающий (в случае с устьем р. Лены) только дельту. Из этих наносов формируется и выдвигается в море тело дельты, образуются дно и берега дельтовых водотоков и водоемов, поверхность и рельеф дельтовой равнины, устьевые бары и др. Часть наносов в арктические дельты приносится речным льдом [2]. В [28] суммарные потери взвешенных наносов в дельте Лены оцениваются в 83–90 %, в [29] – в 70 %, в [6] – в 40–65 %. Активное накопление отложений в водотоках дельты Лены и на ее устьевом взморье требовало периодического дноуглубления с целью поддержания судоходных глубин [30].

Но не все придерживаются этой точки зрения. Так, по результатам сравнения карт, аэрофото- и спутниковых снимков, анализа морфологических изменений в восточной части дельты, частично по данным натурных измерений авторы публикации [31] делают вывод, что бóльшая часть наносов не оседает в дельте, а достигает моря. Новое, более масштабное, сравнение карт и снимков не подтверждает и не опровергает этот вывод [32], свидетельствуя лишь о стабильности МКД. В работе [10] анализировались различия в значениях коэффициента отражения (на снимках Landsat за 2000–2019 гг.) для двух участков – в истоках и устьях главных рукавов. Обнаружено продольное увеличение этого коэффициента в Быковской и Сардахской протоках и его уменьшение в Оленёкской и Туматской. Основная причина – добавление в поток наносов от термоэрозии берегов, прежде всего южной экспозиции, относящихся к едоме, в теплую и солнечную погоду. Это согласуется с данными М.Н. Григорьева, оценившего массу наносов, поступающих в рукава с таких берегов (по 42 участкам общей протяженностью 76,6 км), в 2,15 млн т/год [3]. Но проблема спутниковых данных – это возможность фиксировать лишь взвеси в поверхностном слое потока. А это мелкие, неруслообразующие взвеси, по сути транзитные. Переход от них к общей величине взвесей и осредненной по сечению мутности, реальному русловому балансу наносов требует натурных измерений на разных глубинах и удалении от берега.

Материалы прежних натурных измерений мутности воды, проводившихся на спаде половодья и в меженно-паводочный сезон (при Q на посту Кюсюр <40000 – 30000 м^3/с), показывают либо продольное уменьшение мутности воды [1, 2, 7, 33, 34], либо неоднозначную тенденцию, порой с увеличением мутности [1, 7, 20, 35, 36]. Можно лишь уверенно говорить, по данным многолетнего стационарного мониторинга и экспедиционных измерений, о значительном уменьшении мутности от ВД до о. Столб – в 1,5–2,5 раза.

Во время движения полевого отряда вверх по Быковской протоке (в ночь с 11 на 12 августа 2022 г.) измерения оптической мутности показали ее уменьшение от 7–11 (на участке «зал. Неёлова – примерно 50-й км от истока») до 2–3 NTU. Подобное для гидрометеорологических условий, наблюдавшихся во время экспедиции 2022 г., описано в [7, 10, 35]. Но при сравнении данных этого конкретного «прохода» вдоль Быковской протоки и спутникового снимка от 16 августа увеличения мутности на последнем не обнаружено, даже наоборот (см. ниже). Сама весовая мутность, измеренная в истоке Быковской протоки вечером 12 августа, составила 13–19 мг/л (поверхность). Мутность, измеренная у о-вов Столб и Самойловский, варьировала от 17 до 24 мг/л (поверхность). Это вполне соответствует гидрологическим условиям августа [2, 6] и подтверждает тезис о примерном равенстве мутности воды в основном рукаве и в истоках отделяющихся рукавов [4]. По длине Оленёкской протоки, к створу ниже впадения Булкурской протоки, мутность уменьшилась примерно в 1,5 раза (13 августа) – до 12 мг/л (поверхность). Тогда как в маловодной Булкурской протоке она составила 3,5 мг/л, а в полноводной протоке к югу от о. Сасыл-Ары – 32 мг/л. Различие хорошо видно и на спутниковом снимке. Незначимое снижение мутности отмечено по длине Туматской протоки (15 августа) – до 14–15 мг/л.

Натурные измерения были дополнены результатами дешифрирования снимка Landsat 8 от 16 августа 2022 г., с учетом построенной зависимости между относительными и абсолютными значениями мутности. Они свидетельствуют об уменьшении мутности воды между о-вами Тит-Ары и Столб – с 24,1 до 18,6 мг/л – и далее по Быковской протоке до 16,4 мг/л (в 120 км от о. Столб) (рис. 4, фрагмент А). Уменьшение обнаружено и в Туматской протоке – в 140 км от о. Столб мутность равна ~13,4 мг/л. Обратная ситуация наблюдается для Трофимовской-Сардахской протоки. Здесь мутность 16 августа про-

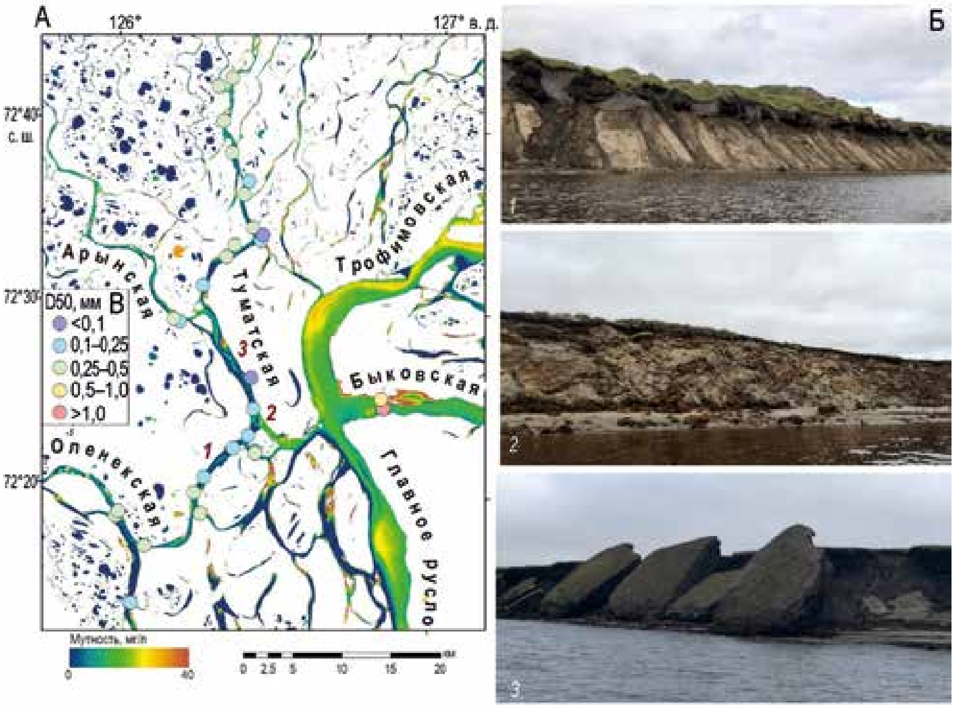

Рис. 4. Пространственное распределение мутности (Landsat 8, от 16.08.2022) (А) с примерами термоабразионных берегов (Б) и данными по средневзвешенной крупности донных наносов (В, легенда). Цифры на снимках (Б) соответствуют цифрам на карте (А)

Fig. 4. SSC spatial distribution (Landsat 8, 16.08.2022) (А) with the examples of thermal abrasion shore types (Б) and average bottom sediment particle size (В). The numbers in the photo (Б) correspond to the numbers on the map (А)

дольно нарастает – до 34,8 мг/л, а также от правого к левому (южной экспозиции) берегу. За многолетний период (с 2000 г.) и на основе >50 ситуативных карт полей мутности воды, полученных по снимкам Landsat с 2000 г., Быковской протоке в июле-сентябре присущ обычно транзитный режим, а уменьшение поверхностной мутности есть только на выходе рукава в зал. Неёлова [10]. Для Оленёкской и Туматской проток уменьшение поверхностной мутности воды оценено в 5,5 и 13 %. Мутность воды в Трофимовской-Сардахской протоке увеличивается на 11,9 % к 130 км.

Выводы по натурным данным были проверены путем сравнения фактической мутности воды (Sф) и мутности, отвечающей транспортирующей способности потока, – Sтр. Ее можно оценить по формуле К.И. Россинского и И.А. Кузьмина [37]:

$$S_{тр} = 0{,}024 \cdot V^3/(hW), \qquad (2)$$

где V – средняя скорость потока (м/с), h – глубина (м), W – гидравлическая крупность частиц (м/с), как функция от диаметра частиц и температуры воды (по В.Н. Гончарову). Средняя крупность отобранных во время экспедиции взвесей и прошедших гранулометрический анализ попадает в диапазон от 0,011 мм (пр. Быковская) до 0,014– 0,019 мм. Это примерно в 2 раза меньше среднего диаметра наносов на посту Кюсюр при тех же Q (по сведениям из Гидрологических ежегодников). Температура воды была 15–16 °С, скорости течения и глубины приведены в таблице. В результате Sф>Sтр (условия для осаждения наносов) обнаружены практически на всех створах, а Sф<Sтр (условия для транзита и наращивания стока наносов) – лишь в истоках Быковской и Арынской проток.

Таким образом, для полноводных и глубоких дельтовых рукавов, с большими скоростями течения, сохраняющих бóльшую часть водного стока до устья, как, например, Быковская и Сардахская протоки, мутность воды в июле-сентябре может не только не уменьшаться, но способна нарастать, прежде всего за счет поступления в поток продуктов размыва аллювиальных берегов и особенно едомных островов, а также на участках перекатов или на выходе с них. Это соответствует выводам из [10]. В конце Быковской протоки скорости течения могут уменьшаться вдвое- втрое [2], особенно на спаде половодья, что приводит к ситуации Sф>Sтр, например на перекате Дашка. По длине проток Оленёкская и Туматская, не говоря уже о более мелких рукавах, сменяются участки как уменьшения, так и увеличения Sтр (как по гидрологическим, так и по морфологическим причинам), что не способствует свободному транзиту наносов. Правобережные берега Оленёкской протоки – это едома с обрывами южной экспозиции. Поэтому осаждение речных взвесей здесь может компенсироваться (в летний сезон) поступлением наносов с берегов (см. рис. 3).

Во время экспедиции был определен вклад одного из ручьев, стекающего с термоэрозионного правобережного склона о. Курунгнах в системе Оленёкской протоки. Измеренная мутность воды соответствует гиперконцентрированным потокам (111 г/л), что формирует вынос взвеси в протоку величиной 6,8 т в сутки. При расчетных расходах наносов в Оленёкской протоке ~50–70 кг/с (или 4300–6050 т/сут.), согласно расчетам из [6] для наблюдавшихся во время экспедиции Q, поступление наносов с одного такого ручья увеличивает расход взвешенных наносов примерно на 0,11–0,16 %.

Учитывая, что подобные временные водотоки широко распространены в дельте, их вклад в продольное изменение стока наносов может быть существенен. Следует отметить, что аналогичные водотоки фиксировались в дельте Лены и ранее [8].

Вторая гидрологическая задача связана с раскрытием характера распределения взвесей и мутности по глубине и ширине потока с целью дешифрирования эхограмм АДПТ, а также определения соотношения между приповерхностной (видимой со спутников, измеряемой с катера и т. п.) и средней мутностью потока – для целей более точного расчета расходов наносов в створах и расширения возможностей использования спутниковых снимков. Последний раз предметно эти соотношения изучались в 1950-х гг. [8]. В Булкурской протоке мутность в приповерхностном и придонном слое составила 3,55 и 5,2 мг/л, в Оленёкской – 11,7 и 13,5 мг/л, Туматской – 16,6 и 32,7 мг/л, Арынской – 14,3 и 17,8 мг/л, в Главном русле – 18,2 и 25,9 мг/л (см. рис. 4). Рассчитанные по эхограммам АДПТ мутности, визуализированные на поперечниках в виде изолиний (см. рис. 3), в большинстве случаев совпали с Sф на срединной вертикали, что свидетельствует о надежности этого метода.

Также обнаружено, что с нарастанием ветро-волновой активности мутность сильно увеличивается. Так, 11 августа Sф у о. Самойловский составляла 24,3 мг/л, 14 августа (штормовой день) – 32,1 мг/л, 15 августа – 14,2 мг/л. Это типичное событие не только при сильном ветре, но и при слабых ветрах – в широких рукавах и на отмелях, которое идентифицируется на спутниковых снимках зоной повышенной мутности и может привести к неверной трактовке данных спутниковой съемки.

Рассчитанные в ПК ASET расходы взвешенных наносов, если сравнивать их с расходами наносов, которые должны быть по имеющейся связи расходов наносов в рукавах с расходами воды на посту Кюсюр [6], за исключением Булкурской и Туматской проток, оказались меньше в 2–2,5 раза. Кроме того, баланс наносов, по данным ПК ASET, редко соблюдается – даже в узлах разветвления. То есть этот метод расчета требует дальнейшего совершенствования.

ДОННЫЕ ОТЛОЖЕНИЯ

Источником донных отложений в русловой сети речных дельт служат взвешенные и влекомые наносы главной реки, поступающие в дельту, а также продукты размыва и переотложения коренных и аллювиально-дельтовых отложений в пределах самой дельты, вынос (реками и ручьями) наносов с местного водосбора дельт. Крупность донных отложений и ее изменения по длине русла могут свидетельствовать о гидролого-морфометрических характеристиках потока, прежде всего во время «высокой воды», о его транспортирующей способности и характере эрозионно-аккумулятивных процессов, о роли боковых источников поступления наносов в русло. Средневзвешенный диаметр 30 проб донных грунтов составил 0,46 мм, что отвечает средней и крупной фракции песка. Максимальная крупность донных отложений отмечена в Быковской протоке и у правого берега (5,58 мм) (см. рис. 4, фрагмент А). Здесь дно русла выстлано галечно-валунными отложениями местного генезиса. По мере удаления от коренного берега в Туматской, Оленёкской и Булкурской протоках донные отложения представлены исключительно песчаными фракциями. Значения средневзвешенной крупности меняются в интервале от 0,1–1 мм. Наиболее тонкие отложения обнаружены в малых поперечных протоках (до 0,088 мм). Во всех пробах, взятых в основных рукавах, доля алевритовых (0,05–0,1 мм) и илистых (<0,05 мм) фракций не превышала 8 %, в среднем составляя 2,7 %. По длине Туматской и Оленёкской проток (на участках измерений) сменялись участки чередования дна, выложенного мелкими (0,1–0,25 мм) и среднезернистыми (0,25–0,5 мм) песками, что подтверждает тезис о чередовании участков русел с Sф>Sтр и Sф<Sтр. Тогда как крупный размер наносов в истоке Быковской протоки говорит о свободном транзите взвесей во время межени.

Из похожих работ известна лишь одна [5]. Согласно ей, средний диаметр отложений в Оленёкской протоке уменьшается вниз по течению от 0,17–0,26 мм до 0,07–0,10 мм (на устьевом баре); сортированность наносов хорошая. В Быковской протоке перекаты сложены крупнозернистыми песками; галька и гравий встречаются вдоль правого берега и на перекатах; остальное слагают средние и мелкие пески, особенно на перекате Дашка. Можно говорить, что материалы экспедиций 1979–1981 и 2022 гг. совпадают.

Результаты обработки грунтов на едомных берегах показали их преимущественно минеральное происхождение. При этом сами грунты представляют собой песчано-илистую смесь с включениями остатков растительности. Они не очень влагонасыщенные: доли сухого вещества в них – от 83,6 до 92,2 %. Эрозия и термоэрозия таких грунтов приводят к поступлению в речной поток относительно мелких частиц, которые по своим размерам соответствуют взвешенным частицам. Еще одно доказательство этого – результаты изучения конуса выноса оврага, расположенного в разрушаемой части едомы правого берега Оленёкской протоки (72,33° с. ш.; 126,28 ° в. д.). Они показали, что доля частиц с размерами <0,1 мкм достигала 40 %.

ВЫВОДЫ

По итогам проводившейся с 10 по 16 августа 2022 г. в дельте реки Лены комплексной гидрологической экспедиции установлено, что распределение водного стока у о. Столб соответствует ранее рассчитанному авторами (в 2016 г.): в Быковскую, Трофимовскую, Туматскую и Оленёкскую протоки поступает 24,9– 25,5, 58– 59,2, 6 и 6,6 % стока р. Лены на посту Кюсюр. В то же время доля Главного русла оказалась несколько ниже расчетной. Получены новые данные по рассредоточению стока в районе о. Самойловский, в узле впадения Булкурской протоки в Оленёкскую и в южной части системы Туматской протоки, а также о распределении скоростей течения в поперечных створах.

В дальнейшем увязка расходов воды в рукавах дельты с расходами воды р. Лены и шириной рукавов (Qрук. = f(QКюсюр, Врук.)) в контексте гидролого-морфологических зависимостей и гидрографических порядков может создать хороший и простой инструмент для расчета расходов воды в не охваченных измерениями рукавах дельты Лены. Измерения расходов и мутности воды пришлись на меженно-паводочный сезон, поэтому измеренная в поверхностном слое мутность воды была сравнительно небольшой – 12–24 мг/л, с минимумом в Булкурской протоке (3,6 мг/л) и максимумом в активной протоке к югу от о. Сасыл-Ары (32,1 мг/л). По глубине мутность возрастала в 1,2–2 раз. То есть одних спутниковых снимков явно недостаточно для оценки переноса речных взвесей в дельте Лены, особенно руслообразующих. По длине Оленёкской и Туматской проток мутность снижалась (в 1,5 и 1,1 раз), что закономерно из-за превышения фактической мутности над транспортирующей мутностью.

Вдоль Быковской протоки мутность, наоборот, нарастала, правда на спутниковом снимке этого не обнаружено.

Мощным дополнительным источником наносов служат размываемые и термоэродируемые берега, особенно по длине Быковской и Оленёкской проток, в солнечную и теплую погоду. Разрушение таких берегов приводит к поступлению в поток частиц, по своим размерам соответствующих взвешенным частицам. Средняя крупность взвесей составила (в гидрологических условиях проведения экспедиции) 0,011–0,019 мм. В узлах разветвления мутность в главном и отходящих рукавах в целом одинаковая. Построены зависимости между весовой и оптической мутностью, а также с величинами обратного рассеяния.

Средневзвешенный диаметр 30 проб донных грунтов составил 0,46 мм, что соответствует средней и крупной фракции песка. Максимальная крупность донных отложений отмечена в Быковской протоке; наиболее тонкие отложения обнаружены в малых поперечных протоках. По длине Туматской и Оленёкской проток сменяются участки чередования дна, выложенного мелкими и среднезернистыми песками.

Конфликт интересов. Авторы заявляют об отсутствии конфликта интересов. Финансирование. Работы выполнены в рамках гранта РНФ № 21-17-00181. Competing interests. The authors declare no conflict of interest.

Funding. The work was carried out within the framework of the RSF grant No. 21-17-00181.

Climate change impacts on streamflow, sediment load and carbon fluxes in the Lena River delta*

1. INTRODUCTION

In the largest periglacial Siberian rivers, the interactions between hydro-climatic factors and the deep permafrost introduce a pronounced specificity in terms of the climate change impact on the hydrological system of deltas. Recent studies show that continuous permafrost regions show increased flows throughout the Eurasian pan-Arctic (Feng et al., 2021). On the one hand, rising temperatures increase snow- or ice-melt. On the other hand, precipitation amounts and intensities might lead to highly concentrated surface runoff in the catchment area and changes in erosion, sediment transport and water chemistry. According to Syvitski et al. (2005), for every 2 °C of warming, a 30 % increase in the sediment flux could result, and for each 20 % increase in river discharge, a 10 % increase in sediment load could follow. The IPCC (Dentener et al., 2013) projected the rise of global-mean surface air temperature (SAT) from 1.4 °C to 5.8 °C by 2100. The discharge of the six largest Eurasian rivers would increase by 315 to 1 260 km3 per year by 2100 (Shiklomanov et al., 2006), constituting an 18 to 70 % increase compared to present conditions. In their modelling study, Morehead et al. (2003) estimated that the sediment flux of six Arctic rivers would significantly increase in a range of up to 122 %. Furthermore, thawing permafrost releases additional sediments to erosion and transport. Predicted warming in the Arctic is expected to affect the extent of the permafrost and ice-covered regions, the amount of precipitation and the productivity of terrestrial and aquatic ecosystems, which will affect river water and sediment discharges to the Arctic Ocean. The degradation of permafrost has recently led to increased runoff, erosion, and associated transport of total suspended matter and nutrients in the lower reaches of the largest Arctic rivers, which has a significant impact on biogeochemical cycles (Shakhova et al., 2007, Wild et al., 2019). Given recent findings that old permafrost-derived organic carbon plays an important role in aquatic ecosystems (Matsuoka et al., 2022), rapid warming is an important hydrological and ecological driver over northern high-latitude regions.

Even though the importance of permafrost thaw on hydrological processes is recognized widely (Vihma et al., 2019), the hydrological processes in the largest deltas of Arctic rivers still need to be considered, due to the complexity and costs of studying hydrological processes in these remote areas. Monitoring coastal systems is a challenging task, since these networks are costly to install and maintain. Delta zones of Arctic rivers have rarely been studied to date (primarily due to difficulties in access), resulting in a general lack of available data. In this regard, the particular exception is the largest Eurasian delta of the Lena River. Here, on Samoylov Island in the central Lena Delta, a Russian–German monitoring site connected to a research station was established in 1998. This monitoring site, together with yearly fieldwork on and around Samoylov Island and in other delta areas, has provided long-term data on, among other things, meteorological, hydrological, and permafrost conditions (Boike et al., 2019). Additionally, the PARTNERS and ArcticGRO programs (Holmes et al., 2012, McClelland et al., 2016a) provide year-round and interannual estimates of changing water composition at the delta apex. Recent field expeditions were carried out between 2005 and 2012 (Fedorova et al., 2015), and another in 2022 by Lomonosov Moscow State University (Chalov and Prokopeva, 2022), and these made numerous measurements of various hydrological parameters.

Long-term hydrological observations are processed at a few locations upstream from the delta and in the delta branches. Recent studies discussed the Lena River's annual discharge increase due to increasing winter flow, as well as increased streamflow and suspended and dissolved material release between the delta apex and branches from the ice complex (Juhls et al., 2020, Magritsky et al., 2018). Based on water temperature monitoring on the Bykovskaya channel, estimates of heat flux show an increasing trend from 1980 (Magritsky et al., 2018). Continuous measurements at Samoilov Island from 1998 to 2011 (Boike et al., 2013) detect no evidence of warming of mean annual air temperatures, and only winter air temperatures have warmed. Permafrost warmed by more than 1 °C at 10.7 m depth, which was related to changes in winter air temperature, net radiation, and snow cover. Through the integration of in-situ monitoring and remote-sensing data (Landsat), a long-term downstream increase along the distributary system of the Lena Delta was identified and attributed to higher discharges and the degradation of permafrost-dominated banks (Chalov et al., 2021, Chalov and Prokopeva, 2022, Chalov and Prokopeva, 2021). Consideration of these data led to the hypothesis that climatic and streamflow drivers (primarily air temperature, solar radiation, water discharges) may influence deltaic permafrost islands, which are increasingly being destabilized and contributing increased sediment load to streamflow along distributaries in the Lena Delta (Chalov et al., 2021). These processes might have important ecosystem impacts due to associated changes in carbon release, which covaries with sediment (Matsuoka

---

* Sergey Chalov, Kristina Prokopeva, Dmitry Magritsky, Vadim Grigoriev, Evgeniya Fingert, Michal Habel, Bennet Juhls, Anne Morgenstern, Pier Paul Overduin, Nikolay Kasimov
https://doi.org/10.1016/j.ecolind.2023.111252.
https://www.sciencedirect.com/science/article/pii/S1470160X23013948

et al., 2022). Understanding of climatic and streamflow drivers of sediment and carbon transport within the Lena River Delta requires the integration of climatic data accessible for this remote region and the identification of long-term historical hydro-climatic trends, which was considered the main goal of this paper.

The paper is based on an innovative integrated approach to capturing hydrological streamflow and sediment transport and quality records for the large Lena River that relies on the existing integrated toolboxes in hydrological studies (e.g., Chalov et al., 2017). Field, observational, remote-sensing, and climate reanalysis data are necessary resources to upscale across this scarce and poorly monitored region. To describe the weather conditions and climatic effects on streamflow and sediment pathways, we rely on ERA5 air temperature data, which is in good correlation with ground-based observations in the Arctic zone (Demchev et al., 2020). Our unique monitoring data and measurements present an opportunity to establish the first comprehensive estimate of the Lena River Delta climatic (precipitation, temperature, radiation, wind) and hydrological (water and sediment discharges) system in the early 21st century with a specific focus on long-term changes of riverine carbon, which is considered to be one of the most heavily impacted constituents of the Arctic biogeochemical cycle due to permafrost degradation and associated active-layer thickening. Therefore, to bridge current gaps in hydro-climatic change assessment for the Lena River Delta, we here investigate long-term hydroclimatic conditions of sediment pathways in this area, with the main objectives being to: (i) identify historical hydro-climatic trends based on ERA5 reanalysis, (ii) assess the current streamflow, sediment discharges, carbon (DOC and POC) concentrations and temperature trends at the delta top, and (iii) assess to what extent the observed trends are linked with the processes within the delta and how they affect the processes within the delta (primary, water distribution over delta distributary branches, suspended sediment budget). To the best of our knowledge, this is the first comprehensive study to integrate the issues of climate changes, sediment transport and water quality over large northern deltas. Our results yielded novel and essential data that could be used to estimate climate change consequences at the northern latitudes.

2. DATA AND METHODS

2.1. Lena delta. Site description

The Lena Delta's area is ~30,000 km^2 (Schneider et al., 2009) and includes a considerable number (over 6 000) of freshwater channels with a total length of 14 600 km (Ivanov et al., 1983) and approximately 29 500 lakes. The Lena Delta is situated in a zone of 500–600-m-thick continuous permafrost (Boike et al., 2013). The active (annually thawed) layer is 30–50 cm thick. The entire delta lies in the tundra zone except for the southern part of the delta. The four main distributaries represent the main sectors of the channel structure: the largest is the Trofimovskaya branch that flows north-east into the Laptev Sea; the second-largest branch by water discharge is the Bykovskaya branch that turns sharply to the east after Stolb Island and flows into the Buor Khaya Gulf; the third- and fourth-largest distributaries are the Olenekskaya branch that flows west into the Kuba Gulf and the Tumatskaya branch that flows north into the Laptev Sea (Fig. 1). The shoreline length from the Olenekskaya branch mouth to the Bykovskaya branch mouth is ~193 km, and the total length of the river network is 14 600 km.

2.2. Climatic data

In this paper three sources of climatic information were used:

1) **Stations of the Russian Federal Service for Hydrometeorology and Environmental Monitoring** (Roshydromet) in Tiksi and Kyusyur, provided by the Russian Research Institute of Hydrometeorological Information – World Data Center. Tiksi station is located 115 km from Stolb Island and 20 km from Neelova Bay, into which the Bykovskaya channel flows, and provides air temperature monitoring data from 1930 and precipitation data from 1933. The Kyusyur station is located 194 km upstream from Stolb Island and provides air temperature and precipitation data from 1925. The length of the data series reaches 113 years (with 9 years missing from 1917 to 1925) for the Kyusyur station and 92 years for the Tiksi station.
2) **Reanalysis ERA5-Land datasets.** The ERA5-Land dataset is available for free public use for data covering the period from 1950 to 2–3 months before the present at a spatial resolution of ~9 km (Muñoz-Sabater, 2019). Four ERA5 meteorological variables were used in this study: 2-meter air temperature (°C); total precipitation (mm); surface net solar radiation (W·m^{-2}) and 4) wind speed (m·s^{-1}). Other components of the hydrological system, and in particular sediment transport, are most affected by these variables during the ice-free period (June–September). ERA5-Land hourly data from 1950 to the present were downloaded in NetCDF format from the Copernicus Climate Data Store (https://cds.climate.copernicus.eu/cdsapp#!/dataset/reanalysis-era5-land?tab=overview). The daily datasets were compared and tested for agreement with observational data from Kyusyur and Tiksi stations. The correlation coefficient between ERA5-Land and Tiksi air temperatures was 0.93, and 0.92 between ERA5-Land and Kyusyur station air temperatures (Appendix A Supplementary data, Mann and Whitney, 1947, Yue et al., 2002).

Two-meter air temperature (K) was converted to °C and hourly data was converted to average day values, and these are further used to compare against sediment transport patterns revealed for particular days. The duration of the temperature dataset is 72 years.

Surface net solar radiation is the difference between downward radiation (amount of solar radiation, also known as shortwave radiation) reaching the surface of the Earth (both direct and diffuse) and reflected solar radiation (amount reflected by the Earth's surface, which is governed by the albedo). This variable too has been gath-

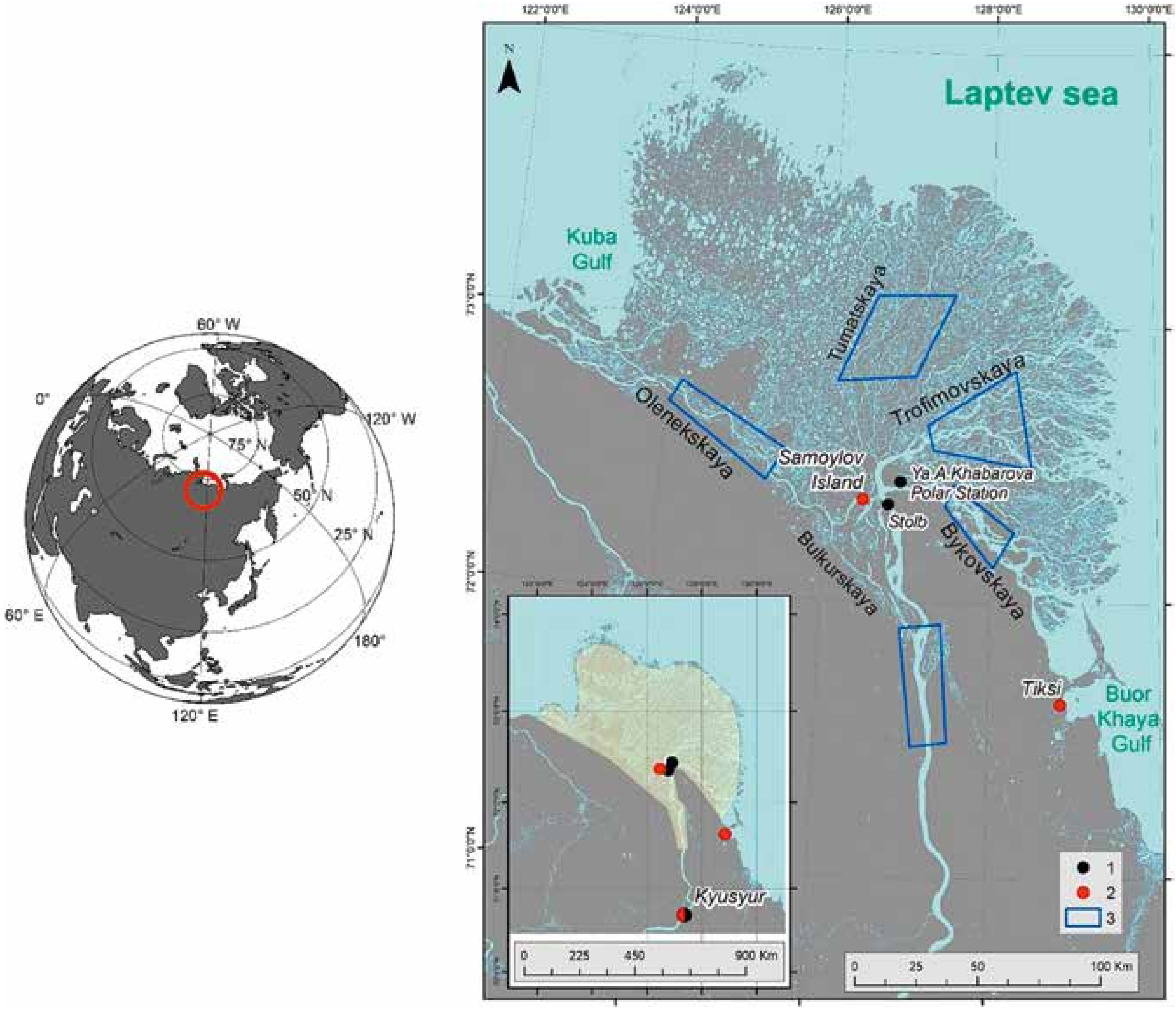

Fig. 1. The Lena Delta study area: 1 – gauging stations; 2 – meteorological stations; 3 – areas for calculating average sediment concentrations representative for particular sectors of the delta (see details in the text); yellow area – ERA5 reanalysis application for Lena Delta.

ered from the beginning of the forecast time to the end of the forecast step for the ERA5-Land reanalysis dataset.

The wind speed monitoring data provide a u-component (eastward component) and a v-component (northward component) of wind, which were converted to wind speed in m s^{-1} as described in Supplementary 2 Eq. (1).

The following characteristics of the ERA5-Land data series and their changes were calculated:

- minimum, mean and maximum values of 2 m air temperature, precipitation, surface net solar radiation and wind speed over 72 years (from 1950 to 2021) and for the months of the open-water period (June–September);
- the Pettitt test, which was applied to calculate the year of the beginning of significant climatic changes (Pettitt, 1979). The Pettitt test is a non-parametric test that has been used in a number of hydroclimatological studies to detect abrupt changes in the mean of the distribution of the meteorological variable (Mallakpour and Villarini, 2016). The description of the test is presented in Supplementary 2–2.
- Linear trend with an estimate of the confidence interval at 95 % significance level for the period of climate change using the non-parametric Spearman's rank correlation coefficient (Spearman's RCC)(Naghettini, 2016) (Supplementary 2–3).

3) **Soil Temperatures.** Soil and permafrost temperature monitoring data were used from the long-term observatory on Samoylov Island (Boike et al., 2019). Here, meteorological parameters and energy balance have been recorded since 1998 and subsurface permafrost temperature since 2006. We used surface (t0) and 0.75 m (t0.75) soil temperatures taken from a measurement chain of temperature sensors installed in a permafrost borehole down to a depth of 22 m at Samoylov Island (Fig. 1). Daily means were calculated from hourly measurements. Permafrost temperature and active-layer thaw depth data were downloaded through the Global Terrestrial Network for Permafrost (GTN-P) database (http://gtnpdatabase.org). The dataset lacks data for the period from June to September. No data are available for the period from 1 June to 24 August in 2006, from 1 August to

30 September in 2015 and from 20 September to 30 September in 2008 and 2021.

Additionally, we calculated accumulated sums and means of air temperature, soil temperature at the soil surface and 0.75 m depth, precipitation, solar net radiation, and wind speed variables over 3, 5, and 7 days (Supplementary 2–4).

2.3. Hydrological data

Long-term hydrological variability was analyzed based on discharge from the Kyusyur gauging station, which characterizes inflow rates to the Lena Delta. Here, the upstream watershed covers 2 430×103 km^2, the delta apex is located 145 km downstream, and the sea (the mouth of the Bykovskaya channel) is 315 km downstream. Water level (H), water discharge (Q) and water temperature (T) have been measured at Kyusyur since 1934, and suspended sediment concentration (SSC) and suspended sediment discharge (R) since 1960. Within the delta, long-term observations were made at the gauging station upstream of the Bykovskaya channel (see Fig. 1) located on the main channel between the delta apex and Stolb Island. The "Stolb Island" polar station has been operating here since the 1950 s (the station is now named "Yu. A. Khabarov").

We compiled a database of daily, mean monthly, and mean annual water levels and discharge for the period 1935–2020 from the Kyusyur gauging station and for 1950–2020 from the Yu. A. Khabarov gauge. Decadal and monthly suspended sediment concentration and average monthly and annual discharges of suspended sediments were analyzed for 1936, 1944, and 1960–2010 at Kyusyur and for 1968–2007 at Khabarov station. Decadal and monthly water temperatures were analyzed for 1935–2019 and 1951–2012. The gaps in the streamflow time-series at the Kyusyur gauge (2012–20) were filled by using separate empirical relationships between water discharges Qmonth and water levels Hmonth (correlation coefficients of 0.9 to 0.99) for each of the individual or pairs of months May, June–July, August–September, October and the remaining winter months.

The gaps in the time-series of average monthly sediment discharges were filled by using average month-

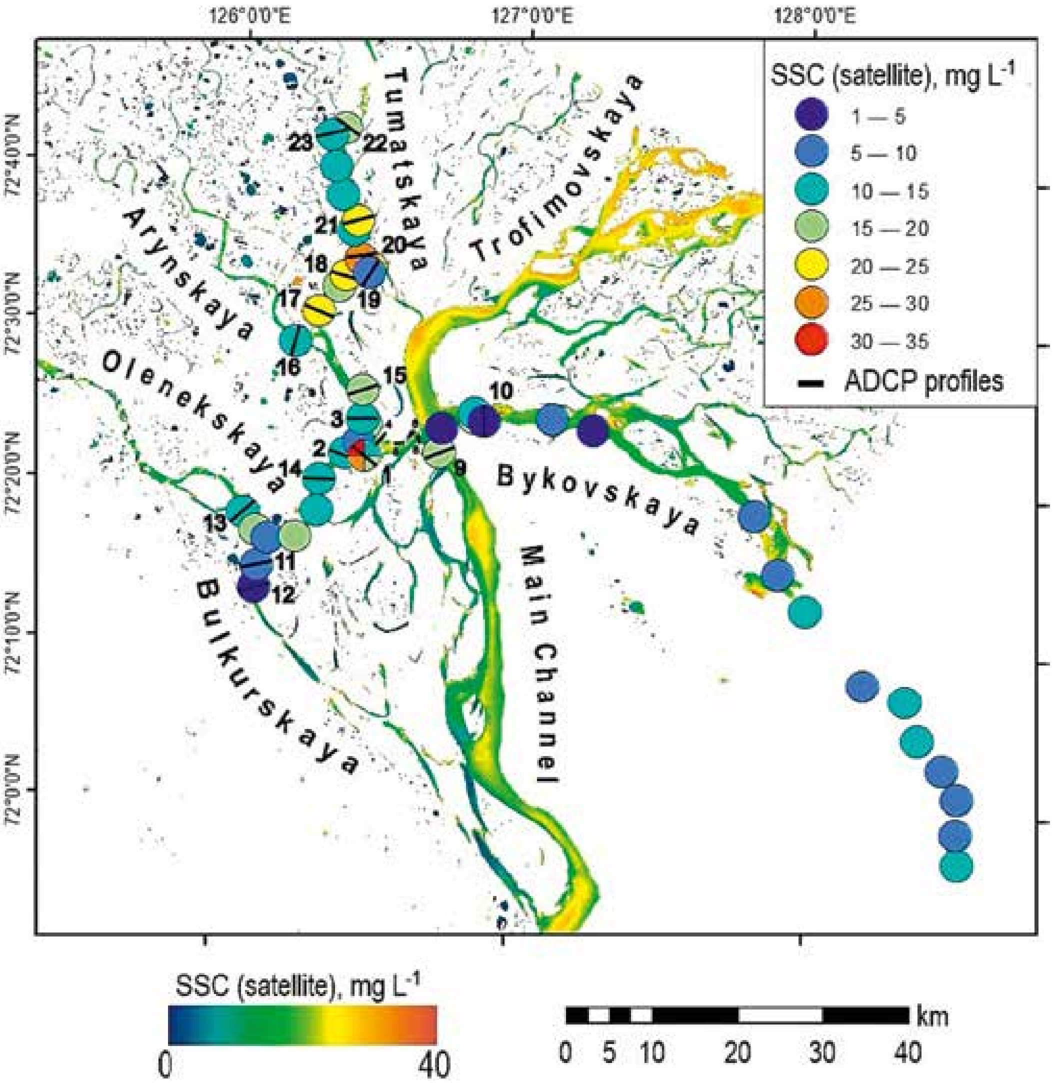

Fig. 2. Measured surface sediment concentrations and water discharges from 10 to 16 August 2022 plotted against satellite-derived (Landsat image from 16 August 2022) SSC map in the upper part of the Lena Delta.

ly water discharges and the power regression $R = aQ^b$, where a = 5.35×10^{-6}, $b = 1.8$ ($R^2 = 0.92$) for May–June and $a = 1.09\times10^{-6}$, $b = 2.02$ ($R^2 = 0.60$) for July–October, for data since 1988 (Magritsky, 2015). The annual values of suspended sediment discharge W_R (million tons/year) were calculated for Kyusyur gauging station. The temporal homogeneity of the time-series was verified using the Fisher (*F-test*), Student (*t-test*), and Mann–Whitney (*U test*) tests for time-correlated and asymmetric series of hydrological characteristics. Independence hypotheses were tested using the Andersen test and the test of the number of series (Supplementary 2–5).

Additionally, water temperature records from both gauges were used to calculate the heat flux W_T as:

$$W_T = c_p \rho T W \tag{1}$$

where c_p is water specific heat capacity ($\text{kJ}\cdot\text{kg}^{-1}\cdot{}^\circ\text{C}^{-1}$), ρ is the density of water ($\text{kg}\cdot\text{m}^{-3}$), T is the average water temperature per decade (°C), and *W* is the volume of water runoff (m^3) per decade. The values of heat runoff for the particular seasons and annual values (W_T,a) were calculated as a sum of 10-day averages.

The Arctic Great Rivers Observatory (ArcticGRO; https://arcticgreatrivers.org/, accessed: 30 April 2023) dataset from Zhigansk gauging station was used to evaluate long-term riverine carbon entering the Lena Delta. This dataset provides data on hydrology and biogeochemistry of the greatest (largest) Arctic rivers (Ob, Yenisei, Lena, Kolyma, Yukon, and Mackenzie) since 2003 at an irregular sampling frequency. Samples represent different hydrographic stages and seasons, with particular emphasis on depth-integrated sampling (for details and protocols, see McClelland et al., 2016b). The database used in our estimates included 87 DOC and POC measurements taken between 12 August 2003 and 25 November 2021 (an average of ~5 samples per year). We assume that the Zhigansk gauging station, which is located ~800 km upstream from the Lena Delta, may not be entirely representative of the discharge to the delta but provides approximate values.

Data on suspended sediment concentration (SSC, $\text{mg}\cdot\text{L}^{-1}$) was collected during comprehensive fieldwork in the Lena Delta conducted from 10 to 16 August 2022. Here, water samples were taken with a filterless submersible 12 V pump from three layers (surface, mid-section, and near-bottom) to account for the vertical distribution of the suspended sediment. For SSC determination, water samples were filtered through pre-weighed and predried (at 105 °C for two hours) membrane filters (pore size 0.45 μm) from the "Millipore" filtration system. The filter samples were then oven-dried (at 105 °C for two hours) and reweighed to determine SSC. The mass of dry sediment was determined by gravitational difference. The SSC was deduced from the measured mass of dry sediment and water sample volume:

$$SSC = \frac{m_2 - m_1}{V} \tag{2}$$

where m^2 is the mass of filter and dried residue (mg), m_1 is the mass of clean filter (mg), and V is the volume of water sample filtered (L) which is defined based on the amount of the sediment in the sample (on average, 2 L). The mass of the membrane filter and wet sediment were measured with a precision of ±0.001 g.

Water sampling for suspended sediment analyses sampling was coupled with simultaneous discharge measurements made using a Teledyne RDInstruments (TRDI) RioGrande WorkHorse 600 kHz ADCP unit mounted on a moving boat. For each sample in a depth profile, the boat was repositioned at its original location and sampling was performed while drifting at the river water velocity. In total, 24 cross-sectional measurements were made in the Bykovskaya, Bulkurskaya, Olenekskaya, Tumatskaya, Arinskaya branches and in the Main Channel (Fig. 2) and aimed to quantify the flow partitioning between delta distributaries. The relative discharges in the particular distributaries of the delta were calculated as:

$$Q_i\,(\%) = Q_i/Q_0 * 100\ \% \tag{3}$$

where Q_i is the discharge (in $\text{m}^3\cdot\text{s}^{-1}$) in an individual distributary and Q_0 is the total discharge (in $\text{m}^3\cdot\text{s}^{-1}$) of the Selenga prior to entering the delta.

2.4. Remote-sensing data

Additionally, long-term changes (between 1999 and 2022) of suspended sediment transport behavior within the delta were retrieved from remote-sensing applications (Chalov et al., 2021, Chalov and Prokopeva, 2022). The SSC was calculated from reflectance intensities (*ρ*) of Landsat images and based on the relationships with SSC data obtained during the field campaign in the Lena River Delta (32 measurements) connected with the available image from 16 August 2022 ($R_2 = 0.76$):

$$\text{SSC} = 1572.1 * \rho_{red} - 25.0 \tag{4}$$

where is bottom of the atmosphere reflectance in the red band (Landsat 8).

Landsat Collection data products were downloaded from the USGS Earth Explorer website from 2000 to 2022 for the Lena Delta. A total of 75 Landsat images for ice-free periods between June and October from 2000 to 22 were used. Suspended sediment concentrations

Table 1. Results of trend analyses of air temperature, total precipitation, surface net solar radiation and wind speed in 1950–2021 based on ERA5-Land reanalysis data.

Meteorological variables	Change year (according to Pettitt test [1])			
air temperature	2000	0.0000*	4.1 °C	6.0 °C
total precipitation	1977	0.9026	170 mm	160 mm
surface net solar radiation	1992	0.0132*	110 $\text{W}\cdot\text{m}^{-2}$	118 $\text{W}\cdot\text{m}^{-2}$
wind speed	1983	0.145	4.86 $\text{m}\cdot\text{s}^{-1}$	4.98 $\text{m}\cdot\text{s}^{-1}$

* Statistically significant (i.e., p-value < 0.05).

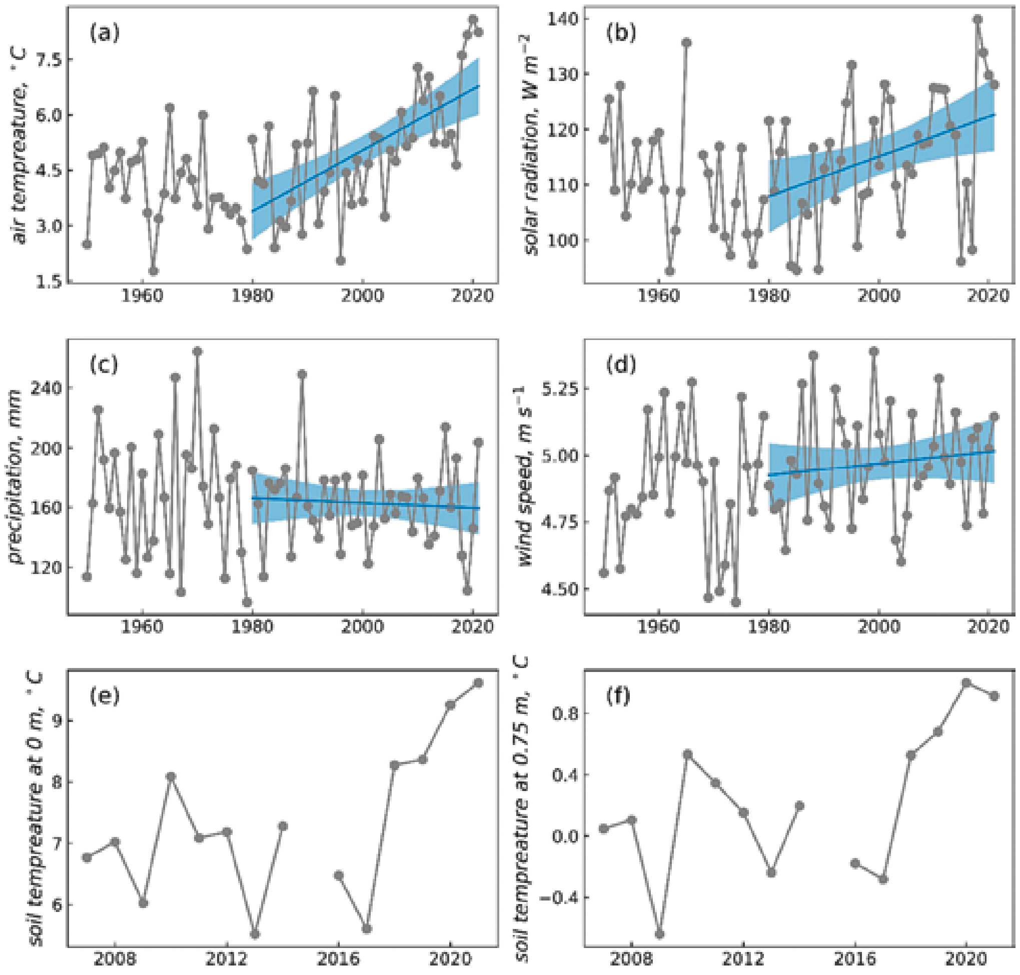

Fig. 3. Long-term changes in mean air temperature (a), surface net solar radiation (b), precipitation (c), wind speed (d) (based on ERA5-Land reanalysis data), soil temperature at 0 m depth (e), soil temperature at 0.75 m depth (f) in the Lena Delta. For a–d, the overall linear trend for 1979–2020 is shown (blue line), with its 95 % confidence interval.

(SSC, mg·L^{-1}) were determined in the Lena River main channel and four deltaic branches: the Bykovskaya, Trofimovskaya, Tumatskaya, and Olenekskaya channels (for additional details, see Chalov et al., 2021, Chalov and Prokopeva, 2022). The images were atmospherically corrected using the SIAC method to remove the effects of atmospheric scattering from an image. SIAC has shown good performance for land surfaces (Yin et al., 2022) and inland water bodies (Sherjah et al., 2023).

Each of the four channels and river upstream from the delta were characterized by an average suspended sediment concentration (SSC) within the selected areas (see Fig. 1), which was estimated for all pixels classified as "water". The non-water pixels were excluded from analyses based on NDWI index and manual classifications. The SSC was calculated as average for particular areas within the delta (shown in Fig. 1 as blue polygons) and refer to near-surface suspended sediment concentrations (approximately 1 m from the water surface (Chalov et al., 2021, Pavelsky and Smith, 2009).

For each of four deltaic branches, SSC change (ΔS_0) was calculated on the basis of the difference between SSC at the upstream area (upstream from the delta, SSC_1) and downstream area (within the particular branch, SSC_2):

$$\Delta S_0 = SSC_2 - SSC_1 \quad (5)$$

Relative sediment changes ΔS (%) were calculated as:

$$\Delta S = \Delta S_0/SSC_1 \quad (6)$$

Three possible ratios between sediment input and output were analyzed: $SSC_2 > SSC_1$, $SSC_2 < SSC_1$, and $SSC_2 \approx SSC_1$, which correspond to either an increase ($\Delta S > 0$) or a decrease ($\Delta S < 0$) in sediment concentrations. These changes are attributed to variations in suspended sediment concentration in the near-surface layer, which is taken as an assumption in our calculations. In particular, we consider that changes in average sediment concentration in the channel profile might be different from those calculated with the above-mentioned methodology.

The ΔS (6) dataset was compared with observed weather conditions (air temperature, radiation, wind) and streamflow inputs to the delta in the period 2000–22. The critical factors influencing sediment load within the delta were identified using correlation analysis, and the corresponding quantitative relationships were established.

3. RESULTS

3.1. Climatic changes in the Lena delta

The trends in air temperatures from reanalysis ERA5-Land datasets are summarized in Table 1. The results suggest a shift toward a warmer climate. Air temperatures increased significantly ($p\text{-value} < 0.05$) according to the Pettitt test. An increase in warming rate was observed between the periods 1950–99 and 2000–21, i.e., the most significant increase in air temperature occurred in the last 20-year period (Table 1). Average air temper-

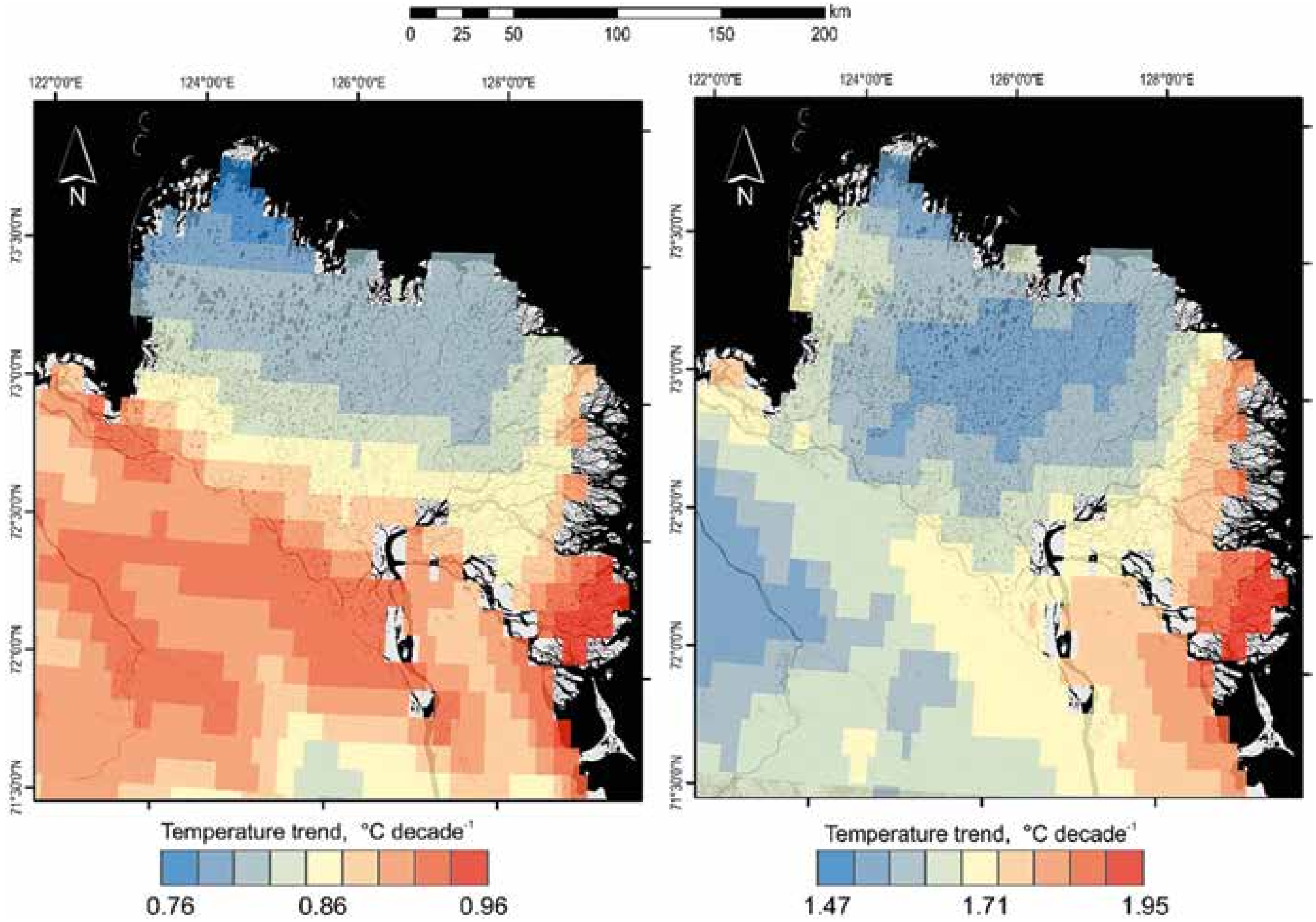

Fig. 4. Map of air temperature trend values in the Lena River Delta: left – from 1979 to 2021, right – from 2000 to 2021.
* Note value ranges represented by color bars differ between maps.

atures were 4.1 °C for the period 1950–99, whereas for the last 20-year period (2000–21) it reached 6.0 °C. Tiksi and Kyusyur weather station's air temperature series based on the Pettitt test also show significant changes in air temperature, with a shift to more rapid warming in 2001 for Tiksi and in 2004 for Kyusyur (p-value < 0.05).

The rate of air temperature rise was 0.86 °C per decade from 1979 to 2021. The subsequent period (2000–21) warmed at 1.61 °C per decade. The significances of the trends by the non-parametric Spearman rank correlation coefficient (1979–2021) were 0.63 and 0.67 at p-value < 0.05 (Fig. 3a), respectively.

The change in warming rate since 2000 was not uniform across the delta. The color-coded map in Fig. 4 shows how average air temperature trends changed. The maximum warming rate reaches 2.11°C per decade. Higher rates are mainly found in the delta's eastern part, near the Bykovskaya channel mouth and along the ridges in the southern part of the delta. Trend values also increase in the south-western part of the delta, along the Olenekskaya channel. The lowest change rates (1.66°C per decade) are observed in the central delta, where air-mass penetration from the Laptev Sea is most likely to have a cooling effect. The value of the trend from 1992 to 2021 in the delta area is lower than the values over the last 20 years (2004–21). In general, as in 2004–21, the higher values of the 1992–2021 trend were observed in the southern part of the delta, with minimum values in the central and northern parts of the delta.

Surface net solar radiation significantly increased from 110 $W\cdot m^{-2}$ (from 1950 to 1992) to 118 $W\cdot m^{-2}$ (from 1993 to 2021) (Fig. 3b). The value of coefficients for 2004–21 is 0.48, but the Spearman rank correlation for the first part of warming (1991–2004) is not significant at p-value < 0.05. Rising surface solar net radiation was 2.64 % per 10 years from 1992 to 2021 and 6.99 % per ten years from 2004 to 2021.

According to the Pettitt test, there were no significant trends in rainfall ($p = 0.9026$) and wind speed values (p-value is 0.145) (Fig. 3c and d). However, non-significant trends were recorded: one upward at the end of the 1980s and one downward from the end of the 2000s. Also, significant statistical changes have not been established for precipitation series at Tiksi and Kyusyur weather stations.

Soil temperature from the observations on the Samoylov Island (Boike et al., 2019) displayed a general increasing tendency, with the higher values after 2017 (Fig. 3e). Compared to t_0, soil temperature at 0.75 m exhibited more stable values over time (Fig. 3f).

3.2. Streamflow input to the delta and partitioning across delta distributaries

The water input to the delta is characterized by the 17,200 $m^3\cdot s^{-1}$ average long-term water discharge of the Lena River at the Kyusyur gauging station (543 km^3 per year average annual runoff W_a) for the period 1927–

2020. These average numbers include linearly interpolated numbers for the years 1927–34 and 2012–20 from the water stage measurements. The streamflow is characterized by relatively small interannual variability (coefficient of variation Cv = 0.12) and high correlation (r[1] = 0.32). The Anderson test t(A) = 3.2 (+) and the test of the number of series t(u) = 2, 12 (+), which are normal for very large rivers, were applied. Wet-dry cycles of water flow are identified (Supplementary 3), among which there was a long dry period in 1939–57 (with the average value of the difference-integral curve (k_{av} = 0.91), medium flow in 1958–2003 (k_{av} = 0.99) and the modern high-water period in 2004–20 (k_{av} = 1.10). The results show an increasing trend in streamflow since 1988 (Spearman's rank correlation coefficient [RCC] [+]) and a particularly large increase in W_a since 2004. W_a increased by 56.3 km^3 per year for the period 1988–2020 compared to 1935–87.

The hydroclimatic changes of the streamflow input to the delta may have a significant impact on hydrological conditions across the delta, especially on flow partitioning between delta distributaries and sediment dynamics. Flow partitioning has rarely been investigated due to the delta's remoteness and size. We collected data of repeated point measurements of water discharge at key locations over the delta. These data include water discharge measurements taken on 12–13 August 2022 (see Fig. 2 and Supplementary 4) and observations reported by Bolshiyanov et al., 2013, Fedorova et al., 2015, and Magritsky et al. (2018). The dataset reveals constant flow partitioning. Over the last 20 years, flow partitioning between main distributaries has remained mostly unchanged: of the Lena's flow input to the delta, approximately 24.9–25.0 % is directed to the Bykovskaya branch, 58–59.2 % to Trofimovskaya, 6% to Tumatskaya, and 6.6 % to Olenekskaya. The difference ratio between various discharges (Bolshiyanov et al., 2013, Magritsky et al., 2018) is less than 0.3 %.

The average annual heat runoff ($W_{T,a}$) of the Lena river is very large (at the Kyusyur gauging station: 16 120×1012 kJ per year for 1935–2019), despite the low water temperatures (average annual T_{june} = 5.2, T_{july} = 14.2, T_{aug} = 12.7 and T_{sept} = 6.3 °C) and a short warm season (ice-free period from June 4 to October 13). This phenomenon is explained by the huge discharge and its increase during the warm season. W_a and WT,a were closely linked (R_2≈0.52). This correlation improves if we take into account the water temperature (R^2≈0.72):

$$W_{T,a}\,(\mathrm{kj} \times 10^{15}) = 0.028\,W_a + 1.416\,\overline{T}_{june\text{-}sept} - 12.9 \quad (7)$$

In Eq. (7), $\overline{T}_{june\text{-}sept}$ is the average water temperature for ice-free June–September. It can be replaced by the corresponding air temperature ($\bar{t}_{june\text{-}sept}$) at the Zhigansk and Kyusyur weather stations (R^2≈0.66):

$$\overline{T}_{june\text{-}sept} = 0.584\,\bar{t}_{june\text{-}sept}\,(\mathrm{Zhigansk}) + \\ + 0.231\,\bar{t}_{june\text{-}sept} \quad (8)$$

The Lena River heat runoff obtained from measurements at the Kyusyur gauging station is underestimated due to the cooling effect of the waters from right-bank tributaries – by about 1 015 kJ per year (Magritsky et al., 2018). The heat runoff of the Lena River is growing due to an increase of water discharges (since 1988) and water temperature (especially since 1997) (Spearman's RCC [+]) (Fig. 5). The difference in WT,a between the periods 1988–2019 and 1935–87 was 1 480 kJ per year, or 9.5 %. The increases in water temperature in June, July–August and September were 1.1, 0.6 and 0.05 °C, respectively. There are the same trends in heat flux within the delta. The relationship between the average monthly water temperatures at the Kyusyur and Khabarov gauging stations is close (R^2 from 0.63 to 0.77). The duration of the period with T ≥0.2 °C has increased by 8 days over the last 30 years (1988–2019).

3.3. Sediment load

During the observation period, the annual sediment runoff at Kyusyur varied between 7.6 (1984) and 53.6 million tons (2005). Runoff and sediment hydrograph coincide to some extent over the long term. There are two trends in annual sediment discharge: WR decreased until 1986–1987 and increased, although at a statistically insignificant rate, in subsequent years by an average rate of 6.1 million tons per year (significant only in the U test [+]) (see descriptions in Supplementary 2). Average annual water flow and sediment runoff exhibit a moderate correlation (R^2≈0.25). As far as sediment conveyance depends on precipitation and water discharge (Costard et al., 2003), these changes can be attributed to snowmelt flood having decreased from 82.7 % in 1936, 1944, 1960–87 to 64.8 % in 1988–2010, and the low-water period contribution to annual flow having increased from 16.8 to 34.9 %. The uniformity of a number of low water values of sediment load was violated both by variance (F-test [+]) and by mean (U test [+]) (for descriptions of test, see Supplementary 2).

Satellite image analysis on the Lena River Delta channels shows that suspended sediment load both increases and decreases along the main distributaries of the delta (Fig. 6). During June (end of spring freshet season), at the end of July, and in August, sediment concentrations tend to increase (ΔS >0), which implies net erosion along the channels. However, during other open-flow conditions, sediment concentrations mostly decrease, which implies net deposition. These changes can be attributed to the water discharges conditions and elevation levels, as well as other hydroclimatic (wind, permafrost thaw) and in-channel (bank erosion) conditions. The whole dataset provides evidence that a downstream sediment transport increase (ΔS > 0) dominates in the Trofimovskaya branch. Here, the downstream increase in surface sediment concentration (for example, from 45 $mg \cdot L^{-1}$ in the main channel to 60 $mg \cdot L^{-1}$ in the Trofimovskaya branch) occurred in 75 % of the observed images. Net deposition is observed at the other three distributaries. In particular, the average relative sediment change ΔS was −22.7 % along the Tumatskaya branch and −8.96 % along the

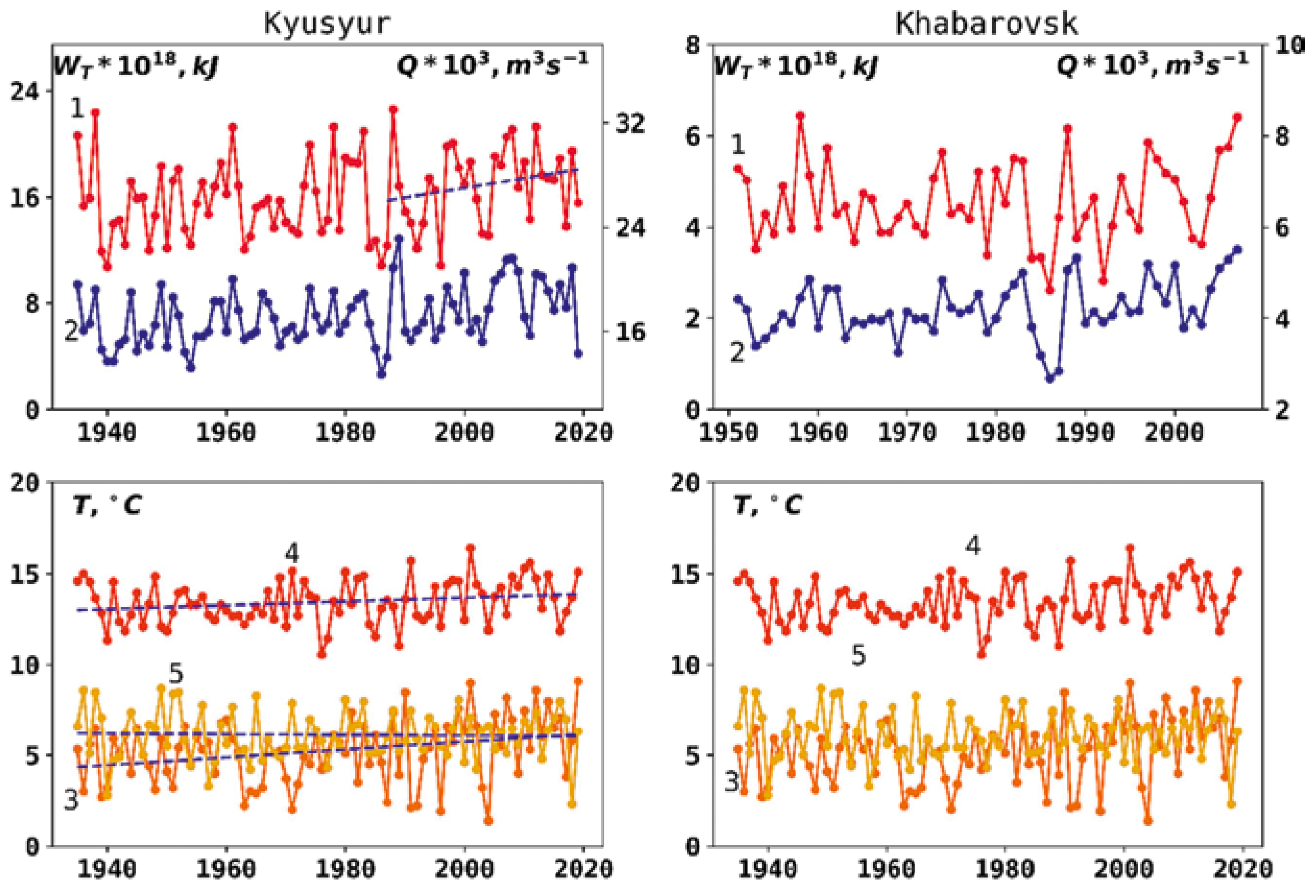

Fig. 5. Long-term fluctuation in the average annual flow of heat (1), discharge (2), and average water temperature for June (3), July–August (4), and September (5) at the Kyusyur (a) and Khabarov (b) gauging stations.

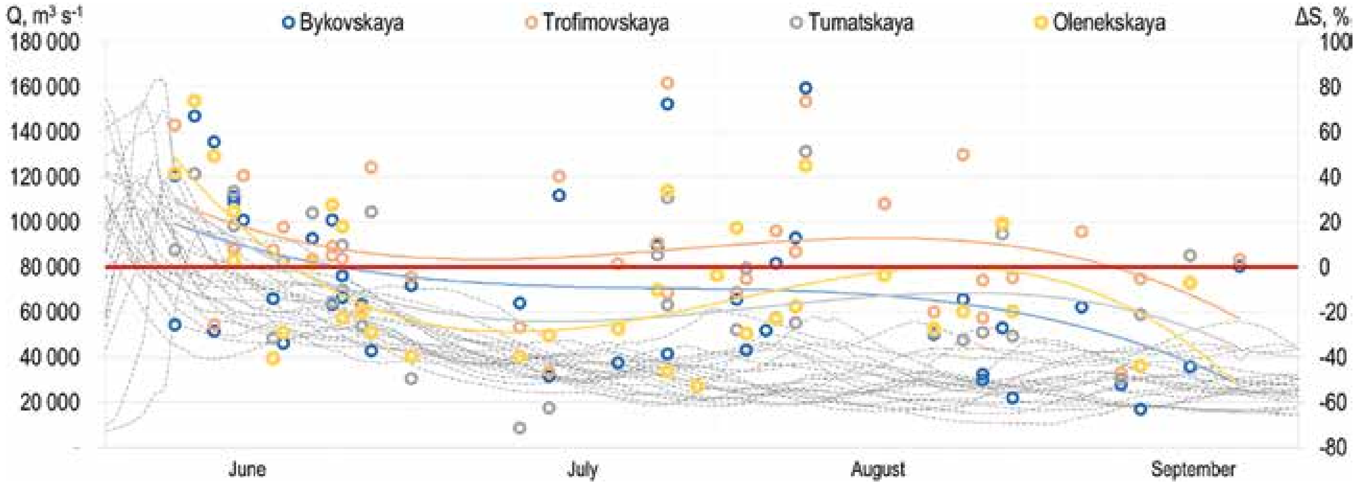

Fig. 6. Seasonal changes in suspended sediment transport ΔS along 4 major distributaries of the delta (based on Landsat data from 2000 to 2022). Dashed gray lines represent water discharges (Q, $m^3 \cdot s{-1}$) on Kyusyur station; solid lines show cubic polynomial regression of suspended sediment (ΔS, %) values.

Olenekskaya branch (a decrease in SSC from 1 $mg \cdot L^{-1}$ in the main channel to 6 $mg \cdot L^{-1}$ in the Olenekskaya channel).

The relationships of relative sediment changes ΔS (%) with climatic parameters are given in Table 2. Relative suspended sediment changes ΔS (%) are constant during the period from 2000 to 2022 and do not correlate to Lena River discharge (see Fig. 6, Supplementary 5 for additional details). As for precipitation datasets, high values of correlations ($r > 0.7$) were found only between these parameters and ΔS (%) in the left Olenekskaya branch, but the correlation is not significant according to Student's t-test at the level of $\alpha = 5$ % due to the shortness of the dataset. For the other parts (Trofimovskaya and Tumatskaya) of the delta, the values of the linear relationships between precipitation and ΔS were less but moderate ($r > 0.3$). Only for the Bykovskaya distributary system was a negative relationship (and no significant correlation) with daily precipitation ($r = -0.22$) found. Sediment load changes are most sensitive to changes in daily wind

Table 2. Correlation matrix between various climatic parameters and SSC change over Lena Delta (Significant correlations according to Student's t-test at the level of α = 5 % are highlighted in bold.).

Parameters	ΔS, %			
	Bykov -skaya	*Trofimov -skaya*	*Tumat -skaya*	*Olenek -skaya*
Daily Tair, °C	0.26	0.11	0.04	0.18
∑3d Tair, °C	0.28	0.07	0.10	0.27
∑5d Tair, °C	**0.31**	0.12	0.12	0.33
∑7d Tair, °C	**0.32**	0.19	0.12	0.32
Daily P, mm	−0.22	0.36	0.46	0.77
3-day precipitation (mean), mm	−0.13	−0.07	0.04	0.53
5-day precipitation (mean), mm	−0.21	−0.33	−0.11	0.24
7-day precipitation (mean), mm	−0.29	−0.27	−0.26	0.03
Daily wind, $m \cdot s^{-1}$	**0.34**	0.22	**0.59**	**0.43**
3-day win (mean), $m \cdot s^{-1}$	**0.37**	**0.40**	**0.58**	**0.44**
5-day wind (mean), $m \cdot s^{-1}$	**0.34**	**0.32**	0.35	**0.34**
Daily SR, $W \cdot m^{-2}$	**0.37**	0.19	0.17	0.17
∑3d SR, $W \cdot m^{-2}$	**0.38**	0.20	0.29	0.26
∑5d SR, $W \cdot m^{-2}$	**0.40**	0.20	0.25	0.32
∑7d SR, $W \cdot m^{-2}$	0.40	0.22	0.26	0.29
Tsoil (0 m), °C	0.15	−0.06	−0.12	0.07
∑3d Tsoil (0 m), °C	0.12	−0.09	−0.04	0.21
∑5d Tsoil (0 m), °C	0.18	0.02	−0.03	0.26
∑7d Tsoil (0 m), °C	0.15	0.08	−0.02	0.17
Tsoil (0.75 m), °C	−0.03	0.18	0.47	0.56
∑3d Tsoil (0.75 m),°C	0.01	0.23	0.49	0.57
∑5d Tsoil (0.75 m),°C	0.00	0.22	0.48	0.56
∑7d Tsoil (0.75 m),°C	−0.04	0.19	0.46	0.53
Delta topset water daily discharge Q, $m^3 \cdot s^{-1}$	0.25	0.05	0.24	0.21

speed ($m \cdot s^{-1}$), in particular 3-day and 5-day average wind speeds, as indicated by significant moderate correlations ($r > 0.3$) across all four major distributaries. Additionally, the subsurface change has the greatest effect on increasing streamflow in the Tumatskaya and Olenekskaya branches: daily soil temperature at the depth of 0.75 m (Tsoil 0.75 m) and sums over 3 (∑3d Tsoil [0.75 m], °C) and 5 (∑5d Tsoil [0.75 m], °C) days are correlated with streamflow discharge.

List of parameters:

1) daily air temperature (Tair) and sums over 3 (∑3d Tair, °C), 5 (∑5d Tair, °C) and 7 (∑7d Tair, °C) days;
2) daily precipitation and mean over 3, 5 and 7 days;
3) daily wind speed and mean over 3 and 5 days;
4) daily solar radiation (SR) and sums over 3 (∑3d SR, $W \cdot m^{-2}$), 5 (∑5d SR, $W \cdot m^{-2}$) and 7 (∑7d SR, $W \cdot m^{-2}$) days;
5) daily soil temperature on the surface (Tsoil 0 m) and sums over sums over 3 (∑3d Tsoil [0 m], °C), 5 (∑5d Tsoil [0 m], °C) and 7 (∑7d Tsoil [0 m], °C) days;
6) daily soil temperature at depth 0.75 m (Tsoil 0.75 m) and sums over 3 (∑3d Tsoil [0.75 m], °C), 5 (∑5d Tsoil [0.75 m], °C) and 7 (∑7d Tsoil [0.75 m], °C) days;
7) delta topset water daily discharge given lag time from Kyusyur to the top of the delta (2 days).

Overall, multilinear regression showed that sums of daily air temperature and wind speed over 3 days make the most pronounced contribution to ΔS variation. However, for the main branch, Trofimovskaya, this connection is not significant (R^2=0.09) according to F-test (p-value < 0.05). For other branches, close connection applies only if $\Delta S > 0$ (Fig. 7) and total R^2=0.22–0.23.

3.4. Carbon riverine transport

The ArcticGRO dataset (see section 2.2) was used to estimate carbon dynamics entering the delta since 2003. POC ($mg \cdot L^{-1}$) and DOC ($mg \cdot L^{-1}$) concentrations correlate with observed daily values of Q (corrected for distance between Zhigansk and Kyusyur) and SSC at Kyusyur gauging station (Table 3). POC mostly depends on sediment transport conditions, but also exhibits a relationship with water discharge. DOC is mostly driven by water discharge, whereas SSC might induce a secondary impact through hydrogeochemical conditions of carbon mineralization. The significant relationship for POC ($R^2 = 0.93$) is:

$$POC = 0.1245 + 7.4 * 10^{-6} * Q + 0.015 * SSC \qquad (9\ )$$

DOC was approximated as a function of Q and SSC ($R^2 = 0.55$):

$$DOC = 6.44 + 10^{-4} * Q - 0.018 * SSC \qquad (10)$$

DOC and POC *in-situ* data vary greatly interannually and seasonally (Fig. 8). The concentrations are highest in spring after the ice break-up and lowest in dry summer months and during the winter low-water period. The Mann–Kendall test and Wald criteria were applied to DOC and POC series to detect a trend. DOC did not show a significant change, partly due to the relative shortness of the period (2003–21) of observations. Based on Mann–Kendall and Wald criteria, there is no significant interannual variability of DOC changes (p-value = 12–13 %) for this relatively short period (2003–21). Conversely, the POC substantially decreased over the studied period (p-value = 0.007–0.008 %) up to −10.7 % per year.

4. DISCUSSION

4.1. Responses of weather conditions, streamflow, and sediment load to climate change

Our study suggests that the Lena Delta has recently demonstrated a shift to more rapid warming. These results were obtained from the ERA5 reanalysis dataset, which is more representative of the whole Lena Delta compared to meteorological stations, since the delta is bounded by high ridges that can impede continental air masses. The predominance of winds from the north and north-east in the summer months can also have impacts that vary locally.

The results of climatic assessments based on ERA5 correlate well with regional observations. According to

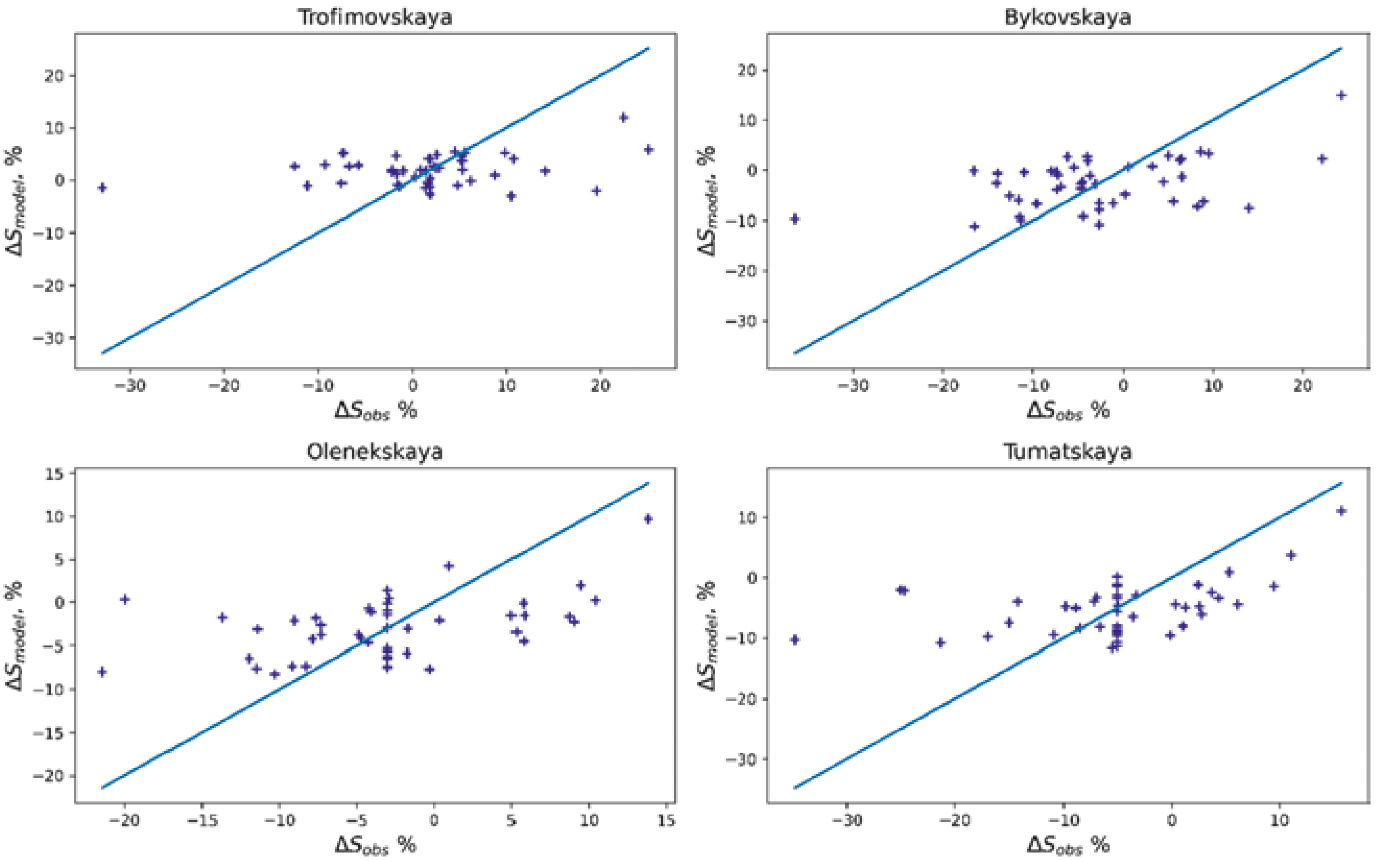

Fig. 7. Relationship between observed daily sediment load change (ΔSobs) and calculated (ΔSmodel) based on air temperature and wind speed data. Blue line denotes ΔSobs = ΔSmodel relation.

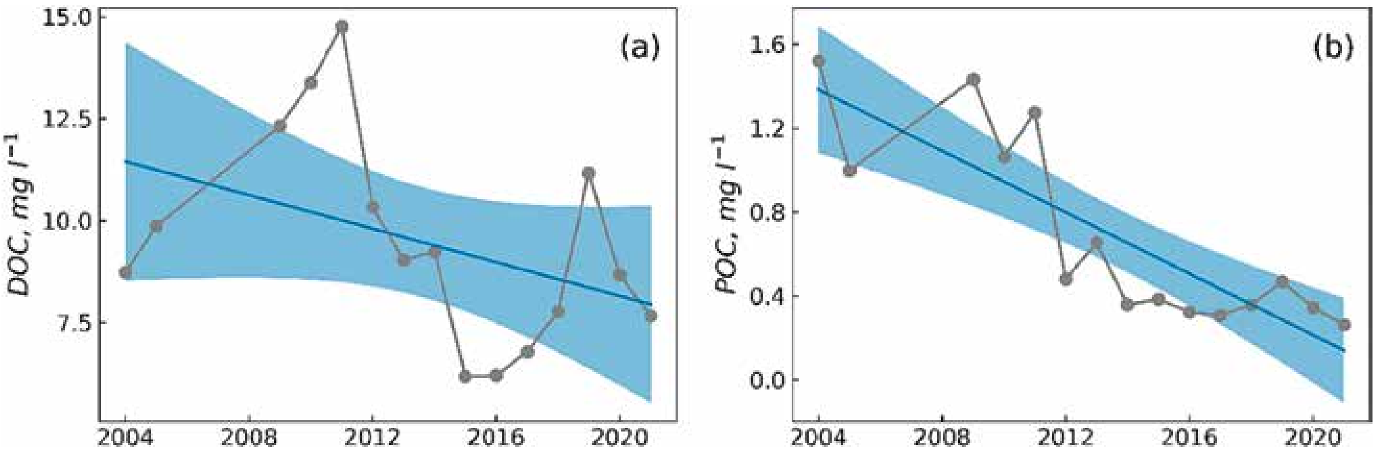

Fig. 8. Long-term changes in (a) DOC and (b) POC concentrations to the Lena Delta. The overall linear trend for 2004–21 is shown (blue line), with its 95% confidence interval; gray point is mean annual value.

Table 3. Correlation ratios between daily POC and DOC concentrations measured at Kyusyur gauging station.

Empty Cell	Q	SSC	POC	DOC
Q	1.00			
SSC	0.69	1.00		
POC	0.82	0.93	1.00	
DOC	0.74	0.42	0.57	1.00

Note: POC and DOC are for the Zhigansk station; SSC and Q are for the Kyusyur station. Q data are corrected for the distance between Zhigansk and Kyusyur.

results based on four observational datasets (NASA's Goddard Institute for Space Studies Surface Temperature version 4 [GISTEMP], the Berkeley Earth temperature dataset [BEST], the Met Office Hadley Centre/Climatic Research Unit version 5.0.1.0 [HadCRUT5] and ERA5 reanalysis), the Arctic region has been warming since 1979 (Rantanen et al., 2022). A previous study (Demchev et al., 2020) showed that, in the coastal zone for May–October, ERA5 overestimates air temperature by an average of 0.29 °C and has a random error of 2.28 °C for daily values. The corresponding values for November–April are 0.27 °C and 2.9 °C. Over the Arctic region, the accuracy of ERA5 net radiation was observed to have a root mean square error of 19.0 $\mathrm{W\cdot m^{-2}}$ and bias of −0.26 $\mathrm{W\cdot m^{-2}}$. ERA5 showed the most similar data distribution to ground observation data compared to other net radiation products (Seo et al., 2020). To compare these processes against a larger spatial scale in the Arctic, we identified warming trends for the Lena basin, as well as others of the largest catchments of Siberia (Ob and Yenisey) based on the same ERA5 dataset. The Lena basin experiences warming rates of annual temperature of 0.25 $\mathrm{°C\cdot decade^{-1}}$ and 0.36 °C·decade−1 of cold-season temperature (November–April) during 1936–2019, which differs a little from the Ob and Yenisei River basins. These trends are significantly slower compared to the Lena Delta (Supplementary 6), which is also warming faster than other Arctic regions. The area north of the Arctic Circle experienced an almost fourfold increase in temperature (0.73 $\mathrm{°C\cdot decade^{-1}}$) compared to the rest of the world (0.19 $\mathrm{°C\cdot decade^{-1}}$) between 1979 and 2021 (Rantanen et al., 2022). Thus, the Lena Delta can be recognized as the world's "hottest spot" in terms of the hydrological consequences of climate change.

The variations in river streamflow, sediment load, and nutrient input to the Lena Delta reflect the impact of the catchment conditions, anthropogenic activities and climate change. However, compared to the climatic trends, there is a significant difference between observed changes at the Kyusyur and Khabarov gauging stations compared with fluctuations in the runoff of the main tributaries in the Lena watershed. The variability of water flow by 43 % was associated with the runoff increase in the upper catchment area by the Tabaga gauging station on the Lena River; 31 % was accounted for by the Aldan River; 20 % was provided with the Vilyui River (Supplementary 3); 6 % is the remaining lateral inflow and channel water balance inconsistencies. The 41 % growth in Wa is provided by an increase in the water content of snowmelt flood (May–July), 29 and 30 % due to the summer–autumn (August–October) and winter low-flow periods. Moreover, the main reasons for the increasing winter runoff and violation of the uniformity of its series are almost equally attributable between natural factors and the impact of the Vilyui reservoir (Berezovskaya et al., 2005, Magritskii, 2008): the operation of the Vilyui reservoir provided additional runoff in winter of ~700 $\mathrm{m^3\cdot s^{-1}}$. The maximum snowmelt flood discharges increased slightly from 134 000 to 138 000 $\mathrm{m^3\cdot s^{-1}}$. The peak of the flood was found to come on average 4 days earlier.

The observed patterns of long-term changes in sediment transport at the top of the Lena Delta compared to other rivers of the Lena basin are even more significant. For example, at the Tabaga gauging station (middle reach of the Lena, ~1800 km upstream), an increase in WR has been detected only since 2006 (Supplementary 7). The main sources of sediments are the Olekma and Chara rivers, since sediment runoff has decreased on the upper Lena. A decreasing trend was detected in the Aldan basin and its tributaries and explained by the reduction in mining activities in the area. The WR fluctuations have been similar to those in the lower reaches of the Vilyui and Lena rivers since the late 1980s, but the increase in the Vilyui sediment runoff is limited by the Vilyui reservoir (Magritsky et al., 2022). The growth and time period recorded at the gauging station over the Lena River Delta were the same as those recorded for Kyusyur. Suspended sediment concentration and sediment flow increased in the Lena downstream due to processes in the middle stream of the Lena River (especially in the Olekma basin), and activation of mechanical and ice-rich bank thermal-erosion in the lower reaches of the Vilyui and Lena rivers.

River flow changes across the northern region of the largest rivers are more heterogeneous. Compared to other large polar rivers, the changes observed in the Lena River hydrological regime have several common features – an increase in air temperature and precipitation have led to intensification of the water cycle (Koutsoyiannis, 2020). Results showed that precipitation fluctuations contributed to most of the runoff variations. We compared the data presented herein with water discharges on the large rivers of the Asian part of Russia, such as Salekhard (Ob River, 1930–2020), Igarka (Yenisey River, 1932–2020), Srednekolymsk (Kolyma River, 1927–2020), Tabaga (Lena River, 1927–2020), Verkhoyansky Perevoz (Aldan River, 1935–2020) and Khatyryk-Homo (Vilyui River, 1935–2020) (Supplementary 3). Thus, total runoff from the Eurasian Arctic basin from 1984 to 2018 increased by 0.22 % and 0.24 % per year. River discharge has substantially decreased in the upper Yenisey but increased in the central region of the Lena basin (Feng et al., 2021).

As for the POC and DOC changes, our results indicate that carbon input to the delta is explained by streamflow and sediment concentration. The observed trend in POC and DOC (Fig. 8) is not representative for the long-term hydroclimatic signal, given that the measurements were taken under different flow conditions and thus represent seasonality. Eqs. (9), (10) show that the increase in average Lena River water discharges from 16 489 $\mathrm{m^3\cdot s^{-1}}$ or 520 km3 (before 1988) to 18 296 $\mathrm{m^3\cdot s^{-1}}$ or 577 $\mathrm{km^3}$ (during 1988–2020) discussed above, lead to 10% POC increase (e.g., from 0.89 to 0.95 $\mathrm{mg\cdot L^{-1}}$, assuming SSC change from 43 to 46 $\mathrm{mg\cdot L^{-1}}$). Similar strong seasonal variations in POC concentrations were previously found for six major Arctic rivers (Yenisey, Lena, Ob, Mackenzie, Yukon, Kolyma) (McClelland et al., 2016a). The discharge-concentration relationships observed here are markedly more evident than those reported for the Yenisey, Mackenzie, Yukon, and Ob. This can be explained by the particularly high proportion of yedoma deposits within its drainage area (Strauss et al., 2021), which contribute to riverine POC fluxes through thermokarst activity and bank erosion (Chalov et al., 2022).

4.2. Factors influencing sediment load in the Lena River delta

The sediment regime observed here differs from that of many river deltas of the world. Deltas of the world's rivers are generally associated with a decrease in hydraulic gradient and a reduction in sediment transport conditions, forming (re)depositional environments that are often characterized by mudflats and tidal wetlands (Fryirs et al., 2007). Increased water discharges and elevation levels favor hydraulic connectivity between the main channels and adjacent deltaic environments (Heiler et al., 1995, Pietroń et al., 2018), enhancing sediment conveyance from the main channel to the deltaic plain and inducing sediment storage. Flooding dynamics govern the net accumulation rates over delta plain across the Mekong River delta, which stores on average 28 % of the incoming sediment load (Binh et al., 2020, Szczuciński et al., 2013). The Selenga River delta, which is the largest tributary of Lake Baikal, can store as much as 34 % of the incoming suspended sediment load (and 67 % of the total sediment load) during high-flow conditions (Chalov et al., 2017, Dong et al., 2016), likely due to an increase in connectivity between channels and floodplain water bodies. These studies also suggested the ability of the delta to store sediment due to evolution of the vegetation cover and seasonal fluctuation of the recipient waterbody's water levels, which can generate backwater effects (Pietroń et al., 2018, Shinkareva et al., 2019).

In the Lena Delta, the observed rise in air temperature and streamflow input coincides with remobilization of sediments. Our study suggests that streamflow conditions, the duration of freezing, frozen, thawing, and unfrozen periods, and riverbank susceptibility to erosion contribute to sediment load through thermokarst activity and bank erosion across the Lena Delta. Increases in streamflow and air temperature impact the rates of freezing/thawing and fluvial bank erosion (Peng et al., 2010). The spring flood inundates the low floodplains and the shallow gullies that are usually dry in the other months (Pertiwi et al., 2021), which do not have extended space to accommodate sediments. The conditions in the Lena River Delta are related to the absence of macrophytes and, thus, this biofiltering effect usually important in the deltas located in the moderate and tropical climate is also negligible (Shinkareva et al., 2019).

The complex interaction between various drivers hampers the establishment of significant relationships between particular factors controlling sediment transport (Table 2). For example, very contrasting sediment transport patterns are observed under the same streamflow conditions. In some cases, the impact of increased water discharges is evident: the highest Lena River water discharge in our satellite imagery dataset (10 June 2018, $Q = 78\,100$ $m^3 \cdot s^{-1}$) coincides with the highest rates of downstream sediment increasing along delta distributaries ($\Delta S = 67.1$ % along Bykovskaya, 41.5 % along Trofimovskaya, 41.5 % along Tumatskaya and 73.9 % along Olenekskaya) (Supplementary 8 – a). It is important to note that the satellite image analysis is limited by the conditions of ice-free flow (from June to September) and the whole dataset generally contains 47 situations (images). This flux within the ice-free period accounts for up to 95 % of the annual sediment yield.

The significant correlations between sediment transport conditions and air and soil temperatures (Table 2) are another example of the impact of hydroclimatic changes on the sediment transport conditions over the delta. As stated by Fedorova et al. (2015), the annual cutoff of riverbank edges during high water produces an unmeasured quantity of suspended and bottom sediments. Additional sediments are washed into the river by thermal erosion and thermal denudation of permafrost banks, which actively thaw under maximal temperatures. These patterns are recorded throughout SSC maps (Supplementary 8 – b and c), which demonstrate a significant increase ($\Delta S > 10$ %) in sediment concentration along the delta. In particular, the soil temperature at the depth of 0.75 m strongly correlated with relative increases in suspended sediment transport. An increase in temperature leads to the activation of the destruction of the riverbanks, which are composed of an ice complex. According to Rachold et al. (2000), sediment volume contribution through thermal erosion processes is almost 2.5 times as great as the fluvial sediment fluxes. Landsat images processing show significant planform change across the Lena Delta. The maximum rate of erosion is observed in the Trofimovskaya branch, whose riverbank sediments mainly consist of yedoma – fine-grained materials rich in organics and ice. This segment of the delta is also noted in our study as the most efficient in sediment mobilization (average $\Delta S = +8.94$ %).

A positive relationship between SSC change (ΔS) and precipitation was observed for the Olenekskaya branch. The effect of precipitation on the SSC increase is associated with the local inflow of turbid waters flowing down from the Verkhoyansky ridges on the left bank. Wind speed rise is associated with higher SSC in the Bykovskaya and Tumatskaya channels. Wind is an important form of natural disturbance that drives SSC by disturbing bed material or blowing of braid bars. Additional impacts on the sediment budget in the Arctic deltas are related to coastal upwelling events, which regularly increase sea-surface turbidity in certain areas adjacent to the Lena Delta in the Laptev Sea and the Kolyma Deltas in the East-Siberian Sea (Osadchiev et al., 2020). These events are formed under strong easterly and south-easterly wind forcing and are estimated to occur during up to 10 % – 30 % of ice-free periods. Combined with intensive coastal erosion (Shakhova et al., 2007), these upwelling events increase sediment concentrations in the most downstream parts of the Lena distributaries.

Stream temperature is another possible factor influencing the frozen banks' thermal erosion and thus increasing sediment transport across the delta (Costard et al., 2007). The water temperature in June, July–August, and September increased by 1.1, 0.6 and 0.05 °C (as shown for the Kyusyur station, see 3.2) which can impact the sediment regime in a long-term perspective. As shown by Gautier et al. (2021), for the lower Lena, water temperatures affect the subsequent thawing of ice, reducing the islands' strength and increasing erosion efficiency. Additionally, thermal effect of global warming on sediment mobilization was proved by experimental studies (Ramalingam and Chandra, 2020), which show that a rise in water temperature causes decreases in both settling flux and degree of deposition.

5. CONCLUSIONS

This study analyzed changes in air and soil temperature, precipitation, and wind speed across the Lena River Delta and their relations with streamflow, sediment load, and carbon fluxes. Along with the substantial increase in air temperatures, there have also been increases in streamflow, sediment, and heat flux input to the delta over recent decades. While the flow partitioning between major distributaries remains constant, the sediment transport conditions have changed significantly. The impact of rising air and soil temperatures on bank degradation and the impact of wind on bottom sediments are considered to be the main drivers of suspended sediment dynamics.

The observed hydroclimatic and sediment transport changes over the Lena Delta are higher than those of the Lena catchment and other major polar rivers. These results imply that the Lena Delta should be recognized as the greatest global hot spot in terms of hydrological consequences of climate change. The significant increase in water and sediment discharge entering the delta and the hydroclimatic impacts on sedimentation patterns across the delta reflect the ongoing climate-driven evolution of the system.

This study provides quantitative results of climate–water–sediment–nutrient variations in the largest polar delta. The main novelty of this study is the integrated picture it provides of long-term changes from a regional perspective. The specific regime of the Lena Delta shines light on a variety of ecological impacts (e.g., production of plant biomass) and biogeochemical impacts (e.g., microbial degradation) controlled by variations in sediment and dissolved (DOC) and particulate organic carbon (POC). The study's results contain valuable information that can be used in developing strategies to cope with and mitigate the dramatic effects of sediment mobilization due to recent global warming in the Arctic, and to detect and predict possible coastal ecosystem degradation in future.

CRediT authorship contribution statement

Sergey Chalov: Conceptualization, Writing – original draft, Investigation. Kristina Prokopeva: Investigation, Methodology. Dmitry Magritsky: Methodology, Investigation. Vadim Grigoriev: Methodology, Validation. Evgeniya Fingert: Data curation, Formal analysis. Michal Habel: Conceptualization. Bennet Juhls: Methodology, Writing – review & editing. Anne Morgenstern: Writing – review & editing. Pier Paul Overduin: Writing – review & editing. Nikolay Kasimov: .

Declaration of Competing Interest

The authors declare that they have no known competing financial interests or personal relationships that could have appeared to influence the work reported in this paper.

Acknowledgements

Fieldworks, study concept and numerical simulations are done within the implementation of Russian Science Foundation project 21-17-00181. Additionally, the remote-sensing processing has been supported by the Kazan Federal University Strategic Academic Leadership Program ("PRIORITY-2030"). The authors greatly acknowledge the support of Samoylov Island Research Station. The authors also acknowledge Mr. Tim